

University of Zagreb

Faculty of Mechanical Engineering and Naval Architecture

Carlo Giorgio Grlj

NUMERICAL ASSESSMENT OF SHIP HYDRODYNAMIC CHARACTERISTICS IN OFF-DESIGN CONDITIONS

Doctoral thesis

Zagreb, 2026.



University of Zagreb

Faculty of Mechanical Engineering and Naval Architecture

Carlo Giorgio Grlj

NUMERICAL ASSESSMENT OF SHIP HYDRODYNAMIC CHARACTERISTICS IN OFF-DESIGN CONDITIONS

Doctoral thesis

Mentor:

Prof. dr. sc. Nastia Degiuli

Zagreb, 2026.



Sveučilište u Zagrebu

Fakultet strojarstva i brodogradnje

Carlo Giorgio Grlj

NUMERIČKO ODREĐIVANJE HIDRODINAMIČKIH ZNAČAJKI BRODA PRI IZVANPROJEKTNIM UVJETIMA

Doktorski rad

Mentor:

Prof. dr. sc. Nastia Degiuli

Zagreb, 2026.

Bibliography data

UDK: xxx.xx

Keywords: computational fluid dynamics, numerical simulations, turbulence models, experimental fluid dynamics, ship hydrodynamics, resistance test, open water test, self-propulsion test, scale effects, loading conditions, slow steaming

Scientific area: Technical sciences

Scientific field: Naval Architecture

Institution: Faculty of Mechanical Engineering and Naval Architecture

Thesis supervisor: Prof. dr. sc. Nastia Degiuli

Number of pages: 286

Number of figures: 36

Number of tables: 15

Number of references: 57

Date of examination: 12^{th} October 2026

Thesis defence committee:

Prof. dr. sc. Željko Tuković,

Prof. dr. sc. Jasna Prpić-Oršić,

Doc. dr. sc. Josip Bašić

Archive: University of Zagreb, Faculty of Mechanical Engineering and Naval Architecture

Acknowledgements

Najprije bih se želio zahvaliti svojoj mentorici, prof. dr. sc. Nastiji Degiuli koja me vodila i pružala podršku tijekom doktorskog studija i izrade ovog doktorskog rada. Njezino znanje, savjeti i poticaj bili su mi od velike važnosti tijekom cijelog ovog razdoblja. Također, želio bih se zahvaliti kolegici doc. dr. sc. Ivani Martić, čija su mi podrška, pomoć i savjeti uvelike olakšali rad i doprinijeli uspješnom završetku doktorskog studija.

Posebno bih se želio zahvaliti svojoj supruzi Mirjam Grlj, koja me strpljivo trpjela i bila mi podrška u svakom trenutku mog sveučilišnog obrazovanja. Tijekom doktorskog studija moja se obitelj proširila, na čemu sam neizmjerno zahvalan. Moja dva sina, Mauro Carlo i Marco, bili su uz mene u svim lijepim, ali i teškim trenucima tijekom ovog razdoblja. Iako možda nisu uvijek bili svjesni toga, svojim su mi osmijesima, prisutnošću i ljubavlju davali dodatnu motivaciju da ustrajem i završim ovaj put.

Naravno, zahvaljujem i svim kolegama s kojima sam tijekom ovih godina mogao podijeliti svoje brige, izazove i svakodnevne muke, ali i brojne lijepe trenutke. Budući da je broj ljudi kojima dugujem zahvalnost velik i nemoguće ih je sve pojedinačno navesti, posebno bih izdvojio Marijana Markovića, s kojim sam tijekom godina proveo mnoge razgovore, od kojih su se brojni ticali naših područja istraživanja.

Zahvalu bih želio uputiti i svojoj obitelji koja me oblikovala u osobu kakva sam danas. Tu su prije svega moji roditelji, Giorgio i Nevenka Grlj, kojima dugujem neizmjernu zahvalnost za svu ljubav, podršku i odricanje tijekom mog odrastanja i obrazovanja. Zahvaljujem i svojim dragim sestrama, Sari Giuliani Strgar i Juditi Kočiš, kao i svom bratu blizancu Lovri Grlju, koji su mi svaki na svoj način bili velika podrška.

Naravno, tu je i moja šira obitelj, čija bi imena, kada bih ih sve počeo nabrajati, zauzela dobar dio ovog doktorskog rada. Stoga im svima, bez pojedinačnog navođenja, upućujem veliko i iskreno hvala na svakom obliku podrške.

Contents

Contents iii

List of Figures v

List of Tables viii

List of Symbols ix

Abstract xiv

Prošireni sažetak xv

1. Introduction 21

1.1. Research background 21

1.2. Motivation 24

1.3. Objectives and hypothesis of the thesis 24

1.4. Scientific contributions of the thesis 25

1.5. Thesis outline 25

2. Materials and methods 27

2.1. Finite volume method 29

2.2. Reynolds averaged Navier-Stokes equations 30

2.3. Turbulence modelling 30

2.3.1. Realizable $k-\varepsilon$ turbulence model 31

2.3.2. Shear stress transport $k-\omega$ turbulence model 31

2.3.3. Reynolds stress model 32

2.4. Transition modelling 32

2.4.1. $\gamma - Re_\theta$ transition model 32

2.5. Dynamic fluid body interaction method 33

2.6. Moving reference frame method 33

2.7. Body force propeller method 34

2.8. Types of numerical simulations 35

2.8.1. Free surface simulations 35

2.8.2. Double body simulations 36

2.8.3. Numerical simulations of the open water test 37

2.8.4. Numerical simulations of the airflow around the ship 37
2.9. Verification and validation studies 39
2.10. Case studies 40
3. Selected results and discussion **43**
3.1. The impact of numerical parameters on ship hydrodynamic characteristics . 43
3.1.1. Turbulence model 43
3.1.2. Discretization schemes 44
3.2. Scale effects on ship hydrodynamic characteristics 47
3.2.1. Propeller open water characteristics 47
3.2.2. Total resistance and its components 50
3.2.3. Propulsion characteristics 53
3.2.4. Nominal and effective wake 56
3.3. Effect of loading conditions and speed on the ship hydrodynamic characteristics 60
3.4. Numerical procedure for the selection of optimal propeller geometric characteristics 72
4. Conclusion **78**
5. Future Work **81**
Bibliography **83**
Curriculum Vitae **90**
List of publications **91**

List of Figures

Figure 1 Classification of GHG emission reduction measures in the maritime sector 21

Figure 2 The dimensions and boundary conditions of the computational domain for FSS 36

Figure 3 The dimensions and boundary conditions of the computational domain for DBS 37

Figure 4 The dimensions and boundary conditions of the computational domain for OWT 38

Figure 5 The dimensions and boundary conditions of the computational domain for OWT 39

Figure 6 Wave patterns obtained with first-order (top-left), second-order (top-right) and third-order (bottom) discretization schemes for convection terms at full scale 45

Figure 7 Wave patterns obtained with first-order (top-left), second-order (top-right) and third-order (bottom) discretization scheme for convection terms at model scale 46

Figure 8 The impact of the temporal discretization on the R_{T} at full scale (left) and model scale (right) 46

Figure 9 The 3D scanned geometry of the propeller (left) and the 3D model used in the numerical simulations (right) 47

Figure 10 The η_{O} as a function of J obtained at different scales 48

Figure 11 The open water curves obtained at model scale with and without the use of the transition model 48

Figure 12 Distributions of the skin friction coefficient on the suction (top), and pressure (bottom) sides without (left) and with (right) the use of the transition model at $J = 0.7$ 49

Figure 13 C_{T} as a function of speed obtained at different scales 50

Figure 14 The components of C_T as a function of speed obtained at different scales . . . 52
Figure 15 The w and t values obtained at different scales and speeds . . . 54
Figure 16 The J, η_O, and η_R values obtained at different scales and speeds . . . 54
Figure 17 The η_H and η_D values obtained at different scales and speeds . . . 55
Figure 18 Contours of v_A/v on the propeller disc obtained at different scales and at model scale with virtual fluid . . . 57
Figure 19 Radial distributions of the circumferentially averaged v_A/v obtained at different scales and at model scale with virtual fluid . . . 58
Figure 20 Contours of v_A/v obtained at different scales and at model scale with virtual fluid in the numerical simulations of the SPT . . . 59
Figure 21 Contours of v_A/v on the propeller disc plane at different speeds . . . 60
Figure 22 Radial distributions of the circumferentially averaged v_A/v at different speeds . . . 61
Figure 23 Contours of v_A/v on the propeller disc plane at different θ_S . . . 61
Figure 24 Radial distributions of the circumferentially averaged v_A/v at different θ_S . . . 62
Figure 25 The C_T values obtained for different θ_S . . . 63
Figure 26 The w values obtained for different θ_S . . . 64
Figure 27 The η_H, η_O, and η_D values obtained for different θ_S . . . 65
Figure 28 The propeller open water curves obtained numerically and experimentally . . . 65
Figure 29 Different container configurations of the post-Panamax 6750 TEU containership . . . 66
Figure 30 The C_N values as a function of Ψ for the considered container configurations . . . 68
Figure 31 Velocity distributions at a profile view cross-section for container configuration 7 at $\theta_S = -0.5°$ (top), $\theta_S = 0°$ (middle) and $\theta_S = 0.5°$ (bottom) . . . 69
Figure 32 Air resistance as a function of speed for different container configurations 70
Figure 33 Velocity distribution for container configurations 1 (top) and 2 (bottom) 71
Figure 34 Flowchart of the proposed numerical procedure . . . 73

Figure 35 3D models of the ships used as case studies 74
Figure 36 The OptiProp graphical interface 77

List of Tables

Table 1 Main particulars of the JBC at full scale and model scale 41
Table 2 Main particulars of the propeller for the JBC 41
Table 3 Main particulars of the post-Panamax 6750 TEU containership at full scale and model scale 42
Table 4 Main particulars of the propellers for the post-Panamax 6750 TEU containership 42
Table 5 The R_T values obtained with RKE, SSTKO and RSM turbulence models at model and full scale 43
Table 6 Comparison of the R_T obtained numerically at model scale and experimentally 44
Table 7 Combinations of the discretization schemes for temporal and spatial discretization 44
Table 8 The main particulars of the considered propeller in the different scales . 47
Table 9 The w_n values obtained at different θ_S 62
Table 10 Air resistance coefficients of the considered container configurations at different θ_S and the respective RD 67
Table 11 Input parameters for the considered ships 74
Table 12 Original and optimal propellers obtained for KCS using different input data 75
Table 13 Original and optimal propellers obtained for JBC using different input data 76
Table 14 Original and optimal propellers obtained for post-Panamax 6750 TEU containership using different input data 76
Table 15 Original and optimal propellers obtained for DTC using different input data 76

List of Symbols

Latin symbols

$\bar{p}$ Mean pressure . . . 30

$\bar{Re}_{\theta t}$ Transition momentum thickness Reynolds number . . . 32

$\bar{u}_i$ Averaged Cartesian components of the velocity . . . 30

$\overline{KG}$ Vertical centre of gravity (from keel) . . . 41

A_E/A_0 Expanded blade area ratio . . . 41

A_F Transverse projected area . . . 38

A_L Lateral projected area . . . 38

A_x, A_θ Body force propeller method constants . . . 34

B Breadth . . . 41

C_μ Model coefficient . . . 31

C_B Block coefficient . . . 41

C_F Frictional resistance coefficient . . . 51

C_T Total resistance coefficient . . . 50

C_{VP} Viscous pressure resistance coefficient . . . 51

C_V Viscous resistance coefficient . . . 50

C_W Wave resistance coefficient . . . 51

C_N Yaw moment coefficient . . . 38

C_{DAX} Longitudinal wind force coefficient . . . 38

C_{DAY} Lateral wind force coefficient . . . 38

D Propeller diameter . . . 41

d/D Hub ratio . . . 41

E_γ Destruction term . . . 33

f_2, f_μ Damping functions . . . 31

F_D Friction deduction force . . . 53

f_i Vector of the resultant force acting on a body . . . 33

f_{β^*} Free-shear modification factor . . . 31

f_β Vortex-stretching modification factor . . . 31

$f_{b\theta}$ Tangential component of the body force . . . 34

f_{bx} Axial component of the body force . . . 34
G_{ij} Buoyancy production term . . . 32
GCI Grid convergence index . . . 40
h_0 Immersion depth of the propeller shaft . . . 73
J Advance coefficient . . . 37
k Turbulent kinetic energy . . . 31
k_{xx} Roll radius of gyration . . . 41
k_{yy} Pitch radius of gyration . . . 41
k_{zz} Yaw radius of gyration . . . 41
K_Q Torque coefficient . . . 48
K_T Thrust coefficient . . . 48
K_T/J^2 Propeller loading . . . 72
L_{PP} Length between perpendiculars . . . 41
L_{WL} Length of waterline . . . 41
m Body mass . . . 33
M_Z Yaw moment . . . 38
M_{ij} Tensor of moments of inertia . . . 33
n Propeller rate of revolution . . . 37
n_i Resultant moment components acting on the body . . . 33
n_j Unit normal vector to the control volume surface . . . 29
p Order of the method . . . 39
P/D Pitch ratio . . . 41
p_{atm} Atmospheric pressure . . . 73
P_k, P_ε, P_ω, P_γ, $P_{\theta t}$ Production terms . . . 31
p_v Vapour pressure . . . 73
P_{ij} Turbulent production term . . . 32
q_A Dynamic pressure . . . 38
R Discriminating ratio . . . 40
R Propeller radius . . . 58
r Grid refinement ratio . . . 39
r' Radial position and propeller tip radius ratio . . . 35

r'_h Propeller hub and tip radii ratio . . . 34
R^2 Coefficient of determination . . . 72
R_T Total resistance . . . 43
r_i Position vector . . . 34
R_{AAX} Longitudinal aerodynamic force . . . 38
R_{AAY} Transverse aerodynamic force . . . 38
RD Relative deviation . . . 40
Re Reynolds number . . . 47
$RMSE$ Root mean squared error . . . 72
S Control volume face surface . . . 29
S Wetted surface area . . . 41
S_ϕ Source term . . . 29
S_k, S_ε, S_ω, S_R User-specified source terms . . . 31
T Draught . . . 41
T Thrust . . . 53
T Turbulent timescale . . . 32
t Thrust deduction fraction . . . 53
T_0 Specific time-scale . . . 31
T_ε The large-eddy time scale . . . 31
u_j Velocity . . . 29
u_{0i} Absolute velocity . . . 34
V Control volume . . . 29
v_A/v Dimensionless axial velocity component . . . 56
v_tip Propeller tip speed . . . 73
w Wake fraction . . . 53
w_Keller Cavitation constraint penalty weight . . . 73
w_n Integral value of the nominal wake . . . 61
$w_{\mathrm{tip,\ speed}}$ Noise constraint penalty weight . . . 73
x_P Longitudinal propeller position (from AP) . . . 41
y^+ Non-dimensional wall distance . . . 32
Z Number of propeller blades . . . 41

z_P Vertical propeller position (from keel) . . . 41

Greek symbols

$\bar{\tau}_{ij}$ Mean viscous stress tensor . . . 30
η_D Quasi-propulsive efficiency . . . 53
η_H Hull efficiency . . . 53
η_O Open water efficiency . . . 47
η_R Relative rotative efficiency . . . 53
Γ Diffusion coefficient . . . 29
γ Intermittency . . . 32
λ Scale . . . 41
μ Dynamic viscosity coefficient . . . 30
μ_t Turbulent eddy viscosity . . . 31
ω Specific dissipation rate . . . 31
ω_j Angular velocity . . . 33
ϕ Transported scalar . . . 29
ϕ_{ij} Pressure-strain tensor . . . 32
Ψ Wind angle of attack . . . 38
ρ Fluid density . . . 29
$\rho\overline{u_i' u_j'}$ Reynolds stress tensor . . . 30
σ_k, σ_ε, σ_ω, σ_f, $\sigma_{\theta t}$, β, β^*, C_{ε_1}, C_{ε_2} Model coefficients . . . 31
θ_S Static trim angle . . . 60
ε Difference between the results obtained with different size grids . . . 39
ε Turbulent dissipation rate . . . 31
ε_0, k_0, ω_0 Ambient turbulence values that counteract turbulence decay . . . 31
ε_{ijk} Levi-Civita symbol . . . 33
ε_{ij} Turbulent dissipation rate tensor . . . 32

Abbreviations

ANN Artificial neural network . . . 72
CFD Computational fluid dynamics . . . 22
CO_2 Carbon dioxide . . . 21
DBS Double body simulation . . . 27

DFBI Dynamic fluid body interaction . . . 33
DNS Direct numerical simulation . . . 30
DTC Duisburg test case . . . 74
EEDI Energy Efficiency Design Index . . . 21
EEOI Energy Efficiency Operational Indicator . . . 21
EFD Experimental fluid dynamics . . . 24
FSS Free surface simulation . . . 27
FVM Finite volume method . . . 27
GA Genetic algorithm . . . 72
GCI Grid Convergence Index . . . 39
GHG Greenhouse gas . . . 21
IMO International Maritime Organization . . . 21
ITTC International Towing Tank Conference . . . 29
JBC Japan bulk carrier . . . 40
KCS Korea Research Institute of Ships and Ocean Engineering containership . . . 74
LES Large eddy simulation . . . 30
MRF Moving Reference Frame . . . 28
OWT Open water test . . . 23
RANS Reynolds-averaged Navier–Stokes . . . 24
ReLU Rectified linear unit . . . 72
RKE Realizable $k-\varepsilon$ . . . 30
RSM Reynolds stress model . . . 30
RST Reynolds stress tensor . . . 30
RT Resistance test . . . 23
SEEMP Ship Energy Efficiency Management Plan . . . 21
SPT Self-propulsion test . . . 23
SSTKO Shear stress transport $k-\omega$ . . . 27
VOF Volume of fluid . . . 27

Other symbols

∇ Displacement volume . . . 41

Abstract

The growing demand for seaborne trade, combined with increasingly stringent environmental regulations introduced by the International Maritime Organization, highlights the urgent need for energy-efficient and sustainable ship operation strategies. One of the most direct and cost-effective measures to reduce fuel consumption and consequently greenhouse gas emissions is slow steaming, i.e., ships operating at speeds lower than their design speed. Although the maritime industry has recognized the environmental and economic potential of slow steaming, current research on the hydrodynamic characteristics of ships sailing under off-design conditions remains limited. Within the framework of this study, a comprehensive numerical investigation is conducted to provide a deeper understanding of ship resistance and propulsion characteristics at both design and off-design conditions. The study focuses on quantifying the impact of slow steaming and different loading conditions on hydrodynamic characteristics and to identify possible improvements for hull-propeller configurations. The influence of numerical parameters on the obtained results at full scale and model scale is investigated. The effects of three turbulence models and discretization schemes for temporal and spatial discretization on the total resistance, its components, ship motions and wave patterns are assessed. The scale effects on the resistance and propulsion characteristics are identified and investigated in detail. The study is further extended to include the effect of loading condition, i.e., container configuration and speed on wind and air resistance of a containership. Based on the obtained results, a numerical procedure was developed for obtaining the optimal propeller geometric characteristics for maximum open water efficiency. The optimization procedure incorporates an artificial neural network trained on experimental data and the genetic algorithm. A standalone application entitled OptiProp is developed. The application integrates the optimization procedure into a simple graphical interface enabling the user to define the ship propulsion characteristics and its operating conditions and to calculate the optimal propeller geometric characteristics.

Keywords: computational fluid dynamics, numerical simulations, turbulence models, experimental fluid dynamics, ship hydrodynamics, resistance test, open water test, self-propulsion test, scale effects, loading conditions, slow steaming

Prošireni sažetak

Uvod

Budući da pomorski promet čini gotovo 3 % globalnih antropogenih emisija ugljikova dioksida, ublažavanje njegova negativnog utjecaja na okoliš postalo je jedan od ključnih ciljeva međunarodnih napora za dekarbonizaciju prometnog sektora. Rastuća potražnja za pomorskim prijevozom robe, zajedno sa sve strožim ekološkim propisima koje je uvela Međunarodna pomorska organizacija, naglašava hitnu potrebu za energetski učinkovitim i održivim strategijama upravljanja brodovima.

Jedna od najpovoljnijih mjera za smanjenje potrošnje goriva, a time i emisije staklenničkih plinova, jest plovidba smanjenom brzinom. Ovakav način plovidbe može dovesti do znatnog smanjenja potrebne snage i potrošnje goriva, čime se izravno smanjuju emisije ispušnih plinova. Međutim, tijekom plovidbe smanjenom brzinom brod operira u izvanprojektnim uvjetima, pri čemu se njegove hidrodinamičke značajke, uključujući otpor i propulzijske značajke, razlikuju od onih pri projektnim uvjetima. Značajke poput stupnja djelovanja brodskog vijka u slobodnoj vožnji, sustrujanja i interakcije trupa i brodskog vijka mogu biti značajno drugačiji, što utječe na ukupni stupanj djelovanja propulzije.

Iako je pomorska industrija prepoznala ekološki i ekonomski potencijal plovidbe smanjenom brzinom, trenutačno dostupna istraživanja hidrodinamičkih značajki brodova pri plovidbi u izvanprojektnim uvjetima i dalje su ograničena. Većina postojećih istraživanja usredotočena su na operativne aspekte, poput uštede goriva i smanjenja emisija, dok su detaljne analize temeljnih hidrodinamičkih mehanizama još uvijek nedostatne.

U okviru ovog istraživanja provedena je opsežna numerička analiza s ciljem detaljnog razumijevanja značajki otpora i propulzije broda pri projektnim i izvanprojektnim uvjetima. Cilj istraživanja je kvantificirati utjecaj plovidbe smanjenom brzinom te stanja krcanja na značajke otpora i propulzije. Također je detaljno istražen utjecaj mjerila na hidrodinamičke značajke broda. Na temelju dobivenih rezultata razvijena je numerička procedura za određivanje optimalnih geometrijskih značajki brodskog vijka s ciljem maksimiziranja stupnja djelovanja brodskog vijka u slobodnoj vožnji.

Cilj i hipoteze istraživanja

Cilj istraživanja je predviđanje utjecaja plovidbe smanjenjom brzinom i različitih stanja krcanja na hidrodinamičke značajke broda, što uključuje otpor broda, koeficijent sustrujanja, raspodjelu nominalnog sustrujanja po disku vijka, koeficijent upijanja (smanjenog poriva), kao i radnu točku brodskog vijka. Istraživanje je temeljeno na sljedećim hipotezama:

1. Primjenom računalne dinamike fluida moguće je odrediti hidrodinamičke značajke broda te polje strujanja oko trupa broda i brodskog vijka pri projektnoj brzini te plovidbi smanjenom brzinom za različita stanja krcanja.

2. Utjecaj mjerila na hidrodinamičke značajke broda može se odrediti primjenom računalne dinamike fluida.

3. Moguće je razviti novi numerički postupak za određivanje optimalnog omjera uspona i promjera brodskog vijka za poboljšanje ukupnog stupnja djelovanja propulzije pri izvanprojektnim uvjetima.

Materijali i metode

Primjenom numeričkih simulacija strujanja oko trupa broda u naravi, utjecaji plovidbe smanjenom brzinom i različitih stanja krcanja na hidrodinamičke značajke broda su istraženi za različite tipove brodova kao što su brod za rasuti teret i kontejnerski brod. U okviru ovog istraživanja korišten je komercijalni programski paket STAR-CCM+ za pripremu numeričkog modela, provođenje numeričkih simulacija te konačno za analizu rezultata. Matematički model temeljen je na Reynoldsovim osrednjenim Navier-Stokesovim jednadžbama (eng. *Reynolds averaged Navier-Stokes equations*, RANS), dok je numerički model temeljen na metodi konačnih volumena (eng. *Finite Volume Method*, FVM). U numeričkim simulacijama primijenjen je model turbulencije kako bi se uskladio broj jednadžbi s brojem nepoznanica. Unutar komercijalnog programskog paketa STAR-CCM+ dostupni su različiti modeli turbulencije, stoga je provedeno detaljno istraživanje utjecaja modela turbulencije na rezultate. S obzirom da su numeričke simulacije provođene za brod i brodski vijak na više mjerila modela, utjecaj prijelaza laminarnog u turbulent-

no strujanje je istražen primjenom modela turbulencije koji uključuje tranzicijski model. Primjenom tranzicijskog modela u numeričkim simulacijama može se procijeniti utjecaj laminarnog strujanja pri različitim mjerilima. Utjecaj modeliranja graničnog sloja u blizini stijenke analiziran je na temelju rezultata numeričkih simulacija sa zidnim funkcijama za opis graničnog sloja te rezultata simulacija u kojima se zidne funkcije ne primjenjuju. Također je istražen utjecaj numeričkih parametara, koji uključuju diskretizacijske sheme za prostornu i vremensku diskretizaciju, na hidrodinamičke značajke broda. Rezultati proizašli iz ovog istraživanja su uspoređeni s rezultatima dobivenim modelskim ispitivanjima. Temeljem validacije rezultata, odabrani su model turbulencije i numerički parametri, koji su primijenjeni u preostalim numeričkim simulacijama. Bitno je naglasiti da se polje strujanja oko trupa broda pri plovidbi u izvanprojektnim uvjetima može znatno razlikovati od polja strujanja oko trupa broda pri plovidbi u projektnim uvjetima. Stoga je ovo istraživanje usredotočeno na utjecaje plovidbe smanjenom brzinom i različitih stanja krcanja na značajke otpora i propulzije broda u mirnoj vodi. U svrhu određivanja ukupnog otpora broda, primijenjene su numeričke simulacije temeljene na viskoznom strujanju sa slobodnom površinom (eng. *Free Surface Simulations*, FSS). Metoda udjela fluida u volumenu (eng. *Volume of Fluid*, VOF) je korištena za određivanje i praćenje položaja slobodne površine. Numeričke simulacije s udvojenim modelom (eng. *Double Body Simulations*, DBS), koje ne uzimaju u obzir utjecaj slobodne površine, su korištene za određivanje viskoznog otpora. Ove simulacije temelje se na duboko uronjenom udvojenom modelu broda pri čemu se pretpostavlja da je dobiveni ukupni otpor jednak viskoznom otporu, s obzirom da kao posljedica zanemarivanja slobodne površine nema stvaranja valova na njoj. Otpor trenja je dobiven integriranjem tangencijalnih naprezanja po oplakanoj površini, dok je viskozni otpor tlaka dobiven integriranjem normalnih naprezanja po oplakanoj površini. U svrhu određivanja otpora valova, viskozni otpor dobiven numeričkim simulacijama s udvojenim modelom oduzima se od ukupnog otpora dobivenog numeričkim simulacijama sa slobodnom površinom. To omogućuje istraživanje utjecaja brzine plovidbe te stanja krcanja na pojedine komponente ukupnog otpora. Dobiveni rezultati ukupnog otpora za brod u naravi su uspoređeni s ekstrapoliranim rezultatima modelskih ispitivanja provedenih u sklopu istraživačkog projekta Hrvatske zaklade za znanost pod naslovom "Održiva plovidba smanjenom brzinom za nisko-ugljično brodarstvo (STARSHIP)" te s rezultatima

dostupnim u literaturi. Kako bi se odredile značajke propulzije odabranih tipova brodova provedene su numeričke simulacije pokusa slobodne vožnje vijka i vlastitog pogona. Utjecaj mjerila na radne značajke brodskog vijka istražene su na temelju rezultata numeričkih simulacija pokusa slobodne vožnje vijka pri različitim mjerilima modela. Numeričke simulacije pokusa slobodne vožnje vijka provedene su korištenjem MRF metode (eng. *Moving Reference Frame*, MRF). Ova metoda se sastoji od referentnog koordinatnog sustava, koji se može zakretati i translatirati u odnosu na nepomični koordinatni sustav. Metoda se temelji na pretpostavci da je kutna brzina tijela konstantna i da je mreža nepomična. U svrhu provođenja numeričkih simulacija pokusa slobodne vožnje vijka proračunska domena je podijeljena na stacionarni i rotirajući dio. Numeričke simulacije pokusa vlastitog pogona broda provedene su primjenom metode masene sile za brodski vijak (eng. *Body force propeller method*), koja modelira učinke brodskog vijka. Ova metoda temelji se na jednolikoj raspodjeli volumenske sile po cilindričnom virtualnom disku. Volumenska sila mijenja se u radijalnom smjeru i njene komponente slijede Goldstein-ov optimum. Točka vlastitog pogona određena je kada se izjednače ukupni otpor i poriv dobiven numeričkim simulacijama pokusa vlastitog pogona broda u naravi. U sklopu numeričkih simulacija pokusa slobodne vožnje vijka određen je stupanj djelovanja vijka u slobodnoj vožnji te koeficijenti poriva i momenta, dok su pomoću numeričkih simulacija pokusa vlastitog pogona određeni broj okretaja vijka te snaga predana vijku. Dobiveni numerički rezultati uspoređeni su s rezultatima dobivenim modelskim ispitivanjima.

Polje sustrujanja je važan parametar pri projektiranju brodskog vijka te se razlikuju efektivno i nominalno sustrujanje. Utjecaj plovidbe smanjenom brzinom i stanja krcanja na nominalno sustrujanje broda je nedovoljno istraženo s obzirom da je vrlo kompliciranо mjeriti nominalno sustrujanje na brodu u naravi. Nominalno sustrujanje broda u naravi određeno je prema postupku opisanom u preporukama ITTC-a (eng. *International Towing Tank Conference*, ITTC) [1]. Dobiveni rezultati su verificirani i validirani usporedbom s rezultatima dobivenim modelskim ispitivanjima. Nominalno sustrujanje broda je validirano usporedbom osrednjenog nominalnog sustrujanja po pojedinom radijusu brodskog vijka te integralne vrijednosti nominalnog sustrujanja dobivenih numeričkim simulacijama i eksperimentalnim ispitivanjima. Pomoću numeričkih simulacija pokusa vlastitog pogona istražen je utjecaj plovidbe smanjenom brzinom i stanja krcanja na koeficijent upijanja

i na efektivno sustrujanje. Pri analizi numeričkih rezultata pokusa vlastitog pogona i određivanju značajki propulzije potrebno je imati na raspolaganju rezultate numeričkih simulacija pokusa otpora i slobodne vožnje vijka. Provedene su opsežne studije verifikacije i validacije kako bi se odredila točnost i valjanost numeričkih modela.

Rezultati

U ovoj doktorskoj disertaciji istražene su hidrodinamičke značajke broda primjenom numeričkih simulacija s naglaskom na utjecaj plovidbe smanjenom brzinom, stanja krcanja te mjerila na otpor i propulzijske značajke broda. Numerički rezultati verificirani su GCI metodom (eng. *Grid Convergence Index method*, GCI) te validirani korištenjem eksperimentalnih podataka dobivenih mjerenjima u bazenu za tegljenje Brodarskog instituta (Jadranbrod d.o.o.) u Zagrebu. Analiza je provedena na post-Panamax kontejnerskom brodu kapaciteta 6750 TEU i brodu za rasuti teret, Japan bulk carrier.

Istražen je utjecaj modela turbulencije i diskretizacijskih shema na numeričke rezultate, pri čemu je utvrđeno da Shear Stress Transport $k-\omega$ model turbulencije ostvaruje najbolje slaganje s eksperimentalnim podacima uz zadovoljavajuće zahtjeve računalnih resursa. Pokazano je da je utjecaj mjerila značajan na ukupni otpor, polje sustrujanja i određene propulzijske značajke. Također je pokazano da su rezultati dobiveni metodom virtualnog fluida na mjerilu modela gotovo jednaki onima dobivenima za brod u naravi korištenjem realnog fluida. Za kontejnerski brod analiziran je utjecaj brzine i trima na ukupni otpor i njegove komponente, propulzijske značajke te na otpor zraka i vjetra. Rezultati pokazuju da stanje krcanja značajno utječe na ukupni otpor i polje sustrujanja, dok je njegov utjecaj na propulzijske značajke manji. Također je pokazano da raspored kontejnera značajno utječe na otpor zraka i vjetra broda.

Na temelju dobivenih rezultata razvijen je optimizacijski postupak koji se sastoji od umjetne neuronske mreže (eng. *Artificial Neural Network*, ANN) i genetski algoritam (eng. *Genetic Algorithm*, GA) za određivanje optimalnih geometrijskih značajki brodskog vijka s ciljem postizanja maksimalnog stupnja djelovanja brodskog vijka u slobodnoj vožnji.

Zaključak

Provedeno istraživanje pokazalo je da numeričke metode predstavljaju pouzdan alat za analizu značajki otpora i propulzije broda u različitim radnim uvjetima te na različitim mjerilima. Verifikacijom i validacijom numeričkih modela potvrđena je njihova sposobnost predviđanja hidrodinamičkih značajki broda s prihvatljivom točnošću.

Ovo istraživanje potvrđuje da numeričke metode, uz odgovarajuću verifikaciju i validaciju, mogu pouzdano predvidjeti hidrodinamičke značajke broda te predstavljaju vrijedan alat u analizi i optimizaciji brodskih sustava. Posebno su istaknuti značaj mjerila i stanja krcanja na značajke otpora i propulzije broda, kao i potencijal primjene metoda umjetne inteligencije u optimizaciji brodskih vijaka.

Dobiveni rezultati predstavljaju doprinos području brodske hidrodinamike i mogu poslužiti kao temelj za daljnja istraživanja energetske učinkovitosti brodova i optimizacije propulzijskih sustava.

Znanstveni doprinos

Znanstveni doprinos ove doktorske disertacije uključuje:

1. Određivanje hidrodinamičkih značajki broda te polja strujanja oko trupa broda i brodskog vijka pri projektnoj brzini te plovidbi smanjenom brzinom za različita stanja krcanja primjenom numeričkih simulacija temeljenih na viskoznom strujanju.
2. Određivanje utjecaja mjerila na hidrodinamičke značajke broda.
3. Razvoj novog numeričkog postupka za određivanje optimalnog omjera uspona i promjera brodskog vijka pri izvanprojektnim uvjetima.

Ključne riječi: računalna dinamika fluida, numeričke simulacije, modeli turbulencije, eksperimentalna dinamika fluida, hidrodinamika broda, pokus otpora, pokus slobodne vožnje vijka, pokus vlastitog pogona, utjecaj mjerila, stanja krcanja, plovidba smanjenom brzinom

1. Introduction

1.1. Research background

Reducing harmful gas emissions into the atmosphere has become a critical priority for the maritime industry. Maritime transport alone accounts for approximately 2.89 % of total anthropogenic carbon dioxide (CO_2) emissions [2]. In response, the International Maritime Organization (IMO) adopted the "Initial IMO Strategy on the Reduction of GHG Emissions from Ships" in 2018, which sets a target to reduce CO_2 emissions by at least 40 % by 2030, relative to 2008 levels [3]. To support this objective, the IMO has introduced several regulatory measures aimed at enhancing energy efficiency and reducing greenhouse gas (GHG) emissions from ships. These include the Energy Efficiency Design Index (EEDI), the Ship Energy Efficiency Management Plan (SEEMP), and the Energy Efficiency Operational Indicator (EEOI) [4].

Xing et al. [5] provided a comprehensive review of measures aimed at mitigating GHG emissions in the maritime sector. They categorised these measures based on their implementation methods into four main groups: technical, operational, eco-friendly fuels, and alternative power sources. Furthermore, such measures can also be classified according to their implementation timeframe as short-term, medium-term, and long-term solutions [6], Figure 1. Among the short-term operational strategies, slow steaming has been recognized

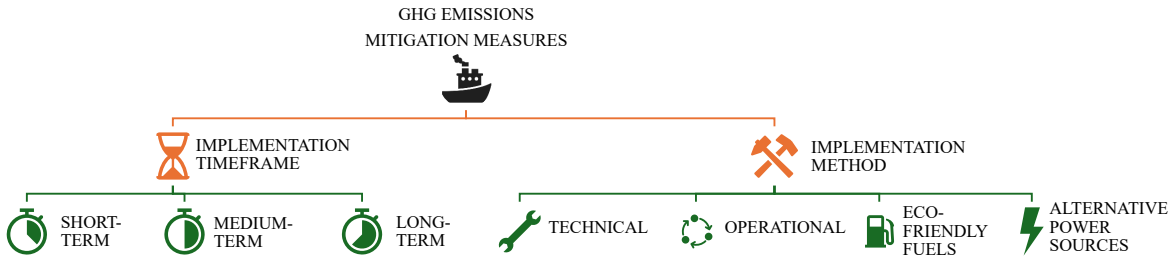


Figure 1. Classification of GHG emission reduction measures in the maritime sector

as particularly effective in reducing GHG emissions. Balcombe et al. [7] found that emissions of harmful gases can be reduced by approximately 20 %, and in some extreme cases, by up to 60 % through slow steaming. Ammar [8] also showed that for a Ro-Ro cargo vessel, a 40 % reduction in speed could lead to a CO_2 emission reduction of up to 78 %, along with an improvement in the EEDI by around 36 % and a reduction in the EEOI

by 71 %. These findings suggest that compliance with the EEDI requirements for the first and the second phases is achievable through speed reduction alone. Degiuli et al. [9] analysed the impact of slow steaming on a Post-Panamax containership operating along a typical route through the Mediterranean Sea. They estimated that a 13.6 % reduction in design speed resulted in approximately a 31 % decrease in fuel consumption and CO_2 emissions, for the analysed sea states. Taskar and Andersen [10] further explored the benefits of speed reduction across various ship types and weather conditions, concluding that a 30 % decrease in speed could lower fuel consumption by up to 45 %. They also emphasised the critical importance of accurately determining the relationship between required power and vessel speed. A cubic relationship is commonly assumed between the required power and sailing speed, however, this assumption does not hold true in many cases [11]. Adland et al. [12] demonstrated that this approximation holds true primarily for vessels operating near their design speed, and proposed an alternative method for estimating the fuel consumption-speed curve. Berthelsen and Nielsen [13] reached a similar conclusion through the analysis of noon report data from 88 tankers in the 35,000-110,000 DWT range. They developed a regression model for the speed-power curve, revealing that the exponent of speed is less than three for speeds below the design speed. Farkas et al. [14] investigated speed reduction requirements to meet the new energy efficiency regulations for existing containerships. The authors emphasised the importance of considering the potential implementation challenges associated with each mitigation measure in order to support the sustainable growth of the maritime transport sector. While slow steaming can significantly reduce GHG emissions, it may also result in a greater number of ships being required to maintain service frequency. Ng [15] proposed a novel method for speed optimisation on selected trade routes with known transit times, enabling a substantial reduction in computation time for specific case studies. Similarly, Wu [16] explored the determination of optimal sailing speeds and concluded that fuel consumption can still be reduced even if the number of vessels increases. More importantly, the study found that higher fuel prices can lead to a lower optimal speed, provided that the resulting fuel cost savings outweigh the additional capital and operational expenditures.

For the assessment of ship behaviour and hydrodynamic characteristics, computational fluid dynamics (CFD) is employed, as demonstrated in the study by Tezdogan et al. [17],

where full-scale numerical simulations were conducted to evaluate the impact of slow steaming on ship behaviour and performance in head seas. Niklas and Pruszko [18] carried out full-scale numerical simulations of the resistance test (RT) and reported good agreement between the numerical results and sea trial data, effectively confirming that full-scale numerical simulations can serve as a viable alternative to traditional towing tank tests. Similarly, Mikkelsen et al. [19] performed full-scale numerical simulations of the RT, open water test (OWT), and self-propulsion test (SPT) and concluded that numerical simulations can predict hydrodynamic performance with accuracy comparable to that of towing tank experiments.

Orych et al. [20] conducted full-scale numerical simulations of the SPT and validated the results using sea trial data, reporting an average error of just 1 % across the considered speed range. Despite the fact that tankers and bulk carriers operate in ballast condition for nearly half of their time at sea, the hydrodynamic characteristics of ships in this condition are rarely studied. Farkas et al. [21] employed CFD to examine the effects of varying draughts on the hydrodynamic characteristics of a bulk carrier. The authors emphasised the need to investigate scale effects and to develop more robust extrapolation methods that incorporate CFD results from both RT and SPT. In a related study, Farkas et al. [22] performed numerical simulations to investigate the nominal wake of a bulk carrier. The authors demonstrated that wall functions can be effectively used for predicting the nominal wake while avoiding excessive number of cells in full-scale simulations. Furthermore, Farkas et al. [23] examined the impact of biofilm on propulsion characteristics, reporting a 36.2 % increase in delivered power due to biofouling. The influence of hard fouling on ship performance was explored in [24], where CFD simulations of the RT, OWT, and SPT were conducted for various hull forms. The authors observed that variations in the impact of biofouling are influenced by several factors, including the proportion of viscous resistance within the total resistance, relative roughness, Reynolds number, and advance coefficient at the self-propulsion point. Mikkelsen and Walther [25] assessed the effect of surface roughness by numerical simulations of the SPT and concluded that incorporating both hull and propeller roughness into the model significantly reduced discrepancies between numerical predictions and speed trial measurements. Yin et al. [26] developed a design methodology for hydrodynamic optimisation, using numerical simulations to improve the

shape of the bulbous bow and hull under slow steaming conditions.

The scale effects on ship resistance and the form factor were analysed by Xiao et al. [27]. The authors demonstrated that both parameters are influenced by the Reynolds number. Korkmaz et al. [28] introduced a method for determining the form factor using CFD and experimental fluid dynamics (EFD), confirming that the form factor depends on speed when applying the ITTC 1957 model ship correlation line for its determination. Lastly, Islam and Soares [29] investigated the effect of trim angle on total resistance using numerical simulations based on Reynolds averaged Navier-Stokes (RANS) equations. By varying both sailing speed and draught, they showed that significant improvements in the ship operational efficiency could be achieved through a dynamic optimisation process.

1.2. Motivation

The efficiency and performance of ships are conventionally analysed under design conditions, which do not always reflect the realities of maritime operations. In recent years, the maritime industry has increasingly adopted operational measures such as slow steaming to reduce fuel consumption and thus the GHG emissions. This shift has highlighted a critical gap in current research: the lack of comprehensive understanding of ship hydrodynamic characteristics in off-design conditions, particularly at reduced speeds and different loading conditions.

Despite the widespread implementation of slow steaming in commercial shipping, most studies still focus on the determination of ship hydrodynamic characteristics in design conditions. This study is motivated by the need to bridge that gap. By systematically analysing ship resistance and propulsion characteristics in both design and off-design conditions, the research aims to provide deeper insight into ship hydrodynamic characteristics across a broader spectrum of operational conditions. The findings not only contribute to the academic understanding of ship hydrodynamic characteristics at various speeds but also at different loading conditions.

1.3. Objectives and hypothesis of the thesis

The objective of this thesis is to predict the effect of slow steaming and different loading conditions on the ship hydrodynamic characteristics. The study focuses on key parameters

such as resistance characteristics, nominal and effective wakes, thrust deduction fraction, as well as the propeller operating point. The research is based on the following hypotheses:

1. CFD can be used for the determination of ship hydrodynamic characteristics and the flow field around the ship hull and propeller at the design and slow steaming speeds for different loading conditions.
2. The scale effect on the ship hydrodynamic characteristics can be determined by CFD.
3. It is possible to develop a new numerical procedure for the determination of optimal pitch ratio for the improvement of overall propulsion efficiency in off-design conditions.

1.4. Scientific contributions of the thesis

The scientific contribution of this thesis includes:

1. The determination of the ship hydrodynamic characteristics and the assessment of flow field around the ship hull and propeller at design and slow steaming speeds for different loading conditions using numerical simulations based on viscous flow.
2. The determination of the scale effect on the ship hydrodynamic characteristics.
3. Development of a new numerical procedure for the determination of optimal pitch ratio in off-design conditions.

1.5. Thesis outline

The structure of the thesis has been designed to systematically address the research objectives and hypotheses, testing the proposed hypotheses and presenting the scientific contributions. The thesis is based on the published articles in the international scientific journals (Articles I-X). The objective is to determine ship hydrodynamic characteristics and the flow field around the ship hull and propeller at design and off-design conditions using CFD simulations. Scale effects on the ship hydrodynamic characteristics are investigated, and a numerical procedure is proposed to obtain the optimal pitch ratio for improving the overall propulsion efficiency in off-design conditions.

Article I provides a detailed overview of the impact of numerical parameters on the total resistance and its components at model scale and full scale. Namely, the effects of turbulence model and different discretization schemes for temporal and spatial discretization on the total resistance, its components, motions, wave patterns and wave cuts are investigated.

In Article II the scale effects on the propeller open water characteristics are assessed. The propeller open water characteristics are determined at different model scales and at full scale using the turbulence model with the transition model enabled.

Articles III and IV present a comprehensive investigation of the scale effects on the resistance and propulsion characteristics of the JBC, whereas Article V examines the scale effects on the resistance and propulsion characteristics of the post-Panamax 6750 TEU containership. Within the articles, the results are compared to the experimental data that are published in Articles VII and VIII.

In Article VI the effects of speed and loading conditions on the nominal wake of the post-Panamax 6750 TEU containership are investigated. The nominal wake was determined using numerical simulations at model scale and the numerical results were validated against the experimental measurements.

Article IX expands the research by providing an analysis of the effect of loading conditions and speed on the wind and air resistance of the post-Panamax 6750 TEU containership. It focuses on the numerical simulations of airflow around the ship hull and superstructure and the determination of wind loads and air resistance acting on the containership.

Finally, the ship resistance and propulsion characteristics obtained both numerically and experimentally enabled the development of a numerical procedure based on a trained artificial neural network, along with an optimization approach using the genetic algorithm, to determine the optimal propeller geometric characteristics with the aim of improving open water efficiency. A tool was developed to enable the calculation of optimal propeller geometric characteristics based on the input ship resistance and propulsion characteristics and its operating conditions. The numerical procedure and its use on the specific case studies are presented in Article X.

2. Materials and methods

The effects of slow steaming and loading conditions on the ship hydrodynamic characteristics are investigated by performing numerical simulations of the flow around different ship types which include a bulk carrier and containership at various scales. For the purpose of this study commercial software package STAR-CCM+ is used to prepare the numerical model, conduct numerical simulations and finally to post-process the results. The mathematical model is based on the RANS equations, while the numerical model is based on the finite volume method (FVM). Different turbulence models are applied in the numerical simulations to close the RANS equations. Since the numerical simulations are conducted for ships and propellers at different scales, the effects of the transition are investigated using the Shear stress transport $k-\omega$ (SSTKO) turbulence model with the $\gamma - Re_\theta$ transition model. By using the transition model within the numerical simulations, the effect of laminar flow at different scales can be assessed. The effect of near-wall modelling is investigated using the results obtained by the numerical simulations with the wall functions applied to solve the boundary layer and the ones without the wall functions. The effects of numerical parameters, which include discretization schemes for spatial and temporal discretization, on the ship hydrodynamic characteristics is also investigated. The results obtained in this study are compared to those obtained from the towing tank tests. Based on the validation study, the turbulence model and numerical parameters are carefully selected for the remaining numerical simulations. It is important to note that while sailing at off-design conditions, the flow field around the ship hull can differ considerably from the flow field around the ship hull at the design conditions. Therefore, the presented study is focused on the effects of slow steaming and different loading conditions on the ship resistance and propulsion characteristics in calm water. To determine the total resistance of a ship, numerical simulations based on the viscous flow with the free surface effects are utilized i.e., free surface simulations (FSS). The volume of fluid (VOF) method is used for locating and tracking the free surface. The double body simulations (DBS), which do not include the free surface effects, are used for the determination of the viscous resistance. DBS consist of a deeply immersed double body model and the obtained total resistance is assumed to be equal to viscous resistance, since

there are no waves generated due to the lack of free surface. The frictional and viscous pressure resistances are obtained by integrating the tangential stresses and pressure over the wetted surface, respectively. Hence, to obtain the wave resistance, the viscous resistance obtained using DBS is subtracted from the total resistance obtained within FSS. This allows the investigation of the influence of the sailing speed and loading condition on each component of the total resistance. The obtained results of the total resistance at full scale are compared with the extrapolated results of the towing tank tests conducted within the Croatian Science Foundation research project entitled "Sustainable slow steaming for low carbon shipping (STARSHIP)" and results available in the literature. To assess the propulsion characteristics of the considered ship types, the numerical simulations of the OWT and SPT are carried out. The scale effects on the propeller performance are investigated using the results of the numerical simulations of the OWT at different scales. The numerical simulations of the OWT are performed using the Moving Reference Frame (MRF) method. MRF is the reference frame that can rotate and translate with the respect to the stationary reference frame. This method is based on the assumption that the angular velocity of the body is constant and that the mesh is rigid. The computational domain is divided into the stationary and rotational parts for the numerical simulations of OWT. The SPT are performed using the body force propeller method, which models the effects of a rotating propeller. The body force propeller method is based on a uniform distribution of volume force over the cylindrical virtual disk. The volume force varies in the radial direction and its components follow the Goldstein optimum. The self-propulsion point is obtained once the total resistance and thrust obtained within the numerical simulations of the SPT at full scale are equal. The open water efficiency, thrust and torque coefficients are determined using the numerical simulations of the OWT, while the rate of revolution and delivered power are assessed using the numerical simulations of the SPT. The obtained results are compared with the results obtained from the towing tank tests. An important parameter for the propeller design is the wake field, where one can distinguish effective and nominal wake. The influence of slow steaming and loading conditions on the nominal wake of a ship is insufficiently studied, since it is very complicated to measure the nominal wake of a full-scale ship. The nominal wake of a full-scale ship is obtained according to the procedure described in the International Towing Tank

Conference (ITTC) recommendations [1]. The obtained results are verified and validated by comparison with those obtained from the towing tank tests. The nominal wake of the ship is validated by comparing the numerically obtained averaged nominal wake at certain radius and integral values of the nominal wake with the experimental data as well as with the contours of the non-dimensional axial velocity on the propeller disk. The effects of slow steaming and loading conditions on the thrust deduction and effective wake are investigated using the numerical simulations of the SPT. To analyse the numerical results of the SPT and determine propulsion characteristics, the results of numerical simulations of RT and OWT are required. Extensive verification and validation studies are conducted to confirm the accuracy and validity of the numerical models. In the following subsections, the numerical methods used in this study are explained in detail.

2.1. Finite volume method

The FVM is a numerical approach that is used to transform the mathematical model into a system of algebraic equations. It involves the discretization of the governing equations both in space and time. In this approach, the computational domain is divided into a finite number of control volumes. The integral form of the governing equations is applied to each control volume, and the fluxes across the control volume faces are approximated using numerical schemes. The FVM ensures the conservation of mass, momentum, and energy within each control volume. The discretized equations are then solved iteratively to obtain the desired flow variables at each control volume centre. The method is based on the general transport equation, which is expressed as follows:

$$\frac{\partial}{\partial t}\int_V \rho\phi \,\mathrm{d}V + \int_S \rho u_j \phi \, n_j \,\mathrm{d}S = \int_S \Gamma \frac{\partial \phi}{\partial x_j} n_j \,\mathrm{d}S + \int_V S_\phi \,\mathrm{d}V \tag{2.1}$$

where ρ is the fluid density, ϕ is the transported scalar, u_j is the velocity , n_j is the unit normal vector to the control volume surface, Γ is the diffusion coefficient, and S_ϕ is the source term. The integrals are taken over the control volume V and its surface S. The first term on the left-hand side represents the transient term, the second term represents the convective term, the first term on the right-hand side represents the diffusive term, and the last term represents the source term.

2.2. Reynolds averaged Navier-Stokes equations

The RANS equations are a special form of Navier-Stokes equations. They are obtained by decomposing the instantaneous flow variables into their mean and fluctuating components, i.e., by applying Reynolds decomposition. The RANS equations for the incompressible and unsteady case read as follows:

$$\frac{\partial \bar{u}_i}{\partial x_i} = 0 \tag{2.2}$$

$$\rho \frac{\partial \bar{u}_i}{\partial t} + \rho \frac{\partial}{\partial x_j}\left(\bar{u}_i \bar{u}_j + \overline{u_i' u_j'}\right) = -\frac{\partial \bar{p}}{\partial x_i} + \frac{\partial \bar{\tau}_{ij}}{\partial x_j} \tag{2.3}$$

where $\bar{u}_i$ is the averaged Cartesian components of the velocity, $\rho\overline{u_i' u_j'}$ is the Reynolds stress tensor (RST), $\bar{p}$ is the mean pressure, and $\bar{\tau}_{ij}$ is the mean viscous stress tensor defined by:

$$\bar{\tau}_{ij} = \mu\left(\frac{\partial \bar{u}_i}{\partial x_j} + \frac{\partial \bar{u}_j}{\partial x_i}\right) \tag{2.4}$$

where μ is the dynamic viscosity coefficient of the fluid. Equations (2.2) and (2.3) present an unclosed system of equations and to be able to solve them turbulence models are applied.

2.3. Turbulence modelling

Turbulence models provide closure of the governing equations by modeling the RST. These models can be broadly classified into eddy-viscosity models and the Reynolds stress model (RSM). Other approaches to turbulence modeling also exist, including large eddy simulation (LES) and direct numerical simulation (DNS), which offer higher-fidelity representations of turbulent flows. However, these methods are computationally more expensive and are typically reserved for specific applications or research purposes. In this study, three turbulence models are used: Realizable $k-\varepsilon$ (RKE) turbulence model, SSTKO turbulence model and RSM. The RANS turbulence models are based on the modelling of the RST. The RKE and SSTKO turbulence models belong to eddy-viscosity models, which are based on the similarity between the molecular gradient-diffusion process and turbulent motion. These types of turbulence models use the Boussinesq approximation to model the RST as follows:

$$-\rho\overline{u_i' u_j'} = \mu_t\left(\frac{\partial \bar{u}_i}{\partial x_j} + \frac{\partial \bar{u}_j}{\partial x_i}\right) - \frac{2}{3}\rho k \delta_{ij} \tag{2.5}$$

where μ_t is the turbulent eddy viscosity, and k is the turbulent kinetic energy.

The RSM computes the components of the RST directly. This allows it to capture the anisotropy of turbulence and predict complex turbulent flows more accurately, albeit at a significantly higher computational cost.

2.3.1. *Realizable* $k-\varepsilon$ *turbulence model*

The RKE turbulence model solves one equation for the turbulent kinetic energy k and one for the turbulent dissipation rate ε. The equations for k and ε read as follows:

$$\frac{\partial}{\partial t}(\rho k)+\frac{\partial}{\partial x_i}(\rho k\bar{u}_i)=\frac{\partial^2 k}{\partial x_i^2}\left(\mu+\frac{\mu_t}{\sigma_k}\right)+P_k-\rho(\varepsilon-\varepsilon_0)+S_k \tag{2.6}$$

$$\frac{\partial}{\partial t}(\rho \varepsilon)+\frac{\partial}{\partial x_i}(\rho \varepsilon\bar{u}_i)=\frac{\partial^2 \varepsilon}{\partial x_i^2}\left(\mu+\frac{\mu_t}{\sigma_\varepsilon}\right)+\frac{1}{T_\varepsilon}C_{\varepsilon 1}P_\varepsilon-C_{\varepsilon 2}f_2\rho\left(\frac{\varepsilon}{T_\varepsilon}-\frac{\varepsilon_0}{T_0}\right)+S_\varepsilon \tag{2.7}$$

where σ_k, σ_ε, C_{ε_1}, and C_{ε_2} are model coefficients, P_k and P_ε are the production terms, ε_0 is the ambient turbulence value that counteracts turbulence decay, S_k and S_ε are the user-specified source terms, T_ε is the large-eddy time scale, T_0 is the specific time-scale, and f_2 is the damping function. With the obtained k and ε, the eddy viscosity is calculated as follows:

$$\mu_t=\rho C_\mu f_\mu\frac{k^2}{\varepsilon} \tag{2.8}$$

where C_μ is the model coefficient and f_μ is the damping function depending on the mean strain rate and mean vorticity as well as k and ε.

2.3.2. *Shear stress transport* $k-\omega$ *turbulence model*

The SSTKO turbulence model is a two-equation model that solves transport equations for the turbulent kinetic energy k and the specific dissipation rate ω:

$$\frac{\partial}{\partial t}(\rho k)+\frac{\partial}{\partial x_i}(\rho k\bar{u}_i)=\frac{\partial^2 k}{\partial x_i^2}(\mu+\sigma_k\mu_t)+P_k-\rho\beta^* f_{\beta^*}(\omega k-\omega_0 k_0)+S_k \tag{2.9}$$

$$\frac{\partial}{\partial t}(\rho \omega)+\frac{\partial}{\partial x_i}(\rho \omega\bar{u}_i)=\frac{\partial^2 \omega}{\partial x_i^2}(\mu+\sigma_\omega\mu_t)+P_\omega-\rho\beta f_\beta(\omega^2-\omega_0^2)+S_\omega \tag{2.10}$$

where P_ω is the production term, σ_ω, β and β^* are the model coefficients, f_{β^*} is the free-shear modification factor, f_β is the vortex-stretching modification factor, S_ω is the user-specified source term, and finally, k_0 and ω_0 are the ambient values that counteract turbulence decay. Menter [30] developed the modified SST $k-\omega$ model by introducing a

blending function that combines the $k-\omega$ model near the wall with the $k-\varepsilon$ model in the far-field. The turbulent eddy viscosity is given with the following equation:

$$\mu_t = \rho k T \tag{2.11}$$

where T is the turbulent timescale.

2.3.3. Reynolds stress model

The RSM consists of solving the transport equation for RST. The transport equation is defined as:

$$\begin{aligned}\frac{\partial}{\partial t}(\rho R_{ij}) + \frac{\partial}{\partial x_i}(\rho R_{ij}\bar{u}_i) = \frac{\partial}{\partial x_m}\left[\left(\mu + \frac{\mu_t}{\sigma_k}\right)\frac{\partial R_{ij}}{\partial x_m}\right] + P_{ij} + G_{ij} - \\ - \frac{2}{3}\Upsilon_M + \phi_{ij} - \rho\varepsilon_{ij} + S_R\end{aligned} \tag{2.12}$$

where P_{ij} is the turbulent production term, G_{ij} is the buoyancy production term, ϕ_{ij} is the pressure-strain tensor, and ε_{ij} is the turbulent dissipation rate tensor. This model requires seven equations to be solved, six equations for the RST components and one equation for the isotropic turbulent dissipation. The quadratic pressure-strain model was used within the simulations with high non-dimensional wall distance y^+ wall treatment to model the pressure-strain term.

2.4. Transition modelling

The turbulence model assumes that the flow is turbulent in the whole flow region. Within the numerical simulations of the OWT at the model scale, the flow is expected to be partly laminar. To model the transition from laminar to turbulent flow, a transition model should is applied.

2.4.1. $\gamma - Re_\theta$ transition model

The correlation-based $\gamma - Re_\theta$ transition model is used within the numerical simulations of the OWT at model scale because it is coupled with the SSTKO turbulence model. The transition model solves two additional transport equations, i.e., intermittency γ and transition momentum thickness Reynolds number $\bar{R}e_{\theta t}$ which read as follows:

$$\frac{\partial}{\partial t}(\rho\gamma) + \frac{\partial}{\partial x_j}(\rho\bar{u}_j\gamma) = \frac{\partial}{\partial x_j}\left[\left(\mu + \frac{\mu_t}{\sigma_f}\right)\frac{\partial\gamma}{\partial x_j}\right] + P_\gamma - E_\gamma \tag{2.13}$$

$$\frac{\partial}{\partial t}(\rho\overline{Re}_{\theta t}) + \frac{\partial}{\partial x_j}(\rho\bar{u}_j\overline{Re}_{\theta t}) = \frac{\partial}{\partial x_j}\left[\sigma_{\theta t}\left(\mu + \mu_t\right)\frac{\partial\overline{Re}_{\theta t}}{\partial x_j}\right] + P_{\theta t} \tag{2.14}$$

where P_γ and $P_{\theta t}$ are the production terms, E_γ is the destruction term, σ_f and $\sigma_{\theta t}$ are the model coefficients. More information on the production, destruction terms and model coefficients can be found in [31]. To accurately solve the laminar and transitional boundary layers, the first cell near the wall must have $y^+ \leq 1$ [32].

2.5. Dynamic fluid body interaction method

In the numerical simulations that include the free surface, the motion of the ship can be modelled using the dynamic fluid body interaction (DFBI) method. In this method the body is assumed to be rigid and thus equations of motion for the centre of mass of the body are solved simultaneously with the fluid flow equations. In this study, the DFBI method was employed to model the translational motion in the direction of z-axis (heave) and rotational motion around the y-axis (pitch) of the ship. In the commercial software package STAR-CCM+, the resultant force and moment acting on the body are calculated and afterwards the equations of motion are solved. The equation for the translation of the centre of mass formulated in the global inertial coordinate system reads as follows:

$$m\frac{\mathrm{d}u_i}{\mathrm{d}t} = f_i \tag{2.15}$$

where m is the mass of the body, u_i is the velocity of the centre of mass, and f_i is the vector of the resultant force acting on the body.

The equations for the rotation of the body formulated in the body local coordinate system are given as:

$$M_{ij}\frac{\mathrm{d}\omega_j}{\mathrm{d}t} + \varepsilon_{ijk}\omega_j M_{kl}\omega_l = n_i \tag{2.16}$$

where M_{ij} (M_{kl}) is the tensor of moments of inertia, ω_j is the angular velocity, n_i is the resultant moment acting on the body, and ε_{ijk} is the Levi-Civita symbol.

2.6. Moving reference frame method

The MRF method consists of defining a reference frame that can rotate and translate relative to the stationary reference frame. The method is based on the assumption that the mesh remains rigid and that the angular velocity of the body is constant. In the

numerical simulations of the OWT, the computational domain is divided into stationary region and a rotating region defined around the propeller geometry. The absolute velocity u_{0i} is expressed in terms of the velocity relative to the MRF, u_{pi},NomenclatureAu_{pi}Velocity relative to the moving reference frame as follows:

$$u_{0i} = u_{pi} + \varepsilon_{ijk}\omega_{pj}r_k \tag{2.17}$$

where r_k is the position vector from the origin of the MRF to the centre of a control volume. In the MRF, the continuity and RANS equations formulated in terms of the relative velocity are as follows:

$$\frac{\partial u_{pi}}{\partial x_i} = 0 \tag{2.18}$$

$$\begin{aligned}\frac{\partial u_{pi}}{\partial t} + u_j\frac{\partial u_{pi}}{\partial x_j} + \varepsilon_{ijk}\frac{\mathrm{d}\omega_{pj}}{\mathrm{d}t}r_k + 2\varepsilon_{ijk}\omega_{pj}u_{pk} + \\ + \varepsilon_{ijk}\varepsilon_{jlm}\omega_{pl}\omega_{pm}r_k = -\frac{1}{\rho}\frac{\partial p}{\partial x_i} + \nu\frac{\partial^2 u_{pi}}{\partial x_j \partial x_j}\end{aligned} \tag{2.19}$$

2.7. Body force propeller method

In the numerical simulations of the SPT, the interaction between the hull and propeller is considered. To model the rotating propeller there is a variety of methods that can be used, such as the sliding or overset mesh approaches, which discretize the propeller geometry. These approaches are considered to be accurate, but are computationally significantly more expensive than simpler methods in which the propeller is not discretized but rather its effects are modelled. One such approach is the body force propeller method, which is based on a uniform distribution of volume force across the cylindrical virtual disk. This force is dependent upon the radial position and follows the Goldstein optimum as follows:

$$f_{bx} = A_x r^* \sqrt{1 - r^*} \tag{2.20}$$

$$f_{b\theta} = A_\theta \frac{r^*\sqrt{1 - r^*}}{r^*(1 - r'_h) + r'_h} \tag{2.21}$$

where f_{bx} and $f_{b\theta}$ are the axial and tangential components of the body force, respectively, A_x and A_θ are functions of thrust and moment as well as the hub and propeller tip radii that define the magnitude of the body force, and r'_h is the ratio between the hub radius

and propeller tip radius. The value r^* is defined as follows:

$$r^* = \frac{r' - r'_h}{1 - r'_h} \tag{2.22}$$

where r' is the ratio between the radial position and propeller tip radius.

2.8. Types of numerical simulations

Different types of numerical simulations are conducted in this study to investigate the effects of slow steaming and loading conditions on the ship resistance and propulsion characteristics. These include FSS, DBS, and simulations of the OWT. For numerical simulations of the RT both the FSS and DBS are conducted for the purposes of the decomposition of the total resistance. For the numerical simulations of the SPT only the FSS are conducted since it is important to include the effects of the free surface to obtain accurate results. The numerical simulations of the OWT are performed without including the effects of the free surface, thus it is assumed that the propeller is submerged entirely. Additional numerical simulations are conducted to obtain the airflow around the ship for the prediction of wind and air resistance. In the following subsections, each type of numerical simulation is explained in detail.

2.8.1. Free surface simulations

The FSS include the VOF method, which is an interface-capturing method for immiscible phases. In this study, it is used for locating and tracking the free surface. The VOF method is based on the concept of volume fraction that represents portion of a phase in a control volume. In this study, two immiscible fluids are considered, i.e., water and air. The computational domain is rectangular shaped and its dimensions are defined according to the ITTC recommendations [33]. The boundaries are placed sufficiently far from the ship as to minimize their effect on the obtained results. To further ensure that the waves do not reflect into the computational domain, the numerical wave damping is applied at the inlet, outlet and side boundaries. The velocity boundary condition is applied at the inlet, top and bottom boundaries, while outlet pressure is applied at the outlet boundary. Symmetry boundary condition is used for the side boundaries, and no slip wall is applied on the hull and rudder surfaces. Figure 2 illustrates the computational domain, including

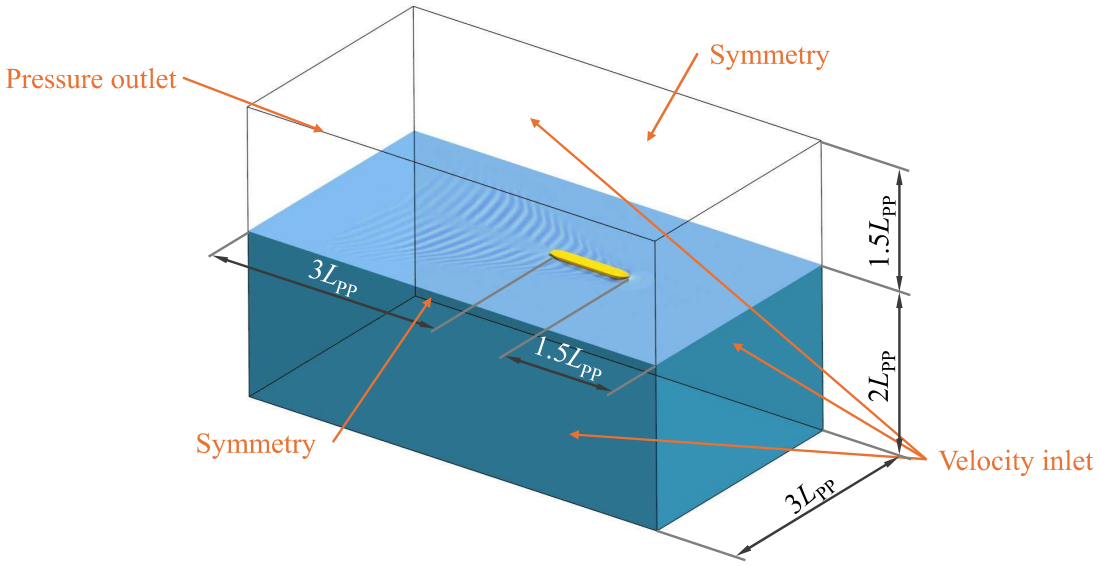


Figure 2. The dimensions and boundary conditions of the computational domain for FSS

the applied boundary conditions and main dimensions. The same setup is used in the numerical simulations of the RT, with only half of the domain considered, divided along the centreline of the ship. For the numerical simulations of RT, symmetry condition is applied at the centreline of the ship to lower the computational cost.

2.8.2. Double body simulations

Contrary to FSS, DBS do not include the effects of the free surface. A symmetry boundary condition is applied at the free surface. The computational domain is also rectangular shaped and its dimensions are the same as those used in the FSS with the exceptions of the height and width of the computational domain. Since air is omitted in the DBS, the height of the computational domain is equal to the water depth. Also, the width is equal to half the width of the computational domain used in FSS, since symmetry is applied at the centreline of the ship. In DBS the velocity inlet is applied only at the inlet boundary, while outlet pressure is applied at the outlet boundary. The no-slip wall is applied on the hull and rudder surfaces and finally, symmetry is applied on the remaining boundaries. Figure 3 shows the computational domain used in the numerical simulations of DBS. The main dimensions of the computational domain and applied boundary conditions are also illustrated.

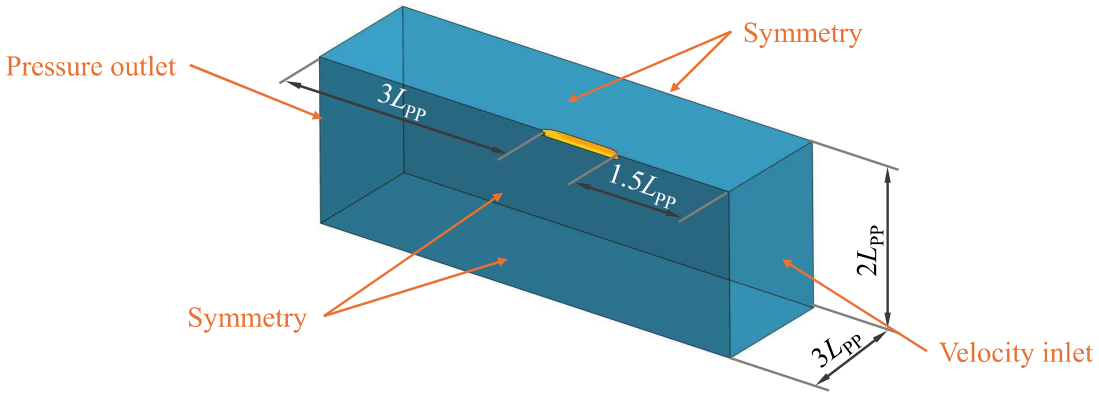


Figure 3. The dimensions and boundary conditions of the computational domain for DBS

2.8.3. Numerical simulations of the open water test

The computational domain in the numerical simulations of the OWT is cylindrical shaped. Within the static region, another cylindrical shaped region is defined, which contains the geometry of the propeller. This region is defined in a rotating reference frame. The radius of the static part of the cylindrical domain is equal to $4D$, while the inlet and outlet boundaries are placed at $5D$ and $15D$ from the propeller, respectively. The boundary conditions applied are as follows: velocity inlet at the inlet boundary, outlet pressure at the outlet boundary, no-slip wall on the propeller, hub, and shaft surfaces and symmetry on the far field boundary. Figure 4 illustrates the computational domain used in the numerical simulations of the OWT, including the applied boundary conditions and main dimensions. The numerical simulations are performed by maintaining a constant rate of revolution n, while varying the advance speed to obtain the open water curves for a range of advance coefficients J.

2.8.4. Numerical simulations of the airflow around the ship

The numerical simulations of the airflow around the containership are conducted to assess the wind and air resistance. These types of numerical simulations are performed according to the ITTC guidelines [34]. The computational domain is cylindrical that consists of a background mesh with an overset mesh embedded in it. The overset mesh region is a smaller cylinder that contains the geometry of the ship. The bottom surface is situated at the position of the free surface. Figure 5 shows the computational domain,

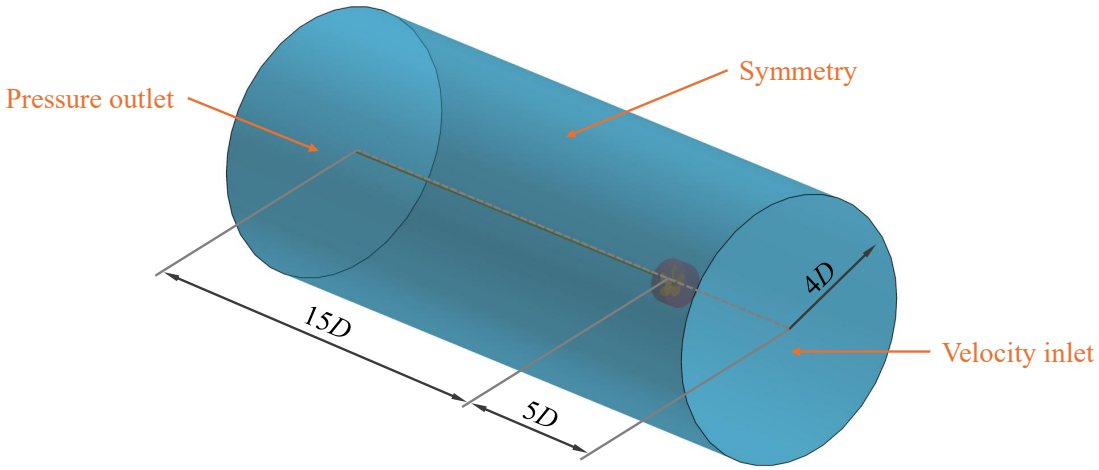


Figure 4. The dimensions and boundary conditions of the computational domain for OWT

boundary conditions, and dimensions.

These type of numerical simulations are performed using the RKE turbulence model since it was successfully used in similar studies [35, 36]. The overset mesh approach is used to enable the simulation of different angles of attack Ψ of the wind. Thus in one run, the simulation is performed from $\Psi = 0°$ to $\Psi = 180°$ with 10° increments. The differences between the numerical simulations for the estimation of wind and air resistance is in the imposed inlet velocity, which is the wind profile for the wind resistance and constant speed for obtaining the air resistance.

In the numerical simulations of the airflow around the post-Panamax 6750 TEU containership the following coefficients are obtained: the longitudinal wind force coefficient C_{DAX}, lateral wind force coefficient C_{DAY} and the yaw moment coefficient C_N. The wind load coefficients are calculated as follows:

$$C_{DAX}(\Psi) = \frac{R_{AAX}(\Psi)}{q_A A_F} \tag{2.23}$$

$$C_{DAY}(\Psi) = \frac{R_{AAY}(\Psi)}{q_A A_L} \tag{2.24}$$

$$C_N(\Psi) = \frac{M_z(\Psi)}{q_A A_L L_{\mathrm{OA}}} \tag{2.25}$$

where A_L and A_F are the lateral and transverse projected areas, respectively, R_{AAX} is the longitudinal aerodynamic force, R_{AAY} is the transverse aerodynamic force, M_Z is the yaw moment, and q_A is the dynamic pressure calculated with the referent wind speeds

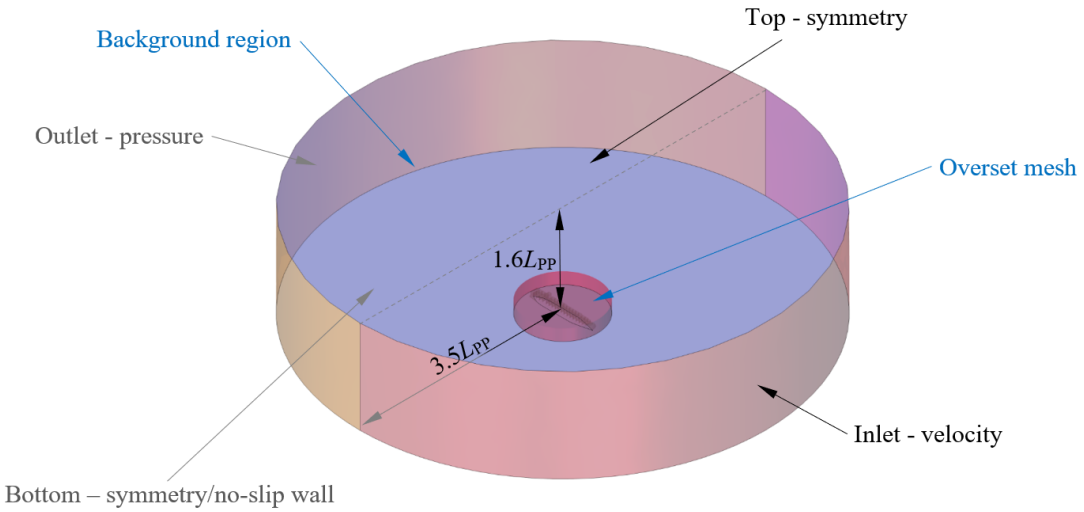


Figure 5. The dimensions and boundary conditions of the computational domain for OWT

depending on the considered component. The calculation of the q_A is described in detail in [34].

2.9. Verification and validation studies

In this study the numerical uncertainty was quantified by employing the Grid Convergence Index (GCI) method [37]. This method is based on Richardson extrapolation and consists of calculating the order of the method p as follows:

$$p = \frac{1}{\ln r_{21}} \cdot \left| \ln \left| \frac{\varepsilon_{32}}{\varepsilon_{21}} \right| + \ln \frac{r_{21}^p - s}{r_{32}^p - s} \right| \tag{2.26}$$

where r is the grid refinement ratio, $\varepsilon = \phi_i - \phi_j$ is the difference between the results ϕ obtained with different grids, $s = \text{sgn}(\varepsilon_{32}/\varepsilon_{21})$, and subscripts 1, 2, and 3 represent the fine, medium, and coarse meshes, respectively. Within the GCI method, the extrapolated values, approximate and extrapolated relative errors are calculated as follows:

$$\phi_{\text{ext}}^{21} = \frac{r_{21}^p \phi_1 - \phi_2}{r_{21}^p - 1} \tag{2.27}$$

$$e_{\text{a}}^{21} = \left| \frac{\phi_1 - \phi_2}{\phi_1} \right| \tag{2.28}$$

$$e_{\text{ext}}^{21} = \left| \frac{\phi_{\text{ext}}^{21} - \phi_1}{\phi_{\text{ext}}^{21}} \right| \tag{2.29}$$

With the caculated values, the GCI is obtained with the following expression:

$$GCI_{\text{fine}}^{21} = \frac{1.25 e_{\text{a}}^{21}}{r_{21}^{p} - 1} \tag{2.30}$$

Four apparent convergence conditions can be distinguished using the discriminating ratio R [38, 39] calculated as:

$$R = \frac{\varepsilon_{21}}{\varepsilon_{32}} \tag{2.31}$$

The following apparent convergence conditions can be identified:

- Monotonic convergence for $0 < R < 1$,
- Oscillatory convergence for $R < 0$ and $|R| < 1$,
- Monotonic divergence for $R > 1$,
- Oscillatory divergence for $R < 0$ and $|R| > 1$.

The calculated GCI is used to obtained the numerical uncertainty due to grid size as well as the time step. Three grids and time steps are used in the verification studies.

For the validation purposes the relative deviation RD is calculated as follows:

$$RD = \frac{\phi_{\text{CFD}} - \phi_{\text{EFD}}}{\phi_{\text{EFD}}} \cdot 100\% \tag{2.32}$$

where the subscripts CFD and EFD indicate the numerical and experimental results, respectively.

Since extensive verification and validation studies have been conducted for each specific case, these results are omitted from Section 3 and can be found in the corresponding published studies.

2.10. Case studies

The effects of slow steaming and loading condition on hydrodynamic characteristics of two ships were investigated. The first ship considered in this study is the Japan Bulk Carrier (JBC), while the second is the post-Panamax 6750 TEU containership.

The JBC is a capesize bulk carrier which was developed by the National Maritime Research Institute at the Yokohama National University, and the Ship Building Research

Centre of Japan. It features a bulbous bow and a transom stern, and it has a high block coefficient. It was never built in full scale, but it was used as a benchmark case study for numerical investigation for the CFD workshop in Tokyo 2015 [40]. The main particulars of the ship are given in Table 1, while the main particulars of the propeller are given in Table 2.

Table 1. Main particulars of the JBC at full scale and model scale

Main particular	**Value**	
Scale λ	1	40.264
Length between perpendiculars L_{PP}, m	280	6.954
Length of waterline L_{WL}, m	285	7.078
Breadth B, m	45	1.118
Draught T, m	16.5	0.410
Displacement volume ∇, m^3	178 420.1	2.733
Wetted surface area S, m^2	19 720.4	12.164
Block coefficient C_{B}	0.858	
Vertical centre of gravity (from keel) $\overline{KG}$, m	13.29	0.330
Roll radius of gyration k_{xx}, m	18	0.447
Pitch radius of gyration k_{yy}, m	70	1.739
Yaw radius of gyration k_{zz}, m	70	1.739
Longitudinal propeller position (from AP) x_{P}, m	4	0.099
Vertical propeller position (from keel) z_{P}, m	5.182	0.129

Table 2. Main particulars of the propeller for the JBC

Main particular	**Value**	
Scale λ	1	40.264
Diameter D, m	8.120	0.202
Pitch ratio P/D	0.736	
Expanded blade area ratio A_{E}/A_0	0.644	
Hub ratio d/D	0.193	
Number of propeller blades Z	5	

The post-Panamax 6750 TEU containership is a benchmark containership developed for the assessment of the performance of the seakeeping analysis codes as a part of the ITTC-ISSC joint workshop in 2014 [41]. This containership was also investigated in an experimental campaign performed at the Brodarski Institute [42] by Degiuli et al. [43], in which its hydrodynamic characteristics were assessed through RT, OWT, and SPT, as well as nominal wake measurements. The main particulars of the containership are given in Table 3, while the main particulars of the propellers are given in Table 4.

Table 3. Main particulars of the post-Panamax 6750 TEU containership at full scale and model scale

Main particular	**Value**	
Scale λ	1	35.18
Length between perpendiculars L_{PP}, m	286.6	8.147
Length of waterline L_{WL}, m	292.37	8.311
Breadth B, m	40	1.137
Draught T, m	11.98	0.341
Displacement volume ∇, m^3	85 556	1.965
Wetted surface area S, m^2	13 325	10.767
Block coefficient C_{B}	0.6231	
Vertical centre of gravity (from keel) $\overline{KG}$, m	16.562	0.471
Roll radius of gyration k_{xx}, m	14.6	0.415
Pitch radius of gyration k_{yy}, m	70.144	1.994
Yaw radius of gyration k_{zz}, m	70.144	1.994
Longitudinal propeller position (from AP) x_{P}, m	6.5048	0.1849
Vertical propeller position (from keel) z_{P}, m	3.9245	0.1112

Table 4. Main particulars of the propellers for the post-Panamax 6750 TEU containership

Main particular	**Value**			
	FPP		**CPP**	
Scale λ	1	35.18	1	35.18
Diameter D, m	7.3	0.2075	7.3	0.2073
Pitch ratio P/D	0.890		1.300	
Expanded blade area ratio A_{e}/A_0	0.750		0.633	
Hub ratio d/D	0.1687		0.2957	
Number of propeller blades Z	4			

3. Selected results and discussion

3.1. The impact of numerical parameters on ship hydrodynamic characteristics

The impact of numerical parameters, specifically the turbulence model, discretization schemes for temporal and spatial discretization on the total resistance and its components, ship motions, wave pattern and wave cuts is investigated in detail in [44]. Numerical simulations are performed at both model and full scale for the determination of ship hydrodynamic characteristics. As the case study, the post-Panamax 6750 TEU containership is used.

3.1.1. Turbulence model

The influence of the turbulence model on the total resistance R_T at model and full scale is given in Table 5, where subscripts S and M indicate full scale and model scale, respectively. The SSTKO turbulence model yields the lowest R_T at both model and full scale. The RSM turbulence model yields the highest R_T at full scale, while at model scale the highest R_T is obtained with the RKE turbulence model. Table 6 shows the comparison between R_T obtained numerically at model scale and experimentally. The RKE turbulence model overpredicts R_T, while both the SSTKO and RSM turbulence models underpredict. The underprediction of R_T is expected since the numerical simulations are performed for smooth hull surface, thus, although the RKE turbulence model shows the lowest RD, it is not selected for further analyses since it overpredicts R_T. The RSM turbulence model is also discarded since it is computationally significantly more expensive than the SSTKO turbulence model. The SSTKO turbulence model is selected for further analyses since it yields the lowest R_T at both model and full scale and its RD from the experimental value is acceptable.

Table 5. The R_T values obtained with RKE, SSTKO and RSM turbulence models at model and full scale

Turbulence model	R_{TS}, kN	R_{TM}, N
RKE	2321.11	96.62
SSTKO	2302.87	87.73
RSM	2356.26	91.35

Table 6. Comparison of the R_T obtained numerically at model scale and experimentally

Turbulence model	$R_{TM,\,CFD}$, N	$R_{TM,\,EFD}$, N	RD, %
RKE	96.617		1.709
SSTKO	87.780	94.994	-7.595
RSM	91.352		-3.834

The influence of the turbulence model on ship motions is negligible at full scale, while at model scale the RSM turbulence model predicts lower sinkage and higher trim values compared to the RKE and SSTKO turbulence models. Also, the wave pattern is not influenced significantly by the selection of the turbulence model.

3.1.2. Discretization schemes

Using the SSTKO turbulence model, a series of numerical simulations are performed systematically to assess the influence of the discretization schemes for both the temporal and spatial discretization on the ship hydrodynamic characteristics. Table 7 shows the different combinations of the discretization schemes used for the temporal, convection and gradient terms. It shows the order of the method applied in each case and for each term.

Table 7. Combinations of the discretization schemes for temporal and spatial discretization

Case	Temporal	Convection	Gradient
1	1st	2nd	2nd
2	1st	1st	2nd
3	1st	3rd	2nd
4	1st	2nd	1st
5	2nd	2nd	2nd
6	1st	1st	1st

The results show a significant influence of the discretization schemes for convection term on the obtained wave pattern. Specifically, the first-order discretization scheme yields lower wave elevations compared to the second and third-order discretization schemes both at full scale and model scale, as shown in Figures 6 and 7.

Similar results are obtained for the discretization schemes for the gradient terms, where higher R_T and a faster convergence is obtained when first-order scheme is applied.

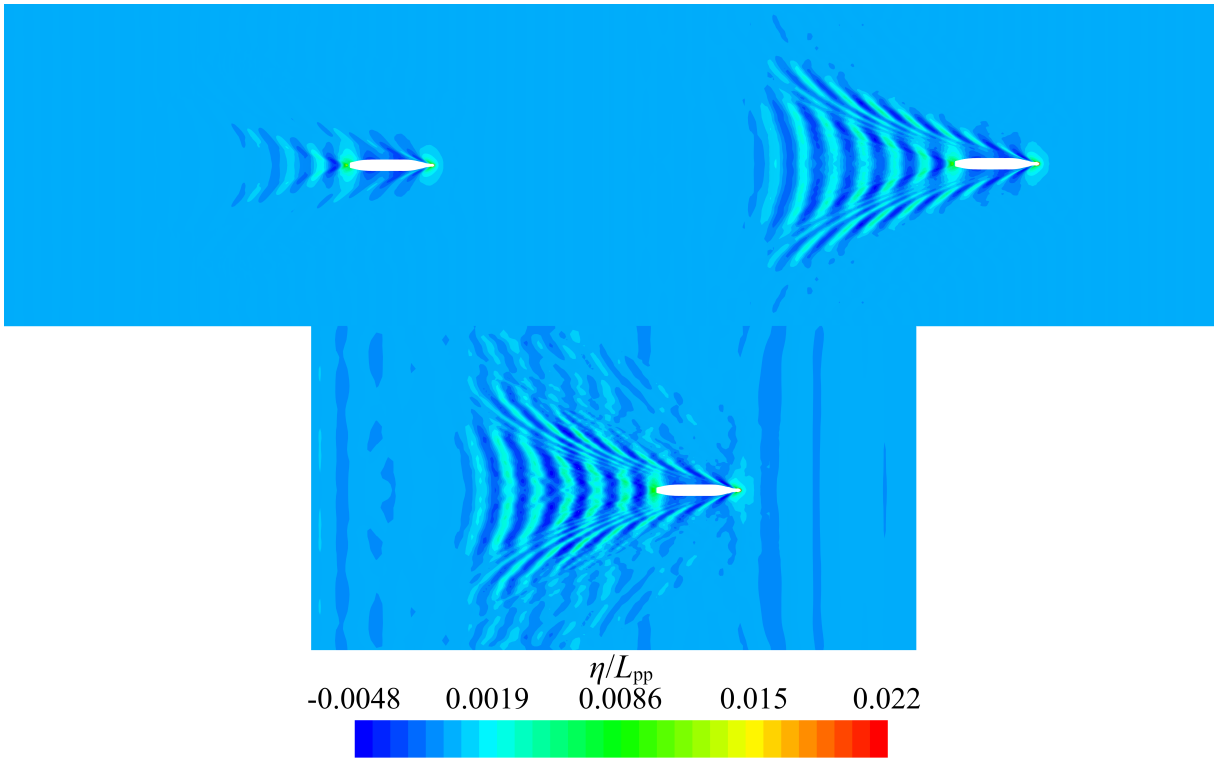


Figure 6. Wave patterns obtained with first-order (top-left), second-order (top-right) and third-order (bottom) discretization schemes for convection terms at full scale

The wave elevations are also lower when first-order discretization scheme is used. Finally, the first-order scheme for the discretization of the temporal term showed faster convergence with no change in the median of R_T at full scale. At model scale, this effect is not significant as can be seen in Figure 8. Thus, the recommended practice for numerical simulations employed in this study is to use first-order discretization scheme for the temporal term and second-order schemes for the convection and gradient terms.

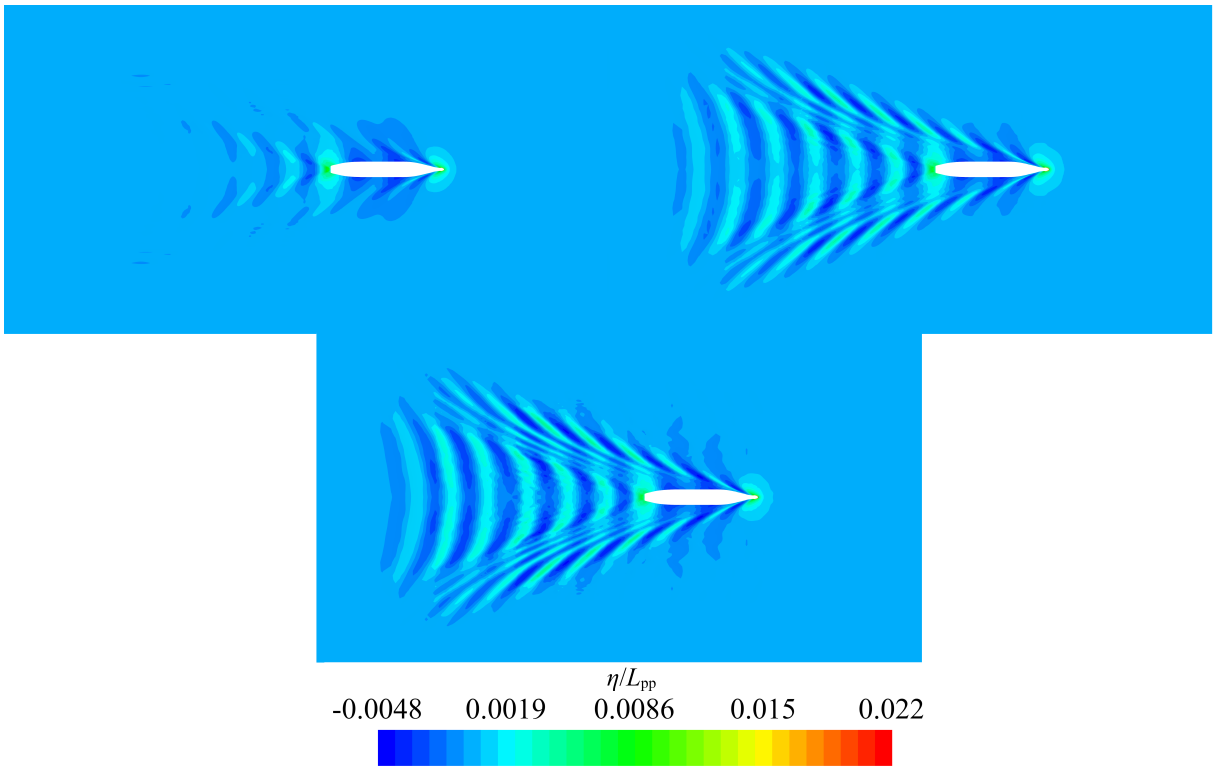


Figure 7. Wave patterns obtained with first-order (top-left), second-order (top-right) and third-order (bottom) discretization scheme for convection terms at model scale

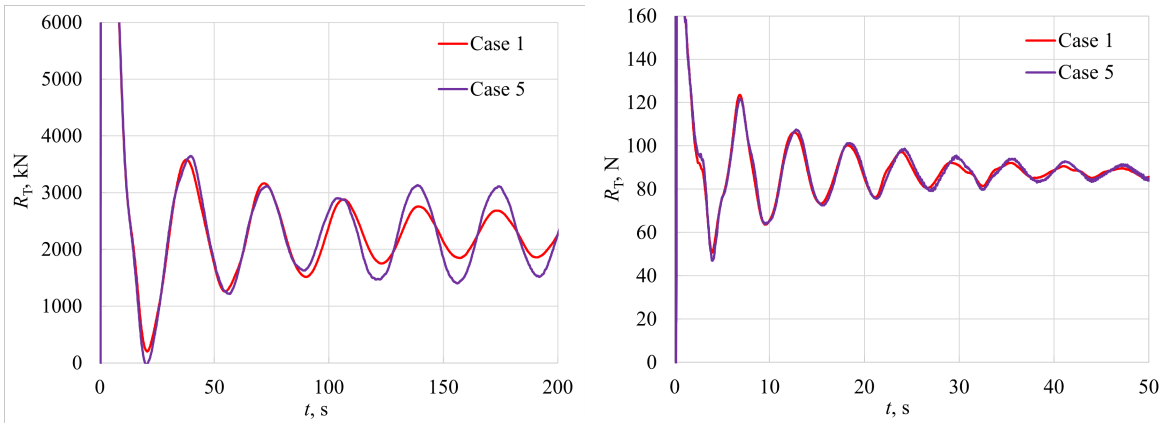


Figure 8. The impact of the temporal discretization on the R_T at full scale (left) and model scale (right)

3.2. Scale effects on ship hydrodynamic characteristics

In this section, the scale effects on ship hydrodynamic characteristics are presented.

3.2.1. Propeller open water characteristics

A series of numerical simulations of OWT are performed to determine the propeller open water characteristics at different model scales and at full scale [45]. Table 8 shows details of the propeller used in the study. It is a 5-bladed, fixed pitch propeller used for the JBC. The geometry of the propeller was obtained with the 3D scanning technique which yields a point cloud. From the point cloud, a 3D model is generated which can be used in numerical simulations, as shown in Figure 9.

Table 8. The main particulars of the considered propeller in the different scales

Scale, λ	**40.264**	**4**	**2**	**1.333**	**1**
Index	M	M1	M2	M3	F
Diameter D, m	0.203	2.040	4.079	6.119	8.158
Rate of revolution n, rps	26.03	8.204	5.801	4.737	4.102
Reynolds number Re	1.298×10^6	4.111×10^7	1.162×10^8	2.136×10^8	3.309×10^8

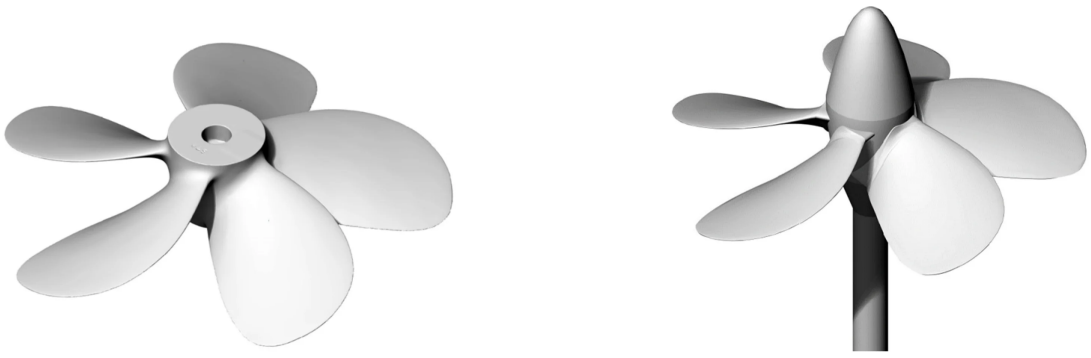


Figure 9. The 3D scanned geometry of the propeller (left) and the 3D model used in the numerical simulations (right)

The open water efficiencies η_O obtained at different scales are presented in Figure 10. The numerically obtained η_O at model scale are extrapolated to full scale using the ITTC 1978 Performance prediction method. The scale effects on η_O are evident increasing with the decrease in scale. The extrapolated values are higher than those obtained at model scale, however still significantly lower than the values obtained at full scale.

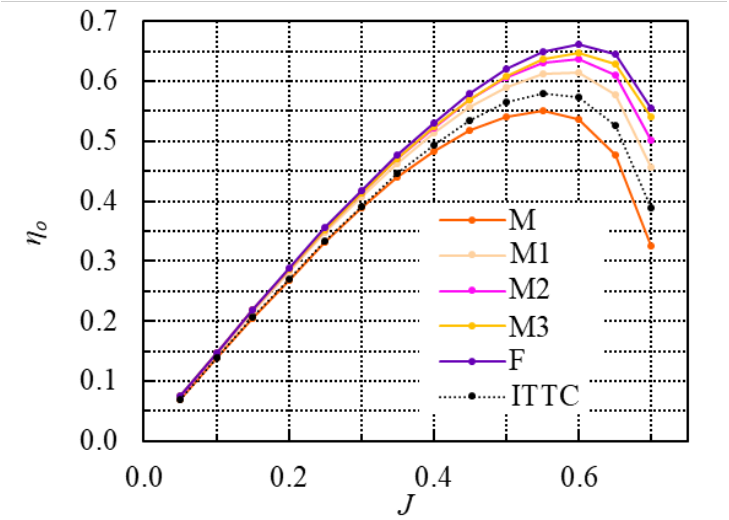


Figure 10. The η_O as a function of J obtained at different scales

The numerical simulations at model scale were performed with and without the use of the transition model to show its impact on the obtained open water curves. Figure 11 shows a comparison between the thrust coefficient (K_T) and torque coefficient (K_Q) as well as η_O obtained with and without transition model. The results show that the transition model has a significant influence on K_Q and consequently on η_O. When the transition model is included, the obtained η_O is significantly higher, which is more pronounced at higher values of J.

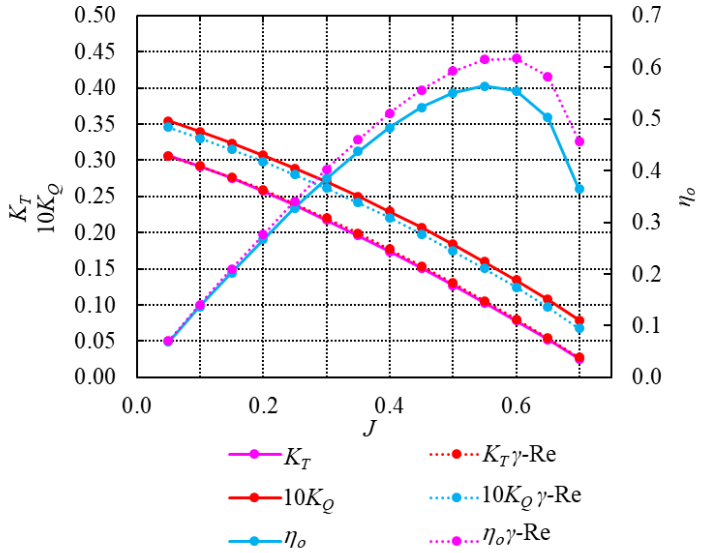


Figure 11. The open water curves obtained at model scale with and without the use of the transition model

Further insight into the effect of transition model on the obtained propeller open water performance is shown in Figure 12 where the distributions of the skin friction coefficient are shown for the cases with and without transition model at $J = 0.7$. It can be seen that significant differences are obtained, where lower skin friction coefficient is obtained with the transition model, compared to the case without the transition model. The lower skin friction leads to lower K_Q, which results in higher η_O when the transition model is included.

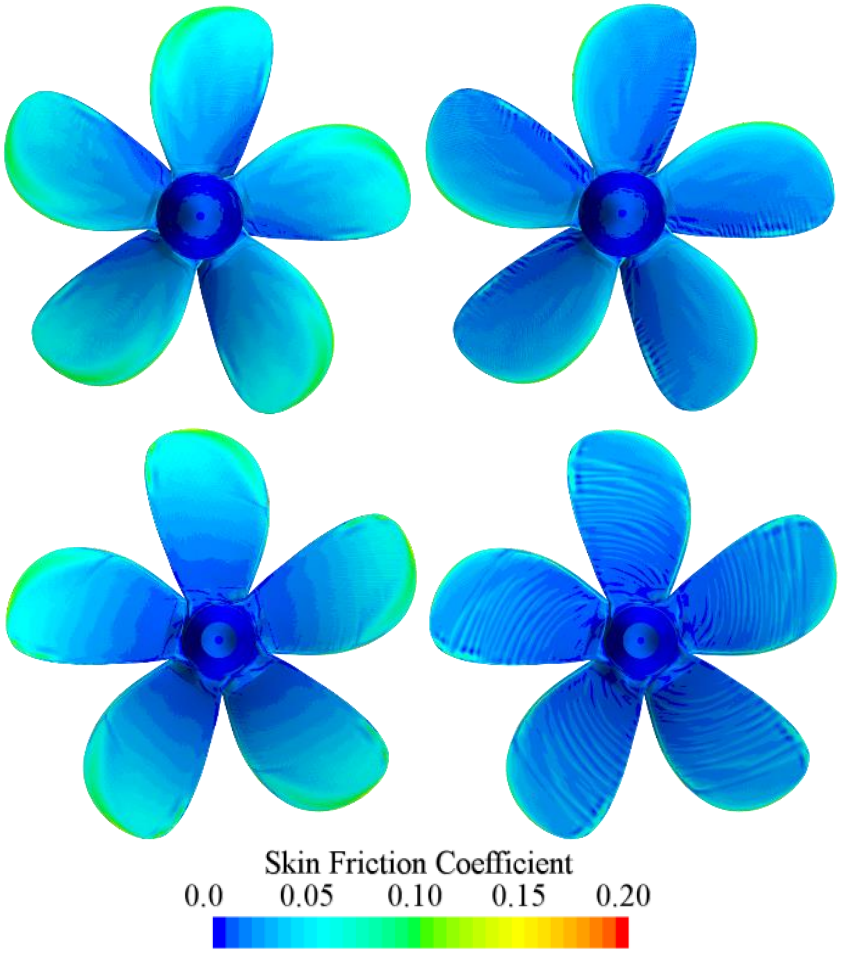


Figure 12. Distributions of the skin friction coefficient on the suction (top), and pressure (bottom) sides without (left) and with (right) the use of the transition model at $J = 0.7$

3.2.2. Total resistance and its components

The total resistance and its components are obtained by performing the FSS and DBS for the JBC at model scales and at full scale [46]. The total resistance coefficient obtained in DBS is considered to be equal to the viscous resistance coefficient C_V since free surface is not present. The wave resistance coefficient is obtained by subtracting the C_V from the total resistance coefficient C_T obtained with the FSS. The results obtained with the real fluid are compared to those obtained from the numerical simulations performed at model scale with the virtual fluid. The virtual fluid is defined to satisfy both the Reynolds as well as Froude similarity simultaneously. Froude similarity is satisfied with the following relationship:

$$v_M = \frac{v_S}{\sqrt{\lambda}} \tag{3.1}$$

where the subscripts M and S refer to model and full scale, respectively. Subsequently, the Reynolds similarity is satisfied by adjusting the dynamic viscosity μ of the fluid as:

$$\frac{\mu_S}{\mu_M} = \lambda^{\frac{3}{2}} \tag{3.2}$$

To obtain total resistance and its components, the obtained forces are multiplied by λ^3. The total resistance coefficient and its components are obtained for a range of sailing speeds from 11 to 16 knots. C_T as a function of speed is shown in Figure 13.

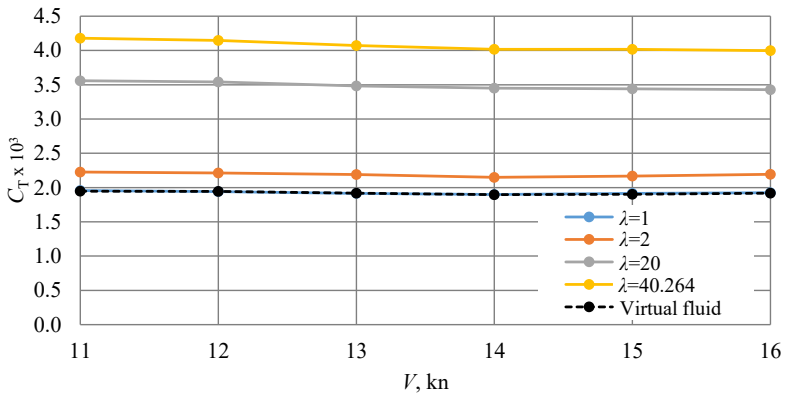


Figure 13. C_T as a function of speed obtained at different scales

The C_T values increase with scale, with the lowest values occurring at full scale and the highest values at model scale. The C_T values obtained from FSS at model scale with virtual fluid are similar to those obtained at full scale with real fluid. The C_T values

obtained at model scale with real fluid is approximately two times larger than the ones obtained at full scale and at model scale with virtual fluid for the entire analysed speed range. The C_T values slightly decrease with the increase of ship speed for the majority of analysed scales.

Figure 14 presents the obtained C_V, viscous pressure resistance coefficient C_{VP}, frictional resistance coefficient C_F, and wave resistance coefficient C_W. Similar results are obtained with DBS for C_V and its components to those obtained with FSS for C_T. The lowest values are obtained at full scale and at model scale with virtual fluid, while the highest are obtained at model scale with real fluid. C_V, C_{VP} and C_F obtained at model scale with real fluid are approximately two times larger than those obtained at full scale with real fluid and model scale with virtual fluid. As for C_W, the lowest value is obtained at model scale with virtual fluid method for a speed of 14 knots. The highest C_W are obtained for the speed of 16 knots at all the considered scales. Regarding the scale effects on C_W, it is noted that the coefficient increases with scale for speeds ranging from 12 to 16 knots. This is not valid for speed of 11 knots, although the results obtained at $\lambda = 20$ and model scale suggest that C_W increases with scale. The numerical simulations with virtual fluid method yield C_W similar to those obtained at full scale with real fluid. It is important to note that C_W is calculated with the results from both FSS and DBS, thus the combined numerical uncertainty from both types of simulations ranges from 0.06 % to 4.69 % depending on scale and type of fluid considered. This is especially important for the JBC since the portion of C_W in C_T ranges from 1.25 % to 4.86 %.

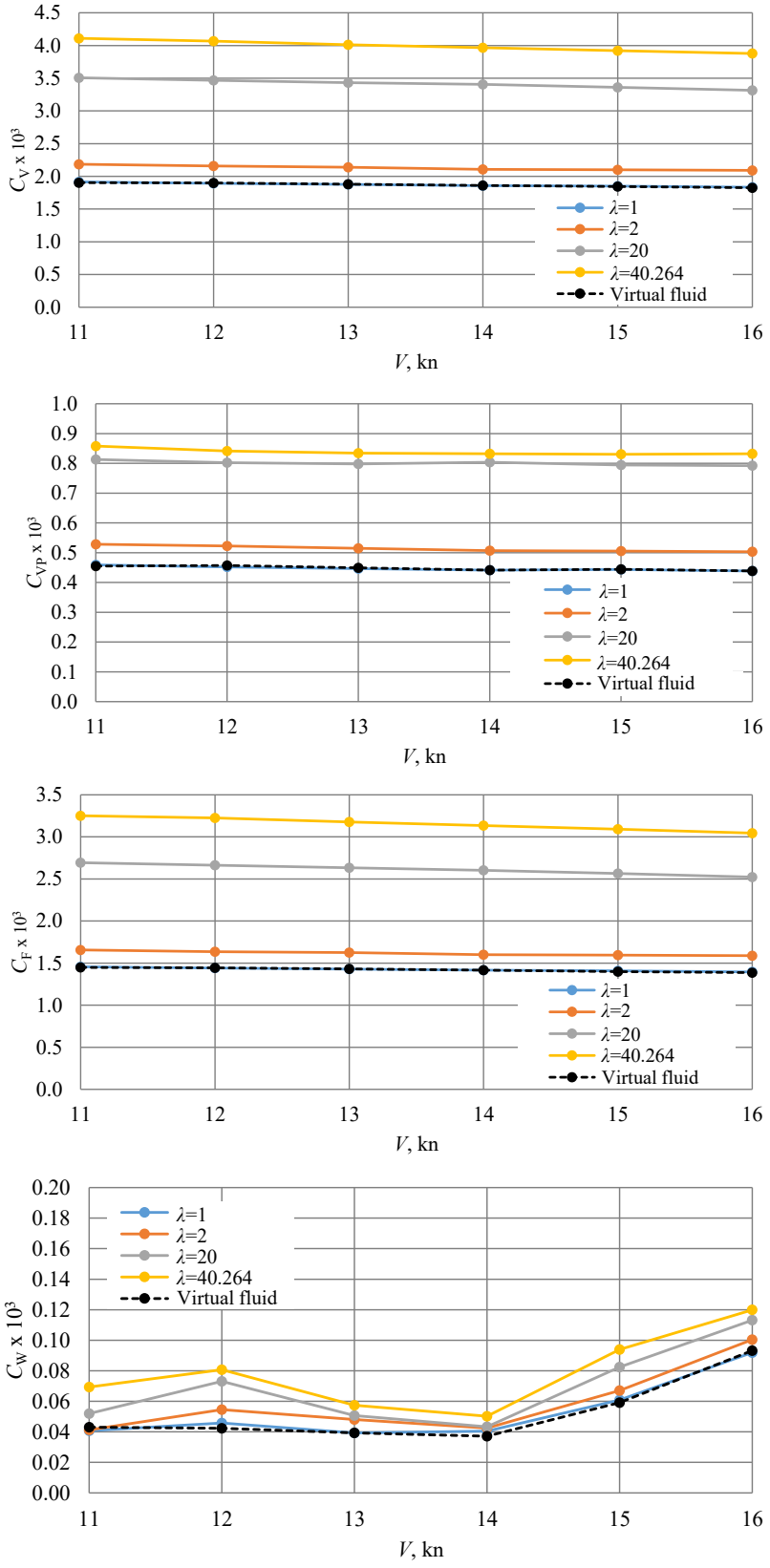


Figure 14. The components of C_T as a function of speed obtained at different scales

3.2.3. Propulsion characteristics

By performing the numerical simulations of RT and SPT, the propulsion characteristics of the JBC are obtained at different model scales and at full scale for speeds in the range from 11 to 16 knots [47]. The following propulsion characteristics are obtained: wake fraction w, thrust deduction fraction t, advance coefficient J, open water efficiency η_{O}, relative rotative efficiency η_{R}, hull efficiency η_{H}, and quasi-propulsive efficiency η_{D}. The self-propulsion points at different model scales are determined when T is equal to R_{T} subtracted by the friction deduction force F_{D} calculated as follows:

$$F_{\mathrm{D}} = \frac{1}{2}\rho S_{\mathrm{M}} v_{\mathrm{M}}^2 (C_{\mathrm{FM}} - C_{\mathrm{FS}}) \tag{3.3}$$

where C_{F} is obtained with the ITTC 1957 model-ship correlation line as follows:

$$C_{\mathrm{F}} = \frac{0.075}{(\log Re - 2)^2} \tag{3.4}$$

Figure 15 shows the obtained w and t at different scales and speeds. The scale effects on w are significant, whereas t does not follow any specific trend in relation to scale. The obtained w is highest at model scale and decreases with scale across the entire speed range. At speeds of 11 and 12 knots, w obtained at model scale with virtual fluid is higher than that obtained at full scale with real fluid, while the opposite is true for speeds ranging from 13 to 16 knots. The numerically obtained J, η_{O}, and η_{R} at different scales and speeds are presented in Figure 16. Both J and η_{O} increase with a decrease in scale. As expected, the values of J and η_{O} obtained at full scale are similar to those obtained at model scale with virtual fluid. η_{R} does not follow a specific trend with respect to scale, although the highest η_{R} is observed at model scale across the entire speed range. However, the obtained differences in η_{R} are negligible compared to those in J and η_{O}. The η_{H} and η_{D} values obtained at different scales and speeds are shown in Figure 17. Both components exhibit no particular trend with regard to speed. The scale effects are noticeable in the obtained η_{H}, which decreases with scale. This can be attributed to the differences in the obtained w, which show a more pronounced impact on the obtained η_{H} compared to t. On the other side, the scale effects on η_{D} are less pronounced, and no specific trend across different scales is observed.

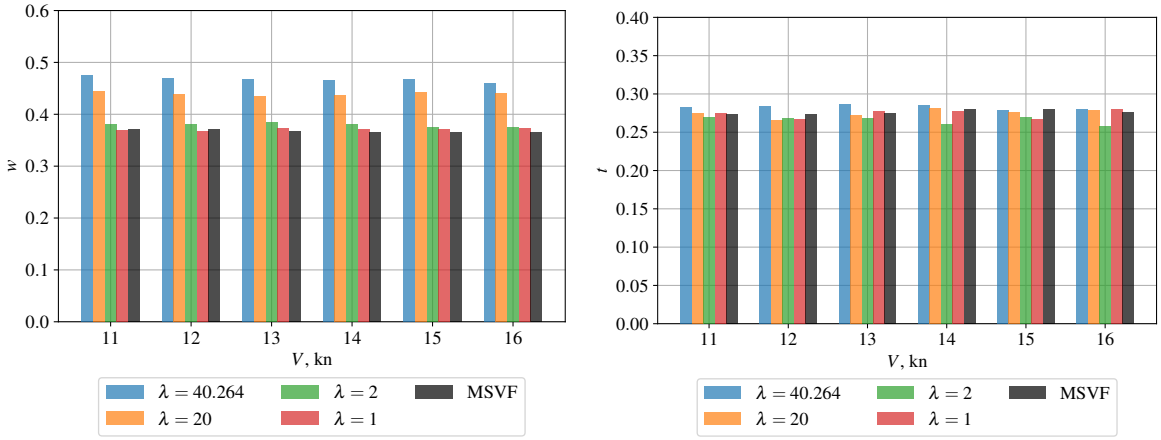


Figure 15. The w and t values obtained at different scales and speeds

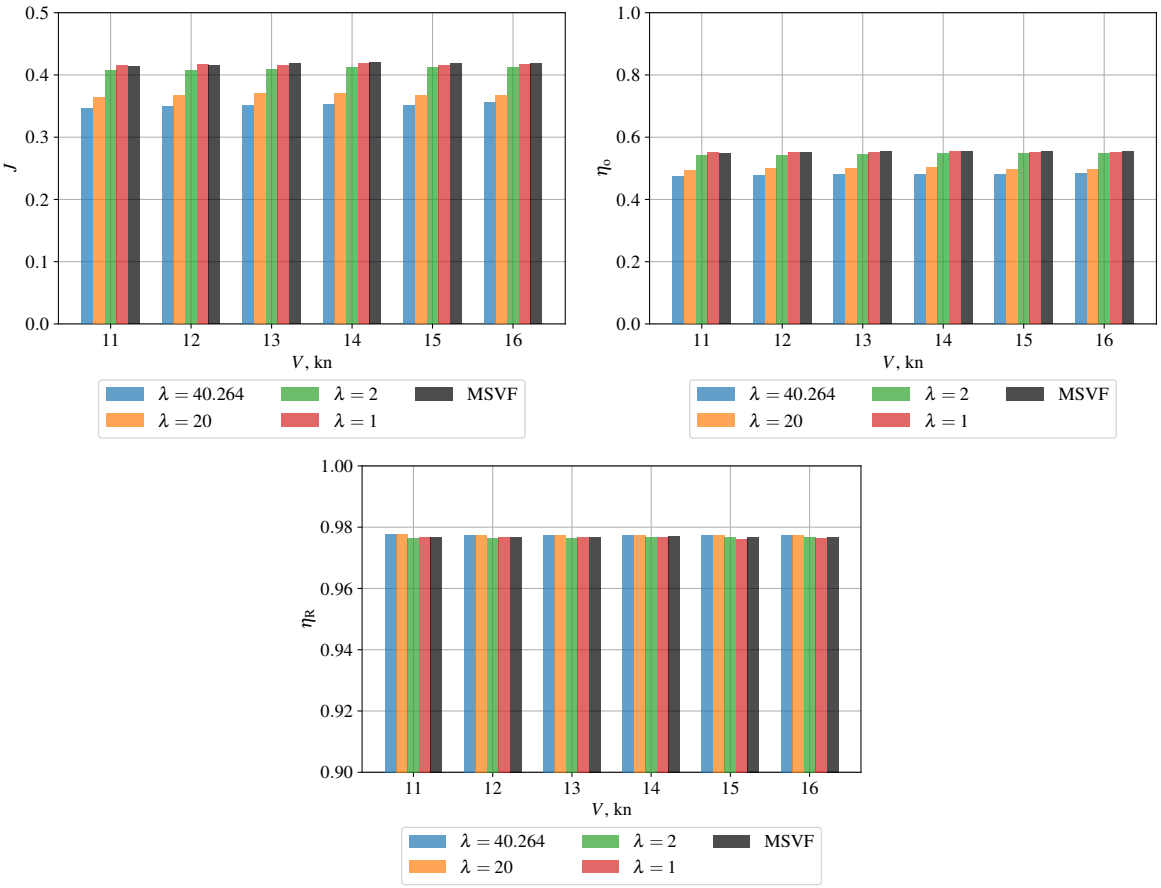


Figure 16. The J, $\eta_{\mathbf{O}}$, and $\eta_{\mathbf{R}}$ values obtained at different scales and speeds

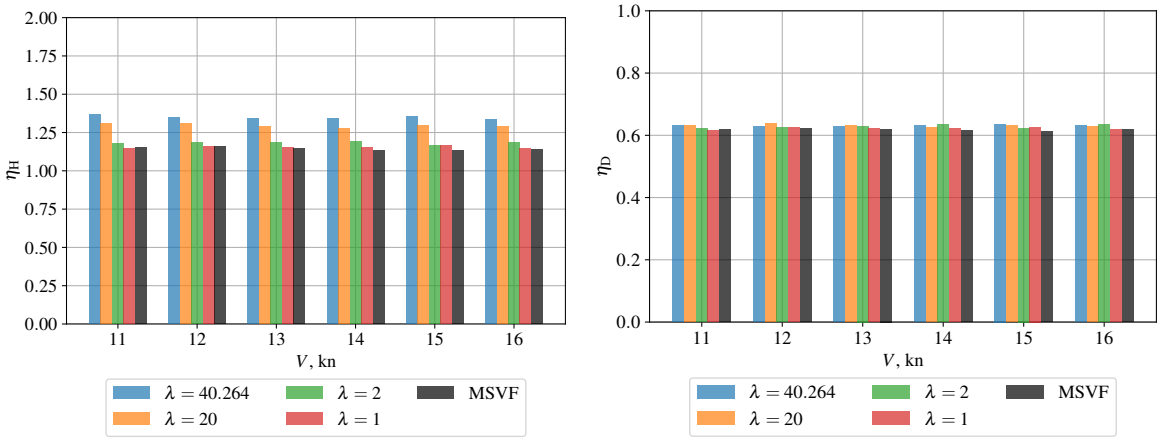


Figure 17. The η_H and η_D values obtained at different scales and speeds

3.2.4. Nominal and effective wake

Finally, the scale effects are assessed on the nominal and effective wakes. Figure 18 shows the contours of the dimensionless axial velocity component v_A/v on the propeller disc obtained at different model scales and full scale with real fluid and at model scale with virtual fluid. These results are obtained in the numerical simulations of RT for the speed of 14 knots. The lowest values of v_A/v are obtained at the angular position of 180° and around the hub in the regions from 0° to 90° and from 270° to 360°. A hook-like shape of the contours is visible under the hub at each scale. The low-speed region is largest at model scale and decreases with scale, confirming that boundary layer thickness also decreases with scale, as previously observed by Wang et al. [48]. The distribution of v_A/v obtained at model scale with virtual fluid is almost the same as the one obtained at full scale with real fluid.

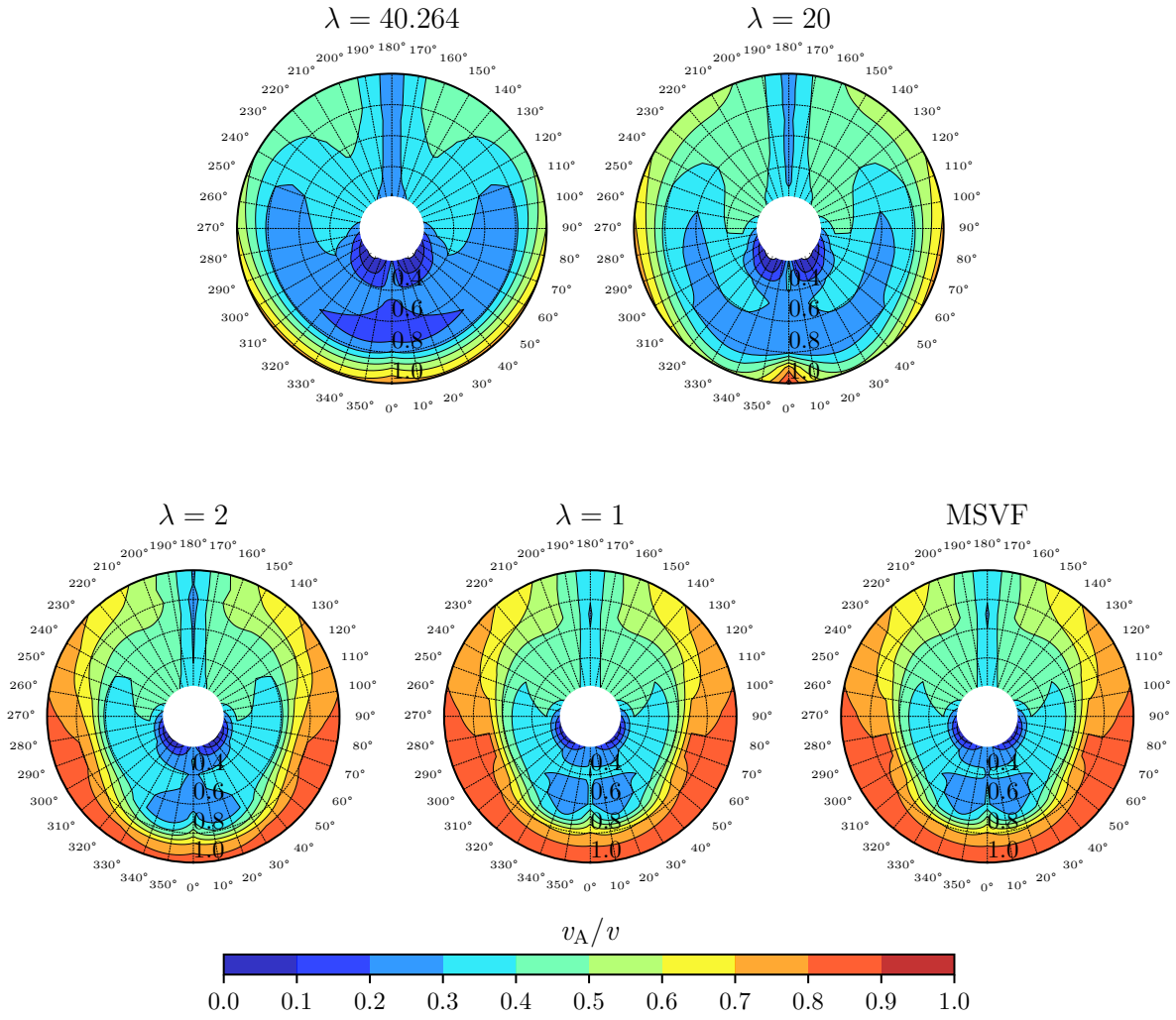


Figure 18. Contours of v_A/v on the propeller disc obtained at different scales and at model scale with virtual fluid

Further insights into the scale effects on the nominal wake are shown in Figure 19. At radial positions in the range from $0.2R$ to $0.4R$, the v_A/v values do not follow any particular trend at different scales. However, at radial positions from $0.5R$ to $1.0R$, v_A/v decreases with the increase in scale. It is observed that v_A/v increases exponentially as the radial position approaches the tip of the propeller disc at model scale and $\lambda = 20$, whereas at other scales, the increase follows a parabolic trend. Close agreement is obtained between v_A/v at full scale with real fluid and at model scale with virtual fluid.

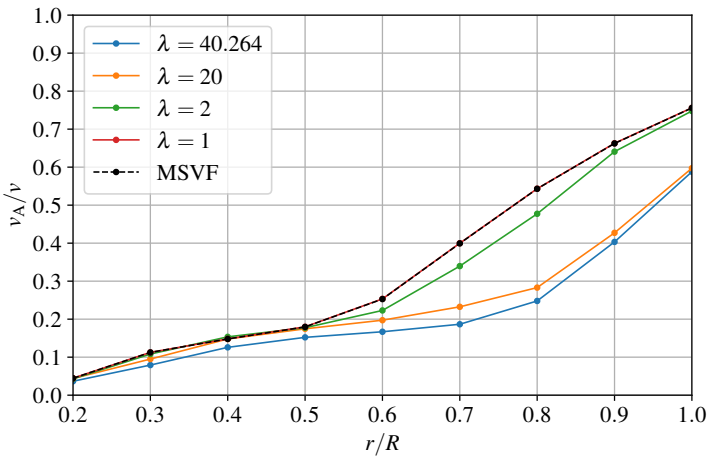


Figure 19. Radial distributions of the circumferentially averaged v_A/v obtained at different scales and at model scale with virtual fluid

The effective wake is presented through the contours of v_A/v at the propeller disc obtained in the numerical simulations of SPT at different scales and at model scale with virtual fluid, as shown in Figure 20. The scale effects on the effective wake are not as pronounced as those on the nominal wake. However, as scale increases, the low-speed regions become more obvious, particularly in the region near the hub of the propeller. The effective wake distribution obtained at model scale with virtual fluid closely matches the one obtained at full scale with real fluid, except in the region near the hub. In this region, the speed reductions are more pronounced at model scale with virtual fluid compared to results obtained at full scale with real fluid.

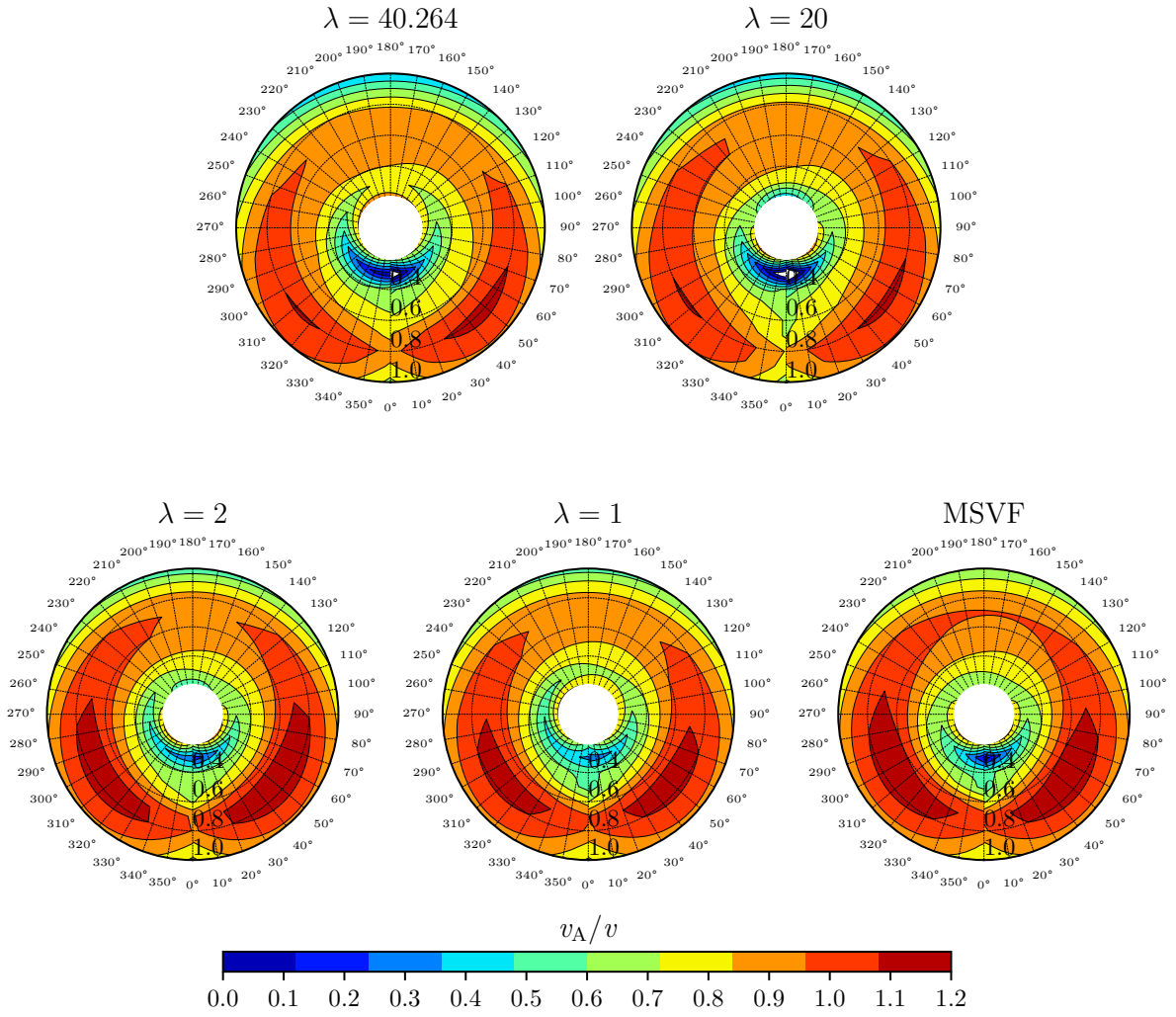


Figure 20. Contours of v_A/v obtained at different scales and at model scale with virtual fluid in the numerical simulations of the SPT

3.3. Effect of loading conditions and speed on the ship hydrodynamic characteristics

From the previous subsection, the effect of speed on resistance characteristics of the ship are negligible. A slight dependence of C_V on speed due to the C_F is shown. Also, C_W, although a small portion of C_T, does show a more pronounced dependence on speed [46]. The effect of speed on the propulsion characteristics, however, was shown to be negligible for the JBC [47]. A more thorough study is conducted to assess the effect of speed and loading conditions on the nominal wake of the post-Panamax 6750 TEU containership [49]. Numerical simulations were performed systematically for different static trim angles θ_S as well as for different speeds. The speeds were defined as 16.02, 19.95, and 23.94 knots. The effect of speed on the nominal wake is shown in Figure 21. The wake peak in the region close to 180° decreases with the increase in speed and the velocity reduction over the entire propeller disc plane is smaller as the ship speed increases.

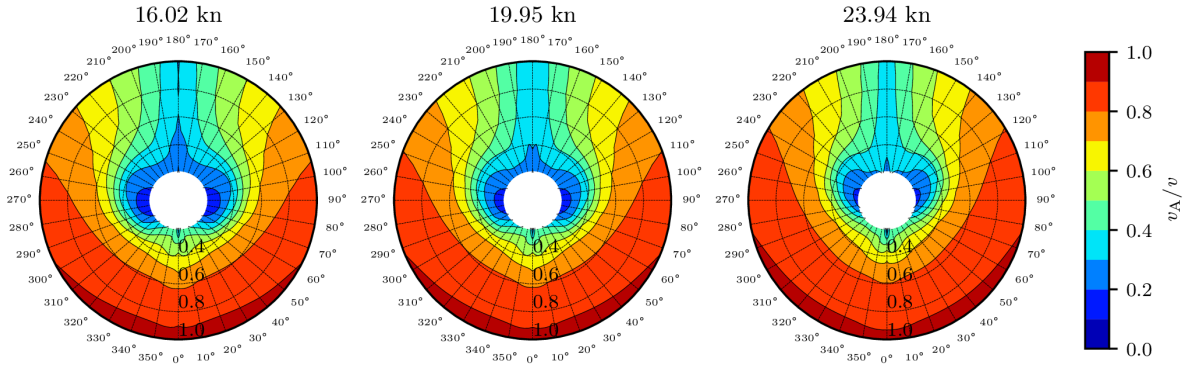


Figure 21. Contours of v_A/v on the propeller disc plane at different speeds

Figure 22 shows the radial distributions of the circumferentially averaged v_A/v obtained at different speeds. It can be seen that the discrepancies between the results obtained at 19.95 and 23.94 knots are larger than those obtained between 16.02 and 19.95 knots.

The loading condition has a significantly stronger influence on the nominal wake than the variations observed across different speeds. Figure 23 shows the contours of v_A/v obtained at θ_S in the range from -0.5° to 0.5° with the increments of 0.25°. It can be seen that the velocity reduction over the entire propeller disc plane is smaller, while the wake peak in the region close to 180° is larger as the θ_S increases. Thus, a more favourable flow

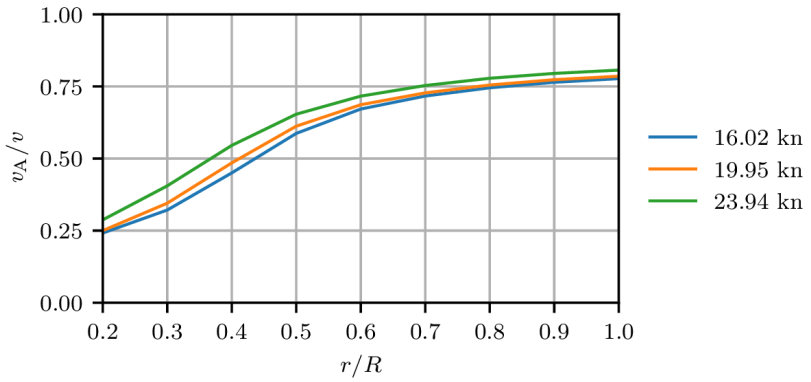


Figure 22. Radial distributions of the circumferentially averaged v_A/v at different speeds

is obtained for trim by stern than for trim by bow compared to even keel. The velocity reductions close to the propeller hub due to the increase in θ_S are insignificant.

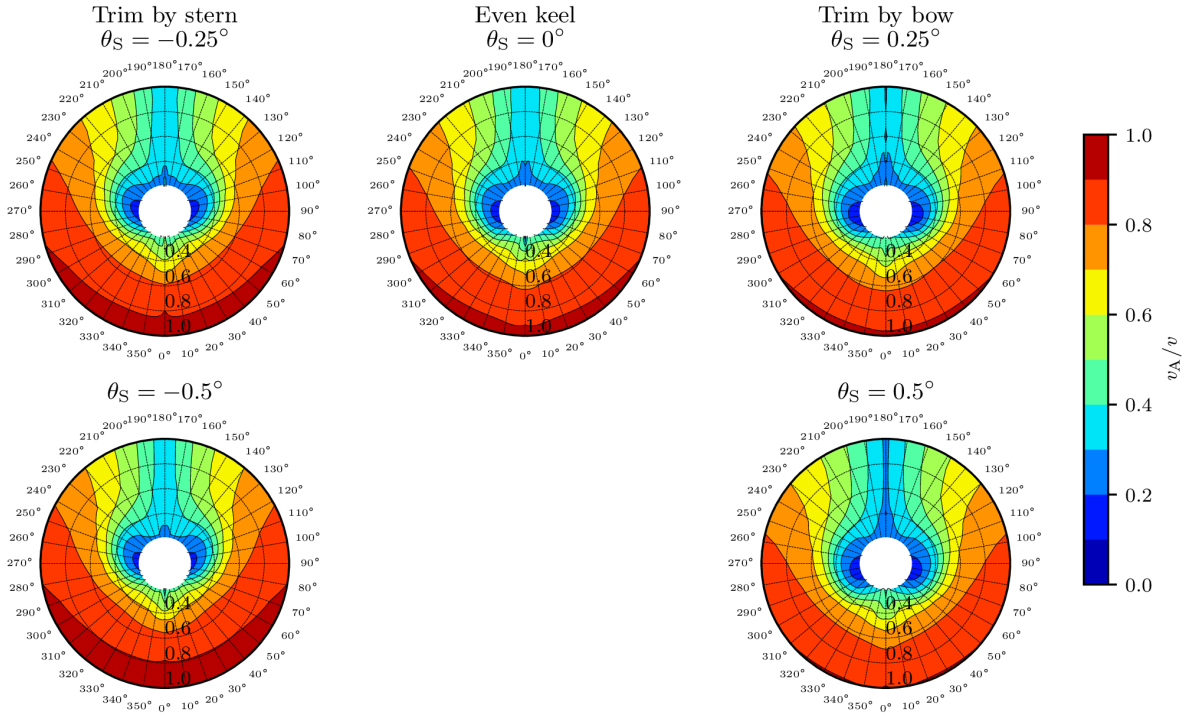


Figure 23. Contours of v_A/v on the propeller disc plane at different θ_S

Radial distributions of the circumferentially averaged v_A/v obtained at different θ_S are shown in Figure 24. A clear trend is visible with the circumferentially averaged v_A/v decreasing with the increase in θ_S at all radial positions. This trend is further emphasized when integral value of the nominal wake w_n is calculated as can be seen in Table 9. The

RD are calculated with respect to the reference value at $\theta_S = 0°$ for different θ_S. The w_n values increase with θ_S and the largest *RD* of -8.31 % is obtained for $\theta_S = -0.5°$.

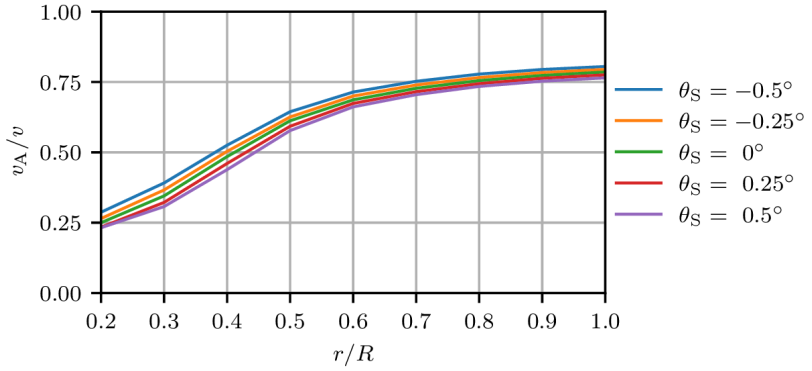


Figure 24. Radial distributions of the circumferentially averaged v_A/v at different θ_S

Table 9. The w_n values obtained at different θ_S

θ_S, °	w_n	*RD*, %
-0.5	0.298	-8.31
-0.25	0.313	-3.69
0	0.325	/
0.25	0.339	4.31
0.5	0.351	8.00

The effect of loading condition on the resistance and propulsion characteristics are assessed for the post-Panamax 6750 TEU containership [50]. Full-scale numerical simulations of the RT and SPT are conducted systematically at different θ_S ranging from -0.5° to 0.5° with 0.25° increments. Additionally, numerical simulations of the OWT are conducted to obtain the required open water characteristics of the propeller for the body force propeller method employed in the numerical simulations of SPT. For θ_S of -0.5° and 0°, the numerical results are compared with the extrapolated measurements from the towing tank. The experimental data is extrapolated with the ITTC 1978 Performance prediction method from 2017 without including the roughness allowance because the numerical simulations are conducted for the smooth rudder and hull surfaces.

The effect of θ_S on C_T is shown in Figure 25. The lowest values occur at even keel, increasing with both positive and negative deviations in θ_S. Contrary, the experimental data shows the lowest C_T at $\theta_S = -0.5°$.

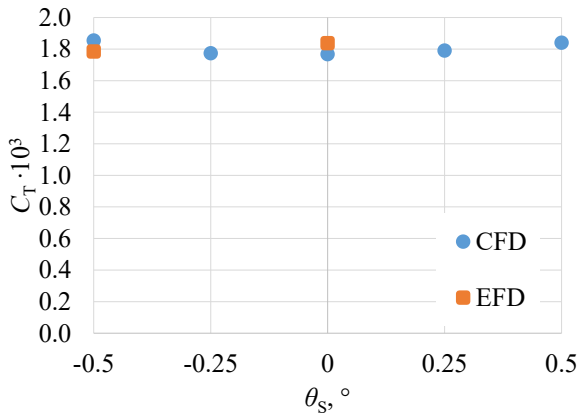


Figure 25. The C_T values obtained for different θ_S

Although C_T is influenced by θ_S, the propulsion components do not exhibit significant differences within the range of θ_S considered. Among the calculated propulsion components, w shows a slight decrease with θ_S up to trim by bow of 0.25°, Figure 26. At trim by bow of 0.5° the numerically obtained w increases slightly. When compared to the experimental data, the numerically obtained w is slightly lower at $\theta_S = -0.5°$ and $\theta_S = 0°$.

The η_H, η_O, and η_D values are presented in Figure 27. No clear trend is observed with respect to θ_S. However, when compared with the experimental data, the numerically

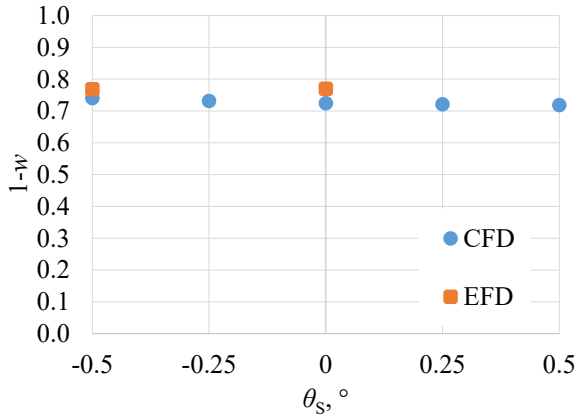


Figure 26. The w values obtained for different θ_S

obtained η_O shows significant discrepancies relative to the measured values. The numerically obtained η_O is significantly higher than the experimental values. This is reflected in the obtained η_D, which results from discrepancies in the open-water curves and is partly attributable to the values of J obtained in the numerical simulations of the SPT. The numerically obtained open water curves and a comparison with the experimental values are shown in Figure 28. The numerically obtained K_T is slightly lower, while K_Q is significantly lower than the experimental values. As a result, η_O is overpredicted, with the discrepancy between numerical and experimental values increasing with J.

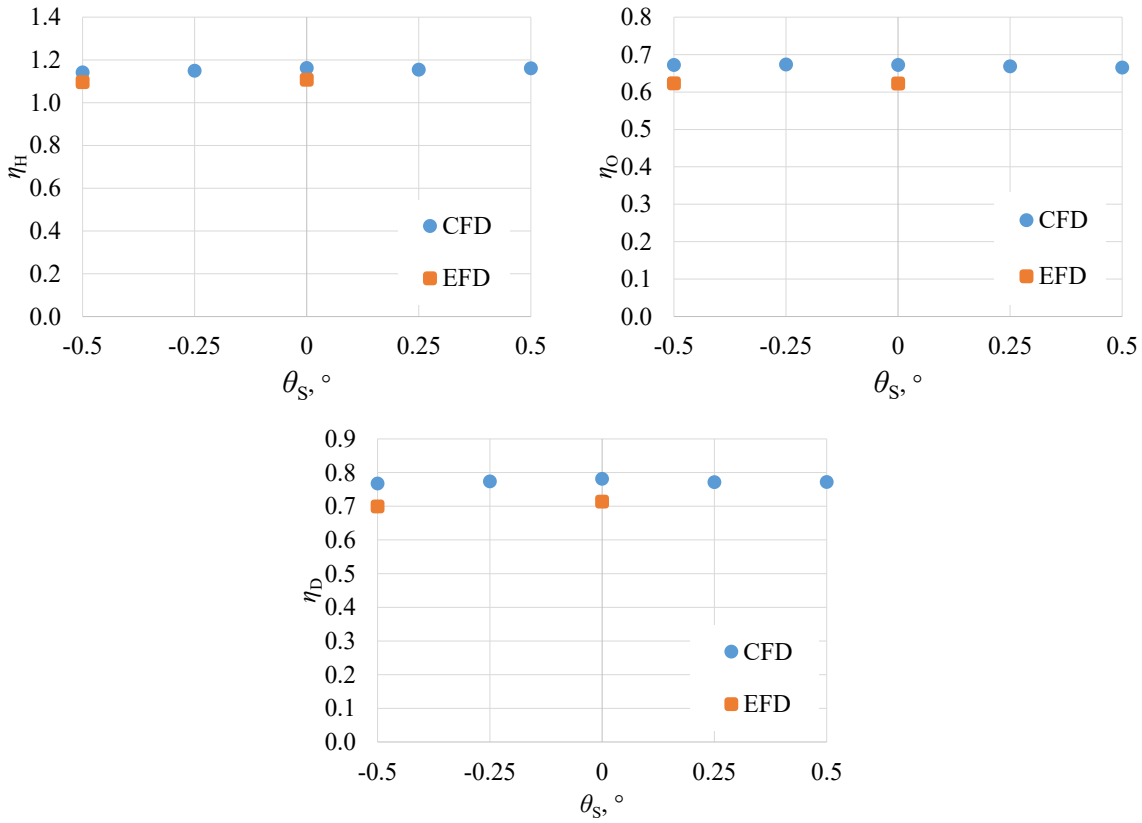


Figure 27. The η_H, η_O, and η_D values obtained for different θ_S

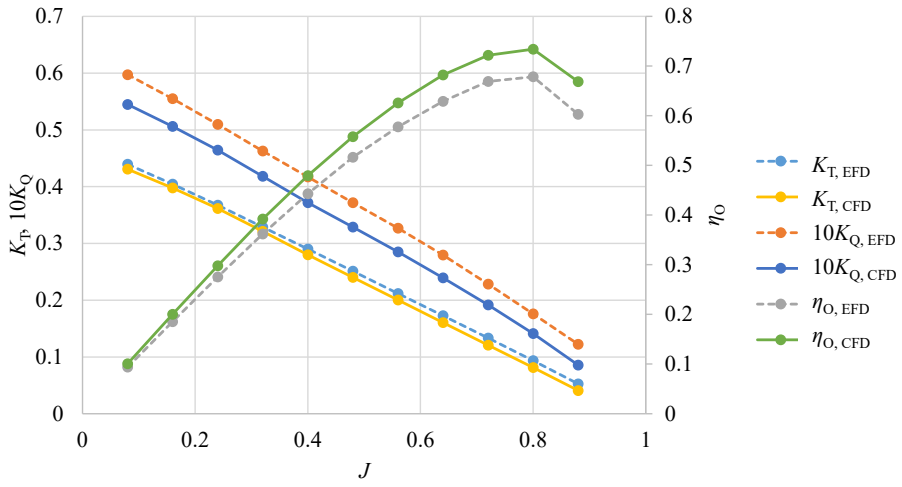


Figure 28. The propeller open water curves obtained numerically and experimentally

Additionally, the influence of different container configurations on wind and air resistance is investigated in [51]. Different container configurations are selected based on the available experimental data provided by Andersen [52]. The container configurations used for the assessment of wind and air resistance of the post-Panamax 6750 TEU containership are shown in Figure 29. A total of 9 container configurations are defined, where the first configuration is the fully loaded containership. This configuration is defined according to IMO Safety of Life at Sea regulation [53], which states that the ship operator has to have a line of sight from the bridge equal to 500 m or two ship lengths, whichever is smaller. Configurations 2 and 3 are defined with no containers and one row of containers loaded above the deck, respectively. The following two configurations are defined by removing the whole stacks in every other bay. In configuration 6, containers are equally loaded with stacks of 6 containers. The last three configurations are defined by streamlining the container configuration and adding more containers in the aft and fore deck.

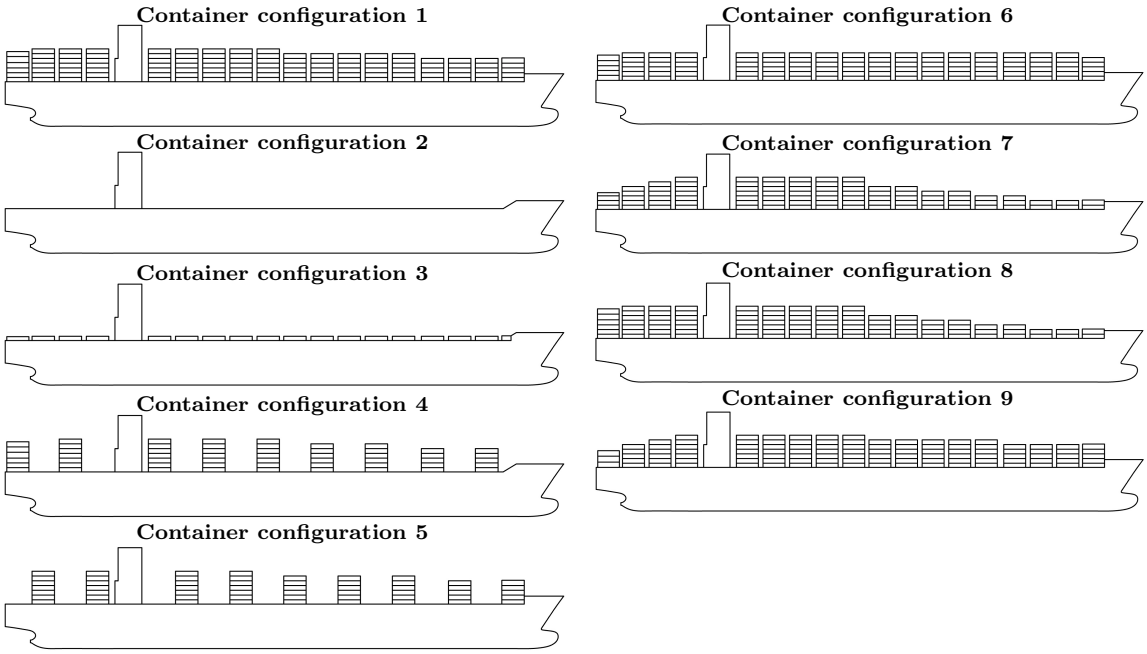


Figure 29. Different container configurations of the post-Panamax 6750 TEU containership

The obtained numerical results show no significant effect of θ_S on C_{DAX} and C_{DAY}, however C_N is affected slightly as shown in Figure 30. A positive θ_S yields higher C_N, while negative θ_S with the same absolute value yields lower C_N over the entire range of Ψ. The highest C_{DAX} is obtained for container configurations 4 and 5, which can be

attributed to the fact that every other bay is empty and thus more recirculation regions occur in the gaps between the container stacks.

Table 10 shows the air resistance coefficient obtained at even keel, $\theta_S = -0.5°$ and $\theta_S = 0.5°$. The presented RD are calculated with respect to the results obtained at even keel. It can be seen that the influence of θ_S on the air resistance coefficient is negligible. The highest absolute value of RD is equal to 6.76 % for container configuration 7 at $\theta_S = -0.5°$ and the lowest RD is obtained for the fully loaded containership at $\theta_S = 0.5°$ and is equal to 0.17 %. The results also show that trim by stern causes an increase, while trim by bow causes a decrease of the air resistance coefficient. Greater differences are obtained for trim by bow for all container configurations except for the empty containership. Figure 31 shows the velocity distribution for container configuration 7, as this configuration yields the highest calculated RD. The reason for the increase in the air resistance coefficient for trim by stern is the larger flow separation region behind the ship compared to that at even keel. The opposite is true for trim by bow, where a smaller flow separation region behind the ship can be noticed compared to even keel. This effect is more pronounced for trim by bow, resulting in higher absolute values of RD.

Table 10. Air resistance coefficients of the considered container configurations at different θ_S and the respective RD

Container configuration	θ_S			RD, %	
	$-0.5°$	$0°$	$0.5°$	$\frac{\phi_{-0.5°}-\phi_{0°}}{\phi_{0°}} \cdot 100$ %	$\frac{\phi_{0.5°}-\phi_{0°}}{\phi_{0°}} \cdot 100$ %
1	0.579	0.578	0.548	0.17	-5.35
2	0.946	0.968	0.959	-2.27	-0.93
3	0.925	0.916	0.894	0.98	-2.4
4	0.728	0.725	0.706	0.41	-2.62
5	0.645	0.643	0.64	0.31	-0.47
6	0.594	0.591	0.573	0.5	-3.14
7	0.679	0.651	0.607	4.3	-6.76
8	0.686	0.66	0.62	3.94	-6.06
9	0.573	0.568	0.55	0.88	-3.17

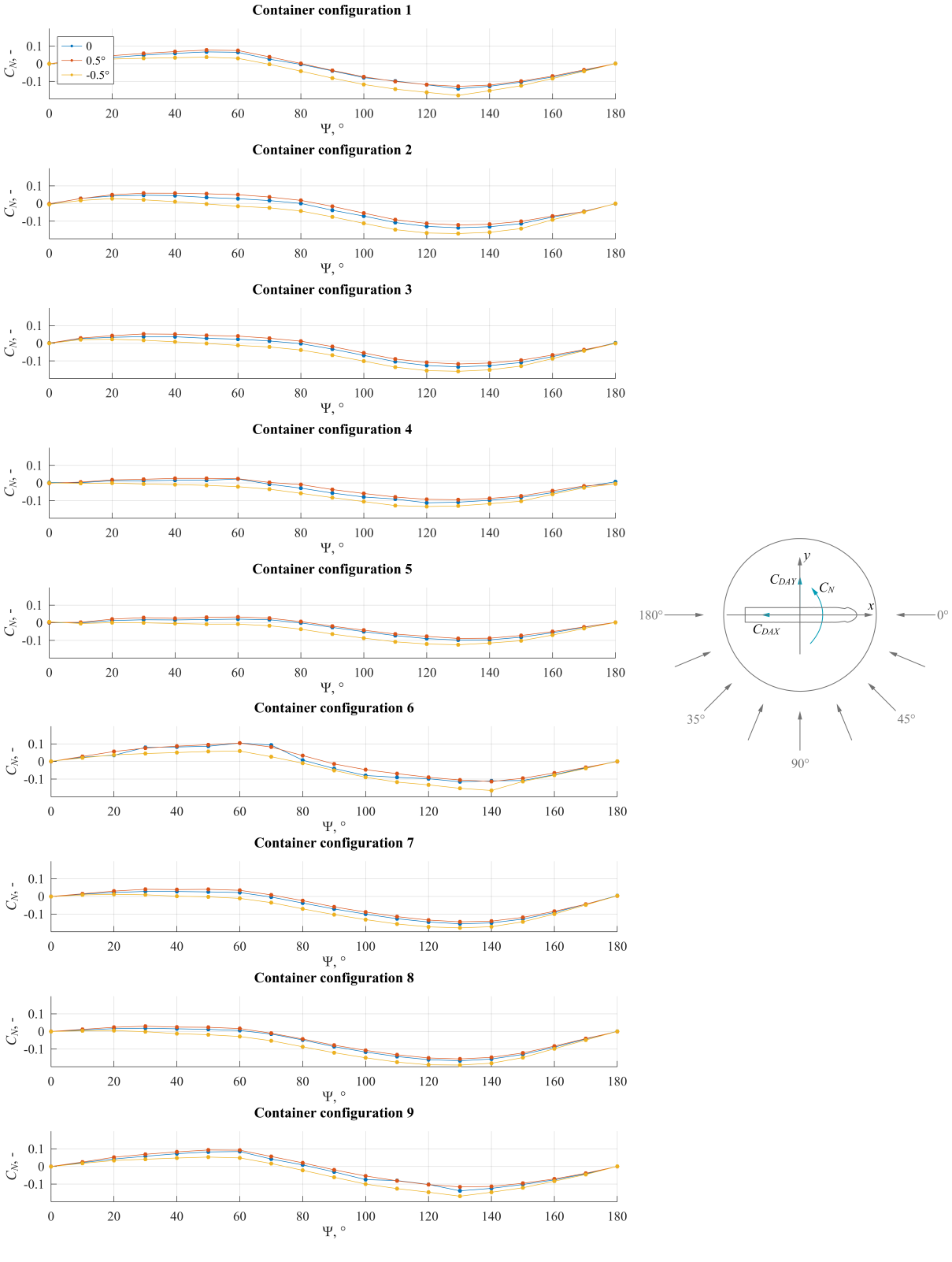


Figure 30. The C_N values as a function of Ψ for the considered container configurations

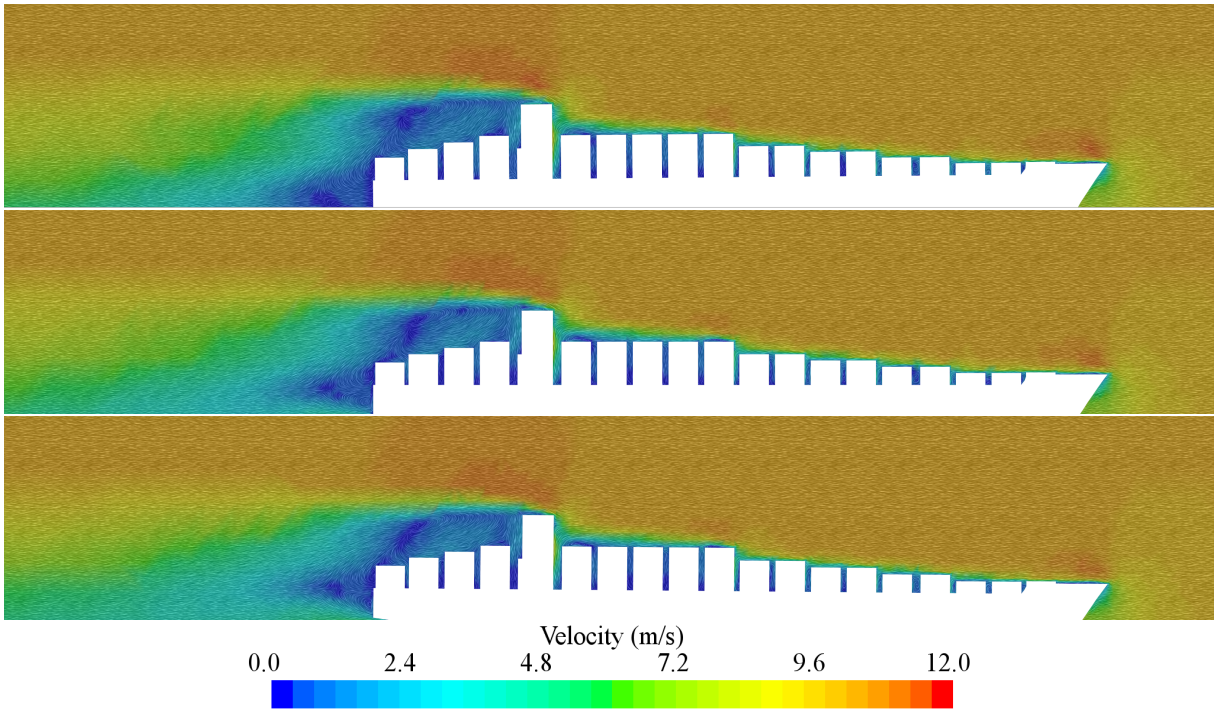


Figure 31. Velocity distributions at a profile view cross-section for container configuration 7 at $\theta_S = -0.5°$ (top), $\theta_S = 0°$ (middle) and $\theta_S = 0.5°$ (bottom)

The influence of speed is investigated within the steady-state numerical simulations by varying the sailing speed. The steps are determined according to the number of iterations needed for the air resistance coefficient to converge. The obtained air resistance is presented in Figure 32 as a function of the speed for the analysed container configurations. The highest air resistance is obtained for container configuration 2, which can be related to higher vorticity behind the superstructure as opposed to container configuration 1, Figure 33. The R_T value for the post-Panamax 6750 TEU containership without superstructure was determined by Grlj et al. [54] to be 2387.2 kN at 25 knots. The portion of air resistance within R_T varies from 3.5 % (container configuration 9) to 5.8 % (container configuration 2).

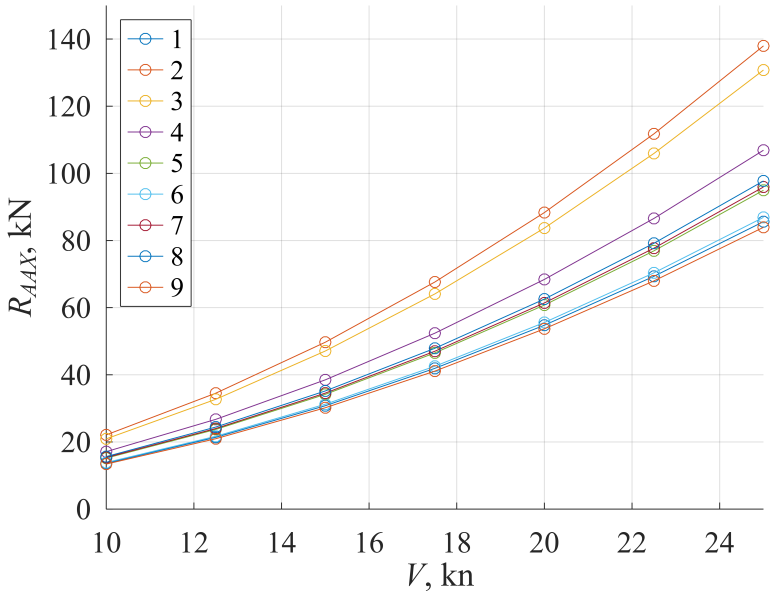


Figure 32. Air resistance as a function of speed for different container configurations

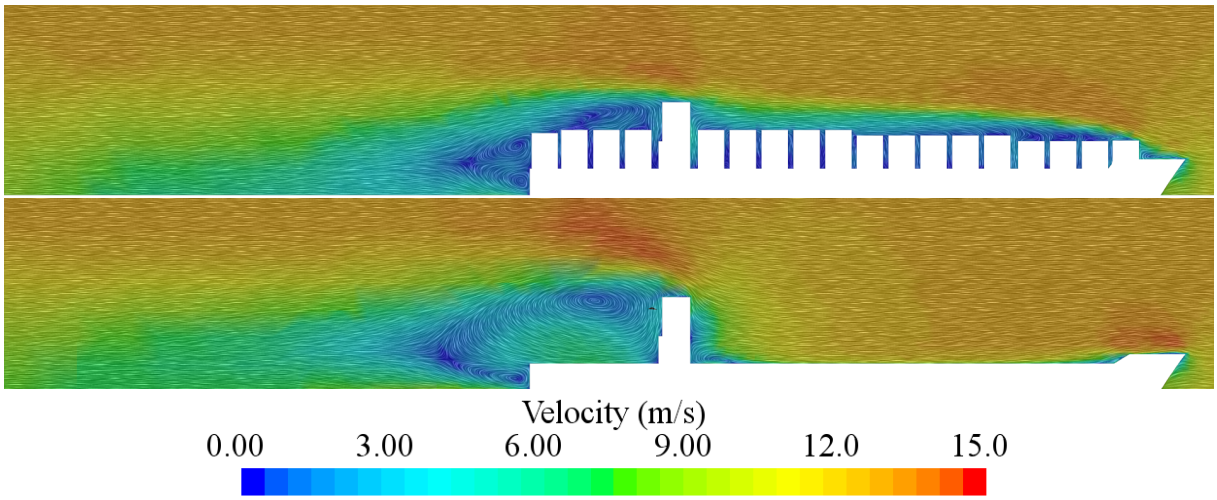


Figure 33. Velocity distribution for container configurations 1 (top) and 2 (bottom)

3.4. Numerical procedure for the selection of optimal propeller geometric characteristics

An optimization procedure is developed by incorporating an artificial neural network (ANN) trained with experimental data into the genetic algorithm (GA) with the aim to find the optimal propeller geometric characteristics for a given ship and its propeller loading K_T/J^2 [55]. The input data can be obtained with different methods including EFD, CFD or low-fidelity empirical methods such as the one proposed by Holtrop and Mennen [56].

The ANN takes the propeller main parameters, i.e., P/D, d/D, A_E/A_0 and Z as inputs, and predicts K_T and K_Q over a range of J. Consequently, the η_O value is calculated. The trained ANN is subsequently integrated into an optimization procedure based on GA. Within the optimization procedure, the propeller geometric characteristics are varied and η_O is obtained for specific K_T/J^2. The objective is to obtain the propeller geometric characteristics that yield the maximum η_O while keeping the design variables within the bounds defined by the training dataset and enforcing cavitation and noise criteria through penalty terms. After the GA converges, the optimal propeller corresponding to the specified design speed is identified, its main geometric parameters are extracted, and the results are reported. Figure 34 shows the proposed numerical procedure.

The database used for the ANN training consists of geometric characteristics of 143 propellers and their respective open water curves from the towing tank tests conducted at the Brodarski Institute (Jadranbrod d.d.) in Zagreb. The optimal ANN consisted of one hidden layer with 10 neurons in total. The activation function used within the neurons is the rectified linear unit (ReLU) defined as follows:

$$y = \mathrm{ReLU}(x) = \begin{cases} x, x > 0 \\ 0, x \leq 0 \end{cases} \tag{3.5}$$

For the training, the 5-fold cross-validation procedure is used. The complete dataset is partitioned into 5 equally sized subsets and the training and validation process is repeated 5 times with each time using one subset as a validation set and the other subsets as training set. The coefficient of determination R^2 and the root mean squared error $RMSE$ are used as performance indicators. The optimal ANN achieved a R^2 of 0.95 and $RMSE$ of 0.2

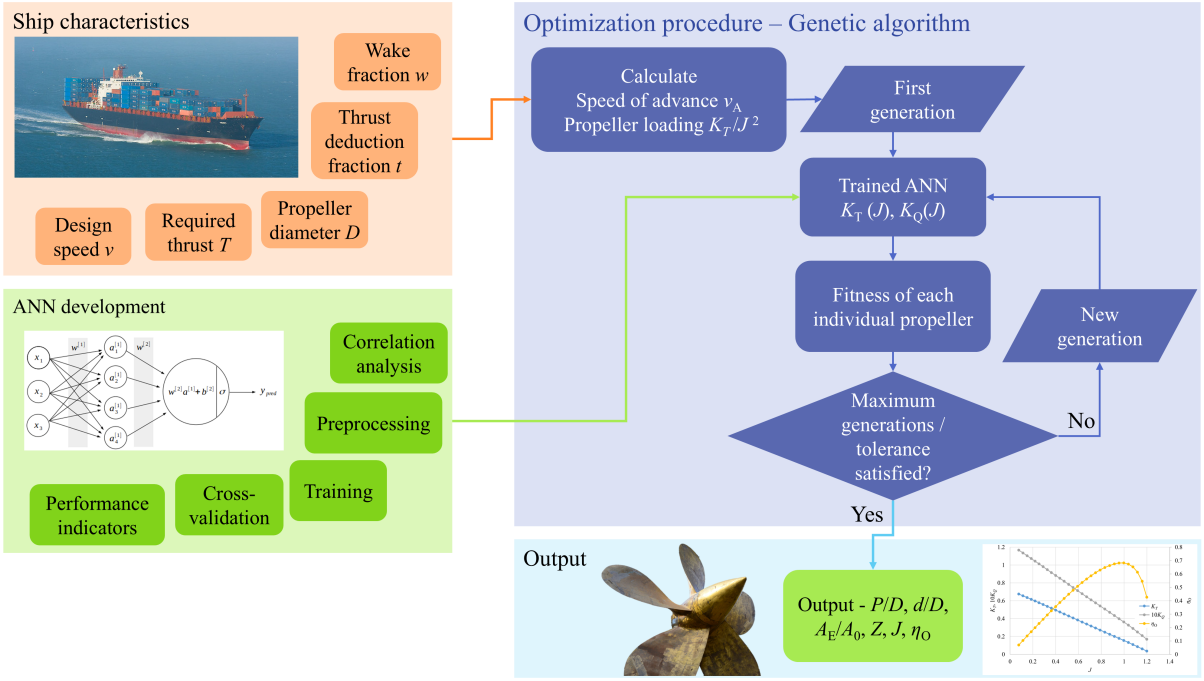


Figure 34. Flowchart of the proposed numerical procedure

on the validation set.

The optimization procedure is then set up with the GA, with the following fitness function:

$$fitness\ function = \eta_O + w_{\text{Keller}} \cdot \max[0, (A_E/A_0)_{\min} - (A_E/A_0)] + \tag{3.6}$$

$$+ w_{\text{tip, speed}} \cdot \max(0, v_{\text{tip}} - v_{\text{tip, max}}) \tag{3.7}$$

where w_{Keller} and $w_{\text{tip, speed}}$ are the cavitation and noise constraint penalty weights, respectively, the minimum expanded area ratio $(A_E/A_0)_{\min}$ and propeller tip speed v_{tip} are defined as follows:

$$(A_E/A_0)_{\min} = \frac{(1.3 + 0.3Z)T}{(p_{\text{atm}} + \rho g h_0 - p_v)D^2} + K \tag{3.8}$$

$$v_{\text{tip}} = Dn\pi \tag{3.9}$$

where p_{atm} and p_v are the atmospheric and water vapour pressure, respectively, h_0 is the immersion depth of the propeller shaft and K is the constant equal to 0.2. Thus, in the objective function, no constraints are taken into account and only the lower and upper bounds are considered. The cavitation and noise constraints are included in the fitness function as penalties. The $v_{\text{tip, max}}$ values are defined as 53 m/s for three- and four-bladed propellers and 46 m/s for five-bladed propellers [57]. The selected population size is equal

to 100, maximum number of generations is 500 and the function tolerance is set to 10^{-4}. To avoid local optima, the GA is performed 10 times in a row from scratch.

Four case study ships are selected: KRISO containership (KCS), JBC, post-Panamax 6750 TEU containership and Duisburg test case (DTC). Figure 35 shows the 3D models of the selected ships, while Table 11 shows the obtained input data with various sources for the design operating conditions.

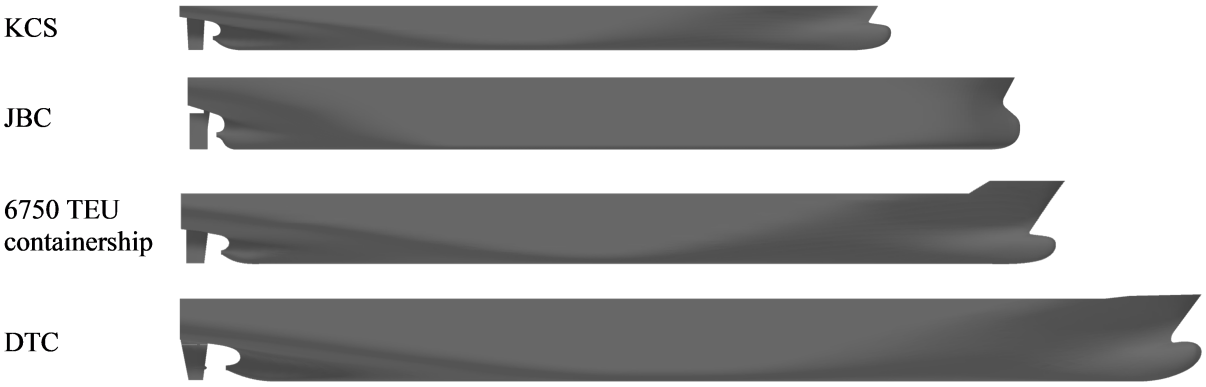


Figure 35. 3D models of the ships used as case studies

Table 11. Input parameters for the considered ships

	KCS			JBC			6750 TEU containership			DTC		
	EFD	**CFD**	**Holtrop**	**EFD**	**CFD**	**Holtrop**	**EFD**	**CFD**	**Holtrop**	**EFD**	**CFD**	**Holtrop**
T, kN	1757	1570	1879	1583	1383	1309	1959	1783	2005	3659	3705	4178
t	0.147	0.133	0.165	0.124	0.270	0.208	0.160	0.158	0.176	0.090	0.110	0.195
w	0.197	0.227	0.218	0.490	0.360	0.583	0.271	0.275	0.222	0.187	0.195	0.294
K_T/J^2	0.327	0.310	0.377	1.847	1.229	2.519	0.482	0.527	0.525	0.451	0.476	0.772

The optimal propeller geometric characteristics are identified and their corresponding geometric and open water characteristics are summarized in Tables 12-15, together with comparisons against the original propellers for each ship. For most ships, the highest η_O is obtained when CFD-derived input data are used, whereas for the DTC the maximum η_O is achieved using EFD data. When Holtrop-Mennen method is used for the input data, the optimal η_O are lower than those of the original propellers except for the post-Panamax 6750 TEU containership where a slightly higher η_O is obtained. Similar results are obtained when EFD-derived input data is used. The optimal P/D values remain close to those of the original propellers, although they are generally higher, with some deviations observed for the JBC. When the input parameters are determined using the

Holtrop-Mennen method, both the achieved η_O and the corresponding geometric characteristics are lower than those obtained using CFD or EFD data, as well as lower than those of the original propellers. The optimal Z is consistently equal to five for all the considered ships, except for the JBC with the Holtrop-Mennen method where the optimization procedure yields a four-bladed propeller. For the post-Panamax 6750 TEU containership, the optimization procedure yields a five-bladed propeller with all the methods applied for obtaining the input data, whereas the original design features four blades. Since propeller performance is strongly influenced by w, the significant differences in the obtained geometric characteristics can be attributed to variations in w predicted by different methods. The smallest differences in w are observed for the KCS and the post-Panamax 6750 TEU containership. Consequently, the optimized geometric characteristics are consistent for these cases. In contrast, the JBC and DTC results exhibit significant differences in w, which leads to corresponding variations in the optimal propeller geometric characteristics. Overall, the optimized propellers demonstrate higher A_E/A_0 compared to the original ones, which is in agreement with the findings from Tadros et al. [57]. In particular, the results obtained for the KCS show close agreement with those reported by Tadros et al. [57]. The optimized KCS propeller exhibits higher η_O, P/D, and A_E/A_0 compared to the original propeller. These results indicate that an optimal propeller design can be successfully obtained using an ANN trained on a small dataset.

Table 12. Original and optimal propellers obtained for KCS using different input data

	Original	**CFD**	**EFD**	**Holtrop**
P/D, kN	0.997	1.186	1.186	1.186
d/D	0.18	0.193	0.193	0.193
A_E/A_0	0.8	0.755	0.738	0.888
Z	5	5	5	5
J	0.679	0.834	0.843	0.822
K_T	0.195	0.228	0.221	0.254
K_Q	0.032	0.046	0.045	0.052
η_O	0.65	0.660	0.664	0.645

Table 13. Original and optimal propellers obtained for JBC using different input data

	Original	**CFD**	**EFD**	**Holtrop**
P/D, kN	0.736	1.106	1.186	0.690
d/D	0.19	0.194	0.193	0.162
A_E/A_0	0.64	0.688	0.738	0.495
Z	5	5	5	4
J	0.351	0.451	0.554	0.292
K_T	0.199	0.376	0.377	0.215
K_Q	0.026	0.060	0.067	0.024
η_O	0.452	0.45	0.50	0.41

Table 14. Original and optimal propellers obtained for post-Panamax 6750 TEU containership using different input data

	Original	**CFD**	**EFD**	**Holtrop**
P/D, kN	0.89	1.186	1.186	1.160
d/D	0.169	0.193	0.193	0.191
A_E/A_0	0.75	0.888	0.888	0.988
Z	4	5	5	5
J	0.622	0.731	0.750	0.749
K_T	0.186	0.307	0.296	0.294
K_Q	0.029	0.060	0.058	0.058
η_O	0.603	0.599	0.609	0.604

Table 15. Original and optimal propellers obtained for DTC using different input data

	Original	**CFD**	**EFD**	**Holtrop**
P/D, kN	0.959	1.160	1.160	1.215
d/D	0.176	0.191	0.191	0.187
A_E/A_0	0.8	0.988	0.988	1.188
Z	5	5	5	5
J	0.615	0.781	0.770	0.678
K_T	0.316	0.276	0.282	0.355
K_Q	0.054	0.055	0.056	0.072
η_O	0.592	0.621	0.615	0.529

Finally, a standalone application called OptiProp is developed using MATLAB App Designer within the software package MATLAB. The application integrates the trained ANN with the optimization procedure based on GA into a user-friendly graphical interface. It enables the user to define the ship propulsion characteristics and its operating conditions. After the calculations are performed, the results are shown within the same graphical interface. The tool provides the propeller geometric parameters, open water characteristics, including K_T, K_Q, and η_O in a table and plots the curves in a diagram. Figure 36 shows the graphical interface of the developed application, where the input and output can be seen.

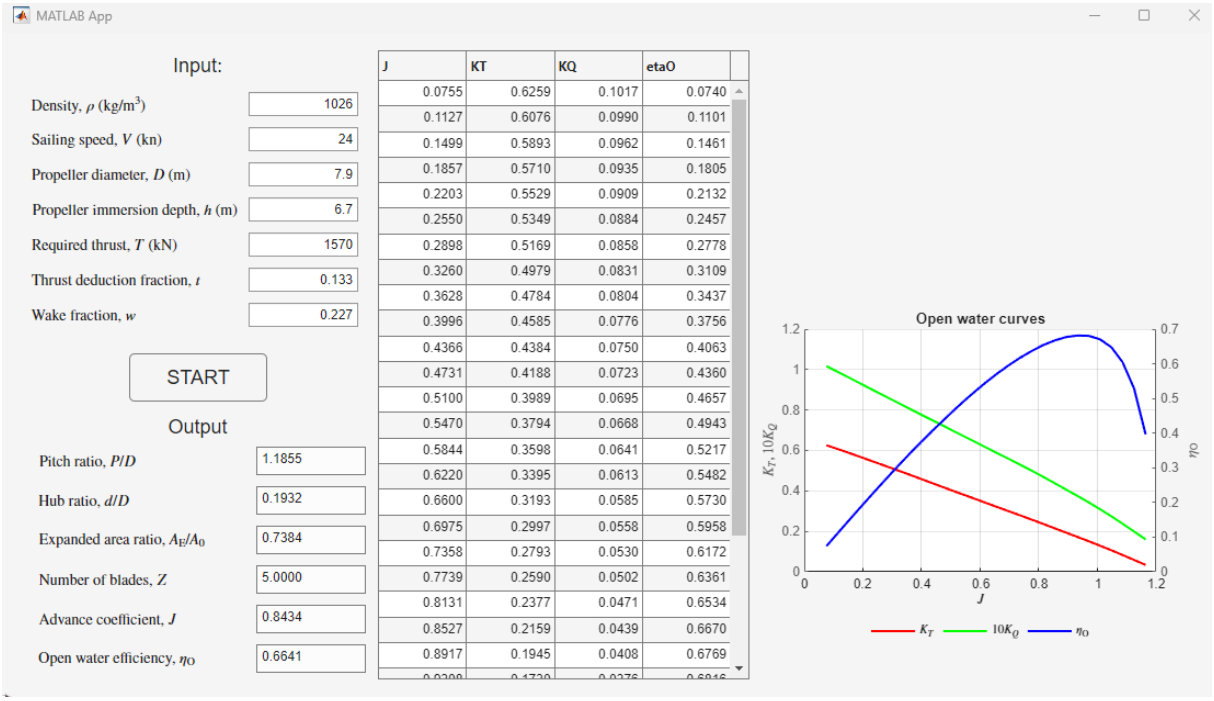


Figure 36. The OptiProp graphical interface

This study demonstrates that optimal propeller geometric characteristics can be obtained for the design operating condition using the proposed method. The same approach can be extended to other loading conditions or operating speeds, provided that appropriate input data are available.

4. Conclusion

In this doctoral dissertation, the ship hydrodynamic characteristics have been determined by employing numerical simulations with the focus on the effects of slow steaming and different loading conditions as well as the scale effects on the ship resistance and propulsion characteristics. The numerical results were thoroughly verified with the GCI method and validated with the experimental data obtained in the towing tank at the Brodarski Institute (Jadranbrod d.o.o.) in Zagreb. Two case study ships were used, namely, the post-Panamax 6750 TEU containership and the JBC.

The thesis commenced with a thorough investigation of the numerical parameters on the obtained results at full scale and model scale. The effects of three turbulence models on the total resistance, its components, ship motions and wave patterns were assessed. After that, the effects of discretization schemes for the convection, gradient and temporal terms were investigated. It was shown that the SSTKO turbulence model yields the lowest resistance at both scales considered, while the relative deviation from the experimental values is acceptable. Regarding the discretization schemes for the temporal and spatial discretization, it was found that the temporal term can be solved with the first-order scheme without impacting the obtained total resistance while speeding up the convergence at full scale. The gradient and convection terms should be solved using second-order schemes to obtain satisfactory results.

Next, the scale effects were investigated in detail using CFD. First, the scale effects on the open water characteristics of the JBC propeller were investigated. The study shows the importance of including the transition model at model scale to ensure that the laminar flow is included, thus yielding results closer to those obtained at full scale. The resistance and propulsion characteristics, as well as wake fields of the JBC were numerically analysed at different model scales and at full scale using the FSS and DBS methods. The virtual fluid approach was also assessed to simultaneously satisfy Reynolds and Froude similarity at model scale. The results showed significant scale effects on the total resistance coefficient and its components, which were highest at model scale with real fluid and lowest at full scale, while the virtual fluid method closely reproduced full-scale results. The wave resistance coefficient increased with scale but exhibited combined

uncertainties of 0.06 % and 4.69 %. Significant scale effects were also observed for the wake fraction and hull efficiency, whereas thrust deduction fraction, relative rotative efficiency, and quasi-propulsive efficiency showed no clear dependency on scale. Analysis of the nominal and effective wakes revealed that the low-speed regions near the propeller hub were most pronounced at model scale and decreased with scale, indicating reduced boundary layer thickness at full scale. Overall, the virtual fluid approach provided wake fields and propulsion characteristics in close agreement with the full-scale results.

The effects of loading conditions and speed on the ship hydrodynamic characteristics were assessed for the post-Panamax 6750 TEU containership. The nominal wake was obtained numerically for different speeds and trim angles. Through the contours and radial distributions of the circumferentially averaged v_A/v, it was shown that the effect of loading condition on the nominal wake is higher than the effect of speed. As the trim angle decreases, higher v_A/v are obtained at the propeller disc. The resistance and propulsion characteristics of the post-Panamax 6750 TEU containership were obtained numerically at full scale for different trim angles. The results show that the total resistance coefficient is lowest at even keel and increases for both bow and stern trim conditions. In contrast, propulsion characteristics showed only minor sensitivity to trim changes. The wake fraction slightly decreased up to a trim by bow of 0.25° and then increased slightly at 0.5° trim by bow. The hull efficiency, open water efficiency, and quasi-propulsive efficiency did not exhibit a clear trend with trim angle. However, significant discrepancies were observed between numerical and experimental open water efficiencies. The numerical simulations overpredicted open water efficiency and consequently quasi-propulsive efficiency because the numerically obtained propeller open water characteristics differed from experimental values. Further, the effect of loading conditions and speed on the wind and air resistance of the post-Panamax 6750 TEU containership were investigated. Nine container configurations were analysed, ranging from a fully loaded ship, defined according to IMO visibility requirements, to partially loaded and streamlined arrangements with varying container distributions. The numerical results indicate that trim angle has negligible effect on longitudinal wind load coefficient and transverse wind load coefficient, while yaw moment coefficient is slightly affected, with positive trim angles producing higher values. The highest longitudinal wind load coefficients were observed for configurations

with alternating empty bays, due to stronger flow recirculation between container stacks. The effect of trim angle on air resistance was generally negligible. Trim by stern slightly increased air resistance, while trim by bow reduced it because of changes in the size of the flow separation region behind the ship. The largest relative deviation in air resistance was 6.76 % for container configuration 7 at $\theta_S = -0.5°$, whereas the smallest deviation was only 0.17 % for the fully loaded configuration at $\theta_S = 0.5°$. The effect of speed was also investigated. The highest air resistance occurred for the empty-deck configuration due to stronger vortices behind the superstructure. Overall, air resistance accounted for approximately 3.5 to 5.8 % of the total resistance of the containership, depending on the container configuration.

The results of this study enabled the development of a numerical procedure that incorporated an ANN trained with experimental data into the optimization procedure based on GA with the aim to find the optimal propeller geometric characteristics for a given ship and its K_T/J^2. For a given ship and its operational conditions, the proposed approach is used to obtain the propeller geometric characteristics that yield the maximum open water efficiency. This approach can likewise be applied to other loading conditions or operating speeds, provided that the appropriate input data are available. The proposed numerical procedure has been implemented within a standalone application written in MATLAB which is provided at https://github.com/carloggrlj/OptiProp.

5. Future Work

As a part of the future work, additional attention should be devoted to the numerical setup of the self-propulsion test through the implementation of more advanced rotating propeller modelling approaches, such as overset mesh and sliding mesh techniques. Compared to the body force propeller method, these approaches enable a more detailed resolution of the interaction between the hull, propeller, and rudder, allowing for improved prediction of ship propulsion characteristics. Their application would be especially valuable for investigating the ship hydrodynamic characteristics in off-design conditions such as slow steaming or different loading conditions.

The numerical approach applied in this study should be extended toward simulations in realistic environmental conditions. The present study focused primarily on calm water, whereas future investigations should consider the combined effects of waves, wind, ship motions, and manoeuvring. Particular emphasis should be placed on the influence of unsteady sea states on propulsion characteristics, wake fields at different loading conditions and at reduced sailing speeds. Furthermore, future studies should investigate transient operational scenarios, including acceleration, deceleration, turning manoeuvres, and course-keeping, since such conditions are highly relevant for ship operation, its fuel consumption, and consequently energy efficiency assessments.

Another important direction for future work is the extension of the analysis to additional ship types and broader operational profiles. The conclusions obtained in this study are based on a bulk carrier and a containership, while future investigations should determine whether similar trends in hydrodynamic characteristics are observed for other ship types, such as Ro-Ro ships, passenger ships, or naval ships sailing in off-design conditions. Moreover, the influence of loading condition could be evaluated using a wider range of trim angles values.

Future studies could also investigate the application of energy saving devices as a means of improving overall propulsion efficiency at slow steaming speeds and different loading conditions. Numerical and experimental analyses could be performed for various pre-swirl stators, ducts, rudder bulbs, fins, and wake equalizing devices in order to evaluate their influence on the ship hydrodynamic characteristics. Since the effectiveness of the

energy saving devices strongly depends on the operating condition, loading conditions, and stern-flow characteristics, additional research is required to determine their performance under off-design conditions, including reduced speeds and varying trim angles. Such investigations could contribute to the development of optimized energy saving devices for improving the overall ship energy efficiency.

The numerical assessment of air and wind resistance could also be further enhanced by incorporating a more detailed container geometries, deck equipment, and realistic atmospheric boundary-layer profiles. Future studies could investigate optimized container configurations aimed at minimizing air resistance. In addition, the interaction between air and water should be examined in greater detail, particularly under strong wind and wave conditions where coupled effects become increasingly significant.

Finally, the developed optimization procedure and the standalone MATLAB application provide a solid basis for further development toward a comprehensive decision-support tool for preliminary ship design. Future work could include the integration of additional optimization objectives and constraints, such as structural limitations or vibration. The incorporation of machine learning approaches trained on larger experimental and numerical databases could further improve the robustness, computational efficiency, and generalization capability of the proposed methodology.

Bibliography

[1] ITTC, , 2014. Practical Guidelines for RANS Calculation of Nominal Wakes ITTC, 7.5-03-03-02. *ITTC-Recommended Procedures and Guidelines*.

[2] Organization, I. M. 2023 IMO Strategy on reduction of GHG emissions from ships, 2023.

[3] Pastra, A., Zachariadis, P., and Alifragkis, A., 2021. The Role of Slow Steaming in Shipping and Methods of CO2 Reduction. *Sustain. Marit. Dom.*, 337–352. https://doi.org/10.1007/978-3-030-69325-1_17.

[4] Demirel, Y. K., Turan, O., and Incecik, A., 2017. Predicting the effect of biofouling on ship resistance using CFD. *Appl. Ocean Res.*, 62, 100–118. https://doi.org/10.1016/j.apor.2016.12.003.

[5] Xing, H., Spence, S., and Chen, H., 2020. A comprehensive review on countermeasures for CO2 emissions from ships. *Renew. Sustain. Energy Rev.*, 134, 110222. https://doi.org/10.1016/j.rser.2020.110222.

[6] Chircop, A., 2019. The IMO initial strategy for the reduction of GHGs from international shipping: A commentary. *Int. J. Mar. Coast. Law.*, 34, 3, 482–512. https://doi.org/10.1163/15718085-13431093.

[7] Balcombe, P., Brierley, J., Lewis, C., Skatvedt, L., Speirs, J., Hawkes, A., and Staffell, I., 2019. How to decarbonise international shipping: Options for fuels, technologies and policies. *Energy Convers. Manag.*, 182, 72–88. https://doi.org/10.1016/j.enconman.2018.12.080.

[8] Ammar, N. R., 2018. Energy- and cost-efficiency analysis of greenhouse gas emission reduction using slow steaming of ships: Case study RO-RO cargo vessel. *Sh. Offshore Struct.*, 13, 8, 868–876. https://doi.org/10.1080/17445302.2018.1470920.

[9] Degiuli, N., Martić, I., Farkas, A., and Gospić, I., 2021. The impact of slow steaming on reducing CO2 emissions in the Mediterranean Sea. *Energy Rep.*, 7, 8131–8141. https://doi.org/10.1016/j.egyr.2021.02.046.

[10] Taskar, B. and Andersen, P., 2020. Benefit of speed reduction for ships in different weather conditions. *Transp. Res. D: Transp. Environ.*, 85, 102337. https://doi.org/10.1016/j.trd.2020.102337.

[11] Psaraftis, H. N. and Lagouvardou, S., 2023. Ship speed vs power or fuel consumption: Are laws of physics still valid? Regression analysis pitfalls and misguided policy implications. *Clean. Logist. Supply Chain*, 7, 100111. https://doi.org/10.1016/j.clscn.2023.100111.

[12] Adland, R., Cariou, P., and Wolff, F. C., 2020. Optimal ship speed and the cubic law revisited: Empirical evidence from an oil tanker fleet. *Transp. Res. E: Logist. Transp. Rev.*, 140, 101972. https://doi.org/10.1016/j.tre.2020.101972.

[13] Berthelsen, F. H. and Nielsen, U. D., 2021. Prediction of ships' speed-power relationship at speed intervals below the design speed. *Transp. Res. D: Transp. Environ.*, 99, 102996. https://doi.org/10.1016/j.trd.2021.102996.

[14] Farkas, A., Degiuli, N., Martić, I., and Grlj, C. G., 2022. Is slow steaming a viable option to meet the novel energy efficiency requirements for containerships? *J. Clean. Prod.*, 374, 133915. https://doi.org/10.1016/j.jclepro.2022.133915.

[15] Ng, M. W., 2019. Vessel speed optimisation in container shipping: A new look. *J. Oper. Res. Soc.*, 70, 4, 541–547. https://doi.org/10.1080/01605682.2018.1447253.

[16] Wu, W. M., 2020. The optimal speed in container shipping: Theory and empirical evidence. *Transp. Res. E: Logist. Transp. Rev.*, 136, 101903. https://doi.org/10.1016/j.tre.2020.101903.

[17] Tezdogan, T., Demirel, Y. K., Kellett, P., Khorasanchi, M., Incecik, A., and Turan, O., 2015. Full-scale unsteady RANS CFD simulations of ship behaviour and performance in head seas due to slow steaming. *Ocean Eng.*, 97, 186–206. https://doi.org/10.1016/j.oceaneng.2015.01.011.

[18] Niklas, K. and Pruszko, H., 2019. Full-scale CFD simulations for the determination of ship resistance as a rational, alternative method to towing tank experiments. *Ocean Eng.*, 190, 106435. https://doi.org/10.1016/j.oceaneng.2019.106435.

[19] Mikkelsen, H., Steffensen, M. L., Ciortan, C., and Walther, J. H., 2019. Ship Scale Validation of CFD Model of Self-propelled Ship. In *MARINE 2019: Computational Methods in Marine Engineering VIII*, 730–741, Gothenburg, Sweden.

[20] Orych, M., Werner, S., and Larsson, L., 2021. Validation of full-scale delivered power CFD simulations. *Ocean Eng.*, 238, 109654. https://doi.org/10.1016/j.oceaneng.2021.109654.

[21] Farkas, A., Degiuli, N., and Martić, I., 2018. Assessment of hydrodynamic characteristics of a full-scale ship at different draughts. *Ocean Eng.*, 156, 135–152. https://doi.org/10.1016/j.oceaneng.2018.03.002.

[22] Farkas, A., Degiuli, N., Martić, I., and Dejhalla, R., 2019. Numerical and experimental assessment of nominal wake for a bulk carrier. *J. Mar. Sci. Technol.*, 24, 4, 1092–1104. https://doi.org/10.1007/s00773-018-0609-4.

[23] Farkas, A., Song, S., Degiuli, N., Martić, I., and Demirel, Y. K., 2020. Impact of biofilm on the ship propulsion characteristics and the speed reduction. *Ocean Eng.*, 199, 107033. https://doi.org/10.1016/j.oceaneng.2020.107033.

[24] Farkas, A., Degiuli, N., Martić, I., and Dejhalla, R., 2020. Impact of hard fouling on the ship performance of different ship forms. *J. Mar. Sci. Eng.*, 8, 10, 1–32. https://doi.org/10.3390/jmse8100748.

[25] Mikkelsen, H. and Walther, J. H., 2020. Effect of roughness in full-scale validation of a CFD model of self-propelled ships. *Appl. Ocean Res.*, 99. https://doi.org/10.1016/j.apor.2020.102162.

[26] Yin, X. B., Lu, Y., Zou, J., and Wan, L., 2019. Numerical and experimental study on hydrodynamic bulbous bow hull-form optimization for various service conditions due to slow steaming of container vessel. *Proc. Inst. Mech. Eng. M: J. Eng. Marit. Environ.*, 233, 4, 1103–1122. https://doi.org/10.1177/1475090218811782.

[27] Xiao, Z., Guo, L., Feng, D., Shuguang, L., and Hu, Z., December 2018. Numerical Study on the Scale Effects of the Ship Resistance and Form Factor. In *2018 IEEE 8th International Conference on Underwater System Technology: Theory and Application*, Wuhan, China.

[28] Korkmaz, K. B., Werner, S., Sakamoto, N., Queutey, P., Deng, G., Yuling, G., Guoxiang, D., Maki, K., Ye, H., Akinturk, A., Sayeed, T., Hino, T., Zhao, F., Tezdogan, T., Demirel, Y. K., and Bensow, R., 2021. CFD based form factor determination method. *Ocean Eng.*, 220, 108451. https://doi.org/10.1016/j.oceaneng.2020.108451.

[29] Islam, H. and Soares, G., 2019. Effect of trim on container ship resistance at different ship speeds and drafts. *Ocean Eng.*, 183, 106–115. https://doi.org/10.1016/j.oceaneng.2019.03.058.

[30] Menter, F. R., 1994. Two-equation eddy-viscosity turbulence models for engineering applications. *AIAA J.*, 32, 8, 1598–1605.

[31] Menter, F. R., Langtry, R. B., Likki, S. R., Suzen, Y. B., Huang, P. G., and Völker, S., 2006. A correlation-based transition model using local variables - Part I: Model formulation. *J. Turbomach.*, 128, 3, 413–422. https://doi.org/10.1115/1.2184352.

[32] Baltazar, J., Rijpkema, D., and de Campos, J. F., 2018. On the use of the {$\gamma-Re_{\theta_t}$} transition model for the prediction of the propeller performance at model-scale. *Ocean Eng.*, 170, 6–19. https://doi.org/10.1016/j.oceaneng.2018.10.005.

[33] ITTC, , 2011. Practical Guidelines for Ship CFD Applications, 7.5-03-02-03. *ITTC-Recommended Procedures and Guidelines*.

[34] ITTC, , 2024. Guideline on the CFD-based Determination of Wind Resistance Coefficients, 7.5-03-02-05. *ITTC - Recommended Procedures and Guidelines*.

[35] Wnek, A. D. and Soares, C. G., 2015. CFD assessment of the wind loads on an LNG carrier and floating platform models. *Ocean Eng.*, 97, 30–36. https://doi.org/10.1016/j.oceaneng.2015.01.004.

[36] Janssen, W. D., Blocken, B., and van Wijhe, H. J., 2017. CFD simulations of wind loads on a container ship: Validation and impact of geometrical simplifications. *J. Wind Eng. Ind.*, 166, 106–116. https://doi.org/10.1016/j.jweia.2017.03.015.

[37] Celik, I. B., Ghia, U., Roache, P. J., Freitas, C. J., Coleman, H., and Raad, P. E., 2008. Procedure for estimation and reporting of uncertainty due to discretization in CFD applications. *J. Fluids Eng. Trans. ASME*, 130, 7, 078001. https://doi.org/10.1115/1.2960953/444689.

[38] Roache, P. J., 2009. *Fundamentals of Verification and Validation*. Hermosa Publishers, New Mexico, USA.

[39] Eça, L. and Hoekstra, M., 2014. A procedure for the estimation of the numerical uncertainty of CFD calculations based on grid refinement studies. *J. Comput. Phys.*, 262, 104–130. https://doi.org/10.1016/J.JCP.2014.01.006.

[40] NMRI, . Tokyo 2015 A Workshop on CFD in Ship Hydrodynamics, 2015.

[41] Kim, Y. and Kim, J.-H., 2016. Benchmark study on motions and loads of a 6750-TEU containership. *Ocean Eng.*, 119, 262–273. https://doi.org/10.1016/j.oceaneng.2016.04.015.

[42] Brodarski Institute, . Report 6655-M. Resistance, self-propulsion and 3D wake measurement test results. Technical report, Zagreb, 2022.

[43] Degiuli, N., Martić, I., Buča, M. P., and Grlj, C. G., 2025. Benchmark study on resistance and propulsion characteristics of a 6750-TEU container ship. *Ocean Eng.*, 319, 120300. https://doi.org/10.1016/j.oceaneng.2025.120300.

[44] Grlj, C. G., Degiuli, N., and Martić, I., 2023. The Impact of Numerical Parameters on the Resistance Characteristics of a Container Ship at the Model and Full Scale. *J. Mar. Sci. Eng.*, 11, 9, 1672. https://doi.org/10.3390/jmse11091672.

[45] Grlj, C. G., Degiuli, N., Farkas, A., and Martić, I., 2022. Numerical Study of Scale Effects on Open Water Propeller Performance. *J. Mar. Sci. Eng.*, 10, 8, 1132. https://doi.org/10.3390/jmse10081132.

[46] Grlj, C. G., Degiuli, N., and Martić, I., 2025. Assessment of the effect of speed and scale on the total resistance and its components for a bulk carrier. *Results Eng.*, 26, 105095. https://doi.org/10.1016/j.rineng.2025.105095.

[47] Grlj, C. G., Degiuli, N., and Martić, I., 2025. Scale effects on the resistance and propulsion characteristics of the Japan Bulk Carrier. *Ocean Eng.*, 339, 122059. https://doi.org/10.1016/j.oceaneng.2025.122059.

[48] Wang, Z. Z., Xiong, Y., Wang, R., Shen, X. R., and Zhong, C. H., 2015. Numerical study on scale effect of nominal wake of single screw ship. *Ocean Eng.*, 104, 437–451. https://doi.org/10.1016/j.oceaneng.2015.05.029.

[49] Grlj, C. G., Degiuli, N., and Martić, I., 2024. Experimental and numerical assessment of the effect of speed and loading conditions on the nominal wake of a containership. *Brodogradnja*, 75, 4, 75405. https://doi.org/10.21278/brod75405.

[50] Grlj, C. G., Degiuli, N., and Martić, I., 2026. A full-scale numerical investigation of a containership resistance and propulsion characteristics at different trim angles. *Results Eng.*, 30, 110318. https://doi.org/10.1016/j.rineng.2026.110318.

[51] Grlj, C. G., Degiuli, N., Tuković, Ž., Farkas, A., and Martić, I., 2023. The effect of loading conditions and ship speed on the wind and air resistance of a containership. *Ocean Eng.*, 273, 113991. https://doi.org/10.1016/j.oceaneng.2023.113991.

[52] Andersen, I. M. V., 2013. Wind loads on post-panamax container ship. *Ocean Eng.*, 58, 115–134. https://doi.org10.1016/j.oceaneng.2012.10.008.

[53] Organization, I. M., 2001. *SOLAS : Consolidated Edition*. London, Great Britain, 3rd edition.

[54] Grlj, C. G., Degiuli, N., Farkas, A., and Martić, I., 2022. The influence of numerical parameters on the total resistance of a container ship. In *Proceedings of The 19th International Congress of the International Maritime Association of the Mediterranean*, 33–40. CRC Press.

[55] Grlj, C. G., Degiuli, N., Martić, I., and Pedišić Buča, M., 2026. Optimization of marine propeller characteristics for maximum open water efficiency using an ANN-GA tool trained on experimental data. *Brodogradnja*, 77, 4, 77405. https://doi.org/10.21278/brod77405.

[56] Holtrop, J. and Mennen, G., 1978. A statistical power prediction method. *Int. Shipbuild. Prog.*, 25, 290, 253–256. https://doi.org/10.3233/ISP-1978-2529001.

[57] Tadros, M., Shi, W., Xu, Y., and Song, Y., 2024. A unified cross-series marine propeller design method based on machine learning. *Ocean Eng.*, 314, 119691. https://doi.org/10.1016/j.oceaneng.2024.119691.

Curriculum Vitae

Carlo Giorgio Grlj was born on December 14, 1995, in Rijeka, Croatia. He holds a master's degree in Aeronautical Engineering from the University of Zagreb, Faculty of Mechanical Engineering and Naval Architecture.

After completing his education at the University of Zagreb, he was employed at the Karlovac University of Applied Sciences as a research assistant on the project funded by the European Union entitled "Research and development of specialized multirotor unmanned aerial vehicles" from 2020 to 2021. From December 2021 he has been employed at the University of Zagreb, Faculty of Mechanical Engineering and Naval Architecture as a research assistant on the Croatian Science Foundation project entitled "Sustainable slow steaming for low carbon shipping, (STARSHIP)". As part of his work on the project, he enrolled in the postgraduate doctoral study Mechanical Engineering, Naval Architecture, Aeronautical Engineering, Metallurgical Engineering at the University of Zagreb, Faculty of Mechanical Engineering and Naval Architecture. From December 2021 he has been developing the website of the international scientific journal Brodogradnja: An International Journal of Naval Architecture and Ocean Engineering for Research and Development. As a part of his doctoral study, he participated at the Chalmers University Workshop at the Chalmers University of Technology in Goethenberg, Sweden. In 2024, he was awarded with the Outstanding Doctoral Student Award in 2023 and in 2025, he received the Annual award of the Society to young scientists and artists for 2024. After the completion of the Croatian Science Foundation research project entitled "Sustainable slow steaming for low carbon shipping (STARSHIP)", he started to work as a researcher on the Croatian Science Foundation research project entitled "Sustainable and Optimized Hull Maintenance Strategy for Ferries in the Adriatic Sea, (SMOOTHS)". From 2024 he is a member of the research team of CA23159 - Decarbonising Waterborne Transportation, contributing to the ship hydrodynamics area within WG2: Hydrodynamic hull design for energy-efficient performance.

Bibliography:

- www.researchgate.net/profile/Carlo-Grlj
- https://orcid.org/0000-0001-5939-0275

List of publications

Article I The Impact of Numerical Parameters on the Resistance Characteristics of a Container Ship at the Model and Full Scale

Carlo Giorgio Grlj, Nastia Degiuli, Ivana Martić. 2023. The Impact of Numerical Parameters on the Resistance Characteristics of a Container Ship at the Model and Full Scale. Journal of marine science and engineering, 11(9), 1672.
https://doi.org/10.3390/jmse11091672

Article II Numerical Study of Scale Effects on Open Water Propeller Performance

Carlo Giorgio Grlj, Nastia Degiuli, Andrea Farkas, Ivana Martić. 2022. Numerical Study of Scale Effects on Open Water Propeller Performance. Journal of marine science and engineering, 10(8), 1132.
https://doi.org/10.3390/jmse10081132

Article III Assessment of the effect of speed and scale on the total resistance and its components for a bulk carrier

Carlo Giorgio Grlj, Nastia Degiuli, Ivana Martić. 2025. Assessment of the effect of speed and scale on the total resistance and its components for a bulk carrier. Results in engineering, 26, 105095.
https://doi.org/10.1016/j.rineng.2025.105095

Article IV Scale effects on the resistance and propulsion characteristics of the Japan Bulk Carrier

Carlo Giorgio Grlj, Nastia Degiuli, Ivana Martić. 2025. Scale effects on the resistance and propulsion characteristics of the Japan Bulk Carrier. Ocean engineering, 339(1), 122059.
https://doi.org/10.1016/j.oceaneng.2025.122059

Article V A full-scale numerical investigation of a containership resistance and propulsion characteristics at different trim angles

Carlo Giorgio Grlj, Nastia Degiuli, Ivana Martić. 2026. A full-scale numerical investigation of a containership resistance and propulsion characteristics at different trim angles. Results in engineering, 30, 110318. https://doi.org/10.1016/j.rineng.2026.110318

Article VI Experimental and numerical assessment of the effect of speed and loading conditions on the nominal wake of a containership

Carlo Giorgio Grlj, Nastia Degiuli, Ivana Martić. 2024. Experimental and numerical assessment of the effect of speed and loading conditions on the nominal wake of a containership. Brodogradnja, 75(4), 75405. https://doi.org/10.21278/brod75405

Article VII Experimental assessment of the hydrodynamic characteristics of a bulk carrier in off-design conditions

Nastia Degiuli, Ivana Martić, Andrea Farkas, Marta Pedišić Buča, Roko Dejhalla, **Carlo Giorgio Grlj**. 2023. Experimental assessment of the hydrodynamic characteristics of a bulk carrier in off-design conditions. Ocean engineering, 280, 114936. https://doi.org/10.1016/j.oceaneng.2023.114936

Article VIII Benchmark study on resistance and propulsion characteristics of a 6750-TEU container ship

Nastia Degiuli, Ivana Martić, Marta Pedišić Buča, **Carlo Giorgio Grlj**. 2025. Benchmark study on resistance and propulsion characteristics of a 6750-TEU container ship. Ocean engineering, 319, 120300. https://doi.org/10.1016/j.oceaneng.2025.120300

Article IX The effect of loading conditions and ship speed on the wind and air resistance of a containership

Carlo Giorgio Grlj, Nastia Degiuli, Željko Tuković, Andrea Farkas, Ivana Martić. 2023. The effect of loading conditions and ship speed on the wind and air resistance of a containership. Ocean engineering, 273, 113991. https://doi.org/10.1016/j.oceaneng.2023.113991

Article X Optimization of marine propeller characteristics for maximum open water efficiency using an ANN-GA tool trained on experimental data

Carlo Giorgio Grlj, Nastia Degiuli, Ivana Martić, Marta Pedišić Buča. 2026. Optimization of marine propeller characteristics for maximum open water efficiency using an ANN-GA tool trained on experimental data. Brodogradnja, 77(4), 77405.
https://doi.org/10.21278/brod77405

Article I

Article published by MDPI in Journal of marine science and engineering on 25 August 2023, available online: https://www.mdpi.com/2077-1312/11/9/1672

Journal of
Marine Science and Engineering

MDPI

Article

The Impact of Numerical Parameters on the Resistance Characteristics of a Container Ship at the Model and Full Scale

Carlo Giorgio Grlj, Nastia Degiuli * and Ivana Martić

Faculty of Mechanical Engineering and Naval Architecture, University of Zagreb, Ivana Lučića 5, 10000 Zagreb, Croatia; carlo.g.grlj@fsb.hr (C.G.G.); ivana.martic@fsb.hr (I.M.)
* Correspondence: nastia.degiuli@fsb.hr

Abstract: Computational Fluid Dynamics (CFD) is a powerful tool used to predict the resistance characteristics of a ship. However, it is important to determine the numerical and modelling errors to assure accurate results. The aim of this study is the investigation of the impact of different numerical parameters on the total resistance, wave pattern and ship motion in numerical simulations at the model and full scale. These include the turbulence model and discretization schemes for convection, gradient and temporal terms within the governing equations. The numerical model used in numerical simulations is based on Reynolds Averaged Navier-Stokes (RANS) equations which are discretized using the Finite Volume Method (FVM). To locate and track the free surface, the Volume of Fluid (VOF) method is employed. The Grid Convergence Index (GCI) method is used for the verification study. The obtained results show that the selection of the discretization scheme for temporal term does not have impact on the median value of the total resistance and that the first-order scheme assures faster convergence in numerical simulations at the full scale. A higher portion of the frictional resistance in the total resistance is obtained with numerical simulations at the model scale in comparison to the full scale.

Keywords: CFD; discretization scheme; turbulence model; container ship; resistance test

check for updates

Citation: Grlj, C.G.; Degiuli, N.; Martić, I. The Impact of Numerical Parameters on the Resistance Characteristics of a Container Ship at the Model and Full Scale. *J. Mar. Sci. Eng.* **2023**, *11*, 1672. https://doi.org/10.3390/jmse11091672

Academic Editor: Kostas Belibassakis

Received: 20 July 2023
Revised: 22 August 2023
Accepted: 22 August 2023
Published: 25 August 2023

Copyright: © 2023 by the authors. Licensee MDPI, Basel, Switzerland. This article is an open access article distributed under the terms and conditions of the Creative Commons Attribution (CC BY) license (https://creativecommons.org/licenses/by/4.0/).

1. Introduction

Nowadays, Computational Fluid Dynamics (CFD) is a commonly used tool for the prediction of flow around the ship and ship hydrodynamic characteristics, since computational power has been increasing continuously. The main advantage of CFD simulations is that it can reduce the required number of expensive towing tank experiments. Another benefit of the numerical simulations over the towing tank experiments is the possibility of avoiding the extrapolation methods by performing full-scale CFD simulations [1]. Recently, Orych et al. [2] conducted a validation study for the delivered power estimated with numerical simulations based on Reynolds Averaged Navier-Stokes (RANS) equations coupled with a body force propeller method for modelling the effects of a rotating propeller, which is based on the lifting line theory. Numerical uncertainty was determined for numerical simulations at the model and full scale, while the validation was based on sea trial results. The authors obtained an average comparison error between the numerically obtained and sea trial results of about 1%, which is considerably lower than the validation uncertainty equal to 7%. Saydam et al. [3] performed numerical simulations of the resistance, open water and self-propulsion tests for a case of a tanker in order to quantify the numerical simulation uncertainties. The authors found an error of 4% for the prediction of the total resistance, while larger uncertainties were obtained for torque predictions and, consequently, the delivered power.

Degiuli et al. [4] investigated the influence of slow steaming on carbon dioxide (CO_2) emissions by using full-scale CFD simulations based on RANS equations for the determination of resistance and propulsion characteristics. Other aspects, such as the influence

of biofouling on resistance, were studied by Demirel et al. [5]. Song et al. [6] emphasized the importance of including the roughness effects within the CFD simulations for the determination of the frictional and viscous resistance of different hull forms. Feng et al. [7] conducted CFD simulations of a KRISO container ship (KCS) in different water depths for the determination of the total resistance and dynamic sinkage. The numerical results were validated against the benchmark experimental results, and the comparison error was between 1% and 4% with larger errors obtained for the model scale numerical simulations. Full-scale CFD simulations were validated by Niklas and Pruszko [8], and the obtained relative deviation of total resistance in calm water was from −10% to 4% compared to the sea trial data and extrapolated towing tank results. The authors emphasized the importance of determining the form factor, which can vary depending on the method used, and thus, it can have a great influence on the ship resistance predictions. Terziev et al. [1] used CFD simulations to investigate the influence of ship speed and scale on the form factor and concluded that it depends on the Froude number for very low ship speeds, while larger differences in the form factor were obtained for different scales and turbulence models. Dogrul [9] pointed out scale effects on the propulsion characteristics, such as nominal wake, thrust deduction fraction, and open-water propeller and propulsion efficiencies for the case of a Joubert BB2 submarine.

Although full-scale CFD simulations may be a good alternative to towing tank tests, since the extrapolation of the measured values is avoided, there is still a need for a more systematic and comprehensive sea trials in order to validate the numerical simulations at the full scale for the determination of the ship resistance characteristics and the nominal wake [10]. In addition, there is a need to investigate the influence of numerical parameters such as the discretization schemes for solving the convection, gradient and temporal terms within the governing equations. Such a study was conducted by Andrun et al. [11], where the authors assessed the effect of different schemes for solving the gradient terms within the Volume of Fluid (VOF) method by conducting numerical simulations of the flow around the model of the Wigley hull. It was concluded that second-order schemes have to be used on realistic hull forms, for which the non-linear effects are more pronounced, to determine the resistance and wave elevation more accurately. A more recent study was conducted by Huang et al. [12], in order to determine the ideal numerical setup for full-scale numerical simulations. The authors showed that the second-order scheme should be used for spatial discretization, while for temporal discretization, either first or second-order schemes can be applied. The effect of different draughts on the hydrodynamic characteristics was investigated by Farkas et al. [13]. Based on the obtained results, the authors concluded that although RSM turbulence model is the most accurate one, by using the Realizable $k-\varepsilon$ (RKE), satisfactory agreement with the extrapolated towing tank results can be obtained. Degiuli et al. [14] numerically investigated the impact of the bulbous bow on the total resistance of a yacht and validated the results by comparing them with the towing tank results. Within the study, the authors achieved satisfactory agreement with the experimentally obtained values for total resistance using different turbulence models.

In this study, numerical simulations of viscous flow around the hull of a container ship are systematically performed in order to assess the effects of different discretization schemes and turbulence models on the hydrodynamic performance in calm water. The effect of numerical parameters are investigated at the model and full scale. The post-Panamax 6750-TEU container ship is chosen since the geometry and inertial properties are available in the literature [15]. An extensive verification study for grid size and time step is performed using the Grid Convergence Index (GCI) method. For numerical simulations at the model scale, a validation study is conducted by comparing the numerical results against the measured values from towing tank tests. The paper is organized as follows. The description of the container ship used in the numerical simulations is provided in Section 2. The mathematical background, the numerical setup and an overview of the verification and validation studies are given in Section 3. The results are discussed in Section 4, and

finally, the conclusions drawn from the comprehensive numerical study are summarized in Section 5.

2. Case Study

The post-Panamax 6750-TEU container ship is selected as a case study. Table 1 shows the geometrical and inertial properties of the model in scale ($\lambda = 35.18$) and full-scale container ship [15], while Figure 1 shows the 3D model used in the simulations.

Table 1. Post-Panamax 6750-TEU container ship data.

Property	Full Scale	Model Scale
λ, -	1	35.18
L_{OA}, m	300.891	8.553
L_{PP}, m	286.6	8.147
L_{WL}, m	281.3	7.996
T, m	11.98	0.341
B, m	40	1.137
Δ, t	85,562.7	1.965
KM, m	18.662	0.531
GM, m	2.1	0.06
KG, m	16.562	0.471
L_{CG} from AP, m	138.395	3.934
k_{xx}, m	14.6	
k_{yy}, m	70.144	
k_{zz}, m	70.144	



Figure 1. Geometry of the post-Panamax 6750-TEU container ship.

The towing tank experiments were conducted at the Brodarski Institute in Zagreb [16]. The resistance tests were carried out in a large towing tank of a length of 276 m, a width of 12.5 m, and a depth of 6 m. The ship model was made of wood at a scale of $\lambda = 35.18$. The resistance tests were conducted at 14 speeds in the range from 12 to 25 knots corresponding to full-scale ship. For purpose of the validation study, the experimental results of the resistance test at 2.168 m/s are used, corresponding to 25 knots for the full-scale ship.

3. Methods

In this study, numerical simulations based on RANS equations are conducted. The Finite Volume Method (FVM) is used for the discretization of the governing equations. A multiphase flow model based on the Eulerian approach; i.e., the VOF method is used for locating and tracking the free surface. To maintain a sharp interface between two fluids, High-Resolution Interface Capturing (HRIC) scheme is used. The Dynamic Fluid Body Interaction (DFBI) model with two degrees of freedom is used to predict the trim and sinkage.

3.1. Mathematical Model

The commercial software package STAR-CCM+ [17] is used in this study. The mathematical model is based on the RANS equations, which are derived from the conservation of mass and momentum laws. For incompressible, unsteady case the RANS equations read as follows:

$$\frac{\partial \bar{u}_i}{\partial x_i} = 0 \tag{1}$$

$$\rho \frac{\partial \bar{u}_i}{\partial t} + \rho \frac{\partial}{\partial x_j}\left(\bar{u}_i \bar{u}_j + \overline{u_i' u_j'}\right) = -\frac{\partial \bar{p}}{\partial x_i} + \frac{\bar{\tau}_{ij}}{\partial x_j} \tag{2}$$

where ρ is the fluid density, $\bar{u}_i$ is the averaged Cartesian components of the velocity vector, $\rho\overline{u_i' u_j'}$ is the Reynolds Stress Tensor (RST), and $\bar{p}$ is the mean pressure. The mean viscous stress tensor $\bar{\tau}_{ij}$ is defined by:

$$\bar{\tau}_{ij} = \mu\left(\frac{\partial \bar{u}_i}{\partial x_j} + \frac{\partial \bar{u}_j}{\partial x_i}\right) \tag{3}$$

where μ is the dynamic viscosity of the fluid. The turbulence models are then used to close the system of Equations (1) and (2) to be able to solve them.

3.2. Turbulence Models

Three turbulence models are used in this study: RKE, Shear Stress Transport $k-\omega$ (SSTKO) and RSM. The RANS turbulence models are based on the modelling of the RST. The RKE and SSTKO turbulence models belong to the group of eddy viscosity models, which are based on the similarity between the molecular gradient-diffusion process and turbulent motion. These types of turbulence models use the Boussinesq approximation to model the RST as follows:

$$-\rho\overline{u_i' u_j'} = \mu_t\left(\frac{\partial \bar{u}_i}{\partial x_j} + \frac{\partial \bar{u}_j}{\partial x_i}\right) - \frac{2}{3}\rho k \delta_{ij} \tag{4}$$

where μ_t is the turbulent eddy viscosity, and k is the turbulence kinetic energy.

The RSM turbulence model calculates the components of the RST directly. Thus, it has the potential to predict complex turbulent fluid flows more accurately by considering the anisotropy of the RST, but at the cost of more computational power. More details regarding the applied turbulence models can be found in the literature [13].

3.3. Realizable $k-\varepsilon$ (RKE) Two-Layer

The Realizable $k-\varepsilon$ Two-Layer turbulence model solves one equation for the turbulent kinetic energy k and one for the turbulent dissipation rate ε. The eddy viscosity is calculated as follows:

$$\mu_t = \rho C_\mu \frac{k^2}{\varepsilon} \tag{5}$$

where C_μ is the model coefficient defined with the following equation:

$$C_\mu = \frac{1}{A_0 + A_S U^* \frac{k}{\varepsilon}} \tag{6}$$

where $A_0 = 4$ and A_S is given by:

$$A_S = \sqrt{6}\cos\phi \tag{7}$$

$$\phi = \frac{1}{3}\arccos\left(\sqrt{6}W\right) \tag{8}$$

$$W = \frac{S_{ij}S_{jk}S_{ki}}{\left(\sqrt{S_{ij}S_{ij}}\right)^3} \tag{9}$$

and U^* is defined as:

$$U^* = \sqrt{S_{ij}\cdot S_{ij} + W_{ij}\cdot W_{ij}} \tag{10}$$

The strain rate tensor is given by the equation:

$$S_{ij} = \frac{1}{2}\left(\frac{\partial u_i}{\partial x_j} + \frac{\partial u_i^T}{\partial x_j}\right) \tag{11}$$

and the rotation rate tensor by:

$$W_{ij} = \frac{1}{2}\left(\frac{\partial u_i}{\partial x_j} - \frac{\partial u_i^T}{\partial x_j}\right) \tag{12}$$

The transport equations for k and ε are defined as:

$$\frac{\partial}{\partial t}(\rho k) + \frac{\partial}{\partial x_i}(\rho k \bar{u}_i) = \frac{\partial^2 k}{\partial x_i^2}\left(\mu + \frac{\mu_t}{\sigma_k}\right) + f_c G_k + G_b - \mathrm{Y}_M - \\ - \rho(\varepsilon - \varepsilon_0) + S_k \tag{13}$$

$$\frac{\partial}{\partial t}(\rho \varepsilon) + \frac{\partial}{\partial x_i}(\rho \varepsilon \bar{u}_i) = \frac{\partial^2 \varepsilon}{\partial x_i^2}\left(\mu + \frac{\mu_t}{\sigma_\varepsilon}\right) + \frac{1}{T_\varepsilon}C_{\varepsilon 1}(f_c Sk + C_{\varepsilon 3}G_b) - \\ - C_{\varepsilon 2}f_2\rho\left(\frac{\varepsilon}{T_\varepsilon} - \frac{\varepsilon_0}{T_0}\right) + S_\varepsilon \tag{14}$$

where $\bar{u}_i$ is the averaged velocity vector, σ_k and σ_ε are the turbulent Schmidt numbers, f_c is the curvature correction factor, G_k is the turbulent production term, G_b is the buoyancy production term, ε_0 is the ambient turbulence value that counteracts turbulence decay, Y_M is the dilatation dissipation, C_{ε_1}, C_{ε_2} and C_{ε_3} are the model depending coefficients, S_k and S_ε are the user-defined source terms, and S is the modulus of the mean strain tensor.

3.4. Shear Stress Transport $k-\omega$ (SSTKO)

The $k-\omega$ turbulence model is a two-equation model that solves transport equations for the turbulent kinetic energy k and another for the specific dissipation ω:

$$\frac{\partial}{\partial t}(\rho k) + \frac{\partial}{\partial x_i}(\rho k \bar{u}_i) = \frac{\partial^2 k}{\partial x_i^2}(\mu + \sigma_k \mu_t) + G_k + G_{nl} + G_b - \\ - \rho\beta^* f_{\beta^*}(\omega k - \omega_0 k_0) + S_k \tag{15}$$

$$\frac{\partial}{\partial t}(\rho \omega) + \frac{\partial}{\partial x_i}(\rho \omega \bar{u}_i) = \frac{\partial^2 \omega}{\partial x_i^2}(\mu + \sigma_\omega \mu_t) + G_\omega + D_\omega - \rho\beta f_\beta(\omega^2 - \omega_0^2) + S_\omega \tag{16}$$

where σ_k, σ_ω, β and β^* are the model depending coefficients, G_{nl} is the non-linear production term, f_β is the free-shear modification factor, f_{β^*} is the vortex-stretching modification factor, and finally, k_0 and ω_0 are the ambient values that counteract turbulence decay. Menter [18] modified the Standard $k-\omega$ model, which blends the $k-\varepsilon$ model in the

far-field with the $k-\omega$ model near the wall. The turbulent eddy viscosity is given with the following equation:

$$\mu_t = \rho k T \tag{17}$$

where T is the turbulent time scale given with the equation:

$$T = \min\left(\frac{\alpha^*}{\omega}, \frac{a_1}{SF_2}\right) \tag{18}$$

where α^* and a_1 are the model coefficients, and F_2 is the blending function coefficient that depends on the distance to the wall.

3.5. Reynolds Stress Model (RSM)

The Reynolds Stress Model consists of solving the transport equation for RST. The transport equation is defined as:

$$\begin{aligned}\frac{\partial}{\partial t}(\rho R_{ij}) + \frac{\partial}{\partial x_i}(\rho R_{ij}\bar{u}_i) = \frac{\partial}{\partial x_m}\left[\left(\mu + \frac{\mu_t}{\sigma_k}\right)\frac{\partial R_{ij}}{\partial x_m}\right] + P_{ij} + G_{ij} - \\ - \frac{2}{3}\Upsilon_M + \phi_{ij} - \rho\varepsilon_{ij} + S_R\end{aligned} \tag{19}$$

where P_{ij} is the turbulent production term, G_{ij} is the buoyancy production term, ϕ_{ij} is the pressure–strain tensor, and ε_{ij} is the turbulent dissipation rate tensor. This model requires seven equations to be solved, six equations for the RST components and one equation for the isotropic turbulent dissipation. The Quadratic Pressure–Strain model was used within the simulations with high y^+ wall treatment to model the pressure–strain term.

3.6. Computational Domain and Boundary Conditions

An unstructured hexahedral mesh is used for the discretization of the computational domain. Only half of the computational domain is created, since the flow is symmetric with respect to the ship symmetry plane. The domain boundaries are placed at a distance to avoid their influence on the flow around the ship hull and consequently on the obtained results. The inlet and bottom boundaries are placed at $2L_{PP}$ from the ship, the top boundary is placed at L_{PP} above the waterline, while the outlet boundary is placed at $4L_{PP}$ behind the ship. The side boundary is placed at $2.5L_{PP}$ to avoid reflection of the waves. Boundary conditions are set as the VOF wave velocity at the inlet, top and bottom boundaries. The pressure outlet is assigned at the outlet boundary, while both sides of the domain are defined as symmetry planes. The no-slip wall boundary condition is set at the hull surface. The computational domain with the respective boundary conditions and its main dimensions is given in Figure 2. In order to prevent wave reflection against the domain boundaries, the wave damping layer approach is used in the numerical simulations. The wave damping is applied at the inlet, outlet and side boundaries.

Different regions around the ship are carefully discretized. The grid is more refined in the area where the free surface is expected to be located as well as the Kelvin wake region behind the ship, following the ITTC recommendations [19]. The region close to the ship hull is refined with more attention given to the bow and stern regions.

The prism layers are carefully generated so that the non-dimensional wall distance y^+ is in the range $30 < y^+ < 100$, i.e., the log-law region [20]. The approximate distance between the wall and the centre of the first prism layer near the wall is calculated as:

$$y = \frac{y^+ L}{0.172 Re^{0.9}} \tag{20}$$

where Re is the Reynolds number. The obtained non-dimensional wall distance y^+ is within the limits, as shown in Figure 3, meaning that the application of wall functions is justified. Figure 4 shows the fine grid with the described refinements, which is used

within the numerical simulations. Figure 5 shows a detailed view of the stern and bow regions. It can be noticed that the prism layers are carefully created to obtain a smooth transition between the prism layers and the rest of the grid. The stretching factor for the prism layers is about 1.5, and the number of prism layers depends on the scale for which the numerical simulations are conducted. A lower number of prism layers are created at the model scale and a higher number at the full scale to achieve a prism layer thickness that assures a smooth transition from prism layers to the rest of the grid. The prism layers are not generated on the deck and transom stern surfaces.

The distributions of the pressure coefficients along the hull surface obtained from numerical simulations at the model and full scale are shown in Figure 6. Lower pressure coefficients are achieved in the bulbous bow region for the model scale in comparison to full scale.

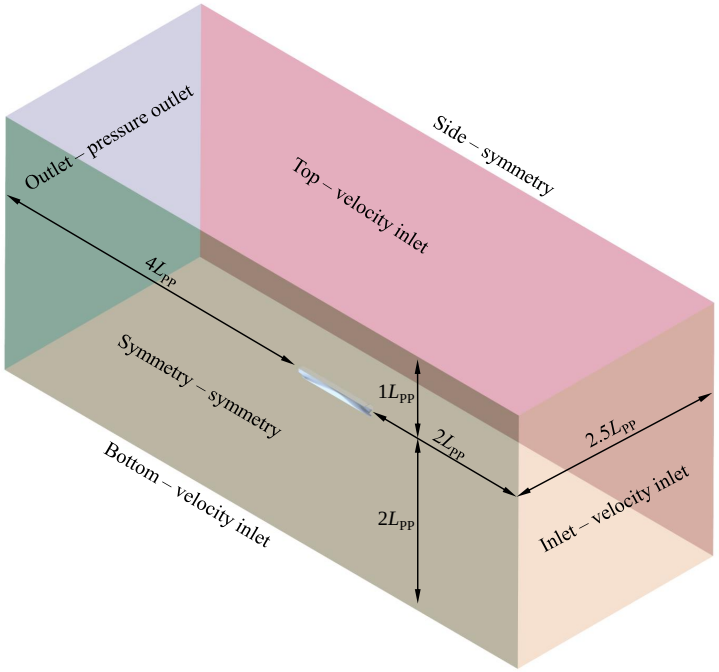


Figure 2. Dimensions and boundaries of the computational domain for the free surface simulations.

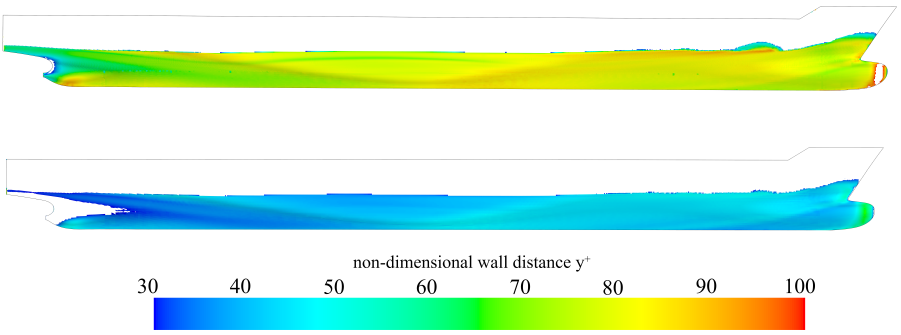


Figure 3. Distribution of the non-dimensional wall distance y^+ on the full scale (**top**) and model scale (**bottom**) hull surface.

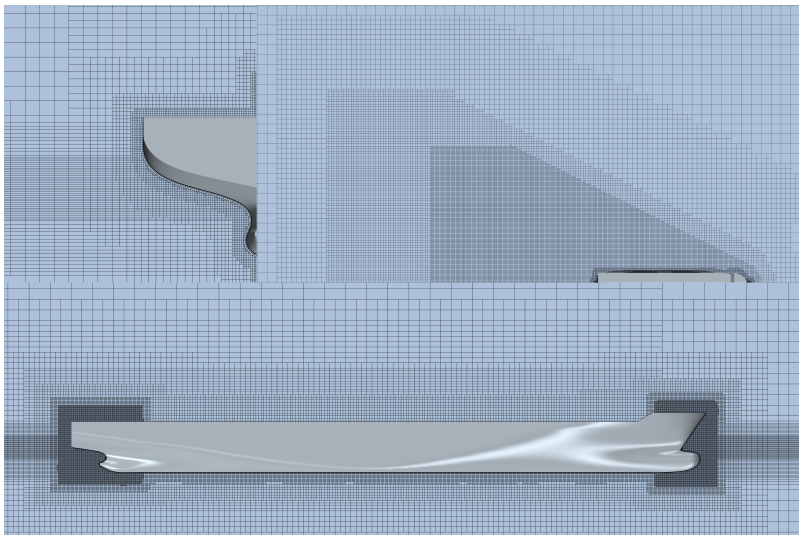


Figure 4. Fine grid with refinements.

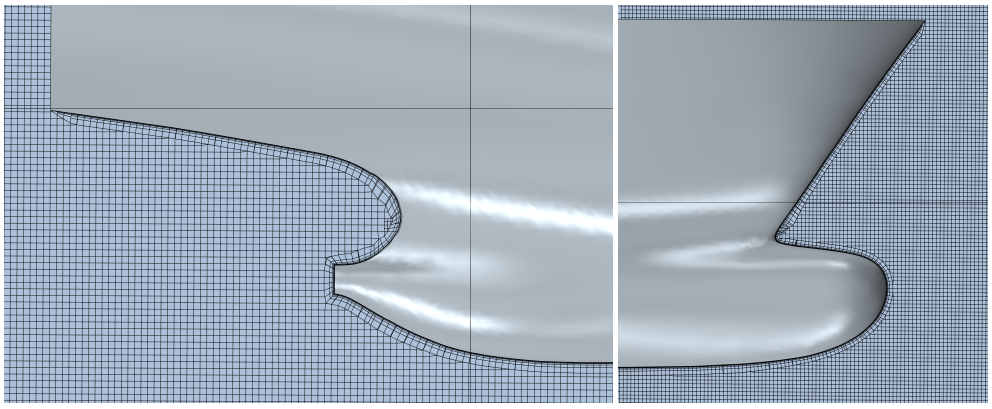


Figure 5. Detailed view of the prism layers at the stern (**left**) and bow (**right**).

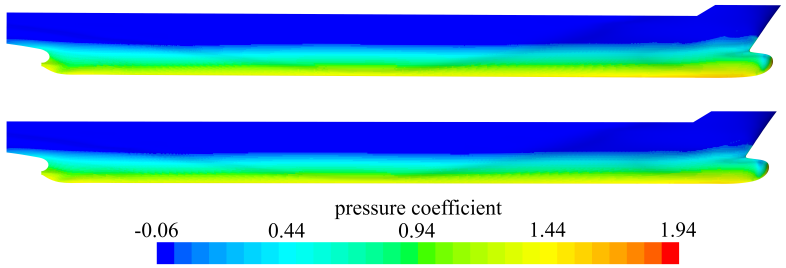


Figure 6. Distribution of the pressure coefficient on the hull surface at full scale (**top**) and model scale (**bottom**).

In the numerical simulations, a speed of 25 knots corresponding to the full-scale ship is used. Froude similarity is used to calculate the speed for the numerical simulations at the model scale.

3.7. The Verification And Validation Study

The GCI method is used for the verification study, which is based on the Richardson extrapolation [21]. This method was successfully used in [20,22,23]. The first step is to calculate the apparent order of the method p using the following equations:

$$p = \frac{1}{\ln r_{21}} \cdot \left| \ln \left| \frac{\varepsilon_{32}}{\varepsilon_{21}} \right| + q(p) \right| \tag{21}$$

$$q(p) = \ln\left(\frac{r_{21}^{p} - s}{r_{32}^{p} - s}\right) \tag{22}$$

$$s = 1 \cdot \mathrm{sgn}\left(\frac{\varepsilon_{32}}{\varepsilon_{21}}\right) \tag{23}$$

where r is the grid refinement ratio, and ε is defined as $\varepsilon_{ij} = \phi_i - \phi_j$, with ϕ being the solutions. The order of the method p is calculated by solving the Equations (21)–(23) iteratively.

Extrapolated values and the approximate and extrapolated relative errors are calculated using the Equations (24)–(26), respectively:

$$\phi_{\mathrm{ext}}^{21} = \frac{r_{21}^{p}\phi_1 - \phi_2}{r_{21}^{p} - 1} \tag{24}$$

$$e_{\mathrm{a}}^{21} = \left|\frac{\phi_1 - \phi_2}{\phi_1}\right| \tag{25}$$

$$e_{\mathrm{ext}}^{21} = \left|\frac{\phi_{\mathrm{ext}}^{21} - \phi_1}{\phi_{\mathrm{ext}}^{21}}\right| \tag{26}$$

Finally, GCI for fine grid can be calculated with following equation:

$$GCI_{\mathrm{fine}}^{21} = \frac{1.25 e_{\mathrm{a}}^{21}}{r_{21}^{p} - 1} \tag{27}$$

The convergence condition R is calculated with the following equation:

$$R = \frac{\varepsilon_{21}}{\varepsilon_{32}} \tag{28}$$

Convergence conditions R are used to evaluate the obtained extrapolated values and are defined as:

- Monotonic convergence: $0 < R < 1$;
- Oscillatory convergence: $R < 0$;
- Divergence: $R > 1$.

The described method can be used for the calculation of the uncertainty due to time step [24]. Fine grid is used, and three time steps are varied in the numerical simulations for the determination of the uncertainty due to time step.

3.8. Discretization Schemes

The RANS equations are discretized in order to be able to numerically solve them. More precisely, the governing Partial Differential Equations (PDE) are transformed into a system of algebraic equations. In this study, different discretization schemes for spatial and temporal discretization are used, and the obtained results are compared. Specifically, the convection terms are solved using three discretization schemes, while the gradient and temporal terms are solved using two discretization schemes.

The convection terms in the segregated flow and turbulence models can be solved using different schemes within the software package STAR-CCM+. The second-order scheme is used for the verification and validation study. Thereafter, first- and third-order schemes are investigated. The results obtained by the first and second-order discretization schemes for gradient terms are then compared. Finally, the investigated parameters, i.e., discretization schemes for gradient, convection terms and temporal discretization are all set as first and second order. An overview of the different combinations used in numerical simulations can be found in Section 4.

4. Results and Discussion

4.1. The Verification and Validation Study

The verification study is performed for time step and grid size at the model and full scale. Time steps are selected according to the ITTC recommendations [19] in the range $0.005L_{WL}/v - 0.01L_{WL}/v$. The largest time step used in this study is $0.02L_{WL}/v$, and hence, the refinement ratio is equal to 2, and consequently, the iterative procedure for obtaining the order of the method p is avoided.

The details of the used grid resolutions are presented in Table 2. The grid spacing value h is defined as:

$$h = \sqrt[3]{\frac{1}{N}\sum_{i=1}^{N}(\Delta V_i)} \tag{29}$$

where N is the total number of cells in the grid, and V_i is the volume of the i-th cell.

Table 2. Details of the used grid resolutions.

Index	N		h, m	
	Model Scale	Full Scale	Model Scale	Full Scale
1	2.3 M	3.7 M	0.189	7.70
2	1.0 M	2.3 M	0.248	8.99
3	0.4 M	1.0 M	0.327	11.99

Tables 3 and 4 show all the calculated variables and the estimation of errors for two verification studies at the model and full scales. The approximated and extrapolated relative errors are presented alongside the GCI. Monotonic convergence is obtained for the full-scale numerical simulations and oscillatory convergence for both verification studies at the model scale. The obtained numerical uncertainty is below 2% for all cases, which shows that the fine grid size and time step are adequate for the remaining numerical simulations. It is worth noting that the obtained GCI for full-scale numerical simulations is slightly higher in comparison to model scale numerical simulations. One of the reasons is the grid setup within the numerical simulations.

Table 3. Verification study for the time step.

Parameter	Model Scale	Full Scale
ε_{32}	−7.906 N	80.524 kN
ε_{21}	1.259 N	31.774 kN
r_{32}	2	2
r_{21}	2	2
R	−0.159	0.395
p	2.650	1.342
e_{a}^{21}	0.014%	0.01%
e_{ext}^{21}	0.003%	0.01%
GCI_{fine}^{21}	0.34%	1.13%

Table 4. Verification study for the grid size.

Parameter	Model Scale	Full Scale
ε_{32}	1.897 N	80.756 kN
ε_{21}	−0.013 N	9.885 kN

Table 4. *Cont.*

Parameter	Model Scale	Full Scale
r_{32}	1.319	1.335
r_{21}	1.314	1.167
R	−0.006	0.123
p	18.142	6.228
e_{a}^{21}	0.0001%	0.44%
e_{ext}^{21}	0.000001%	0.27%
GCI_{fine}^{21}	0.0001%	0.34%

The obtained numerical results for the model scale are validated against the measured values obtained by the towing tank tests. To compare the numerical and experimental results, the relative deviation is calculated as follows:

$$RD = \frac{\phi_{\mathrm{CFD}} - \phi_{\mathrm{EXP}}}{\phi_{\mathrm{EXP}}} \cdot 100\% \tag{30}$$

where ϕ_{CFD} and ϕ_{EXP} are numerically and the experimentally obtained values, respectively. Table 5 shows the numerically and experimentally obtained total resistance and the calculated relative deviations for the speed of 25 knots and three turbulence models. It can be seen that the relative deviations are quite high, but that is in accordance with a previous study conducted by Farkas et al. [13], where the highest relative deviations are obtained using the SSTKO turbulence model. Similar results were shown in a review paper by Pena and Huang [25], where the authors showed that relative deviations of 10% can be expected with eddy viscosity turbulence models when wall functions are applied. It is important to note that the numerical simulations are performed for a smooth hull surface, so underprediction of the total resistance is expected. Thus, although the RKE turbulence model shows the lowest relative deviation, it overpredicts the total resistance. In conclusion, the SSTKO turbulence model is selected since it is the best compromise between the computational time and the accuracy of the results.

Table 5. Validation study for the total resistance.

Turbulence Model	$R_{\mathrm{TM,CFD}}$, N	$R_{\mathrm{TM,EFD}}$, N	RD, %
RKE	96.617	94.994	1.709
SSTKO	87.780		−7.595
RSM	91.352		−3.834

4.2. Turbulence Models

In Section 4.2, the SSTKO turbulence model is compared to the RKE and RSM models. The numerical simulations with the SSTKO turbulence model were conducted until the total resistance converged. After the stable oscillations of the total resistance were reached, the simulations were performed for an additional 200 s for the full scale and around 100 s for the model scale. The medians of these oscillations are calculated, and the obtained total resistances are shown in Table 6.

Table 6. Total resistance obtained with RKE, SSTKO and RSM turbulence model.

Turbulence Model	R_{TS}, kN	R_{TM}, N
RKE	2321.11	96.62
SSTKO	2302.87	87.73
RSM	2356.26	91.35

Figure 7 shows the values of the total resistance as a function of physical time for three turbulence models. The oscillations are caused partly by the trim and sinkage of

the ship. The total resistance obtained with the SSTKO turbulence model at the full scale is slightly lower than for RSM and RKE models, which predict similar results. From Table 6 and Figure 7 it can be seen that the RSM turbulence model yields the highest total resistance at the full scale. Also, the trend of the total resistance curve is almost the same for all three turbulence models. It should be noted that the median values of total resistance obtained by all turbulence models are similar. At the model scale, the trend of the total resistance curve varies significantly with the turbulence model, where the RKE predicts significantly higher values in comparison to the SSTKO and RSM turbulence models. One of the reasons for this is that the numerical setups are different regarding the discretization of the boundary layer, with less prism layers generated at the model scale when compared to the full scale. The reason for the higher values obtained with the RKE turbulence model is that the eddy viscosity is calculated differently than when using the SSTKO turbulence model. This effect is visible at the model scale since the boundary layer is relatively larger when compared to the full scale.

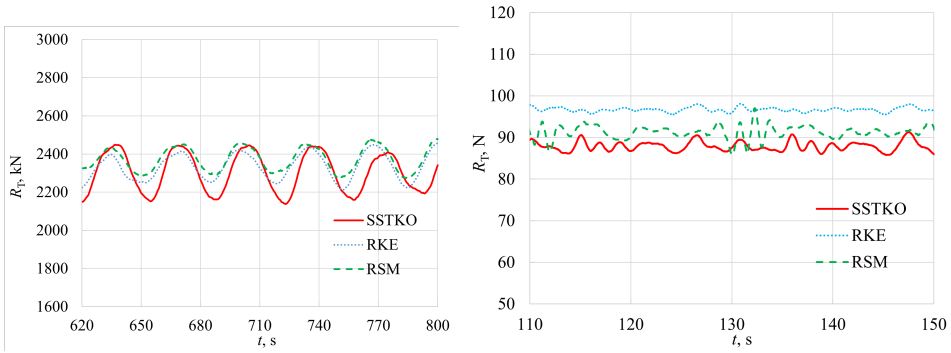


Figure 7. Comparison of total resistance obtained using three turbulence models at full scale (**left**) and model scale (**right**).

Figure 8 shows the sinkage and trim as a function of the physical time at the full scale and model scale. The sinkage obtained with numerical simulations at the model scale is scaled with $\lambda = 35.18$ for the comparison with full-scale results. It can be seen that trim does not depend on the chosen turbulence model at the full scale, while sinkage is slightly lower for the RSM turbulence model. At the model scale, the RSM turbulence model predicts lower sinkage and higher trim values. The sinkage and trim obtained with the RKE and SSTKO turbulence model are nearly the same at the full and model scale. The sinkage and trim obtained using the RSM turbulence model at the model scale are similar to the results at the full scale. However, the trim is lower and sinkage is higher when using the SSTKO and RKE turbulence models at the model scale in comparison to the full scale.

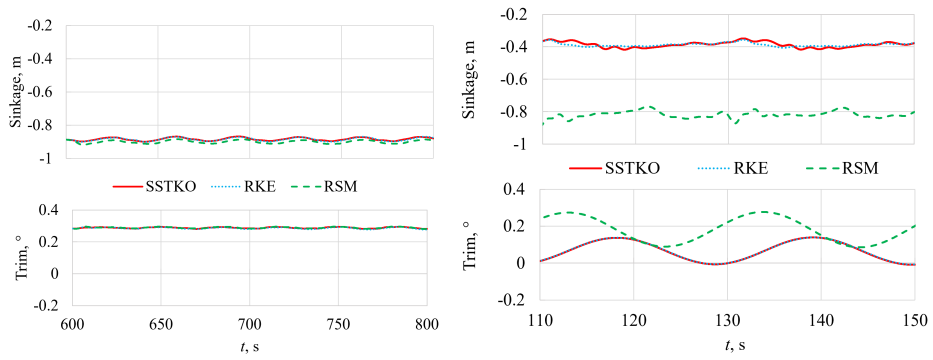


Figure 8. Sinkage and trim values as a function of physical time for three turbulence models at full scale (**left**) and model scale (**right**).

Figure 9 shows the wave elevations along the hull and Figure 10 on the longitudinal cuts located at $B/4$, $B/2$ and B from the centreline of the ship, obtained with different turbulence models at the model and full scale. The wave elevations are presented in the non-dimensional form by dividing the x-axis and wave elevations η with length between perpendiculars L_{PP}. The differences between turbulence models are not significant, although at both scales, there are some discrepancies near the bow. At the full scale, the RSM and SSTKO turbulence model predict similar wave elevations, while the RKE yields slightly different results. Also, at the full scale, the RKE turbulence model predicts a higher wave elevation at longitudinal distance between $0.2L_{PP}$ and $0.3L_{PP}$. Similar results are obtained using the RSM and RKE turbulence model at the model scale but with lower values near the bow in comparison to the full scale.

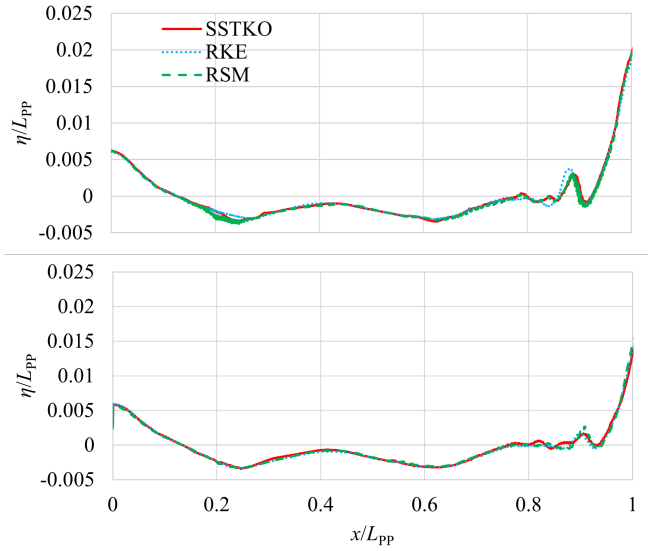


Figure 9. Wave elevations along the hull at full scale (**top**) and model scale (**bottom**) for different turbulence models.

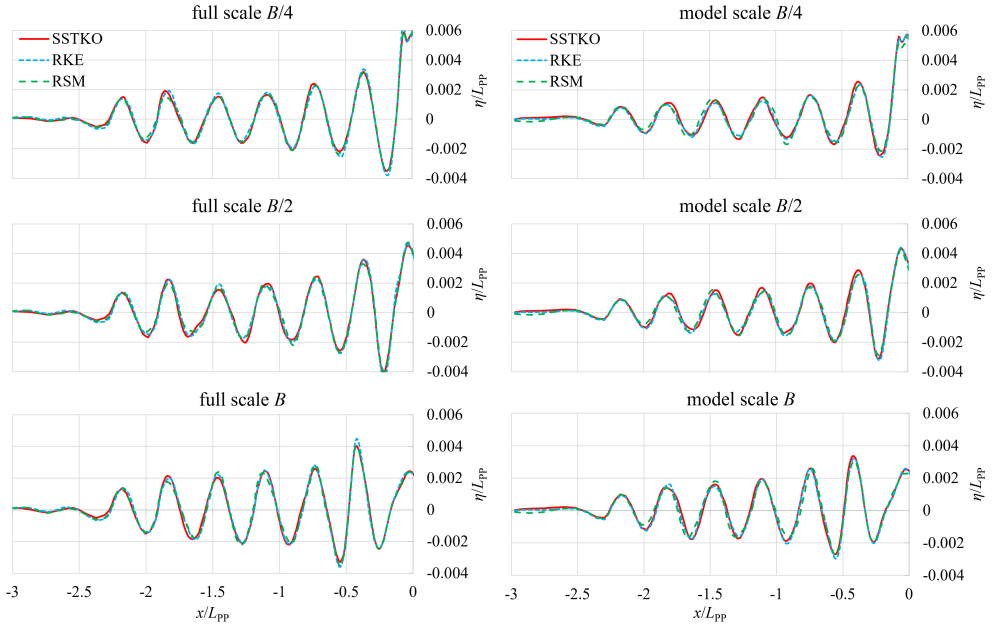


Figure 10. Wave elevations behind the stern at longitudinal cuts $B/4$, $B/2$ and B from the centreline of the ship obtained with numerical simulations at full scale (**left**) and model scale (**right**).

4.3. Discretization Schemes

The impact of the discretization schemes for spatial and temporal discretization is analysed using the fine grid and time step as in the verification study for the full and model scale. The SSTKO turbulence model is used in the remaining numerical simulations. For the cases given in Table 7, the numerical setups are the same at the full and model scales. The STAR-CCM+ default discretization schemes [26] are used in case 1, while remaining cases use different discretization schemes, as shown in Table 7.

Table 7. Different combinations of discretization schemes used in the numerical simulations.

Case	Temporal	Convection	Gradient
1	1st	2nd	2nd
2	1st	1st	2nd
3	1st	3rd	2nd
4	1st	2nd	1st
5	2nd	2nd	2nd
6	1st	1st	1st

4.4. Convection Terms

In this study, the discretization schemes for convection terms are varied within the equations of the turbulence models as well as within the momentum and continuity equations, while maintaining the discretization schemes for gradient and temporal terms as second and first-order, respectively. The considered discretization schemes for convection terms are first-, second- and a hybrid third-order scheme. The third-order scheme is named MUSCL 3rd-order/Central differencing, and it is worth noting that the scheme lowers the order of accuracy in the regions of non-smooth flows.

Figure 11 shows the total resistance values obtained from three numerical simulations at the full scale and three at the model scale. The time range in the graph is displayed from the beginning of the simulations. Using first-order discretization schemes, the total resistance tends to converge considerably faster than in the case with the second-order scheme for the convection terms. Nevertheless, it must be pointed out that the total resistance has higher values for case 2 both at the full and model scale. The amplitudes of the total resistance obtained by second-order discretization scheme are larger and the convergence is much slower than the ones obtained by the first-order scheme. As expected, using the MUSCL 3rd order/Central differencing scheme, the obtained values of total resistance are similar to the ones obtained using second-order scheme. The reason is that this scheme lowers the order of accuracy in the regions of the non-smooth flow.

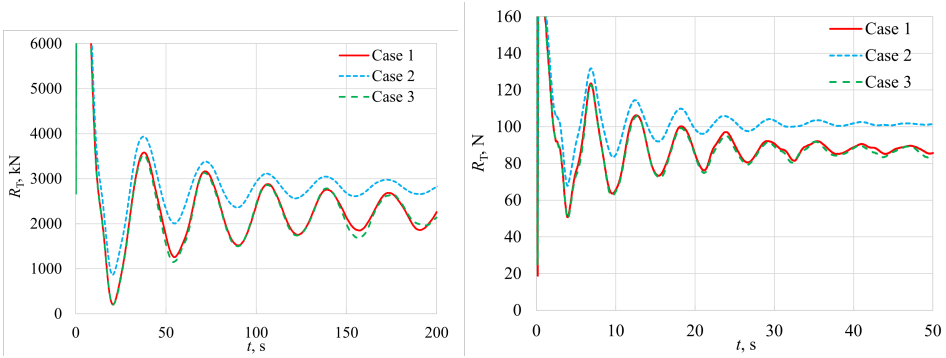


Figure 11. Comparison of three discretization schemes for convection terms at full scale (**left**) and model scale (**right**).

Figure 12 shows the values of sinkage and trim as a function of physical time at the full and model scale. The sinkage obtained with numerical simulations at the model scale is scaled with $\lambda = 35.18$ for the comparison with the full-scale results. There are no significant

differences in the obtained sinkage values other than the slightly lower amplitude of the oscillations in the case when first-order scheme is used. On the other hand, the trim values obtained via the first-order scheme for convection terms show a slightly faster convergence at the full scale, while slightly lower amplitudes are obtained at the model scale. The sinkage and trim depend significantly on the scale, with higher sinkage and lower trim values obtained with numerical simulations at the model scale compared to the full scale.

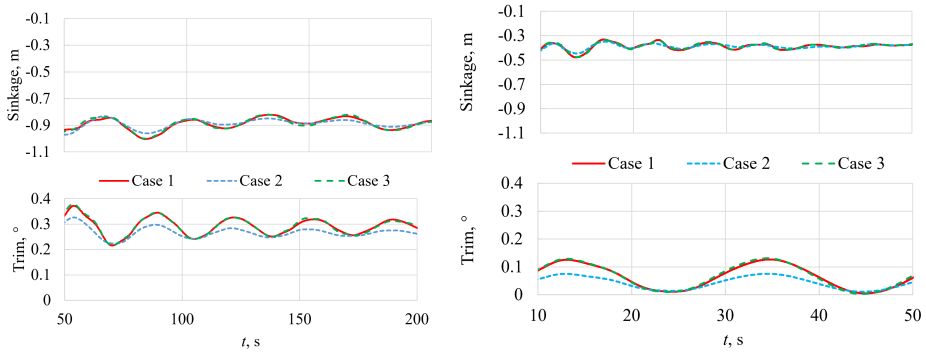


Figure 12. Sinkage and trim values as a function of physical time for different discretization schemes for convection terms at full scale (**left**) and model scale (**right**).

Figures 13 and 14 show the wave patterns obtained using the different discretization schemes for convection terms at the full and model scale. The wave elevations obtained with the first-order schemes are noticeably lower in comparison to the ones obtained using higher order schemes. Also, the Kelvin wake is barely visible both at the full and model scale when using the first-order scheme for convection terms. Non-physical perturbations of the free surface outside the Kelvin region can be seen in case 3, where the hybrid third-order discretization scheme for convection terms is used. This effect is slightly less pronounced for the model scale.

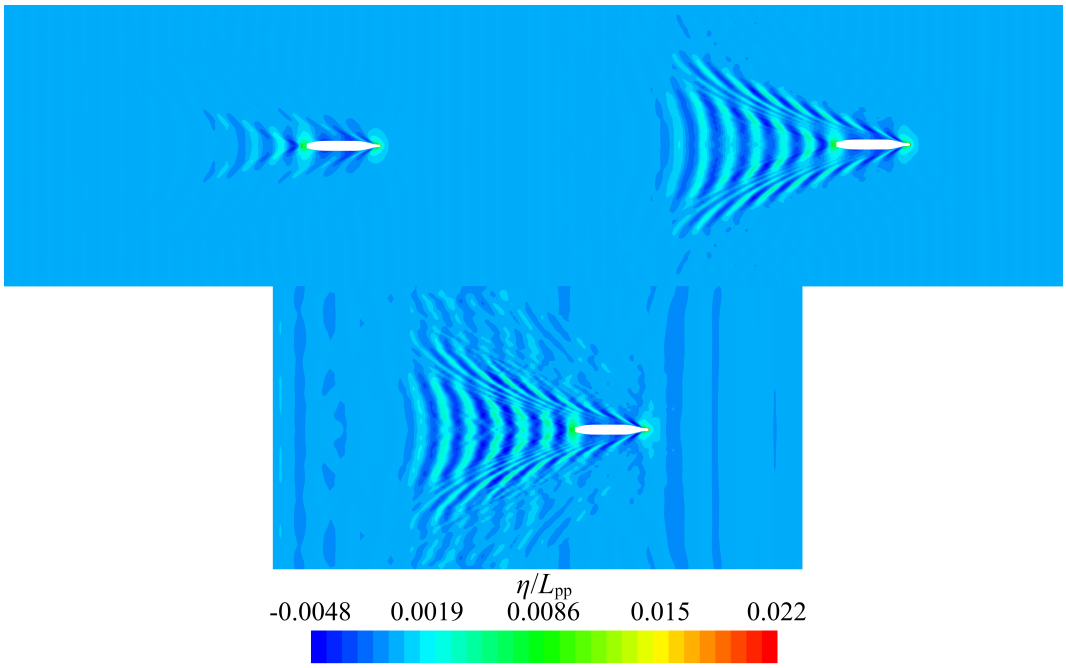


Figure 13. Wave patterns obtained with first-order (**top-left**), second-order (**top-right**) and hybrid third-order (**bottom**) discretization scheme for convection terms at full scale.

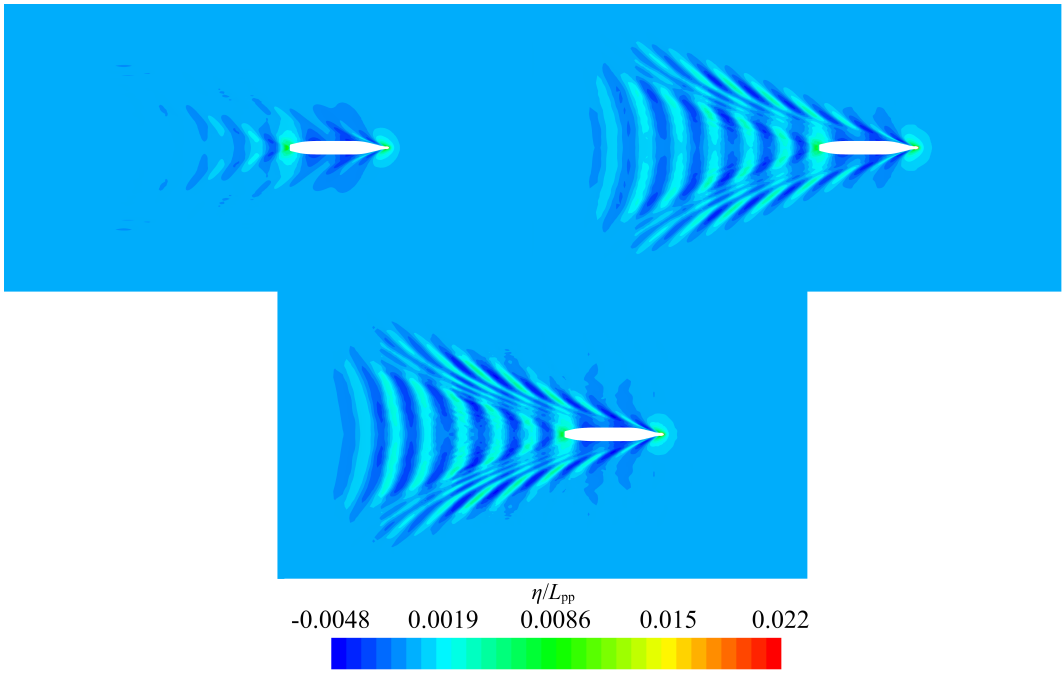


Figure 14. Wave patterns obtained with first-order (**top-left**), second-order (**top-right**) and hybrid third-order (**bottom**) discretization scheme for convection terms at model scale.

Finally, the wave elevations at the centreline of the ship behind the stern and in front of the bow are presented in Figures 15 and 16, respectively, while the wave elevations along the hull are shown in Figure 17. Also, the wave elevations obtained with numerical simulations at the full and model scale behind the stern at longitudinal cuts $B/4$, $B/2$ and B from the centreline of the ship are presented in Figure 18. The results suggest that the choice of the discretization scheme for the convection terms is crucial for the determination of the wave pattern. The wave amplitudes behind the stern decrease significantly faster with first-order scheme in comparison to second and third-order scheme. The same effect can be seen at the full and model scale. The wave elevations along the hull at the model scale are very similar for all three discretization schemes. At the full scale, the first-order scheme yields the lowest elevations, while the hybrid third-order scheme predicts slightly higher elevations.

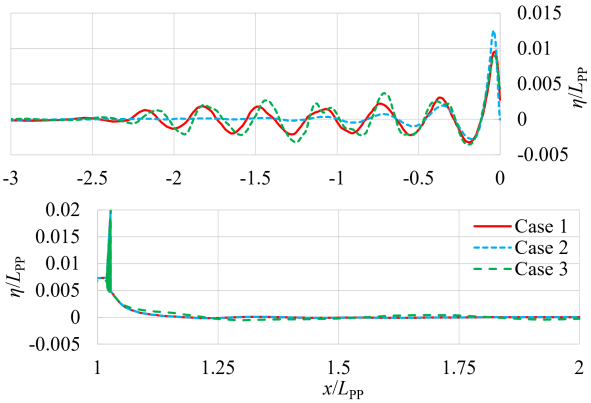


Figure 15. Wave elevations behind the stern (**top**) and in front of the ship (**bottom**), obtained using different discretization schemes for convection terms at full scale.

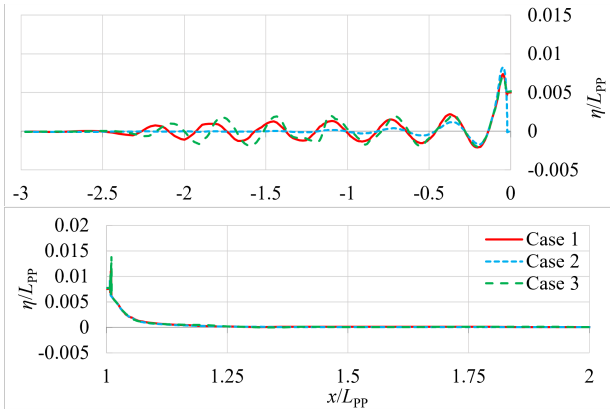


Figure 16. Wave elevations behind the stern (**top**) and in front of the ship (**bottom**), using different discretization schemes for convection terms at model scale.

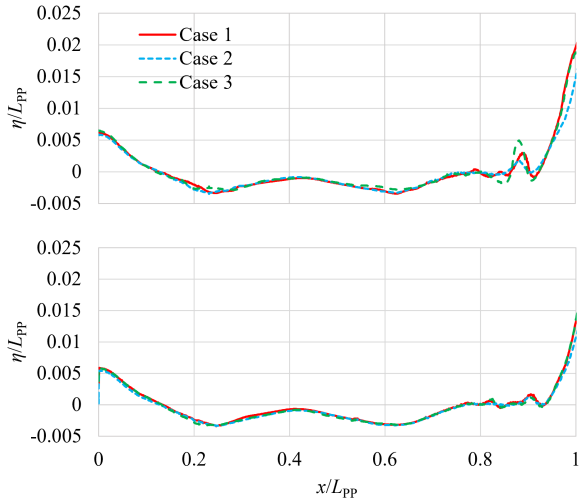


Figure 17. Wave elevations along the hull at full scale (**top**) and model scale (**bottom**) using different discretization schemes for convection terms.

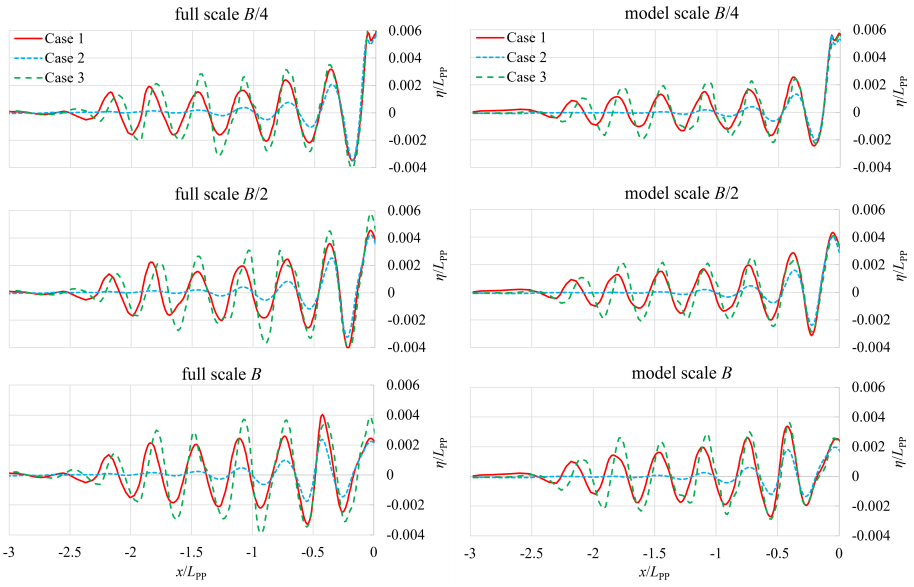


Figure 18. Wave elevations behind the stern at longitudinal cuts $B/4$, $B/2$ and B from the centreline of the ship obtained with numerical simulations at full scale (**left**) and model scale (**right**).

4.5. Gradient Terms

In Section 4.5, the discretization schemes for gradient terms are varied between the first and second order, while the convection terms are kept as second order. The total resistance converges faster with a higher median value using the first-order scheme, as obtained for convection terms in the previous subsection. By comparing Figures 11 and 19, it can be noticed that using the first-order scheme either for gradient or convection terms yields similar results for total resistance. The same is valid for the full and model scale. The main difference between the full and model scale is the faster convergence at the model scale.

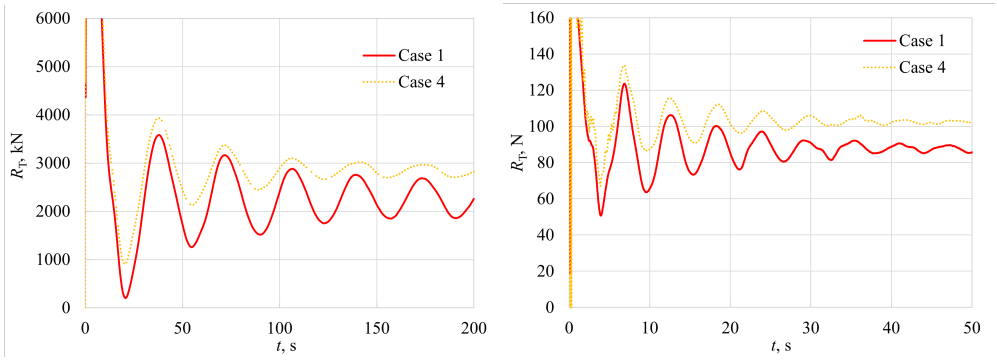


Figure 19. Comparison of two discretization schemes for gradient terms at full scale (**left**) and model scale (**right**).

Figures 20 and 21 show a comparison of the wave elevations at the centreline of the ship, obtained using the first- and second-order scheme for gradient terms at the full and model scales. The wave elevations behind the ship obtained using the first-order scheme are significantly lower than the ones obtained using the second-order scheme. The same is obtained in the previous subsection, where the discretization scheme for convection terms is varied. The wave elevations in front of the ship are almost the same in both cases. Figure 22 shows the wave elevations along the hull for different discretization schemes for gradient terms at the full and model scale. Like in the previous analysis of the discretization schemes for convection terms, the first-order scheme for gradient terms yields lower wave elevations along the hull at the full scale. The differences between two discretization schemes at the model scale are negligible in comparison to the full scale.

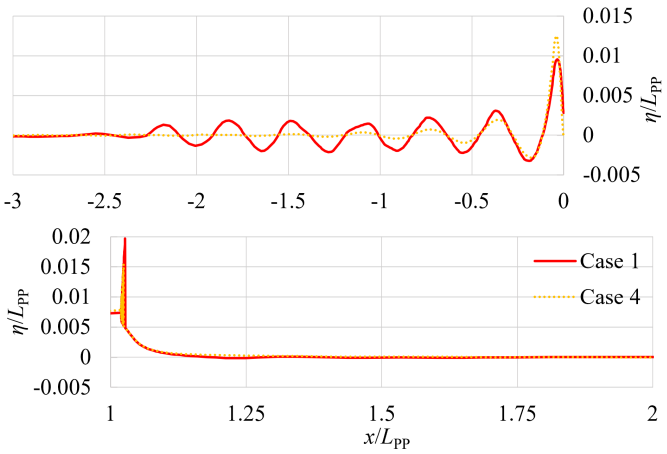


Figure 20. Wave elevations behind the stern (**top**) and in front of the ship (**bottom**), obtained using the first and second-order scheme for gradient terms at full scale.

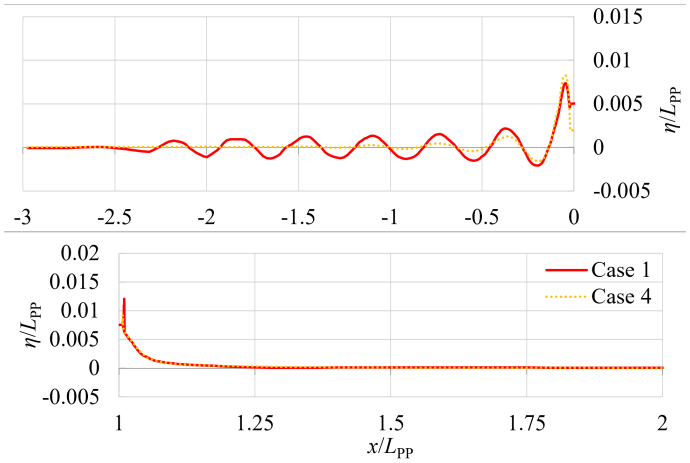


Figure 21. Wave elevations behind the stern (**top**) and in front of the ship (**bottom**), obtained using the first and second-order scheme for gradient terms at model scale.

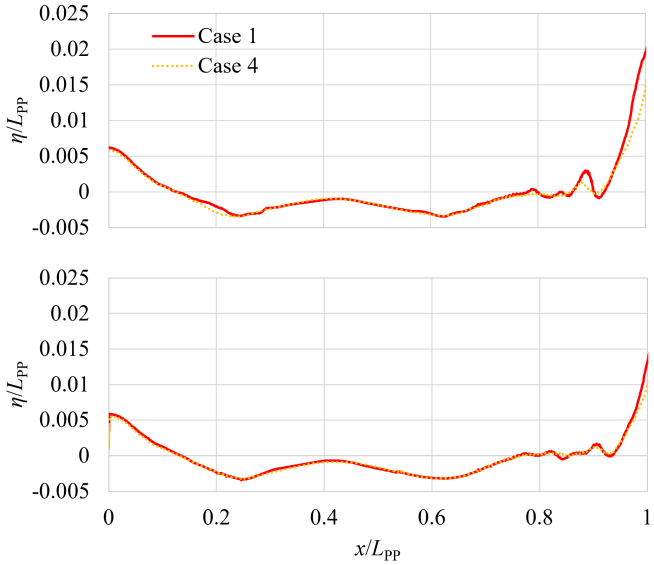


Figure 22. Wave elevations along the hull at full scale (**top**) and model scale (**bottom**) using different discretization scheme for gradient terms.

A comparison between discretization schemes for convection and gradient terms is presented in Figure 23 at the full and model scale in order to assess their impact on numerical results. There are no significant differences between the obtained values of the total resistance at the full and model scale. Thus, it can be concluded that the discretization schemes for solving the convection and gradient terms have a similar impact on the total resistance.

4.6. First-Order vs. Second-Order Schemes

In this Section 4.6, the discretization schemes for all the terms, including temporal discretization, are varied between first and second-order scheme. The details of cases 5 and 6 can be seen in Table 7. The comparison between first- and second-order discretization scheme for gradient, convection and temporal terms is presented in Figure 24 at the full and model scale. A significantly slower convergence of the total resistance is obtained by using the second-order scheme. The oscillations reach higher amplitudes, but with a lower median value. The same is valid for the results obtained using the numerical simulations at the full and model scale, with model scale showing faster convergence using both the first

and second-order discretization scheme, as can be seen from the physical time shown on the abscissa.

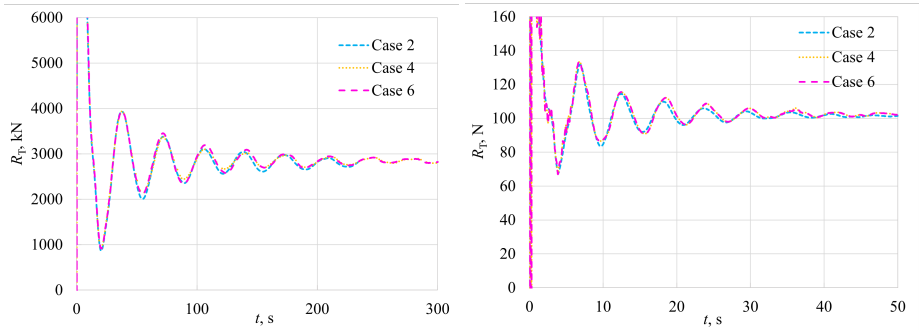


Figure 23. Comparison between first-order scheme for convection and gradient terms at full (**left**) and model scale (**right**).

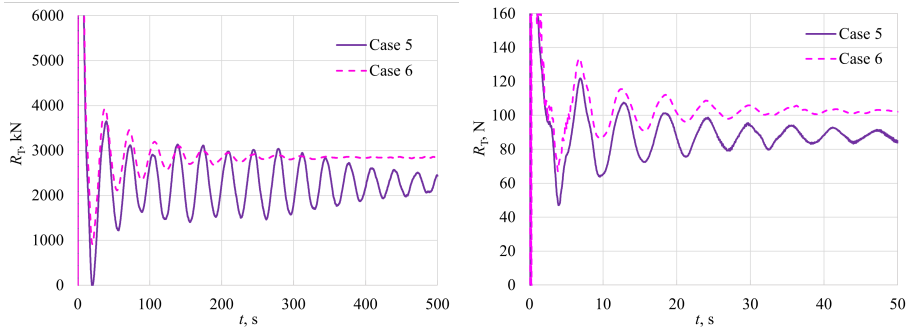


Figure 24. Comparison between first and second-order discretization scheme for gradient, convection terms and temporal discretization at full scale (**left**) and model scale (**right**).

Figures 25 and 26 show the obtained wave elevations at the centreline of the ship at full and model scale, respectively. The numerical dissipation, when first-order scheme is applied, is visible at the full and model scale. Figure 27 shows the wave elevations along the ship hull for the full and model scale, obtained using the first and second-order scheme for convection, gradient and temporal terms. Again, lower elevations can be seen at full scale when the first-order scheme is used, while at model scale, the differences are almost negligible. The impact of the discretization scheme for the temporal term on the total resistance at full and model scale is shown in Figure 28. Faster convergence with no significant effect on the median value is obtained with the first-order discretization scheme for the temporal term. At model scale, this effect is negligible in comparison to full-scale results, nevertheless, it is still visible.

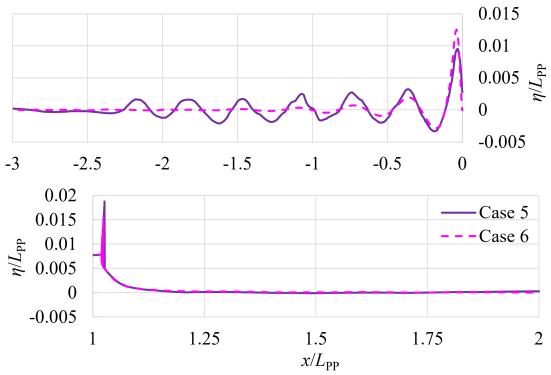


Figure 25. Wave elevations behind the stern (**top**) and in front of the ship (**bottom**), obtained using different discretization schemes for spatial and temporal terms at full scale.

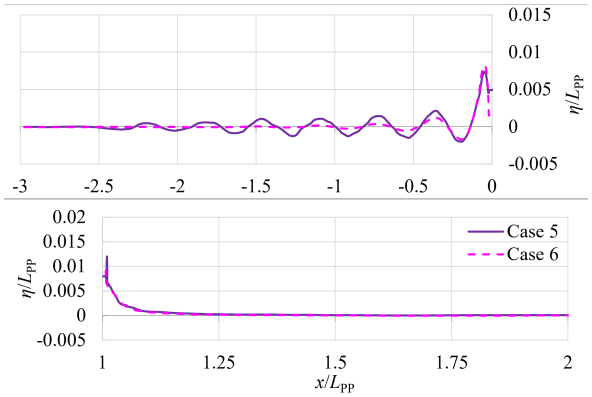


Figure 26. Wave elevations behind the stern (**top**) and in front of the ship (**bottom**), obtained using different discretization schemes for spatial and temporal terms at model scale.

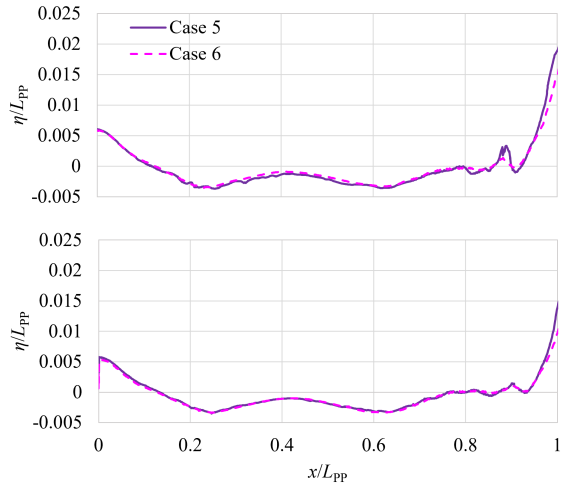


Figure 27. Wave elevations along the hull at full scale (**top**) and model scale (**bottom**) using different discretization schemes for spatial and temporal terms.

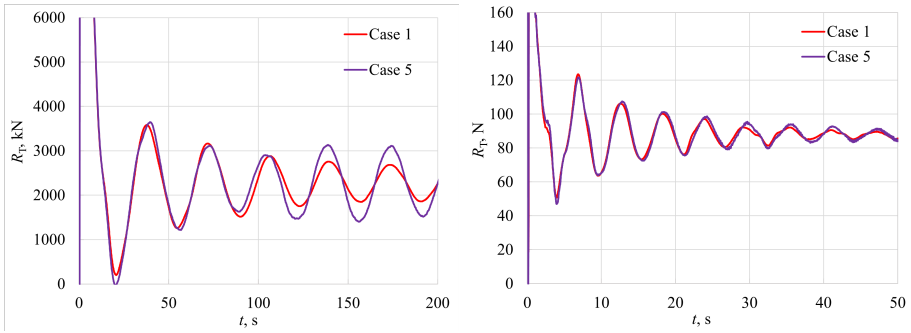


Figure 28. The impact of the temporal discretization on the total resistance at full scale (**left**) and model scale (**right**).

Figure 29 shows the wave elevations behind the stern at longitudinal cuts $B/4$, $B/2$ and B from the centreline of the ship obtained with numerical simulations at the full and model scale. The wave elevations obtained from numerical simulations at the full scale are higher for case 5 in comparison to case 1. On the contrary, at the model scale, the wave elevations behind the ship for case 5 are lower in comparison to case 1. As expected, lower elevations can be seen at sections further away from the centreline of the ship for the full and model scales.

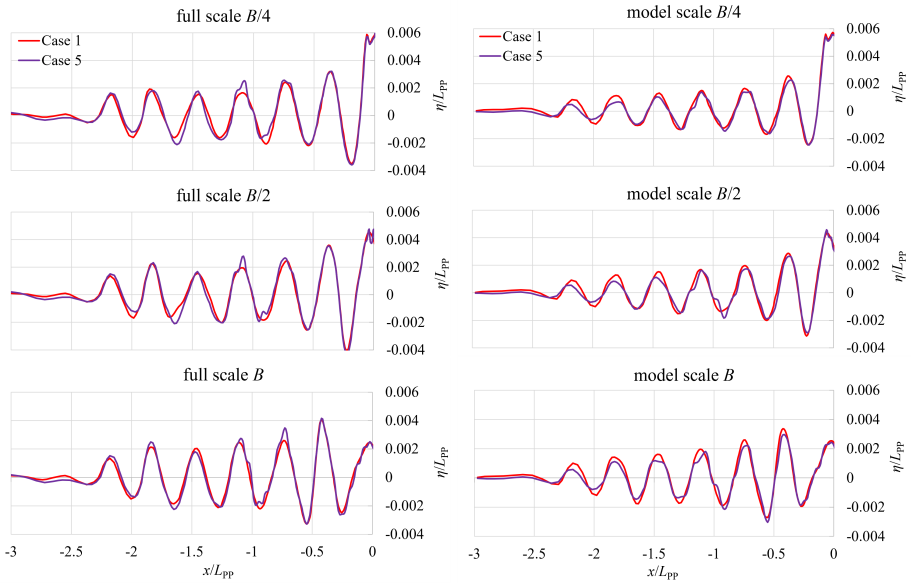


Figure 29. Wave elevations behind the ship at longitudinal cuts $B/4$, $B/2$ and B from the centreline of the ship obtained with numerical simulations at full scale (**left**) and model scale (**right**).

4.7. Resistance Components

In Section 4.7, the total resistance obtained within the free surface simulations is decomposed into the frictional R_F and pressure R_P resistance. These components are obtained by integrating the tangential stress and pressure, obtained with free surface simulations, over the wetted surface, respectively. The results obtained with numerical simulations at the full and model scale are shown in Figures 30 and 31 for the cases listed in Table 7. The frictional resistance is almost the same for all the cases at the full and model scales. The pressure resistance changes with the different discretization schemes more significantly in comparison to the frictional resistance. Also, the portion of the frictional resistance in the total resistance is significantly higher at the model scale, with a median value of 76.2%, than at the full scale, where its portion is 59.5%. It can be concluded that the portion of the frictional resistance decreases, while the portion of the pressure resistance becomes more significant at the full scale in comparison to the model scale.

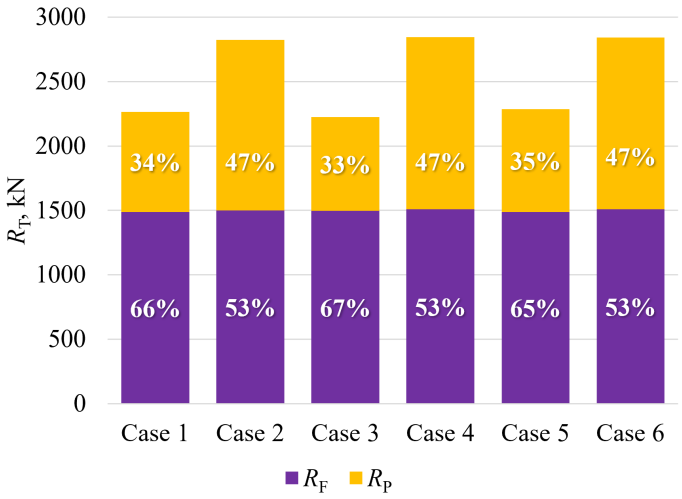


Figure 30. The portions of the total resistance components obtained with numerical simulations at full scale.

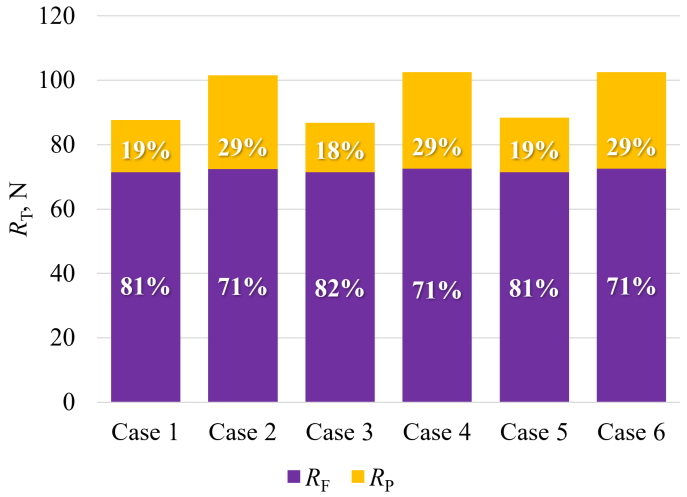


Figure 31. The portions of the total resistance components obtained with numerical simulations at model scale.

Figure 32 shows the portions of the total resistance components obtained with three turbulence models within the numerical simulations at the full and model scale. Similarly to the results of the previous analysis, the median value of the portion of the frictional resistance in the total resistance at the model scale is 82%, which is noticeably higher than that at the full scale, where the median value of the portion of the frictional resistance is 66.7%. The portions of the total resistance components do not change significantly with different turbulence models, even though the total resistance does change.

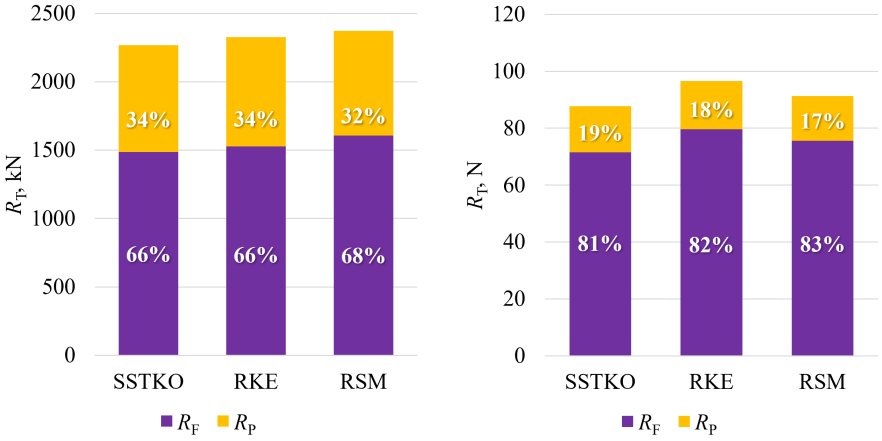


Figure 32. The portions of the total resistance components obtained with different turbulence models within the numerical simulations at full scale (**left**) and model scale (**right**).

5. Conclusions

Numerical simulations of the flow around the model- and full-scale post-Panamax container ship were performed, and the numerical setup was described in detail along with the overview of the meshing process. The grid was refined in the region of the Kelvin wake, the approximate location of the free surface and the boundary layer around the ship hull. In order to apply wall functions, the boundary layer was discretized to maintain the non-dimensional wall distance y^+ in the range $30 < y^+ < 100$. The numerical uncertainty was calculated using the Grid Convergence Index (GCI) method for the grid size and time step. The monotonic convergence of the results was obtained for three grid sizes and three time steps at the full scale, while oscillatory convergence was obtained for numerical simulations at the model scale. A validation study was conducted using the

numerical results obtained with three turbulence models and experimental results from the towing tank. After the verification and validation studies were completed, the impact of different numerical parameters on the total resistance, wave pattern and ship motion was analysed. These included turbulence models and the discretization schemes for the convection, gradient and temporal terms. The considered turbulence models included the Realizable $k-\varepsilon$ (RKE), Shear Stress Transport $k-\omega$ (SSTKO) and Reynolds Stress (RSM). The results have shown that the total resistance obtained using the SSTKO turbulence model at the full scale differs from the ones obtained using RKE and RSM. A similar trend was noticed for numerical simulations at the model scale, where the SSTKO turbulence model yielded lower values of the total resistance in comparison to RKE turbulence model. Also, the total resistance obtained by the RSM turbulence model differs with scale. The total resistance obtained by RSM turbulence model at the full scale is almost the same as the one obtained with RKE, while at the model scale, the values are closer to the ones obtained by SSTKO turbulence model. Slightly lower sinkage values are obtained using the RSM model for the model and full scale, while the trim does not depend on the chosen turbulence model.

For the convection terms, the first-, second- and hybrid third-order discretization schemes were analysed. Faster convergence of the total resistance was obtained when the first-order scheme was applied, but the total resistance was higher than that with the second- and hybrid third-order scheme. Also, the wave pattern obtained with the first-order scheme had lower amplitudes and dissipated faster behind the ship in comparison to the other two schemes. The wave pattern obtained by the hybrid third-order scheme showed some unphysical perturbations in the region outside the Kelvin wake. This effect was slightly less visible at the model scale. Similarly, the impact of the discretization scheme for solving the gradient terms on the numerical results was assessed. The gradient terms in this analysis are solved using the first and second-order discretization scheme. Similar results are obtained as in the analysis of the convection terms. Higher total resistance was obtained with faster convergence when the first-order scheme was applied. The wave elevations at the centreline of the ship had lower amplitudes behind the stern. After the discretization schemes for convection and gradient terms were analysed separately, their impact on the obtained numerical results together with the discretization scheme for temporal terms was assessed. Compared to the second-order scheme, faster convergence with a higher median value of total resistance was obtained with the first-order scheme. Finally, the impact of the discretization scheme for temporal term was assessed. It has been shown that the selection of the discretization scheme for solving the temporal term does not impact the median value of the total resistance and that the first-order scheme assures faster convergence in numerical simulations at the full scale. In numerical simulations at the model scale, the first-order scheme speeds up the convergence of the total resistance as well, but at a slower rate.

Finally, the total resistance was decomposed into frictional and pressure resistance. It has been shown that the frictional resistance does not depend significantly on the discretization scheme for the convection, gradient and temporal terms. On the other hand, the discretization schemes for convection and gradient terms affect the pressure resistance, which is higher when the first-order scheme is used. The total resistance changes with the chosen turbulence model, but the portions of frictional and pressure resistance remain nearly the same. Also, both analyses showed that a higher portion of frictional resistance within the total resistance is obtained with numerical simulations at the model scale in comparison to the full scale.

Author Contributions: Conceptualization, C.G.G., N.D. and I.M.; methodology, C.G.G., N.D. and I.M.; software, C.G.G.; validation, C.G.G., N.D. and I.M.; formal analysis, C.G.G., N.D. and I.M.; investigation, C.G.G., N.D. and I.M.; resources, N.D.; writing—original draft preparation, C.G.G., N.D. and I.M.; writing—review and editing, C.G.G., N.D. and I.M.; visualization, C.G.G.; supervision, N.D.; project administration, C.G.G., N.D. and I.M. All authors have read and agreed to the published version of the manuscript.

Funding: This study was funded by the Croatian Science Foundation under project IP-2020-02-8568.

Institutional Review Board Statement: Not applicable.

Informed Consent Statement: Not applicable.

Data Availability Statement: Not applicable.

Acknowledgments: This study has been fully supported by the Croatian Science Foundation under project IP-2020-02-8568.

Conflicts of Interest: The authors declare no conflicts of interest.

References

1. Terziev, M.; Tezdogan, T.; Demirel, Y.K.; Villa, D.; Mizzi, S.; Incecik, A. Exploring the effects of speed and scale on a ship's form factor using CFD. *Int. J. Nav. Arch. Ocean* **2021**, *13*, 147–162.
2. Orych, M.; Werner, S.; Larsson, L. Validation of full-scale delivered power CFD simulations. *Ocean Eng.* **2021**, *238*, 109654.
3. Saydam, A.Z.; Küçüksu, G.N.; İnsel, M.; Gökçay, S. Uncertainty quantification of self-propulsion analyses with RANS-CFD and comparison with full-scale ship trials. *Brodogradnja* **2022**, *73*, 107–129.
4. Degiuli, N.; Martić, I.; Farkas, A.; Gospić, I. The impact of slow steaming on reducing CO_2 emissions in the Mediterranean Sea. *Energy Rep.* **2021**, *7*, 8131–8141.
5. Demirel, Y.K.; Turan, O.; Incecik, A. Predicting the effect of biofouling on ship resistance using CFD. *Appl. Ocean Res.* **2017**, *62*, 100–118.
6. Song, S.; Demirel, Y.K.; Muscat-Fenech, C.D.M.; Tezdogan, T.; Atlar, M. Fouling effect on the resistance of different ship types. *Ocean Eng.* **2020**, *216*, 107736.
7. Feng, D.; Ye, B.; Zhang, Z.; Wang, X. Numerical Simulation of the Ship Resistance of KCS in Different Water Depths for Model-Scale and Full-Scale. *J. Mar. Sci. Eng.* **2020**, *8*, 745.
8. Niklas, K.; Pruszko, H. Full-scale CFD simulations for the determination of ship resistance as a rational, alternative method to towing tank experiments. *Ocean Eng.* **2019**, *190*, 106435.
9. Dogrul, A. Numerical Prediction of Scale Effects on the Propulsion Performance of Joubert BB2 Submarine. *Brodogradnja* **2022**, *73*, 17–42.
10. Song, K.; Guo, C.; Sun, C.; Wang, C.; Gong, J.; Li, P.; Wang, L. Simulation strategy of the full-scale ship resistance and propulsion performance. *Eng. Appl. Comp. Fluid* **2021**, *15*, 1321–1342.
11. Andrun, M.; Blagojević, B.; Bašić, J. The influence of numerical parameters in the finite-volume method on the Wigley hull resistance. *Proc. Inst. Mech. Eng. M.-J. Eng.* **2019**, *233*, 1123–1132. [CrossRef]
12. Huang, L.; Pena, B.; Thomas, G. Towards a full-scale CFD guideline for simulating a ship advancing in open water. *Ship Technol. Res.* **2023**, 1–17. [CrossRef]
13. Farkas, A.; Degiuli, N.; Martić, I. Assessment of hydrodynamic characteristics of a full-scale ship at different draughts. *Ocean Eng.* **2018**, *156*, 135–152. [CrossRef]
14. Degiuli, N.; Farkas, A.; Martić, I.; Zeman, I.; Ruggiero, V.; Vasiljević, V. Numerical and experimental assessment of the total resistance of a yacht. *Brodogradnja* **2021**, *72*, 61–80. [CrossRef]
15. Kim, Y.; Kim, J.H. Benchmark study on motions and loads of a 6750-TEU containership. *Ocean Eng.* **2016**, *119*, 262–273. [CrossRef]
16. Brodarski Institute. *Report 6655-M. Resistance, Self-Propulsion and 3D Wake Measurement Test Results*; Brodarski Institute: Zagreb, Croatia, 2022.
17. Siemens. STAR-CCM+ User Guide. 2020. Available online: https://www.cfd-online.com/Forums/star-ccm/240557-star-ccm-user-guide-tutorials.html (accessed on 19 July 2023).
18. Menter, F.R. Two-equation eddy-viscosity turbulence models for engineering applications. *AIAA J.* **1994**, *32*, 1598–1605. [CrossRef]
19. ITTC. Practical Guidelines for Ship CFD Applications, 7.5-03-02-03. In *ITTC-Recommended Procedures and Guidelines*; ITTC: Rio de Janeiro, Brazil, 2011.
20. Grlj, C.G.; Degiuli, N.; Farkas, A.; Martić, I. Numerical Study of Scale Effects on Open Water Propeller Performance. *J. Mar. Sci. Eng.* **2022**, *10*, 1132. [CrossRef]
21. Celik, I.B.; Ghia, U.; Roache, P.J.; Freitas, C.J.; Coleman, H.; Raad, P.E. Procedure for estimation and reporting of uncertainty due to discretization in CFD applications. *J. Fluids Eng.* **2008**, *130*, 0780011–0780014.
22. Song, S.; Demirel, Y.K.; Atlar, M.; Dai, S.; Day, S.; Turan, O. Validation of the CFD approach for modelling roughness effect on ship resistance. *Ocean Eng.* **2020**, *200*, 107029. [CrossRef]
23. Mikkelsen, H.; Walther, J.H. Effect of roughness in full-scale validation of a CFD model of self-propelled ships. *Appl. Ocean. Res.* **2020**, *99*, 102162. [CrossRef]
24. Kahramanoglu, E.; Yıldız, B.; Çakıcı, F.; Yilmaz, H. Numerical roll damping prediction of a planing hull. *Ship Offshore Struct.* **2021**, *16*, 363–372. [CrossRef]

25. Pena, B.; Huang, L. A review on the turbulence modelling strategy for ship hydrodynamic simulations. *Ocean Eng.* **2021**, *241*, 110082. [CrossRef]
26. Mikulec, M.; Piehl, H. Verification and validation of CFD simulations with full-scale ship speed/power trial data. *Brodogradnja* **2023**, *74*, 41–62. [CrossRef]

Disclaimer/Publisher's Note: The statements, opinions and data contained in all publications are solely those of the individual author(s) and contributor(s) and not of MDPI and/or the editor(s). MDPI and/or the editor(s) disclaim responsibility for any injury to people or property resulting from any ideas, methods, instructions or products referred to in the content.

Article II

Article published by MDPI in Journal of marine science and engineering on 17 August 2022, available online: https://www.mdpi.com/2077-1312/10/8/1132

Journal of *Marine Science and Engineering*

MDPI

Article

Numerical Study of Scale Effects on Open Water Propeller Performance

Carlo Giorgio Grlj, Nastia Degiuli *, Andrea Farkas and Ivana Martić

Faculty of Mechanical Engineering and Naval Architecture, University of Zagreb, Ivana Lučića 5, 10000 Zagreb, Croatia

* Correspondence: nastia.degiuli@fsb.hr

Abstract: The present study aims to investigate the scale effects of the open water propeller performance using computational fluid dynamics (CFD). The results are presented for the propeller which was previously 3D scanned and digitized. The results obtained using two turbulence models within the numerical simulations are compared. The verification study is conducted to assess the numerical uncertainty and thus obtain the optimal grid size for the numerical simulations. A transition model is used at the model scale to account for the partially laminar flow. The propeller is then scaled, and numerical simulations are performed to assess the scale effects on the open water performance of the considered propeller. The results demonstrate the significant scale effects on open water characteristics however, scale effects are considerably lower when the transition model is applied within the numerical simulations at the model scale.

Keywords: CFD; open water test; scale effect; propeller; transition model; turbulence model

check for updates

Citation: Grlj, C.G.; Degiuli, N.; Farkas, A.; Martić, I. Numerical Study of Scale Effects on Open Water Propeller Performance. *J. Mar. Sci. Eng.* **2022**, *10*, 1132. https://doi.org/10.3390/jmse10081132

Academic Editors: Jasna Prpic-Orsic and Luca Braidotti

Received: 21 July 2022
Accepted: 16 August 2022
Published: 17 August 2022

Publisher's Note: MDPI stays neutral with regard to jurisdictional claims in published maps and institutional affiliations.

Copyright: © 2022 by the authors. Licensee MDPI, Basel, Switzerland. This article is an open access article distributed under the terms and conditions of the Creative Commons Attribution (CC BY) license (https://creativecommons.org/licenses/by/4.0/).

1. Introduction

The open water test (OWT) is carried out in towing tanks to assess the hydrodynamic performance of propellers. These tests are always performed at a model scale since open water tests at full-scale would be expensive and there are no testing sites where such large-scale tests would be feasible. Nowadays, computational fluid dynamics (CFD) is successfully used by many researchers for the assessment of ship propulsion performance. Farkas et al. [1] used numerical simulations for the prediction of the nominal wake in the case of a bulk carrier. The authors noticed significant scale effects in both integral values of nominal wake and circumferential averaged non-dimensional axial velocity distribution. Jang et al. [2] employed numerical simulations of OWT at model scale to assess the influence of pitch motion on the propeller performance. The authors demonstrated that the pitch motion of the ship has a dominant effect on the variation of the propeller performance resulting in the sinusoidal pitch motion of the propeller. Sun et al. [3] used CFD to investigate the vibration and noise reduction effects of an energy-saving device. The obtained results showed that the considered energy-saving device can improve propulsion efficiency and reduce the radiation noise intensity. Multiple different scaling methods have been developed for the extrapolation of the model scale to full-scale results. Helma et al. [4] presented an overview of the different scaling methods and assessed their influence on the full-scale results. The authors divided the scaling methods into statistical, analytical, CFD methods, and a combination of the listed methods. Helma [5] developed a scaling procedure for unconventional propeller designs called the β_i method utilizing the equivalent profile concept. The author showed that the method works well with all propeller geometries since it is independent of the blade loading distribution. It is also important to point out that it needs the results from only one set of open water curves. Extrapolation performed by any of the scaling methods provides accurate and reliable results [6], but experimental OWT is cost-intensive and time-consuming. CFD is a reasonable alternative to towing tank

tests since it is a versatile tool that can be used to predict ship hydrodynamic characteristics in model and full-scale [7]. The authors showed in [7] that the numerical results of the ship resistance in calm water varied from −10% to 4% compared to sea trials data. Mikkelsen and Walther [8] validated the results from the self-propulsion numerical simulations against the results obtained from the sea trials. They showed that the discrepancy between the results can be further lowered using the modified wall functions for the simulation of the surface roughness. The difference between the obtained delivered powers is largely affected by propellers operating at higher Reynolds numbers in full-scale simulations [9]. Another problem with extrapolation to full-scale is the fact that the scaling methods are not accurate enough for unconventional propellers [10]. Multiple authors addressed this issue by simulating the flow around the full-scale propellers with unconventional geometries such as tip-modified propellers [5,11,12]. The hydrodynamic analysis of a tip-loaded propeller was performed using the boundary element method to evaluate the propeller-induced hull pressures in [13]. The predicted hull pressures are in good agreement with the ones obtained in the cavitation tunnel and with unsteady RANS equations at the design and moderately loaded conditions. Dong et al. [12] studied the influence of PPTC-II propeller's tip rake on the scale effects by conducting numerical simulations in full-scale and model scale as well as modifying the propeller geometry with and without the tip rake. The authors compared the results with the ones obtained using the ITTC-1978 method and concluded that the ITTC method must be updated to predict the scale effects on the thrust and torque coefficients more precisely. Li et al. The study by [10] also concluded that ITTC should develop new scaling methods for unconventional propellers. Chen et al. [14] studied the open water hydrodynamic performance of a high skew submarine propeller E1619 and concluded that the difference between the predicted torque coefficient using the ITTC 1978 method and the ones obtained by numerical simulations is not negligible. Furthermore, they concluded that the law of scale effect cannot be analyzed using only two models and that several different scales must be considered. Owen et al. [15] investigated the effect of biofouling on the propeller open water performance using numerical simulations at the model scale where multiple methods for propeller rotation modeling were used, i.e., the moving reference frame (MRF) method and sliding mesh (SM) approach. Minor discrepancies between the open water results obtained from the two methods were shown; thus, the authors decided to retain the MRF method since it is computationally less expensive. The same method was used in [16,17] since it lowers the computational time, and the convergence is faster than using the overset mesh (OM) method. Mikkelsen et al. [18] also used the MRF method for open water simulations; however, in the case of self-propulsion simulations, the MRF method was used only to initialize the flow around the propeller followed by the SM method for the rest of the simulation. A comparison of SM and OM methods was given in [19] for the case of a rotating vertical axis turbine. The authors showed that by increasing the number of cells the results converge faster using the OM method at the cost of 10% higher computational time. Wang et al. [20] used a single-run procedure and OM method to determine the open water curves. The results were compared to the experimental results performed by IIHR (available at the Tokyo 2015 CFD Workshop [21]) and an overall agreement between the results was shown. Bekhit and Lungu [22] performed numerical simulations of resistance and self-propulsion tests with and without the rudder as well as OWT. The obtained results were compared with experimental results, showing an average error of about 3% for the thrust coefficient and 7% for the torque coefficient. Lungu [23] in his later study performed numerical simulations of the resistance, open water, and self-propulsion tests of a 3600 TEU containership, where he showed a 5% difference between the measurements and numerical predictions of thrust and torque coefficients. Farkas et al. [24] compared two methods for assessing the influence of biofouling on the open water propeller characteristics. The verification and validation study were performed for three full-scale propellers and satisfactory agreement was achieved. These results were compared with the results obtained using a propeller performance prediction method for fouled surfaces. The impact of hard fouling on the ship hydrodynamic performance was assessed in [25], where

the authors conducted full-scale CFD simulations of OWT for three propellers and validated the results using the towing tank results. Farkas et al. [26] investigated the effects of biofilm on ship propulsion characteristics. The authors demonstrated the significant impact of biofilm on the ship hydrodynamic performance highlighting the importance of keeping the hull clean. Dogrul [27] investigated the scale effects of a self-propelled submarine where he compared the extrapolated numerical results with the results from full-scale simulations. Gonzalez-Adalid et al. [28] conducted model scale and full-scale numerical simulations for the determination of the performance of two unconventional propellers with the transition model. Good agreement was shown between the results obtained from the fully turbulent, full-scale simulations and the sea trial data. Baltazar et al. [29] also performed the numerical simulations with the transition model at the model scale, but in addition, the paint test results were used for the validation study. The authors showed an increase in thrust of 2–4% when using the transition model. Moran-Guerrero et al. [30] used an improved Gamma Reynolds Theta $(\gamma - Re_\theta)$ correlation-based model for transition prediction, which considers the crossflow effects. Pawar and Brizzolara [31] used the same transition model to simulate the OWT of an open and ducted propeller to assess the discrepancies between experimental and numerical results.

The focus of this study is the investigation of the scale effects of the open water propeller performance. The numerical simulations are conducted for multiple scales ranging from model scale to full-scale. First, the verification study is conducted using the grid convergence index (GCI) method, and the results of the numerical simulations are presented. The rest of the paper is organized as follows: the numerical model and the grid generation are described within Methods section. The results are presented and briefly discussed in the Results section and discussion followed by the conclusions from the present study in the last section.

2. Methods

2.1. Numerical Modeling

The numerical simulations in this study are based on the Reynolds-averaged Navier–Stokes (RANS) equations. For the case of an incompressible fluid, continuity and momentum transport equations for unsteady flow are written as:

$$\frac{\partial \overline{u}_i}{\partial x_i} = 0 \tag{1}$$

$$\rho \frac{\partial \overline{u}_i}{\partial t} + \rho \frac{\partial}{\partial x_j}\left(\overline{u}_i \overline{u}_j + \overline{u'_i u'_j}\right) = -\frac{\partial \overline{p}}{\partial x_i} + \frac{\overline{\tau}_{ij}}{\partial x_j} \tag{2}$$

where $\overline{u}_i$ is the averaged Cartesian components of the velocity vector, $\rho\overline{u'_i u'_j}$ is the Reynolds stress tensor (RST), $\overline{p}$ is the mean pressure, and $\overline{\tau_{ij}}$ is the mean viscous stress tensor defined as:

$$\overline{\tau}_{ij} = \mu\left(\frac{\partial \overline{u}_i}{\partial x_j} + \frac{\partial \overline{u}_j}{\partial x_i}\right) \tag{3}$$

where μ is the dynamic viscosity of the fluid.

To discretize the governing equations, the finite volume method (FVM) is used in the simulations. Within the numerical simulations, the shear stress transport $k - \omega$ (SSTKO) turbulence model is used to close the system of discretized differential equations since it is accurate enough in the near wall and far-field region [32]. The SSTKO is compared with the realizable $k - \varepsilon$ (RKE) turbulence model.

The rotation of the propeller can be modeled using three approaches, i.e., SM, OM, and steady-state simulation using the MRF. In this study, the MRF method [33] is used since it is computationally more efficient compared to the other two approaches [15]. The MRF is a steady-state method that consists of a rotating flow around a stationary mesh.

2.2. Turbulence Models

RANS turbulence models are based on the modeling of RST which is expressed as a function of the mean flow quantities. The turbulence models applied in this study use the concept of turbulent eddy viscosity μ_t to model RST.

2.2.1. Realizable $k-\varepsilon$(RKE) Turbulence Model

This is a two-equation model that solves transport equations for the turbulent kinetic energy k and the turbulent dissipation rate ε. The eddy viscosity in this model is described with the following equation:

$$\mu_t = \rho\, C_\mu \frac{k^2}{\varepsilon} \tag{4}$$

where C_μ is the model coefficient.

The transport equations for k and ε within the RKE model are defined as:

$$\frac{\partial}{\partial t}(\rho k) + \frac{\partial}{\partial x_i}(\rho k \overline{u}_i) = \frac{\partial^2 k}{\partial x_i^2}\left(\mu + \frac{\mu_t}{\sigma_k}\right) + f_c G_k + G_b - \Upsilon_M - \rho(\varepsilon - \varepsilon_0) + S_k \tag{5}$$

$$\frac{\partial}{\partial t}(\rho \varepsilon) + \frac{\partial}{\partial x_i}(\rho \varepsilon \overline{u}_i) = \frac{\partial^2 \varepsilon}{\partial x_i^2}\left(\mu + \frac{\mu_t}{\sigma_\varepsilon}\right) + \frac{1}{T_e} C_{\varepsilon 1}(f_c S k + C_{\varepsilon 3} G_b) - C_{\varepsilon 2}\, f_2\, \rho\left(\frac{\varepsilon}{T_e} - \frac{\varepsilon_0}{T_0}\right) + S_\varepsilon \tag{6}$$

where $\overline{u}_i$ is the averaged velocity vector, f_c is the curvature correction factor, G_k is the turbulent production term, σ_k and σ_ε are turbulent Schmidt numbers, G_B is the buoyancy production term, ε_0 is the ambient turbulence value that counteracts turbulence decay, Υ is the dilatation dissipation, $C_{\varepsilon 1}$, $C_{\varepsilon 2}$ and $C_{\varepsilon 3}$ are the model depending coefficients, S is the modulus of the mean strain tensor, and finally S_k and S_ε are the user-defined source terms.

2.2.2. Shear Stress Transport $k-\omega$ (SSTKO) Turbulence Model

The modified standard $k-\omega$ model blends $k-\varepsilon$ model in the far field with the $k-\omega$ model near the walls. Turbulent eddy viscosity in this model is given by the following equation:

$$\mu_t = \rho k T \tag{7}$$

where T is the turbulent time scale.

The $k-\omega$ turbulence model solves two transport equations for the turbulent kinetic energy k and the specific dissipation ω:

$$\frac{\partial}{\partial t}(\rho k) + \frac{\partial}{\partial x_i}(\rho k \overline{u}_i) = \frac{\partial^2 k}{\partial x_i^2}(\mu + \sigma_k \mu_t) + G_k + G_{nl} + G_b - \rho \beta^* f_{\beta *}(\omega k - \omega_0 k_0) + S_k \tag{8}$$

$$\frac{\partial}{\partial t}(\rho \omega) + \frac{\partial}{\partial x_i}(\rho \omega \overline{u}_i) = \frac{\partial^2 \omega}{\partial x_i^2}(\mu + \sigma_\omega \mu_t) + G_\omega + D_\omega - \rho \beta f_\beta\left(\omega^2 - \omega_0^2\right) + S_\omega \tag{9}$$

where σ_k, σ_ω, β, β^* are the model depending coefficients, G_{nl} is the non-linear production term, $f_{\beta *}$ is the free–shear modification factor, f_β is the vortex–stretching modification factor, and finally k_0 and ω_0 are the ambient values that counteract turbulence decay.

2.3. Transition Model

The turbulence model assumes that the flow is turbulent in the whole flow region. Within the numerical simulations at the model scale, the flow is expected to be partly laminar. To model the transition from laminar to turbulent flow, a transition model should be applied. The correlation-based $\gamma - Re_\theta$ transition model is used within the numerical simulations because it is coupled with the SSTKO turbulence model. The transition model

solves two additional transport equations, i.e., intermittency γ and transition momentum thickness Reynolds number $\overline{Re}_{\theta t}$ which read as follows:

$$\frac{\partial(\rho\gamma)}{\partial t} + \frac{\partial(\rho U_j\gamma)}{\partial x_j} = P_\gamma - E_\gamma + \frac{\partial}{\partial x_j}\left[\left(\mu + \frac{\mu_t}{\sigma_f}\right)\frac{\partial\gamma}{\partial x_j}\right] \tag{10}$$

$$\frac{\partial(\rho\overline{Re}_{\theta t})}{\partial t} + \frac{\partial(\rho U_j\overline{Re}_{\theta t})}{\partial x_j} = P_{\theta t} + \frac{\partial}{\partial x_j}\left[\sigma_{\theta t}(\mu + \mu_t)\frac{\partial\overline{Re}_{\theta t}}{\partial x_j}\right] \tag{11}$$

where U_j is the mean velocity vector, P_γ and $P_{\theta t}$ are the production terms, E_γ is the destruction term, σ_f and $\sigma_{\theta t}$ are the model coefficients. More information on the production, destruction terms and model coefficients can be found in [34]. To accurately solve the laminar and transitional boundary layers, the first cell near the wall must have $y^+ \leq 1$ [29]. Because of this constraint, it is decided to disable the transition model at other scales.

2.4. Open Water Propeller Characteristics

The open water characteristics of a propeller consist of determining the forces and moments acting on the propeller which is operating in a uniform stream without the influence of the hull. To obtain the open water curves, thrust K_T and torque K_Q coefficients need to be determined as functions of the advance coefficient J. The thrust and torque coefficients are defined using the following equations:

$$K_T = \frac{T}{\rho n^2 D^4} \tag{12}$$

$$K_Q = \frac{Q}{\rho n^2 D^5} \tag{13}$$

where T and Q are the thrust and torque, respectively, ρ is the fluid density, n the propeller rate of revolution, and D the propeller diameter. The advance coefficient is defined as follows:

$$J = \frac{v_A}{nD} \tag{14}$$

where v_A is the speed of advance.

Finally, propeller open water efficiency η_o is defined by:

$$\eta_o = \frac{J}{2\pi}\frac{K_T}{K_Q} \tag{15}$$

2.5. Grid Generation

The computational domain is defined as a cylinder that encloses the propeller with the hub and shaft. The domain boundaries are placed sufficiently far from the propeller to avoid their influence on the obtained results. Figure 1 shows the computational domain with the respective dimensions.

For the discretization of the computational domain, the unstructured hexahedral mesh is used. The numerical simulations with the transition model are performed with a grid that has $y^+ \leq 1$, while the remaining simulations are performed with a grid that has $y^+ > 30$ [35]. To obtain the required y^+ values, the distance from the wall to the center of the first prism layer is determined using the following equation:

$$y = \frac{y^+\nu}{u_\tau} \tag{16}$$

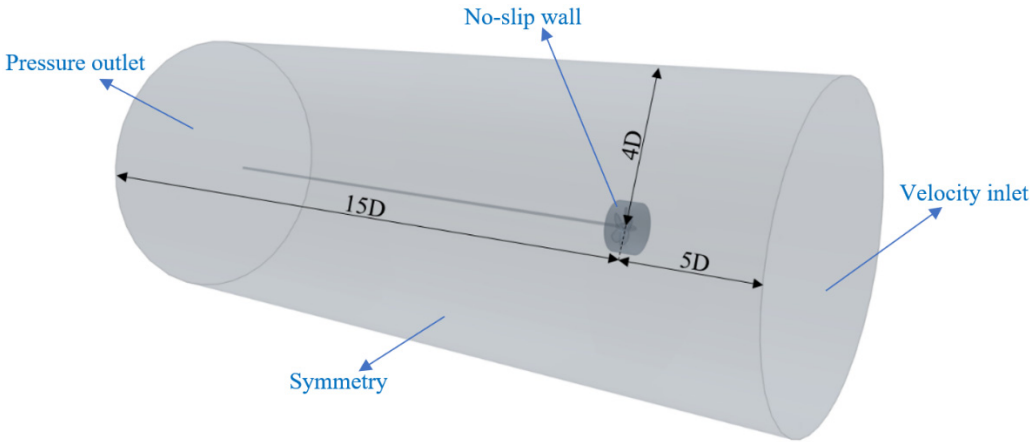


Figure 1. Computational domain for OWT.

The frictional velocity u_τ is calculated as follows:

$$u_\tau = \sqrt{\frac{\tau_w}{\rho}} \tag{17}$$

where the wall shear stress τ_w is calculated using the skin friction coefficient C_f:

$$\tau_w = \frac{1}{2} C_f \rho U_\infty^2 \tag{18}$$

In this study, the skin friction coefficient is determined for a flat plate using the following equation:

$$C_f = 0.0576 Re_d^{-\frac{1}{5}} \tag{19}$$

where Reynolds number depends on the scale. While this is not an exact method for the determination of the height of the first prism layer, it yields satisfactory results. The obtained y^+ values are checked, and it is ensured that $y^+ > 30$ in numerical simulations where wall functions are applied and that $y^+ < 1$ in numerical simulations with the transition model. Special attention is given to the refinement around the propeller and in the MRF zone. The transition from the prism layer to the core mesh is carefully discretized to avoid possible numerical diffusion. A more detailed discussion regarding the influence of y^+ values on the obtained numerical results regarding the open water test can be found in Owen et al. [15].

2.6. Verification Study

The GCI method, based on the Richardson extrapolation is used for the verification study. The GCI method is used to determine the appropriate grid size by determining the grid uncertainty. If the iterative uncertainty is neglected, then the numerical uncertainty consists only of the grid uncertainty. The interested reader can find more details about the method in [24].

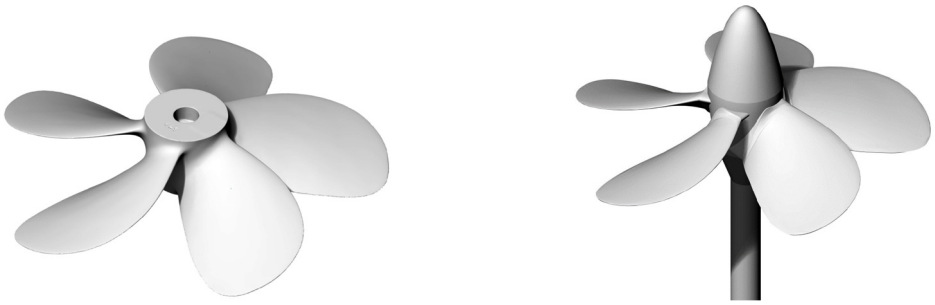
2.7. Case Study

In this study, a propeller is modeled using computer-aided design (CAD) software. The modeled propeller has geometric properties that resemble the one used for the Japan CFD Workshop 2015 for the Japan Bulk Carrier (JBC). The propeller is then scaled and the numerical simulations of OWT are conducted. Figure 2 shows the 3D scan of the propeller model and the CAD model used in the numerical simulations. Table 1 contains the propeller main particulars, and the scales used in the CFD simulations are listed within the same table. The advance coefficients are obtained by changing the speed of advance

with a constant rate of revolution of the propeller. The rate of revolution for different scales is defined using the following equation:

$$n_s = \frac{n_m}{\sqrt{\lambda}} \tag{20}$$

where n_s is the rate of revolution at the specific scale and n_m is the rate of revolution at the model scale.



(**a**) (**b**)

Figure 2. The geometry of the stock propeller. Three-dimensional scan (**a**), CAD model (**b**).

Table 1. The main particulars of the considered propeller in the different scales.

Scale, λ	40.264	4	2	1.333	1
Index	M	M1	M2	M3	F
Diameter, D (m)	0.203	2.040	4.079	6.119	8.158
Rate of revolution, n (rps)	26.03	8.204	5.801	4.737	4.102
Reynolds number, (Re) $(-)$	1.298×10^6	4.111×10^7	1.162×10^8	2.136×10^8	3.309×10^8
Pitch ratio, (P/D) $(-)$			0.736		
Expanded area ratio, $A_e/A_0(-)$			0.644		
Hub ratio, d/D $(-)$			0.193		
Number of blades, Z $(-)$			5		

3. Results and Discussion

3.1. Verification Study

Firstly, the verification study is performed using the numerical simulations at the model scale with the transition model. Since the numerical simulations are steady state, only the GCI for the spatial discretization is calculated. Table 2 shows the data of the used grids where the grid spacing h is calculated using the following equation:

$$h = \sqrt[3]{\frac{1}{N}\sum_{i=1}^{N}(\Delta V_i)} \tag{21}$$

where N is the total number of finite volume cells and V_i is the volume of the i-th cell. The grid refinement ratio is calculated as follows:

$$r_{ij} = \frac{h_i}{h_j} \tag{22}$$

The GCI is calculated for the open water efficiency η_o in the range of advance coefficient from 0.1 to 0.6. Table 3 presents the obtained GCIs with the calculated averages as well. Both the average coarse and fine GCIs are low, and the coarse GCI is under 4 %; thus, the medium grid size is used for the rest of the numerical simulations.

Table 2. Number of cells, grid spacing, and grid refinement ratio for model scale numerical simulations with the transition model.

Index	Number of Finite Volume Cells, N	Grid Spacing, h (m)	Grid Refinement Ratio, r
1	8.8M	0.0098	1.164
2	5.2M	0.0114	
3	3.0M	0.0119	1.040

Table 3. Fine and coarse GCIs for the range of advance coefficients and their average for model scale.

J	GCI_{fine}, %	GCI_{coarse}, %
0.1	1.258	1.71
0.2	1.878	3.14
0.3	5.239	15.25
0.4	0.116	2.21
0.5	0.002	0.55
0.6	0.017	0.65
Average	1.42	3.92

Another verification study is conducted for three full-scale grids with non-dimensional wall distance $y^+ > 30$. The coarse and fine GCIs are calculated for open water efficiency in the considered range of advance coefficients. Table 4 presents the details about the grids, while Table 5 shows the calculated grid convergence indices for the open water efficiency.

Table 4. Number of cells, grid spacing, and grid refinement ratio for full-scale numerical simulations.

Index	Number of Finite Volume Cells, N	Grid Spacing, h (m)	Grid Refinement Ratio, r
1	10.2M	0.3758	1.090
2	8M	0.4075	
3	4.5M	0.0119	1.207

Table 5. Fine and coarse GCI for the range of advance coefficients and their average for full-scale.

J	GCI_{fine}, %	GCI_{coarse}, %
0.1	0.42	0.19
0.2	1.70	1.34
0.3	7.65	8.06
0.4	1.82	2.19
0.5	1.48	1.90
0.6	1.55	2.15
Average	2.44	2.64

This study shows that the average GCIs in the range of advance coefficient from 0.1 to 0.6 are less than 4% and the difference between the coarse and fine GCIs is negligible. Thus, a medium grid size can be used for the full-scale simulations. The grids for the other scales use the same grid setup with varying prism layers to maintain $y^+ > 30$, so it is expected that the GCI will not differ significantly from the two studies presented.

3.2. Turbulence Models

The influence of the turbulence model on the obtained results is investigated using the model scale and full-scale numerical simulations with the medium grid size and the non-dimensional wall distance $y^+ > 30$. Figures 3 and 4 show the open water curves

obtained from the model and full-scale numerical simulations, respectively. The influence of the turbulence model on the results is barely visible for the full-scale case. The relative difference in the open water efficiency for the SSTKO turbulence model is equal to 2.83% for model scale and 0.65% for full-scale. The transition model is disabled for both cases shown in the figures.

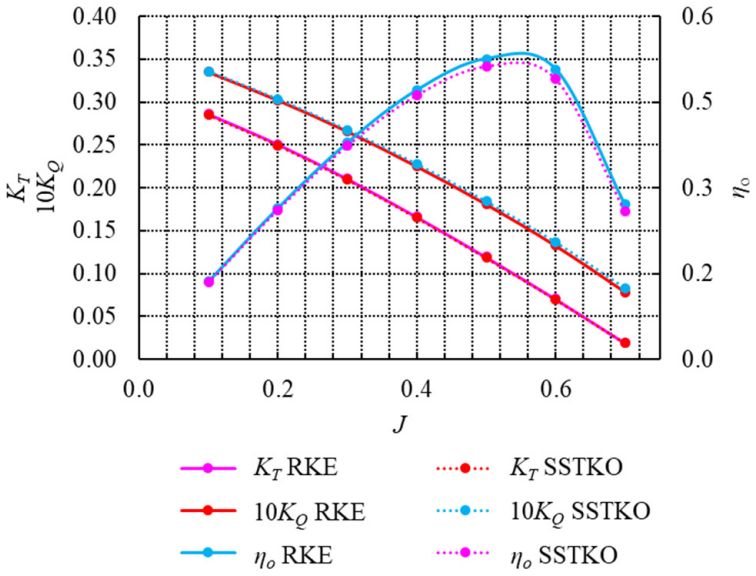


Figure 3. The open water curves of model scale propeller obtained using RKE and SSTKO turbulence models.

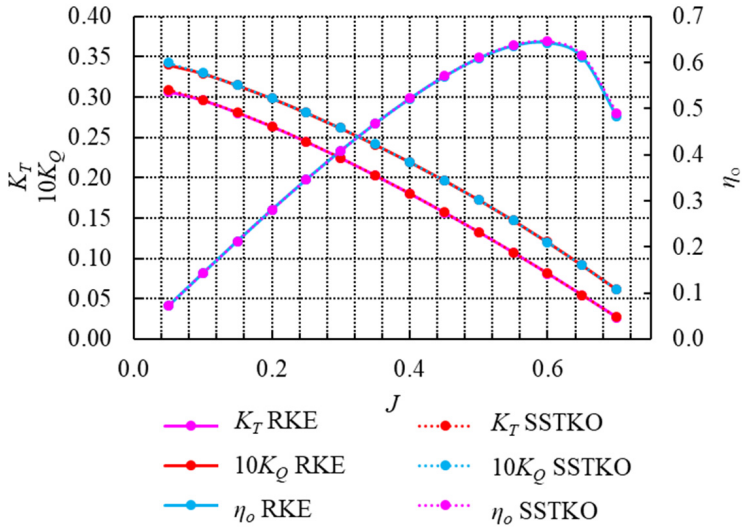


Figure 4. The open water curves of full-scale propeller obtained using RKE and SSTKO turbulence models.

3.3. Model Scale

The numerical simulations at the model scale are performed for non-dimensional wall distance $y^+ > 30$ and $y^+ \leq 1$. The open water curves for the first case are already presented in the previous subsection. Figure 5 shows the open water curves for the numerical simulations at the model scale with and without the transition model for the case with $y^+ \leq 1$. Table 6 shows the numerical values of the relative errors, with respect to the case with the transition model, at different advance coefficients and the average values as well.

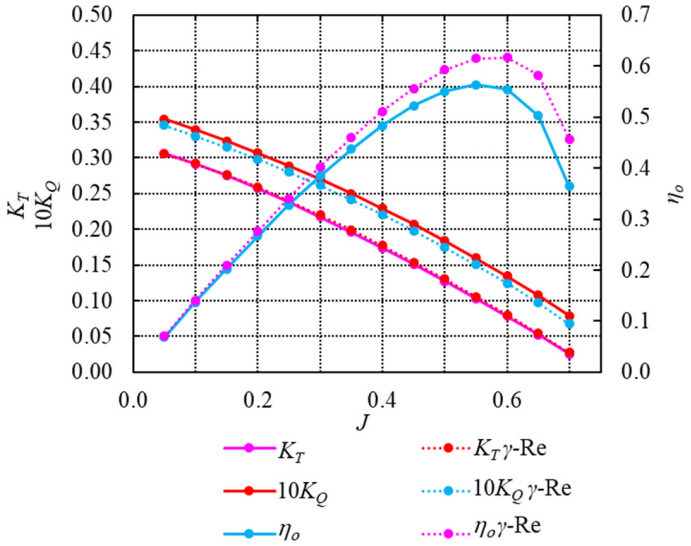


Figure 5. Open water curves for model scale with and without the transition model.

Table 6. Relative differences between the thrust and torque coefficients and open water efficiencies in the range of advance coefficients.

J	K_T, %	$10K_Q$, %	η_o, %
0.2	0.38	2.14	−1.72
0.4	−0.65	4.30	−4.74
0.6	−2.83	8.40	−10.36
0.7	−10.30	17.38	−23.58
Average	3.54	8.06	10.10

The data shows lower values of the torque coefficient for the case with the transition model enabled, which in turn leads to higher values of the open water efficiency. It can be seen that the transition model influences the torque coefficient more in comparison to the thrust coefficient.

Figures 6 and 7 show the distribution of the skin friction coefficient obtained from the model scale numerical simulations. Significant differences between the two cases can be noticed. The skin friction coefficient is lower in the case with the transition model, which is expected considering the partially laminar flow. The lower skin friction leads to lower values of the torque coefficient which results in higher open water efficiencies.

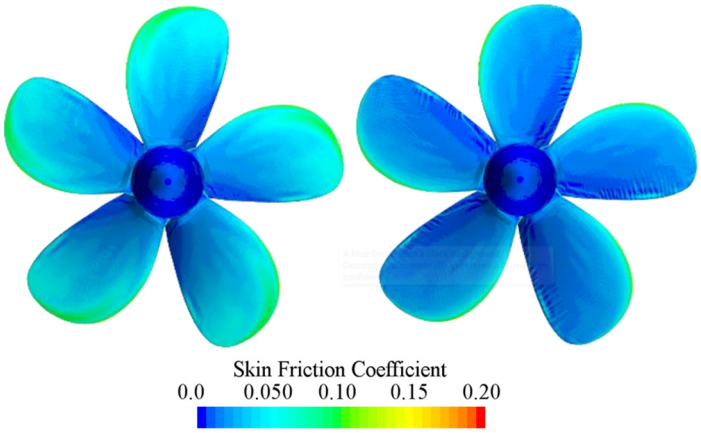


Figure 6. Distribution of the skin friction coefficient on the suction side obtained from numerical simulations at model scale for $J = 0.7$ without transition model (**left**) and with transition model (**right**).

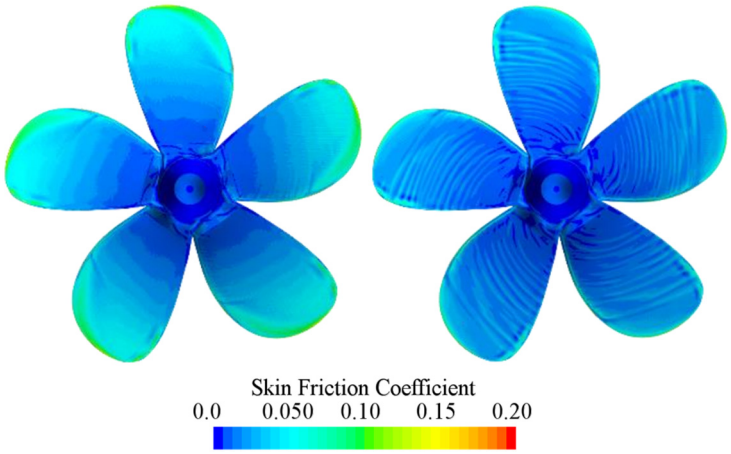


Figure 7. Distribution of the skin friction coefficient on the pressure side obtained from numerical simulations at model scale for $J = 0.7$ without transition model (**left**) and with transition model enabled (**right**).

3.4. Scale Effects

The open water curves obtained from numerical simulations at different scales are compared in this subsection. Figure 8 shows the open water efficiency as a function of the advance coefficient obtained from the simulations at different scales. Figures 9 and 10 show the thrust and torque coefficients, respectively. In Figures 8–10, the numerical results at the model scale are extrapolated to full-scale using the ITTC 1978 Performance Prediction Method (PPM). It can be noticed that the differences between the open water efficiencies are more apparent at higher advanced coefficients. The open water efficiency at the full-scale obtained using ITTC 1978 PPM is higher than at the model scale. However, the extrapolated values of open water efficiency are lower than the ones obtained using numerical simulations in full-scale. This can be attributed to the fact that ITTC 1978 PPM considers a rough full-scale propeller, while in this study smooth full-scale propeller is analyzed.

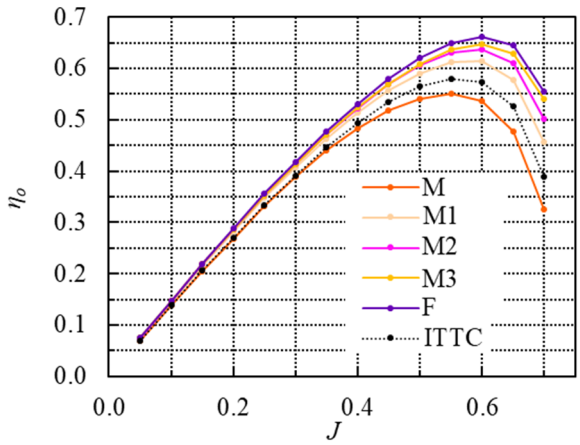


Figure 8. Open water efficiency as a function of advance coefficient for different scales.

Figure 8 shows that the open water efficiency increases with the decrease in scale. Minor discrepancies between the open water efficiencies are visible in the range of lower advance coefficients. The thrust coefficients decrease with the increase in scale, while the torque coefficients decrease with the decrease in scale. This tendency can be seen over the entire range of advance coefficients. It should be noted that the scale effects on the frictional component of the thrust and torque are significant, while the scale effects on the pressure component of the thrust and torque are relatively low [36]. Bhattacharyya et al. [36] noticed that the pressure component has a positive contribution, and the friction component has a negative contribution to the value of propeller thrust at any scale. On the other hand,

the absolute contributions from the pressure and friction components to the total torque are positive at any scale. At higher *Re* numbers, the portion of frictional components in the total torque and thrust values are lower in comparison to the portion of the frictional components in the total torque and thrust values at lower *Re* numbers, since the scale effects of the frictional component of the thrust and torque are significant. Since the frictional component has a positive contribution to the total torque, the torque coefficients will be lower at higher *Re* numbers. On the other hand, since the frictional component has a negative contribution to the total thrust, the thrust coefficients will be higher at higher *Re* numbers.

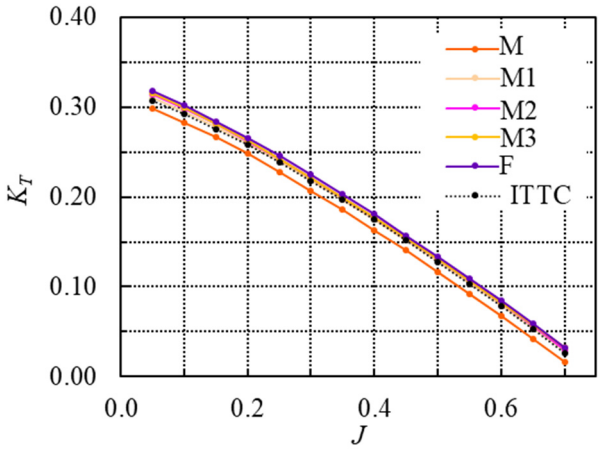


Figure 9. Thrust coefficient as a function of advance coefficient for different scales.

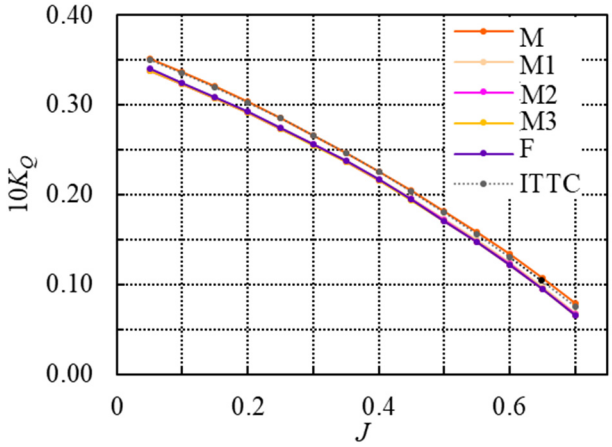


Figure 10. Torque coefficient as a function of advance coefficients for different scales.

Additionally, it is worth noting that the results of model scale numerical simulations have the same non-dimensional wall distance $y^+ > 30$ without the transition model. Large differences can be seen between the results obtained from the model scale simulations and the remaining simulations. This may be attributed to the fact that the scales for model and M1 are significantly different, i.e., $\lambda_M/\lambda_{M1} \approx 10$, and between the other scales the difference is significantly lower.

Table 7 presents the differences between the numerical values obtained for all scales at several advanced coefficients as well as the average values. These differences are calculated using the equation:

$$\Delta\phi = \frac{\phi_x - \phi_M}{\phi_M} \cdot 100\% \tag{23}$$

where ϕ stands for either K_T, K_Q, or η_o, index x denotes either M1, M2, M3, or F, and index M stands for model scale.

Table 7. The change in open water characteristics between the model scale and other scales.

	M1			M2		
J	K_T, %	$10K_Q$, %	η_o, %	K_T, %	$10K_Q$, %	η_o, %
0.1	4.37	−3.84	8.54	5.35	−4.03	9.77
0.2	4.70	−3.76	8.79	5.72	−4.09	10.22
0.3	5.61	−3.71	9.69	6.76	−4.08	11.30
0.4	7.23	−3.94	11.63	8.68	−4.40	13.68
0.5	10.12	−4.80	15.67	11.80	−5.71	18.57
0.6	17.76	−6.85	26.41	20.49	−8.24	31.31
Average	8.30	4.48	13.46	9.80	5.09	15.81
	M3			**F**		
J	K_T, %	$10K_Q$, %	η_o, %	K_T, %	$10K_Q$, %	η_o, %
0.1	5.79	−3.95	10.14	6.62	−3.42	10.39
0.2	5.94	−4.04	10.40	7.12	−3.59	11.10
0.3	6.81	−4.13	11.41	8.39	−3.68	12.53
0.4	8.68	−4.53	13.84	10.62	−4.18	15.45
0.5	11.83	−6.16	19.17	14.09	−5.95	21.30
0.6	21.65	−8.87	33.49	24.46	−8.74	36.38
Average	10.12	5.28	16.41	11.88	4.92	17.86

The highest average change in open water efficiencies is obtained for full-scale and it is equal to 17.86%.

Figures 11 and 12 show the obtained distribution of the skin friction coefficient at the advance coefficient $J = 0.7$ on the pressure and suction side of the propeller. The coefficient is calculated using the same density of the fluid, but with different speeds of advance for each case. It is visible that with the decrease in the scale of the propeller, the skin friction coefficient decreases, which is expected since the Reynolds number increases with the decrease in scale. The values of skin friction coefficient near the propeller hub are low with the tendency to in-crease at higher radii. This can be attributed to the fact that the friction velocity at higher radii is significantly higher. It is worth mentioning that the differences in skin friction co-efficients for M3 and F are insignificant.

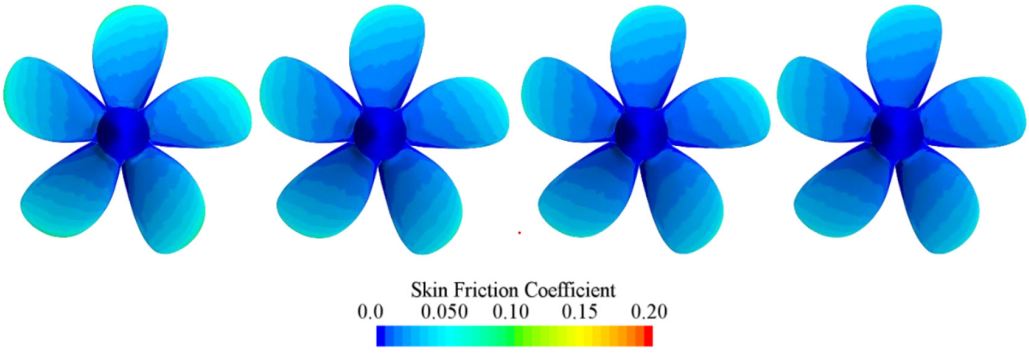


Figure 11. Distribution of the skin friction coefficient obtained from the numerical simulations at different scales on the suction side ($J = 0.7$)—M1 (**first**), M2 (**second**), M3 (**third**), F (**fourth**).

The distributions of the turbulent viscosity ratio (TVR) at $0.75R$ are presented in Figure 13. TVR is defined as the ratio between turbulent viscosity μ_t and dynamic viscosity μ. It is shown that the turbulent viscosity for the model scale is equal to zero, which suggests that the flow is laminar. For other scales, TVR around the blade profile increases with the decrease in scale. It is shown that the flow around the blade is turbulent and that the Reynolds stress increases with the decrease in scale in comparison to viscous shear stress.

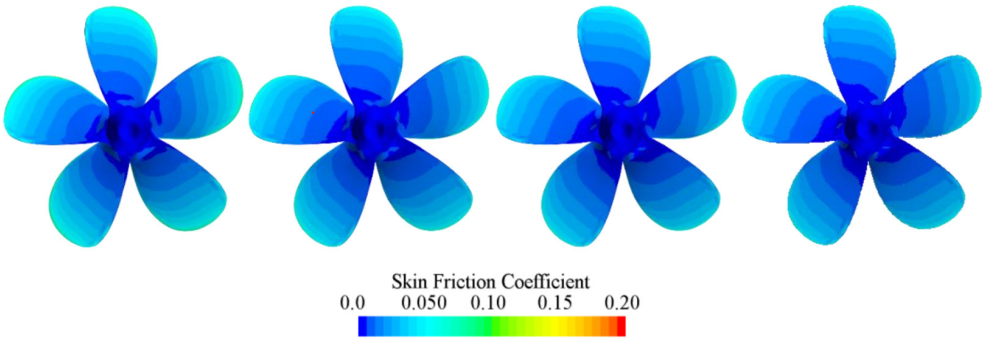


Figure 12. Distribution of the skin friction coefficient obtained from the numerical simulations at different scales on the pressure side ($J = 0.7$)—M1 (**first**), M2 (**second**), M3 (**third**), F (**fourth**).

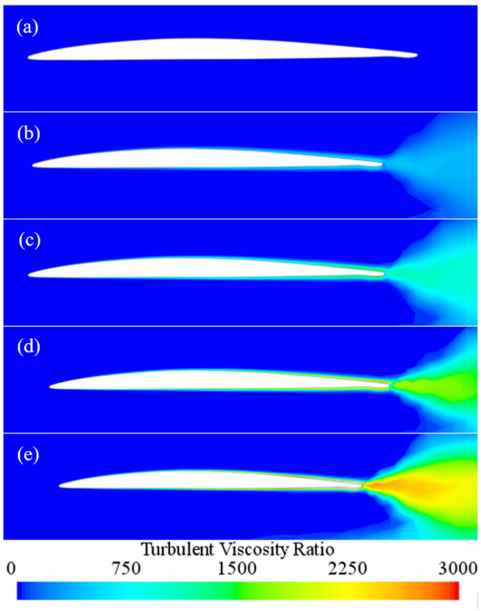


Figure 13. Turbulent viscosity ratio at $0.75R$ for $J = 0.7$ at different scales—M (**a**), M1 (**b**), M2 (**c**), M3 (**d**), F (**e**).

Figure 14 shows the open water efficiency for M1, M2, M3, and F propellers as well as for the model scale obtained with the transition model. It can be seen that the open water efficiency increases once the transition model is applied. From this figure, it can be seen that the impact of the scale effect on open water efficiency is significantly lower if the tran-sition model is applied for the model scale simulations.

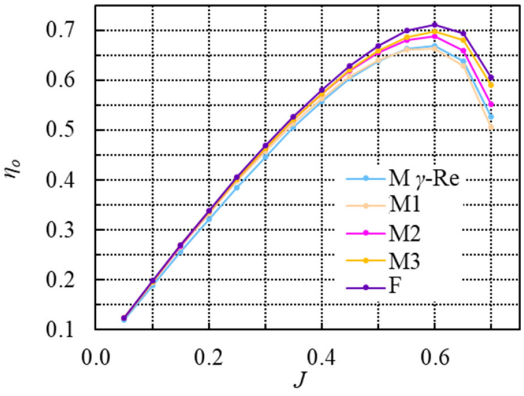


Figure 14. The obtained open water efficiencies.

4. Conclusions

Numerical simulations of the open water test (OWT) are performed at different scales. The simulation setup is described in detail as well as the meshing process. The numerical simulations of the flow around the propeller are carried out using the steady-state moving reference frame (MRF) method. Special attention is given to the grid refinements around the MRF zone and the area around the propeller to predict the flow more accurately. The shear stress transport $k-\omega$ (SSTKO) turbulence model is used to close the system of equations since it can be coupled with the Gamma Reynolds Theta ($\gamma - Re_\theta$) transition model and it is the best compromise between the accuracy and the required computational time. The non-dimensional wall distance y^+ is kept below 1 for the numerical simulations at the model scale, including the transition model, to obtain more accurate results since the laminar flow is present. Within the numerical simulations for other scales, the non-dimensional wall distance is above 30 and the transition model is disabled. The verification study is performed for spatial discretization using the grid convergence index (GCI) method, which shows that the medium size grid is appropriate in terms of computational time and the accuracy of the results. The open water curves are presented for the numerical simulations at the model scale with the transition model, which is compared to the case without the transition model. The results show that when the transition model is applied, the torque coefficient decreases, and thus the open water efficiency increases, which is also confirmed by the distribution of the skin friction coefficient. The scale effects can be noticed from the obtained open water curves, the distribution of the skin friction, as well as the turbulence viscosity ratio (TVR) field. It can be concluded that the open water efficiency increases with the decrease in scale. Finally, a comparison between the numerical simulations at the model scale with the transition model with the numerical simulations at other scales is given. It should be noted that when the transition model is applied, the scale effects on open water characteristics are significantly lower.

Author Contributions: Conceptualization, C.G.G., N.D., A.F. and I.M.; methodology, N.D., A.F. and I.M.; software, C.G.G.; validation, C.G.G.; formal analysis, C.G.G., N.D., A.F. and I.M.; investigation, C.G.G., N.D., A.F. and I.M.; resources, C.G.G., N.D., A.F. and I.M.; writing—original draft preparation, C.G.G., N.D., A.F. and I.M.; writing—review and editing, C.G.G., N.D., A.F. and I.M.; visualization, C.G.G.; supervision, N.D. and A.F.; All authors have read and agreed to the published version of the manuscript.

Funding: This study has been fully supported by the Croatian Science Foundation under project IP-2020-02-8568.

Institutional Review Board Statement: Not applicable.

Informed Consent Statement: Not applicable.

Data Availability Statement: Not applicable.

Acknowledgments: This study has been fully supported by the Croatian Science Foundation under project IP-2020-02-8568.

Conflicts of Interest: The authors declare no conflict of interest.

References

1. Farkas, A.; Degiuli, N.; Martić, I.; Dejhalla, R. Numerical and experimental assessment of nominal wake for a bulk carrier. *J. Mar. Sci. Technol.* **2019**, *24*, 1092–1104. [CrossRef]
2. Jang, Y.H.; Eom, M.J.; Paik, K.J. A Numerical Study on the Open Water Performance of a Propeller with Sinusoidal Pitch Motion. *Brodogradnja* **2020**, *71*, 71–83. [CrossRef]
3. Sun, Y.; Wu, T.; Su, Y.; Peng, H. Numerical Prediction on Vibration and Noise Reduction Effects of Propeller Boss Cap Fins on a Propulsion System. *Brodogradnja* **2020**, *71*, 1–18. [CrossRef]
4. Helma, S.; Streckwall, H.; Richter, J. The Effect of Propeller Scaling Methodology on the Performance Prediction. *J. Mar. Sci. Eng.* **2018**, *6*, 60. [CrossRef]
5. Helma, S. A scaling procedure for modern propeller designs. *Ocean Eng.* **2016**, *106*, 120, 165–174. [CrossRef]

6. Bekhit, A.S.; Lungu, A. Simulation of the POW performance of the JBC propeller. In Proceedings of the AIP Conference Proceedings, Rhodes, Greece, 13–18 September 2019.
7. Niklas, K.; Pruszko, H. Full-scale CFD simulations for the determination of ship resistance as a rational, alternative method to towing tank experiments. *Ocean Eng.* **2019**, *190*, 106435. [CrossRef]
8. Mikkelsen, H.; Walther, J.H. Effect of roughness in full-scale validation of a CFD model of self-propelled ships. *Appl. Ocean Res.* **2020**, *99*, 102162. [CrossRef]
9. Bulten, N.; Stoltenkamp, P. Full scale CFD: The end of the Froude-Reynolds battle. In Proceedings of the Fifth International Symposium on Marine Propulsion, Espoo, Finland, 12–15 June 2017.
10. Li, D.Q.; Lindell, P.; Werner, S. Transitional flow on model propellers and their influence on relative rotative efficiency. *J. Mar. Sci. Eng.* **2019**, *7*, 427. [CrossRef]
11. Brown, M.; Schroeder, S.; Balaras, E. Vortex structure characterization of tip-loaded propellers. In Proceedings of the 4th International Symposium on Marine Propulsors (SMP'15), Austin, TX, USA, 31 May–4 June 2015.
12. Dong, X.Q.; Li, W.; Yang, C.J.; Noblesse, F. RANSE-based simulation and analysis of scale effects on open-water performance of the PPTC-II benchmark propeller. *JOES* **2018**, *3*, 186–204. [CrossRef]
13. Kim, S.; Kinnas, S.A. Prediction of cavitating performance of a tip loaded propeller and its induced hull pressures. *Ocean Eng.* **2021**, *229*, 108961. [CrossRef]
14. Chen, X.; Huang, Y.; Wei, P.; Zhang, Z.; Jin, F. Numerical analysis of scale effect on propeller E1619. In Proceedings of the International Conference on Offshore Mechanics and Arctic Engineering—OMAE, Madrid, Spain, 17–22 June 2018.
15. Owen, D.; Demirel, Y.K.; Oguz, E.; Tezdogan, T.; Incecik, A. Investigating the effect of biofouling on propeller characteristics using CFD. *Ocean Eng.* **2018**, *159*, 505–516. [CrossRef]
16. Tran Ngoc, T.; Luu, D.D.; Nguyen, T.H.H.; Nguyen, T.T.Q.; Nguyen, M.V. Numerical Prediction of Propeller-Hull Interaction Characteristics Using RANS Method. *Pol. Marit. Res.* **2019**, *26*, 163–172. [CrossRef]
17. Vlašić, D.; Degiuli, N.; Farkas, A.; Martić, I. The preliminary design of a screw propeller by means of computational fluid dynamics. *Brodogradnja* **2018**, *69*, 129–147. [CrossRef]
18. Mikkelsen, H.; Steffensen, M.; Ciortan, C.; Walther, J. Ship Scale Validation of CFD Model of Self-propelled Ship. In Proceedings of the MARINE 2019: Computational Methods in Marine Engineering VIII, Göteborg, Sweden, 13–15 May 2019.
19. Mejia, O.D.L.; Mejia, O.E.; Escorcia, K.M.; Suarez, F.; Laín, S. Comparison of Sliding and Overset Mesh Techniques in the Simulation of a Vertical Axis Turbine for Hydrokinetic Applications. *Processes* **2021**, *9*, 1933. [CrossRef]
20. Wang, J.; Zhao, W.; Wan, D. Simulations of Self-Propelled Fully Appended Ship Model at Different Speeds. *Int. J. Comput. Methods* **2019**, *16*, 1840015. [CrossRef]
21. A Workshop on CFD in Ship Hydrodynamics. Available online: https://www.t2015.nmri.go.jp/ (accessed on 19 July 2022).
22. Bekhit, A.S.; Lungu, A. Numerical Study of the Resistance, Free-surface and Self-propulsion Prediction of the KVLCC2 Ship Model. In Proceedings of the International Conference on Traffic and Transport Engineering (ICTTE), Belgrade, Serbia, 27–28 September 2018.
23. Lungu, A. Numerical Simulation of the Resistance and Self-Propulsion Model Tests. *J. Offshore Mech. Arct. Eng.* **2020**, *142*, 021905. [CrossRef]
24. Farkas, A.; Degiuli, N.; Martić, I. The impact of biofouling on the propeller performance. *Ocean Eng.* **2021**, *219*, 108376. [CrossRef]
25. Farkas, A.; Degiuli, N.; Martić, I.; Dejhalla, R. Impact of hard fouling on the ship performance of different ship forms. *J. Mar. Sci. Eng.* **2020**, *8*, 748. [CrossRef]
26. Farkas, A.; Song, S.; Degiuli, N.; Martić, I.; Demirel, Y.K. Impact of biofilm on the ship propulsion characteristics and the speed reduction. *Ocean Eng.* **2020**, *199*, 107033. [CrossRef]
27. Dogrul, A. Numerical Prediction of Scale Effects on the Propulsion Performance of Joubert BB2 Submarine. *Brodogradnja* **2022**, *73*, 17–42.
28. Gonzalez-Adalid, J.; Perez-Sobrino, M.; Gaggero, S.; Gennaro, G.; Moran Guerrero, A. The use of modern computational tools in the design process of unconventional propellers for performance prediction and full-scale extrapolation. In Proceedings of the 19th International Conference on Ship and Maritime Research—NAV 2018, Trieste, Italy, 20–22 June 2018.
29. Baltazar, J.; Rijpkema, D.; Falcão de Campos, J. On the use of the $\Gamma-Re\Theta t$ transition model for the prediction of the propeller performance at model-scale. *Ocean Eng.* **2018**, *170*, 6–19. [CrossRef]
30. Moran-Guerrero, A.; Gonzalez-Gutierrez, L.M.; Oliva-Remola, A.; Diaz-Ojeda, H.R. On the influence of transition modeling and crossflow effects on open water propeller simulations. *Ocean Eng.* **2018**, *156*, 101–119. [CrossRef]
31. Pawar, S.; Brizzolara, S. Relevance of transition turbulent model for hydrodynamic characteristics of low Reynolds number propeller. *Appl. Ocean Res.* **2019**, *87*, 165–178. [CrossRef]
32. Baek, D.G.; Yoon, H.S.; Jung, J.H.; Kim, K.S.; Paik, B.G. Effects of the advance ratio on the evolution of a propeller wake. *Comput. Fluids* **2015**, *118*, 32–43. [CrossRef]
33. Farkas, A.; Degiuli, N.; Martić, I. Assessment of hydrodynamic characteristics of a full-scale ship at different draughts. *Ocean Eng.* **2018**, *156*, 135–152. [CrossRef]
34. Menter, F.R.; Langtry, R.B.; Likki, S.R.; Suzen, Y.B.; Huang, P.G.; Völker, S. A correlation-based transition model using local variables—Part I: Model formulation. *J. Turbomach.* **2006**, *128*, 413–422. [CrossRef]

35. Yao, H.; Zhang, H. Numerical simulation of boundary-layer transition flow of a model propeller and the full-scale propeller for studying scale effects. *J. Mar. Sci. Technol.* **2018**, *23*, 1004–1018. [CrossRef]
36. Bhattacharyya, A.; Krasilnikov, V.; Steen, S. A CFD-based scaling approach for ducted propellers. *Ocean Eng.* **2016**, *123*, 116–130. [CrossRef]

Article III

Article published by Elsevier in Results in engineering on 30 April 2025, available online: https://www.sciencedirect.com/science/article/pii/S2590123025011703

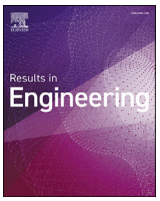
Results in Engineering 26 (2025) 105095



Contents lists available at ScienceDirect

Results in Engineering

journal homepage: www.sciencedirect.com/journal/results-in-engineering



Research paper



Assessment of the effect of speed and scale on the total resistance and its components for a bulk carrier

Carlo Giorgio Grlj, Nastia Degiuli *, Ivana Martić

University of Zagreb, Faculty of Mechanical Engineering and Naval Architecture, Ivana Lučića 5, Zagreb, 10000, Croatia

ARTICLE INFO

Keywords:
CFD
Resistance test
DBS
FSS
Resistance components
Slow steaming

ABSTRACT

Reducing greenhouse gas emissions has become one of the primary goals for maritime transport today. One widely adopted, short-term, and cost-effective operational measure is slow steaming. Therefore, it is essential to assess the resistance characteristics of ships operating at reduced speeds, given that each vessel is optimized for a specific design speed. Computational fluid dynamics is employed to predict the total resistance coefficient and its components and to determine the form factor at various speeds and scales. The numerical approach is based on the Reynolds Averaged Navier-Stokes equations, discretized using the finite volume method. The study employs two numerical approaches: simulations conducted both with and without the presence of the free surface. This allows the decomposition of the total resistance coefficient into its components, namely, frictional, viscous pressure, and wave resistance coefficients. The results show significant scale effects and a minor effect of speed on the total resistance coefficient and its components. The total resistance coefficient and its components decrease as speed increases and scale decreases. The virtual fluid method is employed, and the results show that the total resistance coefficient and its components for the full-scale ship can be derived from numerical simulations conducted at model scale. Although speed has a minor effect on the form factor, significant scale effects are observed.

1. Introduction

The reduction in greenhouse gas (GHG) emissions from maritime transport is essential due to its adverse effect on the Earth's atmosphere. The International Maritime Organization (IMO) has already introduced a strategy in 2018 [1], which is intended to lower the annual GHG emissions from international shipping by 50% by 2050 in comparison to the annual GHG emissions from 2008 [2]. This can be achieved for new ships by decreasing the carbon intensity and strengthening the Energy Efficiency Design Index (EEDI). Tu et al. [3] presented an overview of various GHG abatement measures, which can be divided into technical, operational, and renewable energy utilization measures and alternative fuels. Slow steaming is an efficacious short-term operational measure that has GHG abatement potential of 19% if the sailing speed is reduced by 10% with regard to the considered ship types with the exception of cruise vessels and ferries [3]. Balcombe et al. [4] showed that by applying slow steaming a reduction in fuel consumption and carbon dioxide emissions of 20-30% can be achieved, and in the extreme cases up to 60%. In a similar study conducted by Ammar [5], the author concluded that carbon dioxide emissions of a Ro-Ro cargo vessel can be reduced up to 78% for a speed reduction of 40%. Since January 2023, the operational Carbon Intensity Indicator (CII) has been adopted by the Marine Environment Protection Committee (MEPC), which provides a rating of existing ships ranging from A to E [6]. Hua et al. [7] proposed a speed optimization model designed to maximize economic benefits while complying with the CII requirements set by the MEPC. The authors demonstrated that substantial improvements in annual full load distance can be achieved using the proposed optimization method, all while maintaining a C-rating or better. Zincir [6] showed that at main engine loads of a general cargo ship equal to 38%, fuel savings of 31.5% can be achieved while the CII rating remains A. Thus, the authors confirmed that by applying slow steaming as a measure to mitigate GHG emissions, ships can achieve the target GHG emission reductions set by IMO for 2030 and 2050.

Since slow steaming is a viable measure for the mitigation of GHG emissions and is being applied widely, ships operate in conditions that are considerably different from the design conditions [8]. The determination of ship hydrodynamic characteristics is essential for the prediction of the effect of slow steaming on the ship energy efficiency. Experimental Fluid Dynamics (EFD) and Computational Fluid Dynamics

* Corresponding author.
E-mail address: nastia.degiuli@fsb.unizg.hr (N. Degiuli).

https://doi.org/10.1016/j.rineng.2025.105095
Received 14 March 2025; Received in revised form 3 April 2025; Accepted 24 April 2025
Available online 30 April 2025
2590-1230/© 2025 The Author(s). Published by Elsevier B.V. This is an open access article under the CC BY-NC-ND license (http://creativecommons.org/licenses/by-nc-nd/4.0/).

(CFD) are the most common tools for the determination of ship resistance and propulsion characteristics. Numerical simulations at full scale have been employed to avoid the problems regarding the extrapolation of the results obtained at the model to full scale [9]. Significant scale effects on the ship hydrodynamic characteristics are caused by the fact that Froude similarity is satisfied while the Reynolds number is different for the model and full scale. Guo et al. [10] performed a towing test on a large-scale model for the case of a full-formed ship and found significant scale effects on the residuary resistance. Dogrul et al. [11] investigated the scale effects on resistance components and the form factor by performing numerical simulations at various scales, both with and without the presence of a free surface. The authors obtained considerable scale effects on the residuary resistance coefficient for the KVLCC2 and almost negligible scale effects for the KCS. It was concluded that the reason for the differences in the obtained residuary resistance coefficients is attributed to the different scale effects and portions of the viscous pressure and wave resistances to the total resistance of the KCS and KVLCC2. By conducting numerical simulations of viscous flow Farkas et al. [12] showed that scale effects on the wave resistance coefficient of a tanker were present. The authors proposed considering the scaling of the wave resistance coefficient within the extrapolation methods. Kouh et al. [13] conducted a comprehensive analysis of the scale effect on the form factor for four surface ships and two submerged bodies. The authors used Double Body Simulations (DBS) for the calculation of the form factor and concluded that the form factor increases linearly with the Reynolds number for all the considered ship types and sub-bodies. Farkas et al. [14] examined the impact of applying wall functions in numerical simulations of the resistance test for a handymax bulk carrier. Negligible differences are obtained in numerical simulations with and without the usage of wall functions at model scale and, thus, wall functions were used in the numerical simulations at full scale. The authors found considerable scale effects on the integral value of the nominal wake and the distribution of the circumferentially averaged dimensionless axial velocity. Dogrul [15] investigated the scale effects on the propulsion performance of a Joubert BB2 submarine. Within the study, the author carried out numerical simulations of the resistance test at model and full scale for a range of speeds. The results obtained at model scale were extrapolated with the Hughes' 3D extrapolation method and were compared to the total resistance obtained at full scale. Good agreement was shown between the extrapolated total resistances and those obtained at full scale, with the average absolute relative error lower than 1%. Saydam et al. [16] achieved satisfactory results regarding the determination of the total resistance of a tanker by employing the proposed method for estimating propulsion characteristics. The proposed numerical approach involved conducting numerical simulations of the resistance test at model scale and the obtained numerical results were extrapolated to full scale to predict the propulsion characteristics.

Haase et al. [17] satisfied Froude and Reynolds similarities by adjusting the viscosity of the water to overcome the issues regarding the scale effects on the ship hydrodynamic characteristics in the numerical simulations. Zhao et al. [18] conducted numerical simulations of the self-propulsion test based on the complete similarity theory meaning that the kinematic viscosity of the fluid has been adjusted to maintain the full-scale Reynolds and Froude numbers at the model scale. Similarly, Sezen and Cakici [19] performed numerical simulations with the full similarity technique, i.e., using virtual fluid, at different Froude numbers for the DTMB 5512 ship and showed that it is a viable method for the assessment of the total resistance of a ship at full-scale Reynolds number. Haase et al. [17] applied the same method for the prediction of full-scale resistance of medium-speed catamarans. The main benefit of the presented method is that geometric dimensions are kept at model scale, and thus the numerical simulations require lower computational time. Terziev et al. [20] investigated the scale effects on the resistance components where the authors conducted DBS using the fluid with the altered viscosity, i.e., virtual fluid. More recently, Kim et al. [21] showed that virtual fluid can be applied in the numerical simulations and obtained satisfactory results at model scale without the need to conduct numerical simulations at full-scale, which are computationally more demanding. The authors showed satisfactory agreement between the shear stress distributions, dynamic pressure distributions, and the wake fields obtained with numerical simulations at full scale and model scale with the virtual fluid.

In this study, the scale effects on the total resistance and resistance components for the case of the Japan Bulk Carrier (JBC) are assessed for a wide range of speeds from 11 knots to 16 knots for the full-scale ship. A comprehensive investigation of the scale effects on the total resistance and resistance components is carried out by performing numerical simulations with and without the presence of the free surface. Additionally, the virtual fluid method, which involves adjusting fluid viscosity, is employed to calculate total resistance and its components through numerical simulations at the model scale. To determine the numerical uncertainty comprehensive verification studies are conducted. A validation study is conducted by comparing the numerically obtained results with the experimental results obtained by the same authors [22].

The rest of the paper is structured as follows: the mathematical background, numerical setup, case study, and the decomposition of the total resistance are given in Section 2. The obtained results are given in Section 3 and the main conclusions are drawn in Section 4.

2. Materials and methods

2.1. Mathematical background

The mathematical model is based on the Reynolds Averaged Navier-Stokes (RANS) equations [23], which for the case of incompressible and unsteady flow read as follows:

$$\frac{\partial \bar{u}_i}{\partial x_i} = 0 \tag{1}$$

$$\rho \frac{\partial \bar{u}_i}{\partial t} + \rho \frac{\partial}{\partial x_j}\left(\bar{u}_i \bar{u}_j + \overline{u_i' u_j'}\right) = -\frac{\partial \bar{p}}{\partial x_i} + \frac{\bar{\tau}_{ij}}{\partial x_j} \tag{2}$$

where ρ is the fluid density, $\bar{u}_i$ is the averaged Cartesian components of the velocity vector, $\rho\overline{u_i' u_j'}$ is the Reynolds Stress Tensor (RST), $\bar{p}$ is the mean pressure and $\bar{\tau}_{ij}$ is the mean viscous stress tensor. For the closure of Equations (1) and (2) the Menter's [24] modified Shear Stress Transport $k-\omega$ (SSTKO) turbulence model is applied, as it has proven to be an effective balance between result accuracy and computational efficiency [25–28]. More importantly, the SSTKO turbulence model is considered robust due to its ability to effectively handle adverse pressure gradients and flow separation, which occur specifically in the stern region [11,29]. More details regarding the equations for solving the turbulent kinetic energy k and the specific dissipation rate ω can be found in [30,31].

The governing equations are discretized with the finite volume method, while the volume of fluid method [32] is applied for locating and tracking the free surface. These equations are solved using a segregated approach, the convection and gradient terms are solved with a second-order scheme, and the temporal discretization is carried out with a first-order scheme, in accordance with the recommendations from Grlj et al. [33].

For the decomposition of the total resistance into resistance components, the Free Surface Simulations (FSS) and the DBS were conducted. More details regarding the decomposition of the total resistance can be found in subsection 2.2, while the numerical setups are presented in subsection 2.4.

2.2. Total resistance decomposition

According to Molland et al. [34] the total resistance coefficient C_T can be divided into wave resistance C_W and viscous resistance C_V coefficients:

$$C_T = C_W + C_V \tag{3}$$

Table 1
Main particulars of the JBC.

Main particular	Value			
Scale λ	1	2	20	40.264
Length between perpendiculars L_{PP}, m	280	140	14	6.954
Length of waterline L_{WL}, m	285	142.5	14.25	7.078
Breadth B, m	45	22.5	2.25	1.118
Draught T, m	16.5	8.25	0.825	0.410
Displacement volume ∇, m^3	178 420.1	22 302.51	22.303	2.733

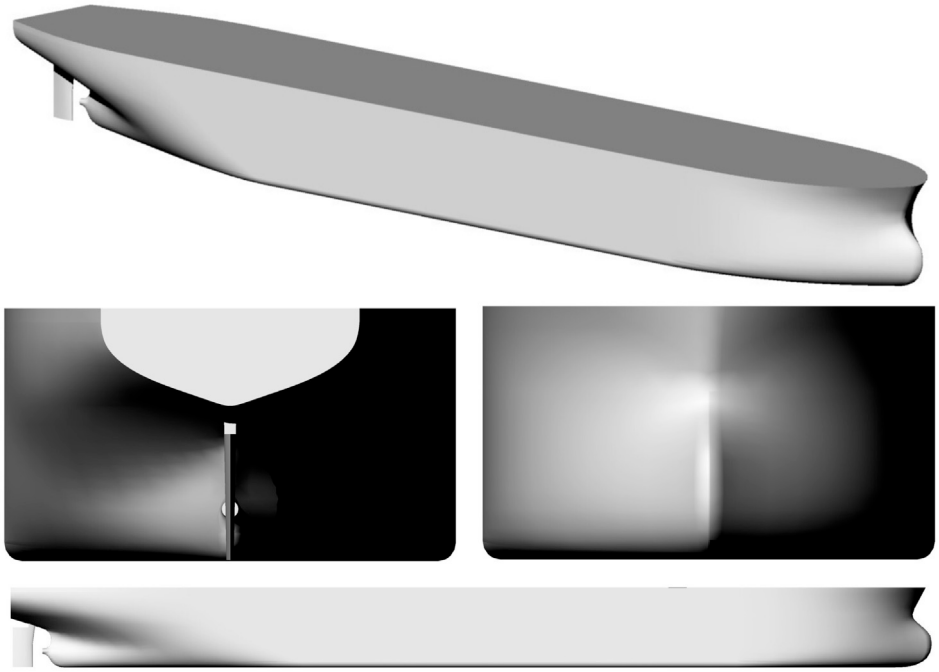


Fig. 1. The three-dimensional model of the JBC.

The total resistance coefficient is obtained by FSS, while the viscous resistance coefficient can be obtained with DBS since the wave resistance can be neglected for a body fully submerged in a fluid with infinite depth [35]. By subtracting the viscous resistance coefficient obtained by DBS from the total resistance coefficient obtained by FSS the wave resistance coefficient is obtained:

$$C_W = C_T - C_V \tag{4}$$

The viscous resistance coefficient can be further decomposed into the frictional resistance coefficient C_F and the viscous pressure resistance coefficient C_{VP} as follows:

$$C_V = C_F + C_{VP} \tag{5}$$

The frictional resistance coefficient is obtained in DBS by the integration of the tangential stresses over the immersed hull surface, while the viscous pressure resistance coefficient is obtained by the integration of pressure stresses over the immersed hull surface [35,36]. The frictional and viscous pressure resistance coefficients are used for the calculation of the form factor k as follows:

$$k = \frac{C_{VP}}{C_F} \tag{6}$$

The coefficient of the total resistance and the resistance components C_X are calculated by dividing the numerically obtained resistance R_X by dynamic pressure and wetted surface as follows:

$$C_X = \frac{R_X}{\frac{1}{2}\rho v^2 S} \tag{7}$$

where v is the ship speed and S is the wetted surface.

2.3. Case study

The numerical simulations of the resistance test are performed for the case of the JBC [37], which features a bulbous bow and a transom stern. The JBC is a capesize bulk carrier developed by the National Maritime Research Institute at the Yokohama National University, and the Ship Building Research Centre of Japan. Table 1 presents the main specifications of the JBC, while Fig. 1 provides a 3D model. A model scale of 40.264, closely matching the original JBC model scale, was used in a comprehensive experimental campaign conducted at the Brodarski Institute in Zagreb, Croatia [22]. Additionally, two other scales were chosen to evaluate the scale effects on the total resistance coefficient and resistance components, alongside the model and full scales.

2.4. Numerical setup

2.4.1. Computational domain

The computational domains in both DBS and FSS consist of a rectangular-shaped box that is discretized with hexahedral finite volumes. Only half of the domain is generated to keep a lower number of cells and reduce the computational time of the numerical simulations. Following the ITTC guidelines for CFD simulations [38], the computational domain extends $1.5L_{PP}$ in front of the bow, $3L_{PP}$ behind the stern, $1.5L_{PP}$ from the side of the ship, and $2L_{PP}$ from the keel. In FSS the top boundary is positioned at $1.5L_{PP}$ above the deck of the ship, while in DBS the top boundary is placed at the free surface. Figs. 2 and 3 show the dimensions of the computational domains of the DBS and

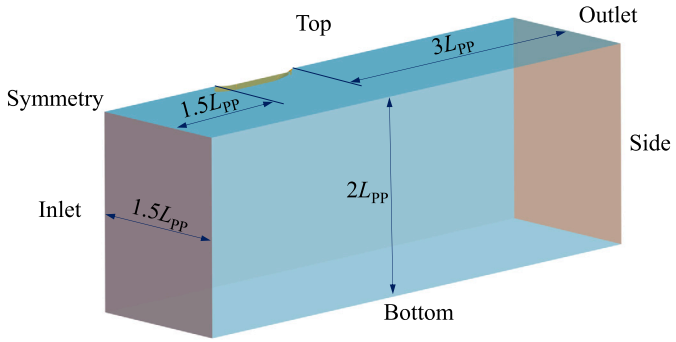


Fig. 2. The computational domain of the DBS.

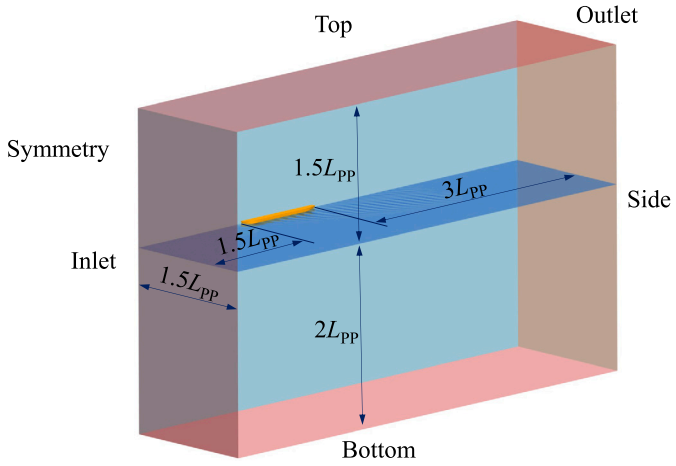


Fig. 3. The computational domain of the FSS.

FSS, respectively, with prescribed boundary conditions. Table 2 shows the boundary conditions applied in DBS and FSS.

The mesh is generated using hexahedral cells with refinements in the bow and stern regions and around the hull. Further refinements are added at the expected location of the free surface and Kelvin wake. Fig. 4 shows the created meshes for the DBS and FSS. It can be noticed that the mesh for DBS was created with the same refinements to maintain

Table 2
The applied boundary conditions.

	Boundary condition	
Boundary	DBS	FSS
Inlet	Inlet velocity	Inlet velocity
Side	Symmetry	Symmetry
Outlet	Outlet pressure	Outlet pressure
Symmetry	Symmetry	Symmetry
Top	Symmetry	Inlet velocity
Bottom	Symmetry	Inlet velocity

the meshes in two different numerical approaches similar. Prism layers were carefully created around the hull surface to keep the dimensionless wall distance y^+ above 30 at the centre of the first cell next to the wall, so wall functions can be applied. Fig. 5 shows the prism layers created near the hull, and in Fig. 6 the obtained dimensionless wall distance in DBS and FSS can be seen. The creation of prism layers was omitted along the deck of the ship.

2.4.2. Virtual fluid

One of the advantages of using CFD over EFD is the fact that the properties of the simulated fluid can be arbitrarily changed [21] and thus, the Reynolds and Froude similarity can be satisfied simultaneously. The same Froude number can be obtained at model and full scale by altering the ship speed assuming that the gravitational acceleration is constant. Froude similarity is satisfied with the following relationship:

$$v_M = \frac{v_S}{\sqrt{\lambda}} \tag{8}$$

where the subscripts M and S denote the speed at model and full scale, respectively. A virtual fluid is defined by adjusting its dynamic viscosity while maintaining the density equal [17]. In this study, the freshwater density is equal to $\rho = 999.49\ \mathrm{kg/m^3}$. The Reynolds similarity is obtained by applying the following relationship:

$$Re_S = Re_M \tag{9}$$

$$\frac{\rho v_S L_{PP,S}}{\mu_S} = \frac{\rho v_M L_{PP,M}}{\mu_M} \tag{10}$$

$$\frac{\mu_S}{\mu_M} = \frac{v_S}{v_M}\lambda \tag{11}$$

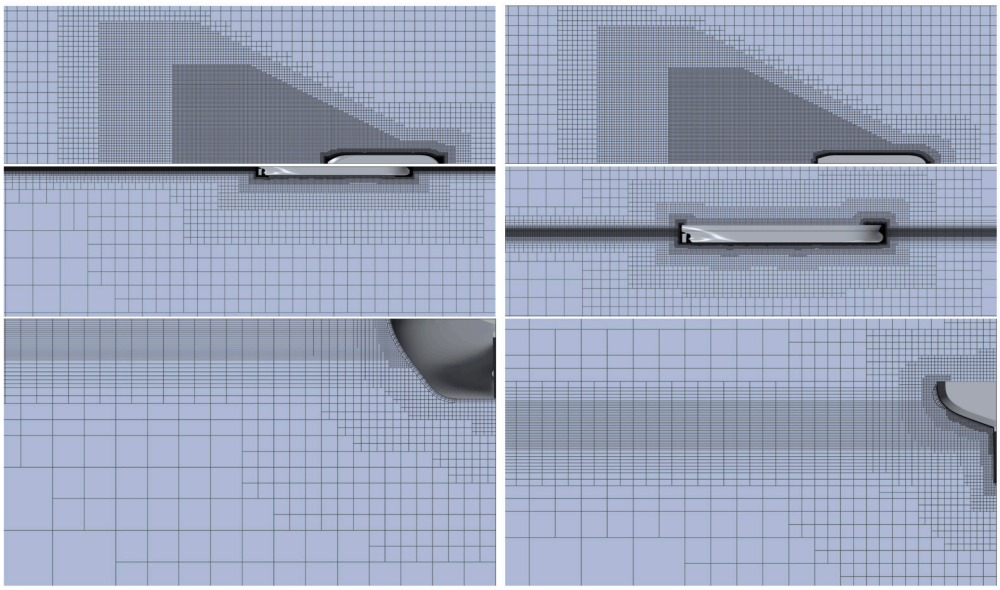


Fig. 4. The generated meshes for the DBS (left) and FSS (right).

Table 3
Numerical conditions at different scales for 14 knots at full scale.

Numerical condition	Value				
Scale λ	1	2	20	40.264	40.264
Fluid type	real				virtual
Density ρ, kg/m^3	999.49				
Dynamic viscosity μ, Pa·s	$1.26 \cdot 10^{-3}$				$4.90 \cdot 10^{-6}$
Reynolds number Re	$1.60 \cdot 10^{9}$	$5.66 \cdot 10^{8}$	$1.79 \cdot 10^{7}$	$6.26 \cdot 10^{6}$	$1.60 \cdot 10^{9}$

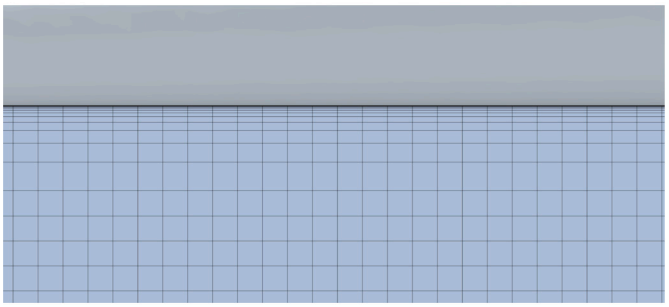


Fig. 5. Prism layers created near the hull.

where μ is the dynamic viscosity of the fluid. If the ratio between the speeds at full and model scales in Equation (11) is substituted with the one obtained from the Froude similarity (8) then Equation (11) reads as follows:

$$\frac{\mu_S}{\mu_M} = \lambda^{\frac{3}{2}} \tag{12}$$

To account for the geometric scaling, the obtained resistance and resistance components are multiplied by λ^3 as shown by Terziev et al. [20]. Table 3 shows the numerical conditions applied in the numerical simulations at different scales with real fluid and virtual fluid. The density was kept constant in all the numerical simulations, while the dynamics viscosity was altered between $1.26 \cdot 10^{-3}$ for the real fluid and $4.9 \cdot 10^{-6}$ for the virtual fluid. The Reynolds number is calculated for 14 knots and varied depending on the scale and the type of fluid considered.

3. Results

3.1. Verification and validation studies

In this study, three verification studies were conducted for each scale and numerical simulations with real and virtual fluids. The verification studies were conducted using the GCI method as presented by Celik et al. [39] and details about the procedure can be found in [40]. Three mesh resolutions were employed, achieved by varying the base size while keeping the same topology. The time step was varied in the range from $\Delta t = 0.00125 L_{PP}/v$ to $\Delta t = 0.005 L_{PP}/v$. Table 4 presents the number of cells used in each numerical simulation for the verification study. It can be seen that the meshes in the numerical simulations at model scale with virtual fluid and the ones at full scale with real fluid are similar. Additionally, the meshes generated in FSS contain approximately 1.4 times more cells than those from DBS.

Table 4
Cell numbers of the meshes used in the verification studies.

FSS					
Fluid type	real				virtual
λ	1	2	20	40.264	40.264
1	5.58M	5.26M	4.34M	3.90M	5.57M
2	2.41M	2.29M	1.84M	1.63M	2.41M
3	0.69M	0.65M	0.75M	0.47M	0.69M
DBS					
Fluid type	real				virtual
λ	1	2	20	40.264	40.264
1	3.98M	3.76M	2.99M	2.65M	3.98M
2	2.22M	2.07M	1.32M	1.15M	1.78M
3	0.96M	0.90M	0.52M	0.44M	0.49M

The verification studies of the total resistance obtained with FSS and DBS are conducted for the mesh resolution and the results are shown in Table 5. Monotonic convergence is obtained for the majority of considered scales, except for scales equal to $\lambda = 2$ and $\lambda = 20$ in FSS where oscillatory convergence can be noticed. The obtained order of the method is satisfactory since it is difficult to obtain exactly $p = 2$. The GCI is less than 4.3% for all conducted numerical simulations, thus the fine mesh is considered to be adequate for the rest of the study.

In Table 6 the obtained results of the verification study for the time step in FSS are presented. Monotonic convergence is achieved for almost all considered scales and types of fluids. Oscillatory convergence is obtained at full scale. The highest GCI equal to 1.01% is obtained for the numerical simulations at $\lambda = 2$. The obtained order of the method p is satisfactory and the obtained GCIs are considered to be reliable. Thus, the fine time step is shown to be adequate for the remaining numerical simulations.

In the validation study, the numerical results at the model scale are compared with experimental results from Degiuli et al. [22] to evaluate the relative deviations, calculated as follows:

$$RD = \frac{R_{T,CFD} - R_{T,EFD}}{R_{T,EFD}} \tag{13}$$

The numerically obtained total resistance for the speeds in the range from 11 knots to 16 knots for full-scale ship are presented in Table 7.

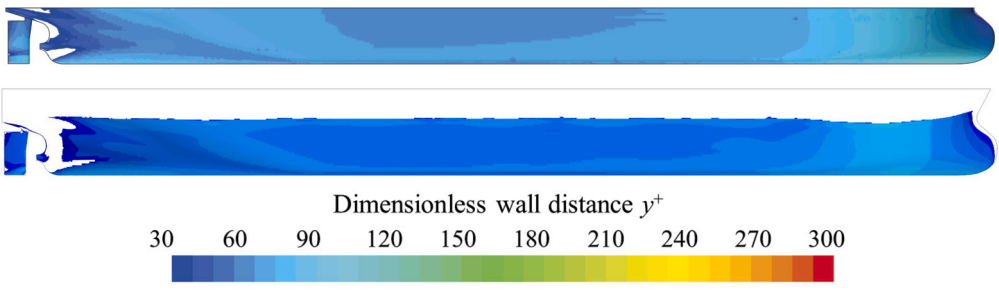


Fig. 6. Dimensionless wall distance y^+ on the first prism layer near the hull obtained with DBS (top) and FSS (bottom).

Table 5
Verification study for the mesh resolution.

	DBS				
Fluid type	real				virtual
λ	1	2	20	40.264	40.264
ϵ_{21}	9.54	2.02	1.36	0.33	0.14
ϵ_{32}	11.24	2.06	1.99	0.82	0.46
R	0.85	0.98	0.68	0.40	0.30
p	1.23	1.93	0.86	1.04	2.05
ϕ_{ext}^{21}	997.08	142.18	230.02	32.44	15.61
e_a^{21}	0.0092	0.0100	0.0058	0.0098	0.0086
e_{ext}^{21}	0.0354	0.0300	0.0224	0.0318	0.0119
GCI_{fine}^{21}	4.27%	3.66%	2.74%	3.86%	1.47%
	FSS				
Fluid type	real				virtual
λ	1	2	20	40.264	40.264
ϵ_{21}	13.21	-1.39	-5.61	0.30	0.20
ϵ_{32}	41.69	3.01	12.95	0.73	0.49
R	0.32	-0.46	-0.43	0.41	0.41
p	2.11	2.07	2.19	1.24	1.38
ϕ_{ext}^{21}	1047.00	153.49	246.17	33.46	15.87
e_a^{21}	0.0124	0.0010	0.0234	0.0087	0.0123
e_{ext}^{21}	0.0157	0.0117	0.0252	0.0211	0.0270
GCI_{fine}^{21}	1.93%	1.47%	3.23%	2.58%	3.28%

Table 6
Verification study for time step in the FSS.

Symbol	Value				
Fluid type	real				virtual
λ	1	2	20	40.264	40.264
ϵ_{21}	-2.18	0.24	1.94	0.13	0.06
ϵ_{32}	4.67	1.04	3.91	0.38	0.25
R	-0.47	0.23	0.50	0.35	0.25
p	1.10	2.13	1.01	1.50	1.98
ϕ_{ext}^{21}	1065.30	151.63	236.14	34.09	16.27
e_a^{21}	0.0021	0.0016	0.0082	0.0039	0.0038
e_{ext}^{21}	0.0018	0.0005	0.0081	0.0021	0.0013
GCI_{fine}^{21}	0.22%	0.06%	1.01%	0.26%	0.16%

Table 7
Results of the validation study.

V, kn	Fr	$R_{T,CFD}$, N	$R_{T,EFD}$, N	RD, %
11	0.107	20.518	21.876	-6.21
12	0.116	24.216	25.682	-5.71
13	0.126	27.880	29.707	-6.15
14	0.136	31.900	34.099	-6.45
15	0.146	36.575	39.466	-7.33
16	0.156	41.419	45.079	-8.12

The total resistance values obtained experimentally by Degiuli et al. [22] are presented in the second column. Relative deviations range from -5.71% and up to -8.12%. Numerical simulations underpredict the total resistance, with the lowest relative deviation of -8.12% obtained for 16 knots. This was expected since in the towing tank tests the model was free to heave and pitch, while the numerical simulations are conducted for a fixed model and thus no dynamic trim is considered. The SSTKO turbulence model was applied as it offers a well-balanced compromise between result accuracy and computational efficiency [35,11]. Additionally, it is a robust model capable of accurately capturing adverse pressure gradients and flow separation, particularly in the stern region [29]. However, Farkas et al. [31] previously demonstrated that the SSTKO turbulence model underpredicts the total resistance.

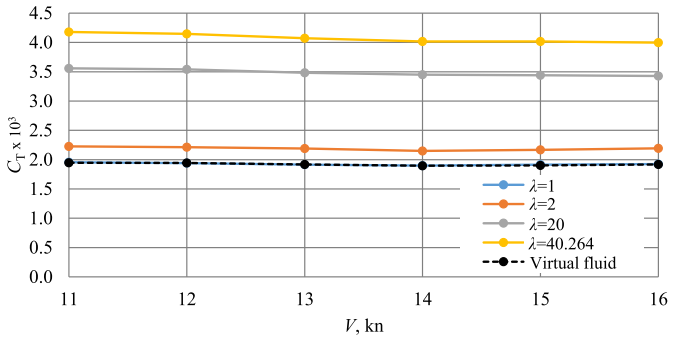


Fig. 7. Total resistance coefficients obtained from the FSS at various speeds and scales.

3.2. Total resistance coefficient

In this subsection, the numerically obtained results for the total resistance coefficient are presented for a wide range of the ship speed from 11 knots to 16 knots corresponding to the full-scale ship. Fig. 7 shows the total resistance coefficients obtained from the FSS for various speeds at different scales with the real fluid and at model scale with the virtual fluid. The total resistance coefficient increases with scale, with the lowest values occurring at full scale and the highest values at model scale. The total resistance coefficients obtained from FSS with virtual fluid are similar to those obtained at full scale. The total resistance coefficient obtained at model scale with real fluid is approximately two times larger than the ones obtained at full scale and at model scale with virtual fluid for the entire analysed speed range. The total resistance coefficient slightly decreases with the increase of ship speed for the majority of analysed scales.

3.3. Total resistance components

In Fig. 8, the viscous resistance coefficient and its components, i.e., frictional and viscous pressure resistance coefficients are presented for speed range from 11 knots to 16 knots obtained at different scales with the real fluid and at model scale with the virtual fluid. Similar results are obtained with DBS for viscous resistance coefficient and its components to those obtained with FSS for the total resistance coefficient. The lowest values are obtained at full scale and at model scale with virtual fluid, while the highest are obtained at model scale with real fluid. The viscous, frictional and viscous pressure resistance coefficients obtained at model scale with real fluid are approximately two times larger than those obtained at full scale with real fluid and model scale with virtual fluid.

The wave resistance coefficient was calculated by subtracting the viscous resistance coefficient obtained with DBS from the total resistance coefficient obtained with FSS. The results are shown in Fig. 9, which indicates that the wave resistance coefficient does not exhibit a consistent trend in relation to speed. The lowest value is obtained at model scale with virtual fluid method for a speed of 14 knots. The highest wave resistance coefficients are obtained for the speed of 16 knots at all the considered scales. Regarding the scale effects on the wave resistance coefficient, it is noted that the coefficient increases with scale for speeds ranging from 12 knots to 16 knots. This is not valid for speed of 11 knots, although the results obtained at $\lambda = 20$ and model scale suggest that the wave resistance coefficient increases with scale. The numerical simulations with virtual fluid method yield wave resistance coefficients similar to those obtained at full scale.

However, it is important to note that the wave resistance coefficient was calculated using results from DBS and FSS, for which the numerical uncertainty should be taken into account. The combined numerical uncertainty of the DBS and FSS ranges from 0.06% up to 4.69% depending on the scale and type of fluid considered. This is important for the JBC

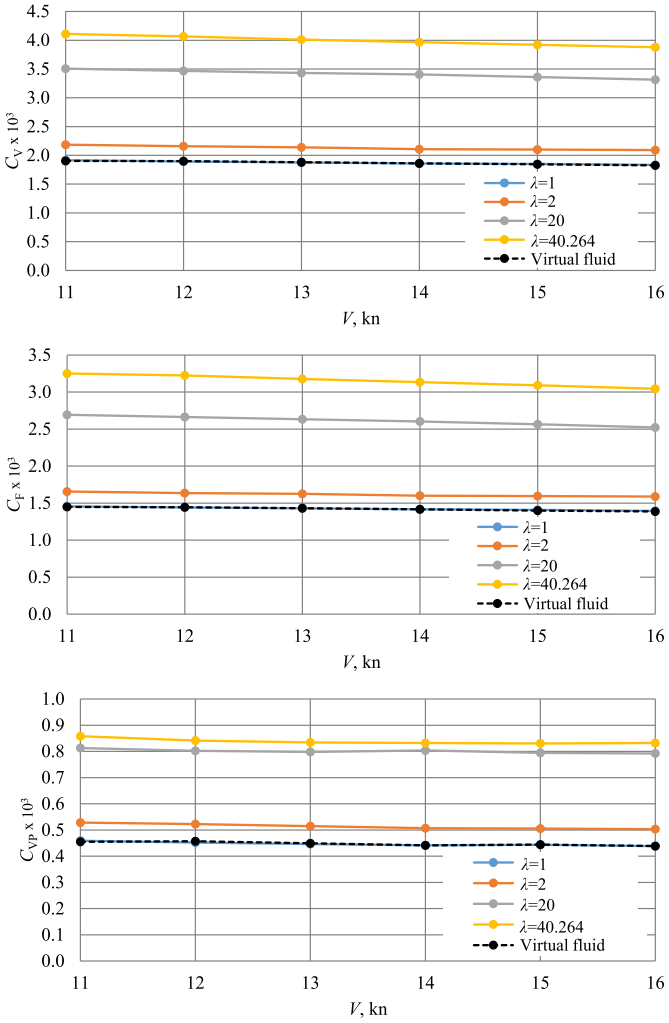


Fig. 8. Viscous (top), frictional (middle), and viscous pressure (bottom) resistance coefficients obtained from the DBS at various speeds and scales.

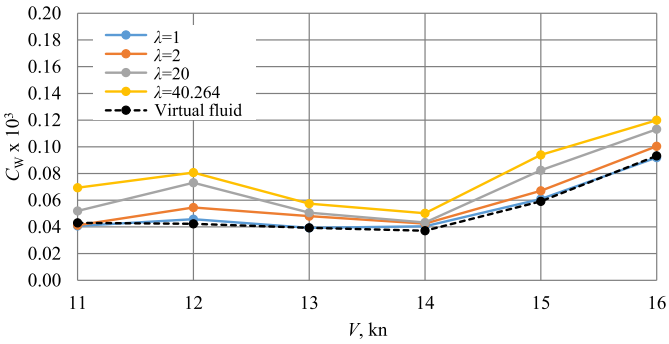


Fig. 9. Wave resistance coefficient obtained for various speeds and at different scales.

since the portion of the obtained wave resistance coefficient in the total resistance coefficient is in the range from 1.25% to 4.86%. The obtained percentages are similar to the results obtained by Dogrul et al. [11] for the KVLCC2. It can be concluded that a low wave resistance coefficient is obtained because the JBC operates at low values of Froude number.

The portion of resistance components to the total resistance are given in Fig. 10. Most of the total resistance coefficient can be attributed to the frictional resistance coefficient which ranges from 72% up to 78%. The viscous pressure resistance coefficient is in the range from 20% to 24%. The effect of speed on the portion of the total resistance components is negligible. The portion of the frictional resistance coefficient in the total resistance coefficient for the speed of 14 knots is equal to 74% at scale of $\lambda = 2$; 75% at scales of $\lambda = 1$, $\lambda = 20$ and at model scale with virtual fluid; while at model scale with real fluid it is equal to 78%. The portion of the viscous pressure resistance coefficient in the total resistance coefficient for the speed of 14 knots ranges from 21% up to 24% with no particular trend. Finally, the wave resistance coefficient is equal to 1% of the total resistance coefficient at $\lambda = 20$ and at model scale with real fluid; while at full scale, $\lambda = 2$ and model scale with virtual fluid it is equal to 2%. The scale effect is evident in the portion of the frictional resistance coefficient to the total resistance coefficient at all investigated speeds, showing an increase with scale, with the exception of full scale and $\lambda = 2$ for speeds of 13 knots and 14 knots. Also, the individual portions of the total resistance components obtained at full scale with real fluid are approximately the same as those obtained at model scale with virtual fluid.

3.4. Form factor

In this subsection, the effect of speed and the scale effects on the form factor are assessed. The form factors calculated with the equation (6) at different speeds and scales with real and virtual fluids are presented in Fig. 11. The impact of speed on the form factor is negligible, as observed at all scales and for both types of fluid at the model scale. Scale effects on the form factor are observed, and for a more detailed analysis, Fig. 12 is provided. Fig. 12 displays the calculated form factor derived from numerical simulations conducted at various scales, excluding the results obtained with virtual fluid. These form factors are compared to the ones calculated using different frictional correlation lines for a flat plate including ITTC 1957 [41], ATTC 1947 [42], Grigson [43], and Katsui [44]. The form factor obtained numerically increases with the Reynolds number, i.e., as the scale decreases, except at full scale, where the form factor is slightly lower than that obtained at $\lambda = 2$. The difference between form factors obtained at model scale and $\lambda = 20$ is more noticeable than the obtained differences between the form factors obtained at $\lambda = 20$ vs. $\lambda = 2$, and $\lambda = 2$ vs. $\lambda = 1$. The numerically obtained form factor displays a trend similar to those derived from the ITTC 1957 and ATTC 1947 lines; however, in those instances, the form factor increases with Reynolds number throughout the entire range. The form factors obtained with the ITTC 1957 line are lower than the ones obtained with the ATTC 1947 line. Both form factors obtained with Katsui and Grigson methods decrease with Reynolds number except the one obtained at model scale with the Katsui method, which is lower than the one obtained at $\lambda = 20$. The form factor obtained numerically is similar to the ones obtained with Katsui and Grigson lines at model scale, while at $\lambda = 2$ and at full scale, shows better agreement with the ones obtained with ITTC 1957 and ATTC 1947.

3.5. Wave pattern

In this subsection, insight into the free surface flow around the ship is given. First, the wave patterns around the ship obtained at different scales and with the virtual fluid method for 14 knots are shown in Fig. 13. It can be observed that there are no noticeable differences between the obtained wave patterns, although some discrepancies can be noticed behind the stern. Thus, more details are provided in Fig. 14, where the wave cuts behind the stern and in front of the bow of the JBC are presented. In front of the bow, the free surface elevations are nearly identical across all considered scales, including the results obtained with the virtual fluid method. However, behind the stern, noticeable differences emerge, with lower free surface elevations observed at higher scales. The results obtained at full scale and at model scale with virtual fluid are almost the same. In the region further away from the stern, the free surface elevations obtained at different scales and with the virtual fluid method show no specific trend.

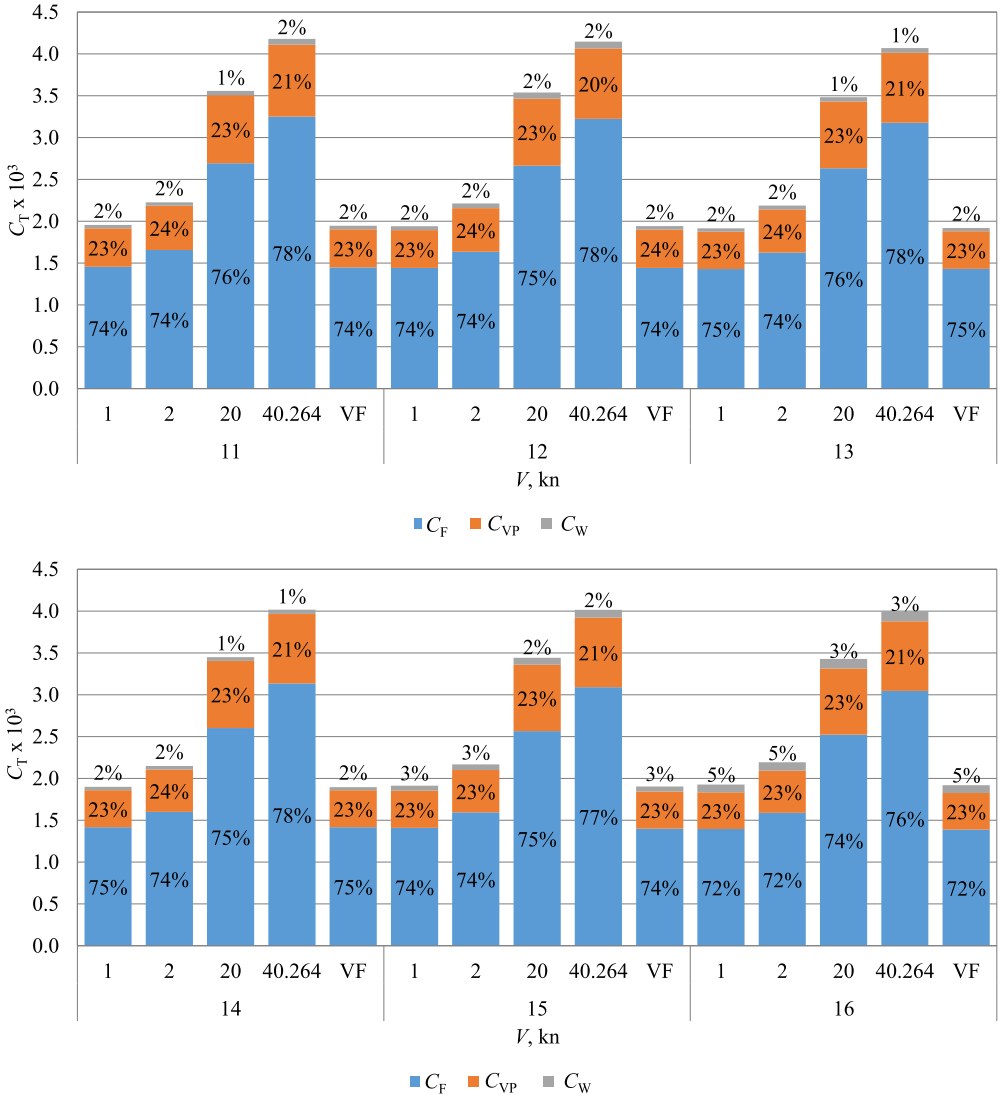


Fig. 10. The decomposition of the total resistance coefficients for speeds between 11 knots and 13 knots (top), and between 14 and 16 knots (bottom).

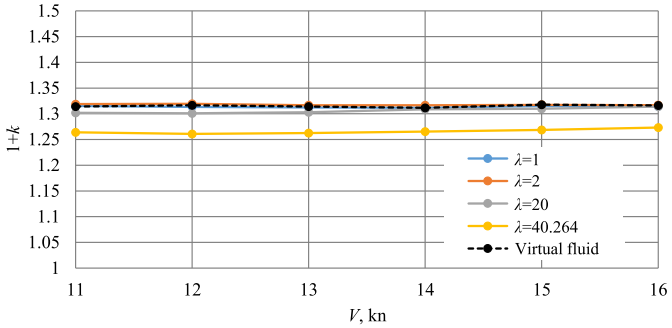


Fig. 11. Form factors obtained at different scales as a function of speed.

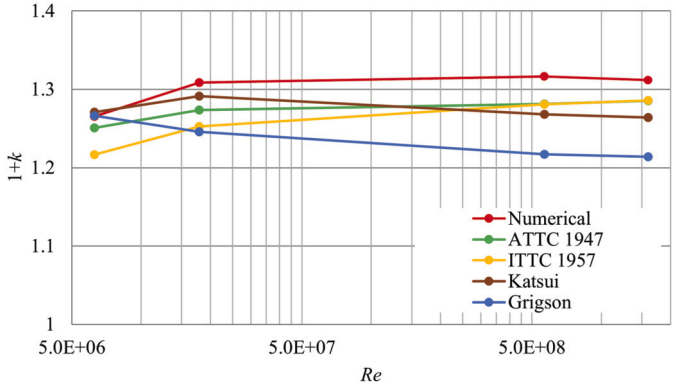


Fig. 12. Form factor obtained with different friction lines as a function of Reynolds number obtained for 14 knots.

Free surface elevations on the hull are depicted in Fig. 15. Similar to the wave cuts behind the stern, lower free surface elevations are obtained at the model scale and $\lambda = 20$. The results obtained at the full scale, $\lambda = 2$, and with the virtual fluid method closely match together along the entire hull with the only exception obtained around $x/L_{PP} = 0.1$, where this trend is not visible.

3.6. Nominal wake

The nominal wake is obtained following the ITTC recommendations for the determination of nominal wake for ships sailing at low and moderate speeds [45]. Since the effects of the free surface, dynamic sinkage, and trim can be neglected for ships sailing at low speeds, the nomi-

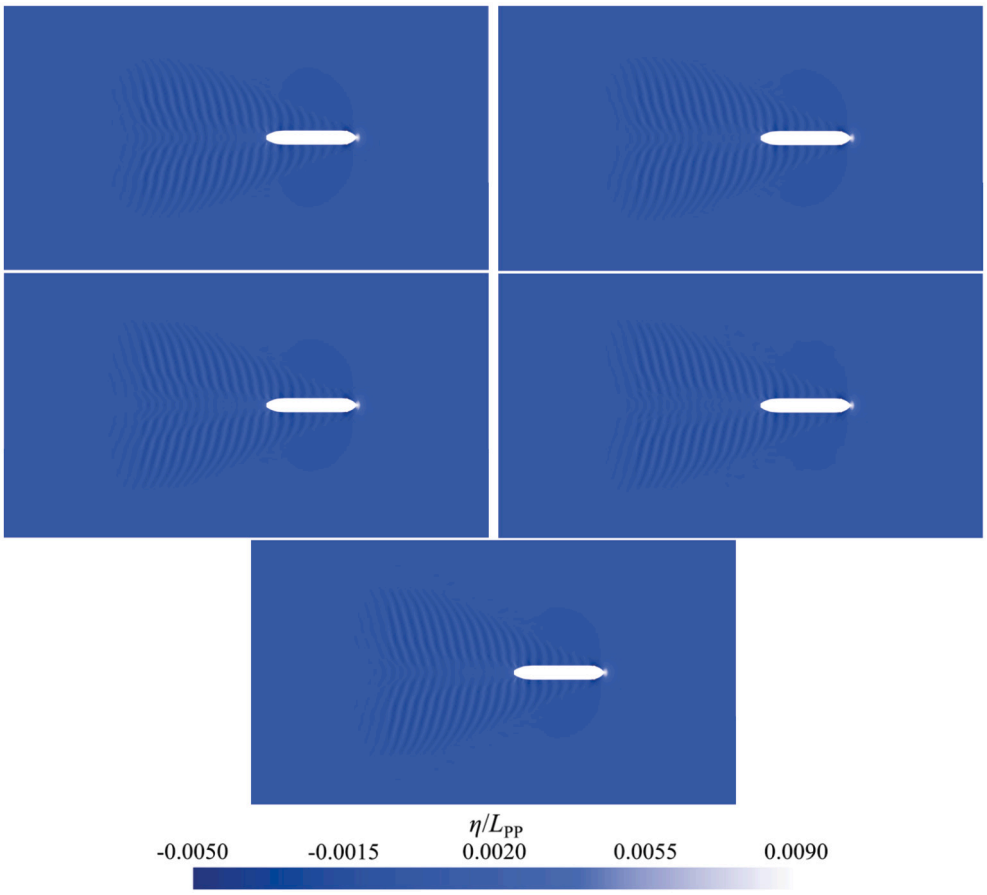


Fig. 13. Wave patterns obtained for $\lambda = 1$ (top-left), $\lambda = 2$ (top-right), $\lambda = 20$ (middle-left), $\lambda = 40.264$ (middle-right) and with virtual fluid method (bottom) at 14 knots.

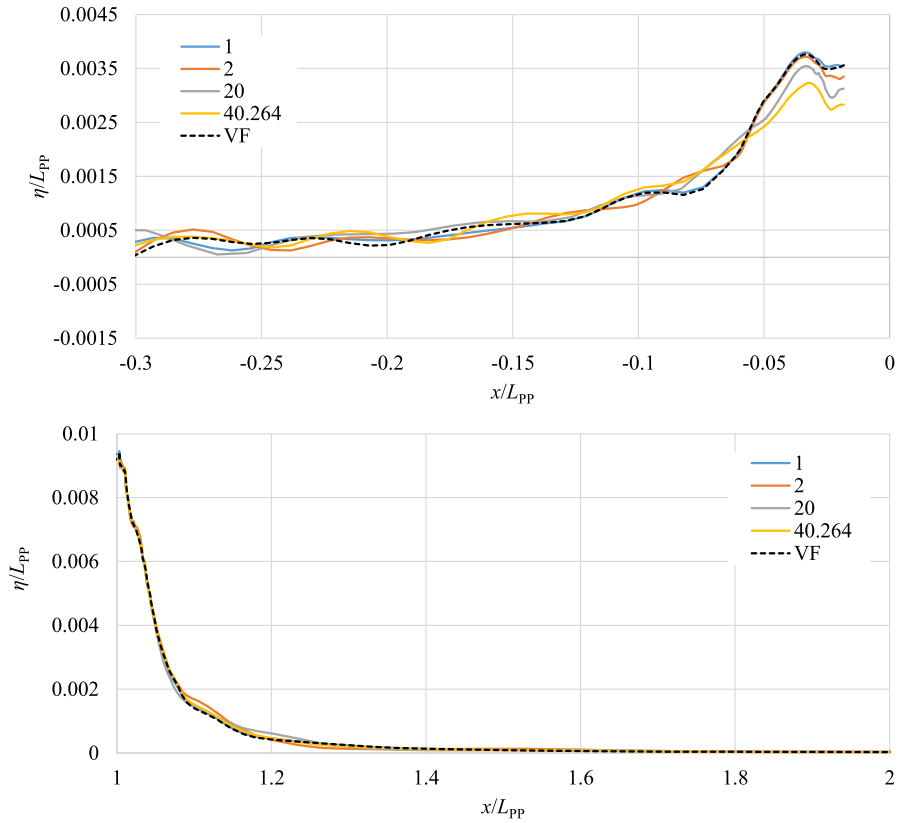


Fig. 14. The wave cut at the symmetry plane of the ship at the centreline behind the stern (top) and in front of the bow (bottom).

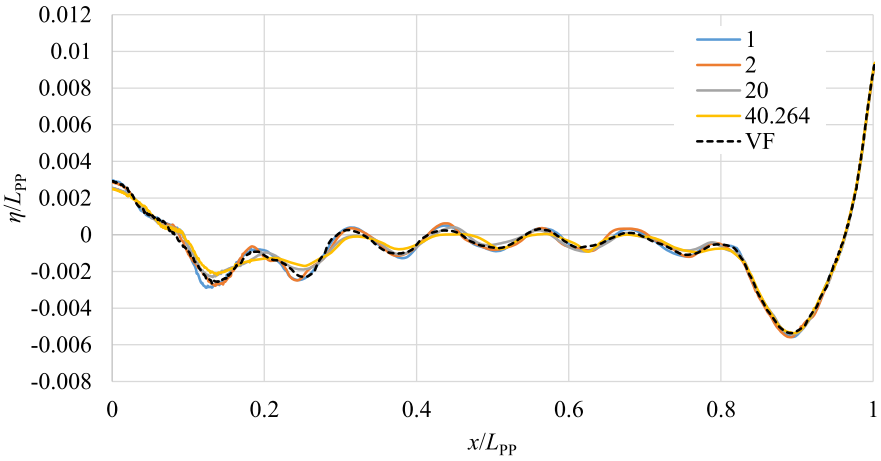


Fig. 15. The free surface elevations on the hull obtained with different scales and fluid types at 14 knots.

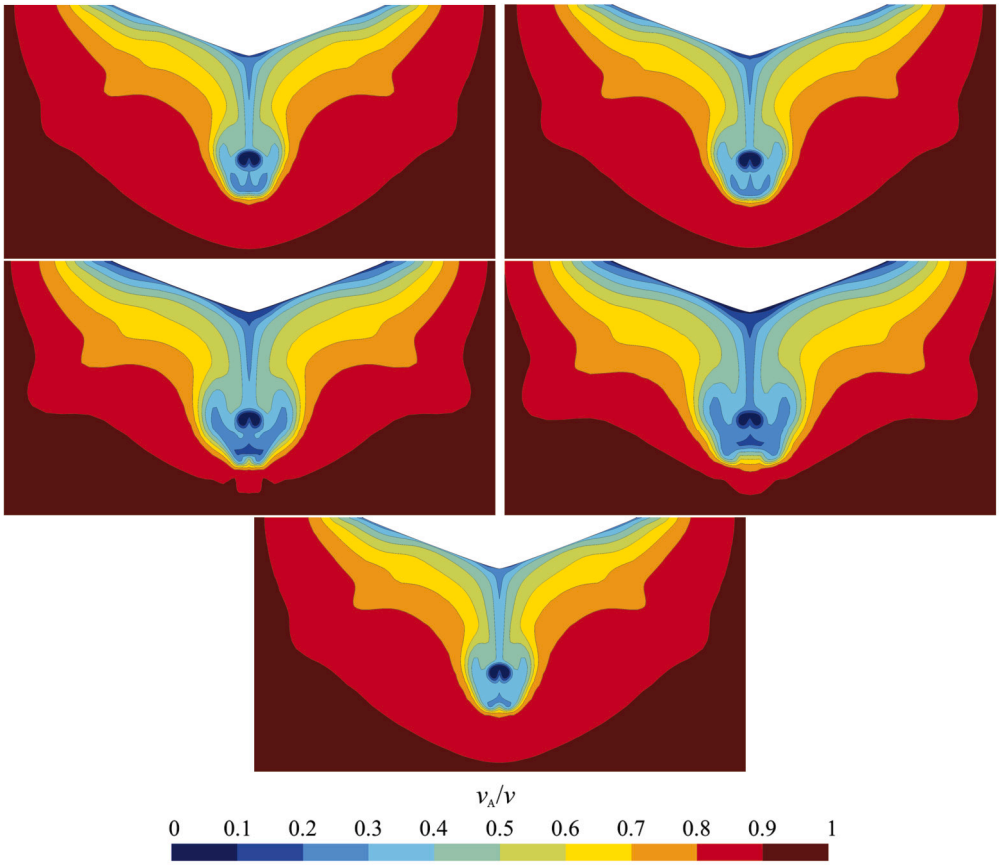


Fig. 16. Dimensionless axial velocity components at the propeller disc plane obtained by DBS at full scale (top-left), $\lambda = 2$ (top-right), $\lambda = 20$ (middle-left), model scale (middle-right) and with the virtual fluid method (bottom) at 14 knots.

nal wake is determined with the DBS. The dimensionless axial velocity components at the propeller disc plane obtained with the numerical simulations at different scales with real fluid and virtual fluid for speed of 14 knots are presented in Fig. 16. Significant scale effects on the nominal wake are evident, as seen by the reductions in axial velocity components that increase with scale. The dimensionless axial velocity components obtained at full scale with the real fluid and model scale with the virtual fluid are nearly the same. The only difference that can be noticed is that the nominal wake obtained with virtual fluid shows lower velocity reductions at the propeller location and near the hull in comparison to the one obtained at full scale with the real fluid.

3.7. Boundary layer

The considerable scale effects on the nominal wake presented in the previous subsection can be addressed to the boundary layer that forms around the hull. The boundary layer is relatively thicker at model scale in comparison to the one obtained at full scale. The obtained boundary layers with the dimensionless axial velocity limited to $v_A/v = 0.9$ at different longitudinal cross-sections are presented in Fig. 17. It can be noticed that the relative thickness of the boundary layer increases with scale. The increased thickness of boundary layer leads to a higher frictional resistance coefficient which has been already shown in the previous subsections. Small differences are obtained between the results

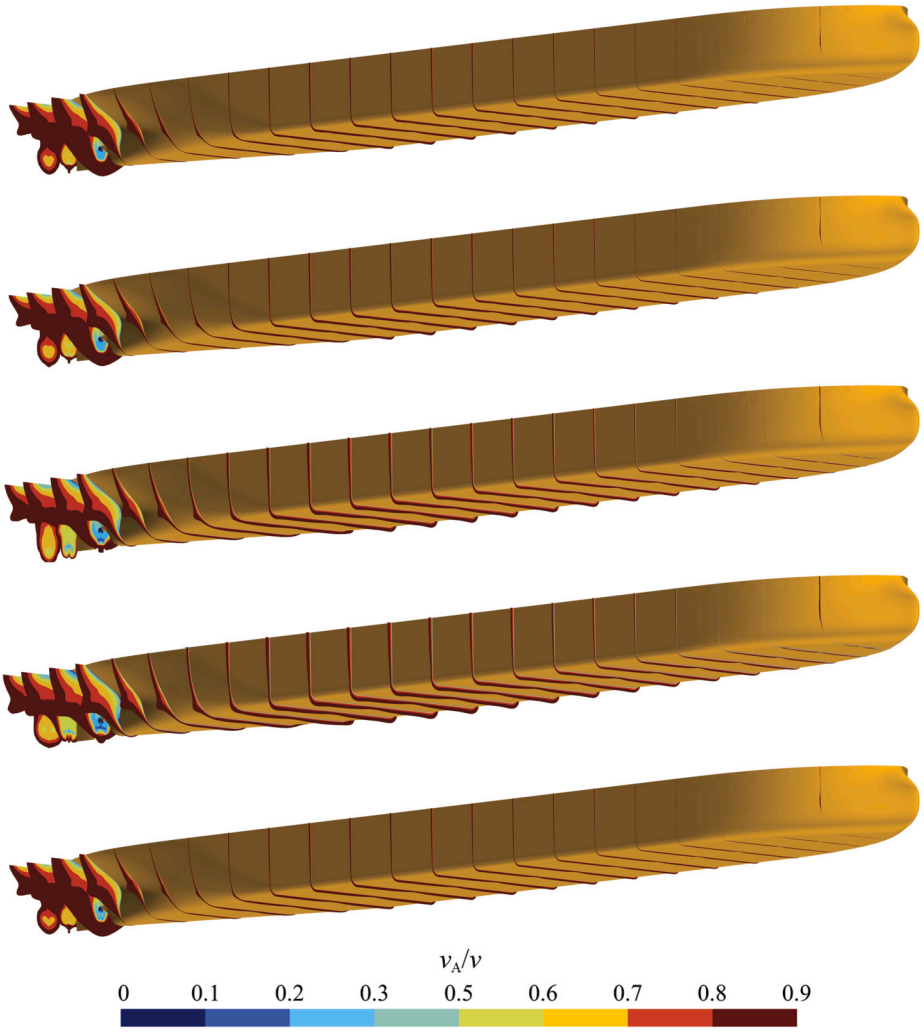


Fig. 17. Boundary layers obtained by DBS at full scale (first), $\lambda = 2$ (second), $\lambda = 20$ (third), model scale (fourth) and with the virtual fluid method (fifth) at 14 knots.

obtained at the model scale with the virtual fluid and those obtained at the full scale with real fluid.

4. Conclusions

Numerical simulations were carried out to investigate the scale effects and the effect of speed on the total resistance coefficient and its components including the form factor. The FSS and DBS were performed to assess the total resistance, the viscous resistance coefficients and its components, i.e., the viscous pressure and the frictional resistance coefficients. The wave resistance coefficient is obtained by subtracting the viscous resistance coefficient from the total resistance coefficient. The results obtained at different scales with real fluid were compared to those obtained from the numerical simulations performed at the model scale with the virtual fluid.

The mathematical background is given, and the numerical setup is elaborated in detail. A thorough verification study was carried out for the estimation of the numerical uncertainty at different scales. The validation study was performed by comparing the numerically obtained results with experimental ones obtained by Degiuli et al. [22]. The presented results include the total resistance coefficient and its components obtained at speeds in the range from 11 to 16 knots for the full-scale ship, at scales equal to 1, 2, 20, and 40.264. Additionally, the form factors are numerically derived from the results of the DBS at various scales and speeds, and are compared with the values calculated using frictional resistance lines from the literature. Finally, the wave patterns, wave cuts at the symmetry plane and along the hull, nominal wakes and boundary layers are presented. Based on this study, the findings can be summarized as follows:

- A slight decrease in the total resistance coefficient and its components with the increase in speed is shown. However, this effect is insignificant when compared to the scale effects on the total resistance coefficient and its components.
- The numerically obtained wave resistance coefficient is shown to depend on the results derived from both the DBS and FSS. For the bulk carrier analysed in this study, the results fall within the limits of numerical uncertainty. Consequently, the findings regarding the wave resistance coefficient should be considered with care.
- It is demonstrated that the total resistance coefficient and its components for the full-scale ship can be determined at model scale if both Froude and Reynolds similarity are met simultaneously, i.e., when the virtual fluid method is used. The total resistance, viscous resistance, frictional resistance, and viscous pressure resistance coefficients obtained by the numerical simulations at model scale with virtual fluid are in close accordance with the ones obtained at full scale when real fluid is considered.
- The effect of speed on the form factor is negligible, while the scale effects on the form factor are significant. The differences between the form factors obtained at model scale and $\lambda = 20$ are higher than the ones obtained between $\lambda = 20$ vs. $\lambda = 2$, and $\lambda = 2$ vs. full scale.

- The wave patterns obtained at different scales and with the virtual fluid method show no significant differences. Further away from the stern, the wave cuts obtained at different scales and with the virtual fluid method show no specific trend.
- The reductions in the dimensionless axial velocity components at the propeller disc plane significantly increase with scale. This is attributed to the growing boundary layer thickness around the hull with increasing scale. The nominal wakes and the boundary layers obtained at full scale with real fluid are in close accordance with those obtained at the model scale with the virtual fluid.

The present study enables the assessment of the scale effects and the effect of speed on the resistance components. The scale effects and the effect of speed on the propulsion components of the JBC will be the focus of a future research.

CRediT authorship contribution statement

Carlo Giorgio Grlj: Writing – review & editing, Writing – original draft, Visualization, Validation, Software, Resources, Methodology, Investigation, Formal analysis, Data curation, Conceptualization. **Nastia Degiuli:** Writing – review & editing, Writing – original draft, Visualization, Validation, Supervision, Resources, Project administration, Methodology, Investigation, Funding acquisition, Formal analysis, Data curation, Conceptualization. **Ivana Martić:** Writing – review & editing, Writing – original draft, Visualization, Validation, Resources, Methodology, Investigation, Formal analysis, Data curation, Conceptualization.

Funding sources

This study was funded by the Croatian Science Foundation under project IP-2020-02-8568.

Declaration of competing interest

The authors declare that they have no known competing financial interests or personal relationships that could have appeared to influence the work reported in this paper.

Acknowledgements

This study has been fully supported by the Croatian Science Foundation under project IP-2020-02-8568. This research was performed using the Advanced computing service provided by University of Zagreb University Computing Centre - SRCE.

Data availability

Data will be made available on request.

References

[1] T.H. Joung, S.G. Kang, J.K. Lee, J. Ahn, The IMO initial strategy for reducing greenhouse gas (GHG) emissions, and its follow-up actions towards 2050, J. Int. Marit. Saf. Environ. Aff. Shipp. 4 (2020) 1–7, https://doi.org/10.1080/25725084.2019.1707938.

[2] A. Chircop, The IMO initial strategy for the reduction of GHGs from international shipping: a commentary, Int. J. Mar. Coast. Law 34 (2019) 482–512, https://doi.org/10.1163/15718085-13431093.

[3] H. Tu, Z. Liu, Y. Zhang, Study on cost-effective performance of alternative fuels and energy efficiency measures for shipping decarbonization, J. Mar. Sci. Eng. 12 (2024) 743, https://doi.org/10.3390/jmse12050743.

[4] P. Balcombe, J. Brierley, C. Lewis, L. Skatvedt, J. Speirs, A. Hawkes, I. Staffell, How to decarbonise international shipping: options for fuels, technologies and policies, Energy Convers. Manag. 182 (2019) 72–88, https://doi.org/10.1016/j.enconman.2018.12.080.

[5] N.R. Ammar, Energy- and cost-efficiency analysis of greenhouse gas emission reduction using slow steaming of ships: case study RO-RO cargo vessel, Sh. Offshore Struct. 13 (2018) 868–876, https://doi.org/10.1080/17445302.2018.1470920.

[6] B. Zincir, Slow steaming application for short-sea shipping to comply with the CII regulation, Brodogradnja 74 (2023) 21–38, https://doi.org/10.21278/brod74202.

[7] R. Hua, J. Yin, S. Wang, Y. Han, X. Wang, Speed optimization for maximizing the ship's economic benefits considering the carbon intensity indicator (CII), Ocean Eng. 293 (2024) 116712, https://doi.org/10.1016/j.oceaneng.2024.116712.

[8] T. Tezdogan, Y.K. Demirel, P. Kellett, M. Khorasanchi, A. Incecik, O. Turan, Full-scale unsteady RANS CFD simulations of ship behaviour and performance in head seas due to slow steaming, Ocean Eng. 97 (2015) 186–206, https://doi.org/10.1016/j.oceaneng.2015.01.011.

[9] K. Niklas, H. Pruszko, Full-scale CFD simulations for the determination of ship resistance as a rational, alternative method to towing tank experiments, Ocean Eng. 190 (2019) 106435, https://doi.org/10.1016/j.oceaneng.2019.106435.

[10] C. Guo, X. Zhong, D. Zhao, Research on scale effect of resistance components for full-formed ship based on large-scale model towing test, J. Mar. Sci. Eng. 11 (2023) 1300, https://doi.org/10.3390/jmse11071300.

[11] A. Dogrul, S. Song, Y.K. Demirel, Scale effect on ship resistance components and form factor, Ocean Eng. 209 (2020) 107428, https://doi.org/10.1016/j.oceaneng.2020.107428.

[12] A. Farkas, N. Degiuli, I. Martić, Numerical simulation of viscous flow around a tanker model, Brodogradnja 68 (2017) 109–125, https://doi.org/10.21278/brod68208.

[13] J.S. Kouh, Y.J. Chen, S.W. Chau, Numerical study on scale effect of form factor, Ocean Eng. 36 (2009) 403–413, https://doi.org/10.1016/j.oceaneng.2009.01.011.

[14] A. Farkas, N. Degiuli, I. Martić, R. Dejhalla, Numerical and experimental assessment of nominal wake for a bulk carrier, J. Mar. Sci. Technol. 24 (2019) 1092–1104, https://doi.org/10.1007/s00773-018-0609-4.

[15] A. Dogrul, Numerical prediction of scale effects on the propulsion performance of Joubert BB2 submarine, Brodogradnja 73 (2022) 17–42, https://doi.org/10.21278/brod73202.

[16] A.Z. Saydam, G.N. Küçüksu, M. İnsel, S. Gökçay, Uncertainty quantification of self-propulsion analyses with RANS-CFD and comparison with full-scale ship trials, Brodogradnja 73 (2022) 107–129, https://doi.org/10.21278/brod73406.

[17] M. Haase, K. Zurcher, G. Davidson, J.R. Binns, G. Thomas, N. Bose, Novel CFD-based full-scale resistance prediction for large medium-speed catamarans, Ocean Eng. 111 (2016) 198–208, https://doi.org/10.1016/j.oceaneng.2015.10.018.

[18] Q.X. Zhao, C.Y. Guo, D.G. Zhao, Study on self-propulsion experiment of ship model with energy-saving devices based on numerical simulation methods, Sh. Offshore Struct. 10 (2015) 669–677, https://doi.org/10.1080/17445302.2014.945765.

[19] S. Sezen, F. Cakici, Numerical prediction of total resistance using full similarity technique, China Ocean Eng. 33 (2019) 493–502, https://doi.org/10.1007/s13344-019-0047-z.

[20] M. Terziev, T. Tezdogan, A. Incecik, A geosim analysis of ship resistance decomposition and scale effects with the aid of CFD, Appl. Ocean Res. 92 (2019) 101930, https://doi.org/10.1016/j.apor.2019.101930.

[21] K.W. Kim, K.J. Paik, S.H. Lee, J.H. Lee, S.Y. Kwon, D. Oh, A numerical study on the feasibility of predicting the resistance of a full-scale ship using a virtual fluid, Int. J. Nav. Archit. 16 (2024) 100560, https://doi.org/10.1016/j.ijnaoe.2023.100560.

[22] N. Degiuli, I. Martić, A. Farkas, M.P. Buča, R. Dejhalla, C.G. Grlj, Experimental assessment of the hydrodynamic characteristics of a bulk carrier in off-design conditions, Ocean Eng. 280 (2023) 114936, https://doi.org/10.1016/j.oceaneng.2023.114936.

[23] M.M.H. Bappy, S.M.R. Hasan, Enhancing inland vessel efficiency: a comprehensive study on the effectiveness of bulbous bow in mitigating resistance in Bangladesh, Results Eng. 24 (2024) 103394, https://doi.org/10.1016/j.rineng.2024.103394.

[24] F.R. Menter, Two-equation eddy-viscosity turbulence models for engineering applications, AIAA J. 32 (1994) 1598–1605, https://doi.org/10.2514/3.12149.

[25] C.G. Grlj, N. Degiuli, A. Farkas, I. Martić, Numerical study of scale effects on open water propeller performance, J. Mar. Sci. Eng. 10 (2022) 1132, https://doi.org/10.3390/jmse10081132.

[26] A. Farkas, N. Degiuli, I. Martić, Assessment of the effect of biofilm on the ship hydrodynamic performance by performance prediction method, Int. J. Nav. Archit. Ocean Eng. 13 (2021) 102–114, https://doi.org/10.1016/j.ijnaoe.2020.12.005.

[27] J. Firouzi, H. Ghassemi, K.A. Vakilabadi, Effect of the cross-flow wake on the hydrodynamic performance of the HSP propeller by the CFD solver, J. Mar. Eng. Technol. 21 (2022) 271–280, https://doi.org/10.1080/20464177.2021.1893136.

[28] X. Yang, Y. Yin, J. Lian, A numerical study on flow field and maneuvering derivatives of KVLCC2 model at drift condition, J. Mar. Eng. Technol. 20 (2021) 52–63, https://doi.org/10.1080/20464177.2019.1680076.

[29] B. Pena, L. Huang, A review on the turbulence modelling strategy for ship hydrodynamic simulations, Ocean Eng. 241 (2021) 110082, https://doi.org/10.1016/j.oceaneng.2021.110082.

[30] Y.K. Demirel, O. Turan, A. Incecik, Predicting the effect of biofouling on ship resistance using CFD, Appl. Ocean Res. 62 (2017) 100–118, https://doi.org/10.1016/j.apor.2016.12.003.

[31] A. Farkas, N. Degiuli, I. Martić, Assessment of hydrodynamic characteristics of a full-scale ship at different draughts, Ocean Eng. 156 (2018) 135–152, https://doi.org/10.1016/j.oceaneng.2018.03.002.

[32] Z. Zhang, L. Song, J. Qi, Q. Hu, J. Sun, Z. Zhang, Research on the optimal spacing resistance reduction technology for ship formation, Results Eng. 24 (2024) 103583, https://doi.org/10.1016/j.rineng.2024.103583.

[33] C.G. Grlj, N. Degiuli, I. Martić, The impact of numerical parameters on the resistance characteristics of a container ship at the model and full scale, J. Mar. Sci. Eng. 11 (2023) 1672, https://doi.org/10.3390/jmse11091672.

[34] A.F. Molland, S.R. Turnock, D.A. Hudson, Ship Resistance and Propulsion, Cambridge University Press, 2017.
[35] A. Farkas, N. Degiuli, I. Martić, Impact of biofilm on the resistance characteristics and nominal wake, Proc. Inst. Mech. Eng. M 234 (2019) 59–75, https://doi.org/10.1177/1475090219862897.
[36] O.K. Kinaci, O.F. Sukas, S. Bal, Prediction of wave resistance by a Reynolds-averaged Navier–Stokes equation–based computational fluid dynamics approach, Proc. Inst. Mech. Eng. M 230 (2016) 531–548, https://doi.org/10.1177/1475090215599180.
[37] NMRI, Tokyo 2015 a workshop on CFD in ship hydrodynamics, https://t2015.nmri.go.jp/index.html, 2015.
[38] ITTC, Practical Guidelines for Ship CFD Applications, 7.5-03-02-03, ITTC-Recommended Procedures and Guidelines, 2011.
[39] I.B. Celik, U. Ghia, P.J. Roache, C.J. Freitas, H. Coleman, P.E. Raad, Procedure for estimation and reporting of uncertainty due to discretization in CFD applications, J. Fluids Eng. Trans. ASME 130 (2008) 078001, https://doi.org/10.1115/1.2960953/444689.
[40] C.G. Grlj, N. Degiuli, Ž. Tuković, A. Farkas, I. Martić, The effect of loading conditions and ship speed on the wind and air resistance of a containership, Ocean Eng. 273 (2023) 113991, https://doi.org/10.1016/j.oceaneng.2023.113991.
[41] ITTC, Resistance Uncertainty Analysis, Example for Resistance Test, 7.5-02-02-02, ITTC-Recommended Procedures, 2002.
[42] J. Carlton, Marine Propellers and Propulsion, Butterworth-Heinemann, 2018.
[43] C.W.B. Grigson, A planar friction algorithm and its use in analysing hull resistance, RINA Trans. Pt. 142 (1999) 76–115.
[44] T. Katsui, H. Asai, Y. Himeno, The proposal of a new friction line, in: Fifth Osaka Colloquium on Advanced CFD Applications to Ship Flow and Hull Form Design, 2005.
[45] ITTC, Practical Guidelines for RANS Calculation of Nominal Wakes, 7.5-03-03-02, ITTC-Recommended Procedures and Guidelines, 2014.

Article IV

Article published by Elsevier in Ocean engineering on 1 July 2025, available online: https://www.sciencedirect.com/science/article/abs/pii/S0029801825017342

Ocean Engineering 339 (2025) 122059

Contents lists available at ScienceDirect

Ocean Engineering

journal homepage: www.elsevier.com/locate/oceaneng

Research paper

Scale effects on the resistance and propulsion characteristics of the Japan Bulk Carrier

Carlo Giorgio Grlj, Nastia Degiuli *, Ivana Martić

University of Zagreb, Faculty of Mechanical Engineering and Naval Architecture, Ivana Lučića 5, Zagreb, 10000, Croatia

ARTICLE INFO

Keywords:
JBC
CFD
Scale effects
Resistance test
Self-propulsion test
Virtual fluid

ABSTRACT

The scale effects on the propulsion characteristics of the Japan Bulk Carrier were investigated using numerical simulations of resistance and self-propulsion tests. The mathematical model was based on Reynolds-averaged Navier Stokes equations and for the closure of the governing equations, the SST $k-\omega$ turbulence model was used. The effects of the rotating propeller were modelled using the body force propeller method. Numerical simulations were systematically conducted across four scales ranging from model to full scale and for a wide range of speeds. Additional numerical simulations were performed at model scale with virtual fluid to satisfy both Froude and Reynolds similarity. A verification study was performed to assess numerical uncertainties, while a validation study was conducted using available experimental data. The obtained numerical results enable a detailed investigation of scale effects on ship resistance and propulsion characteristics. Significant scale effects were observed on the integral value of the nominal wake and the radial distribution of the non-dimensional axial velocity. Additionally, scale effects were shown on the wake fraction and hull efficiency, whereas the scale effects on the thrust deduction fraction and the quasi-propulsive efficiency were minimal. The differences between the numerical results obtained using the virtual fluid method and those at full scale with real fluid fall within the bounds of numerical uncertainty.

1. Introduction

The ship resistance and propulsion characteristics are usually obtained by means of experimental fluid dynamics (EFD). The experimentally measured values have to be extrapolated to full scale using different extrapolation procedures, which can introduce numerous sources of errors, thus adversely impacting the obtained results. Farkas et al. (2019b) conducted model-scale and full-scale numerical simulations for the investigation of scale effects on the nominal wake of a handymax bulk carrier and found significant scale effects on the integral value of the nominal wake as well as the circumferentially averaged non-dimensional axial velocity. Similarly, Wang et al. (2015) performed numerical simulations of the resistance test (RT) without the free surface at different scales for a 4000 TEU containership and showed significant scale effects on the nominal wake field. Also, the authors proposed an extrapolation method for scaling the wake field. The main reason for the scale effects on the nominal and effective wake is the inability to satisfy both Reynolds and Froude numbers simultaneously, thus obtaining a relatively thicker boundary layer at model scale in comparison to full scale (Pena et al., 2020), which leads to higher velocity reductions at the propeller disc plane at model scale (Zhang et al., 2021).

Numerous studies have been conducted recently, emphasizing the potential benefits of using numerical simulations for the determination of ship hydrodynamic characteristics. As a well-established tool in the maritime industry and research, numerical simulations based on the viscous flow can be used to investigate the performance of ships in self-propulsion conditions (Saydam et al., 2022). Niklas and Pruszko (2019) used computational fluid dynamics (CFD) to determine the total resistance of a ship and demonstrated that the calm water resistance obtained in full-scale numerical simulations varied between -10 % and 4 % compared to sea trial data. Their findings confirmed that numerical simulations at full scale can serve as a viable alternative to EFD. Also, it was noticed that the existing methods used for calculating the form factor of innovative hull forms are questionable. Mikulec and Piehl (2023) conducted comprehensive verification and validation studies on full-scale CFD simulations of self-propulsion test (SPT). Their findings indicate that the numerically obtained propeller rate of revolution closely matches sea trial data, with errors ranging from -2.46 % to -4.40 %. Dogrul et al. (2020) investigated the scale effects on the total resistance components of KCS and KVLCC2 using double body and free surface simulations at different scales. The authors showed substantial scale effects on the total resistance and its components as well as on the form

* Corresponding author.
E-mail address: nastia.degiuli@fsb.unizg.hr (N. Degiuli).

https://doi.org/10.1016/j.oceaneng.2025.122059
Received 18 March 2025; Received in revised form 2 June 2025; Accepted 25 June 2025
Available online 1 July 2025
0029-8018/© 2025 Elsevier Ltd. All rights are reserved, including those for text and data mining, AI training, and similar technologies.

factors due to the differences in the calculation of the frictional resistance. Similar results were obtained by Sezen et al. (2021) where the authors investigated the scale effects on the ship hydrodynamic characteristics which include the total resistance, nominal wake, and propulsion characteristics of the Defense Advanced Research Projects Agency (DARPA) Suboff hull form. The authors concluded that the International Towing Tank Conference (ITTC) 1978 performance prediction method can be used with some confidence for the determination of propulsion characteristics of submarines. Terziev et al. (2021) conducted numerical simulations based on Reynolds Averaged Navier-Stokes (RANS) equations to investigate the scale effects and the impact of different turbulence models on the form factor of the KCS hull form. It was shown that the obtained form factor varied between 10 % and 20 % for Froude numbers in the range from 0.02 to 0.06 depending on the chosen turbulence model and scale factor. Korkmaz et al. (2021) investigated the possibility of using a CFD/EFD method for the determination of form factor and concluded that the ITTC 1978 performance prediction method can be improved. Dogrul (2022) conducted numerical simulations of the SPT of a Joubert BB2 submarine and found significant scale effects on the nominal wake, thrust deduction fraction as well as on the open water propeller and propulsion efficiencies. Liu et al. (2024) performed numerical simulations based on RANS equations to analyse a submerged body sailing near the free surface at different speeds. The authors presented the scale effects on the wave pattern, total resistance and its components as well as on the nominal wake. Guo et al. (2017) investigated the scale effects on the nominal wake field of the KCS and developed a method to correct them by deforming the shape of the hull. Can et al. (2020) calculated the effective wake of the KCS with the Telfer's GEOSIM method, based on the numerical results obtained in CFD simulations at different scales. The authors confirmed that the proposed GEOSIM method provides a more accurate determination of the effective wake fraction compared to the ITTC 1978 performance prediction method. Kok et al. (2020) investigated the scale effects on containership squat using numerical simulations and concluded that these effects are negligible. The difference between the non-dimensional squat at model and full scale was found to be approximately 5.32 %. Ma et al. (2024) investigated the scale effects on the flow field behind the KCS sailing in shallow and confined water. The authors found that non-dimensional force and moment coefficients obtained at model scale increase faster with decreasing distance from the shore compared to those obtained at full scale. Zeng et al. (2020) addressed the scale effects on wave-making resistance in shallow water using numerical simulations of RT for Wigley hull and KCS. The results revealed a significantly higher wave-making resistance for the KCS at model scale compared to full scale in very shallow water in the specific range of Froude numbers, prompting the authors to recommend reevaluating the conventional extrapolation method for ships with full hull forms. Haase et al. (2016) addressed scale effects using numerical simulations of resistance test by adjusting the viscosity of the fluid at model scale, thereby satisfying both Froude and Reynolds similarity. Following a similar approach, Sezen and Cakici (2019) used a virtual fluid in their numerical studies of the DTMB 5512 ship at various Froude numbers. Their results demonstrated that this method is effective for estimating total resistance at full-scale Reynolds number. Terziev et al. (2019) further explored scale effects on resistance components by conducting double-body simulations (DBS) using the fluid with modified viscosity.

In this study, the scale effects on the resistance and propulsion characteristics of the Japan Bulk Carrier (JBC) were investigated by performing numerical simulations of RT and SPT, systematically across a range of scales from model to full scale and at different speeds. At model scale, additional numerical simulations were conducted with the virtual fluid method to satisfy both Reynolds and Froude similarity. The rest of the paper is organized as follows: Section 2 provides details of the mathematical and numerical models, while the verification and validation studies are described in detail. In Section 3 results obtained from the numerical simulations are presented and discussed, and at the end, in Section 4 conclusions from this study are drawn and a plan for future studies is given.

Table 1
Main particulars of the JBC.

Main particular	Value			
λ	1	2	20	40.264
L_{PP}, m	280	140	14	6.954
L_{WL}, m	285	142.5	14.25	7.078
B_{WL}, m	45	22.5	2.25	1.118
T, m	16.5	8.25	0.825	0.410
∇, m^3	178 420.1	22 302.51	22.303	2.733

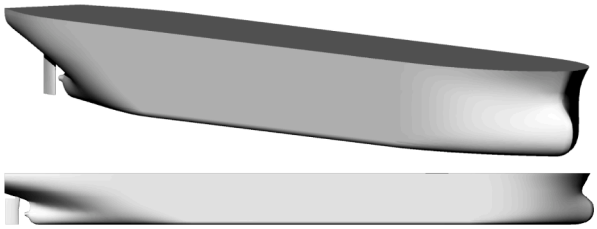


Fig. 1. The 3D model of the JBC used in the numerical simulations.

2. Methods

2.1. Geometry

The JBC was selected as the case study, which include the hull and rudder geometries available online (Nmri, 2015). The JBC model was subjected to extensive experimental campaign in the towing tank at the scale $\lambda = 40.264$ (Degiuli et al., 2023). The 3D model is given in Fig. 1 and the main particulars are presented in Table 1.

2.2. Mathematical model

The commercial software package STAR-CCM+ uses a mathematical model which is based on the RANS equations. The RANS equations for the incompressible and unsteady case read as follows:

$$\frac{\partial \bar{u}_i}{\partial x_i} = 0 \tag{1}$$

$$\rho \frac{\partial \bar{u}_i}{\partial t} + \rho \frac{\partial}{\partial x_j}\left(\bar{u}_i \bar{u}_j + \overline{u_i' u_j'}\right) = -\frac{\partial \bar{p}}{\partial x_i} + \frac{\bar{\tau}_{ij}}{\partial x_j} \tag{2}$$

where ρ is the fluid density, $\bar{u}_i$ is the averaged Cartesian components of the velocity vector, $\rho\overline{u_i' u_j'}$ is the Reynolds Stress Tensor (RST), $\bar{p}$ is the mean pressure, and $\bar{\tau}_{ij}$ is the mean viscous stress tensor defined by:

$$\bar{\tau}_{ij} = \mu\left(\frac{\partial \bar{u}_i}{\partial x_j} + \frac{\partial \bar{u}_j}{\partial x_i}\right) \tag{3}$$

where μ is the dynamic viscosity coefficient of the fluid. Eqs. (1) and (2) present an unclosed system of equations and to be able to solve them turbulence models are applied. In this study, the Shear Stress Transport $k-\omega$ (SSTKO) turbulence model is used since it has already been proven to be a good compromise between the accuracy of the obtained results and the computational time (Dogrul et al., 2020; Farkas et al., 2019a; Grlj et al., 2024; Sun et al., 2020). Moreover, it is a robust turbulence model capable of accurately capturing adverse pressure gradients and flow separation, particularly in the stern region (Pena and Huang, 2021; Song et al., 2021).

2.3. Shear Stress Transport $k-\omega$

The SSTKO is a turbulence model (Menter, 1994) that solves two additional transport equations: one for the turbulent kinetic energy k

and another for the specific dissipation ω:

$$\frac{\partial}{\partial t}(\rho k) + \frac{\partial}{\partial x_i}\left(\rho k \bar{u}_i\right) = \frac{\partial^2 k}{\partial x_i^2}\left(\mu + \sigma_k \mu_t\right) + G_k + G_{nl} + \\ + G_b - \rho \beta^* f_{\beta^*}\left(\omega k - \omega_0 k_0\right) + S_k \tag{4}$$

$$\frac{\partial}{\partial t}(\rho \omega) + \frac{\partial}{\partial x_i}\left(\rho \omega \bar{u}_i\right) = \frac{\partial^2 \omega}{\partial x_i^2}\left(\mu + \sigma_\omega \mu_t\right) + G_\omega + \\ + D_\omega - \rho \beta f_\beta\left(\omega^2 - \omega_0^2\right) + S_\omega \tag{5}$$

where σ_k, σ_ω, β, and β^* are coefficients depending on the model, G_{nl} is the non-linear production term, f_β is the free-shear modification factor, f_{β^*} is the vortex-stretching modification factor, k_0 and ω_0 are the ambient values that counteract turbulence decay (Spalart and Rumsey, 2007).

2.4. Virtual disk model

Within the commercial software STAR-CCM+, various virtual disk models are available for simulating the effects of a rotating propeller. To avoid the computational expense of discretizing the propeller geometry, in this study the body force propeller method was employed. In this approach, a uniform volume force is applied instead of explicitly resolving the propeller geometry, simplifying the numerical simulation while capturing its overall effects on the flow. The volume force is distributed over a cylindrical virtual disk and varies radially according to the Goldstein optimum, as follows:

$$f_{bx} = A_c r^* \sqrt{1 - r^*} \tag{6}$$

$$f_{b\theta} = A_\theta \cdot \frac{r^* \sqrt{1 - r^*}}{r^*(1 - r_h') + r_h'} \tag{7}$$

where f_{bx} and $f_{b\theta}$ are the body force components in the axial and tangential directions, respectively and r^* is calculated as:

$$r^* = \frac{r' - r_h'}{1 - r_h'} \tag{8}$$

where r' and r_h' are given as:

$$r'h = \frac{R_\mathrm{H}}{R_\mathrm{P}} \tag{9}$$

$$r' = \frac{r}{R_\mathrm{P}} \tag{10}$$

where r is the radial coordinate, R_P and R_H are the propeller tip and hub radius, respectively. The constants in the Eqs. (6) and (7) are obtained as follows:

$$A_x = \frac{105}{8} \cdot \frac{T}{\pi \Delta (3R_\mathrm{H} + 4R_\mathrm{P})(R_\mathrm{P} - R_\mathrm{H})} \tag{11}$$

$$A_\theta = \frac{105}{8} \cdot \frac{Q}{\pi \Delta R_\mathrm{P} (3R_\mathrm{H} + 4R_\mathrm{P})(R_\mathrm{P} - R_\mathrm{H})} \tag{12}$$

where T and Q are thrust and torque of the propeller, and Δ is the thickness of the virtual disk. An inflow velocity plane was defined at a distance of $0.1D$ toward the bow and was used to calculate the propeller inflow by averaging the incoming velocity and density. The radius of the inflow plane was set to $1.1R$. Using the velocity averaged over this plane, the advance coefficient was determined, and the corresponding thrust and torque were obtained from the open water curves provided by Grlj et al. (2022). The authors used the moving reference frame method to obtain the open water curves for the selected propeller. The propeller used in the numerical simulations was the same stock propeller that was used in the experiments. The main particulars of the selected propeller are shown in Table 2. The open water curves obtained in numerical simulations of the open water test (OWT) at full scale used in this study are shown in Fig. 2.

Table 2
Main particulars of the propeller.

Main particular	Value			
λ	1	2	20	40.264
D, m	8.120	4.060	0.406	0.202
$P_{0.7R}/D$	0.736			
A_e/A_0	0.644			
d/D	0.193			
Z	5			
Type	Fixed Pitch Propeller (FPP)			

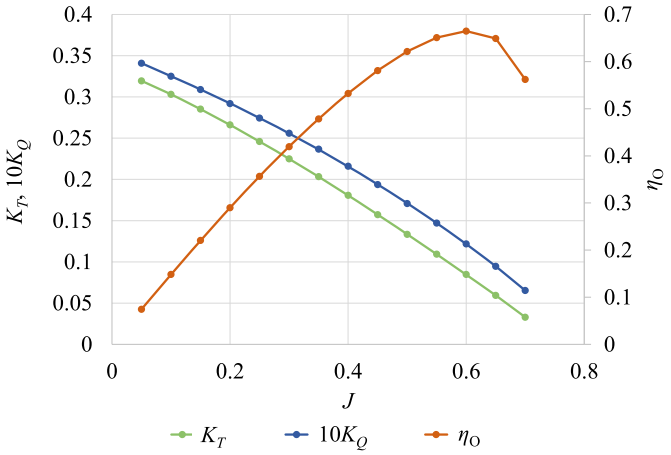


Fig. 2. The open water curves used in the numerical simulations.

2.5. Numerical setup

For this study, the numerical simulations of RT and SPT at full scale and different model scales were conducted. The finite volume method was used for the discretization of the governing equations, which were numerically solved in a segregated manner. The discretization schemes were selected based on Grlj et al. (2023), with convection terms and gradients solved using a second-order scheme, while temporal terms were handled with a first-order scheme. For the validation study, the dynamic fluid body interaction (DFBI) method was used to model the motions of the ship. For the remaining numerical simulations, the ship was kept fixed at even keel to lower the computational resources needed to run the numerical simulations. Additional numerical simulations were conducted using the virtual fluid method to satisfy both Froude and Reynolds similarity, as described by Sezen and Cakici (2019) and more recently by Kim et al. (2024). In these simulations, the water density remained constant, while the dynamic viscosity was adjusted to achieve the same Reynolds number at both model and full scale.

For the validation study, the density and dynamic viscosity were set to match experimental conditions. In other numerical simulations, the density was fixed at 999.49 kg/m^3, and the dynamic viscosity was maintained at $1.258 \cdot 10^{-3}$ Pas, regardless of scale. In the numerical simulations at model scale with virtual fluid, the dynamic viscosity was adjusted to $4.925 \cdot 10^{-6}$ Pas to satisfy simultaneously Reynolds and Froude similarity.

2.5.1. Mesh generation

The computational domain in the numerical simulations of SPT consisted of a rectangular-shaped domain that enclosed the ship, which was discretized using the unstructured hexahedral mesh. Since in the case of the RT the flow is assumed to be symmetrical, only half of the domain was created to lower the total number of cells. The domain boundaries were placed far enough to avoid their influence on the obtained results. The inlet, top, and side boundaries were placed at $1.5L_\mathrm{pp}$ from the ship, outlet at $3L_\mathrm{pp}$ from the stern of the ship, and bottom at $2L_\mathrm{pp}$ from the ship. Prism layers were created near the hull in order to maintain the

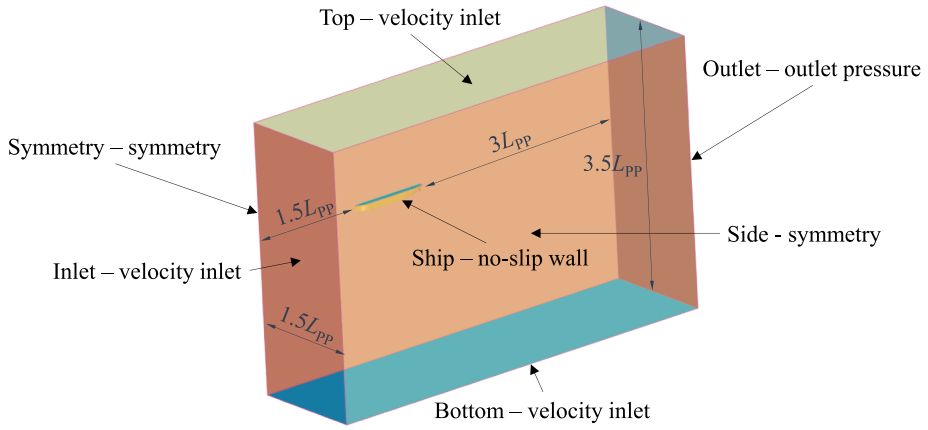


Fig. 3. Computational domain and boundary conditions in the numerical simulations of the RT.

non-dimensional wall distance y^+ higher than 30, thus enabling the computation of the boundary layer using wall functions. The y^+ value is dependent upon the centre of the first cell near the wall y, which was estimated using the following equation:

$$y = \frac{y^+ \nu}{u_\tau} \tag{13}$$

where ν is the kinematic viscosity and the friction velocity u_τ was calculated as follows:

$$u_\tau = \sqrt{\frac{\tau_w}{\rho}} \tag{14}$$

The shear stress τ_w was obtained as:

$$\tau_w = \frac{1}{2} C_f \rho U_\infty^2 \tag{15}$$

where U_∞ is the freestream velocity and C_f is the skin friction coefficient for a flat plate.

Refinements were created in the bow and stern regions as well as in the regions where the free surface and the Kelvin wake were expected. Figs. 3 and 4 show the computational domains with the applied boundary conditions in the numerical simulations of RT and SPT, respectively. The boundary conditions for the inlet and outlet were consistent across all numerical simulations, with a velocity inlet and a pressure outlet. Since in the numerical simulations of the RT only half of the domain was created, symmetry was applied at both sides. Within the numerical simulations of the SPT, the sides were set as velocity inlets. At the bottom and top boundaries, the velocity inlet was set in both types of numerical simulations. Also, it should be noted that the no-slip wall boundary condition was set on the ship and rudder surfaces. In all numerical simulations of RT and SPT, the ship and rudder surfaces were assumed to be smooth.

In Fig. 5 fine grid used in the numerical simulations of the SPT is presented. For the RT simulations, the same grid was sectioned at the symmetry plane.

Fig. 6 shows the distributions of y^+ on the hull obtained in the numerical simulations of SPT at different scales and at model scale with virtual fluid (MSVF). The obtained values of y^+ were above 30 across nearly the entire wetted hull and rudder surfaces, except in the stern region.

2.6. Verification study

To assess simulation uncertainty, a verification study was conducted using the grid convergence index (GCI) method (Celik et al., 2008) for the numerical simulations of SPT at full and different model scales. Since the iteration uncertainty is often one order of accuracy lower than the uncertainty due to time step and two orders of magnitude lower than the one for grid size (Farkas et al., 2019a), its contribution in the calculation of numerical uncertainty was neglected. The GCI method was used for the determination of the numerical uncertainties due to grid size and time step. The apparent order of the method p was calculated using the following equations:

$$p = \frac{1}{\ln r_{21}} \cdot \left| \ln \left| \frac{\varepsilon_{32}}{\varepsilon_{21}} \right| + q(p) \right| \tag{16}$$

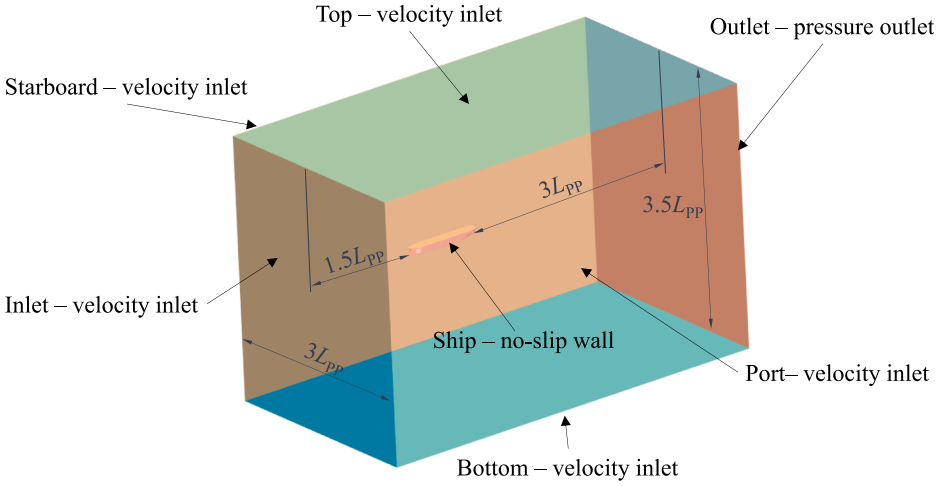


Fig. 4. Computational domain and boundary conditions in the numerical simulations of the SPT.

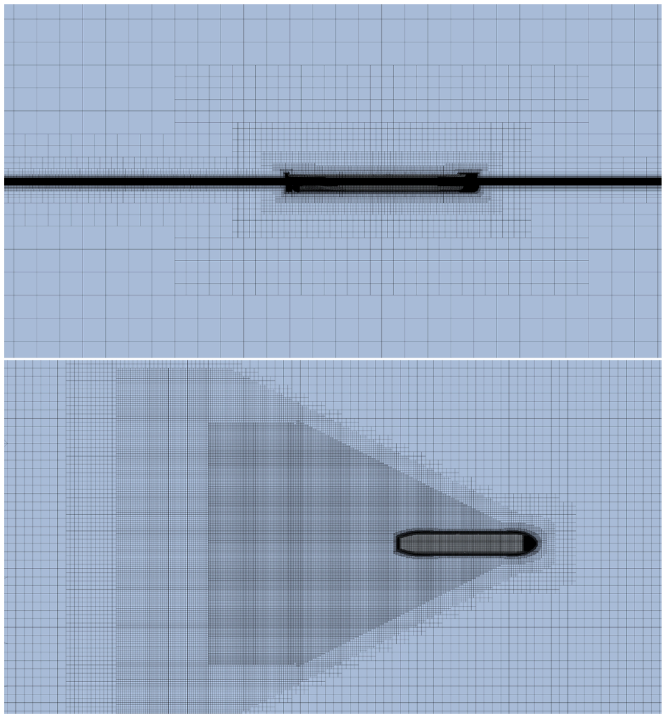


Fig. 5. Symmetry (upper) and top view (lower) cross-sections of the fine grid used in the numerical simulations of SPT.

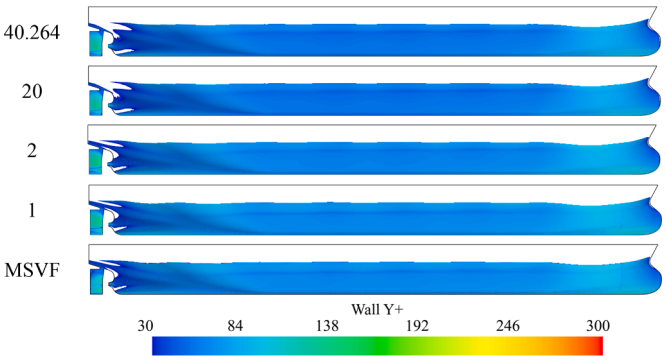


Fig. 6. The y^+ obtained in the numerical simulations of SPT at different scales.

$$q(p) = \ln\left(\frac{r_{21}^p - s}{r_{32}^p - s}\right) \tag{17}$$

$$s = 1 \cdot \mathrm{sgn}\left(\frac{\varepsilon_{32}}{\varepsilon_{21}}\right) \tag{18}$$

where r_{ij} is the grid refinement ratio, ε_{ij} is defined as $\varepsilon_{ij} = \phi_i - \phi_j$, with ϕ being the solution. The p was obtained by iteratively solving the Eqs. (16)–(18). The grid refinement ratio was calculated as the ratio between the grid spacings h of different grids with the following equation:

$$r_{ij} = \frac{h_i}{h_j} \tag{19}$$

where h_i and h_j were calculated in the STAR-CCM+ software package as:

$$h = \sqrt[3]{\frac{1}{N}\sum_{i=1}^{N}(\Delta V_i)} \tag{20}$$

where N is the total number of cells and V_i is the volume of the i-th cell. The extrapolated values, the approximate and extrapolated relative errors were calculated with the following equations:

$$\phi_{\mathrm{ext}}^{21} = \frac{r_{21}^p \phi_1 - \phi_2}{r_{21}^p - 1} \tag{21}$$

$$e_{\mathrm{a}}^{21} = \left|\frac{\phi_1 - \phi_2}{\phi_1}\right| \tag{22}$$

$$e_{\mathrm{ext}}^{21} = \left|\frac{\phi_{\mathrm{ext}}^{21} - \phi_1}{\phi_{\mathrm{ext}}^{21}}\right| \tag{23}$$

Finally, the fine-grid convergence index was calculated with the following equation:

$$GCI_{\mathrm{fine}}^{21} = \frac{1.25 e_{\mathrm{a}}^{21}}{r_{21}^p - 1} \tag{24}$$

The convergence condition is defined as $R = \varepsilon_{21}/\varepsilon_{32}$. According to this criterion, monotonic convergence is obtained when R is positive and its absolute value is less than 1, while oscillatory convergence is observed when R is negative with an absolute value less than 1. If the absolute value of R exceeds 1, the divergence is obtained. In the verification study for the time step, the fine grid with three time steps was used.

2.7. Towing tank experiments

Extensive towing tank experiments were conducted for the case of the JBC at the Brodarski Institute in Zagreb (Brodarski Institute, 2022). The towing tank experiments included the RT, OWT, and SPT at different speeds and loading conditions. The ship model was made out of wood in a scale $\lambda = 40.264$. A trip wire was used in the bow region as a turbulence stimulator as shown in Fig. 8. The resistance curve was obtained using the total resistance R_{T} measured at different Froude numbers. For the OWT, a stock propeller was selected with similar main particulars as the model used in Nmri (2015). The rate of revolution was maintained constant and different advance coefficients were obtained by varying the advance speed. The SPT was conducted with the same stock propeller utilizing the British method (Degiuli et al., 2025, 2023), meaning that a constant towing speed was maintained, and the propeller load was varied. These tests were performed at seven towing speeds. Fig. 7 shows the SPT performed at the design loading condition. The numerical results were compared against the measured values from the towing tank experiments. In the numerical simulations conducted for the validation



Fig. 7. The SPT performed at the Brodarski Institute in Zagreb.



Fig. 8. Trip wire situated in the bow region used as a turbulence stimulator.

study, the ship was allowed to pitch and heave using the DFBI model, replicating the conditions in the towing tank experiments.

As a part of the extensive experimental campaign, the nominal wake of the JBC was also measured. A five-hole Prandtl Pitot tube was used for the wake measurements, which allowed the calculation of the three velocity components based on the measured absolute and static pressures. It is important to note that this is an intrusive method since the Prandtl Pitot tube had to be installed on a support extending from the stern tube and thus causing disturbances in the flow field. The velocity components were obtained at radial positions equal to $0.35R$ (1.409 m), $0.55R$ (2.215 m), $0.74R$ (3.02 m), $0.94R$ (3.825 m) and $1.04R$ (4.228 m) and at angular positions from 0° to 360° with 10° increments. The angular reference was defined such that 0° corresponds to the bottom position of the tube, 90° to starboard, 180° to vertically upward, and 270° to the port side.

2.8. Validation study

The obtained numerical results at model scale were validated against the measured values from the towing tank experiments. The relative deviations RD were calculated between the numerically obtained results (ϕ_{CFD}) and the measured values from the towing tank experiments (ϕ_{EXP}) as follows:

$$RD = \frac{\phi_{CFD} - \phi_{EXP}}{\phi_{EXP}} \cdot 100\ \% \tag{25}$$

3. Results and discussion

3.1. Verification study

The verification study was performed for the numerical simulations of the SPT at full scale and various model scales, including numerical simulations with virtual fluid. The R_T, T, Q, and rate of revolution n were analysed. In Table 3, details of the grids used in the verification study are shown, while the time steps are presented in Table 4. Comparable grid sizes were generated in the numerical simulations at both the model scale with the virtual fluid and the full scale with the real fluid. The primary reason for the higher number of cells in the model-scale simulations with virtual fluid is the increased number of prism layers required to ensure a smooth transition between the prism layers and the base mesh. Fine time steps were calculated as $\Delta t = 0.125\ \% \cdot L_{PP}/v$, while the medium and coarse time steps were determined by multiplying the fine time step by factors of 2 and 4, respectively.

Table 4
Time steps used in the verification study.

λ	Δt_1, s	Δt_2, s	Δt_3, s
1	0.047	0.094	0.188
2	0.033	0.066	0.132
20	0.011	0.022	0.044
40.264	0.0074	0.0148	0.0296
MSVF	0.0074	0.0148	0.0296

Table 5
Verification study results for R_T.

	λ	ε_{32}, N	ε_{21}, N	R	p	ϕ^{21}_{ext}, N	GCI^{21}_{fine}, %
Grid size	1	124620	20810	0.17	6.18	1330300	0.42
	2	10670	5350	0.50	2.36	182440	3.71
	20	7.49	3.54	0.47	2.12	279.58	1.88
	40.264	2.12	0.33	0.16	5.62	39.93	0.25
	MSVF	1.46	0.35	0.24	4.59	20.76	0.80
Time step	1	117030	-14380	-0.12	3.03	1336800	0.19
	2	1050	-0120	-0.11	3.15	188040	0.01
	20	1.95	0.39	0.20	2.33	283.76	0.04
	40.264	0.24	-0.01	-0.05	4.25	40.01	0.002
	MSVF	0.34	0.07	0.20	2.31	20.87	0.10

Tables 5–8 present the verification study results for grid size and time step. The obtained GCI was below 1 % in most of the cases, with few exceptions, primarily at scales $\lambda = 2$ and $\lambda = 20$, where the GCI exceeded 1 %. In the verification study for n, the GCI values at $\lambda = 20$ and model scale for grid size were higher, likely due to the lower p. Monotonic convergence was obtained for R_T, T, and Q in the verification study for grid size. However, in the verification study for time step, oscillatory convergence was observed at full scale, $\lambda = 2$, and model scale. In the verification study for grid size, oscillatory convergence was predominant for n, with full scale being the only case where monotonic convergence was achieved. Regarding the time step, monotonic convergence was observed at every scale considered except at full scale, where oscillatory convergence occurred. The verification studies showed that the fine grid size and time step are adequate for the numerical simulations of SPT.

3.2. Resistance test

In this subsection, the results obtained in the numerical simulations of RT are presented. The obtained results from the numerical simulations at model scale were directly validated with the measured values from the towing tank. Table 9 shows the obtained R_T at different model speeds (v_M). It can be seen that R_T was underpredicted with the relative deviations being lower than -7 % for all speeds. One of the reasons is the selected turbulence model, which was shown to yield the highest relative deviations of R_T, as noticed by Farkas et al. (2018). Additionally, due to errors in the manufacturing process, the physical ship model used in the towing tank was not identical to the 3D model used in the numerical simulations. Furthermore, the moment of inertia used in the simulations was taken from available literature, as it was not measured for the actual physical model used in the experiments.

Fig. 9 compares the nominal wake obtained numerically at model scale with the wake measured in the towing tank and the one provided

Table 3
Grids used in the verification study.

λ	N_1	N_2	N_3	h_1, m	h_2, m	h_3, m	r_{32}	r_{21}
1	10.73M	4.62M	1.94M	4.907	6.499	8.671	1.334	1.324
2	10.20M	4.34M	1.83M	2.495	3.317	4.426	1.334	1.329
20	8.31M	3.54M	1.37M	0.267	0.355	0.488	1.374	1.330
40.264	7.37M	3.14M	1.20M	0.137	0.183	0.253	1.383	1.336
MSVF	10.81M	4.65M	1.88M	0.122	0.161	0.218	1.354	1.320

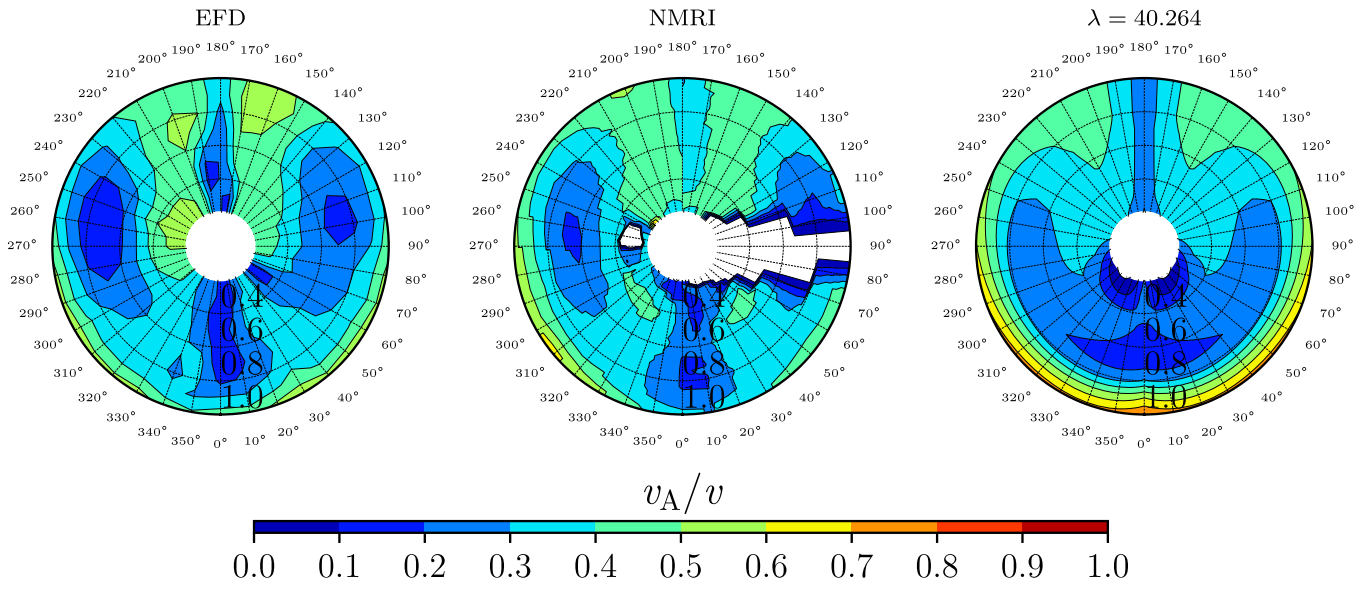


Fig. 9. Comparison between the nominal wakes obtained experimentally, numerically at model scale, and results available online (Nmri, 2015).

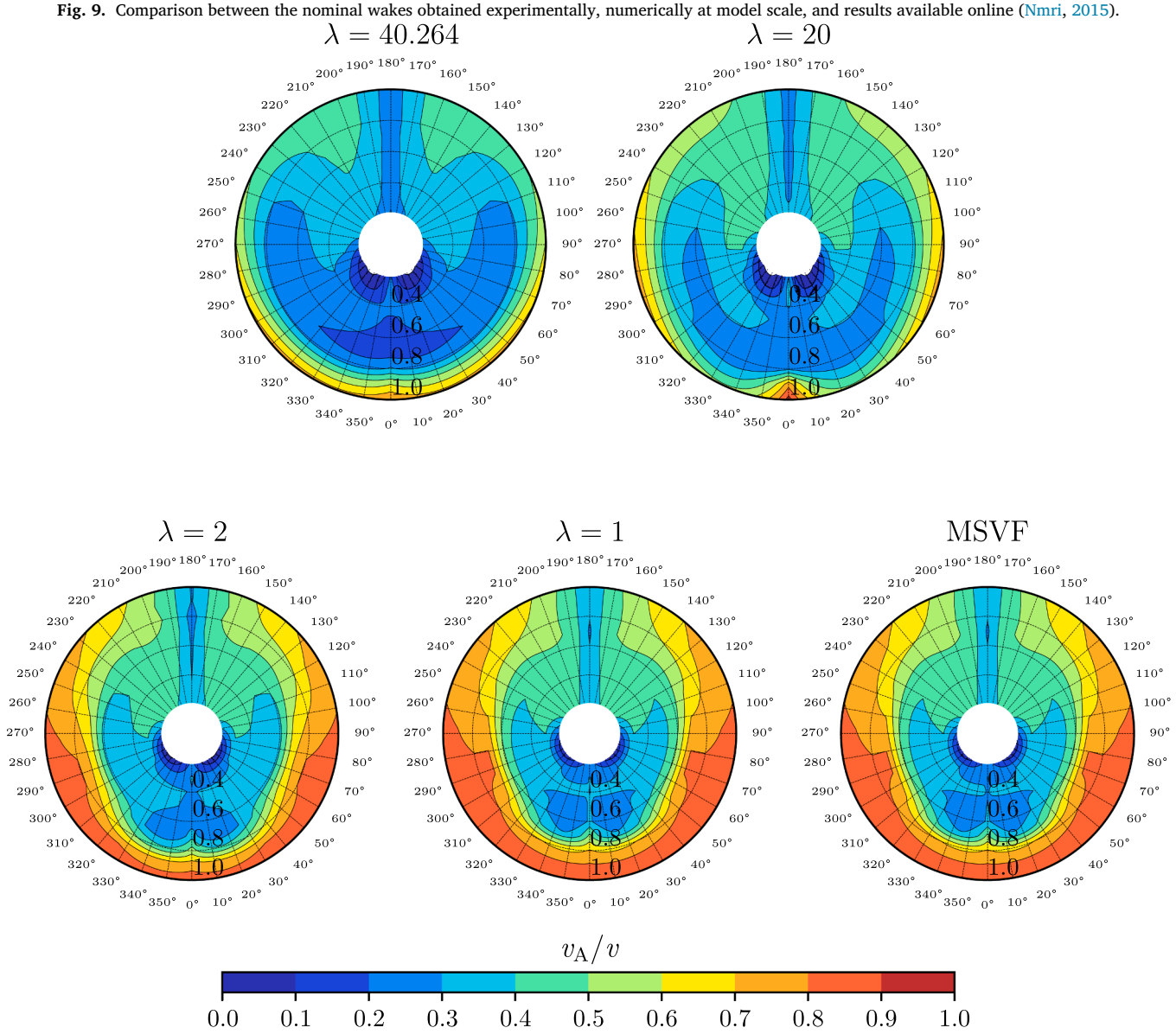


Fig. 10. Nominal wakes obtained numerically at different scales and at model scale with virtual fluid.

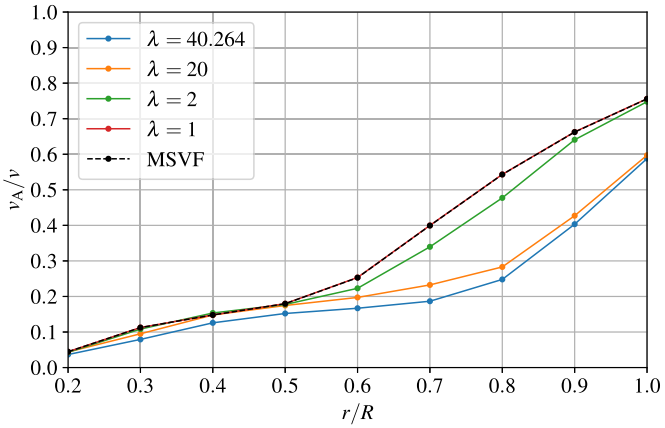


Fig. 11. Radial distribution of the v_A/v obtained at different scales.

Table 6
Verification study results for T.

	λ	ε_{32}, N	ε_{21}, N	R	p	ϕ_{ext}^{21}, N	GCI_{fine}^{21}, %
Grid size	1	124630	20880	0.17	6.16	1330300	0.42
	2	10690	5360	0.50	2.36	182450	3.71
	20	7.50	3.55	0.47	2.12	206.71	2.54
	40.264	2.12	0.34	0.16	5.62	26.514	0.38
	MSVF	1.46	0.35	0.24	4.59	22.422	0.74
Time step	1	275520	-14500	-0.05	4.25	1335600	0.08
	2	1080	-120	-0.11	3.14	188040	0.01
	20	1.94	0.39	0.20	2.32	210.91	0.06
	40.264	0.24	-0.01	-0.05	4.25	26.595	0.003
	MSVF	0.34	0.07	0.20	2.32	22.539	0.09

Table 7
Verification study results for Q.

	λ	ε_{32}, Nm	ε_{21}, Nm	R	p	ϕ_{ext}^{21}, Nm	GCI_{fine}^{21}, %
Grid size	1	103870	6860	0.07	9.41	1325000	0.05
	2	4150	1530	0.37	3.43	91250	1.25
	20	0.31	0.05	0.15	5.76	10.107	0.14
	40.264	0.05	0.001	0.03	11.39	0.6274	0.01
	MSVF	0.03	0.003	0.11	7.31	0.5507	0.11
Time step	1	266320	-12930	-0.05	4.37	1326200	0.06
	2	510	-60	-0.11	3.14	92180	0.01
	20	0.09	0.02	0.20	2.36	10.11	0.05
	40.264	0.005	-0.0002	-0.03	4.87	0.6275	0.001
	MSVF	0.01	0.002	0.21	2.26	0.5508	0.10

Table 8
Verification study results for n.

	λ	ε_{32}, rpm	ε_{21}, rpm	R	p	ϕ_{ext}^{21}, rpm	GCI_{fine}^{21}, %
Grid size	1	-0.476	-0.027	0.06	9.93	80.017	0.003
	2	0.112	-0.056	-0.50	2.39	82.658	0.09
	20	1.834	-1.420	-0.77	0.84	89.016	7.81
	40.264	2.060	-1.418	-0.69	1.21	86.751	5.01
	MSVF	4.614	-0.342	-0.07	8.67	83.228	0.05
Time step	1	8.435	0.635	-0.08	3.73	79.963	0.08
	2	0.600	0.473	0.79	0.34	80.832	2.68
	20	0.310	0.042	0.14	2.87	84.050	0.01
	40.264	0.309	0.016	0.05	4.25	83.408	0.001
	MSVF	0.42	0.084	0.20	2.31	83.174	0.03

Table 9
Validation study for the numerical simulations of RT.

V, kn	v_M, m/s	$R_{T,\,CFD}$, N	$R_{T,\,EFD}$, N	RD, %
11	0.892	20.858	21.950	-4.80
12	0.973	23.888	25.820	-6.28
13	1.054	28.063	29.960	-6.46
14	1.135	32.522	34.380	-4.20
15	1.216	38.229	39.210	-3.70
16	1.297	43.716	44.860	-1.76

Table 10
Integral values of the nominal wake obtained at different scales and at model scale with virtual fluid.

	$\lambda = 40.264$	$\lambda = 20$	$\lambda = 2$	$\lambda = 1$	MSVF
w_n	0.652	0.609	0.475	0.436	0.436
RD, %	/	-6.59 %	-27.15 %	-33.13 %	-33.13 %

by Nmri (2015), which was measured using Particle Image Velocimetry (PIV). Qualitatively, the numerical results show good agreement with the towing tank measurements and the NMRI data. A hook-like shape in the wake contours is evident beneath the hub in all cases. However, the numerically predicted speed reductions are generally lower than those measured in the towing tank, particularly at angular positions between 0°-90° and 270°-360°. A part of the reason for the lower speed reductions is the fact that the nominal wake was extracted from the numerical simulation of RT that included the rudder, whereas in the towing tank measurements, the rudder was removed to allow the installation of the five-hole Prandtl Pitot tube behind the stern. Among the three cases, the Nmri (2015) data show the lowest speed reductions at the angular position of 180°.

Since the ship model tested in the towing tank follows Froude identity, ensuring equal Froude numbers between the model and the full-scale ship, a disparity in Reynolds number arises. Consequently, the model exhibits a relatively thicker boundary layer compared to the full-scale ship (Carlton, 2018). The nominal wakes are presented in Fig. 10 with the contours of the non-dimensional axial velocity v_A/v obtained in the numerical simulations of RT at different scales and at model scale with virtual fluid for speed of 14 kn. The lowest values of v_A/v are obtained at the angular position of 180° and around the hub in the region from 0° to 90° and from 270° to 360°. A hook-like shape of the contours is visible under the hub at each scale. The low-speed region is largest at model scale and decreases as the scale decreases, confirming that boundary layer thickness also decreases with scale, as previously observed by Wang et al. (2015). The distribution of v_A/v obtained at model scale with virtual fluid is almost the same as the one obtained at full scale with real fluid.

Fig. 11 shows the radial distributions of v_A/v obtained at different scales and at model scale with virtual fluid. At radial positions in the range from $0.2R$ to $0.4R$, the v_A/v does not follow any particular trend at different scales. However, at radial positions from $0.5R$ to $1.0R$, the v_A/v decreases with the increase in scale. It is observed that v_A/v increases exponentially as the radial position approaches the tip of the propeller disc at model scale and $\lambda = 20$, whereas at other scales, the increase follows a parabolic trend. Close agreement is obtained between the v_A/v at full scale and model scale with virtual fluid.

A more detailed representation of the nominal wake is given in Fig. 12, where the circumferential distributions of v_A/v at different radii are shown. The scale effects on the circumferential distributions of v_A/v are more pronounced at radii ranging from $0.6R$ to $1.0R$ compared to those observed at lower radii. The lowest v_A/v values are obtained at model scale and the v_A/v values increase with a decrease in scale, due to the relatively thinner boundary layer forming at lower scales. However, exceptions to this trend occur at radii between $0.8R$ and $1.0R$, where lower v_A/v values are observed at $\lambda = 20$ for angular positions between 10°–60°, and 300°–350°, compared to those at model scale. At radii $0.4R$ and $0.5R$ the scale effects on the v_A/v values are negligible. Almost no differences are observed in the circumferential distributions of v_A/v at all radii when comparing full scale and model scale with virtual fluid.

Finally, in Table 10 the integral values of the nominal wake w_n obtained at different scales and at model scale with virtual fluid are presented. The scale effects on w_n are evident, as RD increases with the decrease in scale. The calculated RD, with respect to the nominal wake obtained at model scale, ranges from -6.59 % for $\lambda = 20$ and up to -33.13 % for full scale and model scale with virtual fluid.

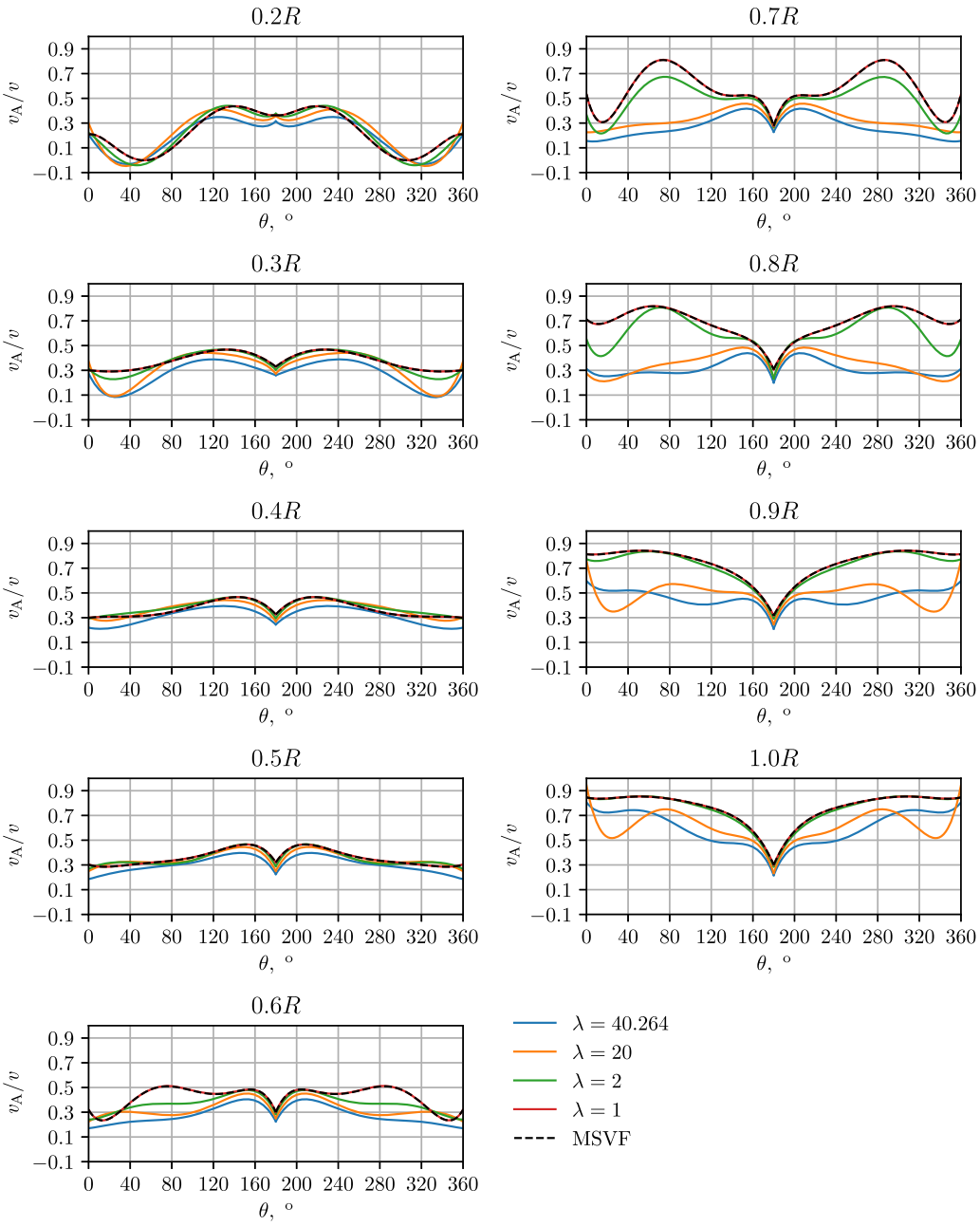


Fig. 12. Circumferential distributions of v_A/v at radii in the range from $0.2R$ to $1.0R$.

Table 11
Validation study of the numerical simulations of SPT.

v_M, m/s	n_M, 1/s	$R_{T,\,CFD}$, N	$R_{T,\,EFD}$, N	RD, %	T_{CFD}, N	T_{EFD}, N	RD, %
0.850	6.0	29.501	28.112	4.94	11.592	10.797	7.36
0.929	6.7	34.351	33.461	2.66	14.471	13.808	4.80
1.010	8.2	40.881	40.777	0.26	22.496	23.287	-3.40
1.089	7.7	45.220	46.287	-2.30	18.691	19.407	-3.69
1.180	8.5	52.733	54.598	-3.41	22.852	24.041	-4.95
1.260	9.2	59.858	60.8924	-1.70	26.816	28.166	-4.79
1.340	10.3	67.750	70.8385	-4.36	34.350	36.287	-5.34

In Fig. 13 the C_T values obtained at different scales and speeds are presented. The C_T values obtained at model scale were nearly half of those at full scale, with scales $\lambda = 2$ and $\lambda = 20$ following the same trend. At model scale and $\lambda = 20$, C_T decreases slightly with speed in the range of 11 kn–14 kn, wheras at $\lambda = 2$ and full scale, C_T does not follow a specific trend. The C_T values obtained at model scale with virtual fluid are nearly identical to those obtained at full scale with real fluid. However, larger differences are observed at speeds of 15 kn and 16 kn.

To gain a deeper understanding of the physical basis of scale effects on total resistance, the individual resistance components, namely frictional resistance and pressure resistance, were calculated. The frictional resistance was obtained by integrating the tangential shear stresses

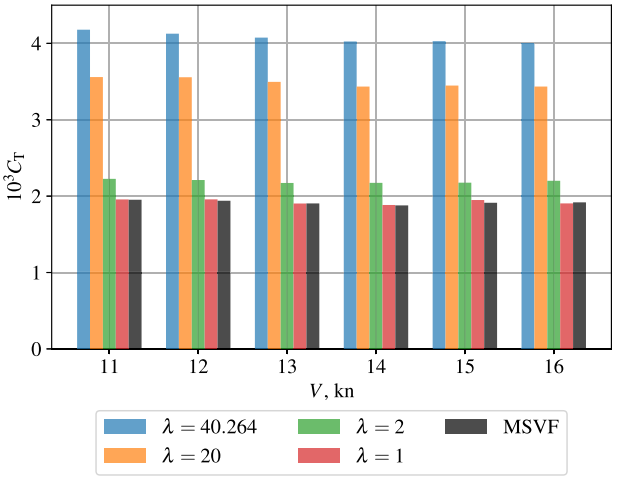


Fig. 13. The obtained C_T values at different scales and speeds.

acting on the hull surface, while the pressure resistance was determined by integrating the normal pressures. Both components were then nondimensionalized to yield their respective coefficients. Subsequently, the contributions of each resistance coefficient to the total resistance coefficient were computed, and the results are presented in Fig. 14. It was observed that the contribution of the frictional resistance coefficient to the total resistance coefficient increases with scale, a trend that is consistent across the entire range of speeds considered. As the speed increases, the contribution of the frictional resistance coefficient to the total resistance coefficient decreases.

3.3. Self-propulsion test

The results obtained in the numerical simulations of the SPT are compared against the measured values from the towing tank. Since the SPT was performed using the British method, only a single propeller rate of revolution is considered for each speed in the validation study. Table 11 shows the numerically and experimentally obtained R_T and T at each speed for single rate of revolution, along with the associated relative deviations RD. At lower speeds, R_T and T are overpredicted at lower speeds, with maximum RD of 4.94 % and 7.36 %, respectively. At higher speeds, however, R_T and T are underpredicted, with the highest absolute RDs of 4.36 % and 5.34 %, respectively. The average absolute RD for R_T is 2.8 %, while for T it is 4.9 %. The larger discrepancies observed between the numerically and experimentally obtained T values can be attributed to the method used to model the effects of the rotating propeller, i.e., the body force propeller approach. In this method, the propeller is not discretized, instead, force distributions derived from OWT are imposed within the numerical simulations of SPT. Despite this simplification, the RD between the numerically and experimentally obtained R_T remain within acceptable limits, with errors below 5 %.

The numerical simulations of SPT at different scales were conducted for speeds in the range from 11 kn to 16 kn, corresponding to the full-scale ship. The presented propulsion components consist of wake w and thrust deduction t fractions, hull efficiency η_H, the propeller advance ratio J, propeller efficiency in open water η_O, relative rotative

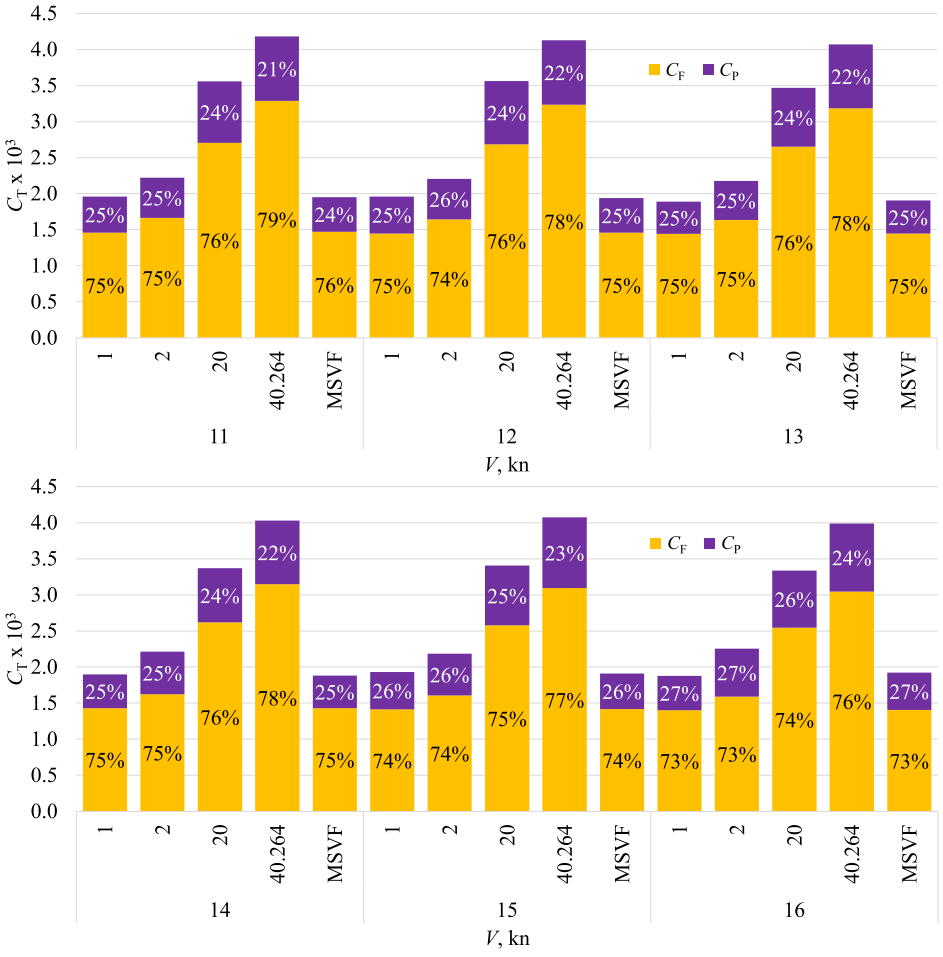


Fig. 14. Portions of the frictional and pressure resistance coefficients in total resistance coefficient obtained at different speeds.

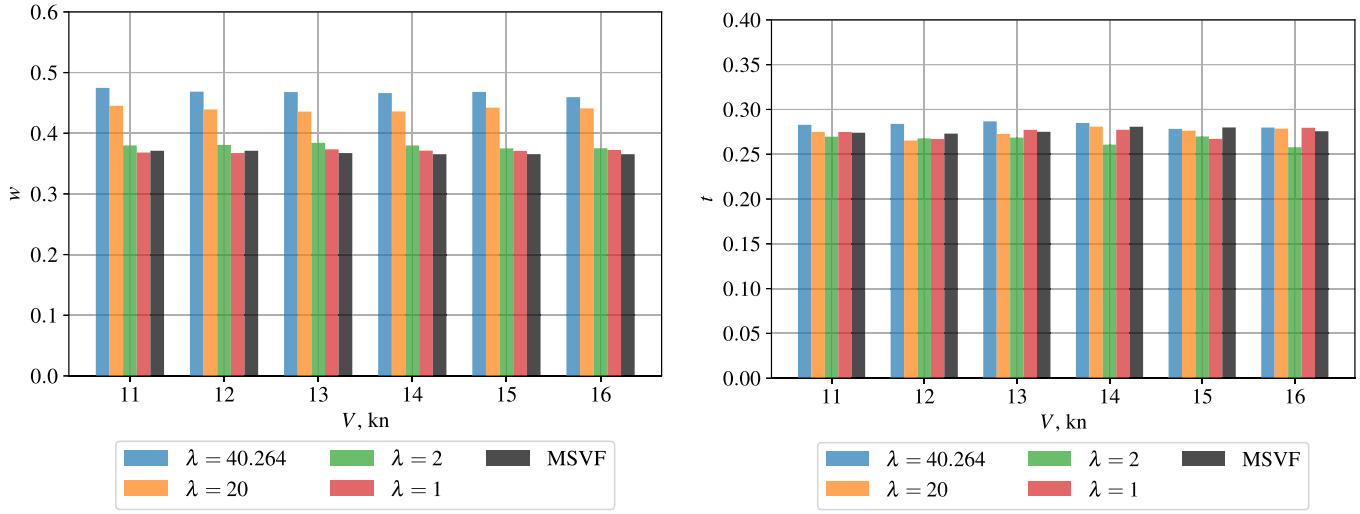


Fig. 15. The obtained w (left) and t (right) at different scales and speeds.

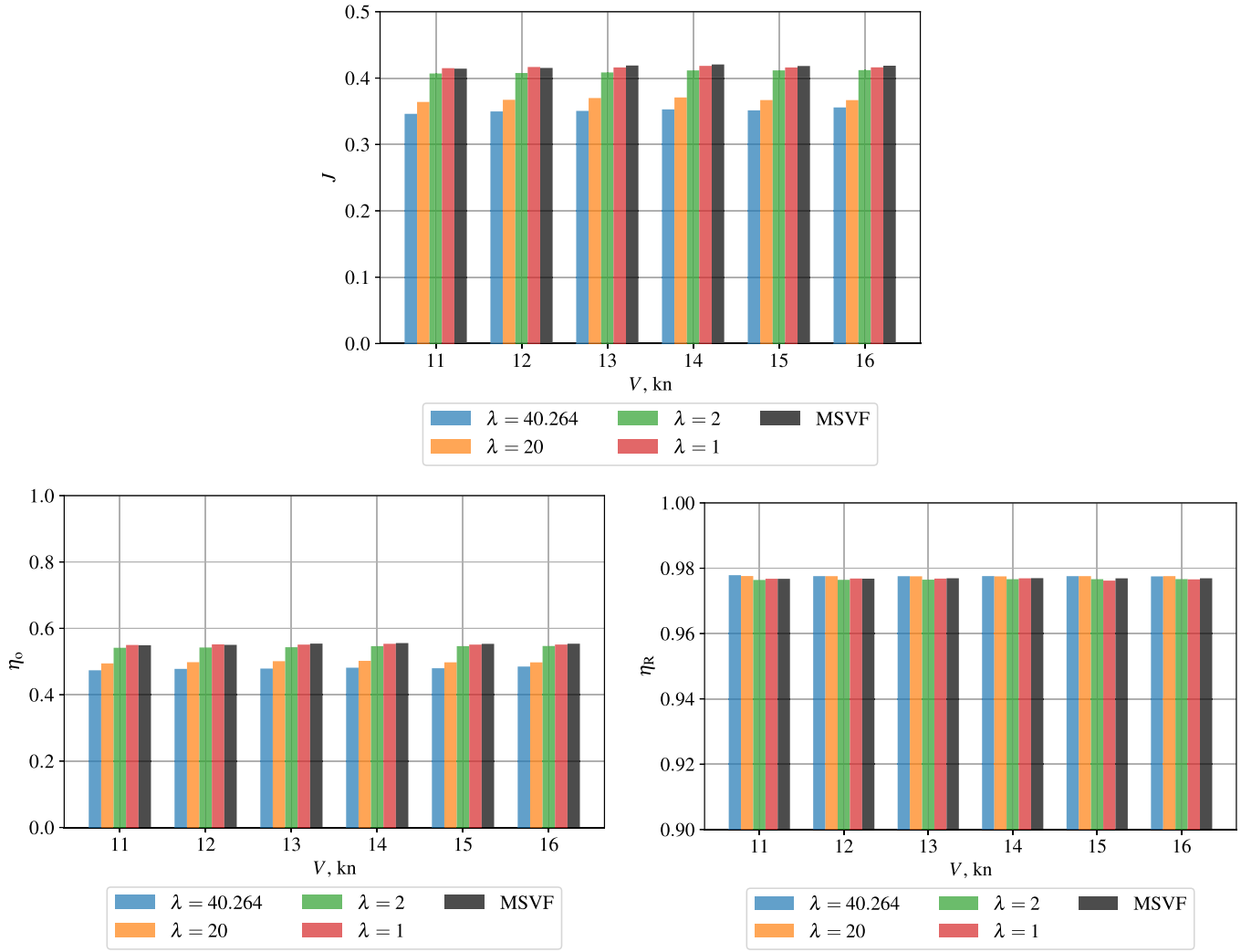


Fig. 16. The obtained J (top), η_O (bottom-left), and η_R (bottom-right) at different scales and speeds.

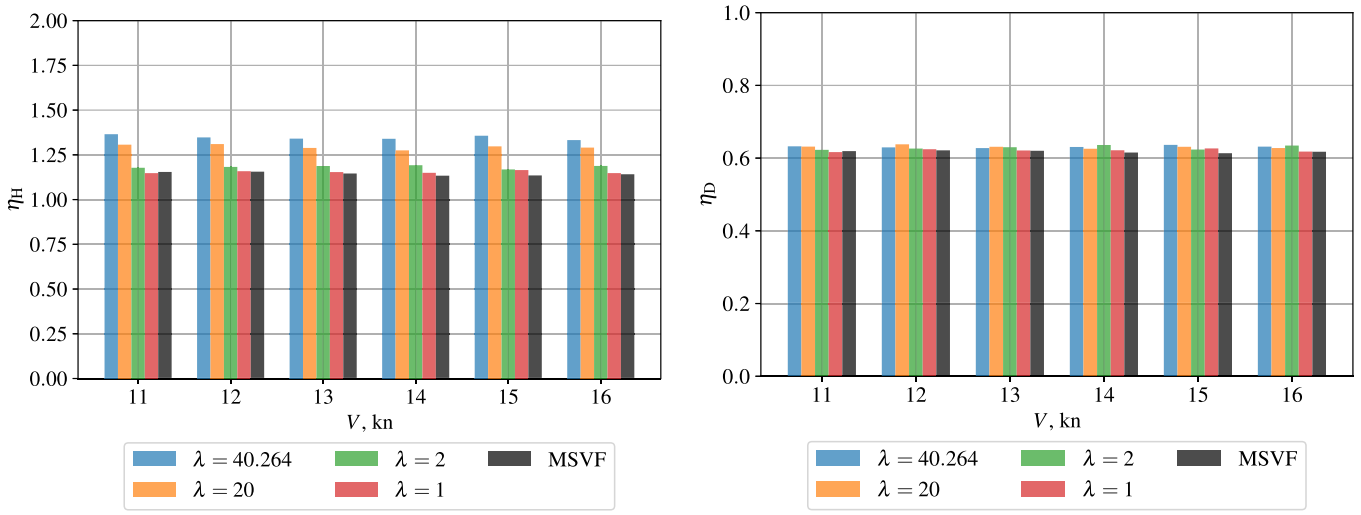


Fig. 17. The obtained η_H (left), η_D (right) at different scales and speeds.

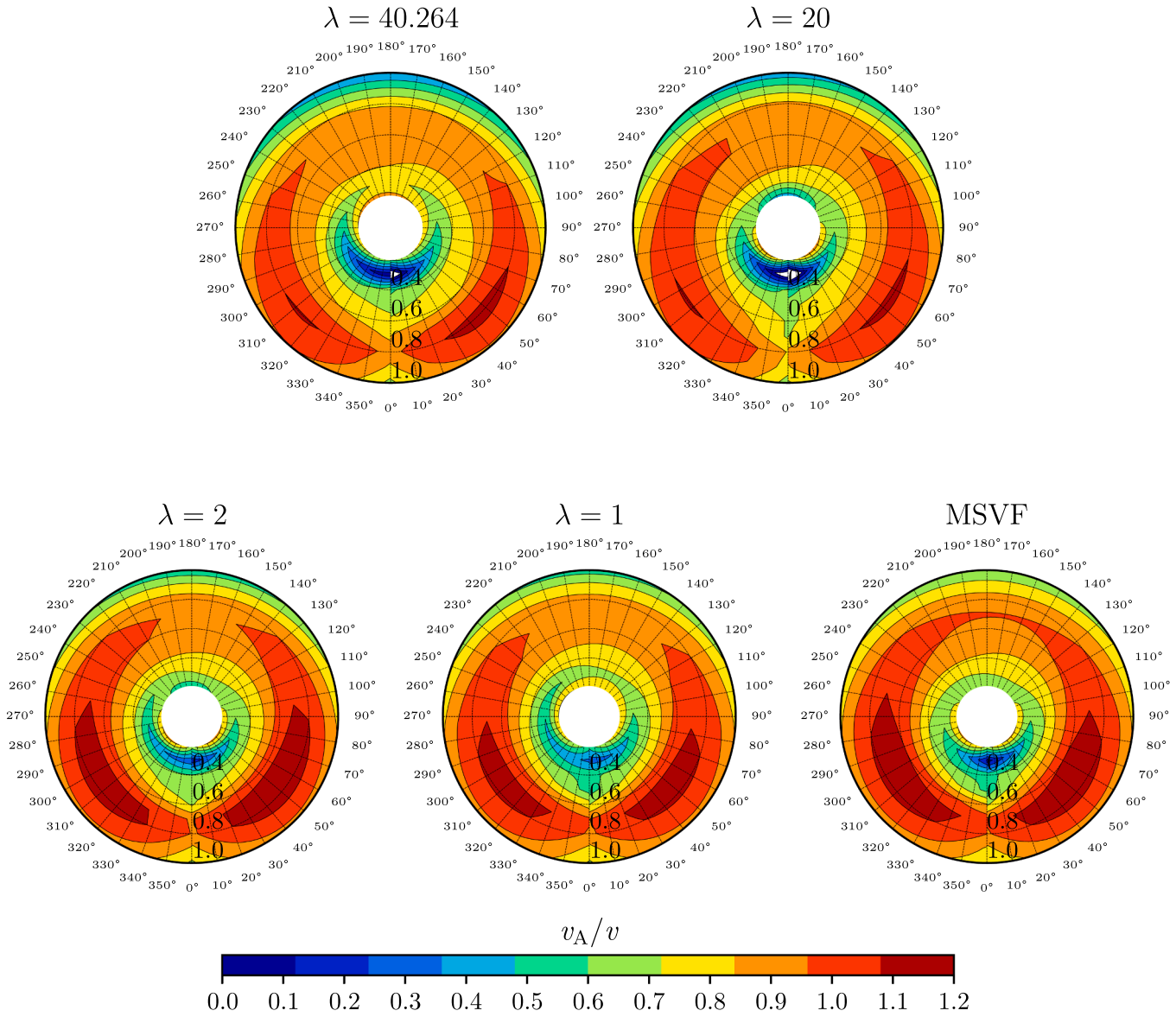


Fig. 18. Effective wake distributions obtained at different scales and at model scale with virtual fluid.

efficiency η_R, and quasi-propulsive efficiency η_D. The self-propulsion point was determined when T was equal to the R_T subtracted by the friction deduction force (F_D). This was done to account for the reduction in frictional resistance at full scale in comparison to model scale (ITTC, 2014), which was calculated as follows:

$$F_D = \frac{1}{2}\rho S_M v_M^2 (C_{FM} - C_{FS}) \tag{26}$$

where S_M is the wetted surface, and C_{FM} and C_{FS} are the frictional resistance coefficients at model and full scale, respectively. The frictional resistance coefficient was obtained with the ITTC 1957 model-ship correlation line:

$$C_F = \frac{0.075}{(\log Re - 2)^2} \tag{27}$$

Fig. 15 shows the obtained w and t at different scales and speeds. The scale effects on w are significant, whereas t does not follow any specific trend in relation to scale. The obtained w is highest at model scale and decreases with scale across the entire speed range. At speeds of 11 kn and 12 kn, w obtained at model scale with virtual fluid is higher than that obtained at full scale with real fluid, while the opposite is true for speeds ranging from 13 kn to 16 kn.

The numerically obtained J, η_O, and η_R at different scales and speeds are presented in Fig. 16. Both J and η_O increase with a decrease in scale. As expected, the values of J and η_O obtained at full scale are similar to those obtained at model scale with virtual fluid. η_R does not follow a specific trend with respect to scale, although the highest η_R is observed at model scale across the entire range of speeds. However, the obtained differences in η_R are negligible compared to those in J and η_O.

The η_H and η_D values obtained at different scales and speeds are shown in Fig. 17. Both components exhibit no particular trend with regard to speed. The scale effects are noticeable in the obtained η_H, which decreases as scale decreases. This can be attributed to the differences in the obtained w, which show more impact on the obtained η_H compared to t. On the other side, the scale effects on η_D are less pronounced, and no specific trend across different scales is observed.

The effective wake is presented through the distributions of v_A/v obtained in the numerical simulations of SPT at different scales and at model scale with virtual fluid, as shown in Fig. 18. The scale effects on the effective wake are not as pronounced as those on the nominal wake. However, as scale increases, the low-speed regions become more prominent, particularly in the region near the hub of the propeller. The effective wake distribution obtained at model scale with virtual fluid closely matches the one obtained at full scale with real fluid, except in the region near the hub. In this region, the speed reductions are more pronounced at model scale with virtual fluid compared to results obtained at full scale with real fluid.

4. Conclusions and future work

In this study, numerical simulations of RT and SPT were systematically conducted at four scales, ranging from model to full scale, for sailing speeds between 11 kn and 16 kn, corresponding to the full-scale ship. Additional numerical simulations were performed at model scale with virtual fluid to satisfy both Froude and Reynolds similarity. The numerical simulations were based on RANS equations, with the SSTKO turbulence model applied to close the governing equations. The governing equations were discretized using the finite volume method to obtain a numerically solvable system of algebraic equations. The volume of fluid method was employed to simulate the two-phase flow of water and air. In the numerical simulations of SPT, the body force propeller method was used to model the effects of a rotating propeller behind the stern. An extensive verification study was carried out for the numerical simulations of SPT for R_T, T, Q, and n to quantify numerical uncertainty resulting from grid size and time step. For the numerical simulations of RT, half of the domain was used, maintaining the same mesh setup as in the numerical simulations of SPT. The validation study was performed at model scale for both types of simulations, using the available experimental data from towing tank tests. In the validation study, the ship was allowed to pitch and heave, whereas for the remaining numerical simulations, it was fixed at even keel. In numerical simulations with real fluid, the density and viscosity of the fluids remained constant across all scales. However, in the numerical simulations at model scale with virtual fluid, the dynamic viscosity was adjusted to match the Reynolds number at full-scale.

The verification study showed that the numerical uncertainty is relatively low, with the obtained GCI values being lower than 1 % in most cases. Monotonic convergence was achieved for R_T, T, and Q in the verification study for grid size, and for n in the verification study for time step. In other cases, oscillatory convergence was obtained. The verification study showed that the fine grid and time step were appropriate for the remaining numerical simulations.

The validation study of the numerical simulations of RT showed that R_T was consistently underpredicted, with RD values lower than -7 % for all considered speeds. The nominal wake was analysed at different scales and at model scale with virtual fluid. The low-speed region was largest at model scale and decreased with scale. The distribution of the v_A/v obtained at model scale with virtual fluid closely matched that obtained at full scale with real fluid. Radial distributions of v_A/v showed a decrease with increasing scale at radii from $0.5R$ to $1.0R$. Circumferential distributions indicated that the lowest v_A/v was obtained at model scale, with speed increasing as scale descreases. The calculated RD of w_n, obtained numerically and experimentally, ranged from -6.59 % at model scale to -33.13 % at full scale.

The validation study of the numerical simulations of SPT showed that R_T and T were overpredicted at lower speeds and underpredicted at higher speeds. The average absolute RD for R_T was 2.8 %, while for T was equal to 4.9 %. The results indicated that the scale effects had a more significant impact on w compared to t. The obtained J and η_O increased scale decreased, while the scale effects on η_R were negligible. η_H decreased with scale, while the scale effects on η_D were less pronounced. The effective wake distributions revealed that the low-speed regions became more visible as scale increased, particularly near the propeller hub. The effective wake distribution obtained at model scale with virtual fluid closely matched that obtained at full scale with real fluid, except in the region near the hub.

This study provides a detailed analysis of the scale effects and the impact of speed on the resistance and propulsion characteristics of the JBC. The results obtained at model scale with virtual fluid aligned closely with those obtained at full scale with real fluid. Future study will be focused on the determination of scale effects on the ship hydrodynamic characteristics using numerical simulations of SPT with a fully discretized propeller.

CRediT authorship contribution statement

Carlo Giorgio Grlj: Writing – review & editing, Visualization, Investigation, Conceptualization, Writing – original draft, Software, Methodology, Data curation, Validation, Resources, Formal analysis; **Nastia Degiuli:** Visualization, Resources, Investigation, Formal analysis, Writing – review & editing, Supervision, Project administration, Funding acquisition, Data curation, Writing – original draft, Validation, Methodology, Conceptualization; **Ivana Martić:** Writing – original draft, Methodology, Data curation, Writing – review & editing, Visualization, Resources, Investigation, Validation, Formal analysis, Conceptualization.

Declaration of competing interest

The authors report there are no competing interests to declare.

Acknowledgment

This study has been fully supported by the Croatian Science Foundation under project IP-2020-02-8568. This research was performed using the Advanced computing service provided by University of Zagreb University Computing Centre - SRCE.

References

Brodarski Institute, 2022. Report 6652-M. Resistance, Self-Propulsion and 3D Wake Measurement Test Results. Technical Report. Brodarski Institute. Zagreb.

Can, U., Delen, C., Bal, S., 2020. Effective wake estimation of KCS hull at full-scale by GEOSIM method based on CFD. Ocean Eng.. Vol. 218. https://doi.org/10.1016/j.oceaneng.2020.108052

Carlton, J., 2018. Marine Propellers and Propulsion. Butterworth-Heinemann.

Celik, I.B., Ghia, U., Roache, P.J., Freitas, C.J., Coleman, H., Raad, P.E., 2008. Procedure for estimation and reporting of uncertainty due to discretization in cfd applications. J. Fluids Eng. Trans. ASME 130, 78001. https://doi.org/10.1115/1.2960953/444689

Degiuli, N., Martić, I., Buča, M.P., Grlj, C.G., 2025. Benchmark study on resistance and propulsion characteristics of a 6750-TEU container ship. Vol. 319. Ocean Eng.. https://doi.org/10.1016/j.oceaneng.2025.120300

Degiuli, N., Martić, I., Farkas, A., Buča, M.P., Dejhalla, R., Grlj, C.G., 2023. Experimental assessment of the hydrodynamic characteristics of a bulk carrier in off-design conditions. Vol. 280. Ocean Eng.. https://doi.org/10.1016/j.oceaneng.2023.114936

Dogrul, A., 2022. Numerical prediction of scale effects on the propulsion performance of joubert bb2 submarine. Brodogradnja 73, 17–42. https://doi.org/10.21278/brod73202

Dogrul, A., Song, S., Demirel, Y.K., 2020. Scale effect on ship resistance components and form factor. Ocean Eng.. Vol. 209. https://doi.org/10.1016/j.oceaneng.2020.107428

Farkas, A., Degiuli, N., Martić, I., 2018. Assessment of hydrodynamic characteristics of a full-scale ship at different draughts. Ocean Eng.. Vol. 156. https://doi.org/10.1016/j.oceaneng.2018.03.002

Farkas, A., Degiuli, N., Martić, I., 2019a. Impact of biofilm on the resistance characteristics and nominal wake. Proc. Inst. Mech. Eng. M 234, 59–75. https://doi.org/10.1177/1475090219862897

Farkas, A., Degiuli, N., Martić, I., Dejhalla, R., 2019b. Numerical and experimental assessment of nominal wake for a bulk carrier. J. Mar. Sci. Technol. 24, 1092–1104. https://doi.org/10.1007/s00773-018-0609-4

Grlj, C.G., Degiuli, N., Farkas, A., Martić, I., 2022. Numerical study of scale effects on open water propeller performance. J. Mar. Sci. Eng. 10, 1132. https://doi.org/10.3390/jmse10081132

Grlj, C.G., Degiuli, N., Martić, I., 2023. The impact of numerical parameters on the resistance characteristics of a container ship at the model and full scale. J. Mar. Sci. Eng. 11, 1672. https://doi.org/10.3390/jmse11091672

Grlj, C.G., Degiuli, N., Martić, I., 2024. Experimental and numerical assessment of the effect of speed and loading conditions on the nominal wake of a containership. Brodogradnja 75, 75405. https://doi.org/10.21278/brod75405

Guo, C., Wu, T., Zhang, Q., Luo, W., Su, Y., 2017. Numerical simulation and experimental studies on aft hull local parameterized non-geosim deformation for correcting scale effects of nominal wake field. Brodogradnja 68, 77–96. https://doi.org/10.21278/brod68105

Haase, M., Zurcher, K., Davidson, G., Binns, J.R., Thomas, G., Bose, N., 2016. Novel cfd-based full-scale resistance prediction for large medium-speed catamarans. Ocean Eng. 111, 198–208. https://doi.org/10.1016/j.oceaneng.2015.10.018

ITTC, 2014. Practical Guidelines for Ship Self-Propulsion CFD. ITTC 7.5-03-03-01, ITTC-Recommended Procedures and Guidelines.

Kim, K.W., Paik, K.J., Lee, S.H., Lee, J.H., Kwon, S.Y., Oh, D., 2024. A numerical study on the feasibility of predicting the resistance of a full-scale ship using a virtual fluid. Int. J. Nav. Archit. 16, 100560. https://doi.org/10.1016/j.ijnaoe.2023.100560

Kok, Z., Duffy, J., Chai, S., Jin, Y., Javanmardi, M., 2020. Numerical investigation of scale effect in self-propelled container ship squat. Appl. Ocean Res. 99, 102143. https://doi.org/10.1016/j.apor.2020.102143

Korkmaz, K.B., Werner, S., Sakamoto, N., Queutey, P., Deng, G., Yuling, G., Guoxiang, D., Maki, K., Ye, H., Akinturk, A., Sayeed, T., Hino, T., Zhao, F., Tezdogan, T., Demirel, Y.K., Bensow, R., 2021. CFD based form factor determination method. Vol. 220. Ocean Eng.. https://doi.org/10.1016/j.oceaneng.2020.108451

Liu, S., He, G., Wang, Z., Zhang, C., Zhang, Z., 2024. Scale effects on the hydrodynamic performance of a submerged body. Ocean Eng. 305, 117899. https://doi.org/10.1016/j.oceaneng.2024.117899

Ma, Z., Li, N., Zeng, Q., Deng, X., Shi, C., 2024. Influence of scale effect on flow field offset for ships in confined waters. Brodogradnja 75, 75106. https://doi.org/10.21278/brod75106

Menter, F.R., 1994. Two-equation eddy-viscosity turbulence models for engineering applications. AIAA J. 32, 1598–1605. https://doi.org/10.2514/3.12149

Mikulec, M., Piehl, H., 2023. Verification and validation of cfd simulations with full-scale ship speed/power trial data. Brodogradnja 74, 41–62. https://doi.org/10.21278/brod74103

Niklas, K., Pruszko, H., 2019. Full-scale CFD simulations for the determination of ship resistance as a rational, alternative method to towing tank experiments. Vol. 190. Ocean Eng.. https://doi.org/10.1016/j.oceaneng.2019.106435

Nmri, 2015. Tokyo 2015 a workshop on CFD in ship hydrodynamics. https://t2015.nmri.go.jp/index.html.

Pena, B., Huang, L., 2021. A review on the turbulence modelling strategy for ship hydrodynamic simulations. Ocean Eng.. 241. https://doi.org/10.1016/j.oceaneng.2021.110082

Pena, B., Muk-Pavic, E., Fitzsimmons, P., 2020. Detailed analysis of the flow within the boundary layer and wake of a full-scale ship. Ocean Eng.. Vol. 218. https://doi.org/10.1016/j.oceaneng.2020.108022

Saydam, A.Z., Kucuksu, G.N., Insel, M., Gokcay, S., 2022. Uncertainty quantification of self-propulsion analyses with rans-cfd and comparison with full-scale ship trials. Brodogradnja 73, 107–129. https://doi.org/10.21278/brod73406

Sezen, S., Cakici, F., 2019. Numerical prediction of total resistance using full similarity technique. Vol. 33. China Ocean Eng.. https://doi.org/10.1007/s13344-019-0047-z

Sezen, S., Delen, C., Dogrul, A., Atlar, M., 2021. An investigation of scale effects on the self-propulsion characteristics of a submarine. Appl. Ocean Res. 113, 102728. https://doi.org/10.1016/j.apor.2021.102728

Song, K., Guo, C., Sun, C., Wang, C., Gong, J., Li, P., Wang, L., 2021. Simulation strategy of the full-scale ship resistance and propulsion performance. Eng. Appl. Comput. Fluid Mech. 15, 1321–1342. https://doi.org/10.1080/19942060.2021.1974091

Spalart, P.R., Rumsey, C.L., 2007. Effective inflow conditions for turbulence models in aerodynamic calculations. AIAA J. 45, 2544–2553. https://doi.org/10.2514/1.29373

Sun, W., Hu, Q., Hu, S., Su, J., Xu, J., Wei, J., Huang, G., 2020. Numerical analysis of full-scale ship self-propulsion performance with direct comparison to statistical sea trail results. J. Mar. Sci. Eng. 8, 24. https://doi.org/10.3390/jmse8010024

Terziev, M., Tezdogan, T., Demirel, Y.K., Villa, D., Mizzi, S., Incecik, A., 2021. Exploring the effects of speed and scale on a ship's form factor using cfd. Int. J. Nav. Archit. Ocean Eng. 13, 147–162. https://doi.org/10.1016/j.ijnaoe.2020.12.002

Terziev, M., Tezdogan, T., Incecik, A., 2019. A geosim analysis of ship resistance decomposition and scale effects with the aid of cfd. Appl. Ocean Res. 92, 101930. https://doi.org/10.1016/j.apor.2019.101930

Wang, Z.Z., Xiong, Y., Wang, R., Shen, X.R., Zhong, C.H., 2015. Numerical study on scale effect of nominal wake of single screw ship. Ocean Eng. 104, 437–451. https://doi.org/10.1016/j.oceaneng.2015.05.029

Zeng, Q., Hekkenberg, R., Thill, C., Hopman, H., 2020. Scale effects on the wave-making resistance of ships sailing in shallow water. Ocean Eng. 212, 107654. https://doi.org/10.1016/j.oceaneng.2020.107654

Zhang, Y.X., Lai, M.Y., Ni, Y.G., Feng, L., 2021. Cfd study of hull wakes in oblique flow at model and full scales. Appl. Ocean Res. 112, 102689. https://doi.org/10.1016/j.apor.2021.102689

Article V

Article published by Elsevier in Results in engineering on 29 March 2026, available online: https://www.sciencedirect.com/science/article/pii/S2590123026013526

Results in Engineering 30 (2026) 110318



Contents lists available at ScienceDirect

Results in Engineering

journal homepage: www.sciencedirect.com/journal/results-in-engineering



A full-scale numerical investigation of a containership resistance and propulsion characteristics at different trim angles

Carlo Giorgio Grlj, Nastia Degiuli *, Ivana Martić

University of Zagreb Faculty of Mechanical Engineering and Naval Architecture, Ivana Lučića 5, Zagreb, 10000, Croatia

ARTICLE INFO

Keywords:
CFD
Full scale
6750 TEU Containership
Self-propulsion test

ABSTRACT

This study presents a comprehensive full-scale numerical investigation of the resistance and propulsion characteristics of a post-Panamax 6750 TEU containership at various trim angles. The numerical simulations are conducted using Reynolds averaged Navier-Stokes equations coupled with the shear stress transport $k-\omega$ turbulence model. The dynamic fluid body interaction method is employed to allow the ship to freely heave and pitch, while the effects of the rotating propeller in the numerical simulations of the self-propulsion test are modelled using the virtual disk method. A thorough verification study is performed to ensure the accuracy and reliability of the numerical results. A validation study was also conducted through comparison with the available experimental data, showing good agreement. The findings demonstrate that the adopted numerical approach accurately predicts the ship resistance and propulsion characteristics across different trim angles. The results highlight the significant influence of trim on ship performance, providing valuable insights for optimizing trim angle during its operation.

1. Introduction

Accurate prediction of ship resistance and propulsion characteristics plays a crucial role in the early stages of ship design, as these parameters directly influence hull optimization, fuel efficiency, and overall vessel performance. Computational Fluid Dynamics (CFD) has become an indispensable tool in this process, allowing detailed analysis of flow phenomena around the hull and propeller that are difficult to capture experimentally. With continuous advancements in numerical methods, turbulence modelling, and computational resources, CFD simulations have evolved from simplified model-scale analyses to reliable full-scale predictions that can complement or even replace traditional towing tank experiments. Niklas and Pruszko [1] demonstrated that full-scale CFD simulations are capable of accurately predicting ship resistance characteristics, achieving agreement with experimental data comparable to towing tank tests. Similarly, Orych et al. [2] conducted a comprehensive validation study of full-scale self-propulsion test (SPT) simulations, showing excellent correlation between numerical and experimental resultsSulovsky et al. [3] conducted full-scale CFD simulations of the SPT for a post-Panamax containership, applying the actuator disk or virtual disk method to capture the effects of propeller rotation. The numerical results showed that the developed actuator disk model is capable of accurately predicting ship propulsion characteristics by comparing the obtained results with sea trial data. These studies highlight the growing reliability of full-scale CFD approaches as a powerful and cost-effective alternative to experimental testing in modern ship hydrodynamics. Another approach for simulating the effects of the rotating propeller include a hybrid RANS/Boundary Element Method (BEM) as employed by Calcagni et al. [4] within the CFD simulations of the SPT for the KRISO containership (KCS). The authors showed good agreement with the experimental data regarding the propeller loads, while some discrepancies were observed for the wake field. Similarly, BEM was employed by Testa et al. [5] to assess the hydrodynamic characteristics of different propeller models in oblique flow. The main findings demonstrate that the proposed BEM approach is capable of accurately capturing the unsteady blade pressures as well as the thrust and torque of the propeller.

Carrica et al. [6] proposed a numerical methodology for simulating a self-propelled ship at model scale using the overset mesh technique, in which the propeller is fully discretized and resolved within the flow domain. A feedback controller was implemented to automatically adjust the propeller rotational speed to achieve the self-propulsion condition. The approach was validated using three benchmark ship geometries: the KRISO Very Large Crude Carrier (KVLCC1), the David Taylor Model Basin (DTMB) 5613 surface combatant (ONR Tumblehome), and the KCS. Building on this work, the same authors extended the methodology to full-scale simulations [7]. In that study, they performed numerical analyses of the resistance test (RT), open-water test (OWT), and SPT at full scale to determine the propulsion characteristics of the KCS. The

* Corresponding author.
E-mail address: nastia.degiuli@fsb.unizg.hr (N. Degiuli).

https://doi.org/10.1016/j.rineng.2026.110318
Received 5 February 2026; Received in revised form 11 March 2026; Accepted 27 March 2026
Available online 29 March 2026
2590-1230/© 2026 The Authors. Published by Elsevier B.V. This is an open access article under the CC BY-NC-ND license (http://creativecommons.org/licenses/by-nc-nd/4.0/).

results demonstrated good agreement between the full-scale numerical predictions and the corresponding model-scale experimental data obtained in accordance with the International Towing Tank Conference (ITTC) procedures, thereby confirming the validity and accuracy of the proposed CFD-based approach.

Mikulec and Piehl [8] performed an extensive verification and validation study of full-scale CFD simulations. The verification results were satisfactory, and the validation study showed good agreement for the numerically predicted propeller rate of revolution. However, significant discrepancies were observed between the numerically predicted delivered power and the values obtained from sea trials. The authors attributed these deviations to insufficient information regarding the onboard logging system installed on the analysed vessel. Similarly, Quist et al. [9] performed a validation study of full-scale numerical simulations that accounted for measured hull roughness and welding seams. Their findings emphasized that incorporating hull roughness effects into full-scale CFD simulations is essential for accurately predicting delivered power and achieving closer agreement with experimental or operational data. Mikkelsen and Walther [10] investigated the influence of hull roughness on ship propulsion characteristics through full-scale CFD simulations. Their results revealed significant discrepancies between the numerical predictions and sea trial measurements when the standard empirical roughness formulation proposed by Townsin was applied. These discrepancies were notably reduced when modified wall functions were implemented to account more accurately for surface roughness effects. More recently, Lopes et al. [11] performed full-scale CFD simulations of the resistance test to assess scale effects on ship resistance. The numerical predictions were evaluated against experimental measurements acquired at full scale, showing that the total resistance was underpredicted in the whole range of considered Froude numbers. The authors attributed this to the omission of hull roughness in the numerical simulations.

Although CFD simulations are widely used in ship design, they are also valuable for examining how various parameters influence ship resistance and propulsion performance during operation. Since trim optimization is one of the measures recommended by the International Maritime Organization (IMO) to improve overall ship energy efficiency [12], understanding how trim angle affects resistance and propulsion is essential. Numerous studies have investigated the impact of trim on resistance and propulsion characteristics [13–15], primarily through numerical simulations at model scale. Islam and Soares [16] investigated the total resistance of a containership at three Froude numbers and draught conditions using numerical simulations, concluding that the optimal trim varies with both draught and Froude number. A similar conclusion was reached by Sun et al. [17]. Mahmoodi et al. [18] examined the propulsion characteristics of a VLCC tanker at various trim angles using model-scale CFD simulations. They reported that a 0.2° bow-down trim yielded reduced total resistance and propeller thrust, alongside an increase in propulsive efficiency.

Building on the authors' previous analysis of speed and trim angle effects on the nominal wake at model scale [19], this study concentrates on validating full-scale resistance and propulsion characteristics predicted by numerical simulations for a post-Panamax 6750 TEU containership. The numerical simulations are performed at several trim angles while maintaining a constant displacement, and the corresponding resistance and propulsion characteristics are evaluated. A thorough verification study is conducted, and the results are presented for different types of numerical simulations. The rest of the paper is organised as follows: Section 2 describes the methods used in the numerical simulations, including the geometry, mathematical background, numerical setup, and the calculation of propulsion components. Section 3 presents the verification study and the results of the conducted numerical simulations, along with a discussion of the findings. Finally, Section 4 summarizes the main conclusions drawn from this study.

Table 1
Post-Panamax 6750 TEU containership main particulars.

Main particular	Symbol	Unit	Value
Scale ratio	λ	-	1
Length between perpendiculars	L_{PP}	m	286.6
Length, overall	L_{OA}	m	300.9
Length of waterline	L_{WL}	m	292.37
Breadth	B	m	40
Draught	T	m	11.98
Area of wetted surface	S	m^2	13 325
Displacement volume	∇	m^3	85 556
Longitudinal centre of buoyancy (from midship)	L_{CB}	m	-5.07
Vertical centre of buoyancy (from keel)	Z_{CB}	m	6.62
Longitudinal propeller position (from AP)	x_P	m	6.51
Vertical propeller position (from keel)	z_P	m	3.91

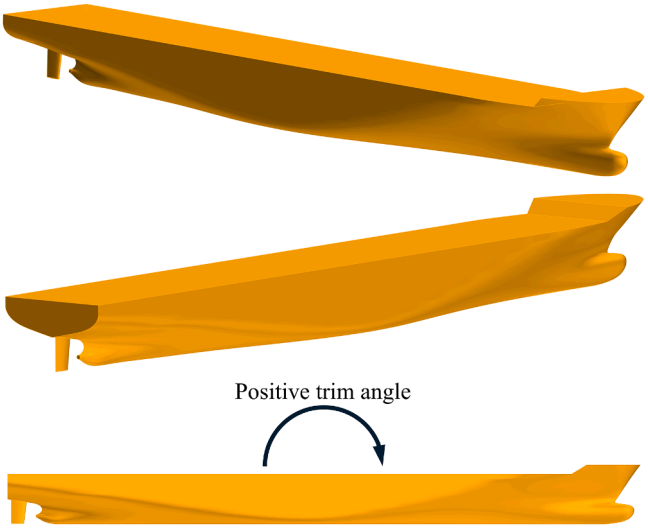


Fig. 1. The 3D representation of the post-Panamax 6750 TEU containership employed in the numerical simulations.

2. Methods

2.1. Geometry

For the case study, a post-Panamax 6750 TEU containership was selected. The geometry of the containership is given by Kim and Kim [20], where the authors presented the results of the benchmark study conducted during the 2nd ITTC-ISSC joint workshop in 2014 for the assessment of ship motions and loads. Subsequently, the same containership model was employed in a comprehensive experimental investigation performed at the Brodarski Institute in Zagreb at a model scale of $\lambda = 35.18$ [21]. The 3D model is depicted in Fig. 1, and the corresponding main particulars are summarized in Table 1.

The rudder and propeller were not available originally since the containership model was first used as a benchmark study for the assessment of the ship motions and loads. Therefore, Degiuli et al. [21] defined a rudder and selected two stock propellers. The rudder and propellers were selected based on ship characteristics, the available space behind the stern of the containership, and the required clearance from the keel. From the two propellers, the fixed pitch propeller (FPP) was used in the present study. Its main particulars are given in Table 2.

Since the CFD simulation were conducted at different trim angles, Table 3 summarizes the length of waterline and draughts for each trim angle considered in this study.

Table 2
Containership propeller main particulars.

Main particular	Symbol	Unit	Value
Propeller diameter	D	m	7.3
Pitch ratio	$P_{0.75R}/D$	-	0.8901
Expanded blade area ratio	A_E/A_0	-	0.75
Hub ratio	d/D	-	0.1687
Number of propeller blades	Z	-	4
Direction of rotation	-	-	Clockwise

2.2. Mathematical background

The numerical simulations rely on the Reynolds averaged Navier-Stokes (RANS) formulation, requiring the solution of the continuity and momentum equations that read as follows:

$$\frac{\partial \bar{u}_i}{\partial x_i} = 0 \tag{1}$$

$$\rho \frac{\partial \bar{u}_i}{\partial t} + \rho \frac{\partial}{\partial x_j}\left(\bar{u}_i \bar{u}_j + \overline{u_i' u_j'}\right) = -\frac{\partial \bar{p}}{\partial x_i} + \frac{\partial \bar{\tau}_{ij}}{\partial x_j} \tag{2}$$

where ρ is the fluid density, $\bar{u}_i$ is the averaged Cartesian components of the velocity vector, $\rho\overline{u_i' u_j'}$ is the Reynolds Stress Tensor (RST), $\bar{p}$ is the mean pressure, and $\bar{\tau}_{ij}$ is the mean viscous stress tensor. For the closure of RANS equations, the Shear Stress Transport $k-\omega$ (SSTKO) turbulence model is used in this sutdy because it was previously shown that it is a reasonable compromise between solution accuracy and computational expense [22,23]. The SSTKO turbulence model belongs to the eddy viscosity models, where the RST is modelled using the Boussinesq hypothesis. Details on the additional transport equations for the kinetic energy and the specific dissipation rate can be found in [24]. The governing equations were discretized and solved using the commercial software STAR-CCM+ (version 2306, build 18.04.009).

2.2.1. Moving reference frame

The numerical simulations of the OWT are performed under steady-state conditions using the Moving Reference Frame (MRF) approach. In this method, a reference frame rotates relative to a stationary frame. It assumes a rigid mesh and a constant angular velocity of the rotating body. The computational domain is divided into a stationary region and a rotating region surrounding the propeller geometry. The absolute velocity, u_{0i}, is expressed in terms of the velocity relative to the MRF, u_{pi}, as follows:

$$u_{0i} = u_{pi} + \varepsilon_{ijk}\omega_{pj} r_k \tag{3}$$

where ω_{pj} is the angular velocity and r_k is the position vector from the origin of the MRF to the centre of a control volume. In the MRF, the continuity and RANS equations, formulated using the relative velocity, take the following form:

$$\frac{\partial u_{pi}}{\partial x_i} = 0 \tag{4}$$

$$\frac{\partial u_{pi}}{\partial t} + u_j \frac{\partial u_{pi}}{\partial x_j} + \varepsilon_{ijk}\frac{\mathrm{d}\omega_{pj}}{\mathrm{d}t} r_k + 2\varepsilon_{ijk}\omega_{pj}u_{pk} + \\ + \varepsilon_{ijk}\varepsilon_{jlm}\omega_{pl}\omega_{pm} r_k = -\frac{1}{\rho}\frac{\partial p}{\partial x_i} + \nu \frac{\partial^2 u_{pi}}{\partial x_j \partial x_j} \tag{5}$$

where ν is the kinematic viscosity.

2.2.2. Dynamic fluid body interaction method

Within the CFD simulations of the RT and SPT the containership was allowed to freely heave and pitch by employing the Dynamic Fluid Body Interaction (DFBI) method as implemented in the commerical software STAR-CCM+. The remaining degrees of freedom were disabled in the numerical simulations. With the resultant force and moment acting on the body, the equations of motion are solved and the new position and orientation of the rigid body are obtained. The equations of motion are given as:

$$m\frac{\mathrm{d}u_i}{\mathrm{d}t} = f_i \tag{6}$$

$$M_{ij}\frac{\mathrm{d}\omega_j}{\mathrm{d}t} + \varepsilon_{ijk}\omega_j M_{kl}\omega_l = n_i \tag{7}$$

where m is the mass of the body, u_i is the velocity of the centre of mass, f_i is the resultant force acting on the rigid body, $M_{ij}(M_{kl})$ is the tensor of moments of inertia, $\omega_j(\omega_l)$ is the angular velocity, n_i is the resultant moment acting on the rigid body and ε_{ijk} is the Levi-Civita symbol. As the input for the DFBI method, the mass of the ship, position of the centre of gravity, and the moments of inertia are specified. Depending on whether a symmetry condition was applied at the ship centreline, the total ship mass was halved accordingly. The mass was determined from the displacement volume and the fluid density. For each trim angle, the displacement volume was calculated using CAD software, and the centre of gravity was aligned with the centre of buoyancy to maintain the same static trim condition.

2.2.3. Virtual disk method

Within the CFD simulations of the SPT, the effects of the rotating propeller were modelled using the virtual disk method [25]. It is the most common approach for simulating the effects of the rotating propeller since it significantly decreases the computational effort needed to perform the numerical simulations [8,24]. It consists of applying a uniform volume force at the position of the propeller. The volume force is applied as a distribution over a cylindrical virtual disk following the Goldstein optimum, as described below:

$$f_{bx} = A_c r^* \sqrt{1-r^*} \tag{8}$$

$$f_{b\theta} = A_\theta \cdot \frac{r^*\sqrt{1-r^*}}{r^*(1-r_h') + r_h'} \tag{9}$$

where f_{bx} and $f_{b\theta}$ denote the components of the body force along the axial and tangential directions, respectively and r^* is calculated as:

$$r^* = \frac{r' - r_h'}{1 - r_h'} \tag{10}$$

where r' and r_h' are given as:

$$r_h' = \frac{R_H}{R_P} \tag{11}$$

$$r' = \frac{r}{R_P} \tag{12}$$

where r is the radial coordinates, R_P and R_H are the propeller tip and hub radius, respectively. The constants A_x and A_θ are obtained as follows:

$$A_x = \frac{105}{8} \cdot \frac{T}{\pi\Delta(3R_H + 4R_P)(R_P - R_H)} \tag{13}$$

$$A_\theta = \frac{105}{8} \cdot \frac{Q}{\pi\Delta R_P(3R_H + 4R_P)(R_P - R_H)} \tag{14}$$

where T and Q are thrust and torque of the propeller, and Δ is the thickness of the virtual disk.

As indicated by Equations (13) and (14), the virtual disk method requires the open water curves to determine the body force components. The open water curves in this study are derived at full scale by performing numerical simulations of the OWT. In the numerical simulations of the SPT, the thrust is set equal to the total resistance, which enables the determination of the propeller rate of revolution at the self-propulsion point.

Table 3
Post-Panamax 6750 TEU containership main particulars at each trim angle.

Main particular	Symbol	Unit	Value				
Trim angle	θ_S	°	−0.5	−0.25	0	0.25	0.5
Length of waterline	L_{WL}	m	291.78	292.02	292.37	291.20	291.65
Draught at aft perpendicular	T_A	m	12.84	12.28	11.98	11.14	10.55
Draught at midship	T_M	m	11.86	11.93	11.98	12.04	12.08
Draught at forward perpendicular	T_F	m	10.56	11.34	11.98	12.64	13.27
Longitudinal centre of buoyancy (from midship)	L_{CB}	m	-9.7392	-7.4042	-5.07	-2.9525	-0.8274

2.3. Numerical setup

The numerical simulations of the RT, OWT, and SPT are conducted at full scale. The governing equations are discretized using the finite volume method to obtain an algebraic system of equations, which are solved in a segregated manner. The numerical simulations were conducted in accordance with the ITTC Practical guidelines for CFD applications [26]. The free surface position is located and tracked using the Volume of Fluid (VOF) method [27,28] within the CFD simulations of the RT and SPT. The second-order upwind scheme is used for the spatial discretization of the convection terms in the momentum equations, while the second-order central difference scheme is applied for the diffusive terms. The pressure-velocity coupling is achieved using the SIMPLE algorithm. An implicit second-order scheme is employed for the temporal discretization. The simulations are run in a transient manner until a periodic steady state is reached, which is determined by monitoring the total resistance R_T in the numerical simulations of RT and the thrust T and torque Q in the case of numerical simulations of the OWT and SPT. The numerical simulations were carried out on a high-performance computing cluster provided by the University of Zagreb Computing Centre - SRCE. The CFD simulations were performed using 96 cores on a single node and required approximately one day or two days to complete, depending on the type of CFD simulation.

The fluid is defined as seawater, with a viscosity of 1.22×10^{-3} Pas and a density of $1026.02\,kg/m^3$. The numerical simulations are conducted at different trim angles ranging from -0.5° to 0.5° in increments of 0.25°. The draught is adjusted beforehand to maintain the same displacement volume for all trim angles. All the CFD simulation were performed at speed of 23 knots, which corresponds to a Froude number of $Fr = 0.221$.

The computational domain used in the CFD simulations of the RT and SPT consists of a rectangular region enclosing the entire ship, discretized with an unstructured hexahedral mesh. For the RT simulations, the flow is assumed to be symmetric, allowing only half of the domain to be modelled in order to reduce the total cell count. The domain boundaries are positioned sufficiently far from the hull to prevent any influence on the numerical solution. Specifically, the inlet, top, and side boundaries are located at $1.5L_{PP}$ from the ship, the outlet at $3L_{PP}$ downstream of the stern, and the bottom boundary at $2L_{PP}$ beneath the ship. Figs. 2 and 3 present the computational domains for the CFD simulations of the SPT and RT, including the corresponding boundary conditions and the regions of mesh refinement.

The meshes are finer near the bow and stern and in the areas around the free surface and Kelvin wake. Special care was taken in the region of the virtual disk to ensure that the mesh resolution is adequate to capture the Gaussian shape function along the thickness of the virtual disk. The inlet and outlet boundary conditions are identical in both types of numerical simulations, employing a velocity inlet and a pressure outlet. In the RT simulations, only half of the domain is generated due to flow symmetry; therefore, symmetry boundary conditions are imposed on both sides of the domain. The same boundary conditions are applied at the side boundaries in the numerical simulations of the SPT. For both RT and SPT cases, the top and bottom boundaries are also specified as velocity inlets. Finally, no-slip wall boundary conditions are applied on the ship hull and rudder surfaces.

For the OWT, the computational domain is 1/4 section of a cylinder, with the propeller placed at the centre, Fig. 4. Periodic boundary condition is used to lower the number of cells needed for the computation. The radius of the cylinder is set to $1.5D$ from the propeller axis, while the length extends $3D$ upstream and $5D$ downstream of the propeller. In the numerical simulations of the OWT, the region around the propeller is refined.

Prism layers are generated along the hull, rudder, and propeller surfaces to ensure that the non-dimensional wall distance y^+ remains greater than 30, thereby permitting the application of wall functions for boundary-layer modelling. The first-cell height y, which directly determines the resulting y^+ is estimated following the procedure described by Grlj et al. [24]. Fig. 5 shows the distributions of y^+ on the hull, rudder, and propeller surfaces obtained in the numerical simulations of SPT, RT, and OWT. The obtained y^+ values remained above 30 throughout the wetted areas of both the hull and rudder. The area close to the propeller hub exhibited y^+ values slightly below 30. However, this region has a negligible impact on the open water characteristics.

A detailed verification study for the numerical simulations of RT, OWT, and SPT are conducted to assess the numerical uncertainty due to grid size and time step. The results of the performed verification study are presented in Section 3.

2.4. Propulsion components

The output of the CFD simulations of RT and SPT were the following resistance and propulsion components: total resistance R_T, thrust T, torque Q, propeller rate of revolution n, and advance coefficient J. With the obtained values, the wake w and thrust deduction t fractions were calculated as follows:

$$w = 1 - \frac{J\,Dn}{v} \tag{15}$$

$$t = 1 - \frac{R_{T,\,RT}}{T} \tag{16}$$

where v is the ship speed, and the subscript RT indicate the type of the numerical simulation, which in this case is the resistance test. Next, the hull efficiency η_H, open water efficiency η_O, and the overall propulsive efficiency η_D were determined as follows:

$$\eta_H = \frac{1-t}{1-w} \tag{17}$$

$$\eta_O = \frac{K_{T,\,OWT}}{K_{Q,\,OWT}} \frac{J}{2\pi} \tag{18}$$

$$\eta_D = \eta_H \cdot \eta_O \cdot \eta_R \tag{19}$$

where $K_{T,\,OWT}$ and $K_{Q,\,OWT}$ are the thrust and torque coefficients, respectively, calculated using the obtained J and the open water curves. The relative rotative efficiency η_R is assumed to be equal to 1 since the virtual disk method was employed [3,29]. With the obtained Q and n, the delivered power P_D can be calculated using the following expression:

$$P_D = 2\pi nQ \tag{20}$$

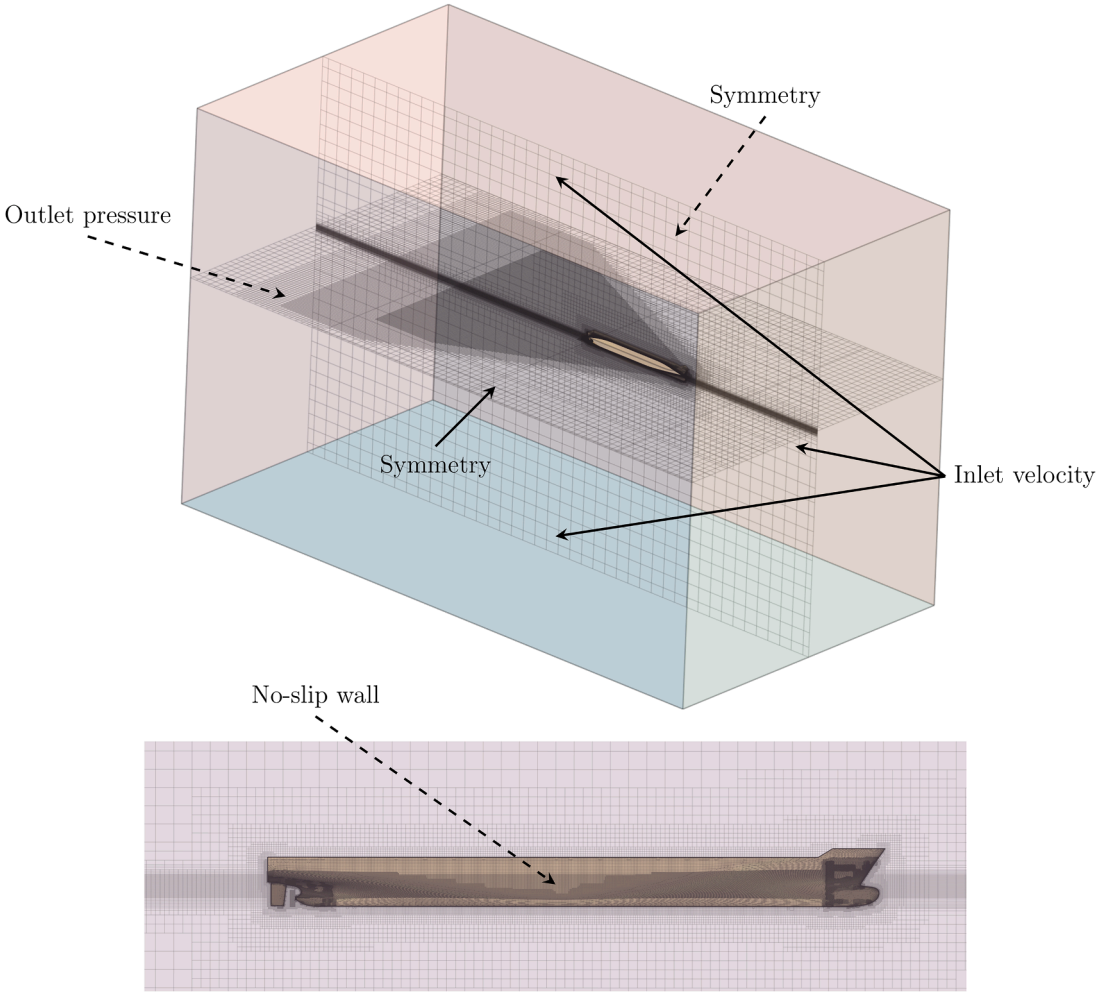


Fig. 2. Computational domain and applied boundary conditions in the CFD simulations of the SPT.

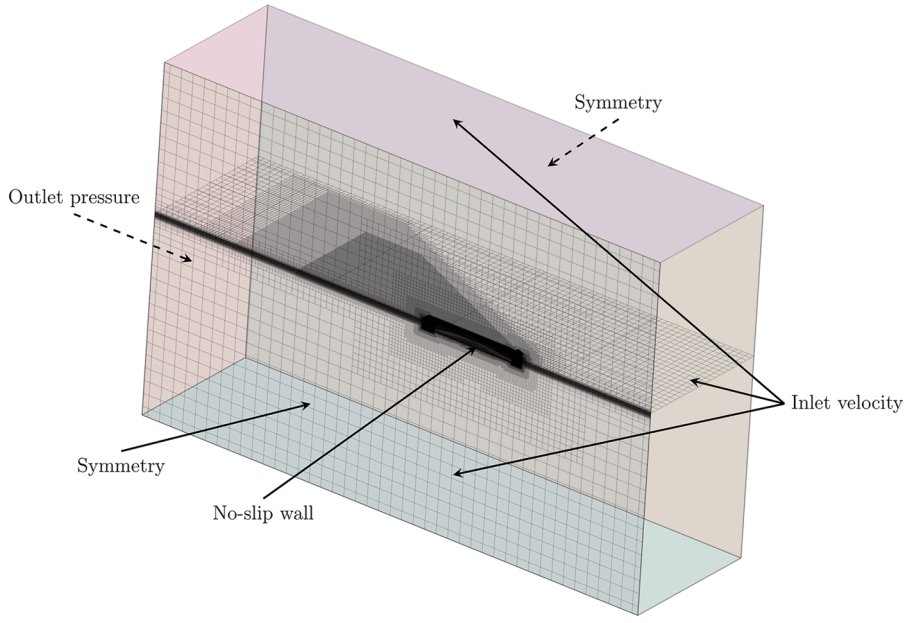


Fig. 3. Computational domain and applied boundary conditions in the CFD simulations of the RT.

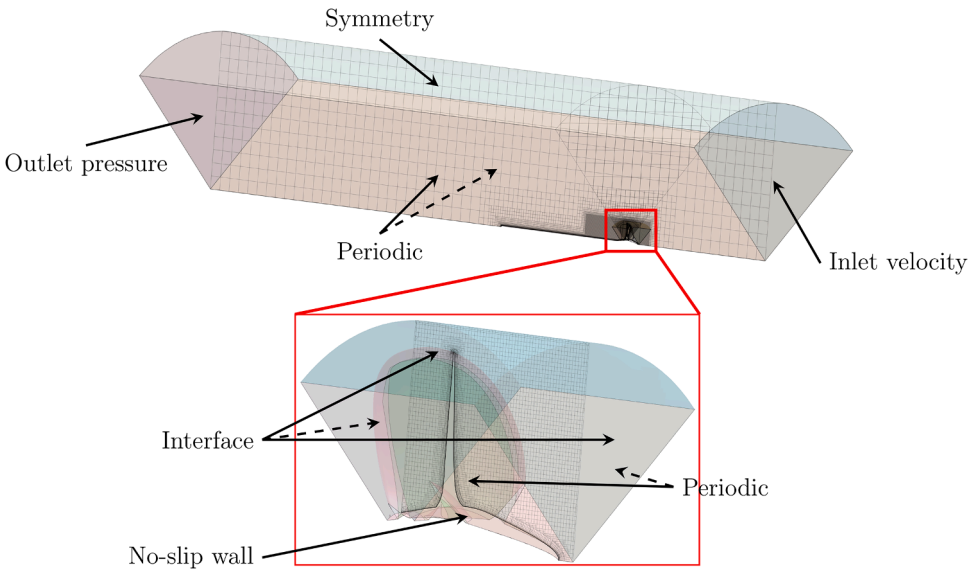


Fig. 4. Computational domain and applied boundary conditions in the CFD simulations of the OWT.

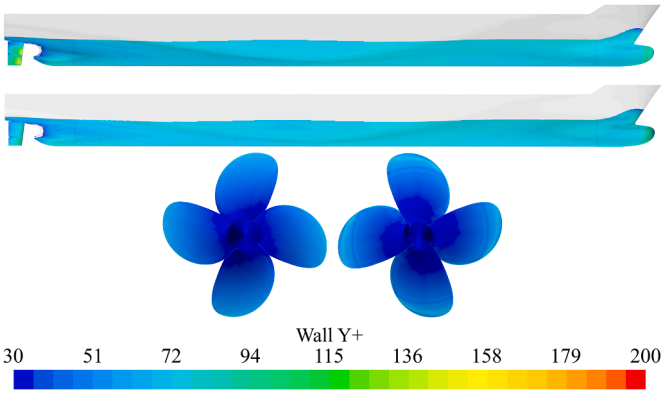


Fig. 5. The y^+ obtained in the numerical simulations of SPT (top), RT (middle), and OWT (bottom).

3. Results and discussion

3.1. Verification study

Simulation uncertainty is assessed through a verification study by employing the Grid Convergence Index (GCI) method (Celik et al., 2008), which quantifies the numerical uncertainties arising from both grid size and time step selection. Details on the method are provided by [24]. Since the CFD simulations of OWT are conducted as steady state, the verification study for the time step is not performed for this type of simulation. For the CFD simulations of the RT, the total resistance R_T, sinkage z, and dynamic trim θ_V were analysed, while for the CFD simulations of the SPT, additionally, the torque Q and propeller rate of revolution n were taken into account. Finally, for the CFD simulations of OWT, the open water efficiency η_O was considered.

Details of the grids employed in the verification study are provided in Table 4. The number of cells is denoted with N, while h and r represent the grid spacing and refinement ratio, respectively. The subscripts 1, 2, and 3 indicate the fine, medium and coarse meshes, respectively. It can be seen that the grids in the CFD simulations of the SPT have nearly double the number of cells compared to the RT. This is because only half of the domain is modelled in the CFD simulations of RT. The refinement ratio is maintained approximately around 1.4, with the exception of the numerical simulations of the OWT were lower values are obtained. The

Table 4
Grids used in the verification study for the CFD simulations of the RT.

Parameter	RT	OWT	SPT
N_1	5 900 859	3 625 983	11 131 465
N_2	1 998 021	2 347 144	3 681 606
N_3	687 104	951 768	1 241 059
h_1	4.753	0.299	4.847
h_2	6.820	0.346	7.009
h_3	9.734	0.463	10.071
r_{32}	1.427	1.338	1.437
r_{21}	1.435	1.157	1.446

fine time step in the CFD simulations of the RT and SPT is calculated as $\Delta t = 0.125\ \% \cdot L_{PP}/v$. The medium and coarse time steps are calculated by multiplying the fine time step by factors of 2 and 4, respectively. The considered time steps are equal to 0.03, 0.06, and 0.12 for fine, medium, and coarse time steps, respectively. For the assessment of the numerical uncertainty due to time step, the fine grid is used.

Table 5 presents the results of the verification study for the CFD simulations of the RT, including the those for grid size as well as time step. The table includes the differences between the results obtained with fine and medium grid sizes/time steps ε_{21}, and between medium and coarse grid sizes/time steps ε_{32}. Additionally, the convergence criterion R, and observed order of the method p are shown. Finally, the GCI for the fine grid size/time step GCI^{21}_{fine} is presented. It can be seen that the obtained GCI is lower than 1 % in most of the cases, and lower than 4 % for the case of z in the verification study of grid size. In almost all the cases monotonic convergence is achieved, except for the θ_V in the verification study of grid size, where oscillatory convergence is observed.

Table 6 presents the results of the verification study for the numerical simulations of OWT. In this case, the numerical uncertainty due to grid size is assessed for each advance coefficient J considered. It can be seen that divergence is obtained for the cases of $J = 0.16 \div 0.32$, thus the calculation of the GCI is omitted in these cases. For other cases monotonic convergence is obtained, and the value p is satisfactory, except for $J = 0.08$. The obtained GCI is lower than 3 % in most cases, except for $J = 0.48$ where a higher value of 7.33 % is obtained. Despite this, the differences between the results obtained with fine and medium grids, as well as between medium and coarse grids, are negligible.

Table 5
Verification study for the CFD simulations of the RT.

	Grid size R_T	z	θ_V
ϵ_{21}	3.087 kN	-0.00433 m	-0.00004°
ϵ_{32}	58.707 kN	-0.00640 m	0.00171°
R	0.053	0.676	-0.025
p	8.285	1.133	10.364
GCI^{21}_{fine}	0.01 %	3.34 %	0.003 %
	Time step		
ϵ_{21}	3.424 kN	-0.00008 m	-0.00011°
ϵ_{32}	10.726 kN	-0.00131 m	-0.00072°
R	0.319	0.061	0.150
p	1.647	4.042	2.736
GCI^{21}_{fine}	0.11 %	0.002 %	0.05 %

Table 6
Verification study for the CFD simulations of the OWT.

Grid size J	ϵ_{21}	ϵ_{32}	R	p	GCI^{21}_{fine}
0.08	-0.0011	-0.0013	0.837	21.678	0.07 %
0.16	-0.0029	-0.0025	1.138	/	/
0.24	-0.0051	-0.0037	1.389	/	/
0.32	-0.0069	-0.0054	1.291	/	/
0.4	-0.0050	-0.0084	0.593	3.219	2.21 %
0.48	-0.0034	-0.0080	0.421	0.683	7.33 %
0.56	-0.0022	-0.0064	0.347	1.554	1.80 %
0.64	-0.0014	-0.0057	0.250	2.984	0.49 %
0.72	-0.0014	-0.0061	0.223	3.461	0.37 %
0.8	-0.0022	-0.0086	0.257	2.858	0.74 %
0.88	-0.0053	-0.0179	0.296	2.253	2.60 %

Table 7
Verification study for the CFD simulations of the SPT.

	Grid size R_T	Q	n	z	θ_V
ϵ_{21}	43.8130	43.9026	0.0125	-0.0039	0.0004
ϵ_{32}	91.6190	84.0504	-0.0150	-0.0068	0.0010
R	0.478	0.522	-0.830	0.579	0.380
p	2.067	1.825	0.509	1.543	2.698
GCI^{21}_{fine}	2.27 %	2.39 %	4.02 %	1.94 %	0.75 %
	Time step				
ϵ_{21}	-1.0443	-0.7624	0.0002	0.00003	-0.0001
ϵ_{32}	12.4008	12.3825	0.0030	0.0006	-0.0002
R	-0.110	-0.089	0.030	0.022	0.353
p	3.186	3.495	5.075	5.494	1.502
GCI^{21}_{fine}	0.01 %	0.01 %	0.0002 %	0.0001 %	0.15 %

Finally, the results of the verification study for the CFD simulations of the SPT are presented in Table 7. It can be seen that the obtained GCI due to grid size is below 5 % in all the cases. The convergence is monotonic in almost all the cases, and the obtained values of p are satisfactory. Oscillatory convergence is obtained for n. Regarding the verification study for time step, the obtained GCI is very low in all the cases, below 1 %. The obtained values p are slightly higher than 2 for R_T and θ_V, while significantly higher values are obtained for n and z, which explains the lower GCI. Monotonic convergence is obtained for n, z, and θ_V, while oscillatory convergence is observed for R_T and Q.

3.2. Resistance and propulsion characteristics

In this subsection, the numerical results obtained at different trims are presented and discussed. The numerical results obtained at even keel and trim by stern $\theta_S = -0.5°$ are compared to the experimental data from Degiuli et al. [21]. The measurements in the towing tank were previously extrapolated using the ITTC 1978 Performance prediction method from

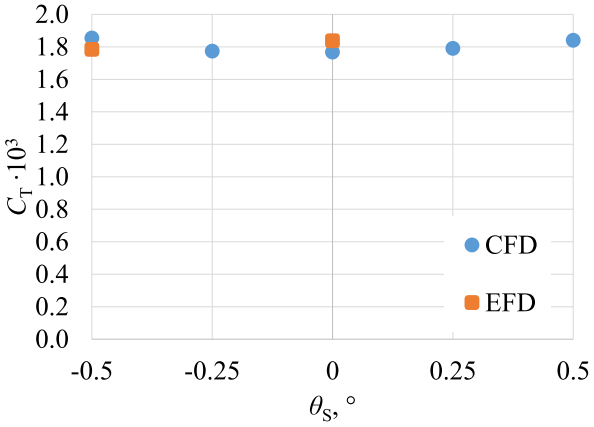


Fig. 6. Total resistance coefficient C_T obtained in the CFD simulations of the RT at different trim angles for ship speed of 23 knots.

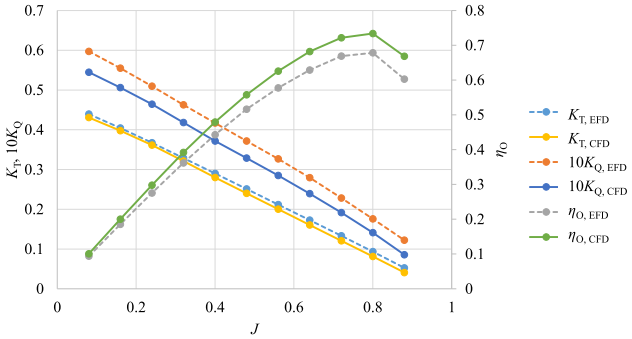


Fig. 7. Propeller open water curves obtained numerically and experimentally.

2017 [30], in which the roughness allowance is neglected, since the full-scale CFD simulations were conducted for smooth rudder and hull surfaces, as well as the propeller surfaces in the CFD simulations of the OWT.

First, the numerically obtained total resistance coefficient C_T at different trim angles is presented in Fig. 6. The numerical simulations predict the lowest C_T at even keel, while the highest values are obtained at $\theta_S = -0.5°$ and $\theta_S = 0.5°$. The experimental data shows the lowest C_T at $\theta_S = -0.5°$.

In Fig. 7, the propeller open water curves obtained numerically and experimentally are presented. The experimental measurements obtained in the OWT were extrapolated using the scale effect corrections for the propeller characteristics from the ITTC 1978 Performance prediction method [30]. Large discrepancies are observed between the numerical and experimental results. While the numerically obtained thrust coefficient K_T is slightly lower than the experimental values, the numerically obtained torque coefficient K_Q is significantly lower in the entire range of J. This leads to higher values of open water efficiency η_O obtained numerically compared to the experimental results. The discrepancies between the numerical and experimental η_O increase with J.

Fig. 8 presents the obtained w and t. The experimental w is slightly higher than the numerical values at trim by stern $\theta_S = -0.5°$ and at even keel. As the trim angle increases, the numerical values decrease up to trim by bow of 0.25°. At trim by bow of 0.5°, the numerically obtained w increases slightly. The numerically obtained t closely matched the experimental values. There is no specific trend observed for various trims, although a slight decrease of t can be observed, but these differences are within the numerical uncertainty.

Next, the η_H, η_O, and η_D are presented in Fig. 9. The numerically obtained η_H are slightly lower than the experimental values at trim by stern $\theta_S = -0.5°$ and at even keel. The numerically obtained η_O is significantly higher than the experimental values, which is partially a consequence

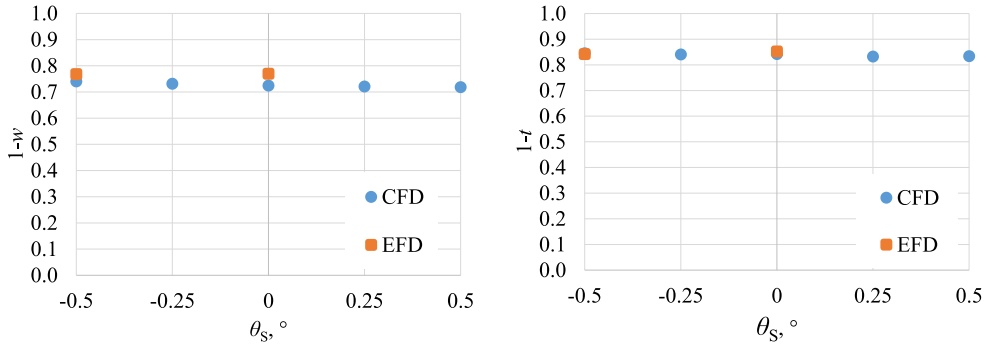


Fig. 8. Comparison of numerically predicted w and t at different trim angles with corresponding experimental results for ship speed of 23 knots.

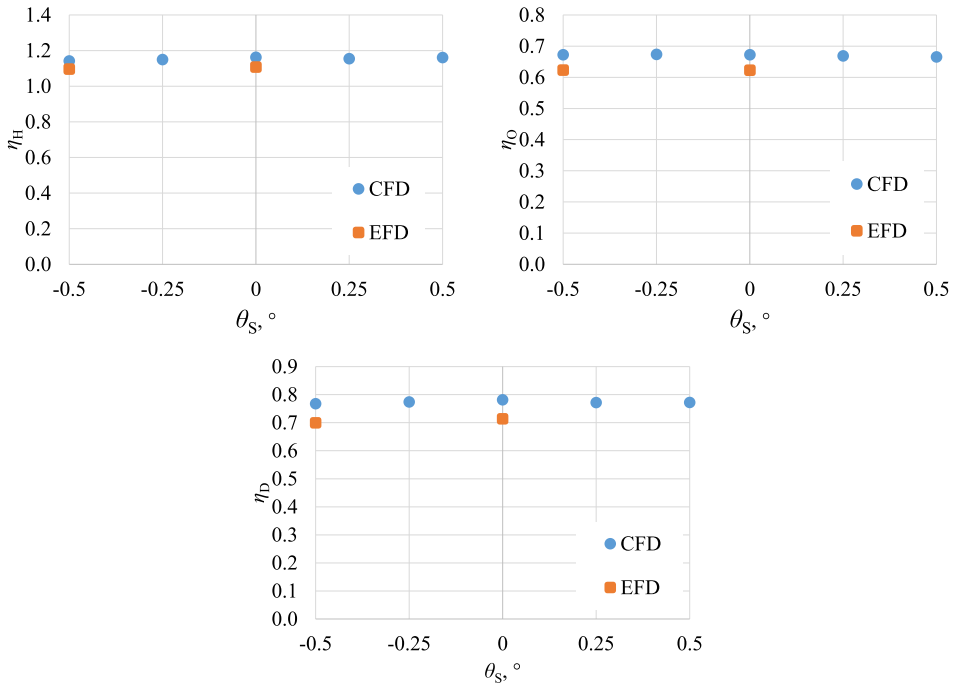


Fig. 9. Comparison of numerically predicted η_H, η_O, and η_D at different trim angles with corresponding experimental results for ship speed of 23 knots.

of the discrepancies observed in the open water curves and partially due to the obtained advance coefficient in the CFD simulations of the SPT. As a result, the numerically obtained η_D is also higher than the experimental values. No specific trend is observed in the obtained efficiencies at different trim angles.

Finally, Fig. 10 presents the obtained P_D and n, respectively. The numerically obtained P_D is higher than the experimental values at trim by stern $\theta_S = -0.5°$, while slightly lower value is obtained at even keel. As the trim angle increases, the numerically obtained P_D decreases slightly up to trim angle of 0°. The numerically obtained n at trim angle of -0.5° and at even keel are lower than the experimental values. As the trim angle increases, the numerically obtained n decreases slightly up to trim angle of 0.25°, while at trim angle of 0.5° a slight increase is observed.

Table 8 summarizes the results of the validation study by presenting the relative deviations RD between the numerically and experimentally obtained resistance and propulsion characteristics at trim by stern $\theta_S = -0.5°$ and at even keel. The RD is calculated as follows:

$$RD = \frac{\phi_{CFD} - \phi_{EFD}}{\phi_{EFD}} \cdot 100\,\% \tag{21}$$

where ϕ is the considered physical value, and the subscripts CFD and EFD indicate the values obtained numerically and experimentally, respectively. It can be seen that the RD are below 11 % in all the cases. The highest RD are obtained for η_D at both trim angles, which is mainly due to the discrepancies observed in the η_O. The lowest RD is obtained for C_T at $\theta_S = 0°$ where it is equal to 0.55 %. Dispite the differences in the RD obtained for efficiency coefficients, the RD obtained for P_D and n are below 6 % at both trim angles. The numerically obtained n are

Table 8
Relative deviations between the resistance and propulsion characteristics obtained numerically and experimentally for ship speed of 23 knots.

	$\theta_S = -0.5°$	$\theta_S = 0°$
$1 - w$	-3.61 %	-5.85 %
$1 - t$	1.15 %	-1.18 %
η_H	4.94 %	4.95 %
η_O	8.03 %	8.00 %
η_D	10.70 %	9.48 %
P_D	1.61 %	-4.00 %
n	-3.45 %	-5.64 %
C_T	8.50 %	0.55 %

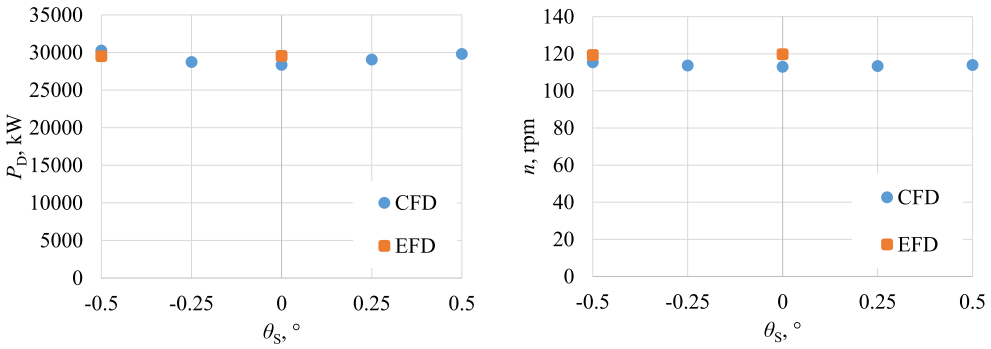


Fig. 10. Comparison of numerically predicted P_D and n at different trim angles with corresponding experimental results for ship speed of 23 knots.

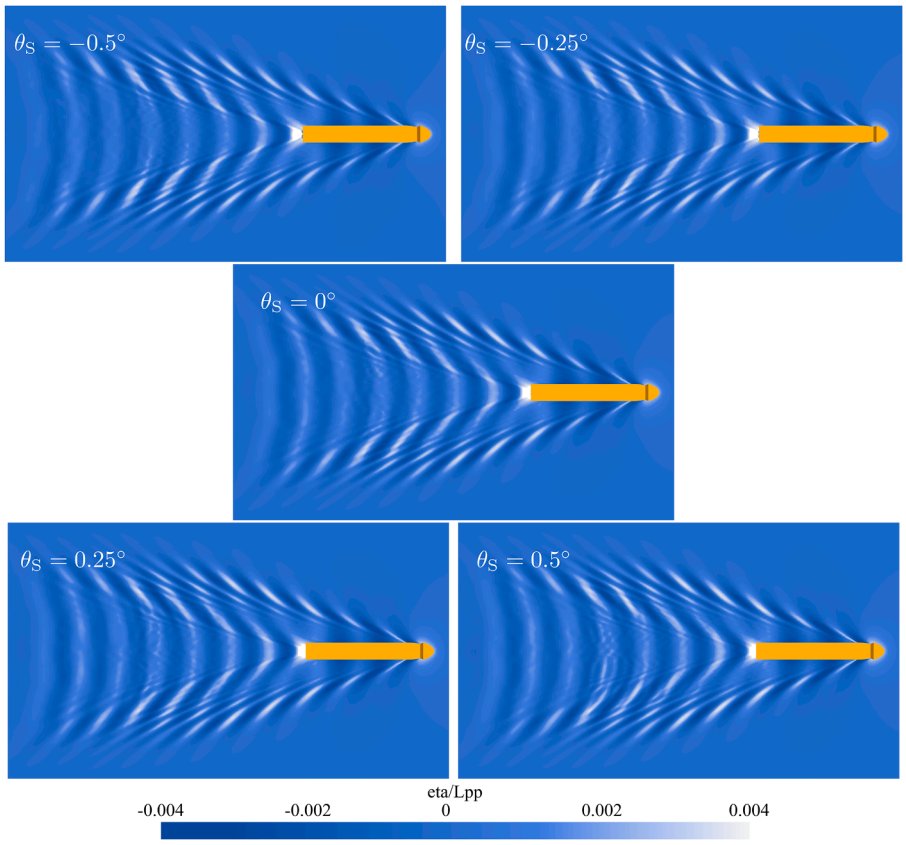


Fig. 11. Wave patterns obtained in CFD simulations of the SPT at different trim angles for ship speed of 23 knots.

underpredicted at both trim angles, while the P_D is slightly overpredicted at $\theta_S = -0.5°$ and underpredicted at even keel.

3.3. Flow insights

In this subsection, the flow field around the containership, obtained in the CFD simulations of the SPT at various trim angles, is examined. Fig. 11 shows the resulting wave patterns, where an increase in trim angle leads to a more pronounced bow wave. More importantly, the stern wave shifts closer to the transom as the trim angle increases. At negative trim angles (trim by stern), the transom becomes immersed, causing the stern wave to move farther away from the hull.

A more detailed view of the numerically obtained wave patterns is shown in Fig. 12. Wave cuts at different longitudinal cross-sections both behind the stern and ahead of the bow obtained at different trim angles are presented. The wave cuts confirm the observations made from the wave patterns in Fig. 11. At negative trim angles, the stern wave is located farther from the stern, while as the trim angle increases, it moves closer to the stern. The bow wave becomes more pronounced with increasing trim angle. The only exception is the wave cut ahead of the bow at the cross-section $y = 0$, where a change in trend is visible close to the bow.

Further insight is provided in Fig. 13, which presents the velocity field in a longitudinal centreline section together with streamlines on the hull. The stern wave pattern is clearly captured. A recirculation zone forms directly behind the transom at negative trim angles, as indicated by the red circle, while the stern wave moves further away from the transom. This occurs because the transom becomes increasingly immersed at negative trim angles. As the trim angle increases, this recirculation zone gradually diminishes and eventually disappears.

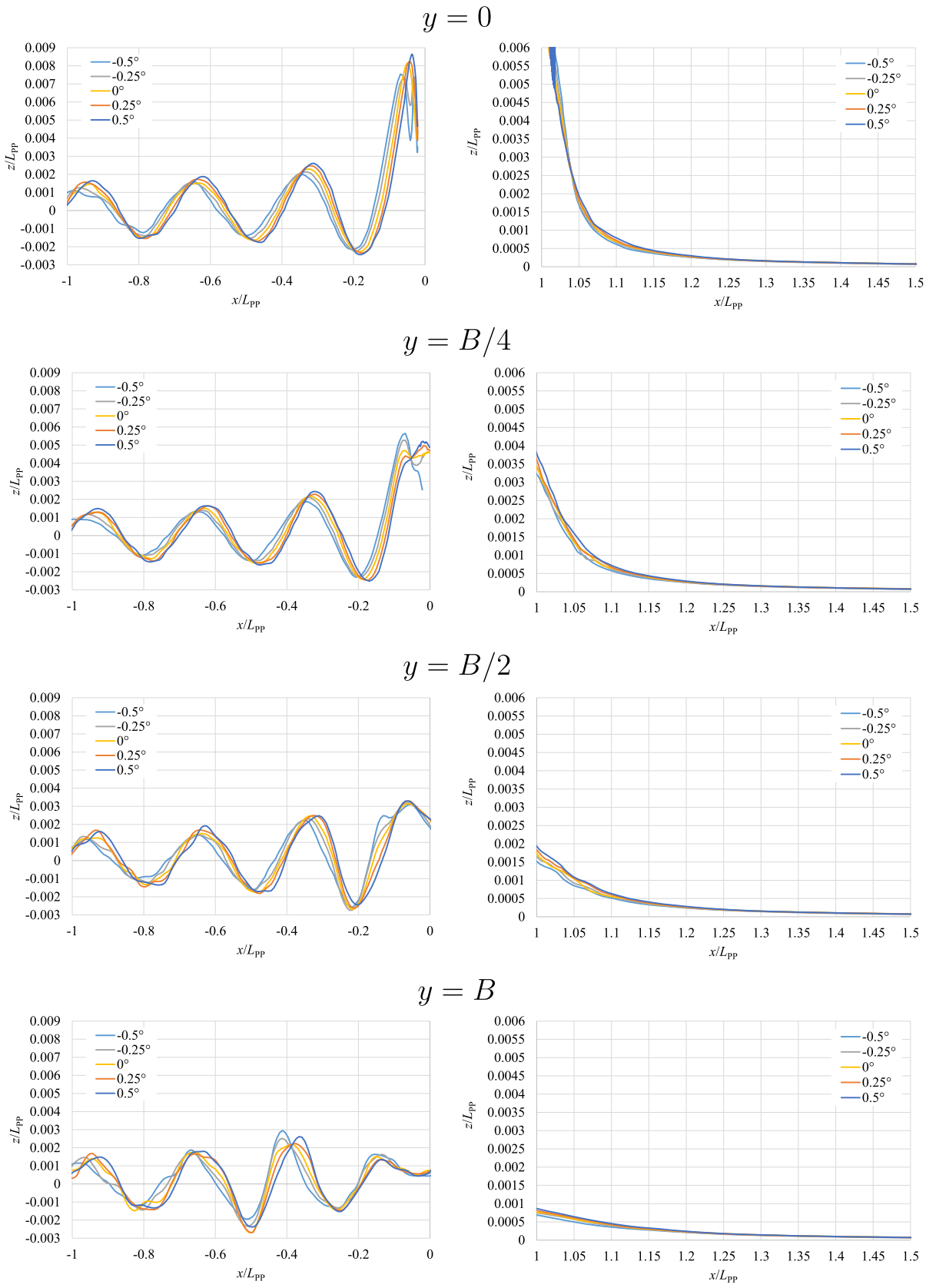


Fig. 12. Wave cuts at different longitudinal cross-sections behind the stern (left) and ahead of the bow (right) obtained at different trim angles for ship speed of 23 knots.

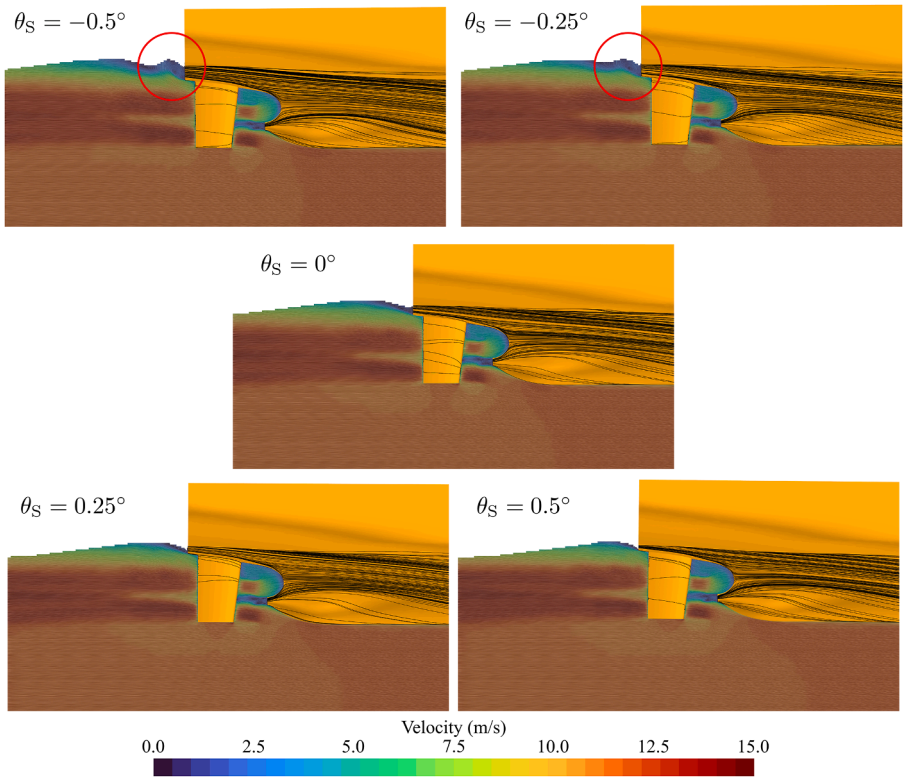


Fig. 13. Velocity field on the longitudinal cross-section at the ship centreline and streamlines on the ship hull in the stern region for ship speed of 23 knots.

4. Conclusions and future work

In this study, the effects of trim on the resistance and propulsion characteristics of a full-scale post-Panamax 6750 TEU containership were investigated using CFD simulations. The CFD simulations of the resistance, open water, and self-propulsion tests were conducted at different trims ranging from -0.5° to 0.5° with increments of 0.25°. The virtual disk method was employed in the numerical simulations of self-propulsion test to model the effects of the rotating propeller. An extensive verification study was performed using the grid convergence index method to assess the numerical uncertainty due to grid size and time step.

The numerical results obtained at even keel and trim by stern of 0.5° were compared to the experimental data. The numerical simulations predicted the lowest total resistance coefficient at even keel, while the experimental data showed the lowest values at trim by stern of 0.5°. The numerically predicted higher open-water efficiency led to an increase in quasi-propulsive efficiency compared to the experimental results. The numerically obtained thrust deduction fraction closely matched the experimental values, while the wake fraction showed some discrepancies with the experimental data. No specific trend was observed in the obtained efficiencies at different trim angles. The delivered power obtained numerically was higher than the experimental values at trim by stern of 0.5°, while slightly lower value was obtained at even keel.

Insights into the flow field around the post-Panamax 6750 TEU containership were provided. The wave patterns obtained in the CFD simulations of the self-propulsion test showed that with an increase in trim angle, the bow wave becomes more pronounced, and the stern wave shifts closer to the stern. Further, the velocity field on the longitudinal cross-section at the centreline of the containership revealed a recirculation zone forming directly behind the transom at negative trim angles, which gradually diminishes and eventually disappears as the trim angle increases.

This study showed that full-scale CFD simulations can provide satisfactory predictions of the resistance and propulsion characteristics at different trim angles when compared to the extrapolated measurements from the towing tank. Future work will focus on a more detailed analysis of the propulsion characteristics at various trim angles by discretizing the propeller geometry and employing the overset mesh approach to model the rotation of the propeller. In addition, future investigations will examine the effect of trim angle on resistance and propulsion characteristics in waves. Such numerical simulations would allow for a more comprehensive assessment of the ship hydrodynamic characteristics under realistic operating conditions.

Funding

This work was funded by the Croatian Science Foundation under the project number IP-2025-02-4779.

CRediT authorship contribution statement

Carlo Giorgio Grlj: Writing – review & editing, Writing – original draft, Visualization, Validation, Software, Resources, Methodology, Investigation, Formal analysis, Data curation, Conceptualization; **Nastia Degiuli:** Writing – review & editing, Writing – original draft, Visualization, Validation, Supervision, Resources, Project administration, Methodology, Investigation, Funding acquisition, Formal analysis, Data curation, Conceptualization; **Ivana Martić:** Writing – review & editing, Writing – original draft, Visualization, Validation, Resources, Methodology, Investigation, Formal analysis, Data curation, Conceptualization.

Data availability

Data will be made available on request.

Declaration of competing interest

The authors declare that they have no known competing financial interests or personal relationships that could have appeared to influence the work reported in this paper.

Acknowledgements

This work was supported by the Croatian Science Foundation under the project number IP-2025-02-4779. This research was performed using the Advanced computing service provided by University of Zagreb University Computing Centre - SRCE.

References

[1] K. Niklas, H. Pruszko, Full-scale CFD simulations for the determination of ship resistance as a rational, alternative method to towing tank experiments Ocean Eng., 190, 2019, 106435 https://doi.org/10.1016/j.oceaneng.2019.106435
[2] M. Orych, S. Werner, L. Larsson, Validation of full-scale delivered power CFD simulations. Ocean Eng, 238, 2021. https://doi.org/10.1016/j.oceaneng.2021.109654
[3] I. Sulovsky, S. Mewes, O.E. Moctar, J. Prpić-Oršić, CFD study on a full-scale ship performance in a representative sea state Ocean Eng., 333, 2025, 121519 https://doi.org/10.1016/j.oceaneng.2025.121519
[4] D. Calcagni, G. Dubbioso, A. Capone, F. Ortolani, R. Broglia, A generalized hybrid RANSE/BEM approach for the analysis of hull-propeller interaction in off-design conditions, J. Mar. Sci. Eng. 9 (2021) 482. https://doi.org/10.3390/jmse9050482
[5] C. Testa, L. Greco, J. Bosschers, Marine propeller shaft loading analysis in moderate oblique-flow conditions Ocean Eng., 262, 2022, 112199 https://doi.org/10.1016/j.oceaneng.2022.112199
[6] P.M. Carrica, A.M. Castro, F. Stern, Self-propulsion computations using a speed controller and a discretized propeller with dynamic overset grids, J. Mar. Sci. Technol. 15 (2010) 316–330. https://doi.org/10.1007/s00773-010-0098-6
[7] A.M. Castro, P.M. Carrica, F. Stern, Full scale self-propulsion computations using discretized propeller for the KRISO container ship KCS, Comput. Fluids 51 (2011) 35–47. https://doi.org/10.1016/j.compfluid.2011.07.005
[8] M. Mikulec, H. Piehl, Verification and validation of CFD simulations with full-scale ship speed/power trial data, Brodogradnja 74 (2023) 41–62. https://doi.org/10.21278/brod74103
[9] N.A. Quist, R.H. Christensen, H. Mikkelsen, J.H. Walther, Validation of a full scale CFD simulation of a self-propelled ship with measured hull roughness and effect of welding seams on hull resistance, Appl. Ocean Res. 141 (2023) 103746. https://doi.org/10.1016/j.apor.2023.103746
[10] H. Mikkelsen, J.H. Walther, Effect of roughness in full-scale validation of a CFD model of self-propelled ships, Appl. Ocean Res. 99 (2020). https://doi.org/10.1016/j.apor.2020.102162
[11] R. Lopes, A. Eslamdoost, R. Johansson, S. Roychoudhury, R.E. Bensow, P. Hogström, D. Ponkratov, Resistance prediction using CFD at model- and full-scale and comparison with measurements Ocean Eng., 321, 2025. https://doi.org/10.1016/j.oceaneng.2025.120367
[12] I. Martić, B. Anušić, N. Degiuli, C.G. Grlj, Numerically investigating the effect of trim on the resistance of a container ship in confined and shallow water, Appl. Sci. 14 (2024) 6570. https://doi.org/10.3390/app14156570
[13] T.H. Le, M.T. Vu, V.N. Bich, N.K. Phuong, N.T.H. Ha, T.Q. Chuan, T.N. Tu, Numerical investigation on the effect of trim on ship resistance by RANSE method, Appl. Ocean Res. 111 (2021) 102642. https://doi.org/10.1016/j.apor.2021.102642
[14] E. Shivachev, M. Khorasanchi, A. H. Day, Trim influence on Kriso container ship (KCS): an experimental and numerical study, in: 36th International Conference on Ocean, Offshore and Arctic Engineering, Trondheim, Norway, 2017. https://doi.org/10.1115/OMAE2017-61860
[15] J. Wang, D. Wan, M. Abdel-Maksoud, CFD Investigations of ship propulsion performance at different trim angles, in: Proceedings of the Thirtieth (2020) International Ocean and Polar Engineering Conference, the Thirtieth (2020) International Ocean and Polar Engineering ConferenceShanghai, China, 2020, pp. 2338–2344.
[16] H. Islam, G. Soares, Effect of trim on container ship resistance at different ship speeds and drafts Ocean Eng., 183, 2019. https://doi.org/10.1016/j.oceaneng.2019.03.058
[17] J. Sun, H. Tu, Y. Chen, D. Xie, J. Zhou, A study on trim optimization for a container ship based on effects due to resistance, J. Ship Res. 60 (2016) 30–47. https://doi.org/10.5957/jsr.2016.60.1.30
[18] H. Mahmoodi, I. Ghamari, A. Hajivand, M. Mansoori, A CFD investigation of the propulsion performance of a low-speed VLCC tanker at different initial trim angles Ocean Eng., 275, 2023. https://doi.org/10.1016/j.oceaneng.2023.114148
[19] C.G. Grlj, N. Degiuli, I. Martić, Experimental and numerical assessment of the effect of speed and loading conditions on the nominal wake of a containership, Brodogradnja 75 (2024) 75405. https://doi.org/10.21278/brod75405
[20] Y. Kim, J.H. Kim, Benchmark study on motions and loads of a 6750-TEU containership Ocean Eng., 119, 2016. https://doi.org/10.1016/j.oceaneng.2016.04.015
[21] N. Degiuli, I. Martić, M.P. Buča, C.G. Grlj, Benchmark study on resistance and propulsion characteristics of a 6750-TEU container ship. Ocean Eng., 319, 2025. https://doi.org/10.1016/j.oceaneng.2025.120300
[22] C.G. Grlj, N. Degiuli, I. Martić, The impact of numerical parameters on the resistance characteristics of a container ship at the model and full scale, J. Mar. Sci. Eng 11 (2023) 1672. https://doi.org/10.3390/jmse11091672
[23] C.G. Grlj, N. Degiuli, I. Martić, 2025A. assessment of the effect of speed and scale on the total resistance and its components for a bulk carrier, Results Eng. 26 (2025) 105095. https://doi.org/10.1016/j.rineng.2025.105095
[24] C.G. Grlj, N. Degiuli, I. Martić, 2025b. Scale effects on the resistance and propulsion characteristics of the Japan Bulk Carrier Ocean Eng., 339, 2025. https://doi.org/10.1016/j.oceaneng.2025.122059
[25] Z. Ma, N. Li, Q. Zeng, X. Deng, C. Shi, Influence of scale effect on flow field offset for ships in confined waters, Brodogradnja 75 (2024) 75106. https://doi.org/10.21278/brod75106
[26] Ittc, Practical Guidelines for Ship CFD Applications, 7, 2024 ITTC-Recommended Procedures and Guidelines,
[27] L. Liang, Z. Baoji, Z. Hao, G. Jiaye, T. Zheng, G. Shuhui, B. Yuanbiao, Z. Xu, Study on numerical simulation and mitigation of parametric rolling in a container ship under head waves, Brodogradnja 75 (2024) 75305. https://doi.org/10.21278/brod75305
[28] Y. Wei, J. Zhang, K. Liu, J. Pan, L. Zhang, W. Chen, Q. Zhang, Numerical study of the influence of hydrofoil hydrodynamic performance considering near-free surface, Brodogradnja 76 (2025) 76108. https://doi.org/10.21278/brod76108
[29] D. Villa, S. Gaggero, T. Gaggero, G. Tani, G. Vernengo, M. Viviani, An efficient and robust approach to predict ship self-propulsion coefficients, Appl. Ocean Res. 92 (2019). https://doi.org/10.1016/J.APOR.2019.101862
[30] Ittc, 1978 ITTC Performance Prediction Method, 7, 2017. ITTC-Recommended Procedures and Guidelines

Article VI

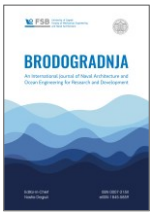
Article published by Faculty of Mechanical Engineering and Naval Architecture of the University of Zagreb in Brodogradnja: an international journal of naval architecture and ocean engineering for research and development on 1 September 2024, available online: https://brodogradnja.fsb.hr/vol-75-no-4-75405/

Brodogradnja Volume 75 Number 4 (2024) 75405

journal homepage: www.brodogradnja.fsb.hr

Brodogradnja

An International Journal of Naval Architecture and Ocean Engineering for Research and Development



Experimental and numerical assessment of the effect of speed and loading conditions on the nominal wake of a containership

Carlo Giorgio Grlj[1*], *Nastia Degiuli*[1], *Ivana Martić*[1]

[1]*University of Zagreb, Faculty of Mechanical Engineering and Naval Architecture, Ivana Lučića 5, Zagreb, 10000, Croatia*

ARTICLE INFO

Keywords:
EFD
CFD
containership
loading conditions
nominal wake
RANS

ABSTRACT

An important aspect of the design of the propeller is the determination of the nominal wake. In this study, the nominal wake of a Post Panamax containership is determined numerically and experimentally at different speeds and loading conditions. The numerical simulations are based on the Reynolds averaged Navier Stokes equations, which are discretized using the finite volume method and the system of equations is closed using the Shear stress transport $k-\omega$ turbulence model. The nominal wake is determined with numerical simulations that model the effects of the free surface and without the free surface included, i.e., double body simulations. The verification study is conducted to assess the numerical uncertainty for the grid size and time step. The validation study includes a comparison of the contours of the dimensionless axial velocity component, the radial distributions of the circumferentially averaged dimensionless axial velocity components, and the integral values of the nominal wake. The effect of speed is more noticeable for the results obtained with EFD in comparison to the numerically obtained results, which is especially pronounced for the integral value of the nominal wake. The integral value of the nominal wake increases with the increase in the trim angle.

1. Introduction

The most important aspect of the propeller design is the nominal wake, which is measured at the propeller disc plane. The determination of the nominal wake is crucial for the propeller blade section design and local pitch, but also for the purpose of the efficiency evaluation of the Energy Saving Devices (ESD) [1]. Conventional methods for determining the full-scale nominal wake rely on the measured nominal wake at the model scale in the towing tank. However, due to the lack of validation studies, it is impossible to draw conclusions regarding the different wake field scaling procedures.

Significant scale effects on the nominal wake are present since it is strongly affected by viscous effects [2]. The scale effects are manifested through lower values of the axial velocity at the propeller disc plane at the model scale when compared to the full scale [3]. Zhang et al. [4] analysed the nominal wake in oblique flow using numerical simulations at model and full scale and showed a lower mean wake fraction at full-scale

* Corresponding author.
E-mail address: carlo.g.grlj@fsb.unizg.hr

http://dx.doi.org/10.21278/brod75405
Submitted 03.07.2024; Accepted 26.08.2024.
ISSN 0007-215X; eISSN 1845-5859

numerical simulations compared to the model scale. The reason for this is that the nominal wake is largely affected by the viscous effects such as the relative thickness of the boundary layer which is larger at the model scale compared to the one at full scale. Similarly, Dogrul et al. [5] conducted numerical simulations of the viscous flow around the KRISO Containership (KCS) and the KRISO Very Large Crude Carrier 2 (KVLCC2) at different scales. The authors observed lower axial velocities on the propeller disc plane at lower Reynolds numbers and showed significant scale effects on the nominal wake. Pena et al. [6] investigated the aft end boundary layer and the wake of a full-scale general cargo ship using numerical simulations based on the Improved Delayed Detached Eddy Simulation (IDDES), which combines the Reynolds Averaged Navier-Stokes (RANS) and the Large Eddy Simulation (LES) approaches. It was found that the lower axial velocities in the nominal wake are caused by a negative pressure gradient and flow separation near the propeller.

Conventionally, towing tank tests are employed for the determination of the nominal wake at the model scale. Since measurements of the nominal wake are expensive and time-consuming, Computational Fluid Dynamics (CFD) at model and full scale is employed as an alternative. As shown by Farkas et al. [3], the scaling of the nominal wake is avoided by conducting numerical simulations of viscous flow around the full-scale ship, and consequently, the errors introduced by the scaling methods proposed by the International Towing Tank Conference (ITTC) are eliminated. The authors concluded that this is an important benefit of employing numerical simulations at full scale for the optimization of the stern flow and also for the validation of ESD performance. Pena et al. [7] pointed out that there is a lack of clear and concise guidelines for the investigation of the boundary layer around a full-scale ship. The authors investigated the effect of three turbulence models on the obtained boundary layer and nominal wake of a full-scale ship. The study showed that the lowest discrepancies between the numerical results and sea trial measurements are obtained using the IDDES approach. Alongside the determination of the nominal wake, it is important to assess the hull-propeller interaction [8, 9]. Sakamoto et al. [10] investigated the stern wake of two full-scale merchant ships using numerical simulations of the resistance and self-propulsion tests and showed that it is important to include the effects of surface roughness for the prediction of the nominal wake, total wake, and power.

The importance of taking into account surface conditions such as hard fouling or biofilm in the numerical simulations was pointed out by Farkas et al. [11]. The authors performed CFD simulations of the open water test to assess the impact of biofouling on the open water characteristics of the propeller and proposed a performance prediction method for fouled surfaces. It was concluded that further studies are needed to assess the impact of surface conditions on the propeller performance operating in the wake of the ship hull. The impact of soft fouling such as biofilm on the nominal wake was assessed by Farkas et al. [12] and it was shown that the integral value of the nominal wake of a bulk carrier can decrease by up to 7 % due to the presence of the biofilm.

Wang et al. [13] determined the scale effects on the nominal wake for the case of a 4000 TEU containership using CFD. The authors performed numerical simulations without considering the effects of the free surface, i.e., Double Body Simulations (DBS). The results obtained with DBS were compared to those obtained with Free Surface Simulations (FSS). The authors showed the negligible effect of the free surface on the nominal wake. However, the dependence of the mean axial wake on the Reynolds number was shown and a new method for scaling the nominal wake was proposed. Shin et al. [14] conducted a numerical investigation of the nominal wake in regular head waves for the KVLCC2 at the model scale for the full loading condition. The axial mean velocities in short wave conditions showed similar trends as in calm water. On the other hand, the significant impact of the large vertical motions on the nominal wake was shown in medium and long wave conditions. Mikkelsen et al. [15] indicated fluctuations in the nominal wake fraction of up to 39 % of the mean nominal wake fraction due to the large vertical motions of a KCS containership sailing in waves. Dai et al. [16] investigated the impact of head and oblique waves on the propulsive factors using CFD and obtained a decrease in wake fraction, hull efficiency, and propulsive efficiency in oblique waves in comparison to calm water conditions. Farkas et al. [17] assessed the scale effects on the wave resistance of a tanker and pointed out the importance of implementing a scaling procedure for the wave resistance coefficient in the existing extrapolation procedures.

Sun et al. [18] performed numerical simulations of the self-propulsion test for a commercial bulk carrier and showed the importance of determining the scale effects on the effective wake. The authors showed that modelling of the free surface as well as including the surface roughness can have a significant impact on the determination of the delivered power. Guo et al. [19] studied the scale effects on the nominal wake of the KCS model by modifying the aft hull to obtain a wake field similar to the one of the full-scale ship. The results were validated using the particle image velocimetry and the authors proposed a new method for eliminating the errors due to the scale effects on the nominal wake. Can et al. [20] determined the effective wake with numerical simulations of the self-propulsion test by using geometrically similar models within the CFD simulations to predict the effective wake at full scale. The proposed method showed better agreement of the obtained effective wake fractions with the results obtained by full-scale CFD simulations in comparison to those obtained using the ITTC 1978 extrapolation procedure.

Numerous studies have been conducted to assess various effects on the nominal wake, such as the effects of scale, surface roughness, fouling conditions, wave heading, and turbulence model. However, to the best of the authors' knowledge, insufficient research has been carried out to assess the effects of speed and loading conditions on the nominal wake. In addition, a detailed insight into the circumferential distribution of the different velocity components at the propeller plane is rarely given in similar studies. Thus, the aim of this study is the experimental and numerical determination of the nominal wake of the Post Panamax 6750 TEU containership with an emphasis on the effect of speed and loading conditions on the nominal wake distribution. The effect of the free surface on the nominal wake is assessed by comparing the results obtained with DBS and FSS. The rest of the paper is organized as follows. Section 2 provides the mathematical background of the numerical simulations and experimental setup. The case study, numerical setup, and verification and validation studies are presented within the same section. The results are given in Section 3, discussing the impact of speed and loading conditions on the nominal wake distribution. Finally, in Section 4 the conclusions of the study are summarized, and a plan for future work is given.

2. Methods

2.1 Geometry

A Post Panamax 6750 TEU containership is used as a case study for the experimental and numerical assessment of the nominal wake [21]. Table 1 shows the main particulars of the Post Panamax 6750 TEU containership at full scale and model scale, while Figure 1 presents the body plan and the 3D model.

Table 1 Post Panamax 6750 TEU containership main particulars

Main Particular	Full scale	Model scale
Scale λ	1	35.18
Length between perpendiculars L_{PP}, m	286.60	8.147
Length overall L_{OA}, m	303.98	8.641
Breadth at waterline B_{WL}, m	40.00	1.137
Draught T, m	11.98	0.341
Displacement volume ∇, m3	85 634	1.967
Roll radius of gyration k_{xx}, m	14.60	0.415
Pitch radius of gyration k_{yy}, m	70.144	1.994
Yaw radius of gyration k_{zz}, m	70.144	1.994
Longitudinal centre of gravity (from AP) x_{CG}, m	138.395	3.934
Vertical centre of gravity z_{CG}, m	16.562	0.471

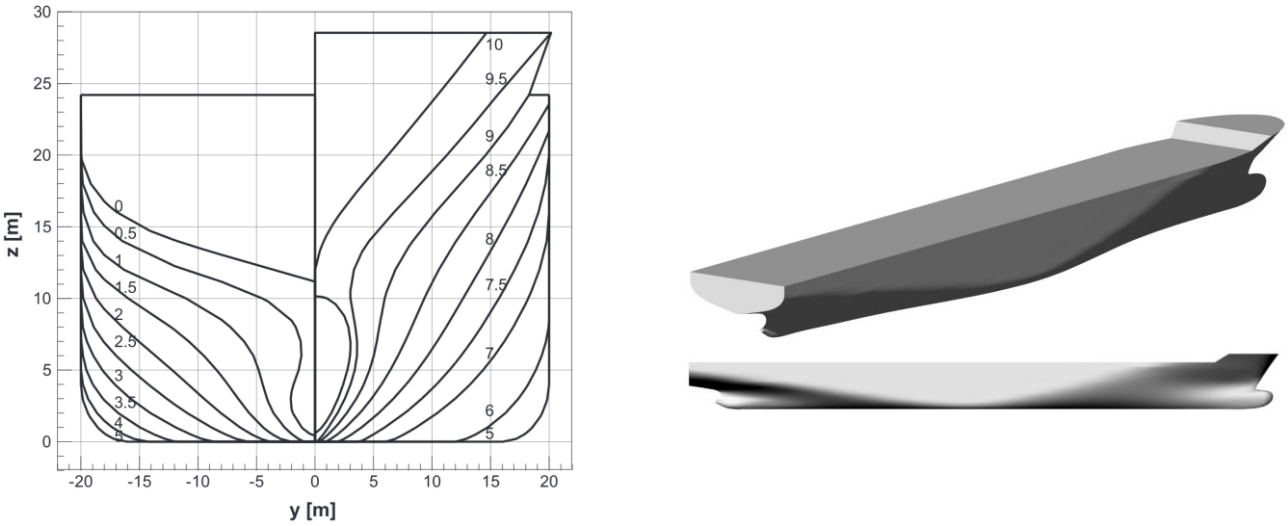


Fig. 1 The body plan and the 3D model of the Post Panamax 6750 TEU containership

The experimental and numerical investigations were performed for the ship at even keel at speeds of 19.95 kn and 16.02 kn, while for a ship trimmed by stern with a trim angle of -0.5° at 19.95 kn, corresponding to the full-scale ship. The loading conditions were defined by varying the trim while maintaining the same displacement volume as shown in Table 2. An additional numerical simulation was conducted at 23.94 kn, corresponding to the full-scale ship, for the assessment of the effect of speed on the nominal wake. The two speeds of 16.02 kn and 23.94 kn were selected as ±20 % of the design speed which is equal to 19.95 kn.

Table 2 Investigated loading conditions of the containership model

	Trim by stern		Even keel	Trim by bow	
Trim angle θ_S, °	−0.5	−0.25	0	0.25	0.5
Length of waterline L_{WL}, m	8.294	8.301	8.314	8.199	8.112
Draught at midship T_M, m	0.337	0.339	0.341	0.341	0.342
Draught at aft perpendicular T_A, m	0.372	0.354	0.341	0.326	0.313
Draught at forward perpendicular T_F, m	0.303	0.322	0.341	0.359	0.377

2.2 Experimental setup

An extensive experimental campaign was conducted at the Brodarski Institute in Zagreb for the case of the Post Panamax 6750 TEU containership [22], including resistance, open water, and self-propulsion tests and the measurements of the nominal wake at model scale $\lambda = 35.18$.

Model tests were performed in a large towing tank with a length of 276 m, a width of 12.5 m, and a depth of 6 m. It is equipped with a towing carriage with a maximum speed of 14 m/s. The wake measurements were performed using the five-hole Prandtl Pitot tube, shown in Figure 2. The axial v_A, radial v_R, and tangential v_T velocity components were calculated based on the difference between the measured absolute and static pressures in axial, radial, and tangential directions. The five-hole Prandtl Pitot tube was attached to a support extending from the stern tube, with the tube head positioned on the propeller disc plane 0.1112 m in front of the aft perpendicular. The velocity components were measured at multiple radial positions corresponding to 0.34R (0.035 m), 0.53R (0.055 m), 0.72R (0.075 m), 0.92R (0.095 m) and 1.01R (0.105 m). At each radial position, the velocity components were measured at angular positions in the range from 0° to 350° with 10° increments. The angular position of 0° corresponds to the bottom position of the tube, 90° to the starboard, 180° to the position of the tube vertically upwards, and 270° to the port side.

The towing speed was defined as 19.95 kn corresponding to the full-scale ship. A lower speed of 16.02 kn was selected for the even keel loading condition to assess the effect of ship speed on the nominal wake. The temperature of the water during the wake measurements was 13.7°C, the density 999.2 kg/m^3, the kinematic viscosity $1.179 \cdot 10^{-6}$ m^2/s, and the respective dynamic viscosity 0.001178 Pa·s. It should be noted that the five-hole Prandtl Pitot tube is an intrusive method for measuring the velocity components since the instrument has to be placed within the measuring domain. As such, it can introduce disturbances in the flow field, and thus it is important to use a measuring device with low uncertainty. In its long-term practice, Brodarski Institute has developed reliable calibration procedures for measuring devices and in that regard has gained confidence in its experimental results. The uncertainty of the Prandtl Pitot tube is within the range of ±3 %.

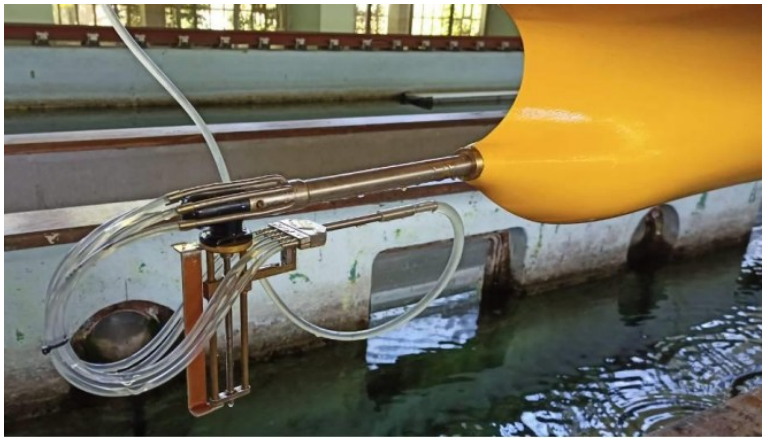


Fig. 2 Five-hole Prandtl Pitot tube mounted behind the stern of the containership model

2.3 Mathematical model

The mathematical model used in the numerical simulations is based on the RANS equations. The governing equations arise from the conservation of mass and momentum laws. For the incompressible and unsteady case, the governing equations read as follows:

$$\frac{\partial \overline{u}_i}{\partial x_i} = 0 \tag{1}$$

$$\rho \frac{\partial \overline{u}_i}{\partial t} + \rho \frac{\partial}{\partial x_j}\left(\overline{u}_i \overline{u}_j + \overline{u_i' u_j'}\right) = -\frac{\partial \overline{p}}{\partial x_i} + \frac{\overline{\tau}_{ij}}{\partial x_j} \tag{2}$$

where ρ is the fluid density, $\overline{u}_i$ is the averaged Cartesian components of the velocity vector, $\rho\overline{u_i' u_j'}$ is the Reynolds Stress Tensor (RST), $\overline{p}$ is the mean pressure, and $\overline{\tau}_{ij}$ is the mean viscous stress tensor defined by:

$$\overline{\tau}_{ij} = \mu\left(\frac{\partial \overline{u}_i}{\partial x_j} + \frac{\partial \overline{u}_j}{\partial x_i}\right) \tag{3}$$

where μ is the dynamic viscosity of the fluid. The Finite Volume Method (FVM) is used for the discretization of the RANS equations (1) and (2).

The obtained system of equations is unclosed and thus a turbulence model needs to be applied to solve the discretized RANS equations. In this study, the Shear Stress Transport $k-\omega$ (SSTKO) turbulence model is used since it was already proven to be a good compromise between the accuracy of the obtained results and the computational time needed for the assessment of the nominal wake [3, 18, 5]. The SSTKO is a turbulence model that solves two additional transport equations for the turbulent kinetic energy k and for the specific dissipation ω:

$$\frac{\partial}{\partial t}(\rho k)+\frac{\partial}{\partial x_i}(\rho k \bar{u}_i)=\frac{\partial^2 k}{\partial x_i^2}(\mu+\sigma_k \mu_t)+G_k+G_{nl}+G_b-\rho\beta^* f_{\beta^*}(\omega k-\omega_0 k_0)+S_k \quad (4)$$

$$\frac{\partial}{\partial t}(\rho \omega)+\frac{\partial}{\partial x_i}(\rho \omega \bar{u}_i)=\frac{\partial^2 \omega}{\partial x_i^2}(\mu+\sigma_\omega \mu_t)+G_\omega+D_\omega-\rho\beta f_\beta(\omega^2-\omega_0^2)+S_\omega \quad (5)$$

where σ_k, σ_ω, β^* and β are model-depending coefficients, G_{nl} is the non-linear production term, f_β is the free-shear modification factor, f_{β^*} is the vortex-stretching modification factor, and k_0 and ω_0 are the ambient values that counteract turbulence decay.

2.4 Numerical setup

For this study, two types of numerical simulations were conducted at model scale using the commercial software package STAR-CCM+ [23]. The first type is the DBS, where the symmetry boundary condition is applied at the waterline surface, while the second type is a numerical simulation that includes the effects of the free surface, i.e., FSS. The former is conducted following the ITTC recommendations [24] for the determination of the nominal wake for ships at low and moderate speeds. The Volume of Fluid (VOF) method is used in the FSS for locating and tracking the free surface. For the validation study, the Dynamic Fluid Body Interaction (DFBI) is used to model the ship motions by enabling two degrees of freedom, i.e., heave and pitch in the FSS simulations. Table 3 shows the overview of the conducted numerical simulations in this study. The numerical results are validated and compared to the experimentally obtained results for even keel at 16.02 kn and 19.95 kn and for a trim angle of -0.5° at 19.95 kn.

Table 3 Test matrix of the conducted numerical simulations

Speed, kn	$\theta_S = -0.5°$	$\theta_S = -0.25°$	$\theta_S = 0°$	$\theta_S = 0.25°$	$\theta_S = 0.5°$
16.02	/	/	DBS FSS	/	/
19.95	DBS FSS	FSS	DBS FSS	FSS	FSS
23.94	/	/	FSS	/	/

In both types of simulations, the computational domain consists of a rectangular box with the fixed bare hull of the containership embedded, which is discretized using an unstructured hexahedral mesh. It is assumed that the flow is symmetrical with respect to the symmetry plane of the ship and thus only half of the computational domain is created to lower the number of cells, and consequently to lower the computational time. The grid generation was performed carefully, paying attention to the discretization of the boundary layer. Wall functions were applied in both types of numerical simulations for solving the boundary layer. Thus, the dimensionless wall distance y^+ is maintained above 30 on the hull of the containership. To achieve the desired dimensionless wall distance, prism layers are created around the hull. The required distance from the wall to the centre of the first prism layer near the wall was estimated using the skin friction coefficient for a flat plate defined as:

$$C_f = 0.0576 Re^{-\frac{1}{5}} \quad (6)$$

The resulting equation for the determination of the distance between the wall and the centre of the first prism layer near the wall is defined as follows:

$$y = \frac{y^+ \nu}{\sqrt{0.0288 Re^{-\frac{1}{5}} v^2}} \tag{7}$$

where ν is the kinematic viscosity of the water, Re is the Reynolds number, and v is the ship speed. Figure 3 shows the obtained dimensionless wall distance y^+ in the DBS and FSS. In both cases, the obtained dimensionless wall distance values are higher than 30 over the entire hull except for a small area in the stern region.

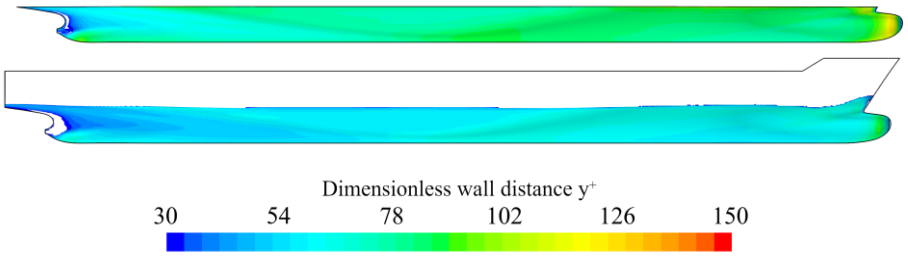


Fig. 3 The obtained dimensionless wall distance y^+ in the DBS (top) and FSS (bottom)

The generated grids vary depending on the ship speed and the type of simulations. In both FSS and DBS, the grid is refined near the hull with further refinements in the bow and stern regions. Special attention was given to the discretization around the propeller disc plane. Figures 4 and 5 show the detailed view of the generated grids for DBS and FSS, respectively. It should be noted that within the FSS, the expected locations of the free surface and the Kelvin wake were refined as well.

To further improve the stability of the FSS as well as to avoid wave reflections from the walls, the wave damping method is applied at the inlet, outlet, and side boundaries. The method was introduced by Choi and Yoon [25] and it introduces resistance to the vertical motion to dampen the waves near the boundaries to avoid their reflection. The resistance term is added to the equation for the vertical velocity component as follows:

$$S_z^d = \rho(f_1 + f_2 |w|) r^d w \tag{8}$$

where f_1 and f_2 are parameters of the damping model, r^d is the damping strength indicator, w is the vertical velocity component, and ρ is the water density.

The computational domain consists of six boundaries which are placed far enough to avoid their effect on the obtained results following the ITTC recommendations [26]. The inlet and the side boundaries are placed at $1.5L_{PP}$ from the ship. The inlet velocity is applied at the inlet boundary and the symmetry boundary condition is applied at the side and symmetry boundaries. The outlet boundary is set at $3L_{PP}$ from the ship and constant pressure is applied in both DBS and FSS. The difference between the two types of numerical simulations is the selection of the boundary conditions of the top and bottom boundaries. In DBS, the top boundary is set at the waterline, and the symmetry boundary condition is applied at both the top and bottom boundaries, while in FSS the velocity inlet is set at the top and bottom boundaries. The bottom boundary is placed at $2L_{PP}$ from the ship and the top boundary in FSS at $1.5L_{PP}$ from the ship. The hull surface is assumed to be smooth, and the boundary condition is set as the no-slip wall. A detailed view of the computational domain with a focus on the boundary conditions and the main dimensions are shown in Figures 6 and 7 for the DBS and FSS, respectively.

The effect of numerical parameters on the obtained results was investigated by Grlj et al. [27] in detail. Based on this study, the first-order discretization scheme is chosen for the temporal discretization, while the

convection and gradient terms are solved using the second-order discretization scheme within the FSS [28]. Within DBS the temporal terms are not solved since it is a steady-state simulation.

It should be noted that the numerical simulations are performed for smooth hull and with the assumption of a fully developed turbulent flow in the whole computational domain. In the experimental study, a tripwire is placed in the bow region to stimulate the flow to become turbulent, thus forming a turbulent boundary layer around the hull.

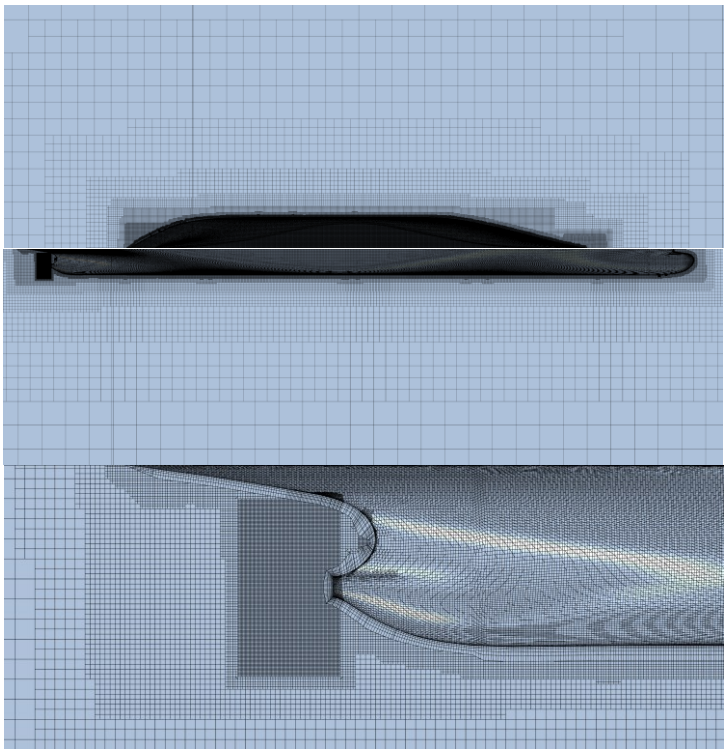


Fig. 4 Detailed view of the generated grids for the DBS

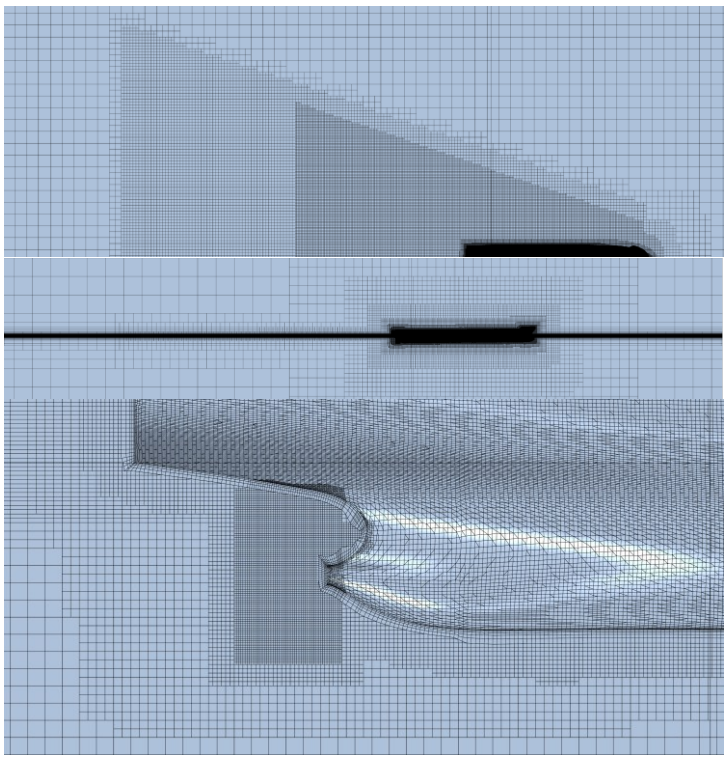


Fig. 5 Detailed view of the generated grids for the FSS

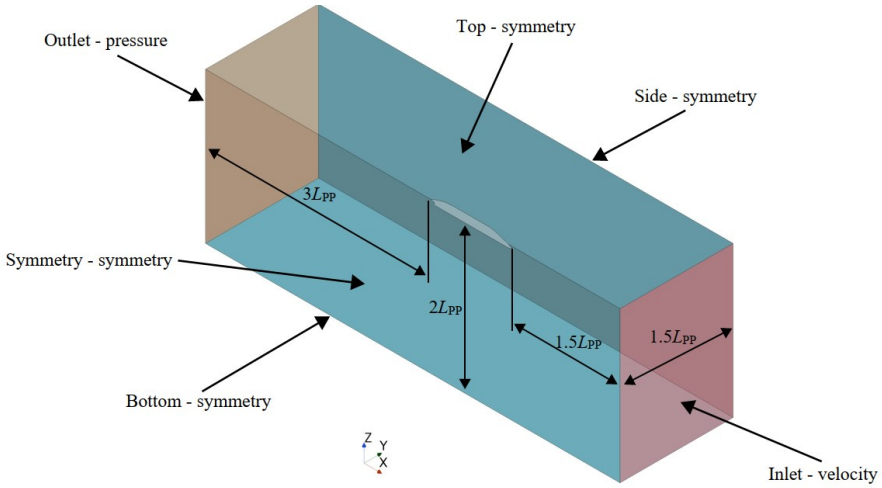


Fig. 6 Detailed view of the computational domain of the DBS with boundary conditions and main dimensions

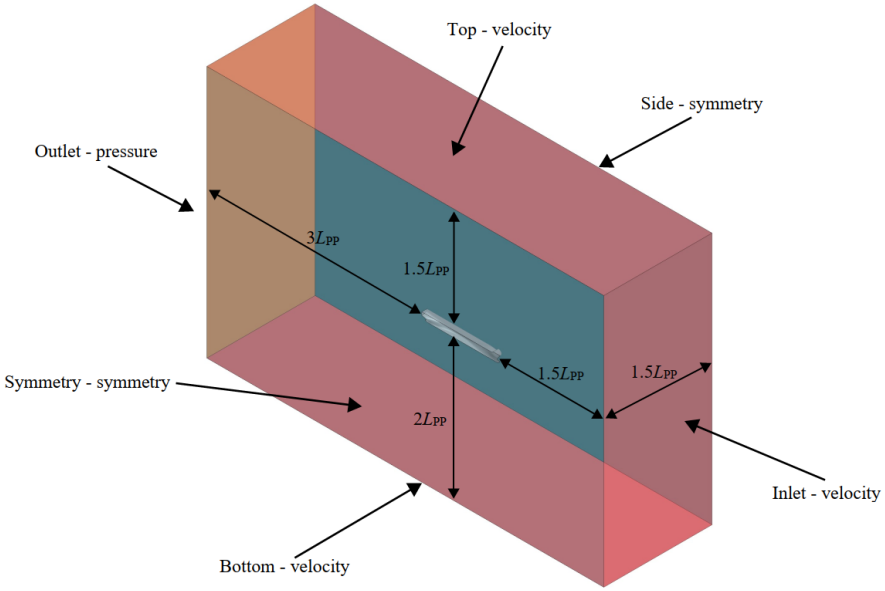


Fig. 7 Detailed view of the computational domain of the DBS with boundary conditions and main dimensions

2.5 Verification and validation studies

For the determination of the numerical simulation uncertainty, the Grid Convergence Index (GCI) method, as proposed by Celik et al. [29], is used. The apparent order of the method p is calculated using the following equation:

$$p = \frac{1}{\ln r_{21}} \cdot \left| \ln \left| \frac{\varepsilon_{32}}{\varepsilon_{21}} \right| + \ln \left(\frac{r_{21}^{p} - s}{r_{32}^{p} - s} \right) \right| \tag{9}$$

where r_{ij} is the grid refinement ratio, ε_{ij} is defined as $\varepsilon_{ij} = \phi_i - \phi_j$, with ϕ being the solution, and s is defined as $s = 1 \cdot \mathrm{sgn}(R)$ with R being the discriminating ratio [30]. The discriminating ratio defines the convergence behaviour as:

1. Monotonic convergence: $0 < R < 1$,
2. Monotonic divergence: $R > 1$,
3. Oscillatory convergence: $R < 0$ and $|R| < 1$,

4. Oscillatory divergence: $R < 1$ and $|R| > 1$.

The order of the method p can be obtained by solving equation (9) using fixed-point iteration. The grid refinement ratio is calculated as the ratio between different grid spacings h:

$$r_{ij} = \frac{h_i}{h_j} \tag{10}$$

where h_i and h_j are calculated for each grid using the following equation:

$$h = \sqrt[3]{\frac{1}{N}\sum_{i=1}^{N}(\Delta V_i)} \tag{11}$$

where N is the total number of cells and V_i is the volume of the *i*-th cell. With the refinement ratio and the obtained order of the method, the extrapolated values can be calculated as:

$$\phi_{\text{ext}}^{21} = \frac{r_{21}^{p}\phi_1 - \phi_2}{r_{21}^{p} - 1} \tag{12}$$

The approximate relative error is calculated as follows:

$$e_{\text{a}}^{21} = \left| \frac{\phi_1 - \phi_2}{\phi_1} \right| \tag{13}$$

The extrapolated relative error is defined as:

$$e_{\text{ext}}^{21} = \left| \frac{\phi_{\text{ext}}^{21} - \phi_1}{\phi_{\text{ext}}^{21}} \right| \tag{14}$$

Finally, the grid convergence index is calculated with the following equation:

$$GCI_{\text{fine}}^{21} = \frac{1.25\, e_{\text{a}}^{21}}{r_{21}^{p} - 1} \tag{15}$$

For the purpose of the validation study, the relative deviations between the numerically obtained results (ϕ_{CFD}) and the measured values from the towing tank (ϕ_{EFD}) are calculated as follows:

$$RD = \frac{\phi_{\text{CFD}} - \phi_{\text{EXP}}}{\phi_{\text{EXP}}} \cdot 100\% \tag{16}$$

3. Results and Discussion

3.1 Verification study

Two verification studies were conducted for the grid size and one for the time step. The first verification study was performed for the grid size in the DBS. Two verification studies were conducted for the grid size and time step in the FSS. Details about the grids used in DBS and FSS can be found in Table 4 and Table 5, respectively. Both tables show the number of cells, grid spacings, and refinement ratios. In the verification study for the time step, a refinement ratio between the fine and medium, and coarse and medium time steps is

equal to two. The time steps were chosen according to the ITTC recommendations [26] for standard pseudo-transient resistance computations as $\Delta t = 0.005 \div 0.01 L_{PP} / U$.

Table 4 Grids used in the verification study of the DBS

Index	Number of cells N	Grid spacing h, m	Refinement ratio r_{ij}
1	4.5M	0.122	1.275
2	2.2M	0.156	1.462
3	0.7M	0.228	

Table 5 Grids used in the verification study of the FSS

Index	Number of cells N	Grid spacing h, m	Refinement ratio r_{ij}
1	3.5M	0.162	1.263
2	1.7M	0.204	1.385
3	0.6M	0.282	

Table 6 shows the obtained results of the verification study for the grid size in the DBS. It can be seen that the obtained numerical uncertainty is slightly below 4 %, which confirms that the fine grid is adequate for the numerical simulations. Monotonic convergence is achieved, and the order of method p is below 2 which may indicate that the obtained GCI is overpredicted.

Table 7 shows the results of the verification studies for the grid size and time step in the FSS. The results show that the monotonic convergence was achieved in both studies with the obtained GCI for the time step lower than 1 %. The obtained numerical uncertainty for the grid size is slightly higher than 4 % but the order of method p suggests that the GCI for the grid size is overpredicted. Nevertheless, the obtained numerical uncertainties are satisfactory and thus the fine grids are used in the remaining numerical simulations.

Table 6 Verification study for the grid size of the DBS

Parameter	Value
ε_{21}, N	-0.0036
ε_{32}, N	-0.0084
R	0.4301
p	1.2580
ϕ_{ext}^{21}, N	0.3385
e_{a}^{21}	0.0110
e_{ext}^{21}	0.0300
GCI_{fine}^{21}, %	3.87

Table 7 Verification study for the grid size and time step of the FSS

Parameter	Grid size	Time step
ε_{21}, N	-0.0040	-0.0050
ε_{32}, N	-0.0044	-0.0200
R	0.9091	0.2500
p	1.2990	2
ϕ_{ext}^{21}, N	0.3363	0.3267
e_{a}^{21}	0.0123	0.0154
e_{ext}^{21}	0.0336	0.0051
GCI_{fine}^{21}, %	4.35	0.64

3.2 Validation study

The results obtained with numerical simulations were compared with the towing tank measurements. The measurements were taken at five radii and at each radius the velocity was measured at 36 angles, covering the range from 0°to 360° with an increment of 10°. Figure 8 shows the measured velocity components for all loading conditions and speeds at different radial positions. These results were interpolated for the purpose of the validation study and the assessment of the effects of ship speed and loading conditions on the nominal wake.

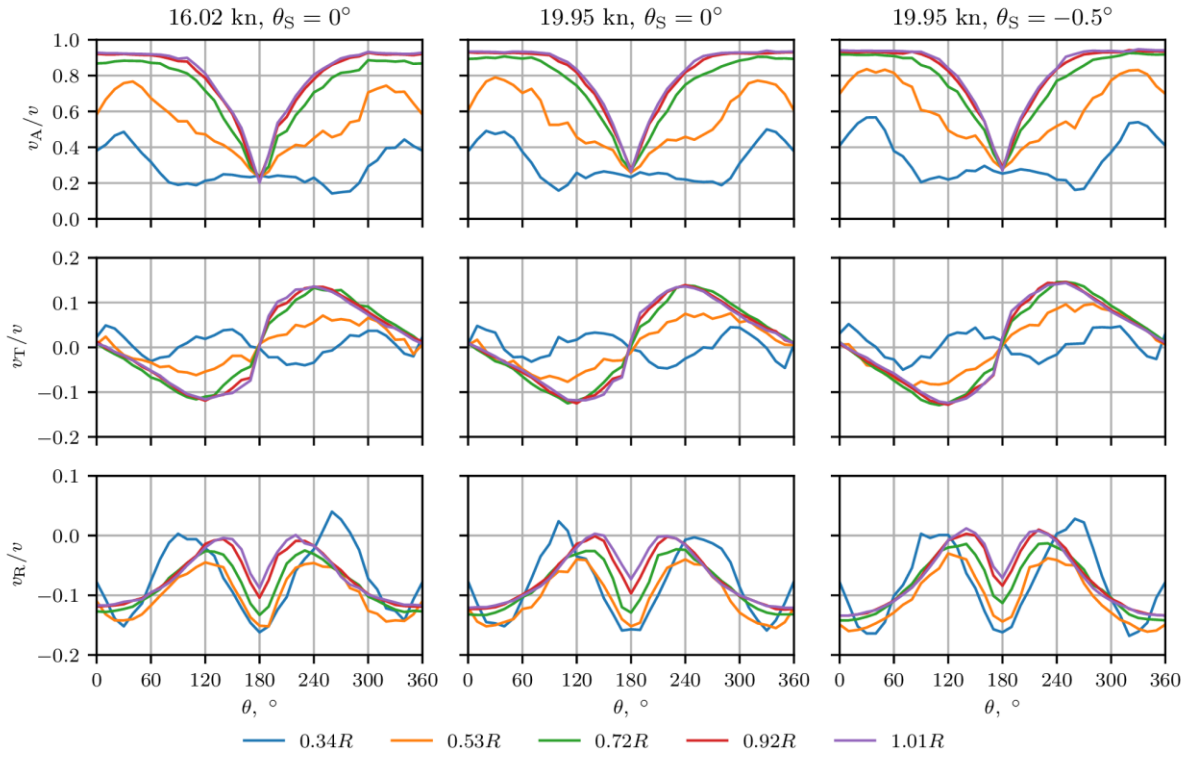


Fig. 8 Circumferential distribution of the axial (top row), tangential (middle row), and radial (bottom row) velocity components measured in the towing tank for even keel at 19.95 kn and 16.02 kn, and for a trim angle of -0.5° at 19.95 kn

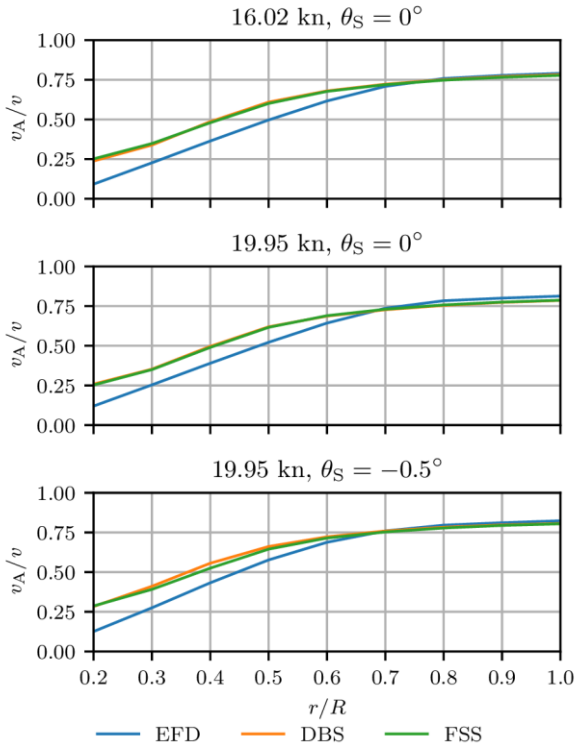


Fig. 9 The radial distribution of the circumferentially averaged dimensionless axial velocity components at different speeds and loading conditions

The radial distributions of the circumferentially averaged dimensionless axial velocity component were calculated at different radial positions and compared to the ones obtained with FSS and DBS as shown in Figure 9. It can be seen that the circumferentially averaged dimensionless axial velocity components are significantly overpredicted at radial positions from 0.2R to 0.6R for both loading conditions and ship speeds. The relative deviations decrease with the increase of the radius. The circumferentially averaged dimensionless axial velocity components are underpredicted for all loading conditions from 0.8R to 1.0R. The highest and the lowest discrepancies are obtained with FSS for even keel at 16.02 kn and 19.95 kn, respectively.

Table 8 shows the results of the validation study for the integral values of the nominal wake. The relative deviations between the results obtained with Experimental Fluids Dynamics (EFD) and DBS, and EFD and FSS are presented. Lower discrepancies are obtained with FSS in comparison to DBS, especially for a trim angle of -0.5° at 19.95 kn and for even keel at 16.02 kn.

Table 8 The validation study for the integral values of the nominal wake

Speed, kn	θ_S, °	$w_{n,\,EFD}$	$w_{n,\,DBS}$	$w_{n,\,FSS}$	RD_{DBS}, %	RD_{FSS}, %
16.02	0	0.375	0.329	0.336	-12.27	-10.40
19.95	0	0.351	0.323	0.329	-7.98	-6.27
19.95	-0.5	0.326	0.288	0.298	-11.66	-8.59

3.3 Effect of speed

In this subsection, the nominal wakes obtained with EFD, FSS, and DBS at different speeds are compared. Figure 10 shows the contours of the dimensionless axial velocity component on the propeller disc plane obtained with EFD, FSS, and DBS at two speeds. It can be noticed that a larger wake peak in the region close to 180° at the speed of 16.02 kn was obtained by EFD in comparison to 19.95 kn. In addition, the velocity reduction is larger over the entire propeller disc plane for the speed of 16.02 kn. On the other hand, differences

between the dimensionless axial velocity components obtained for the analysed speeds were not captured entirely by DBS and FSS. The velocity reduction in the region close to the propeller hub obtained with FSS is larger than the one with DBS for both speeds. It can be seen that in the region close to the propeller hub, the EFD results show a higher velocity reduction in comparison to the results obtained numerically. The results obtained with FSS show better agreement with the EFD results than those obtained with DBS. Therefore, the remaining numerical simulations are carried out with the free surface effects included.

The contours of the dimensionless axial velocity component obtained with FSS at 16.02 kn, 19.95 kn, and 23.94 kn are shown in Figure 11. It can be noticed that the wake peak in the region close to 180° decreases with the increase in speed. The velocity reduction over the entire propeller disc plane is smaller as the ship speed increases.

Figure 12 shows the circumferential distribution of the dimensionless axial velocity component at different radial positions, while in Figures 13 and 14 the dimensionless tangential and radial velocity components are presented, respectively. In Figure 15 the differences between the dimensionless axial velocity components obtained at 16.02 kn and 19.95 kn with EFD can be seen at all radial positions. The numerical results show that these differences are present only at radial positions from $0.2R$ to $0.6R$. On the other hand, as can be seen from Figure 13 the differences between the dimensionless tangential velocity components obtained at 16.02 kn and 19.95 kn are negligible. The differences between the numerical results and those obtained by EFD can be noticed, especially at radial positions from $0.2R$ to $0.5R$. The differences between the dimensionless radial velocity components obtained numerically and by EFD are more pronounced than the other velocity components at all radial positions. The comparison between the circumferential distributions of the axial, tangential, and radial velocity components obtained with FSS at 16.02 kn, 19.95 kn, and 23.94 kn is presented in Appendix A.

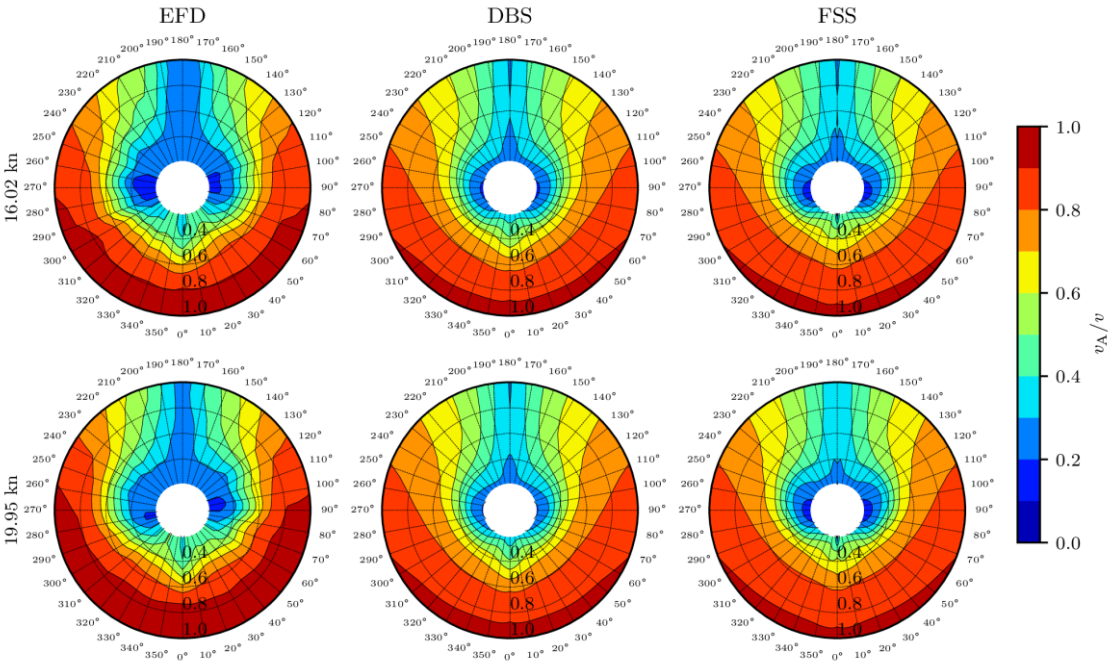


Fig. 10 Contours of the dimensionless axial velocity component on the propeller disc plane obtained with EFD, DBS, and FSS at different speeds

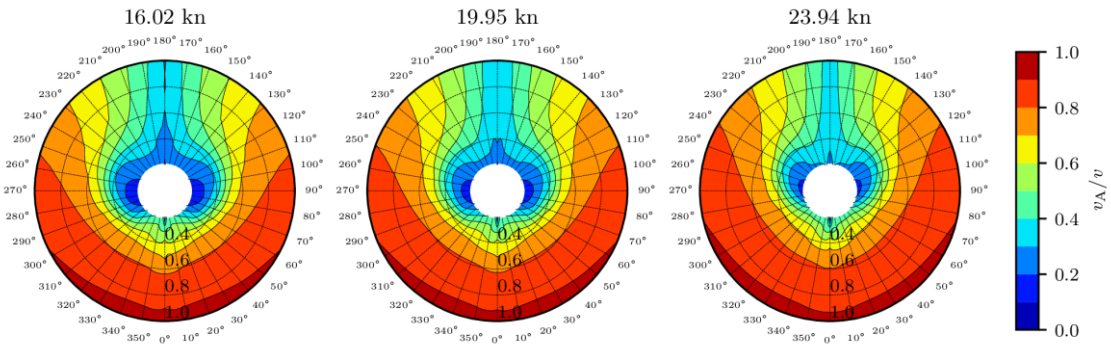


Fig. 11 Contours of the dimensionless axial velocity component on the propeller disc plane obtained with FSS at different speeds

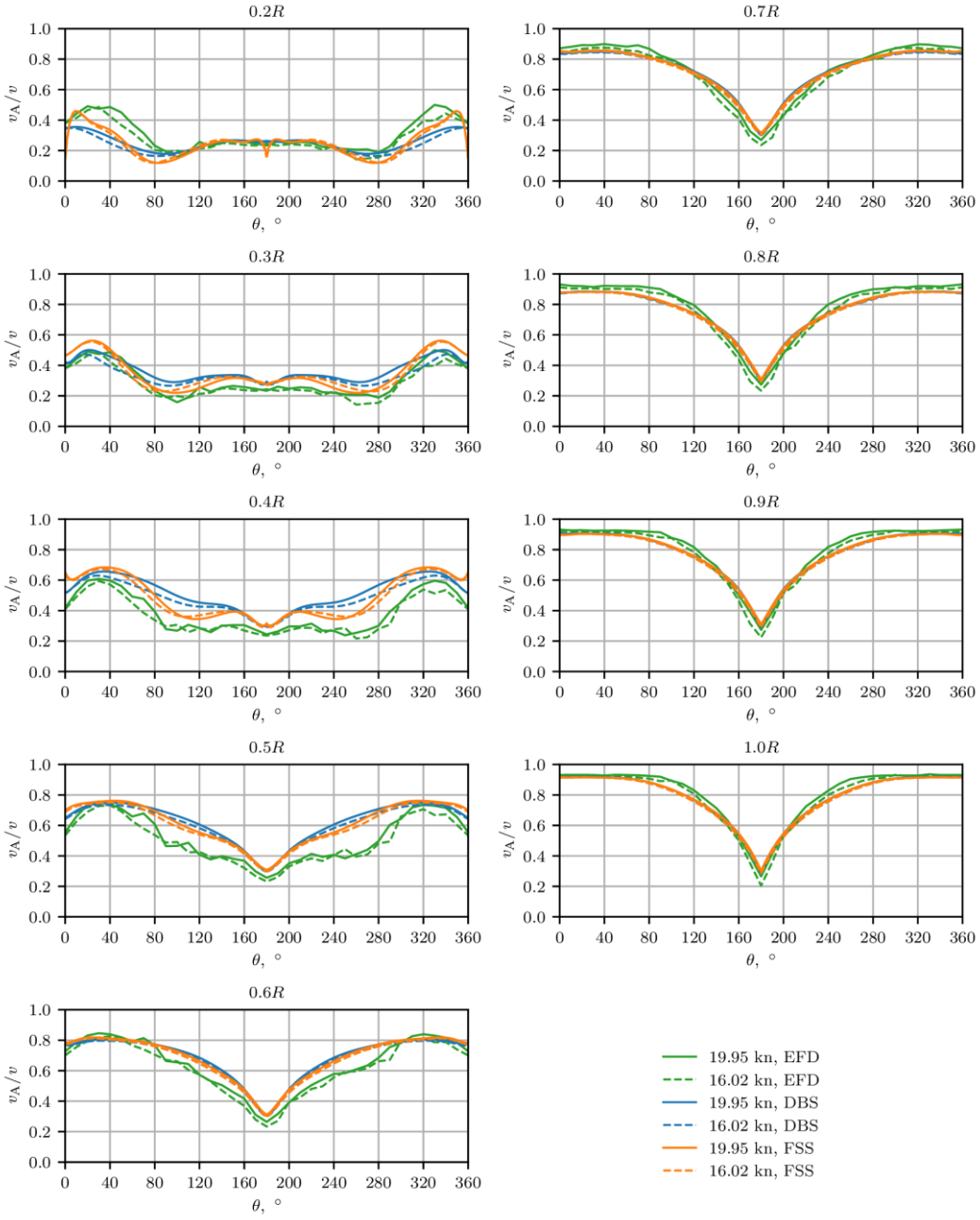


Fig. 12 Circumferential distributions of the axial velocity component for even keel at 19.95 kn and 16.02 kn

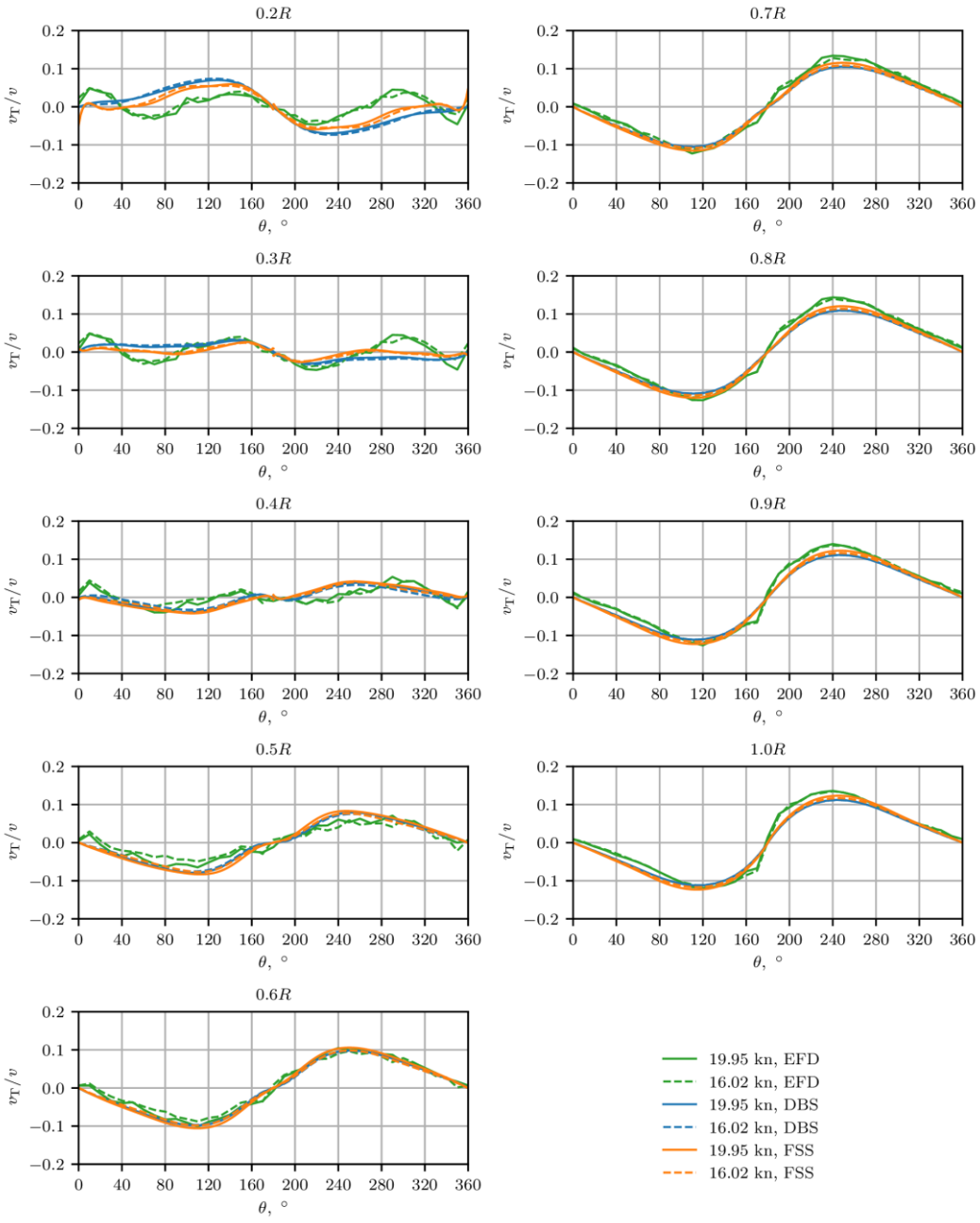


Fig. 13 Circumferential distributions of the tangential velocity component for even keel at 19.95 kn and 16.02 kn

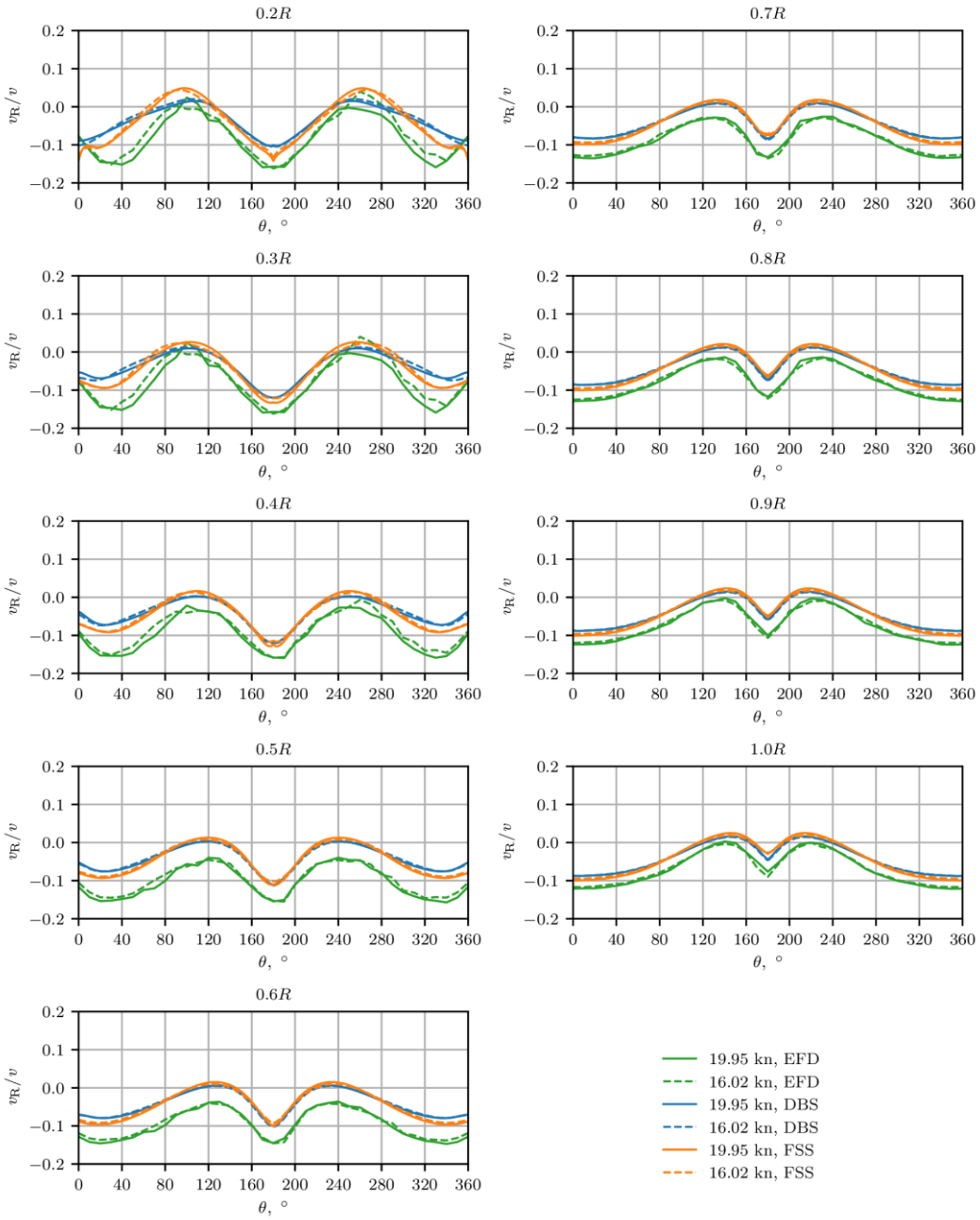


Fig. 14 Circumferential distributions of the radial velocity component for even keel at 19.95 kn and 16.02 kn

The radial distributions of the circumferentially averaged axial velocity component obtained with EFD, DBS, and FSS at 19.95 kn and 16.02 kn are presented in Figure 15. A slight effect of speed on the circumferentially averaged axial velocity component can be seen, with the relative deviations obtained with DBS and FSS ranging from -0.4 % to -8 % and from -1 % to -7 %, respectively. The effect of speed is more noticeable for the results obtained with EFD with the relative deviations being in the range from -3 % up to 23 %. It should be noted that the relative deviations are calculated with respect to the results obtained at 19.95 kn. The relative deviations between the results obtained at the analysed speeds decrease with the increase of the radius. Figure 16 shows the obtained radial distributions of the circumferentially averaged axial velocity component obtained with FSS at 16.02 kn, 19.95 kn, and 23.94 kn. It can be seen that the relative deviations between the results obtained at 19.95 kn and 23.94 kn are larger than those obtained between 16.02 kn and 19.95 kn.

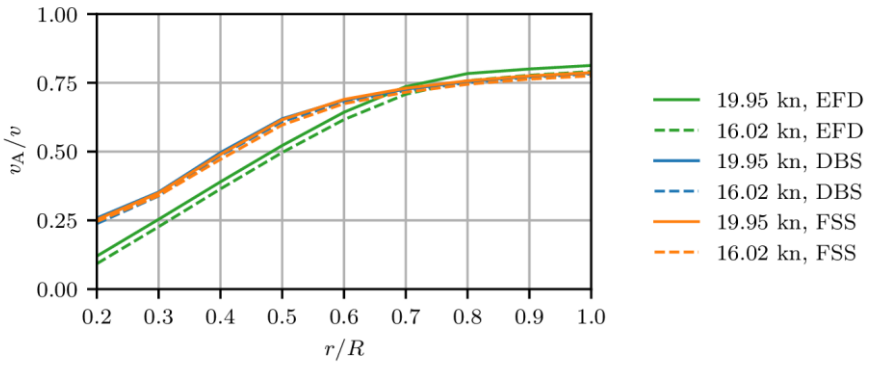


Fig. 15 Radial distributions of the circumferentially averaged dimensionless axial velocity component obtained with EFD, DBS, and FSS at 19.95 kn and 16.02 kn

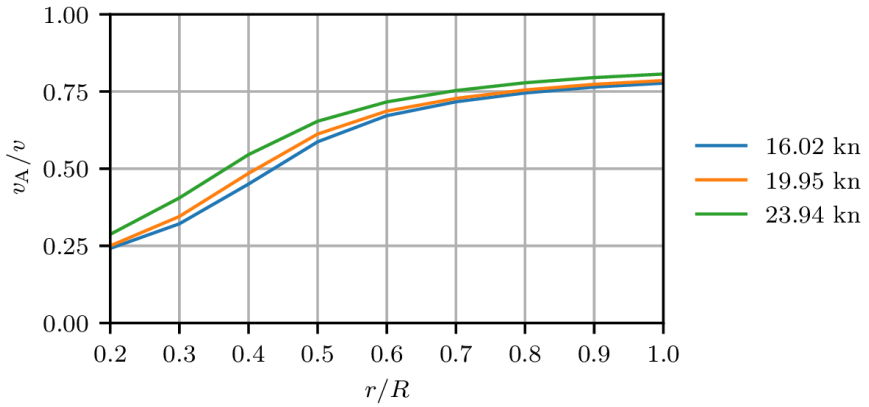


Fig. 16 Radial distributions of the circumferentially averaged dimensionless axial velocity component obtained with FSS at 16.02 kn, 19.95 kn, and 23.94 kn

The integral values of the nominal wake obtained with EFD, DBS, and FSS for even keel at 16.02 kn and 19.95 kn, and with FSS at 23.94 kn are calculated as the average value of the dimensionless axial velocity component on the propeller disc plane, Table 9. The relative deviations between the integral values of the nominal wake at 16.02 kn and 19.95 kn obtained with EFD, DBS, and FSS are 6.84 %, 1.86 %, and 4.62 %, respectively. The relative deviation obtained with FSS at 19.95 kn and 23.94 kn is -9.85 %. The effect of speed is underpredicted with both DBS and FSS at 16.02 kn, even though the results obtained with FSS are in better agreement with those obtained with EFD. As can be seen from Table 9, the integral values of the nominal wake obtained at 16.02 kn are slightly higher than those obtained at 19.95 kn, while the lowest integral value of the nominal wake is obtained at 23.94 kn.

Table 9 Integral values of the nominal wake obtained at different speeds

Speed, kn	$w_{n,\,EFD}$	$w_{n,\,DBS}$	$w_{n,\,FSS}$
16.02	0.375	0.329	0.340
19.95	0.351	0.323	0.325
23.94	/	/	0.293

3.4 Effect of loading condition

In this subsection, the results obtained with CFD and EFD for different loading conditions are presented. The contours of the dimensionless axial velocity component obtained with EFD, DBS, and FSS are shown in Figure 17. It can be seen that smaller velocity reductions are obtained with EFD, DBS, and FSS for the trim angle of -0.5° in comparison to even keel. In the region close to the propeller tip radius, the velocity reductions obtained with EFD are smaller than those obtained with DBS and FSS. On the other hand, the velocity

reductions near the propeller hub obtained by EFD are larger than those obtained numerically. Again, the results obtained with FSS show better agreement with the EFD results. Additional FSS were conducted for trim angles of -0.25°, 0.25°, and 0.5°. The obtained contours of the dimensionless axial velocity component are presented in Figure 18. It can be seen that the velocity reduction over the entire propeller disc plane is smaller, while the wake peak in the region close to 180° is larger as the trim angle increases. Thus, a more favourable flow is obtained for trim by stern than for trim by bow compared to even keel. The velocity reductions close to the propeller hub due to the increase in the trim angle are insignificant.

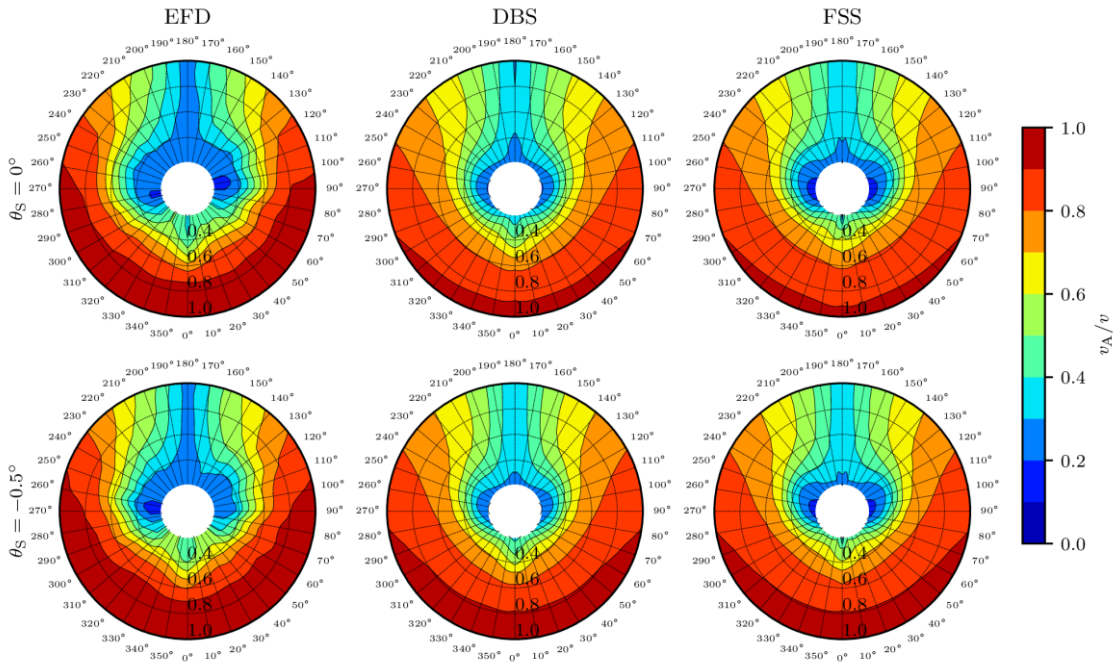


Fig. 17 Contours of the dimensionless axial velocity component on the propeller disc plane obtained with EFD, DBS, and FSS for different loading conditions

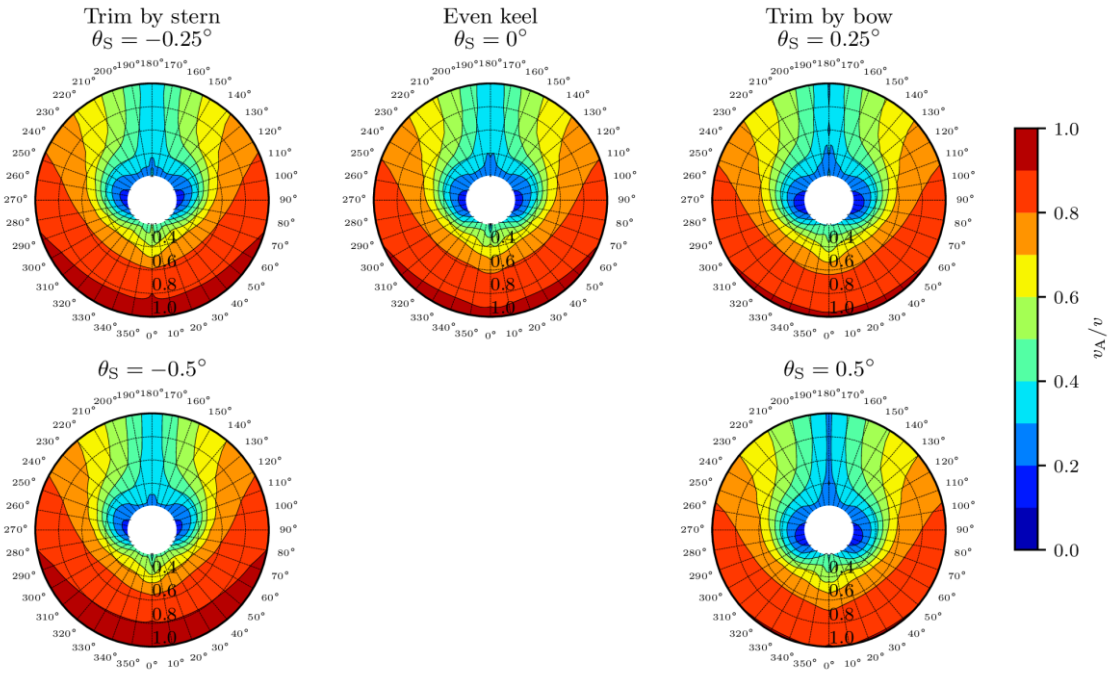


Fig. 18 Contours of the dimensionless axial velocity component on the propeller disc plane obtained with FSS for different loading conditions

Figures 19, 20, and 21 show the circumferential distribution of the dimensionless axial, tangential, and radial velocity components, respectively. The effect of the loading condition on the obtained results can be seen in the entire range of radial positions from $0.2R$ to $1.0R$. Higher discrepancies between the results obtained at the investigated loading conditions can be seen at lower radial positions for all velocity components, especially for the axial and tangential velocity components. Lower values of the dimensionless axial and tangential velocity components are obtained for even keel compared to the trim angle of -0.5° in the entire range of the angular positions. On the other hand, the obtained dimensionless radial velocity components are higher for even keel compared to the trim angle of -0.5° at angular positions from 0° to 80° and 280° to 360°. The differences between the dimensionless radial velocity components obtained numerically and by EFD are more pronounced than the other velocity components at all radial positions. The comparison between the circumferential distributions of the axial, tangential, and radial velocity components obtained with FSS for different loading conditions is presented in Appendix B.

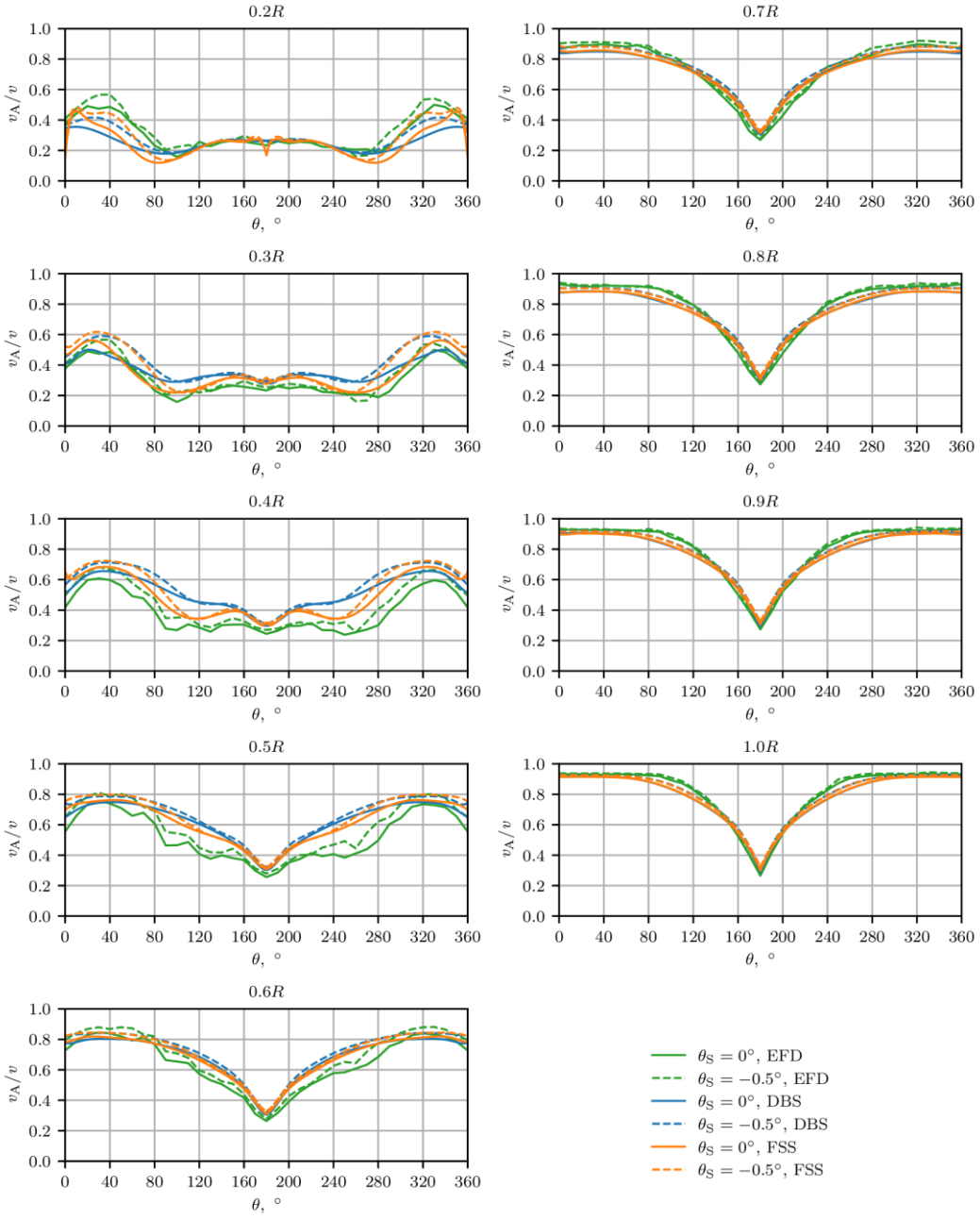


Fig. 19 Circumferential distributions of the axial velocity component for even keel and trim angle of -0.5° at 19.95 kn

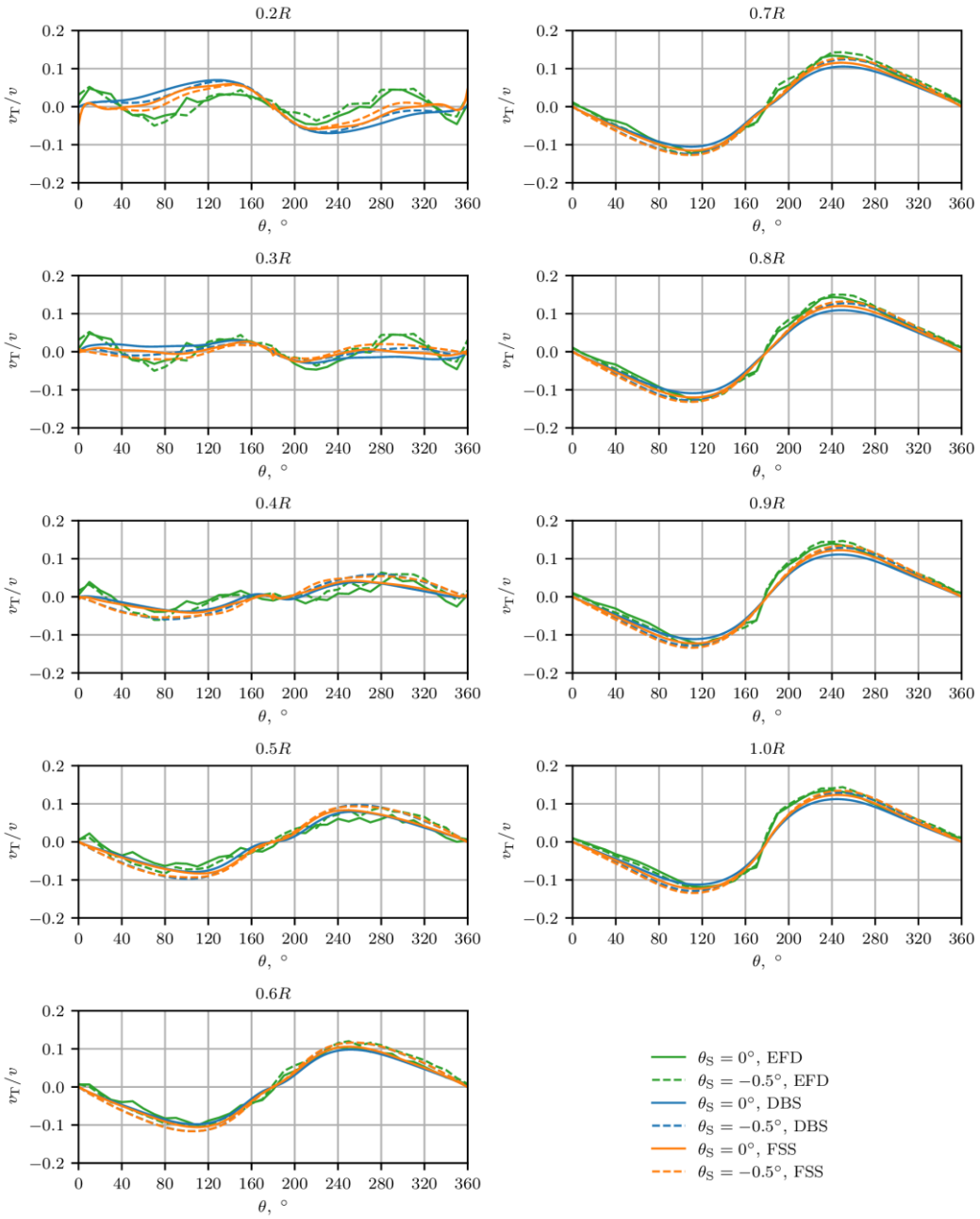


Fig. 20 Circumferential distributions of the tangential velocity component for even keel and trim angle of -0.5° at 19.95 kn

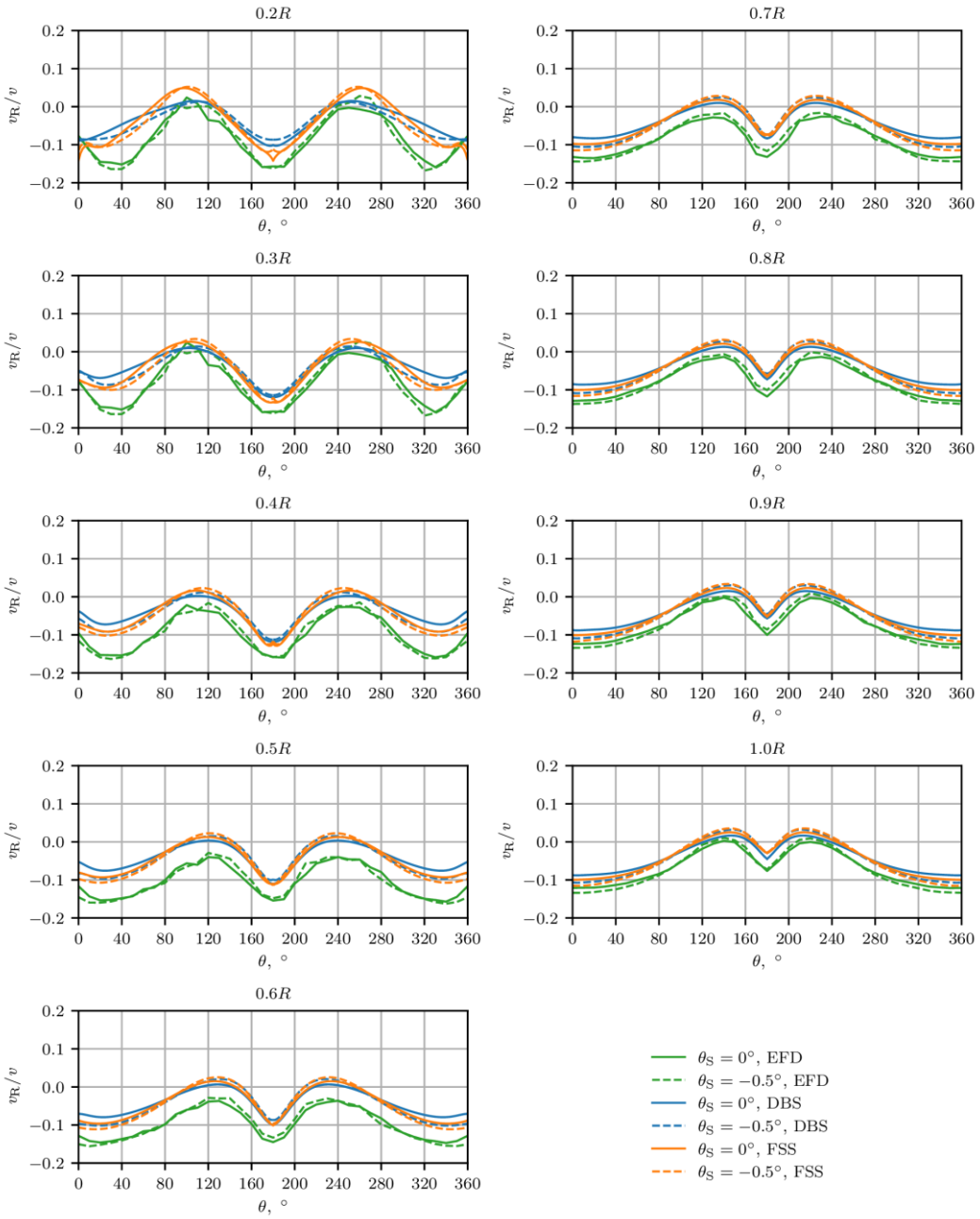


Fig. 21 Circumferential distributions of the radial velocity component for even keel and trim angle of -0.5° at 19.95 kn

Radial distributions of the circumferentially averaged axial velocity component obtained with EFD, DBS, and FSS for even keel and a trim angle of -0.5° are presented in Figure 22. It can be seen that the effect of the loading condition on the circumferentially averaged axial velocity component is significant, with the relative deviations between the results obtained by EFD being up to 11 % at the radial positions 0.4R and 0.5R. The relative deviations between the results obtained numerically are up to 16 % at 0.3R for DBS and 15 % at 0.2R for FSS. The relative deviations for the analysed loading conditions decrease with the increase of the radius. It should be noted that the relative deviations are calculated with respect to the results obtained for even keel. The circumferentially averaged axial velocity components obtained with FSS for trim angles of -0.5°, -0.25°, 0°, 0.25°, and 0.5° are presented in Figure 23. It can be noticed that the circumferentially averaged axial velocity component decreases with the increase in trim angle over the entire range of the radial positions.

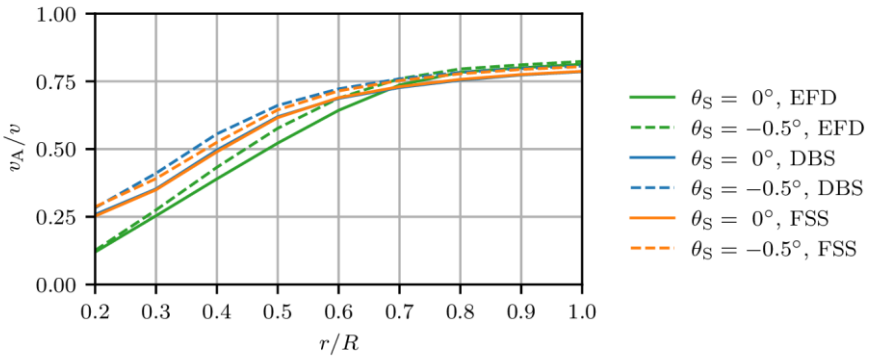


Fig. 22 Radial distributions of the circumferentially averaged dimensionless axial velocity component obtained with EFD, DBS, and FSS for even keel and trim angle of -0.5°

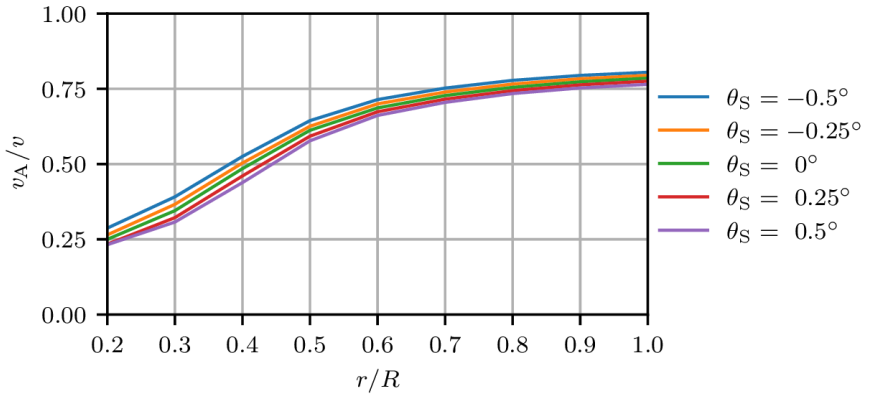


Fig. 23 Radial distributions of the circumferentially averaged dimensionless axial velocity component obtained with FSS for different trim angles

Table 10 Integral values of the nominal wake obtained for even keel and trim angle of -0.5°

	$\theta_S = 0°$	$\theta_S = -0.5°$	RD, %
$w_{n,\,EFD}$	0.351	0.326	-7.12
$w_{n,\,DBS}$	0.323	0.288	-10.84
$w_{n,\,FSS}$	0.325	0.298	-8.31

Table 11 Integral values of the nominal wake obtained with FSS for different trim angles

θ_S, °	$w_{n,\,FSS}$	RD, %
-0.5	0.298	-8.31
-0.25	0.313	-3.69
0	0.325	/
0.25	0.339	4.31
0.5	0.351	8.00

Table 10 shows the obtained integral values of the nominal wake for different loading conditions. The largest effect of the loading condition on the integral value of the nominal wake is predicted by DBS for a trim angle of -0.5°, with a relative deviation of -10.84 %, while the smallest effect is predicted by EFD with a relative deviation of -7.12 %. The effect of the loading condition is overpredicted with DBS and FSS, even

though the results obtained with FSS are in better agreement with those obtained with EFD. As can be seen from Table 11, the integral values of the nominal wake obtained with FSS increase with the increase in trim angle. The largest relative deviation of -8.31 % is obtained between the trim angle of -0.5° and even keel.

4. Conclusions and future work

The focus of this study is the assessment of the effects of speed and loading conditions on the nominal wake of a Post Panamax 6750 TEU containership. The analysis is carried out based on the measurements from the towing tank and the results of the numerical simulations. The presented results include the contours and the radial distributions of the dimensionless axial velocity component as well as the circumferential distributions of the axial, tangential, and radial velocity components determined at different radial positions, and the integral values of the nominal wake. The results obtained with DBS were compared with those obtained using FSS. Based on this study, the following conclusions are drawn:

- Relative deviations between the numerically and experimentally obtained circumferentially averaged dimensionless axial velocity component decrease with the increase of the radius. The dimensionless axial velocity component obtained numerically is overpredicted at radial positions from $0.2R$ to $0.7R$, and slightly underpredicted above $0.7R$. The results obtained with FSS show slightly better accordance with the EFD results than those obtained with DBS. The velocity reductions obtained numerically are larger than those obtained experimentally in the entire propeller disc plane, except in the region close to the propeller hub.
- A larger wake peak in the region close to 180° at a speed of 16.02 kn is obtained by EFD in comparison to 19.95 kn. The results obtained with FSS show that the velocity reduction over the entire propeller disc plane is smaller as the ship speed increases, which was not captured entirely by DBS. The differences between the dimensionless radial velocity components obtained numerically and by EFD are more pronounced than the other velocity components. A slight effect of speed on the axial velocity component can be seen at radial positions closer to the propeller hub for DBS and FSS. The differences between the dimensionless axial velocity components obtained at 16.02 kn and 19.9 kn with EFD can be seen at all the radial positions. Only a slight effect of speed on the circumferentially averaged axial velocity is observed. The effect of speed is more noticeable for the results obtained with EFD in comparison to the numerically obtained results, which is especially pronounced for the integral value of the nominal wake.
- Smaller reductions of the dimensionless axial velocity component are obtained for a trim angle of -0.5° in comparison to even keel with both EFD and CFD. The effect of the loading condition can be noticed in the obtained circumferential distributions of all velocity components. The effect of the loading condition on the circumferentially averaged dimensionless axial velocity component is more pronounced at radial positions closer to the propeller hub. Similar results are seen for the circumferentially averaged axial velocity for which the relative deviations between the results obtained numerically are up to 16 % at $0.3R$ for DBS and 15 % at $0.4R$ for FSS with respect to the results obtained for even keel. The relative deviations for the considered loading conditions decrease with the increase in radius. The integral value of the nominal wake obtained by FSS increases with the increase in trim angle. The largest effect of the loading condition on the integral value of the nominal wake is obtained with DBS with a relative deviation of -10.84 % between a trim angle of -0.5° and even keel. The results obtained with FSS are in better agreement with those obtained with EFD.

This study provides valuable experimental data for CFD benchmark studies as well as numerical results for the nominal wake obtained using DBS and FSS at the model scale. Future studies will focus on the assessment of the scale effects on the ship propulsion characteristics, which will include an assessment of the scale effects on the nominal wake. This will be a step further in the improvement of the existing extrapolation procedures for the nominal wake.

A. Appendix

Figures A1-A3 show the circumferential distributions of the dimensionless axial, tangential, and radial velocity components at radial positions from $0.2R$ to $1.0R$, obtained with FSS at different speeds.

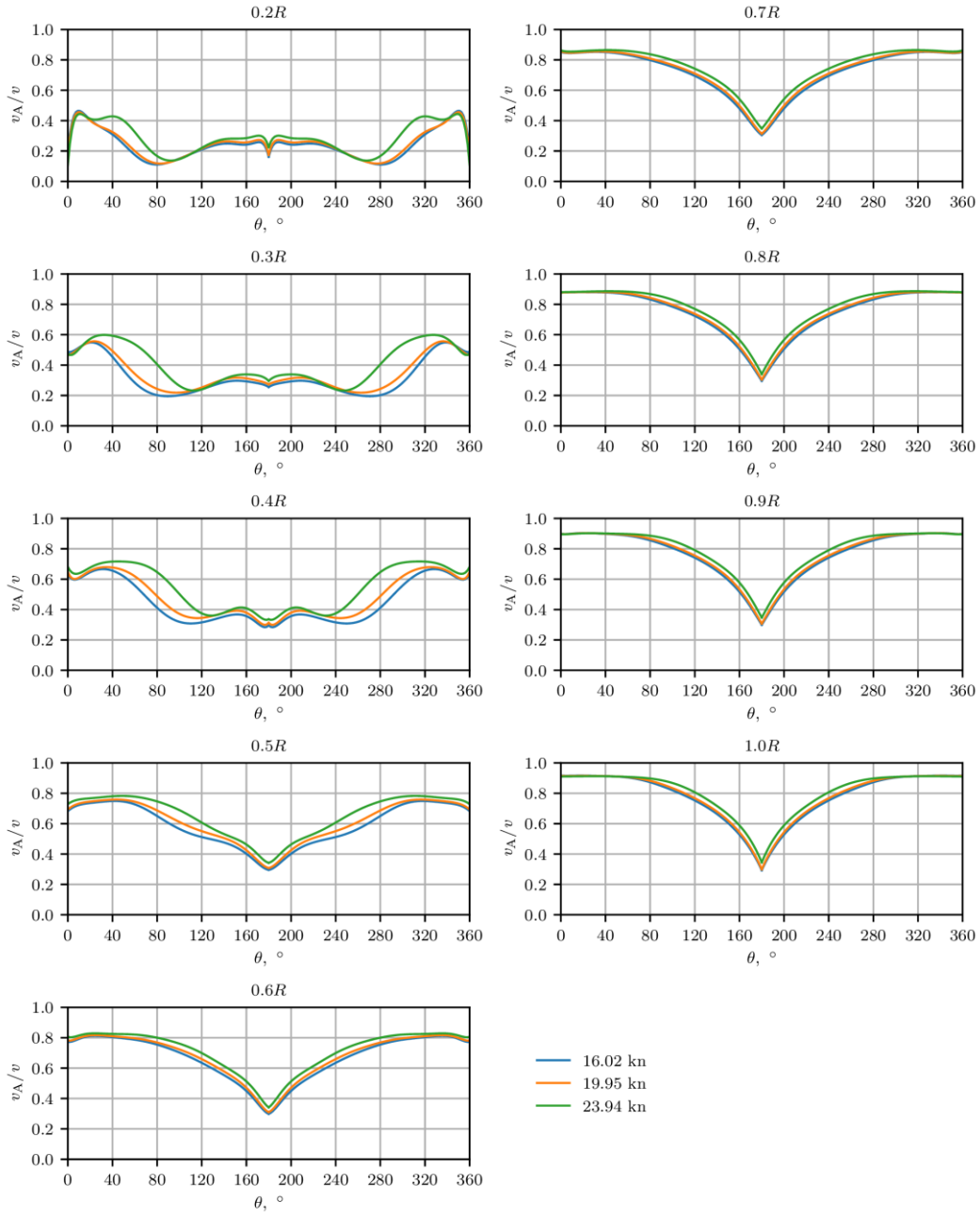


Fig. A1 Circumferential distributions of the axial velocity component obtained with FSS at different speeds

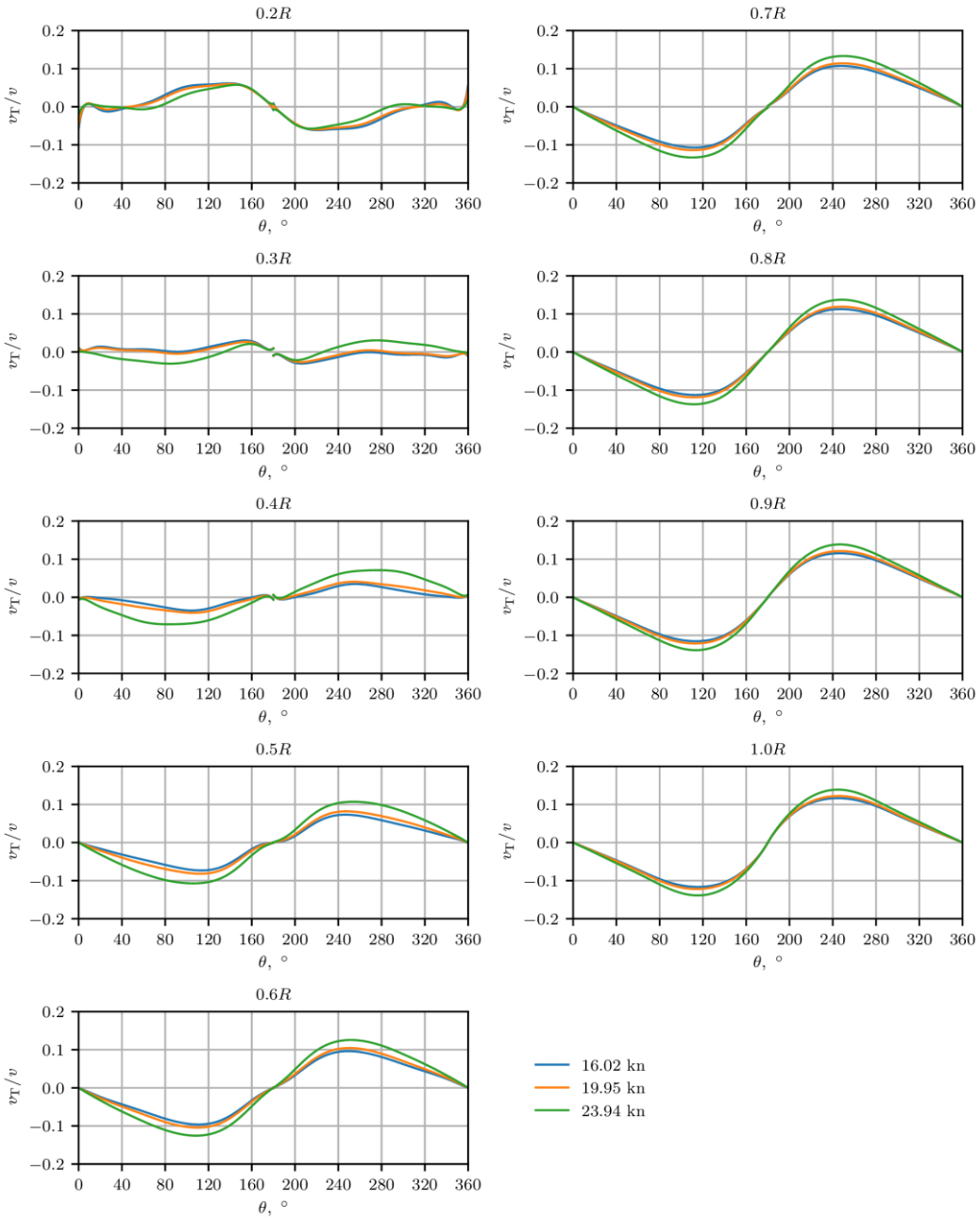


Fig. A2 Circumferential distributions of the tangential velocity component obtained with FSS at different speeds

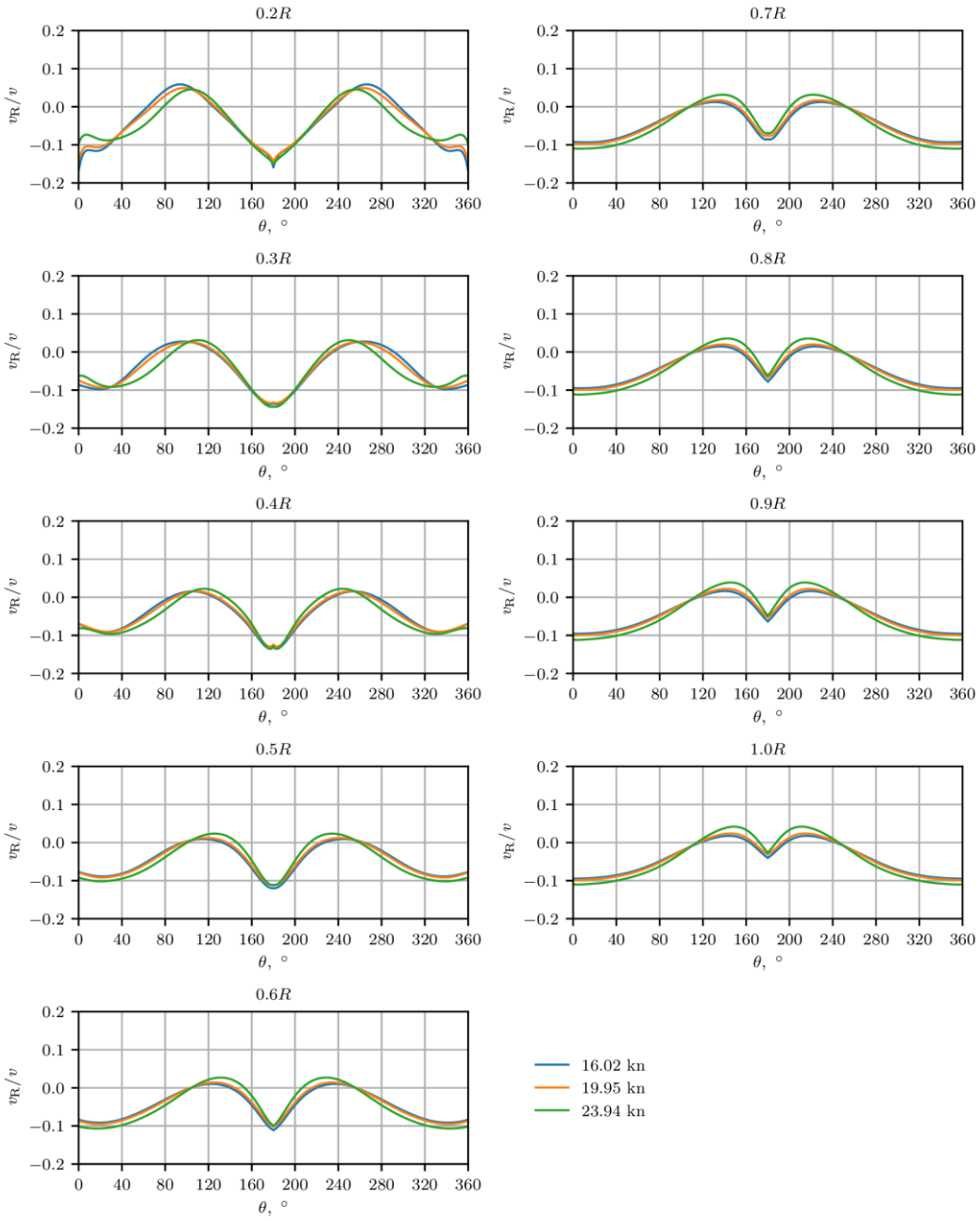


Fig. A3 Circumferential distributions of the radial velocity component obtained with FSS at different speeds.

B. Appendix

Figures B1-B3 show the circumferential distributions of the dimensionless axial, tangential, and radial velocity components at radial positions from $0.2R$ to $1.0R$, obtained with FSS for different loading conditions.

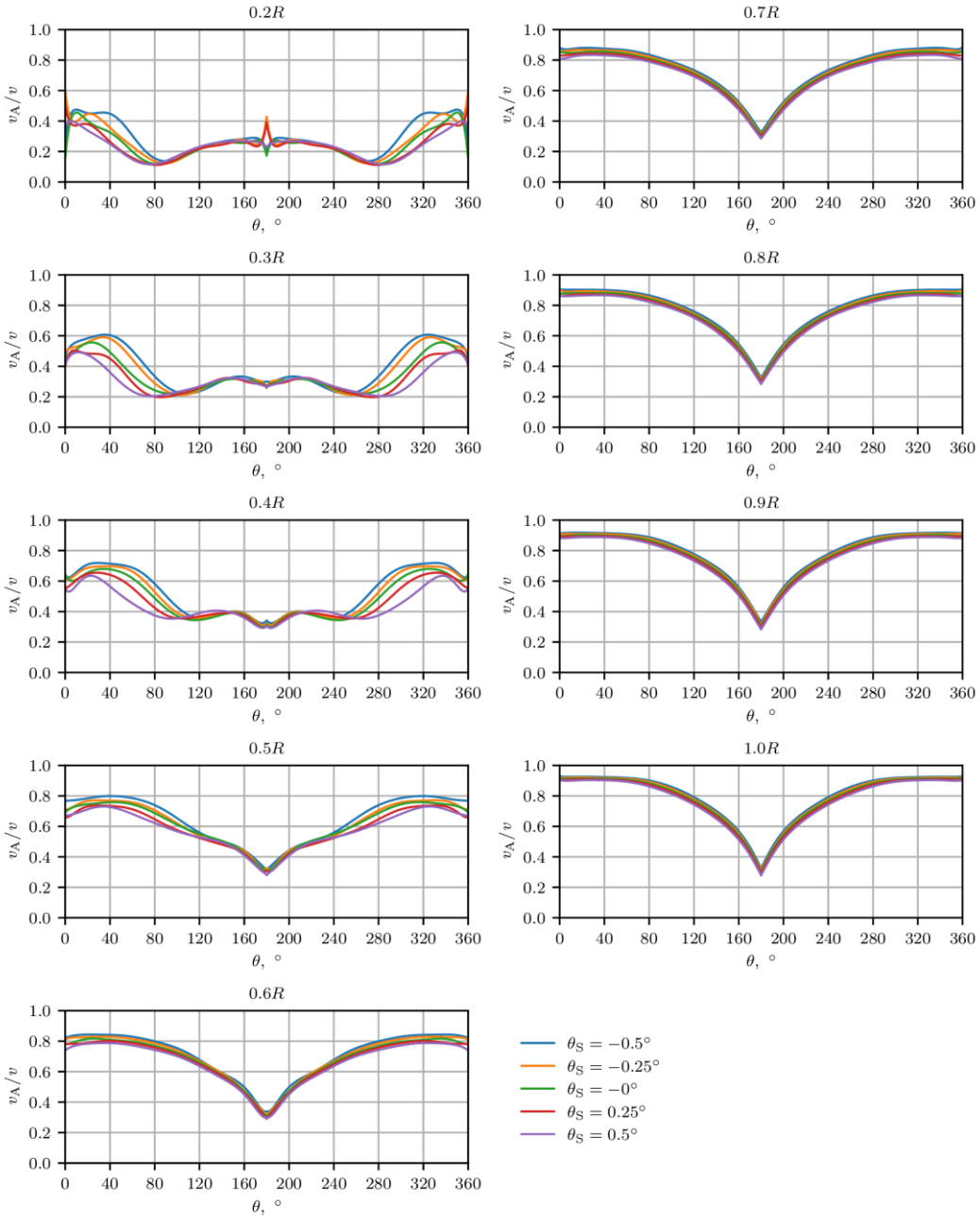


Fig. B1 Circumferential distributions of the axial velocity component obtained with FSS for different loading conditions

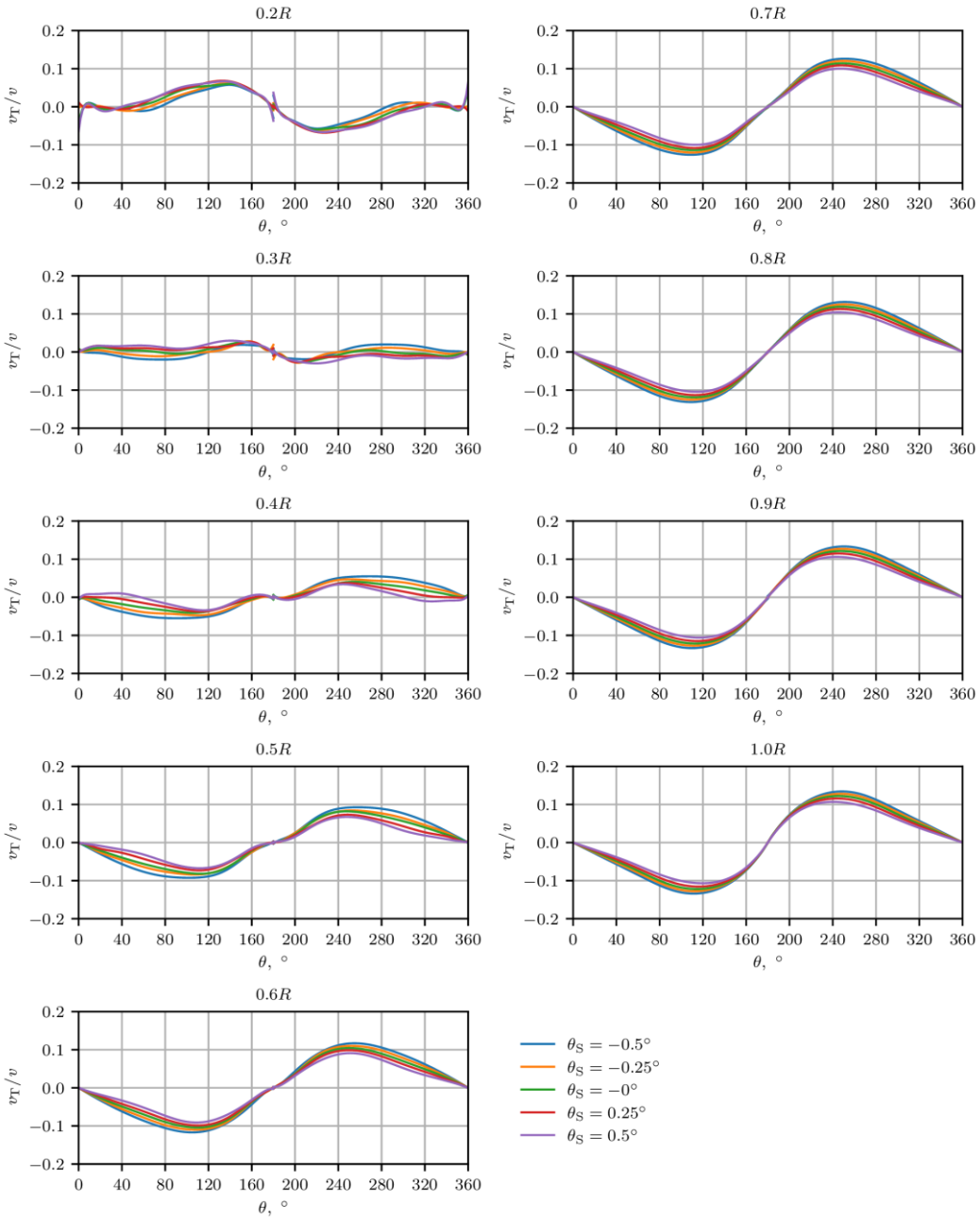


Fig. B2 Circumferential distributions of the tangential velocity component obtained with FSS for different loading conditions

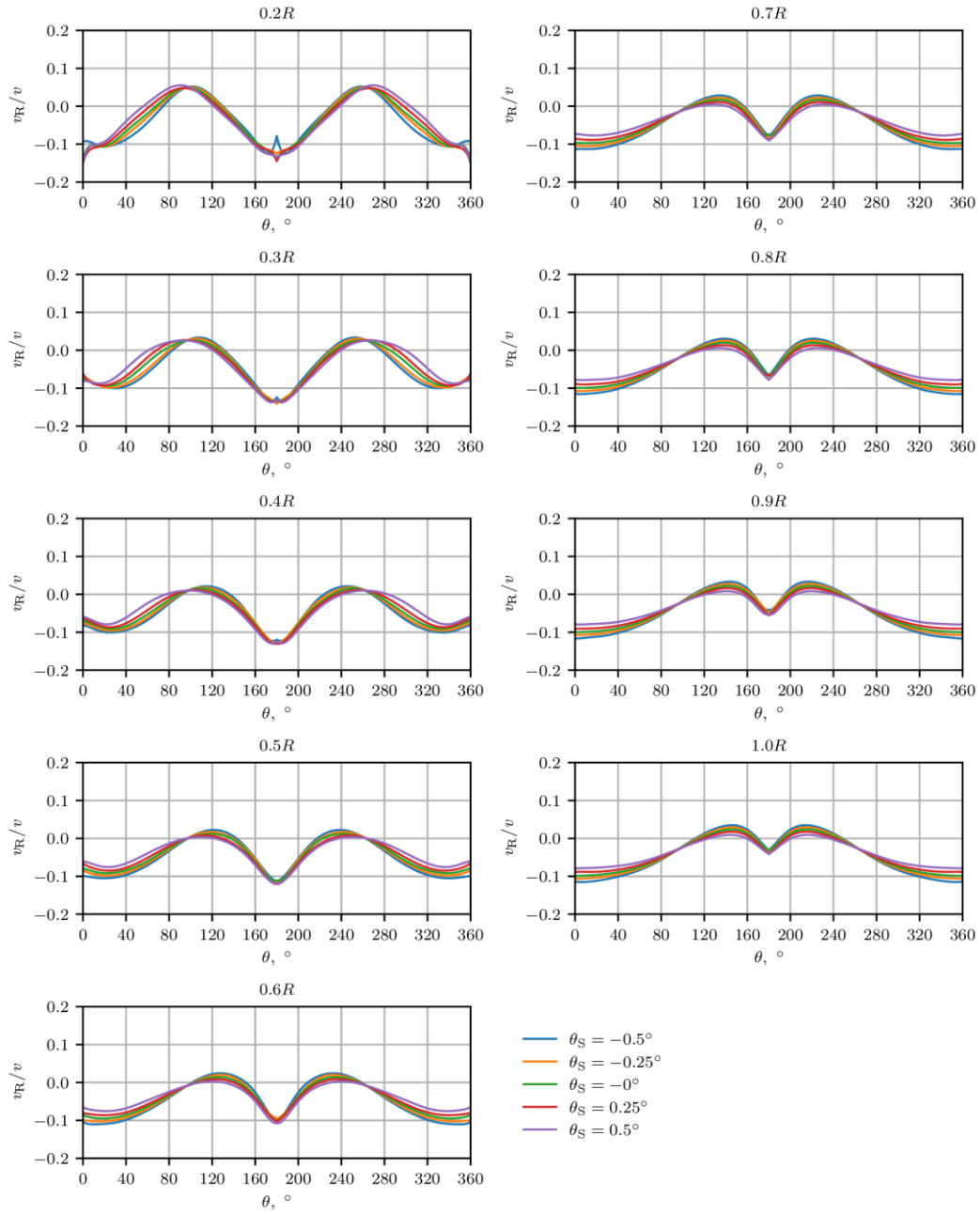


Fig. B3 Circumferential distributions of the radial velocity component obtained with FSS for different loading conditions

FUNDING

This study was funded by the Croatian Science Foundation under project IP-2020-02-8568.

ACKNOWLEDGEMENTS

This study has been fully supported by the Croatian Science Foundation under project IP-2020-02-8568.

REFERENCES

[1] Park, S., Oh, G., Rhee, S. H., Koo, B. Y., Lee, H., 2015. Full scale wake prediction of an energy saving device by using computational fluid dynamics. *Ocean Engineering*, 101, 254–263. https://doi.org/10.1016/j.oceaneng.2015.04.005

[2] Regener, P., Mirsadraee, Y., Andersen, P., 2018. Nominal vs. effective wake fields and their influence on propeller cavitation performance. *Journal of marine science and technology*, 6(2), 34. https://doi.org/10.3390/jmse6020034

[3] Farkas, A., Degiuli, N., Martić, I., Dejhalla, R., 2019. Numerical and experimental assessment of nominal wake for a bulk carrier. *Journal of marine science and technology*, 24, 1092–1104. https://doi.org/10.1007/s00773-018-0609-4

[4] Zhang, Y. X., Lai, M. Y., Ni, Y. G., Feng, L., 2021. CFD study of hull wakes in oblique flow at model and full scales. *Applied Ocean Research*, 112, 102689. https://doi.org/10.1016/j.apor.2021.102689

[5] Dogrul, A., Song, S., Demirel, Y. K., 2020. Scale effect on ship resistance components and form factor. *Ocean Engineering*, 209, 107428. https://doi.org/10.1016/j.oceaneng.2020.107428

[6] Pena, B., Muk-Pavic, E., Fitzsimmons, P., 2020a. Detailed analysis of the flow within the boundary layer and wake of a full-scale ship. *Ocean Engineering*, 218, 108022. https://doi.org/10.1016/j.oceaneng.2020.108022

[7] Pena, B., Muk-Pavic, E., Thomas, G., Fitzsimmons, P., 2020b. An approach for the accurate investigation of full-scale ship boundary layers and wakes. *Ocean Engineering*, 214, 107854. https://doi.org/10.1016/j.oceaneng.2020.107854

[8] Liu, J. Z., Zou, Z. J., Guo, H. P., Chen, C. Z., 2023. A study on the interaction among hull, engine and propeller during self-propulsion of a ship. *Ocean Engineering*, 286, 115702. https://doi.org/10.1016/j.oceaneng.2023.115702

[9] Dogrul, A., 2022. Numerical prediction of scale effects on the propulsion performance of Joubert BB2 submarine. *Brodogradnja*, 73(2), 17–42.

[10] Sakamoto, N., Kobayashi, H., Ohashi, K., Kawanami, Y., Windén, B., Kamiirisa, H., 2020. An overset RaNS prediction and validation of full scale stern wake for 1,600TEU container ship and 63,000 DWT bulk carrier with an energy saving device. *Applied Ocean Research*, 105, 102417. https://doi.org/10.1016/j.apor.2020.102417

[11] Farkas, A., Degiuli, N., Martić, I., 2021. The impact of biofouling on the propeller performance. *Ocean Engineering*, 219, 108376. https://doi.org/10.1016/j.oceaneng.2020.108376

[12] Farkas, A., Degiuli, N., Martić, I., 2020. Impact of biofilm on the resistance characteristics and nominal wake. *Proceedings of the Institution of Mechanical Engineers, Part M: Journal of Engineering for the Maritime Environment*, 234, 59–75. https://doi.org/10.1177/1475090219862897

[13] Wang, Z. Z., Xiong, Y., Wang, R., Shen, X. R., Zhong, C. H., 2015. Numerical study on scale effect of nominal wake of single screw ship. *Ocean Engineering*, 104, 437–451. https://doi.org/10.1016/j.oceaneng.2015.05.029

[14] Shin, H. W., Paik, K. J., Jang, Y. H., Eom, M. J., Lee, S., 2020. A numerical investigation on the nominal wake of KVLCC2 model ship in regular head waves. *International Journal of Naval Architecture and Ocean Engineering*, 12, 270–282. https://doi.org/10.1016/j.ijnaoe.2020.01.001

[15] Mikkelsen, H., Shao, Y., Walther, J. H., 2022. Numerical study of nominal wake fields of a container ship in oblique regular waves. *Applied Ocean Research*, 119, 102968. https://doi.org/10.1016/j.apor.2021.102968

[16] Dai, K., Li, Y., Gong, J., Fu, Z., Li, A., Zhang, D., 2022. Numerical study on propulsive factors in regular head and oblique waves. *Brodogradnja*, 73(1), 37–56. https://doi.org/10.21278/brod73103

[17] Farkas, A., Degiuli, N., Martić, I., 2017. Numerical simulation of viscous flow around a tanker model. *Brodogradnja*, 68(2), 109–125. https://doi.org/10.21278/brod68208

[18] Sun, W., Hu, Q., Hu, S., Su, J., Xu, J., Wei, J., Huang, G., 2020. Numerical analysis of full-scale ship self-propulsion performance with direct comparison to statistical sea trail results. *Journal of Marine Science and Engineering*, 8(1), 24. https://doi.org/10.3390/jmse8010024

[19] Guo, C., Wu, T., Zhang, Q., Luo, W., Su, Y., 2017. Numerical simulation and experimental studies on aft hull local parameterized non-geosim deformation for correcting scale effects of nominal wake field. *Brodogradnja*, 68(1), 77–96. https://doi.org/10.21278/brod68105

[20] Can, U., Delen, C., Bal, S., 2020. Effective wake estimation of KCS hull at full-scale by GEOSIM method based on CFD. *Ocean Engineering*, 218, 108052. https://doi.org/10.1016/j.oceaneng.2020.108052

[21] Kim, Y., Kim, J. H., 2016. Benchmark study on motions and loads of a 6750-TEU containership. *Ocean Engineering*, 119, 262–273. https://doi.org/10.1016/j.oceaneng.2016.04.015

[22] Brodarski Institute, 2022. Report 6652-M. resistance, self-propulsion and 3D wake measurement test results. *Brodarski Institute*.

[23] Siemens, 2020. STAR-CCM+ User Guide.

[24] ITTC, 2017. Practical guidelines for RANS calculation of nominal wakes ITTC.

[25] Choi, J., Yoon, S. B., 2009. Numerical simulations using momentum source wave-maker applied to RANS equation model. *Coastal Engineering*, 56, 1043–1060. https://doi.org/10.1016/j.coastaleng.2009.06.009

[26] ITTC, 2011. Practical guidelines for ship CFD applications, 7.5-03-02-03. *ITTC-Recommended Procedures and Guidelines*.

[27] Grlj, C. G., Degiuli, N., Martić, I., 2023. The impact of numerical parameters on the resistance characteristics of a container ship at the model and full scale. *Journal of Marine Science and Engineering*, 11(9), 1672. https://doi.org/10.3390/jmse11091672

[28] Mikulec, M., Piehl, H., 2023. Verification and validation of CFD simulations with full-scale ship speed/power trial data. *Brodogradnja*, 74(1), 41–62. https://doi.org/10.21278/brod74103

[29] Celik, I. B., Ghia, U., Roache, P. J., Freitas, C. J., Coleman, H., Raad, P.E., 2008. Procedure for estimation and reporting of uncertainty due to discretization in CFD applications. *ASME. Journal of Fluids Engineering*, 130, 078001. https://doi.org/10.1115/1.2960953

[30] Eça, L., Hoekstra, M., 2014. A procedure for the estimation of the numerical uncertainty of CFD calculations based on grid refinement studies. *Journal of Computational Physics*, 262, 104–130. https://doi.org/10.1016/j.jcp.2014.01.006

Article VII

Article published by Elsevier in Ocean engineering on 30 May 2023, available online: https://www.sciencedirect.com/science/article/abs/pii/S0029801823013203

Ocean Engineering 280 (2023) 114936



Contents lists available at ScienceDirect

Ocean Engineering

journal homepage: www.elsevier.com/locate/oceaneng





Experimental assessment of the hydrodynamic characteristics of a bulk carrier in off-design conditions

Nastia Degiuli [a,*], Ivana Martić [a], Andrea Farkas [a], Marta Pedišić Buča [b], Roko Dejhalla [c], Carlo Giorgio Grlj [a]

[a] University of Zagreb, Faculty of Mechanical Engineering and Naval Architecture, Ivana Lučića 5, Zagreb, 10000, Croatia
[b] Brodarski Institute, Avenija Većeslava Holjevca 20, Zagreb, 10000, Croatia
[c] University of Rijeka, Faculty of Engineering, Vukovarska 58, Rijeka, 51000, Croatia

ARTICLE INFO

Keywords:
Experimental data
JBC
Loading condition
Extrapolation method
Resistance characteristics
Propulsion characteristics
CFD benchmark

ABSTRACT

This paper presents an extensive experimental study on the resistance and propulsion characteristics of the Japan Bulk Carrier in off-design conditions. The experimental campaign is carried out for a ship model at a scale of 40.264 for three loading conditions. Resistance, open water, and self-propulsion tests were performed at the Brodarski Institute for a wide range of speeds. Four extrapolation methods, based on different assumptions, were applied to predict the resistance and propulsion characteristics of the full-scale ship from model-scale experiments. The differences between the results obtained by different extrapolation methods and the effect of loading conditions on ship resistance and propulsion characteristics are discussed. This study provides a benchmark database for the validation of Computational Fluid Dynamics simulations.

1. Introduction

Ship energy efficiency is determined by the ship hull and propulsion system, as well as speed, draught, and trim during the ship operation (Shivachev et al., 2020). Traditionally, the ship hull is optimised for the design speed and design loading condition. During its lifetime, the ship operates in a range of different speeds, draughts, and trims, i.e. in conditions that are significantly different from those for which it was designed and optimised. Thus, sailing in off-design conditions can cause several occurrences, such as a change in propulsion efficiency, a change in the level of vibration, increased specific fuel oil consumption, or an inefficient heat recovery system. Therefore, it is necessary to investigate the ship's overall performance in off-design conditions. The introduction of slow steaming in recent years has pointed out how inefficient it is to optimise a ship for one speed and one draught (Shivachev et al., 2020). Cargo ships are designed to transport a certain amount of cargo, implying the specification of trim conditions. Trim has a significant effect on ship resistance, and trim optimisation can bring significant savings in fuel consumption. For each draught, there is a trim condition that results in minimum total resistance. One of the easiest and cheapest methods in the energy efficiency measures recommended by IMO is trim optimisation, which can be achieved by ballast water management and load distribution. This does not require any hull shape or propulsion system modifications (IMO, 2016). Numerous investigations have shown that sailing under optimal trim conditions can lead to fuel savings of 2–5% (Shivachev et al., 2020) and consequently to reductions in greenhouse gas emissions. Grlj et al. (2023) have indicated for the case of a containership that trim has an effect on wind and air resistance, with trim by bow leading to a decrease, and trim by stern to an increase, in air resistance in comparison to an even keel condition.

As already mentioned, ship resistance and propulsion characteristics in off-design conditions are considerably different from those for which the ship is optimised. Even though the slow steaming approach is recognised by the maritime transport industry, the research performed so far related to ship hydrodynamic characteristics at slow steaming speed is insufficient. In addition, the downsides of slow steaming should be taken into account, such as the longer duration of sailing on the route leading to higher route costs and a lower number of routes per year (Degiuli et al., 2021b), as well as significantly reduced engine loads which can lead to fouling of the main engine (Farkas et al., 2022).

Even though tankers and bulk carriers sail for 40–50% of their time in ballast loading conditions, investigations related to ship hydrodynamic characteristics in those conditions are rarely given any consideration. Bulk carriers typically sail in various loading conditions

* Corresponding author.
E-mail address: nastia.degiuli@fsb.hr (N. Degiuli).

https://doi.org/10.1016/j.oceaneng.2023.114936
Received 22 March 2023; Received in revised form 8 May 2023; Accepted 23 May 2023
Available online 30 May 2023
0029-8018/© 2023 Elsevier Ltd. All rights reserved.

depending on the cargo content in each hold. Most bulk carriers sail in light ballast conditions when the weather conditions are favourable, with all double bottom, hopper, topside wing, and peak tanks filled. In the light ballast condition, the ship usually has a displacement of 40–50% of the displacement in full load condition. On the other hand, bulk carriers sail in heavy ballast conditions when harsh weather is expected or met. In this particular loading condition, the above-mentioned ballast tanks are filled, and, in addition, one or several holds are flooded, resulting in a displacement of 50–65% of the displacement in a full load condition (Regulations Governing Ballast Management, 2023). When in the ballast condition, the breadth-draught ratio changes significantly compared to the full load condition (Legović and Dejhalla, 2015). This causes a significant change in the underwater hull form and the ship hydrodynamic characteristics. Bulk carriers often have a bulbous bow, whose effects on the ship hydrodynamic characteristics are complex and vary with, amongst other things, the loading condition of the ship. Bulbous bows are employed to reduce the ship resistance, and for full hull forms at lower speeds, the bulbous bow could be the most efficient in the ballast condition, influencing the flow around the ship and thus the propulsion characteristics as well (Molland et al., 2017). From the propulsion point of view, the draught should be sufficient to accommodate the propeller without significantly reducing the propeller efficiency. However, the propulsion characteristics can substantially change with the change in the loading condition of the ship. For example, the wake fraction in the ballast condition tends to be 5–15% larger than that in the design loading condition (Molland et al., 2017). Similar findings were obtained by Farkas et al. (2018) in the numerical assessment of the nominal wake. In addition, a larger hub vortex was obtained in the light ballast condition compared to the design loading condition (Farkas et al., 2018).

Kim et al. (2001) performed model tests and analysed the flow characteristics around three modern hull forms of one container ship and two very large crude oil carriers. The results contribute to the benchmark database for the validation of the numerical tools. The flow characteristics, i.e. the velocity and wave profiles around the model of an LNG carrier equipped with a propeller and rudder, were measured by Van et al. (2006). Knowing the flow characteristics around the ship hull is essential for the design of a ship with enhanced hydrodynamic performance. The overall performance of a ship under various operating conditions can be improved by optimising the bulbous bow. Yin et al. (2019) performed an optimisation process and proposed an innovative design for the bulbous bow of a container ship. The authors performed model tests for the original and optimised hull form which showed a reduction in the total resistance higher than 10%, especially at lower speeds. The integration of computer-aided design and Computational Fluid Dynamics (CFD) was applied in the optimisation procedure of the bulbous bow of an ocean-going trawler (Zhao et al., 2021). The authors validated the obtained results of the total resistance by performing towing tank tests and concluded that using the proposed optimisation method could lead to a decrease in the total resistance of a trawler. Degiuli et al., 2021a investigated numerically and experimentally the effect of three bow shapes on the total resistance of a yacht. The obtained results showed that the decrease in the total resistance due to bulbous bow could reach 7%. To improve the flow field around the transom stern, Song et al. (2020) analysed the influence of different angles of a stern flap attached to a DTMB 5415 ship model on the total resistance and flow characteristics. The authors showed that the stern flap increases the boundary layer thickness in the vicinity of its location while reducing the speed in the propeller plane, which was over-predicted at the model scale in comparison to the full scale. Farkas et al. (2019) concluded that the scale effects on the nominal wake could be avoided by performing numerical simulations of viscous flow around a full-scale ship. To avoid the scale effects and improve the prediction of the full-scale ship performance, Min and Kang (2010) proposed a new extrapolation procedure based on the International Towing Tank Conference (ITTC) 1978 Performance Prediction Method and validated the obtained results by comparison with the sea trial data. Niklas and Pruszko (2019) compared the results of towing tank tests, numerical simulations, and sea trial data and concluded that the difference in the form factor obtained by various methods was significant. Consequently, the total resistance in calm water varied from −6% to 11% in comparison to sea trial measurements. Additionally, the authors concluded that for innovative hull forms, extrapolation methods and methods for the calculation of the form factor become questionable. Saydam et al. (2022) compared the numerically obtained total resistance of a full-scale ship with the extrapolated data of towing tank tests for a tanker, while the delivered power was compared with the sea trial data. The methodology for the assessment of the self-propulsion characteristics proposed by the authors enables the prediction of hull and propeller performance at reduced propeller loading.

In this paper, resistance, open water, and self-propulsion tests are performed for a wide range of speeds and for three loading conditions to investigate ship resistance and propulsion characteristics in off-design conditions. Since bulk carriers often sail at draughts different from the designed one, the Japan Bulk Carrier (JBC) was selected as the case study. The presented results contribute to the research performed so far related to ship hydrodynamic characteristics at slow steaming speed and in off-design conditions, which are insufficient. The obtained experimental results present a valuable contribution to the database for benchmarking the CFD software. The organisation of the paper is as follows. Section 2 provides a description of the case study. The experimental campaign is explained in detail in Section 3. In Section 4, different methods used for the extrapolation of the model scale data are given. Section 5 presents the obtained experimental results, as well as the results of the extrapolation methods, which are followed by a discussion. Finally, the conclusions drawn from the comprehensive experimental campaign are briefly summarised in Section 6, along with plans for future studies.

2. Case study

The research object of this study is the JBC, which has a transom stern and bulbous bow. Considering the limited availability of experimental data, the authors believe that the performed comprehensive experimental study presents a valuable contribution to benchmark data for the validation of CFD simulations.

The resistance, open water, and self-propulsion tests were performed for a wide range of speeds and three loading conditions. The hull lines of the JBC are given in Fig. 1, and the 3D model is given in Fig. 2. The main particulars of the JBC at the model and full scale at the design, light ballast, and heavy ballast draughts are given in Table 1. It should be noted that the longitudinal centre of buoyancy shown in Table 1 is given with respect to the midship, where the positive value denotes the fore of the midship section, while the negative value denotes the aft of the midship section. A model scale of 40.264 was chosen, and this scale is very close to the scale used for the original model of the JBC, for which the scale was 40.0.

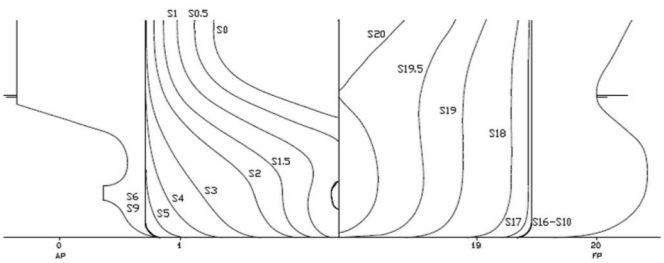


Fig. 1. Hull lines of the JBC.



Fig. 2. 3D model of the JBC.

3. Experimental setup

The ship model scale was primarily chosen so that that the diameter of the propeller model was larger than 200 mm. Care was also taken to avoid any blockage effect, i.e. the impact of the side walls and bottom of the towing tank on the measurement results, and that the displacement of the model was within acceptable limits for handling and operations.

Model tests were conducted in the facility of the Brodarski Institute, which now operates within the company Croatian Shipbuilding Corporation – Jadranbrod (Brodarski Institute, 2022). All tests were carried out in a large towing tank of a length of 276 m, a width of 12.5 m, and a depth of 6 m. It is equipped with a towing carriage with a maximum speed of 14 m/s.

The ship model was manufactured from Obeche wood, on a five-axis CNC milling machine whose positional accuracy is ± 0.2 mm. Figs. 3–5 show certain stages of the manufacturing of the wooden ship model. After the entire surface of the model was properly sanded and smoothed, the model was finally painted with yellow varnish. Afterwards, the model was placed on a measuring device, on which the centreline, sections, and water lines (draughts) were marked with a black marker.

The model was additionally equipped with a propeller and rudder, Fig. 6. It is very important to pay attention to their position in relation to the hull. The 3D model of the rudder is available at (NMRI, 2015). Upon completion of the model, a tripwire of a diameter of 1 mm was placed at the position of the theoretical section 19as a turbulence stimulator.

One of the main criteria for selecting the propeller was that its main particulars were most similar to the particulars of the original propeller for the JBC, Table 2. The geometry of the propeller is presented in Fig. 7. The pitch and maximum blade section thickness at different radii are given in Table 3. The open water diagram of the model and full-scale propeller is given in Fig. 8, and the open water characteristics for the propeller model are presented in Table 4.

Before each test, appropriate ballasting and trimming of the ship was carried out. The mass of the model was within 0.05% of the accurately calculated displacement, and the trim was within ± 0.5 mm of the indicated waterline at the four checked positions on the bow and stern perpendiculars and on the port and starboard sides at the midship of the model.

The setup for the experiments included outfitting the model with measurement equipment and a drive system, as described in more detail in Subsections 3.1-3.3. The experiments that were carried out were the resistance, open water, and self-propulsion tests.



Fig. 3. Preparation of the initial workpiece.



Fig. 4. Milling procedure in a five-axis milling machine.

Table 1
The main particulars of the JBC at the model and full scale at three loading conditions.

Main particular	Design draught		Light ballast draught		Heavy ballast draught	
	Full scale	Model scale	Full scale	Model scale	Full scale	Model scale
Length between perpendiculars, L_{PP}, m	280	6.9541	280	6.9541	280	6.9541
Length of waterline, L_{WL}, m	285.02	7.0787	278.23	6.9102	278.82	6.9248
Breadth, B, m	45	1.1176	45	1.1176	45	1.1176
Draught at forward perpendicular, T_F, m	16.50	0.4097	7.22	0.1792	9.70	0.2409
Draught at aft perpendicular, T_A, m	16.50	0.4097	10.01	0.2487	11.40	0.2831
Draught at midship, T_M, m	16.50	0.4097	8.61	0.2139	10.55	0.2620
Wetted surface area, S, m^2	19592	12.0848	14646	9.0340	15793	9.7417
Displacement volume, ∇, m^3	178232	2.7305	89149	1.3657	110683	1.6956
Longitudinal centre of buoyancy, L_{CB}, m	7.12	0.1767	4.34	0.1078	6.82	0.1694
Vertical centre of buoyancy, Z_{CB}, m	8.45	0.2099	4.37	0.1086	5.36	0.1331
Block coefficient, C_B	0.8575		0.7688		0.8065	
Midship section coefficient, C_M	0.9981		0.9963		0.9970	
Longitudinal prismatic coefficient, C_P	0.8586		0.7735		0.8092	
Waterplane area coefficient, C_{WP}	0.9075		0.8717		0.8806	



Fig. 5. Model with a second layer of basic coating with previous painting and manual sanding.

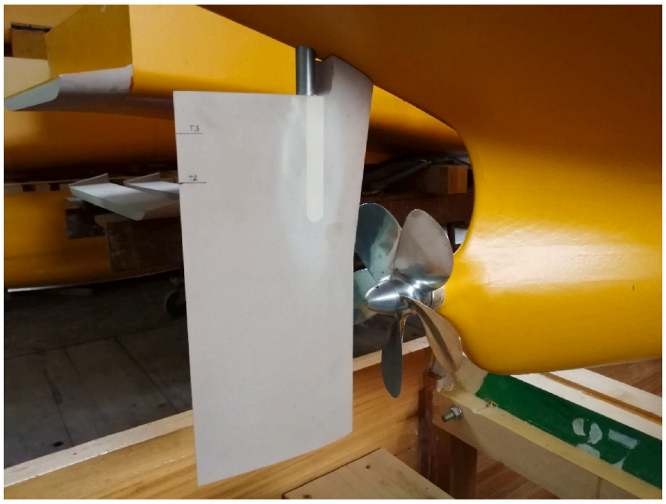


Fig. 6. Rudder and propeller models of the JBC.

Table 2
The main particulars of the propeller model.

Propeller particulars	Original JBC propeller	BI Propeller V–570 (R)
Diameter, D, m	8.120	8.121
Pitch ratio at 0.75R, $P_{0.75R}/D$	0.750	0.736
Expanded blade area ratio, A_E/A_0	0.500	0.644
Ratio of the hub diameter to the propeller diameter (hub ratio), d/D	0.180	0.193
Number of propeller blades, Z	5	
Type of propeller	FPP	

3.1. Resistance test

In the scope of the resistance tests, the following quantities were measured.

- the model speed, i.e. the carriage speed, measured as a distance against time using an incremental encoder and an electronic counter;
- total resistance, measured with a resistance dynamometer;
- running trim, measured with an inclinometer;
- sinkage, measured with a potentiometer;
- water temperature, measured with a thermometer, at a depth close to half of the model draught at the beginning and at the end of each test.

All devices used for data acquisition were calibrated prior to the measurements. The resistance dynamometer was calibrated internally with weights that were calibrated externally. The calibration measurement chain consisting of an amplifier, filter, and A/D converter was the same as the one used for the measurements. Appropriate calibrated devices were used to calibrate the other measuring instruments.

The ship model was connected to the towing carriage through a resistance dynamometer, and it was free to heave and pitch. In order to prevent yawing or swaying motions, guides were placed on the bow and stern of the model. As a standard procedure, zero instrument readings were taken before each run of the model through the towing tank. The waiting time between successive runs was determined based on experience, and it was estimated that a minimum of 20 min was sufficient for the appropriate conditions, i.e. calm water in the towing tank.

The resistance tests were conducted for the design, light, and heavy ballast draughts. The speed range for all three tests was 0.73–1.459 m/s, which corresponds to 9–18 knots for the full-scale ship, and at least 18 measurement points were covered within this range. Repeatability was checked, and the results obtained were within 1%. Based on the sampling, the mean value during the run was determined, and the duration of the measurement signal was at least 20 s.

3.2. Open water test

For the purposes of conducting the open water test, the propeller model was mounted on the drive shaft of a propeller dynamometer. The immersion of the propeller model axis was 1.5D. Within this test, the following quantities were measured:

- speed of the carriage, i.e. speed of advance of the propeller model;
- propeller thrust, measured with a propeller dynamometer;
- propeller torque, measured with a propeller dynamometer;
- propeller rate of revolutions, measured with a revolution counter;
- water temperature, measured with a thermometer.

The propeller dynamometer was calibrated prior to the measurements, and the calibration measurement chain consisting of an amplifier, filter, and A/D converter was the same as the one used for the measurements. The test was carried out in a way that at the same rate of revolution, the propeller model advanced through the water at different speeds, from zero speed up to the speed at which thrust and torque took on negative values. The step chosen for the velocity was quite small and was 0.25 m/s, while propeller revolutions of 26 per second were chosen to achieve a Reynolds number above $6{\cdot}10^5$.

3.3. Self-propulsion test

For the purpose of the self-propulsion tests, the ship model was additionally outfitted with a propeller model, a propeller dynamometer, and an electric motor drive. The quantities measured during each run were the same as the ones measured during the resistance tests. Additionally, propeller thrust, torque, and the propeller rate of revolution were measured as well. These devices were also calibrated with weights prior to the measurement. An end-to-end type of calibration was performed, i.e. the same data acquisition system and software used during the tests with the propeller model were applied. The cables were also the same. The electronic system used throughout testing included amplifiers, low-pass filters, an A/D converter and software. In the calibration process, the Nyquist sampling theorem was consistent with the data rate of the digitised filtered signal to eliminate the aliasing problem. The measurement of the propeller rate of revolution was carried out using an incremental angle encoder.

The British method was applied, and it includes a constant speed of the ship model at a variable load of the ship propeller model, which means that for each speed of the ship model, several measurements were made with a different rate of revolution of the propeller model. Tests were carried out for design draught in the speed range of 0.85–1.34 m/s

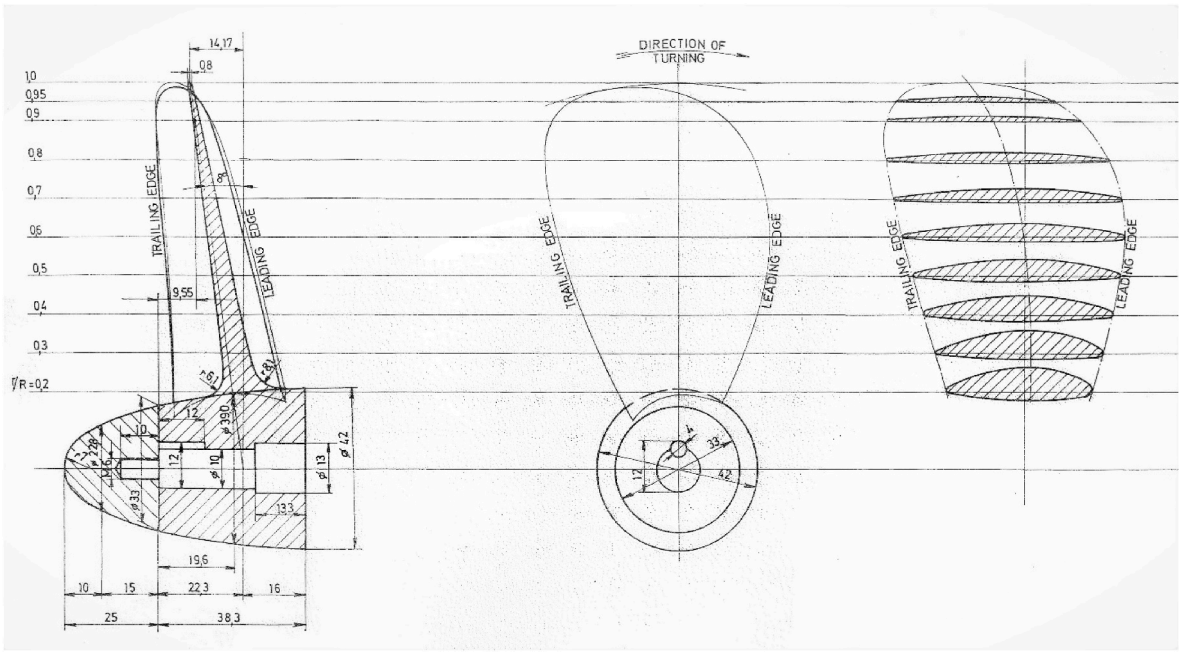


Fig. 7. Geometry of the propeller BI Propeller V–570 (R) (original drawing) (Brodarski Institute, 2022).

Table 3
Pitch and maximum blade section thickness at different radii.

r/R	r, mm	P, mm	t_{MAX}, mm
0.2	20.17	137.2	8.5
0.3	30.25	138.5	7.5
0.4	40.34	140.1	6.6
0.5	50.42	142.0	5.6
0.6	60.50	144.6	4.6
0.7	70.59	148.4	3.7
0.8	80.67	154.4	2.7
0.9	90.76	161.3	1.7
0.95	95.8	164.4	1.2
1.0	100.84	167.3	0.8

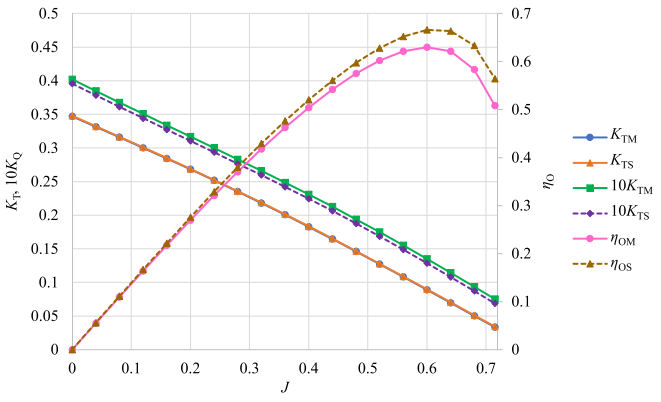


Fig. 8. Open water diagram of the model and full-scale propeller.

which corresponds to 10.5–16.5 knots for the full-scale ship, light ballast draughts in the speed range of 1.013–1.420 m/s which corresponds to 12.5–17.5 knots for the full-scale ship, and for heavy ballast draughts in the speed range 0.929–1.420 m/s which corresponds to 11.5–17.5 knots for the full-scale ship. Self-propulsion tests were carried out for seven speeds for the design and heavy ballast loading condition and for six speeds for the light ballast loading condition. For each speed, between four and seven rates of revolution were taken, which made it possible to obtain an extensive amount of data for further analysis. Given that the hull has a block coefficient larger than 0.85, it was expected that some level of instabilities, such as flow separation, might occur, and therefore it was advisable to carry out the tests in such a way that the measurement points were densely distributed.

Table 4
Open water characteristics for the propeller model.

J_M	K_{TM}	$10K_{QM}$	η_{OM}
0	0.3471	0.4021	0
0.04	0.3316	0.3849	0.0548
0.08	0.316	0.3677	0.1094
0.12	0.3003	0.3507	0.1635
0.16	0.2844	0.3338	0.217
0.2	0.2683	0.3169	0.2695
0.24	0.2519	0.3	0.3208
0.28	0.2352	0.2831	0.3703
0.32	0.2181	0.266	0.4175
0.36	0.2007	0.2487	0.4622
0.4	0.1828	0.231	0.5038
0.44	0.1646	0.2128	0.5416
0.48	0.1461	0.1941	0.5749
0.52	0.1273	0.175	0.6021
0.56	0.1083	0.1552	0.6215
0.6	0.0891	0.135	0.6299
0.64	0.0698	0.1144	0.6212
0.68	0.0504	0.0935	0.5835
0.715	0.0336	0.0753	0.5079

Before the measurement itself, the shaft losses, i.e. frictional losses, were checked on the model equipped only with the "dummy hub", ensuring that there was no interference with the measured data. Besides, before each run, zero readings of each measured value were checked. The data derived from the experiment, namely thrust, torque, and towing force, were first plotted against the square of the rate of revolution and then against the towing force. The corresponding curves were faired, and the ship's self-propulsion points were taken from the diagram.

Measurement uncertainty was calculated on the basis of bias and precision errors (ITTC, 2021). However, precision errors were estimated on the basis of some previous designs of similar characteristics (model

size, scale, and displacement) since it is not a common procedure to conduct additional extensive measurements for each design. Bias errors were determined on the basis of the detailed analysis, thus eliminating some sources of errors which were recognised as negligible (amounting to less than 0.1%), such as impact of the hull ballasting, carriage speed accuracy, and water temperature measurement accuracy. Calibration is considered among the most influential sources of errors including the end-to-end approach, i.e. the dynamometer and acquisition system (amplifier, low pass filters, AD converters and software). The combined uncertainty of bias and precision errors amounts for a single measurement to 0.53% for resistance force, 0.62% for thrust force, 0.78% for torque, and 0.017% for revolutions.

4. Extrapolation methods

4.1. ITTC 1957 Performance Prediction Method

In 1957, the ITTC proposed a method for extrapolating the results of towing tank tests from model to full scale based on the Froude resistance decomposition. By using this method, one can calculate the total resistance of a full-scale ship in the following manner (Bertram, 2000):

$$R_{TS} = \frac{1}{2} C_{TS} \rho_S v_S^2 S_S \tag{1}$$

where C_{TS} is the total resistance coefficient of a full-scale ship, ρ_S is the mass density of fluid, v_S is the ship speed, and S_S is the wetted surface area. The index S denotes values for the full-scale ship. The coefficient C_{TS} is determined using the following equation:

$$C_{TS} = C_{FS} + C_R + C_A \tag{2}$$

where C_{FS} is the frictional resistance coefficient of a full-scale ship, C_R is the residuary resistance coefficient being the same for the model and full-scale ship, and C_A is the incremental resistance coefficient for the model ship correlation. C_{FS} is obtained using the ITTC 1957 model-ship correlation line as follows:

$$C_F = \frac{0.075}{(\log Re - 2)^2} \tag{3}$$

where Re is the Reynolds number.

According to the Froude resistance decomposition, C_R does not depend on the model scale (λ) , and therefore it can be determined from the towing tank results.

To account for scale effects on the resistance components, C_A is added. The values C_A differ between various towing tanks. In the Brodarski Institute, the correlation allowance is determined as the total correlation allowance coefficient based on the database of trial results of more than 1000 vessels, and the procedure is developed by monitoring parameters such as displacement, block and prismatic coefficients, main dimensions, the ratios of the main dimensions, etc., regarding the power prognosis for a particular project. The values taken for different loading conditions are given in Table 5.

Self-propulsion tests were conducted according to the British method. The self-propulsion point of a ship was obtained at the propeller load that corresponds to the skin friction correction calculated as:

$$F_D = \frac{1}{2} \rho_M v_M^2 S_M (C_{FM} - C_{FS} - C_A) \tag{4}$$

Table 5
Incremental resistance coefficient.

Loading condition	$C_A \cdot 10^3$
Design draught	−0.1
Light ballast draught	0
Heavy ballast draught	−0.05

where index M denotes the values for the ship model.

By equalising the difference between the total resistance of the model and thrust with the skin friction correction, $R_{TM} - T_M = F_D$, the propeller rate of revolution (n) for the self-propulsion point of a ship can be determined. The propeller rate of revolution and speed for a full-scale ship can be determined using the Froude similarity law for a certain speed as follows:

$$n_S = \frac{n_M}{\sqrt{\lambda}} \tag{5}$$

$$v_S = v_M \sqrt{\lambda} \tag{6}$$

It is important to note that the thrust and torque for the full-scale ship are obtained by means of scaling laws. The values for the model scale should be multiplied by λ^3 and the density scale λ_ρ for thrust, and λ^4 and the density scale λ_ρ for torque to obtain values for the full-scale ship.

Once the resistance and thrust for a full-scale ship at a certain speed are calculated, the thrust deduction fraction (t) can be easily calculated. The wake fraction (w) is determined using the thrust and torque identity approach. In the ITTC 1957 extrapolation procedure, it is assumed that there are no scale effects on w i.e., $w_M = w_S$. The scale effects on the results of the open water test are also neglected.

4.2. ITTC 1978 Performance Prediction Method

Nowadays, the ITTC 1978 Performance Prediction Method is widely used by towing tanks. The total resistance coefficient of a full-scale ship is decomposed as follows:

$$C_{TS} = (1+k) C_{FS} + C_W + \Delta C_F \tag{7}$$

where k is the form factor obtained by Prohaska's method, C_W is the wave resistance coefficient being the same for the model and full-scale ship, and ΔC_F is the roughness allowance that can be calculated as:

$$\Delta C_F = 0.001 \cdot \left[105 \left(\frac{k_S}{L_{WL}} \right)^{\frac{1}{3}} - 0.64 \right] \tag{8}$$

where k_S is the roughness equal to $k_S = 150 \cdot 10^{-6}$ m.

The thrust and torque coefficients are extrapolated to full scale as follows:

$$K_{TS} = K_{TM} + 0.3Z \frac{c}{D_S} \frac{P_S}{D_S} \Delta C_D \tag{9}$$

$$K_{QS} = K_{QM} - 0.25Z \frac{c}{D_S} \Delta C_D \tag{10}$$

where Z is the number of propeller blades, P_S/D_S is the pitch ratio, c is the chord length at radius $0.75R$, D_S is the propeller diameter at full scale, and ΔC_D is the difference between C_{DM} and C_{DS} defined as follows:

$$C_{DM} = 2 \left(1 + 2 \frac{t_M}{c_M} \right) \left(\frac{0.044}{Re_{co}^{1/6}} - \frac{5}{Re_{co}^{2/3}} \right) \tag{11}$$

$$C_{DS} = 2 \left(1 + 2 \frac{t_S}{c_S} \right) \left(1.89 + 1.62 \log \frac{c_S}{k_p} \right)^{-2.5} \tag{12}$$

where t is the maximum blade thickness at the radius $0.75R$ and k_p is the propeller blade roughness equal to $k_p = 30 \cdot 10^{-6}$ m.

Re_{co} in equation (11) is the Reynolds number at $0.75R_M$ calculated as follows:

$$Re_{co} = \frac{v_{co} c_M}{\nu_M} \tag{13}$$

where v_{co} is given as:

$$v_{co} = \sqrt{v_{AM}^2 + (0.75\pi n_M D_M)^2} \tag{14}$$

Based on the thrust identity approach, the propeller advance ratio at model scale (J_M) can be calculated. With J_M known, w_M can also be determined. Thrust deduction fraction, which is the same for the model and the full-scale ship, can be calculated as:

$$t = 1 + \frac{F_D - R_{TM}}{T_M} \tag{15}$$

where F_D is calculated based on equation (4) being $C_A = \Delta C_F$.

The relative rotative efficiency (η_R) can be calculated as follows:

$$\eta_{RM} = \eta_{RS} = \frac{K_{QM,OWT}}{K_{QM,SPT}} \tag{16}$$

where $K_{QM,SPT}$ is the torque coefficient obtained in the self-propulsion test, and $K_{QM,OWT}$ is the torque coefficient obtained in the open water test.

The wake fraction for the full-scale ship should be corrected as follows:

$$w_S = w_M \frac{C_{FS}}{C_{FM}} + (t + 0.04)\left(1 - \frac{C_{FS}}{C_{FM}}\right) \tag{17}$$

To obtain n_S, the curve for a parameter $(K_T/J^2)_S$ has to be drawn in an open-water diagram for the full-scale ship, and the intersection of $(K_T/J^2)_S$ and K_{TS} curves gives the design point and consequently J_S. The parameter $(K_T/J^2)_S$ is determined as follows:

$$\left(\frac{K_T}{J^2}\right)_S = \frac{T_S}{\rho_S D_S^2 v_{AS}^2} = \frac{S_S}{2D_S^2} \cdot \frac{C_{TS}}{(1-t)(1-w_S)^2} \tag{18}$$

Afterwards, the torque coefficient and propeller efficiency in open water can be read from the diagrams $K_{QS} = f(J_S)$ and $\eta_{OS} = f(J_S)$, respectively. The propeller rate of revolution for the full-scale ship can be calculated as follows:

$$n_S = \frac{(1 - w_S)v_S}{J_S D_S} \tag{19}$$

The torque and thrust of the full-scale ship are determined as:

$$Q_S = \frac{K_{QS}}{\eta_R} \rho_S n_S^2 D_S^5 \tag{20}$$

$$T_S = \left(\frac{K_T}{J^2}\right)_S J_S^2 \rho_S n_S^2 D_S^4 \tag{21}$$

The delivered power and quasi-propulsive efficiency coefficient of the full-scale ship are then:

$$P_{DS} = 2\pi Q_S n_S \tag{22}$$

$$\eta_{DS} = \eta_{OS}\eta_R\eta_{HS} \tag{23}$$

4.3. ITTC 1978 Performance prediction Method (1999)

In 1999, the ITTC proposed a modification of the ITTC 1978 Performance Prediction Method with regard to the wake fraction of the full-scale ship:

$$w_S = (t + 0.04) + (w_M - t - 0.04)\frac{(1+k)C_{FS} + \Delta C_F}{(1+k)C_{FM}} \tag{24}$$

where 0.04 accounts for the rudder effect.

4.4. ITTC 1978 Performance prediction method (2017)

The 19th ITTC suggested a modification of the roughness allowance:

$$\Delta C_F = 0.044\left[\left(\frac{k_s}{L_{WL}}\right)^{1/3} - 10Re^{-1/3}\right] + 0.000125 \tag{25}$$

The correlation allowance was separated from the roughness allowance and is calculated as follows:

$$C_A = 0.001 \cdot (5.68 - 0.6 \log Re) \tag{26}$$

However, each towing tank should use its own model-ship correlation based on the systematic comparison between the sea trial results and the results obtained from the model tests. This correction takes into account any systematic error during the model tests and prediction procedures, as well as any facility bias.

5. Results

5.1. Experimental results

The total resistance coefficient of the ship model as a function of speed is shown in Fig. 9 for the design, light ballast, and heavy ballast draughts. The form factors were determined by means of Prohaska's method and are as follows: $k = 0.2988$, $k = 0.2921$, and $k = 0.3687$ for the design, light ballast and heavy ballast draughts, respectively. The total resistance of the ship model is given in Table 6 and Fig. 10.

The ship model during the resistance test at speed $v_M = 1.221$ m/s for the design, light, and heavy ballast draughts is shown in Figs. 11, 13 and 15, respectively. The ship model during the self-propulsion test at speed $v_M = 1.176$ m/s for the design, light, and heavy ballast draughts is shown in Figs. 12, 14 and 16, respectively.

5.2. Extrapolated results

In this section, the resistance and propulsion characteristics of the full-scale ship for three loading conditions obtained using four extrapolation methods are presented. As stated in Section 4, the applied extrapolation methods are ITTC 1957, ITTC 1978, ITTC 1978 (1999), and ITTC 1978 (2017).

5.2.1. Design draught

In this subsection, the resistance and propulsion characteristics of the full-scale ship for the design draught obtained using four extrapolation methods are presented in Figs. 17–21. The resistance and propulsion characteristics given within these figures are the total resistance coefficient, the thrust deduction fraction, the relative rotative efficiency, the wake fraction, the propeller advance ratio, the propeller efficiency in open water, the hull efficiency, the propeller rate of revolution, the

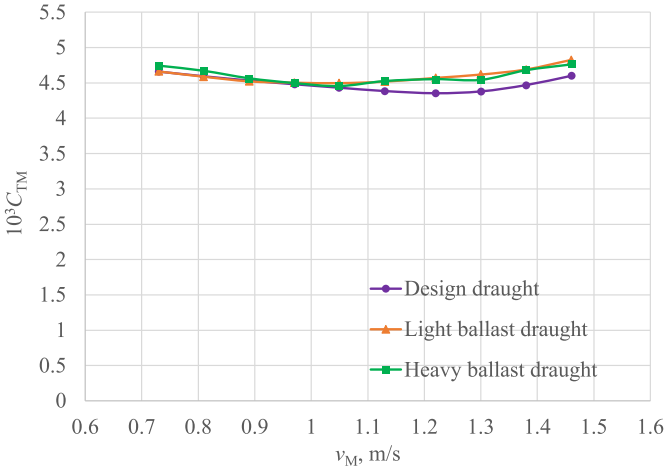


Fig. 9. Total resistance coefficient of ship model as a function of speed.

Table 6
Total resistance of the ship model for design, light ballast, and heavy ballast draught.

Fr	v_M, m/s	V, knots	R_{TM}, N		
			Design draught	Light ballast draught	Heavy ballast draught
0.088	0.73	9	15.130	11.314	12.445
0.097	0.809	10	18.318	13.674	15.049
0.107	0.89	11	21.876	16.312	17.792
0.116	0.97	12	25.682	19.255	20.820
0.126	1.049	13	29.707	22.535	24.116
0.136	1.13	14	34.099	26.272	28.436
0.146	1.221	15	39.466	30.982	33.399
0.156	1.3	16	45.079	35.540	37.778
0.166	1.38	17	51.841	40.673	43.864
0.175	1.46	18	59.740	46.836	49.967

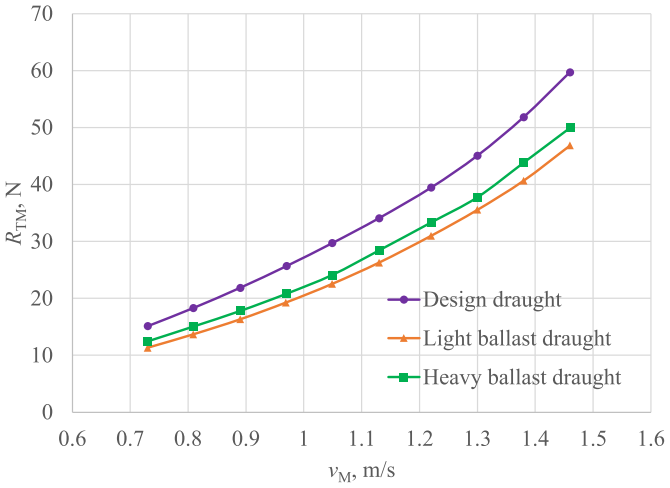


Fig. 10. Total resistance of the ship model as a function of speed.

delivered power, and the quasi-propulsive efficiency coefficient.

As can be seen in Fig. 17, the trend of the curves for the total resistance coefficient for the full-scale ship is similar for all extrapolation methods. The obtained extrapolated values show significant differences when the ITTC 1957 extrapolation method is applied in comparison to other extrapolation methods. On the other hand, the total resistance coefficients obtained by ITTC 1978 (1999) and ITTC 1978 (2017) are almost identical since the roughness allowance is taken into account in the same way. The differences between the results obtained using ITTC 1978 (2017) and the results obtained using ITTC 1978 and ITTC 1978 (1999) lie in the fact that the ITTC 1978 (2017) methods take into account the roughness and the correlation allowance separately. In the same figure, it can be seen that the thrust deduction fraction is similar for all applied extrapolation methods and is the same for the model and the full-scale ship.

The relative rotative efficiency is shown in Fig. 18. It can be seen that the trend of the curves obtained by all extrapolation methods is the same. However, the values obtained using the ITTC 1957 method are lower at lower speeds. For speeds greater than 15 knots, the differences between the obtained results vanish. The results obtained by ITTC 1978 (1999) and ITTC 1978 (2017) are almost identical. On the other hand, the wake fraction obtained by the ITTC 1957 method is significantly different and larger in comparison to the results obtained by other methods, with the trend of the curve being completely different. The reason is that the ITTC 1957 method assumes that there are no scale effects on the wake fraction. The wake fraction obtained by the ITTC 1978 method is lower compared to the wake fraction obtained by the ITTC 1978 (1999) and ITTC 1978 (2017) methods. Starting from 1999, the ITTC proposed a modification of the ITTC 1978 Performance Prediction Method with regards to the wake fraction of the full-scale ship according to equation (24). The differences obtained between the ITTC 1978 (1999) and ITTC 1978 (2017) methods are attributed to the fact that in the ITTC 1978 (2017) method the correlation allowance was separated from the roughness allowance. As can be seen from Fig. 18, the scale effects on the wake fraction are more pronounced at lower



Fig. 11. Fore part (left) and aft part (right) of the ship model during the resistance test at $v_M = 1.221$ m/s for design draught.



Fig. 12. Fore part (left) and aft part (right) of the ship model during the self-propulsion test at $v_M = 1.176$ m/s for the design draught.



Fig. 13. Fore part (left) and aft part (right) of the ship model during the resistance test at $v_M = 1.221$ m/s for the light ballast draught.



Fig. 14. Fore part (left) and aft part (right) of the ship model during the self-propulsion test at $v_M = 1.176$ m/s for the light ballast draught.

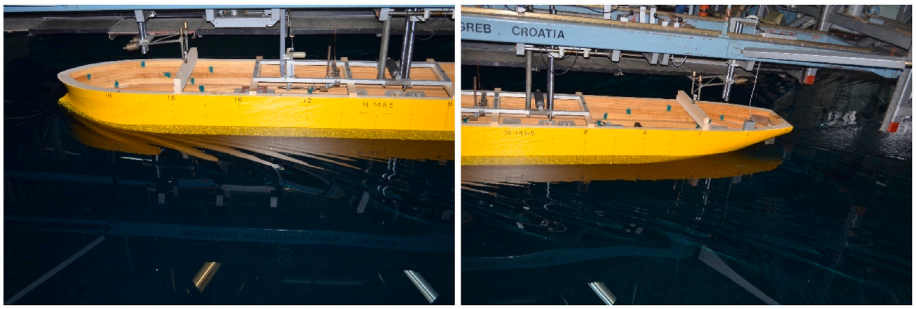


Fig. 15. Fore part (left) and aft part (right) of the ship model during the resistance test at $v_M = 1.221$ m/s for the heavy ballast draught.

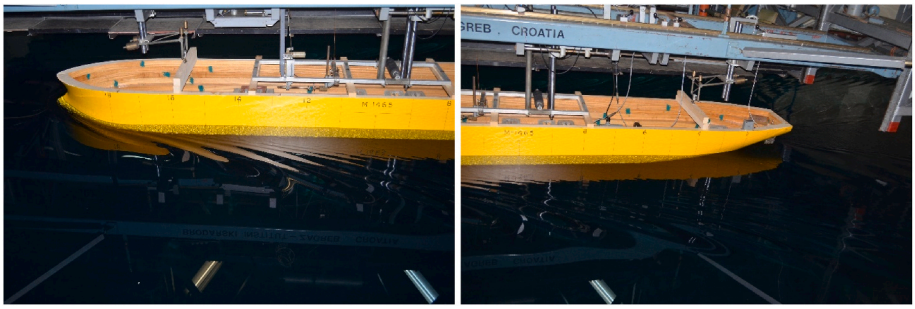


Fig. 16. Fore part (left) and aft part (right) of the ship model during the self-propulsion test at $v_M = 1.176$ m/s for the heavy ballast draught.

speeds.

The propeller advance ratio and efficiency in open water, Fig. 19, are significantly underpredicted by the ITTC 1957 method in comparison to other methods. In the ITTC 1957 method, it is assumed that there are no scale effects on the propulsion characteristics. The propeller advance ratio obtained by the ITTC 1957 method is significantly lower than other methods, and, consequently, the propeller efficiency in open water is lower as well. Since $C_{DM} > C_{DS}$ for a given J, $K_{QS} < K_{QM}$ and $K_{TS} < K_{TM}$, leading to $\eta_{OS} > \eta_{OM}$. Additionally, since the propeller operates at lower values of an advance ratio when the ITTC 1957 method is used, the efficiency in open water is lower. This can be attributed to the fact that the propeller operates at an advance ratio which is lower than the advance ratio for which the efficiency in open water has its maximum.

Hull efficiency for the full-scale ship is significantly overpredicted by the ITTC 1957 method in comparison to other methods, with a decreasing trend, unlike the hull efficiency obtained by other methods, which are almost the same, Fig. 20. Large differences among the obtained results are a consequence of the significantly overpredicted wake fraction by the ITTC 1957 method. The trend of the quasi-propulsive efficiency coefficient obtained by ITTC 1957 for lower speeds is

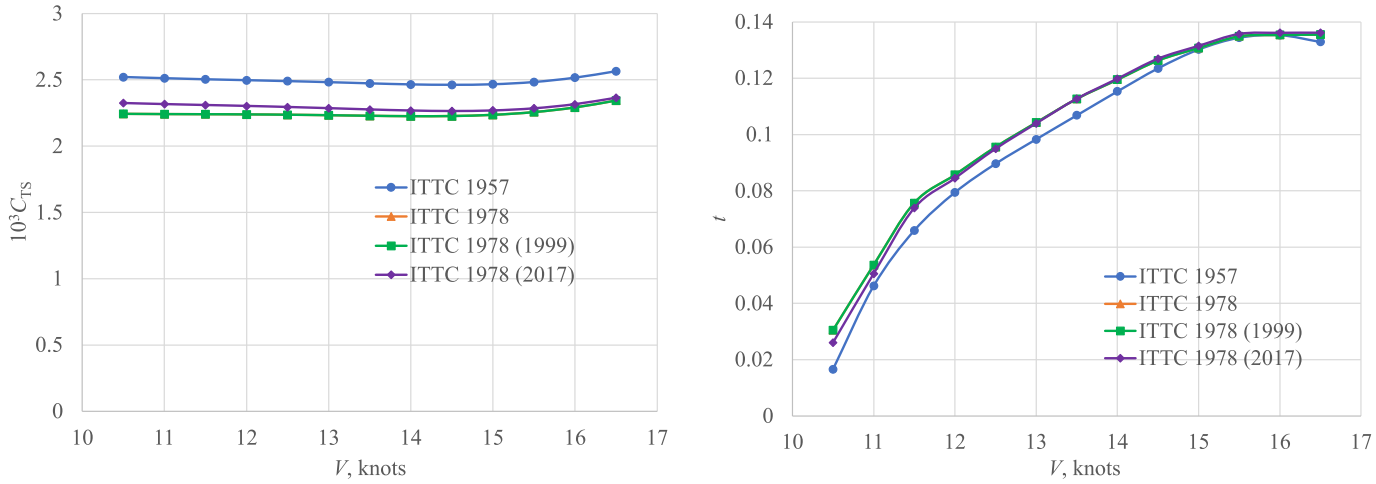


Fig. 17. Total resistance coefficient (left) and thrust deduction fraction (right) as a function of ship speed obtained using different extrapolation methods.

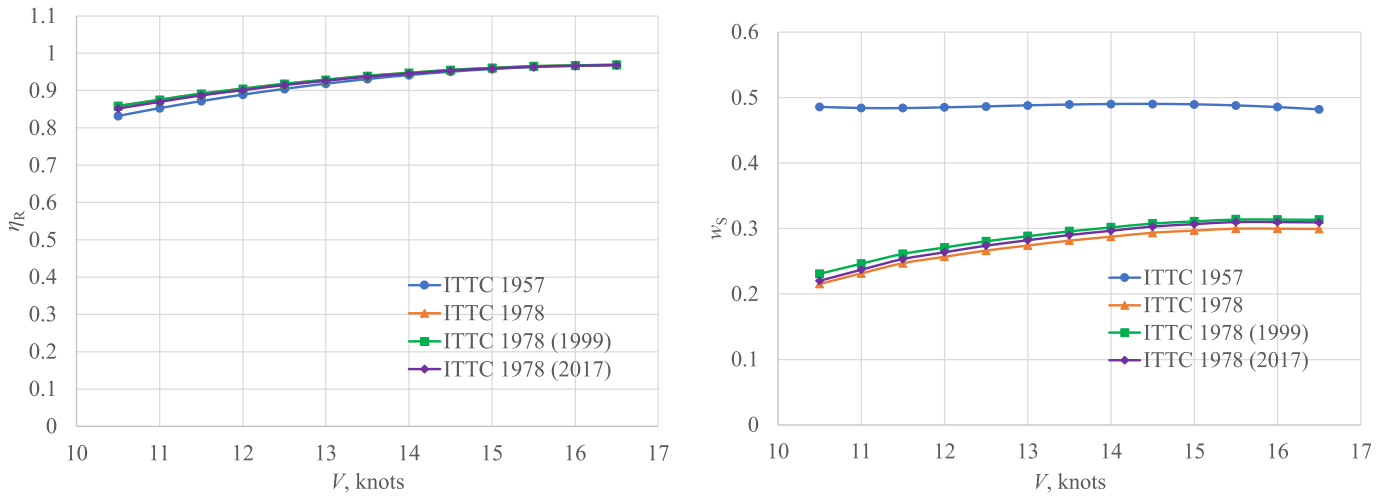


Fig. 18. Relative rotative efficiency (left) and wake fraction (right) as a function of ship speed obtained using different extrapolation methods.

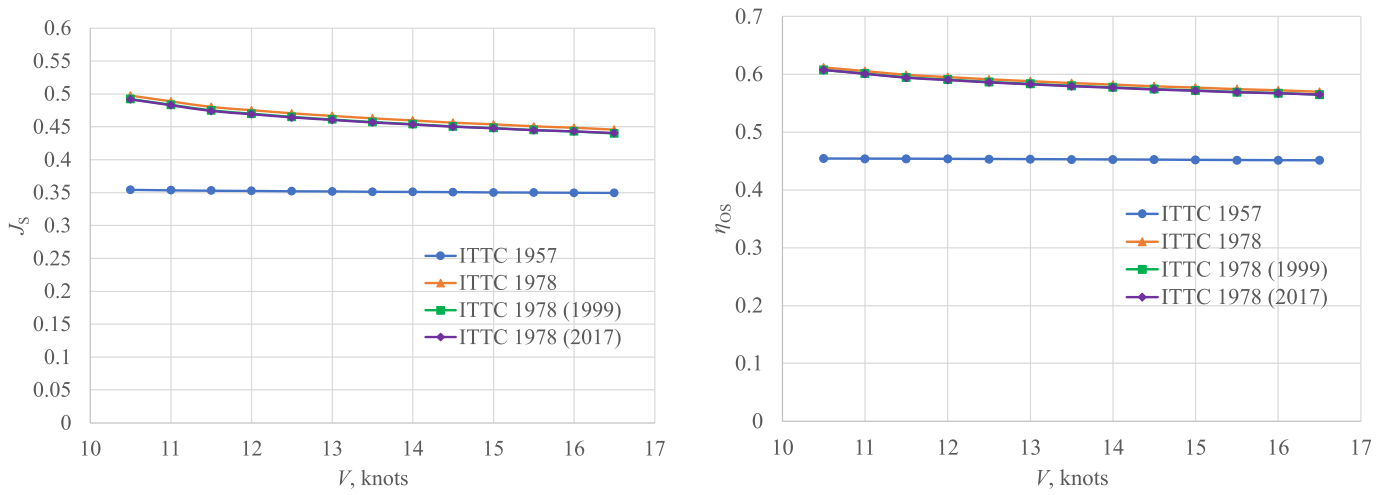


Fig. 19. Propeller advance ratio (left) and propeller efficiency in open water (right) as a function of ship speed obtained using different extrapolation methods.

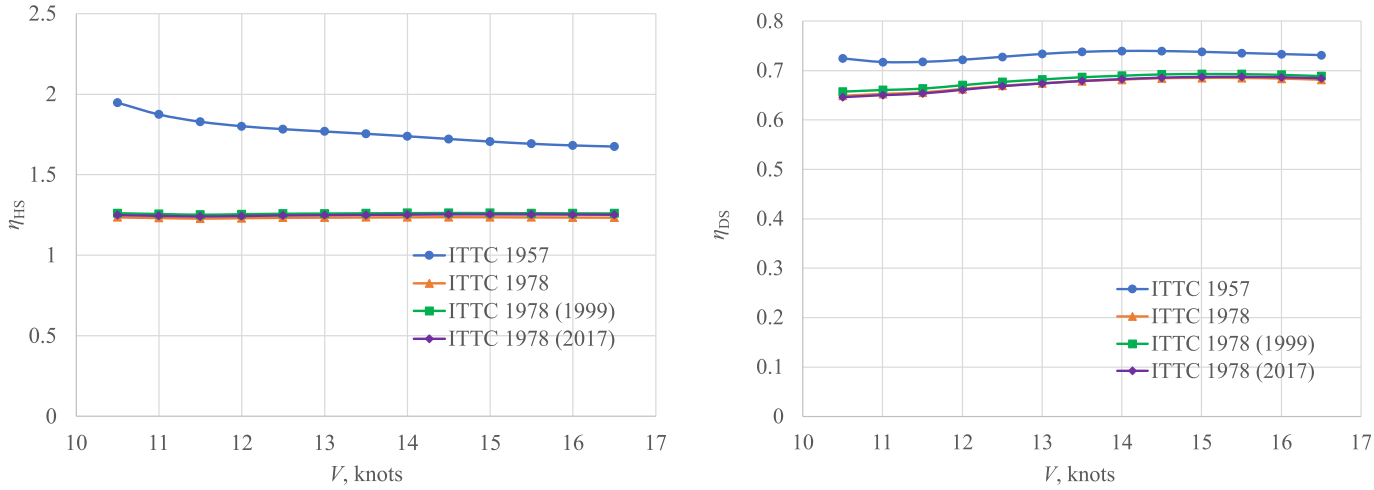


Fig. 20. Hull efficiency (left) and quasi-propulsive efficiency coefficient (right) as a function of ship speed obtained using different extrapolation methods.

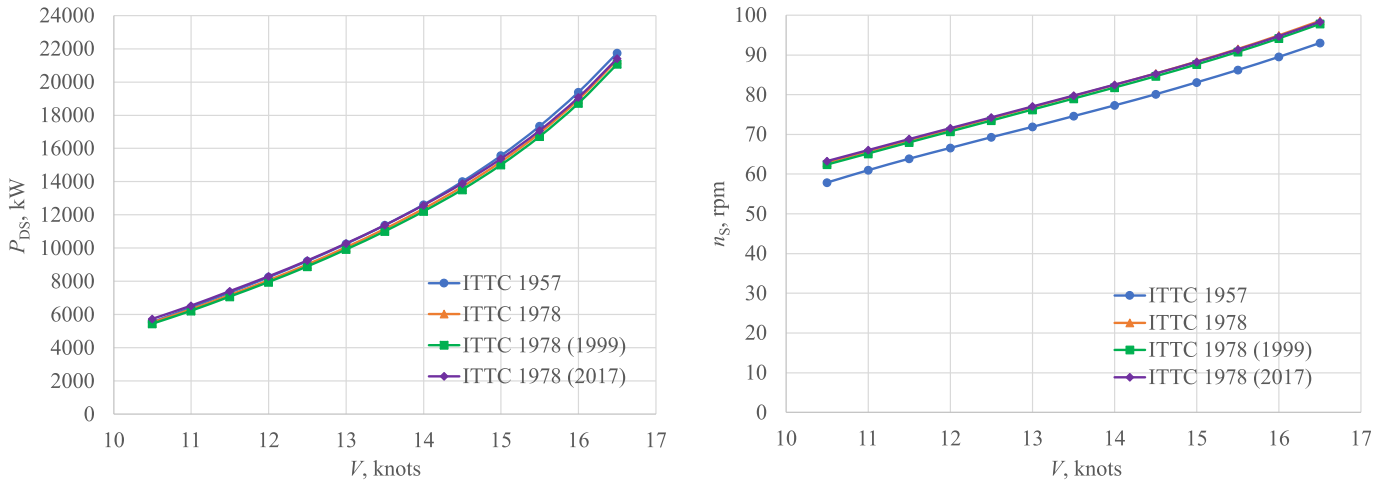


Fig. 21. Delivered power (left) and propeller rate of revolution (right) as a function of ship speed obtained using different extrapolation methods.

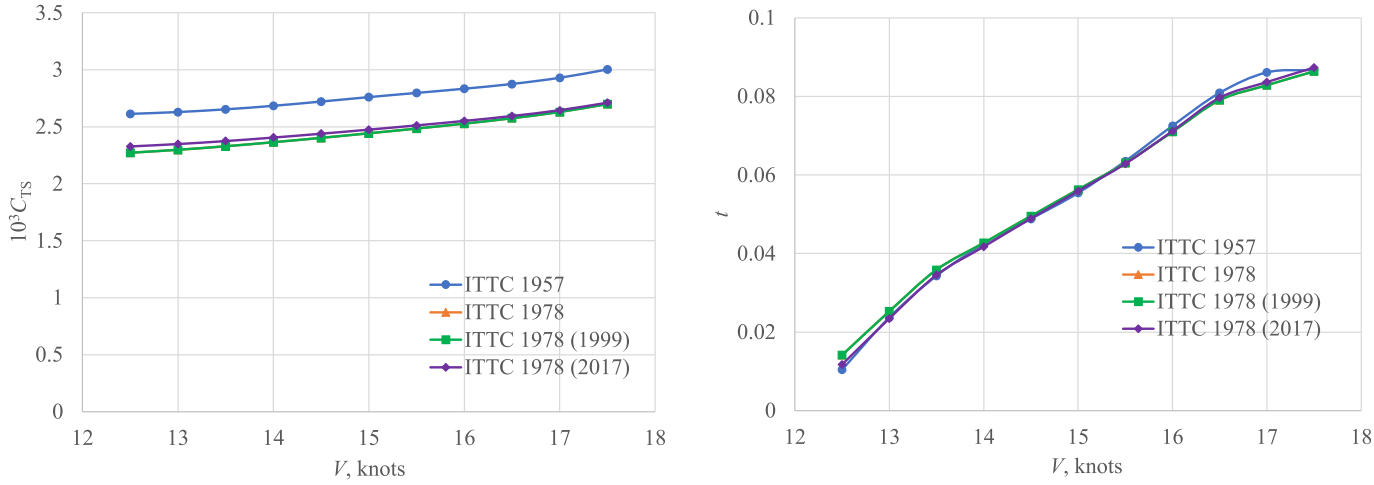


Fig. 22. Total resistance coefficient (left) and thrust deduction fraction (right) as a function of ship speed obtained using different extrapolation methods.

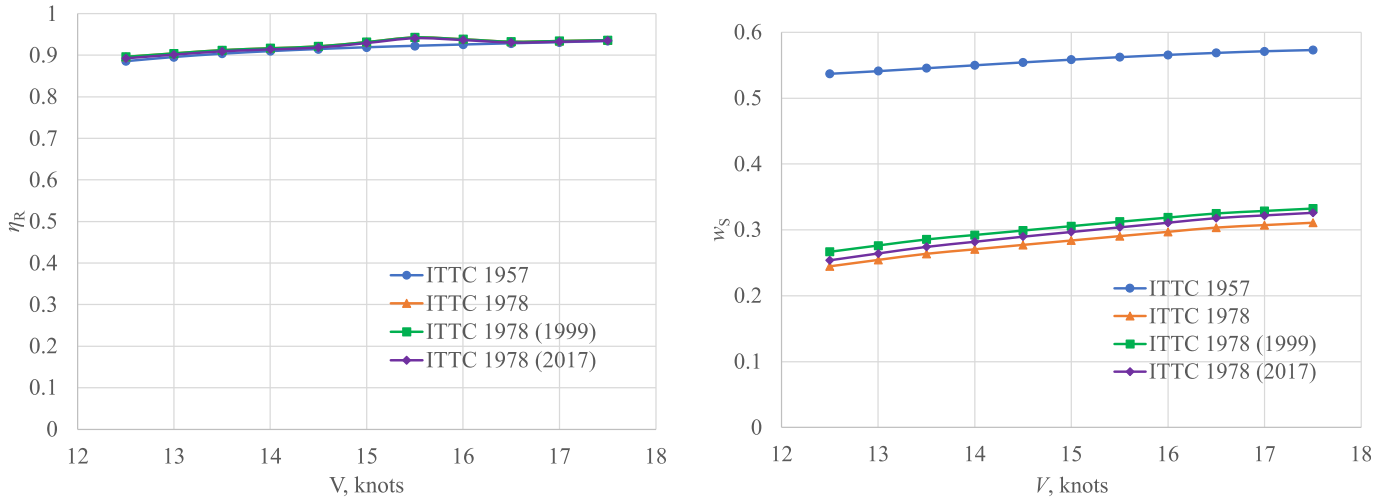


Fig. 23. Relative rotative efficiency (left) and wake fraction (right) as a function of ship speed obtained using different extrapolation methods.

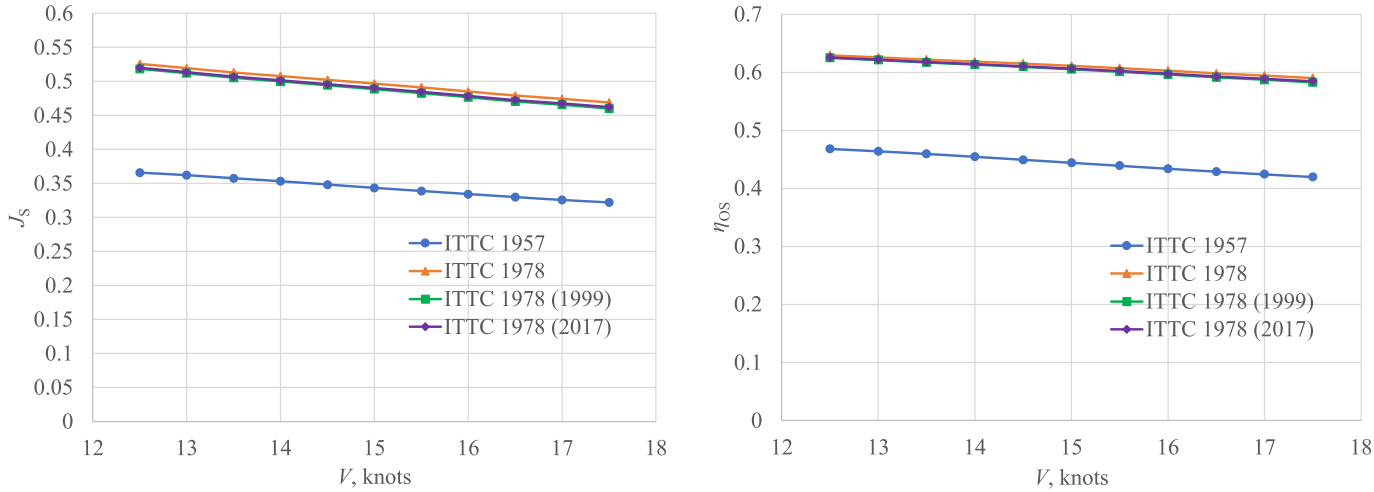


Fig. 24. Propeller advance ratio (left) and propeller efficiency in open water (right) as a function of ship speed obtained using different extrapolation methods.

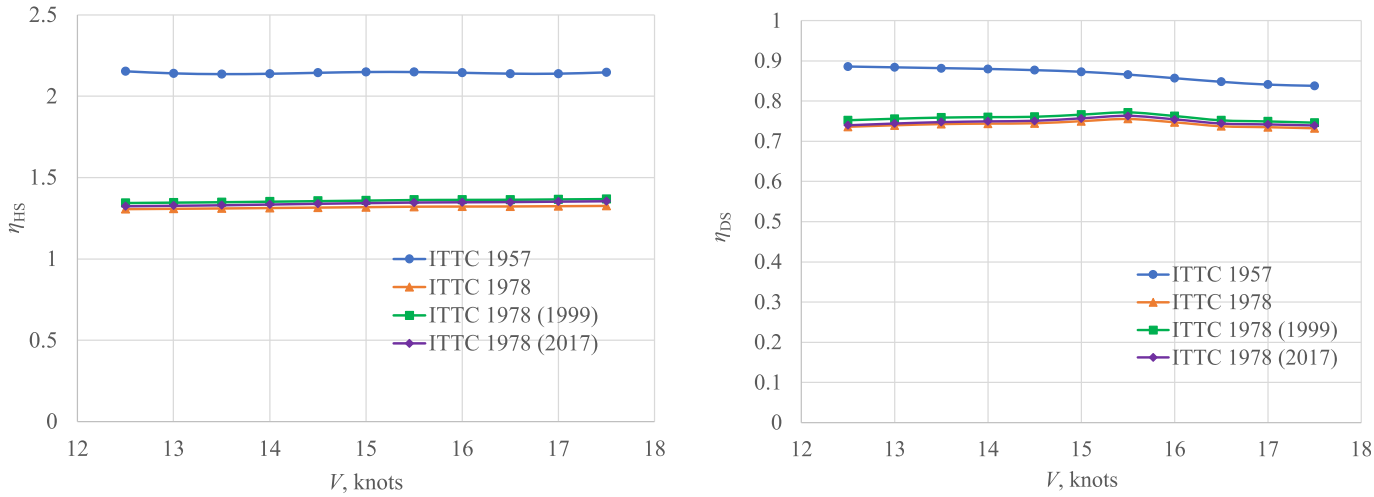


Fig. 25. Hull efficiency (left) and the quasi-propulsive efficiency coefficient (right) as a function of ship speed obtained using different extrapolation methods.

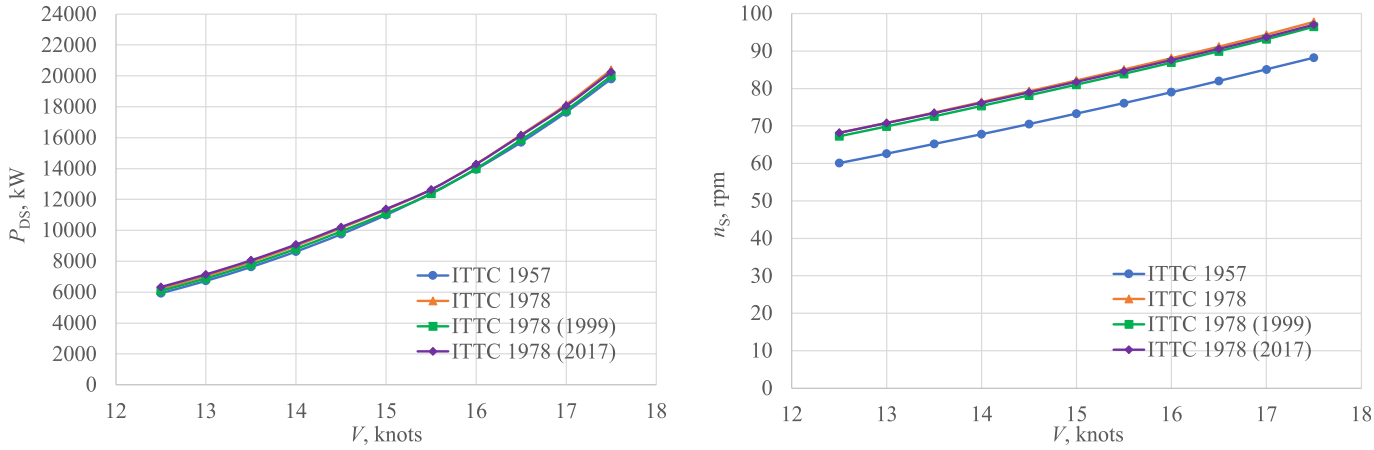


Fig. 26. Delivered power (left) and propeller rate of revolution (right) as a function of ship speed obtained using different extrapolation methods.

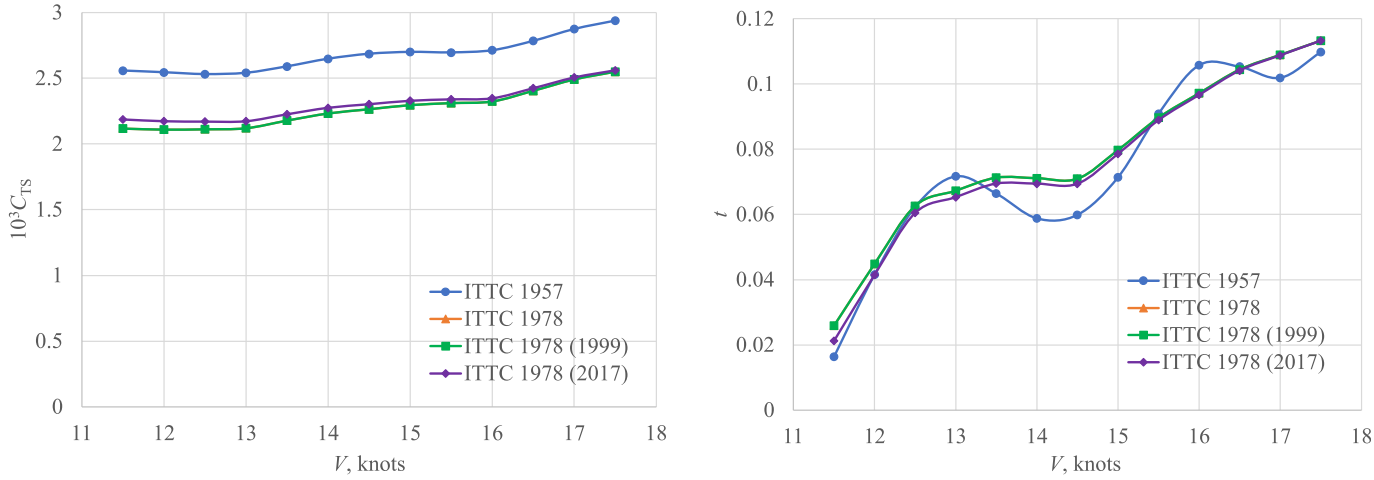


Fig. 27. Total resistance coefficient (left) and thrust deduction fraction (right) as a function of ship speed obtained using different extrapolation methods.

different in comparison to other methods, with the pronounced minimum, due to the large value of hull efficiency. For the same reason, the results obtained by the ITTC 1957 method are noticeably higher when compared to other methods.

The delivered power and propeller rate of revolution as a function of ship speed obtained using different extrapolation methods are given in Fig. 21. The trend of the curves for the propeller rate of revolution is the same for all extrapolation methods. However, the rate of revolution

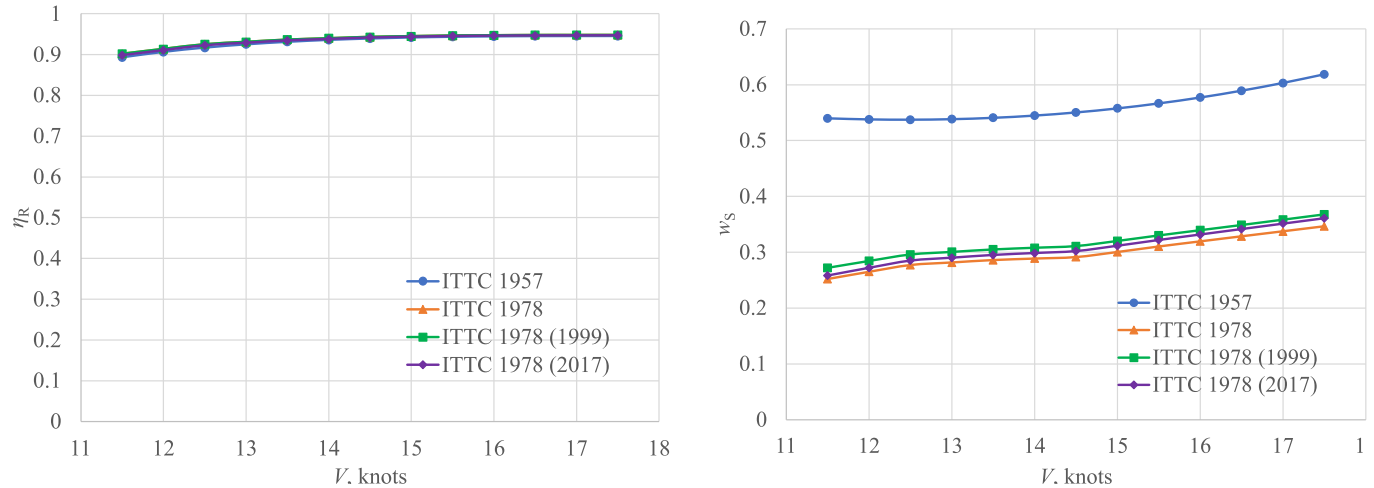


Fig. 28. Relative rotative efficiency (left) and wake fraction (right) as a function of ship speed obtained using different extrapolation methods.

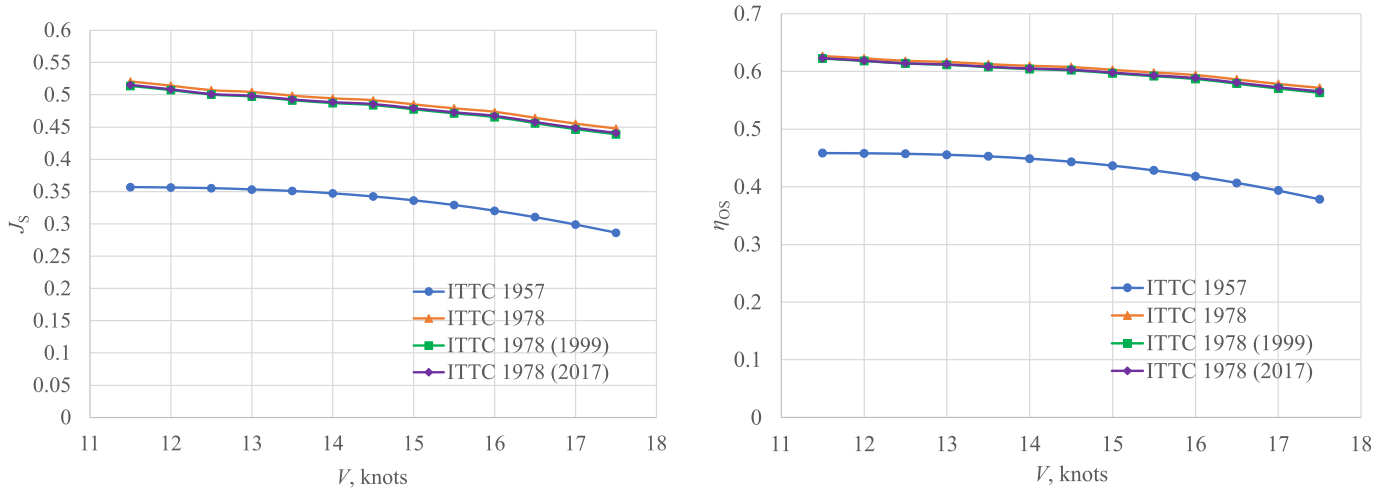


Fig. 29. Propeller advance ratio (left) and propeller efficiency in open water (right) as a function of ship speed obtained using different extrapolation methods.

obtained by the ITTC 1957 method is approximately 5 rpm lower in comparison to other methods. The delivered power for the full-scale ship is almost the same for all investigated extrapolation methods.

5.2.2. Light ballast draught

In this subsection, the resistance and propulsion characteristics of the full-scale ship for the light ballast draught obtained using four extrapolation methods are presented in Figs. 22–26.

The trend of the curves for the total resistance coefficient for the full-scale ship is similar for all extrapolation methods, Fig. 22. As can be seen from Fig. 22, the total resistance coefficient obtained using the ITTC 1957 method is significantly larger in comparison to other extrapolation methods. On the other hand, the total resistance coefficients obtained by ITTC 1978 (1999) and ITTC 1978 (2017) are almost identical. The thrust deduction fraction is similar for all extrapolation methods, Fig. 22.

The relative rotative efficiency for the light ballast condition is shown in Fig. 23. It can be seen that the relative rotative efficiency obtained for 15, 15.5, and 16 knots increases in comparison to the results obtained for other analysed speeds. The wake fraction obtained by the ITTC 1957 method is significantly different and larger in comparison to the results obtained by other methods, with the same trend of the curve.

The propeller advance ratio and efficiency in open water are presented in Fig. 24 which shows that the propeller advance ratio is significantly underpredicted by the ITTC 1957 method in comparison to other methods. Since the propeller advance ratio obtained by the ITTC 1957 method is significantly lower than other methods, the propeller efficiency in open water is lower as well. In comparison to the results obtained with the ITTC 1957 method for the design condition, where propeller efficiency in open water is almost the same for all speeds, for the light ballast condition the trend of the curve is a decreasing one, similar to the curves obtained by other extrapolation methods.

Hull efficiency given in Fig. 25 is significantly overpredicted by the ITTC 1957 method, with a trend different from the ones obtained by other extrapolation methods, where the trend of the curve for hull efficiency is an increasing one. The trend of the quasi-propulsive efficiency coefficient obtained by the ITTC 1957 method is different in comparison to other methods. The curve obtained by the ITTC 1957 method has a decreasing trend, while the curves obtained by other extrapolation methods show a maximum value at 15.5 knots.

Delivered power and the propeller rate of revolution as a function of ship speed obtained using different extrapolation methods are given in Fig. 26. Similar to the design condition, in the light ballast condition, the propeller rate of revolution is underpredicted by the ITTC 1957 method, while the delivered power obtained by all investigated extrapolation methods is almost the same.

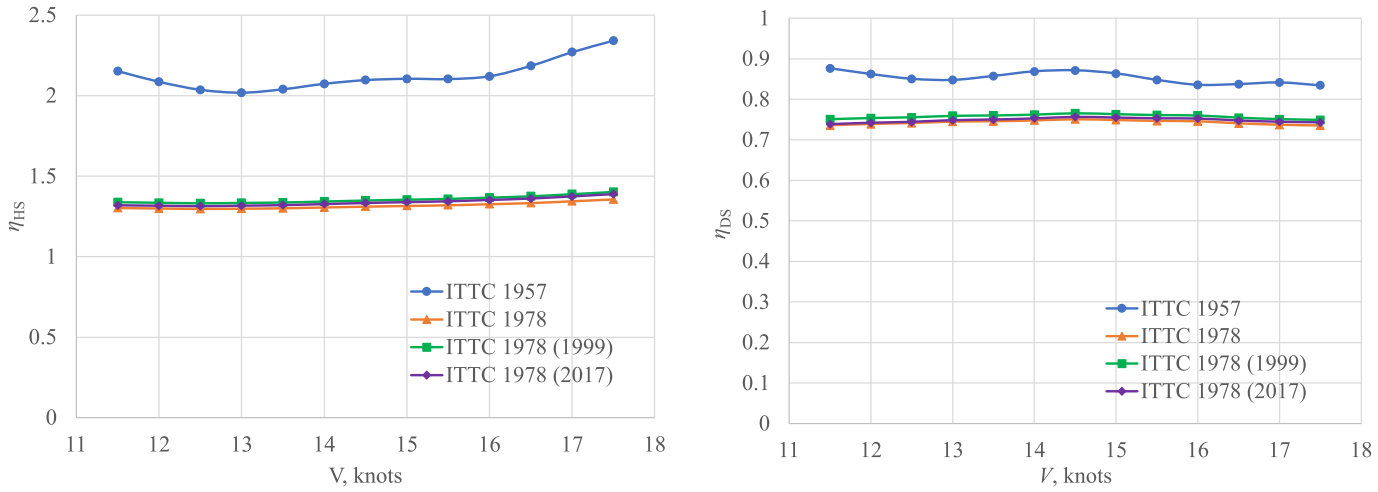


Fig. 30. Hull efficiency (left) and the quasi-propulsive efficiency coefficient (right) as a function of ship speed obtained using different extrapolation methods.

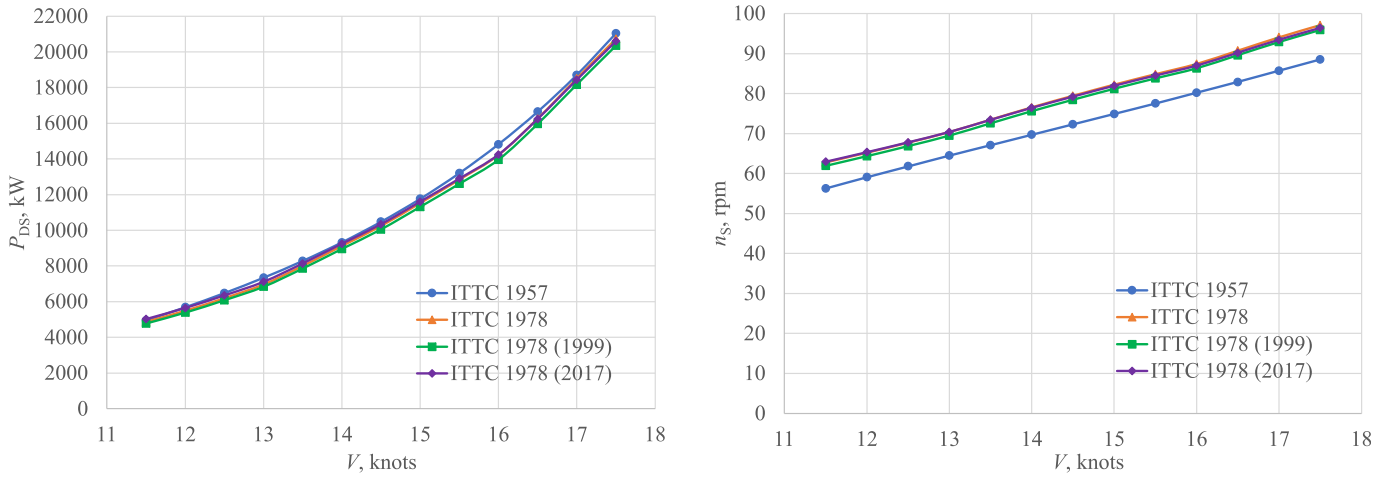


Fig. 31. Delivered power (left) and the propeller rate of revolution (right) as a function of ship speed obtained using different extrapolation methods.

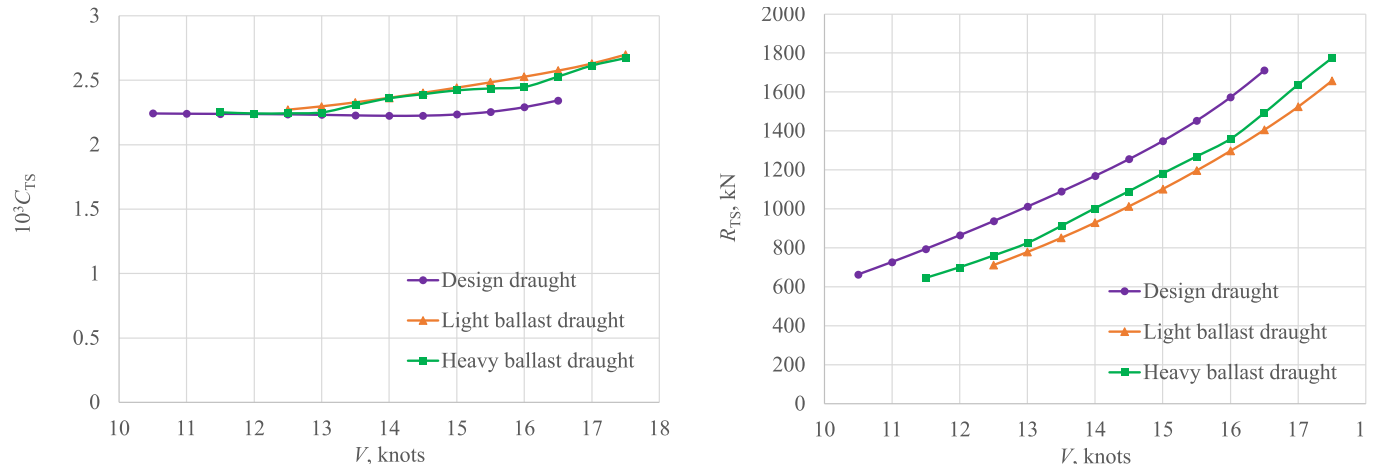


Fig. 32. Total resistance coefficient (left) and total resistance (right) as a function of ship speed for three loading conditions.

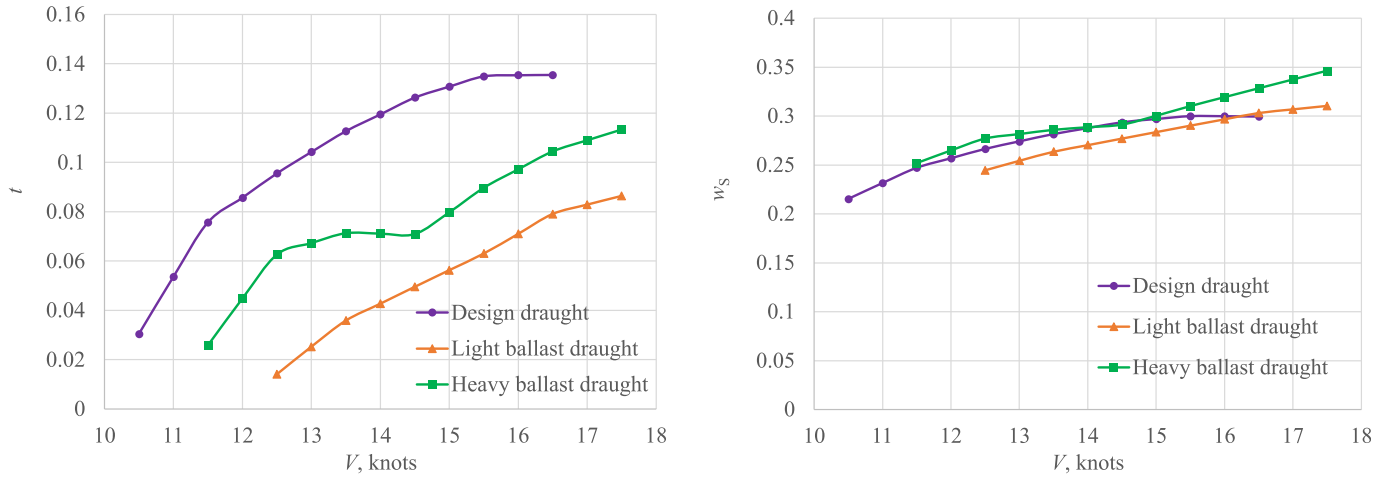


Fig. 33. Thrust deduction fraction (left) and wake fraction (right) as a function of ship speed for three loading conditions.

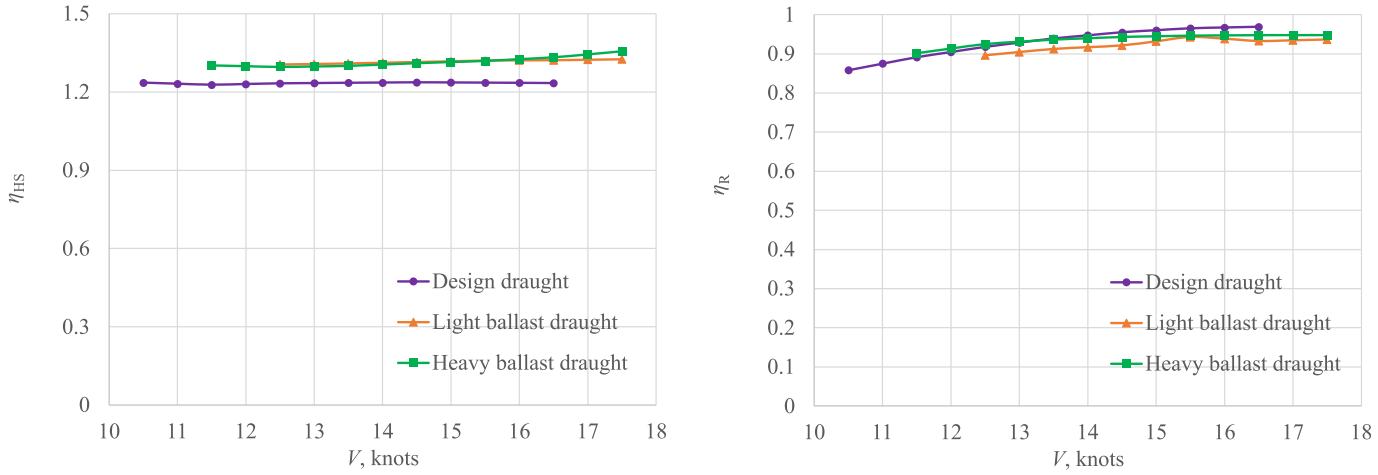


Fig. 34. Hull efficiency (left) and relative rotative efficiency (right) as a function of ship speed for three loading conditions.

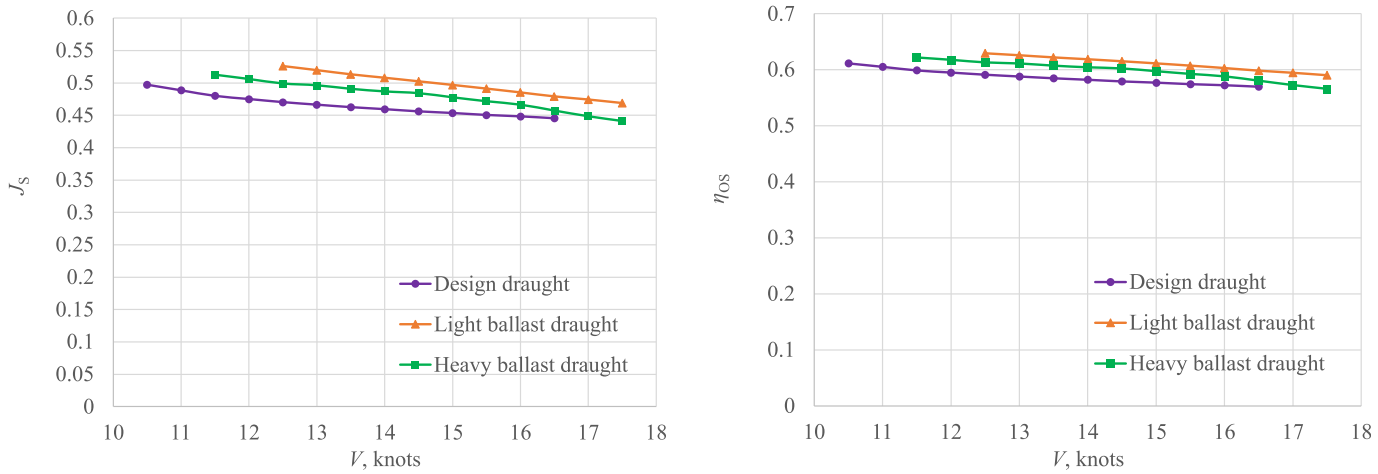


Fig. 35. Propeller advance ratio (left) and propeller efficiency in open water (right) as a function of ship speed for three loading conditions.

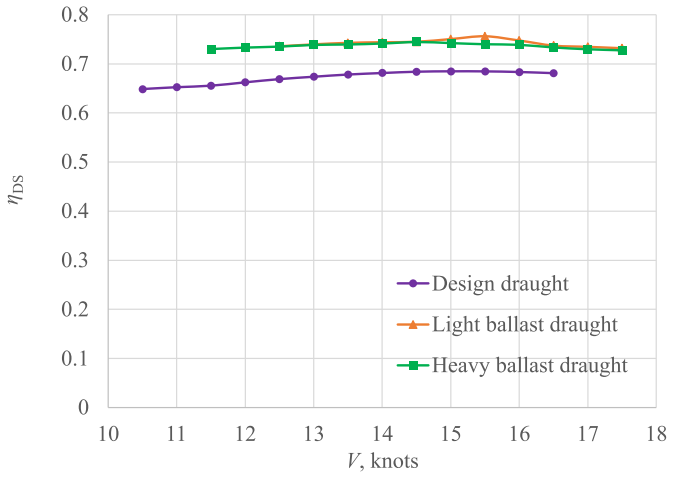


Fig. 36. Quasi-propulsive efficiency coefficient as a function of ship speed for three loading conditions.

5.2.3. *Heavy ballast draught*

In this subsection, the resistance and propulsion characteristics of the full-scale ship for the heavy ballast draught obtained using four extrapolation methods are presented in Figs. 27–31.

No humps or hollows were observed in the curve for the total resistance coefficient, either for the design or for the light ballast draught. For the heavy ballast draught, the presence of both humps and hollows is evident for specific speeds, Fig. 27. Unlike the design draught, the thrust deduction fraction has humps and hollows as well, especially when extrapolated by the ITTC 1957 method. The thrust deduction fraction obtained by ITTC 1978 and ITTC 1978 (1999) is identical and very close to the one obtained by ITTC 1978 (2017).

The differences in relative rotative efficiency for the heavy ballast condition obtained by the analysed extrapolation methods are almost constant for the entire speed range, Fig. 28. Similar to the design and light ballast draught, the wake fraction obtained by the ITTC 1957 method is significantly larger and with a different trend in comparison to the results obtained by other methods.

The propeller advance ratio is again significantly underpredicted by the ITTC 1957 method in comparison to other methods, causing lower propeller efficiency in open water, Fig. 29. Similar to the light ballast condition, the trend of the curve for propeller efficiency in open water is a decreasing one.

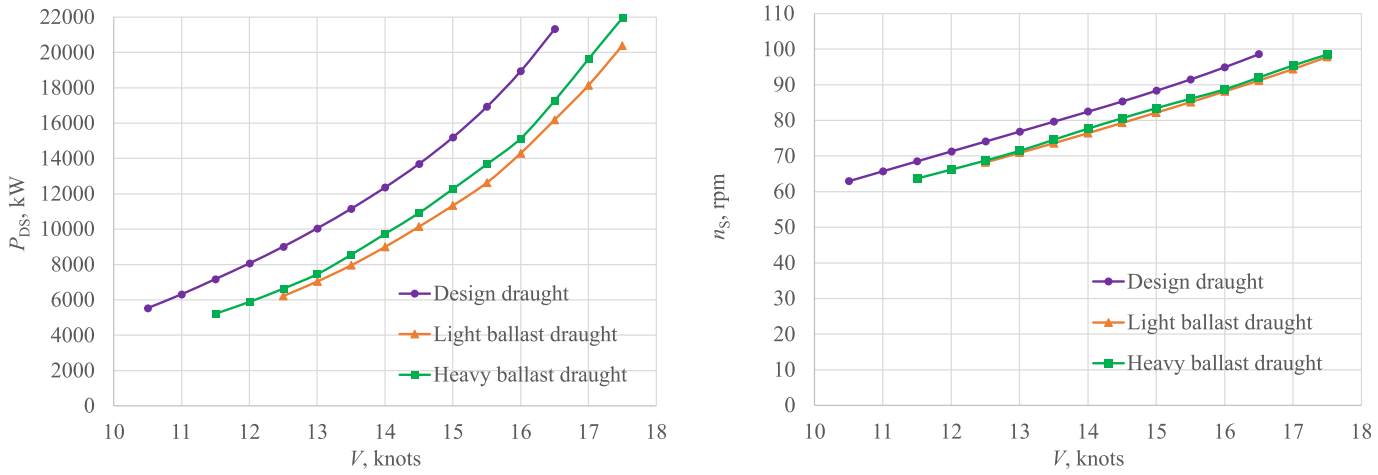


Fig. 37. Delivered power (left) and propeller rate of revolution (right) as a function of ship speed for three loading conditions.

Hull efficiency for the heavy ballast condition is overpredicted by the ITTC 1957 method, with a trend different from the one obtained by other extrapolation methods, and with pronounced humps and hollows due to the trend of thrust deduction fraction, Fig. 30. Consequently, the quasi-propulsive efficiency coefficient obtained by the ITTC 1957 method has two humps and two hollows at particular speeds.

Delivered power and the propeller rate of revolution as a function of ship speed obtained using different extrapolation methods are given in Fig. 31. In the heavy ballast condition, the propeller rate of revolution is underpredicted by the ITTC 1957 method, similar to the design and light ballast. The delivered power obtained by all investigated extrapolation methods is almost the same as obtained for the design and light ballast draught.

5.3. Impact of the loading condition on the resistance and propulsion characteristics

In this subsection, the results extrapolated by the ITTC 1978 method are presented.

As can be seen from Fig. 32, the total resistance for the design draught is larger than those obtained for the light and heavy ballast draughts. The total resistance coefficient for light and heavy ballast draughts is larger in comparison to the design draught for speeds above 13.5 knots, Fig. 32. It can be seen that for particular speeds, the total resistance coefficient for the light and heavy ballast draughts is almost the same. The total resistance is 17.5–24.1% lower for the light ballast draught and 12.4–18.9% lower for the heavy ballast draught in comparison to the total resistance for the design draught. It should be noted that the wetted surface area for the light ballast condition is 25.2% smaller than for the design draught, while for the heavy ballast draught it is 19.2% smaller.

Thrust deduction fraction and wake fraction for three loading conditions are presented in Fig. 33, while hull efficiency is given in Fig. 34. The hull efficiency for the design draught is smaller than the other two draughts since the thrust deduction fraction is larger for the design draught. The values of hull efficiency for the light and heavy ballast draughts are almost the same since both the thrust deduction fraction and wake fraction for the heavy ballast draught are larger in comparison to the light ballast draught, Fig. 33. As can be seen from Fig. 35, the obtained values of the propeller advance ratio for the design draught are lower than the ones for the light and heavy ballast draughts, leading to lower values of the propeller efficiency in open water.

The values for the quasi-propulsive efficiency obtained for the light and heavy ballast draughts are almost the same for the entire speed range except for 15.5 knots, Fig. 36, and larger than for the design draught. The delivered power is 24.1–31% lower for the light ballast draught and 19.1–26.2% lower for the heavy ballast draught in comparison to the total resistance for the design draught, Fig. 37. It can be noticed that differences between the delivered power for the design and the other two draughts are more significant than those for the total resistance, which can be explained by the lower values of quasi-propulsive efficiency obtained for the design draught. Currently, there is no extrapolation method that takes into account all scale effects and provides satisfactory results for different types of ships and loading conditions (Terziev et al., 2022) .

6. Conclusion

In this study, an extensive experimental campaign was conducted to assess the ship resistance and propulsion characteristics of the JBC for three loading conditions. The resistance and self-propulsion tests were carried out at the design, light ballast, and heavy ballast draughts for a wide range of speeds. The open water test was carried out for the propeller whose main particulars were most similar to the particulars of the original propeller for the JBC. The obtained results of the model tests were extrapolated to full-scale using four extrapolation methods, i.e. ITTC 1957, ITTC 1978, ITTC 1978 (1999), and ITTC 1978 (2017). Based on the extrapolated results, it can be seen that the values obtained by the ITTC 1957 method are significantly different from other extrapolation methods that provide similar results. It was shown that the ITTC 1957 extrapolation method overpredicts the resistance in comparison to the ITTC 1978 extrapolation method and its later modifications. In comparison with the ITTC 1957 extrapolation method, in the ITTC 1978 extrapolation method the thrust deduction factor and the relative rotative efficiency are the same for the model and full-scale ship, while on all other propulsion characteristics corrections for scale effects are applied. However, the delivered power for the full-scale ship obtained by all extrapolation methods is the same for the entire speed range, while the propeller rate of revolution is underestimated by the ITTC 1957 method in comparison to other methods.

Without sea trial data, one can argue which quantities contribute to the overprediction of the resistance by the ITTC 1957 extrapolation method. The JBC is a design developed for academic studies and no sea trial data are available. Therefore, it cannot be strictly determined whether it might be better to follow the later ITTC guidelines. It should be noted that the results extrapolated by the ITTC 1978 extrapolation method and its later modifications are based on the standard value for hull roughness due to the lack of measured data for the JBC.

The resistance and propulsion characteristics for different loading conditions are compared for the full-scale ship based on the ITTC 1978

method. Due to the lower values of the quasi-propulsive efficiency for the design draught, the differences between the delivered power for the design and the other two draughts are more significant than those for the total resistance. The propeller rate of revolution is almost the same for the light and heavy ballast draughts for the entire speed range. The limitations of the extrapolation procedures in general are well-known scale effects since model tests are carried out at Froude similarity while Reynolds similarity cannot be fulfilled simultaneously. For this reason, the towing tanks must rely on the experience and databases of both model tests and sea trial data. The absence of sea trial data prevents the development of a reliable and accurate full-scale extrapolation method, especially when it comes to the off-design conditions of ships.

In this paper, an investigation of the resistance and propulsion characteristics of a ship in off-design conditions, such as slow steaming and different loading conditions, was carried out experimentally. This is especially important for ships such as tankers and bulk carriers since almost half of their operational time is spent in ballast conditions. On the other hand, the introduction of slow steaming, with the aim of increasing the energy efficiency of ships, requires a thorough analysis of the ship hydrodynamic characteristics at speeds lower than the design one in order to evaluate the real benefits of slow steaming. The experimental data given in this paper represent a valuable contribution to clarifying the change in hydrodynamic characteristics at different loading conditions for a wide range of speeds. The authors believe that the research carried out in this study will provide a valuable benchmark database for the numerical analysis of ship hydrodynamic performance in off-design conditions. Future study will focus on the numerical assessment of the resistance and propulsion characteristics for different loading conditions. The scale effects on the ship resistance and propulsion characteristics will also be investigated and quantified.

Funding

This study was funded by the Croatian Science Foundation under project IP-2020-02-8568.

CRediT authorship contribution statement

Nastia Degiuli: Conceptualization, Data curation, Formal analysis, Funding acquisition, Investigation, Methodology, Project administration, Resources, Supervision, Validation, Visualization, Writing – original draft, Writing – review & editing. **Ivana Martić:** Conceptualization, Data curation, Formal analysis, Investigation, Methodology, Resources, Validation, Visualization, Writing – original draft, Writing – review & editing. **Andrea Farkas:** Conceptualization, Data curation, Formal analysis, Investigation, Methodology, Resources, Validation, Visualization, Writing – review & editing. **Marta Pedišić Buča:** Conceptualization, Data curation, Formal analysis, Investigation, Methodology, Resources, Validation, Writing – original draft, Writing – review & editing. **Roko Dejhalla:** Conceptualization, Formal analysis, Investigation, Methodology, Validation, Visualization, Writing – review & editing. **Carlo Giorgio Grlj:** Data curation, Formal analysis, Investigation, Methodology, Validation, Visualization, Writing – review & editing, All authors have approved Credit author statement.

Declaration of competing interest

The authors declare that they have no known competing financial interests or personal relationships that could have appeared to influence the work reported in this paper.

Data availability

Data will be made available on request.

Acknowledgements

This study has been fully supported by the Croatian Science Foundation under project IP-2020-02-8568.

References

Bertram, V., 2000. Practical Ship Hydrodynamics. Butterworth-Heinemann, Oxford, Great Britain.
Brodarski Institute, 2022. Report M-1465. Technical Report. Brodarski Institute, Zagreb.
Degiuli, N., Farkas, A., Martić, I., Zeman, I., Ruggiero, V., Vasiljević, V., 2021a. Numerical and experimental assessment of the total resistance of a yacht. Brodogradnja 72 (3), 61–80.
Degiuli, N., Martić, I., Farkas, A., Gospić, I., 2021b. The impact of slow steaming on reducing CO2 emissions in the Mediterranean Sea. Energy Rep. 7, 8131–8141.
Farkas, A., Degiuli, N., Martić, I., 2018. Assessment of hydrodynamic characteristics of a full-scale ship at different draughts. Ocean Eng. 156, 135–152.
Farkas, A., Degiuli, N., Martić, I., Dejhalla, R., 2019. Numerical and experimental assessment of nominal wake for a bulk carrier. J. Mar. Sci. Technol. 24, 1092–1104.
Farkas, A., Degiuli, N., Martić, I., Grlj, C.G., 2022. Is slow steaming a viable option to meet the novel energy efficiency requirements for containerships? J. Clean. Prod. 374, 133915.
Grlj, C.G., Degiuli, N., Tuković, Ž., Farkas, A., Martić, I., 2023. The effect of loading conditions and ship speed on the wind and air resistance of a containership. Ocean Eng. 273, 113991.
IMO, 2016. Guidelines for the development of a ship energy efficiency management plan (SEEMP). MEPC 282 (70). Annexes 9 and 10.
ITTC, 2021. Recommended Procedures and Guidelines, General Guideline for Uncertainty Analysis in Resistance Tests 7 (5), 02-02-02.
Kim, W.J., Van, S.H., Kim, D.H., 2001. Measurement of flows around modern commercial ship models. Exp. Fluid 31 (5), 567–578.
Legović, D., Dejhalla, R., 2015. Numerical hydrodynamic optimisation of a tanker hull form. In: Towards Green Marine Technology and Transport–Proceedings of the 16th International Congress of the International Maritime Association of the Mediterranean, IMAM 2015, Pula, Croatia, 21–24 September 2015. CRC Press/Balkema, Leiden, the Netherlands.
Min, K.S., Kang, S.H., 2010. Study on the form factor and full-scale ship resistance prediction method. J. Mar. Sci. Technol. 15, 108–118.
Molland, A.F., Turnock, S.R., Hudson, D.A., 2017. Ship Resistance and Propulsion. Cambridge University Press.
Niklas, K., Pruszko, H., 2019. Full-scale CFD simulations for the determination of ship resistance as a rational, alternative method to towing tank experiments. Ocean Eng. 190, 106435.
NMRI, 2015. Tokyo 2015 a Workshop on CFD in Ship Hydrodynamics. Japan Bulk Carrier. JBC. https://www.t2015.nmri.go.jp/jbc_gc.html.
Regulations Governing Ballast Management, 2023. https://www.hydracaptainsclub.gr/regulations-governing-ballast-management/.
Saydam, A.Z., Küçüksu, G.N., İnsel, M., Gökçay, S., 2022. Uncertainty quantification of self-propulsion analyses with RANS-CFD and comparison with full-scale ship trials. Brodogradnja 73 (4), 107–129.
Shivachev, E., Khorasanchi, M., Day, S., Turan, O., 2020. Impact of trim on added resistance of KRISO container ship (KCS) in head waves: an experimental and numerical study. Ocean Eng. 211, 107594.
Song, K.W., Guo, C.Y., Wang, C., Sun, C., Li, P., Zhong, R.F., 2020. Experimental and numerical study on the scale effect of stern flap on ship resistance and flow field. Ships Offshore Struct. 15 (9), 981–997.
Terziev, M., Tezdogan, T., Incecik, A., 2022. Scale effects and full-scale ship hydrodynamics: a review. Ocean Eng. 245, 110496.
Van, S.H., Kim, W.J., Yoon, H.S., Lee, Y.Y., Park, I.R., 2006. Flow measurement around a model ship with propeller and rudder. Exp. Fluid 40, 533–545.
Yin, X.B., Lu, Y., Zou, J., Wan, L., 2019. Numerical and experimental study on hydrodynamic bulbous bow hull-form optimisation for various service conditions due to slow steaming of container vessel. Proc. IME M J. Eng. Marit. Environ. 233 (4), 1103–1122.
Zhao, C., Wang, W., Jia, P., Xie, Y., 2021. Optimisation of hull form of ocean-going trawler. Brodogradnja 72 (4), 33–46.

Article VIII

Article published by Elsevier in Ocean engineering on 6 January 2025, available online: https://www.sciencedirect.com/science/article/abs/pii/S0029801825000150

Ocean Engineering 319 (2025) 120300

Contents lists available at ScienceDirect

Ocean Engineering

journal homepage: www.elsevier.com/locate/oceaneng

Research paper

Benchmark study on resistance and propulsion characteristics of a 6750-TEU container ship

Nastia Degiuli [a,*], Ivana Martić [a], Marta Pedišić Buča [b], Carlo Giorgio Grlj [a]

[a] University of Zagreb, Faculty of Mechanical Engineering and Naval Architecture, Ivana Lučića 5, Zagreb, 10000, Croatia
[b] Brodarski Institute, Avenija Većeslava Holjevca 20, Zagreb, 10000, Croatia

ARTICLE INFO

Keywords:
Experimental data
Container ship
FPP
CPP
Resistance and propulsion characteristics
CFD benchmark

ABSTRACT

This paper presents an experimental assessment on the resistance and propulsion characteristics in calm water of the Post Panamax 6750-TEU container ship featuring a transom stern and bulbous bow at a 1:35.18 scale. The resistance and self-propulsion tests were conducted in the large towing tank of Brodarski Institute, covering a broad range of speeds. The experimental uncertainty assessment for the self-propulsion test encompasses both bias and precision errors, evaluated for two Froude numbers. Self-propulsion tests were conducted following the British method, using both fixed pitch and controllable pitch propeller models to gain insight into the hull-propeller interaction. The obtained experimental results are extrapolated using the ITTC 1957 method with the correlation allowance derived from a database of trial results. Given the lack of experimental data regarding resistance and propulsion characteristics for the Post Panamax 6750-TEU container ship, this comprehensive study makes a valuable contribution by providing benchmark data for validating CFD simulations.

1. Introduction

Despite advancements in computational resources enabling numerical methods based on computational fluid dynamics (CFD) to serve as cost-effective and time-efficient alternatives to traditional experimental testing, whether for final design validation or exploring innovative solutions, physical experiments continue to play a significant role in the field. To ensure the reliability and validity of numerical results, a validation study should be conducted by comparing them with experimental data at model scale or with extrapolated data (Liang et al., 2024) and sea trial data for full-scale ships (Mikulec and Piehl, 2023). This necessitates ongoing experimental campaigns using ship models of modern designs and innovative solutions.

Yin et al. (2019) conducted a hydrodynamic optimization study focusing on the design of the bulbous bow to enhance performance under slow steaming conditions for a container ship. While the numerical simulations were performed within the optimization procedure, the experimental tests conducted for the original and optimal hull forms revealed a reduction in the total resistance of more than 10 % in comparison to the original hull form. Guo et al. (2021) analysed the flow around the bow of a research type of ship using silk threads and stereoscopic particle image velocimetry (SPIV) to investigate the phenomenon of bubble sweep-down. Xue et al. (2024) explored the possibility of using the non-refrigerated synthetic model of ice made from polypropylene to simulate ship behaviour in broken ice within a conventional non-refrigerated towing tank, instead of requiring a specialized ice tank. This approach significantly reduces both the time and resources needed for testing, overcoming the problem of a limited amount of data due to these difficulties (Lee et al., 2023). By performing resistance and self-propulsion tests for various loads in calm water and waves for the DTC ship model, Saettone et al. (2021) concluded that propeller loading and ship motions have minimal effect on the relative rotative efficiency. The hull efficiency shows significant sensitivity to ship motions only in the presence of very large wave amplitudes. Since the propulsive efficiency is predominantly affected by variations in the propeller open-water efficiency, overload tests conducted in calm water offer a reliable assessment of propulsion efficiency in waves for the chosen vessel. An interaction between the hull, propeller, and rudder is experimentally investigated for a multi-purpose dry cargo ship with both the conventional and gate rudder systems (Köksal et al., 2024) in calm water and in waves. The authors highlighted the superior performance of the gate rudder system configuration over the conventional one in both conditions, showing enhanced interaction with the hull and propeller, and contribution to the ship performance in oblique waves.

* Corresponding author.
E-mail address: nastia.degiuli@fsb.hr (N. Degiuli).

https://doi.org/10.1016/j.oceaneng.2025.120300
Received 25 November 2024; Received in revised form 20 December 2024; Accepted 2 January 2025
Available online 6 January 2025
0029-8018/© 2025 Elsevier Ltd. All rights are reserved, including those for text and data mining, AI training, and similar technologies.

Shivachev et al. (2020) conducted an experimental and numerical investigation on the impact of trim on the motions and added resistance in waves for the KCS ship model. Their findings indicated that trim has a negligible effect on ship motions. Additionally, the optimal trims in calm water and short waves are similar, whereas the optimal trim in long waves differs from the one in calm water. Su et al. (2023) conducted both experimental and numerical tests on a new type of shallow-water seismic survey ship designed to overcome the limitations of traditional ships. These limitations, including deep draughts and heavy loads, prevent traditional seismic survey ships from meeting the demands of shallow-water marine resource exploration. Zhou et al. (2021) assessed experimentally and numerically the effect of a passing DTMB 5145 model, on a moored KCS model alongside a closed quay. By analysing the transient ship motions, generated waves, as well as hydrodynamic forces acting on the moored ship, the authors highlighted that critical parameters affecting the transient interaction are the speed, water depth, and separation distance.

Resistance tests for bare and appended wind-assisted ships at leeway angles, i.e. Delft Wind-Assist Series, were carried out to validate the Reynolds Averaged Navier-Stokes (RANS) solver used to calculate hydrodynamic forces of wind-assisted commercial ships (van der Kolk et al., 2019). Through a comprehensive experimental study on the resistance and propulsion characteristics of the Japan Bulk Carrier (JBC) in calm water under off-design conditions, Degiuli et al. (2023) established a benchmark database for validating CFD codes. In addition, the authors applied four extrapolation procedures to predict the resistance and propulsion characteristics of a ship at full scale. A comparative analysis of numerically obtained results, experimental data, and sea trial data for the benchmark ship MV Regal (Krasilnikov et al., 2023) revealed that both the delivered power and propeller rate of revolution were underestimated in the numerical and experimental studies when compared to the sea trial data.

Kinaci et al. (2020) demonstrated that satisfactory results can be achieved using smaller-scale models, such as the 1/100 scale DTC ship model used in resistance and self-propulsion tests. To offer guidance for navigation in canals, a series of towing tank tests were carried out on a scaled model of the Kriso Container Ship (KCS) for a wide range of water depth to ship draught ratio at various speeds (Elsherbiny et al., 2019). The experiments were carried out using a 1/75 scale ship model, with the authors noting an experimental uncertainty of over 90 % for sinkage and trim at low sailing speeds. Delen and Bal (2024) assessed the experimental uncertainty of the propulsion characteristics for the Office of Naval Research Tumblehome (ONRT) ship model at two Froude numbers. By repeating the tests, it was determined that the uncertainties affecting key parameters were, in decreasing order of significance, thrust, torque, and propeller rate of revolution.

In this study, the experimental campaign was conducted on a Post Panamax 6750-TEU container ship, which served as a benchmark study for ship motions and loads, carried out by members of the International Towing Tank Conference (ITTC) and the International Ship and Offshore Structure Congress (ISSC) (Kim and Kim, 2016). The experiments in regular head waves were conducted at the Korea Research Institute of Ships and Ocean Engineering (KRISO) for the ship model in a scale of 1/70 consisting of eight segmented hull parts connected to the flexible backbone. Eleven institutions compared the results obtained by 17 numerical codes and obtained satisfactory agreement with the experimental data regarding the heave, pitch, and vertical bending moment in linear test conditions, while some discrepancies were noticed in the case of non-linear test conditions. Wang et al. (2022) employed a non-linear 3D panel method to assess the hydroelastic analysis and concluded that the nonlinear hydrostatic restoring forces, along with first-order wave forces, play a dominant role, and their nonlinear effects become more pronounced as sailing speed increases. Additionally, slamming forces are highly sensitive to changes in wave direction, and the high-frequency impacts between the hull and waves must be carefully considered in head waves under severe conditions. The same 1/65 scale ship model, consisting of nine segments, was used to experimentally investigate wave-induced motions and loads in oblique regular waves without forward speed (Kim et al., 2023). The study analysed the effect of wave steepness on the ship motions, as well as on horizontal and vertical bending moments. Additionally, the effects of the mooring system were examined. Significant efforts were made to gain insight into the phenomena occurring in steep waves and to establish a validation case for computing the vertical bending moment in extreme wave conditions (Horel et al., 2019; Bouscasse et al., 2022). Waskito et al. (2020) experimentally investigated the spatial distribution of wave-induced unsteady pressure across the hull of a 6750-TEU container ship model in waves for the first time, which involved simultaneous pressure measurements at numerous locations on the hull, utilizing pressure sensors. Grlj et al. (2024) assessed the effects of loading conditions and speed on the nominal wake of a 6750-TEU containership experimentally and numerically. The authors concluded that the effect of speed observed experimentally is more pronounced than that obtained through numerical methods, particularly for the integral value of the nominal wake.

Although numerous experimental campaigns have focused on the responses and loads of the 6750-TEU container ship in waves, to the best of the authors' knowledge resistance and self-propulsion tests in calm water have not been conducted so far. In this paper, an extensive experimental campaign of resistance, open water, and self-propulsion tests for a wide range of speeds is carried out. The results of the measurement uncertainty analysis are presented, encompassing both bias and precision errors. Bias errors were determined based on measurements conducted at two Froude numbers. The experimental results offer a valuable contribution to the database used for benchmarking CFD software, while also addressing a gap in the existing literature concerning available experimental data for the 6750-TEU containership model. The remainder of the paper is organized as follows: Section 2 introduces the case study, while Section 3 provides a detailed description of the experimental setup. Section 4 outlines the methodology for assessing experimental uncertainty, and Section 5 explains the approach used to extrapolate model-scale results to full-scale ship. The experimental and extrapolated results are presented in Section 5, with the conclusions summarized in Section 6.

2. Case study

This study focuses on a Post Panamax 6750-TEU container ship, characterized by a transom stern and a bulbous bow. Due to the absence of experimental data on its resistance and propulsion characteristics, the authors assert that this extensive experimental investigation significantly contributes to the benchmark data needed for validating CFD simulations. Resistance, open-water, and self-propulsion tests were performed over a broad range of speeds. The hull lines of the container ship are depicted in Fig. 1, while Fig. 2 provides a visualization of the 3D model. Table 1 outlines the main particulars of the container ship at both model and full scale. Notably, the longitudinal center of buoyancy in Table 1 is referenced to the midship. Positive values indicate a position forward of the midship section, while negative values represent a position aft.

The model tests of a proposed container ship were conducted with two stock propeller models, i.e. fixed pitch propeller, FPP, which belongs to the Wageningen B series, and controllable pitch propeller, CPP at a single pitch. The ship model was manufactured in a geometrical scale of $\lambda = 35.18$ in accordance with the diameter of the selected stock FPP. The propeller diameter was not predetermined; instead, it was derived based on the available space at the stern.

As no marine engine is available to match the required power and revolutions within the speed range corresponding to the design speeds of container ships, the second phase of testing involved measurements with a CPP featuring an increased pitch to further reduce the propeller rate of revolution. The diameter of the CPP remains the same as that of the FPP, measuring $D = 7.3$ m. The main particulars of the CPP and FPP are

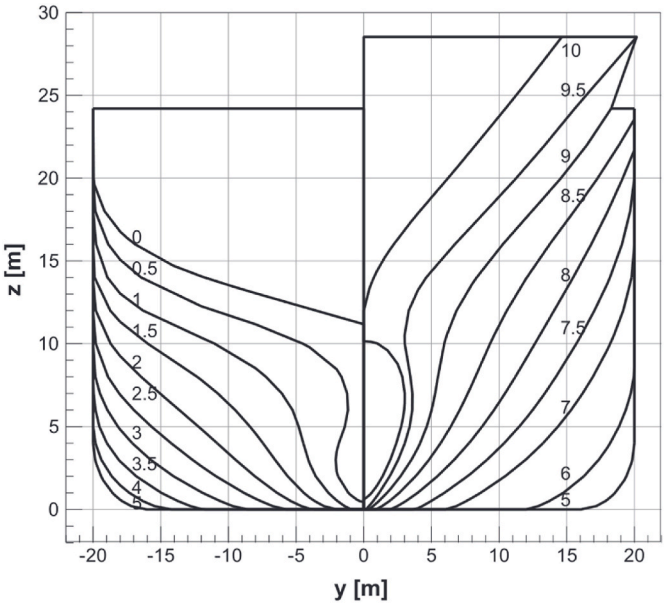


Fig. 1. Hull lines of a 6750-TEU containership (Kim and Kim, 2016).

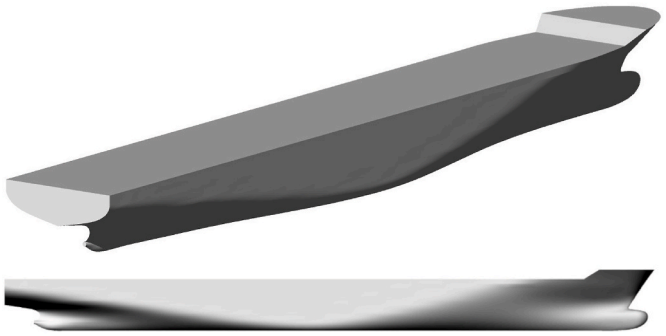


Fig. 2. 3D model of a 6750-TEU containership.

Table 1
The main particulars of a 6750-TEU containership at the model and full scale.

Main particular	Design draught	
	Full scale	Model scale
Scale, λ	1	35.18
Length between perpendiculars, L_{PP}, m	286.58	8.1460
Length of waterline, L_{WL}, m	292.37	8.3107
Breadth, B, m	40	1.1370
Draught at midship, T_M, m	11.98	0.3405
Wetted surface area (bare hull), S, m^2	13325	10.7668
Displacement volume (bare hull), ∇, m^3	85556	1.9650
Longitudinal centre of buoyancy, L_{CB}, m	−5.07	−0.1440
Vertical centre of buoyancy, Z_{CB}, m	6.62	0.1882
Block coefficient, C_B	0.6231	
Midship section coefficient, C_M	0.9850	
Longitudinal prismatic coefficient, C_P	0.6317	
Waterplane area coefficient, C_{WP}	0.7838	

given in Table 2, while the 3D models are presented in Figs. 3 and 4.

3. Experimental setup

The model tests were carried out at the Brodarski Institute (Brodarski Institute, 2022) in a large towing tank measuring 276 m in length, 12.5 m in width, and 6 m in depth, with a towing carriage capable of reaching speeds up to 14 m/s. The ship model scale was selected to ensure that the propeller model's diameter exceeded 200 mm. Additionally, measures were taken to prevent any blockage effects, such as interference from the towing tank's side walls and bottom, and to ensure the model's displacement remained within manageable limits for handling and operations. Details about the manufacturing process of the ship model are explained in detail by Degiuli et al. (2023). Fig. 5 illustrates the stages of the wooden ship model's construction. After thoroughly sanding and smoothing the model's surface, it was given a final coat of yellow varnish, as shown in Fig. 6. The model was further fitted with a propeller and rudder, as shown in Fig. 7, with careful attention given to their alignment with the hull. A 3D model of the rudder is included as supplementary material, while the 3D model of the bare hull can be found at (ISSC, 2021). Once the model was completed, a 1 mm diameter tripwire was placed at the location of theoretical section 19 to act as a turbulence stimulator.

Table 2
The main particulars of propeller models.

Propeller particulars	FPP	CPP
Diameter, D	0.2075 m	0.2073 m
Pitch ratio at 0.75R, $P_{0.75R}/D$	0.8901	1.3
Expanded blade area ratio, A_E/A_0	0.75	0.633
Ratio of the hub diameter to the propeller diameter (hub ratio), d/D	0.1687	0.2957
Number of propeller blades, Z	4	
Direction of rotation	Clockwise	Counterclockwise

Prior to each test, the ship model was carefully ballasted to ensure that its mass was within 0.05% of the precisely calculated displacement. The experimental setup involved outfitting the model with the necessary measurement equipment and a drive system. Resistance, open water, and self-propulsion tests were performed. More details about the measurement equipment, calibration procedures, and the calibration measurement chain can be found in (Degiuli et al., 2023). The ship model was attached to the towing carriage via a resistance dynamometer, enabling it to move freely in heave and pitch. Guides were positioned at the bow and stern to restrict yaw and sway motions. As part of the standard procedure, zero readings of the instruments were recorded prior to each test run. A waiting period of at least 20 min between successive runs was observed to ensure stable and calm water conditions in the towing tank.

The open water tests were conducted using two stock propeller models: V–645 (FPP, right-handed) and V–1324 (CPP, left-handed). During the test, the propeller model was mounted on a horizontal shaft, with the shaft's centerline positioned one and a half times the diameter below the water surface. The test involved advancing the propeller model through the water at various speeds, from zero to the point where thrust and torque became negative while maintaining a constant rate of revolution. The chosen speed increments were 0.5 m/s, with the propeller rate of revolutions equal to 25.01 rps for the FPP and 20.01 rps for the CPP to achieve a Reynolds number above $6{\cdot}10^5$. For the self-propulsion tests, the ship model was equipped with a propeller model, a propeller dynamometer, and an electric motor. The British method was used, where the speed of the ship model remained constant while the propeller model operated at variable loads. For each speed, multiple measurements were taken with different propeller rates of revolution. Before testing, shaft losses due to friction were verified on the model using a "dummy hub" to ensure no interference with the measured data. Additionally, zero readings for all measured values were checked before each run.

4. Experimental uncertainty

The self-propulsion tests were conducted with the ship model M-1468 and stock propeller model V-1324 at the design draught corresponding to $T = 11.98$ m in full scale. The analysis considers two measurement points: one corresponding to the lowest tested speed $V = 16.0$ kn ($v_M = 1.38$ m/s; $Fr = 0.173$) and the other to the highest

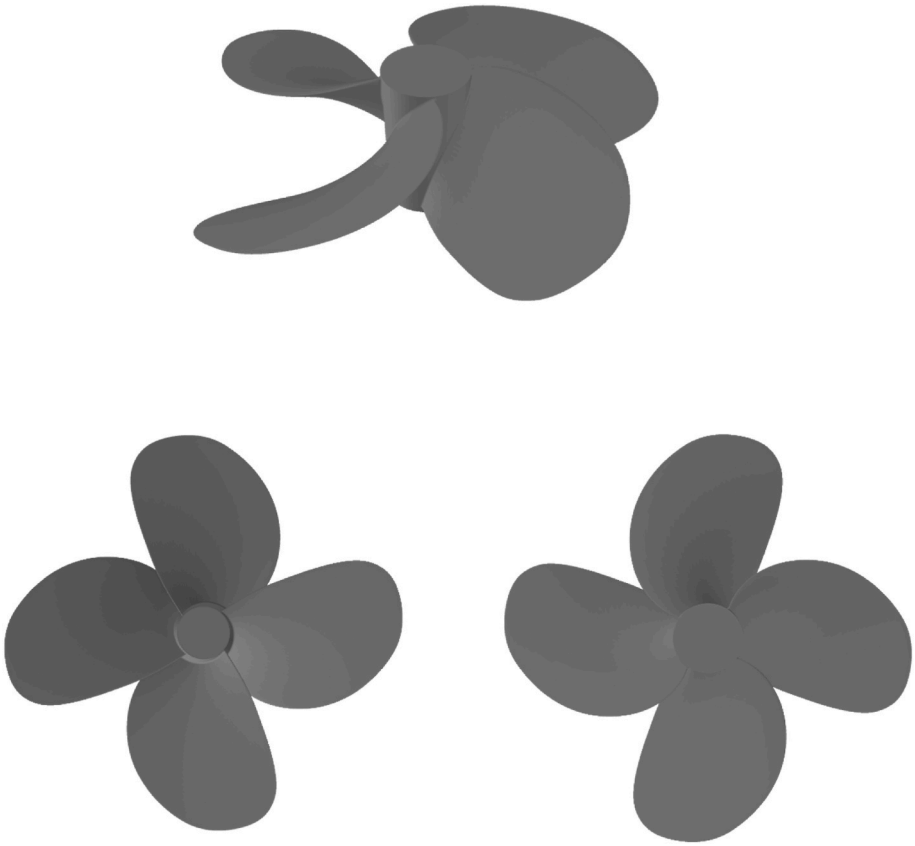


Fig. 3. 3D model of the FPP propeller V–645 (upper), pressure side (lower left) and suction side (lower right).

tested speed $V = 22.0$ kn ($v_M = 1.91$ m/s; $Fr = 0.212$). The measurement uncertainty analysis included both bias and precision errors, with bias errors calculated based on the two Froude numbers mentioned before. Precision errors were determined through analysis of repetitive tests conducted under self-propulsion conditions as part of the routine measurement uncertainty checks for the facility. These tests were performed on several displacement hulls of similar size and range of measured values. Repetitive tests should be conducted in multiple sets, with the model removed from the water and re-installed between each set. The analysis was based on four sets of runs, with each set containing at least two runs under identical conditions. The analysis included results obtained by testing several models, and the standard deviation was calculated. In that way, random errors in the setup such as model misalignment, trim, heel, etc. were taken into account. Bias errors encompassed the following groups of values: hull geometry, propeller geometry, water condition (temperature, density, viscosity), model i.e. carriage speed, propeller rate of revolution, measured resistance force, towing force, thrust, and torque as well as thrust and torque coefficients. Sources of errors contain the following categories: calibration, data acquisition, data reduction, and conceptual bias. It should be noted that certain sources of error do not apply to specific groups of analysed values.

When considering hull geometry as a source of error, the main contributors are model length and wetted surface. The bias error for model length is $B(L) = 2$ mm (0.024 % of L). The bias error for the wetted surface is $B(S) = 0.00804$ m^2 (0.08 % of $S = 10.7668$ m^2) and accounts for potential differences in model dimensions (length, breadth, draught) as well as errors in model loading (uncertainty of mass of model weights). Propeller geometry is highly complex, making errors related to it challenging to estimate accurately. The difference in diameter is identified as the primary contributor, with its associated bias error quantified as $B(D) = 0.0001$ m (0.048 % of the nominal diameter $D = 0.2073$ m). The uncertainty in temperature measurement also impacts the accuracy of density and viscosity values. The total bias limit includes calibration, data reduction, and conceptual errors. The bias error for density is $B(\rho) = 0.804$ kg/m^3 and for the viscosity is $B(\nu) = 7.5{\cdot}10^{-9}$ m^2/s (0.41 % of kinematic viscosity of fresh water).

The measurement of carriage speed was based on the pulse count of wheel rotations; thus, factors such as pulse count, wheel diameter, and the time base of the D/A and A/D conversion cards all contribute to measurement uncertainty. An optical encoder was used to track wheel rotation. Taking into account all parameters the total bias error for the speed measurement is $B(v_{M1}) = 0.0031$ m/s for carriage speed equal to $v = 1.38$ m/s (corresponding to $V = 16.0$ kn for the full-scale ship), i.e. 0.22 % of the nominal speed, and $B(v_{M2}) = 0.00298$ m/s for carriage speed equal to $v = 1.91$ m/s (corresponding to $V = 22.0$ kn for the full-scale ship), i.e. 0.16 % of the nominal speed. The rate of revolution of the propeller model was determined through pulse counting and A/D conversion at a specified time base, with an optical encoder used to track the rotation. The obtained bias errors are as follows: $B(n_1) = 0.0235$ rps or 0.374 % of 6.29 rps (revolutions obtained at speed corresponding to $V = 16.0$ kn for the full-scale ship), and $B(n_2) = 0.0235$ rps or 0.209 % of 8.91 rps (revolutions obtained at speed corresponding to $V = 22.0$ kn for the full-scale ship).

The resistance force measurement was carried out using a transducer calibrated with weights. These weights were calibrated in a certified laboratory outside the facility to a specified class, with their tolerance certified to be ± 0.002 % for each individual weight. Bias errors encompassed the tolerance of the weights, data acquisition accuracy, load cell misalignment, A/D conversion accuracy, and the effects of the rod to which the transducer was attached, which vary based on rod length and inclination. Total uncertainty consists of the total bias limit and total precision limit and it is equal to $(R_T) = 0.167$ N. Since the precision limit is dominant, there are no differences between the values

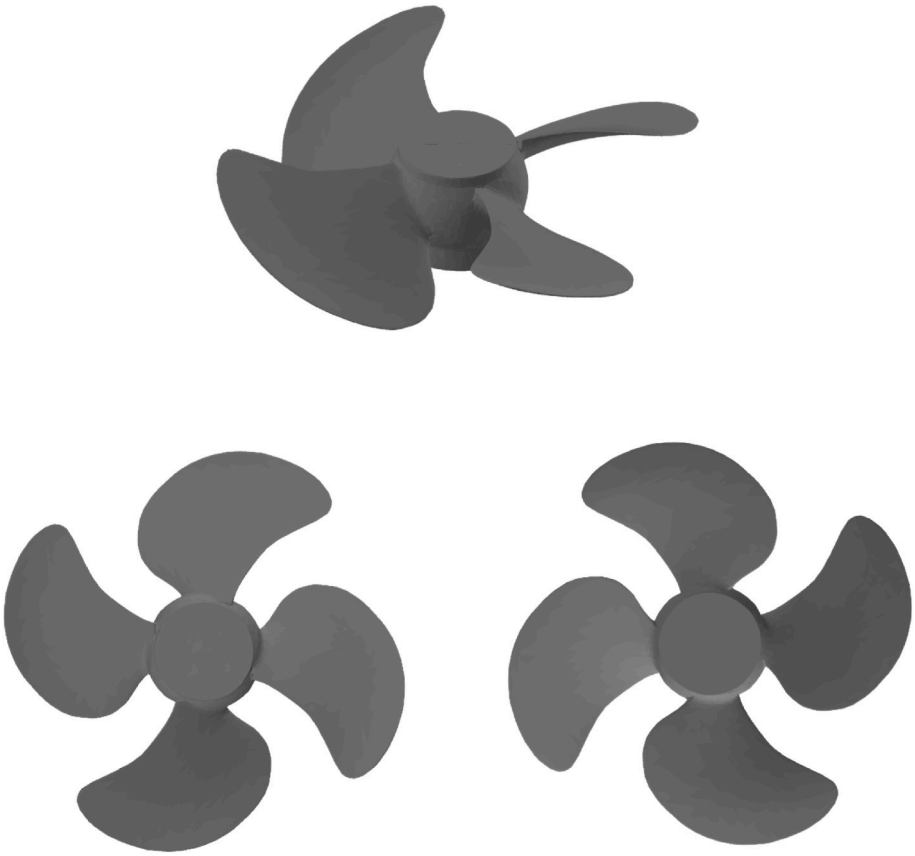


Fig. 4. 3D model of the CPP propeller V–1324 (upper), pressure side (lower left) and suction side (lower right).

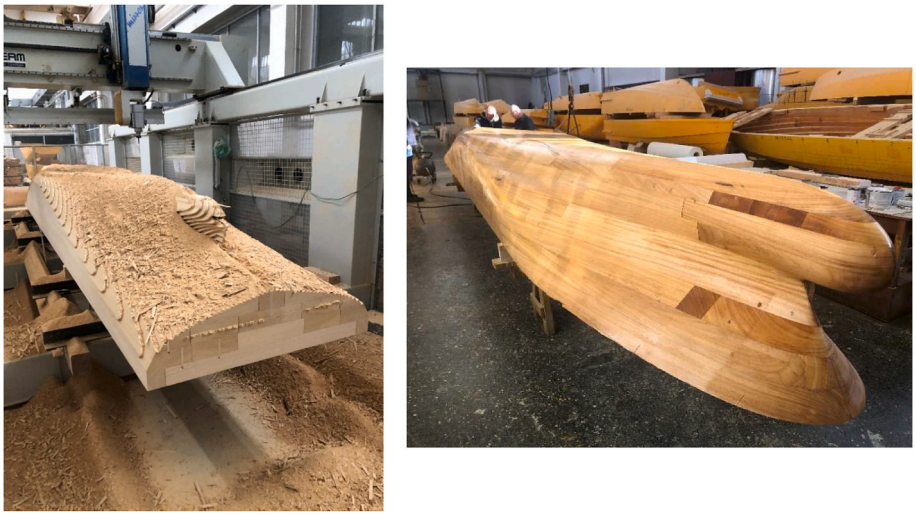


Fig. 5. Milling procedure (left) and model with the basic coating applied (right).

obtained for lower and higher tested speeds. The total uncertainty of resistance force is used in the self-propulsion test as a bias error.

When the model is towed through the water horizontal towing force is measured. Bias errors are comparable to those found in resistance measurement, in addition to errors that arise from the formula used to calculate the external towing force. Taking into account the aforementioned sources of error total bias errors for external towing force are $B(F_D) = 0.275$ N (1.36 % of the skin friction correction for the speed corresponding to $V = 16.0$ kn for the full-scale ship), and $B(F_D) = 0.341$ N (0.91 % of the skin friction correction for the speed corresponding to $V = 22.0$ kn for the full-scale ship).

Thrust was measured with the propeller dynamometer and bias error was affected by calibration, data acquisition, and A/D conversion. Calibration was performed in a manner similar to that of the resistance force transducer, utilizing weights that have been calibrated to a specific class. Data acquisition error was determined based on the definition provided by Coleman and Steele (1999), where the $\pm$ 2 SEE band around the regression curve encompasses 95 % of the data points. This band represents the confidence interval for the curve fit. The torque dynamometer was calibrated using weights applied at a specific distance

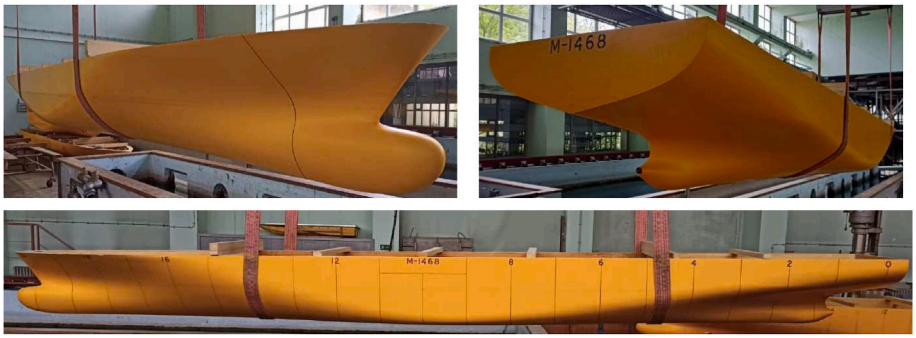


Fig. 6. Various views of the finished containership model.



Fig. 7. Rudder and FPP propeller of a 6750-TEU containership.

from the shaft line to generate the moment. Therefore, in addition to the certified tolerance of the weights, the measurement uncertainty of the moment arm length also impacts the accuracy. Sources of error are calibration, data acquisition, and A/D conversion. Data acquisition error was determined in the same manner as for the thrust. The total precision limit for both thrust and torque was defined based on repetitive tests for similar projects. The total uncertainties of thrust and torque are given in Table 3.

Accordingly, thrust and torque coefficients were calculated for the two speeds of interest, along with their respective thrust and torque values. The total bias errors for thrust coefficient are $B(K_T) = 0.000955$ (0.34 % of the skin friction correction for the speed corresponding to $V = 16.0$ kn for the full-scale ship), and $B(K_T) = 0.001618$ (0.58 % of the skin friction correction for the speed corresponding to $V = 22.0$ kn for the full-scale ship). The total bias errors for torque coefficient are $B(K_Q) = 0.000445$ (0.83 % of the skin friction correction for the speed corresponding to $V = 16.0$ kn for the full-scale ship), and $B(K_Q) = 0.000320$ (0.62 % of the skin friction correction for the speed corresponding to $V = 22.0$ kn for the full-scale ship). All calculated bias errors are summarized in Table 4.

5. ITTC 1957 Performance prediction method

The conversion from model to full-scale ship was performed using the ITTC-1957 extrapolation method, applying the total correlation allowance $C_A = -0.35 \cdot 10^{-3}$. At the Brodarski Institute, the correlation allowance is calculated as a total correlation allowance coefficient, derived from an extensive database of trial results encompassing over 1000 ships. The extrapolation method is based on the assumption that the residuary resistance coefficient C_R remains constant for the ship and model at the same Froude number:

$$C_R = C_{RM} = C_{TM} - C_{FM} \tag{1}$$

The total resistance coefficient was determined as follows:

$$C_{TS} = C_{FS} + C_R + C_A \tag{2}$$

The frictional resistance coefficient was determined according to the ITTC 1957 model-ship correlation line based on the Reynolds number Re:

$$C_F = \frac{0.075}{(\log Re - 2)^2} \tag{3}$$

During the tests, sinkage at the longitudinal center of buoyancy at rest, as well as the dynamic trim, were recorded. The sinkage for the full-scale ship was determined as follows:

$$z_S = z_M \lambda \tag{4}$$

The self-propulsion tests were conducted using the British method, which involves testing at various propeller loads. The self-propulsion point of the ship was identified at the propeller load corresponding to the skin friction correction, which was calculated using the total correlation allowance as follows:

$$F_D = \frac{1}{2} \rho_M v_M^2 S_M (C_{FM} - C_{FS} - C_A) \tag{5}$$

The propeller rate of revolution n_M was achieved when the difference between the total resistance and thrust equaled the skin friction correction.

The ship speed and the propeller rate of revolution for the full-scale ship were calculated based on the Froude similarity law as reads:

$$v_S = v_M \sqrt{\lambda} \tag{6}$$

$$n_S = \frac{n_M}{\sqrt{\lambda}} \tag{7}$$

Table 3
Total uncertainty (bias and precision limits taken into account).

Parameter	$Fr = 0.173$		$Fr = 0.212$	
	Value	%	Value	%
$U(T)$	0.122 N	0.6	0.122 N	0.3
$U(Q)$	0.0022 Nm	0.27	0.0036 Nm	0.22

Table 4
Calculated total bias limits.

Parameter	$Fr = 0.173$		$Fr = 0.212$	
	Value	%	Value	%
$B(v_M)$	0.0031 m/s	0.22	0.00298 m/s	0.16
$B(n)$	0.0235 rps	0.374	0.0235 rps	0.209
$B(F_D)$	0.275 N	1.36	0.341 N	0.91
$B(K_T)$	0.000955	0.34	0.001618	0.58
$B(K_Q)$	0.000445	0.83	0.000320	0.62

Thrust and torque for the full-scale ship were determined through scaling laws. To calculate the thrust for the full-scale ship the model scale values are multiplied by the density scale λ_ρ and λ^3, and to calculate torque with λ_ρ and λ^4.

The thrust deduction fraction (t) was calculated based on the total resistance and thrust values for a full-scale ship, while the wake fraction (w) was calculated using the thrust and torque identity method. No scale effects on wake fraction and open water characteristics are taken into account within the ITTC 1957 extrapolation procedure.

6. Results

6.1. Experimental results

Resistance tests were carried out over a speed range of 12–25 knots, corresponding to the full-scale ship. The ship model was equipped with a rudder, and a trip wire was installed at station 19 to act as a turbulence stimulator. During the experiments, the water temperature was equal to 12.6 °C with the corresponding density of 999.34 kg/m^3 and kinematic viscosity of $1.215{\cdot}10^{-6}$ m^2/s. During the resistance test, total resistance, sinkage, and trim were measured, and the obtained results are presented in Table 5. The total resistance coefficients were determined using a dynamic wetted surface area of 10.907 m^2. The Froude numbers presented in Table 5 were calculated based on a waterline length of 8.3107 m. Negative sinkage values across the entire speed range indicate an increase in draught, whereas negative trim values signify a trim by bow. The results of the open water tests for V–645 and V–1324 propeller models are presented in Figs. 8 and 9, respectively.

The self-propulsion tests covered a significantly broad speed range from 16 to 23 kn corresponding to full scale to align with the focus on investigating slow steaming regimes. Typically, self-propulsion tests are conducted around the design speed and the tested range is narrow, tailored to the power requirements near the speeds attainable at trial and in service. The experimental campaign was conducted as part of a scientific project aimed at investigating the impact of reduced sailing speeds on hydrodynamic characteristics, engine performance, and shaft vibrations. The obtained results, particularly the relationship between the required engine power and the rate of revolutions, revealed that there is no suitable marine diesel engine currently available for this specific ship. In the second phase of testing, to achieve a further reduction in the propeller rate of revolution, self-propulsion tests were conducted using the CPP stock model. The left-handed CPP model V–1324, with appropriate diameter, expanded area ratio, and the number of blades was selected for this purpose. Based on the self-propulsion test results obtained with the FPP stock model, the pitch of the CPP was set to $P_{0.7R}/D = 1.3$, and relevant self-propulsion tests were performed. The measured rate of revolutions, thrust, torque, and towing force in self-propulsion tests obtained with FPP and CPP for various speeds are given in Tables 6 and 7, respectively. As the self-propulsion tests were conducted using the British method, the rate of revolutions varied for each tested speed.

Table 5
The results of the resistance test.

v_M, m/ s	Fr	C_{TM}	z_M, m	τ, °
1.04	0.115	3.689	−0.0013	−0.008
1.13	0.125	3.621	−0.0017	−0.011
1.209	0.134	3.592	−0.0017	−0.012
1.3	0.144	3.596	−0.0024	−0.015
1.39	0.154	3.594	−0.0028	−0.017
1.469	0.163	3.568	−0.0031	−0.02
1.56	0.173	3.571	−0.0035	−0.023
1.65	0.183	3.553	−0.0042	−0.027
1.73	0.192	3.437	−0.0051	−0.036
1.82	0.202	3.488	−0.0059	−0.039
1.91	0.212	3.555	−0.0066	−0.043
1.99	0.22	3.548	−0.0074	−0.051
2.08	0.23	3.523	−0.0046	−0.036
2.17	0.24	3.708	−0.008	−0.041

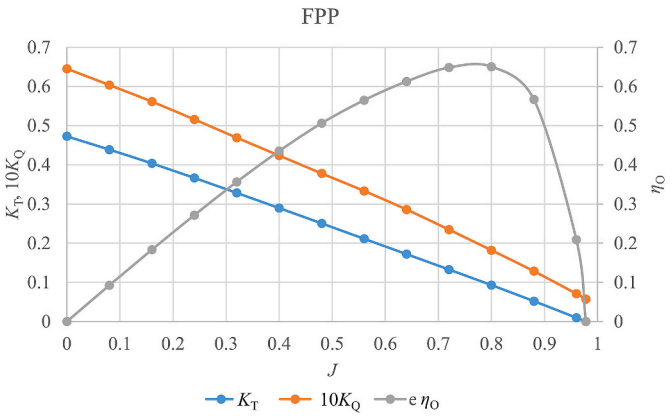


Fig. 8. Open water diagram of the FPP.

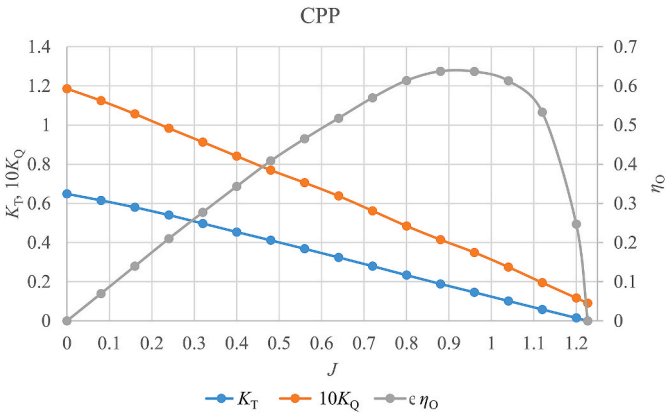


Fig. 9. Open water diagram of the CPP.

6.2. Extrapolated results

In the lower speed range $V = 16 - 18.5$ kn, the propeller delivered power obtained with the CPP model was, on average, 2 % lower compared to the reference values obtained with the FPP model, Fig. 10. For higher speeds $V = 19 - 22$ kn, the delivered power obtained with the CPP model was, on average, 2.6 % higher compared to the reference values obtained with the FPP model. The results of self-propulsion tests show minimal differences in propeller thrust. In the lower speed range $V = 16 - 20$ kn the propeller thrust with the CPP model was, on average, 1.2 % lower compared to the reference values obtained with the FPP propeller, while for higher speeds $V = 20.5 - 22$ kn, the propeller thrust with the CPP model was, on average, 0.2 % higher than the reference values of the FPP model.

The propeller rate of revolution is significantly affected by the pitch increment applied to the CPP, which has the same diameter, number of blades, and a slightly lower area ratio when compared to FPP. Increasing the pitch ratio $P_{0.7R}/D$ from 0.8901 to 1.3 led to an average reduction in the propeller rate of revolution of 17 %, Fig. 11. Contrary, the propeller advance ratio of CPP is on average 21.3 % higher in the entire speed range when compared to FPP, Fig. 12. The wake fractions as a function of ship speed obtained with FPP and CPP are presented in Fig. 13. The wake fractions obtained with CPP are, on average, 2.5 % lower than the

Table 6
Measurements from the self-propulsion test conducted with FPP.

v_M, m/ s	N_M, 1/s	T_M, N	Q_M, Nm	F_D, N
1.38	6.21	9.097	0.3216	30.083
1.38	6.8	13.563	0.4577	26.083
1.38	7.41	18.519	0.6088	21.653
1.38	8.01	23.871	0.7719	16.86
1.38	8.6	29.583	0.946	11.759
1.56	8.1	20.747	0.6959	29.891
1.56	8.7	26.613	0.8746	24.643
1.56	9.3	32.869	1.0653	19.033
1.56	9.91	39.559	1.2692	13.054
1.73	9.31	28.696	0.9363	33.723
1.73	9.91	35.341	1.1389	27.771
1.73	10.5	42.354	1.3526	21.482
1.73	11.1	49.872	1.5817	14.769
1.82	9.8	31.681	1.0269	37.381
1.82	10.41	38.722	1.2415	31.045
1.82	11	46.091	1.4661	24.473
1.82	11.6	53.939	1.7053	17.43
1.91	10.5	37.096	1.1967	39.196
1.91	11.1	44.664	1.4274	32.433
1.91	11.71	52.58	1.6687	25.342
1.91	12.31	60.964	1.9242	17.848
1.99	11.21	43.261	1.3968	40.074
1.99	11.8	51.15	1.6372	32.999
1.99	12.4	59.59	1.8945	25.448
1.99	13.01	68.41	2.1633	17.573

Table 7
Measurements from the self-propulsion test conducted with CPP.

v_M, m/ s	N_M, 1/s	T_M, N	Q_M, Nm	F_D, N
1.38	5	7.685	0.3371	30.99
1.38	5.5	12.182	0.5044	27.00
1.38	6	17.051	0.6857	22.684
1.38	6.5	22.413	0.8853	17.915
1.38	6.9	27.01	1.0564	13.84
1.38	7.3	31.848	1.2364	9.547
1.38	7.7	36.982	1.4275	5.001
1.38	8.1	42.341	1.627	0.235
1.38	8.5	48.053	1.8396	−4.839
1.56	6.6	19.008	0.7663	30.986
1.56	7.21	26.146	1.032	24.658
1.56	7.81	33.835	1.3182	17.822
1.56	8.4	42.05	1.6239	10.545
1.65	7.21	23.899	0.9636	32.331
1.65	7.6	28.855	1.1481	27.94
1.65	8.01	34.285	1.3502	23.121
1.65	8.4	39.813	1.556	18.214
1.65	8.81	45.785	1.7783	12.915
1.73	7.51	25.535	1.0395	36.35
1.73	8.01	32.17	1.2865	30.462
1.73	8.51	39.22	1.5489	24.198
1.73	9.01	46.663	1.8259	17.601
1.73	9.51	54.573	2.1203	10.581
1.73	10	62.859	2.4287	3.22
1.73	10.5	71.602	2.7541	−4.531
1.82	7.7	25.529	1.0524	42.745
1.82	8.31	33.785	1.3596	35.411
1.82	8.9	42.538	1.6854	27.651
1.82	9.5	51.993	2.0374	19.252
1.82	10.11	62.056	2.4119	10.315
1.91	8.31	30.847	1.2545	44.73
1.91	8.9	39.582	1.5796	36.994
1.91	9.5	49.053	1.9322	28.565
1.91	10.1	59.09	2.3057	19.681

ones obtained with FPP in a speed range $V = 16 - 19.5$ kn. As can be seen from Fig. 14, in a speed range $V = 16 - 19$ kn, the thrust deduction fractions achieved with the CPP are, on average, 7.9 % lower than those obtained with the FPP. At the two highest tested speeds, the thrust deduction fractions achieved with the CPP are approximately 1.3 % higher compared to those obtained with the FPP.

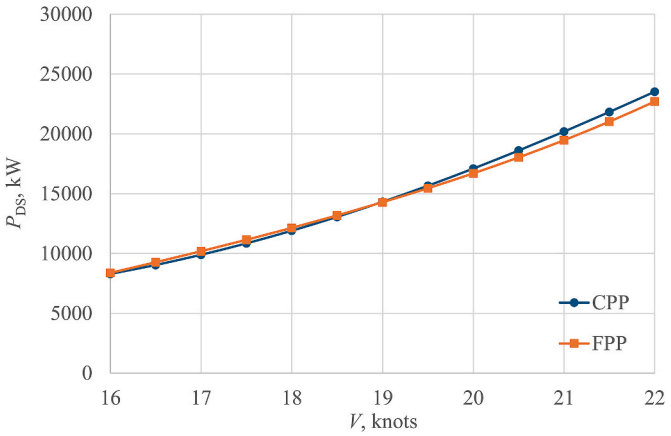


Fig. 10. Delivered power obtained with FPP and CPP.

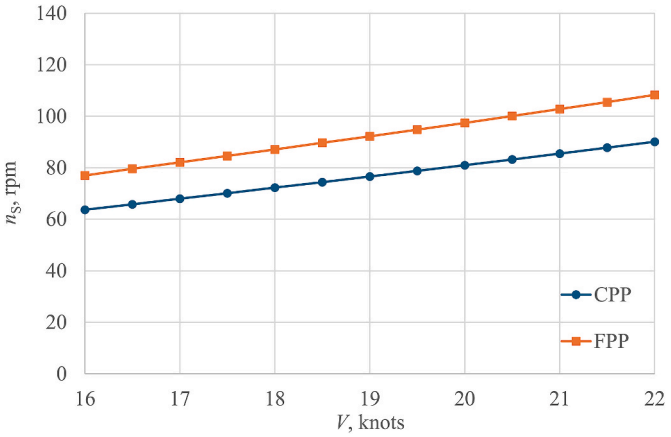


Fig. 11. Rate of revolution obtained with FPP and CPP.

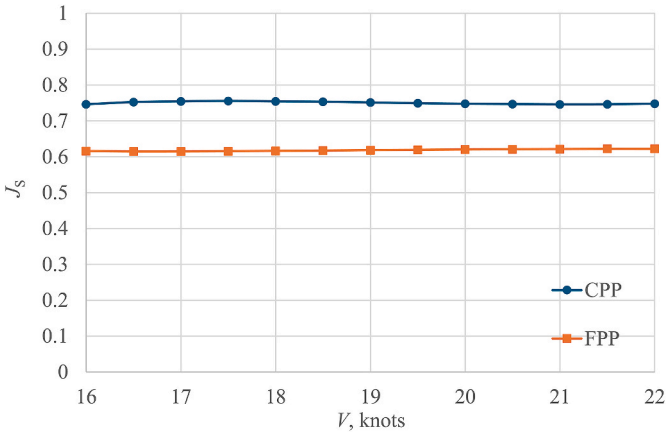


Fig. 12. Propeller advance ratio obtained with FPP and CPP.

The differences between the hull efficiency obtained with FPP and CPP are negligible in the entire speed range, Fig. 15. The propeller efficiency in open water obtained with FPP is higher than the one obtained with CPP in the entire speed range, Fig. 16. Relative rotative efficiency presented in Fig. 17, is on average 3.2 % higher for CPP in comparison to FPP in a speed range $V = 16 - 19$ kn. In the lower speed range $V = 16 - 18.5$ kn, the quasi-propulsive efficiency coefficient obtained with the CPP model was, on average, 2 % higher compared to the reference values obtained with the

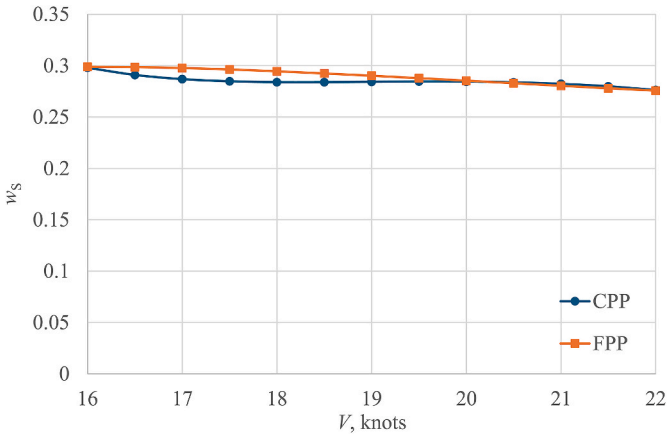


Fig. 13. Wake fraction obtained with FPP and CPP.

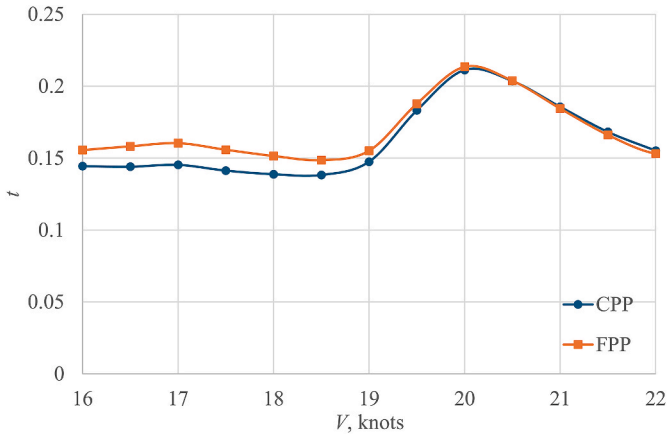


Fig. 14. Thrust deduction fraction obtained with FPP and CPP.

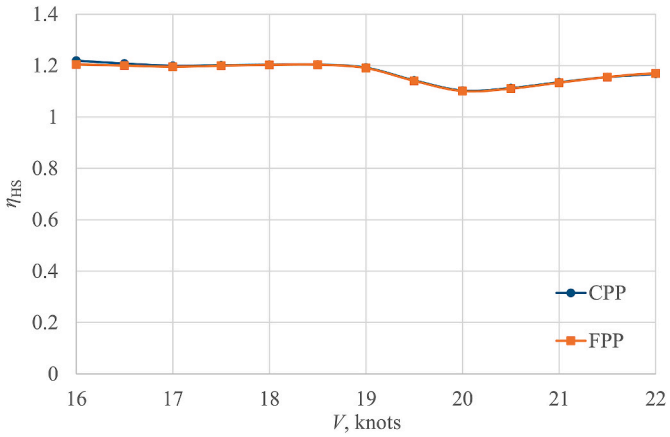


Fig. 15. Hull efficiency obtained with FPP and CPP.

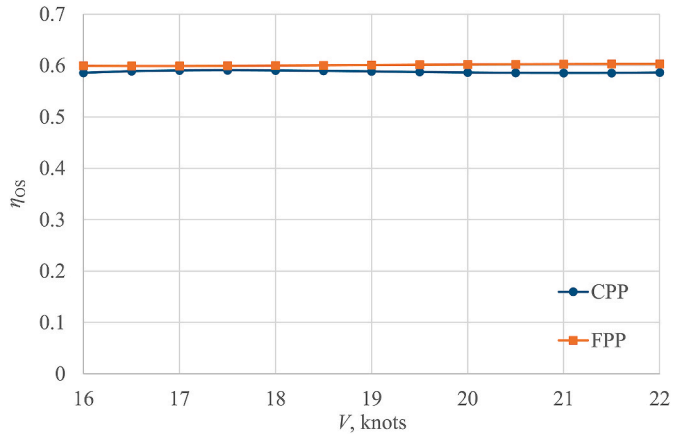


Fig. 16. Propeller efficiency in open water obtained with FPP and CPP.

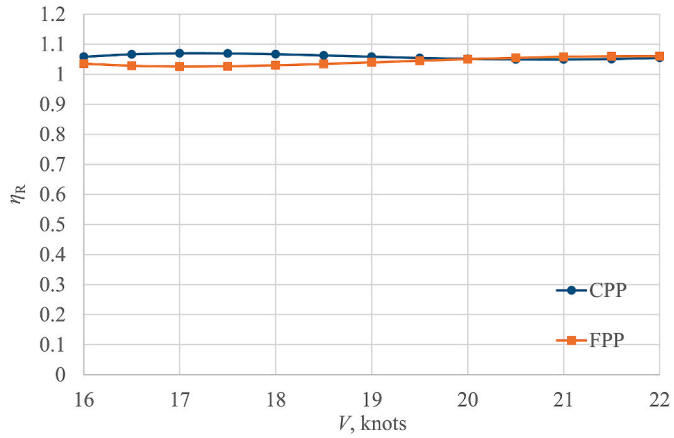


Fig. 17. Relative rotative efficiency obtained with FPP and CPP.

FPP model, Fig. 18. For higher speeds $V = 19 - 22$ kn, the quasi-propulsive efficiency coefficient obtained with the CPP model was, on average, 2.5 % lower compared to the reference values obtained with the FPP model.

7. Conclusion

Although many experimental studies have examined the responses and loads of the 6750-TEU container ship in wave conditions, resistance and self-propulsion tests in calm water have not been reported to date. This paper presents an extensive experimental campaign encompassing resistance, open water, and self-propulsion tests across a wide range of speeds for a ship model in a scale of 35.18. The test were carried out at the Brodarski Institute, Zagreb in a large towing tank. The results of the self-propulsion tests were presented for various propeller loads following the British method. The experimental uncertainty was evaluated following the procedure recommended by the ITTC. The results of

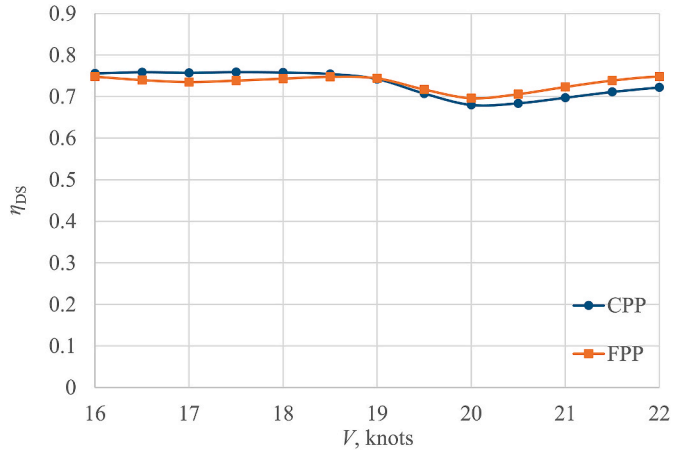


Fig. 18. Quasi-propulsive efficiency coefficient obtained with FPP and CPP.

the measurement uncertainty analysis were presented, encompassing both bias and precision errors. Bias errors were calculated based on two Froude numbers.

The experimental campaign was undertaken as part of a scientific project focused on investigating the effects of reduced sailing speeds on hydrodynamic performance, engine efficiency, and shaft vibrations. Notably, the results, specifically the correlation between required engine power and rate of revolutions, highlighted the absence of a suitable marine diesel engine for this particular ship. Therefore, in addition to the fixed pitch propeller, self-propulsion tests were conducted using a controllable pitch propeller at a single pitch to further reduce the rate of revolutions. The experimental data were extrapolated using the ITTC 1957 performance prediction method, following the standard practice at the Brodarski Institute. The results obtained with fixed and controllable pitch propellers were then compared. The findings provide a valuable addition to the benchmarking database for validating CFD simulations and fill a significant gap in the existing literature regarding experimental data for the 6750-TEU containership model.

CRediT authorship contribution statement

Nastia Degiuli: Writing – review & editing, Writing – original draft, Visualization, Validation, Supervision, Resources, Project administration, Methodology, Investigation, Funding acquisition, Formal analysis, Data curation, Conceptualization. **Ivana Martić:** Writing – review & editing, Writing – original draft, Visualization, Validation, Project administration, Methodology, Investigation, Formal analysis, Data curation, Conceptualization. **Marta Pedišić Buča:** Writing – review & editing, Writing – original draft, Validation, Resources, Methodology, Investigation, Formal analysis, Data curation, Conceptualization. **Carlo Giorgio Grlj:** Writing – review & editing, Writing – original draft, Visualization, Validation, Project administration, Methodology, Investigation, Formal analysis, Data curation.

Funding

This study was funded by the Croatian Science Foundation under project IP-2020-02-8568.

Declaration of competing interest

The authors declare that they have no known competing financial interests or personal relationships that could have appeared to influence the work reported in this paper.

Acknowledgements

This study has been fully supported by the Croatian Science Foundation under project IP-2020-02-8568.

Appendix A. Supplementary data

Supplementary data to this article can be found online at https://doi.org/10.1016/j.oceaneng.2025.120300.

References

Bouscasse, B., Merrien, A., Horel, B., De Hauteclocque, G., 2022. Experimental analysis of wave-induced vertical bending moment in steep regular waves. J. Fluid Struct. 111, 103547.
Brodarski Institute, 2022. Report M-1468. Technical Report. Brodarski Institute, Zagreb.
Coleman, H.W., Steele, W.G., 1999. Experimentation and Uncertainty Analysis for Engineers, second ed. John Wiley & Sons, Inc., New York, NY.
Degiuli, N., Martić, I., Farkas, A., Pedišić Buča, M., Dejhalla, R., Grlj, C.G., 2023. Experimental assessment of the hydrodynamic characteristics of a bulk carrier in off-design conditions. Ocean. Eng. 280, 114936.
Delen, C., Bal, S., 2024. Experimental analysis of self-propelled characteristics with uncertainty analysis of ONR tumblehome hull. Ocean. Eng. 307, 118230.
Elsherbiny, K., Tezdogan, T., Kotb, M., Incecik, A., Day, S., 2019. Experimental analysis of the squat of ships advancing through the New Suez Canal. Ocean. Eng. 178, 331–344.
Grlj, C.G., Degiuli, N., Martić, I., 2024. Experimental and numerical assessment of the effect of speed and loading conditions on the nominal wake of a containership. Brodogradnja 75 (4), 75405.
Guo, C.Y., Kuai, Y.F., Wang, W., Han, Y., Xu, P., Fan, Y.W., 2021. Experimental study on bow flow field of scientific research ship based on flow visualisation. Ocean. Eng. 235, 109412.
Horel, B., Bouscasse, B., Merrien, A., de Hauteclocque, G., 2019. Experimental assessment of vertical shear force and bending moment in severe sea conditions. In: International Conference on Offshore Mechanics and Arctic Engineering, vol. 58783. American Society of Mechanical Engineers, V003T02A031.
ISSC, 2021. Loads committee – benchmark. https://github.com/BV-DR/ISSC_2021_LOADS_BENCHMARK.
Kim, S., Bouscasse, B., Ducrozet, G., Delacroix, S., De Hauteclocque, G., Ferrant, P., 2023. Experimental investigation on wave-induced bending moments of a 6,750-TEU containership in oblique waves. Ocean. Eng. 284, 115161.
Kim, Y., Kim, J.H., 2016. Benchmark study on motions and loads of a 6750-TEU containership. Ocean. Eng. 119, 262–273.
Kinaci, O.K., Gokce, M.K., Delen, C., 2020. Resistance experiments and self-propulsion estimations of Duisburg Test Case at 1/100 scale. Ship Technol. Res. 67 (2), 109–120.
Köksal, Ç.S., Aktas, B., Gürkan, A.Y., Sasaki, N., Atlar, M., 2024. Experimental assessment of hull, propeller, and the gate rudder system interaction in calm water and oblique waves. Ocean. Eng. 312, 119144.
Krasilnikov, V., Skjefstad, V.S., Koushan, K., Rambech, H.J., 2023. A calibration study with CFD methodology for self-propulsion simulations at ship scale. J. Mar. Sci. Eng. 11 (7), 1342.
Lee, S.J., Jung, K.H., Ku, N., Lee, J., 2023. A comparison of regression models for the ice loads measured during the ice tank test. Brodogradnja 74 (3), 1–15.
Liang, L., Hao, Z., Chaonan, Z., Jinbiao, C., Baoji, Z., Xiangen, B., Shengyao, S., Qian, C., Weijia, Z., 2024. Study on the effect of marine propeller wake on sediment siltation in a shallow water channel. Brodogradnja 75 (3), 1–22.
Mikulec, M., Piehl, H., 2023. Verification and validation of CFD simulations with full-scale ship speed/power trial data. Brodogradnja 74 (1), 41–62.
Saettone, S., Taskar, B., Steen, S., Andersen, P., 2021. Experimental measurements of propulsive factors in following and head waves. Appl. Ocean Res. 111, 102639.
Shivachev, E., Khorasanchi, M., Day, S., Turan, O., 2020. Impact of trim on added resistance of KRISO container ship (KCS) in head waves: an experimental and numerical study. Ocean. Eng. 211, 107594.
Su, S., Wu, Y., Xiong, Y., Guo, F., Liu, H., Cheng, Q., 2023. Experiment and numerical simulation study on resistance performance of the shallow-water seismic survey vessel. Ocean. Eng. 279, 113889.
Van der Kolk, N.J., Keuning, J.A., Huijsmans, R.H.M., 2019. Part 1: experimental validation of a RANS-CFD methodology for the hydrodynamics of wind-assisted ships operating at leeway angles. Ocean. Eng. 178, 375–387.
Wang, H., Duan, W., Chen, J., Ma, S., 2022. A numerical method to compute flexible vertical responses of containerships in regular waves. Ocean. Eng. 266, 112828.
Waskito, K.T., Kashiwagi, M., Iwashita, H., Hinatsu, M., 2020. Prediction of nonlinear vertical bending moment using measured pressure distribution on ship hull. Appl. Ocean Res. 101, 102261.
Xue, Y., Zhong, K., Ni, B.Y., Li, Z., Bergström, M., Ringsberg, J.W., Huang, L., 2024. A combined experimental and numerical approach to predict ship resistance and power demand in broken ice. Ocean. Eng. 292, 116476.
Yin, X.B., Lu, Y., Zou, J., Wan, L., 2019. Numerical and experimental study on hydrodynamic bulbous bow hull-form optimization for various service conditions due to slow steaming of container vessel. Proc. IME M J. Eng. Marit. Environ. 233 (4), 1103–1122.
Zhou, L., Abdelwahab, H.S., Soares, C.G., 2021. Experimental and CFD investigation of the effects of a high-speed passing ship on a moored container ship. Ocean. Eng. 228, 108914.

Article IX

Article published by Elsevier in Ocean engineering on 24 February 2023, available online: https://www.sciencedirect.com/science/article/abs/pii/S002980182300375X

Ocean Engineering 273 (2023) 113991

Contents lists available at ScienceDirect

Ocean Engineering

journal homepage: www.elsevier.com/locate/oceaneng

The effect of loading conditions and ship speed on the wind and air resistance of a containership

Carlo Giorgio Grlj, Nastia Degiuli *, Željko Tuković, Andrea Farkas, Ivana Martić

University of Zagreb, Faculty of Mechanical Engineering and Naval Architecture, Ivana Lučića 5, Zagreb, 10000, Croatia

ARTICLE INFO

Handling Editor: A.I. Incecik

Keywords:
CFD
Wind resistance
Air resistance
Container configuration
Trim
Ship speed

ABSTRACT

Although air resistance is relatively low in comparison to the total resistance of a ship, in the case of containerships, it can vary depending on the loading conditions and the layout of the stored containers. Over the years, containerships have increased in size and thus the air resistance has increased due to the increased windage area. The present study aims to assess the effect of different container configurations and trim on wind and air resistance as well as the influence of ship speed on air resistance. Numerical simulations based on viscous flow around a post Panamax 6750-TEU containership were conducted for open sea conditions. The verification studies for the grid size and time step were conducted and a validation study was performed using the available experimental results. The numerical results are reported with the non-dimensionalized wind load coefficients using the ITTC recommendations for the determination of the representative wind velocity. It is shown that the trim angle has the greatest influence on the moment coefficient, while the largest air resistance is obtained for the empty containership. The results also show that trim by bow causes lower values of air resistance, while trim by stern leads to higher values in comparison to an even keel condition. Finally, the portion of air resistance in the total resistance varies from 3.5% up to 5.8% for container configurations 9 and 2, respectively.

1. Introduction

As containership size has been increasing over the years, the projected windage areas are increasing and consequently so is the portion of wind resistance in the total resistance. Therefore, it is increasingly important to determine wind resistance as accurately as possible rather than taking it into account through the sea margin. This will allow for a more accurate assessment of fuel consumption to determine the ship energy efficiency in realistic sailing conditions. To determine ship wind and air resistance, computational aerodynamics can be used in the ship design process. Computational Fluid Dynamics (CFD) has already become a commonly used approach in problems related to ship hydrodynamics. Farkas et al. (2019) conducted numerical simulations of viscous flow around a typical Handymax bulk carrier at model scale and full-scale to assess the nominal wake. The authors performed extensive verification and validation studies, while the effect of wall functions and different turbulence models on the results was investigated. Farkas et al. (2018) investigated the effect of different loading conditions on the hydrodynamic characteristics of a bulk carrier using CFD simulations. The numerical results were validated against the extrapolated experimental results using five extrapolation methods. The authors emphasized the importance of using CFD based on viscous flow to improve the reliability of extrapolation methods. Zhang et al. (2021) established roll motion stability prediction methods for a trimaran vessel in regular and irregular waves and wind loads with a varying configuration layout using CFD. Vinayak et al. (2021) analysed changes in oceanic wind and wave conditions in the last 27 years. The authors conducted numerical simulations of ship navigation for three ship types and assessed the changes in travel time and fuel consumption due to changes in wave and wind conditions. Wang et al. (2019) performed an experimental and numerical investigation of a 1900 TEU containership at model scale to assess the wind load coefficients and wave resistance. The authors pointed out the importance of analysing the coupled wind and wave loads and showed the effects of their interaction. Majidian and Azarsina (2019) conducted several numerical simulations with different numerical setups to develop a model for the determination of wind resistance. The numerical setup was validated against the available pressure distributions for an Akron airship. The obtained numerical results were compared with the available voyage data for different wind speeds and directions. Finally, the authors developed a regression equation for air resistance in the range of the yaw angle from 0° to 40°.

* Corresponding author.
E-mail address: nastia.degiuli@fsb.hr (N. Degiuli).

https://doi.org/10.1016/j.oceaneng.2023.113991
Received 22 December 2022; Received in revised form 27 January 2023; Accepted 14 February 2023
Available online 24 February 2023
0029-8018/© 2023 Elsevier Ltd. All rights reserved.

Nomenclature

ANN	Artificial Neural Network
CFD	Computational Fluid Dynamics
EFD	Experimental Fluid Dynamics
FVM	Finite Volume Method
GCI	Grid Convergence Index
GRNN	Generalized Regression Neural Network
IMO	International Maritime Organization
ITTC	International Towing Tank Conference
LNG	Liquefied Natural Gas
RANS	Reynolds Averaged Navier-Stokes
RKE	Realizable $k-\varepsilon$
RST	Reynolds Stress Tensor
A_{VX}	Transverse projected (frontal windage) area
A_{VY}	Lateral projected (side windage) area
B	Breadth
C, D	Normal and tangential components of the aerodynamic force
C_{DAX}, C_{DAY}	Longitudinal and transverse wind load coefficients
C_s	Roughness constant
$C_{\varepsilon 1}$, $C_{\varepsilon 2}$, $C_{\varepsilon 3}$	Turbulence model depending coefficients
C_μ	Model coefficient
e_{a}^{21}	Approximate relative error
e_{ext}^{21}	Extrapolated relative error
f_c	Curvature correction factor
GCI_{fine}^{21}	Fine-grid convergence index
G_k	Turbulent production term
G_b	Buoyancy production term
h	Grid spacing
H_{BR}, H_L	Representative heights
k	Turbulent kinetic energy
k_s	Equivalent sand-grain roughness height
L_{OA}	Length, overall
L_{PP}	Length between perpendiculars
L_{WL}	Length of waterline
M_z	Moment around the vertical axis
N	Total number of cells
p	Apparent order of the method
$\overline{p}$	Mean pressure
q_A	Dynamic pressure
R_{AAX}, R_{AAY}	Longitudinal and transverse forces
Re	Reynolds number
r	Refinement ratio
S	Modulus of the mean strain tensor
S_k, S_ε	User-defined source terms within the turbulence model
T	Draught
T_{mid}	Draught at midship
T_{aft}	Draught at aft perpendicular
T_{fwd}	Draught at forward perpendicular
$U(z)$	Velocity profile
U_{G}	Grid size uncertainty
U_{ref}	Reference velocity
U_{SN}	Simulation numerical uncertainty
U_{T}	Time step uncertainty
u^*	Frictional velocity
$\overline{u}_i$	Averaged Cartesian components of the velocity vector
V_{AA}	Representative wind speed
V_{A1}, V_{A2}	Height average wind velocities
V_i	Volume of the i-th cell
y^+	Non-dimensional wall distance
z_0	Aerodynamic roughness length
z_{ref}	Reference height
α	Velocity profile exponent
∇	Displacement volume
ε	Turbulent dissipation rate
ε_0	Ambient turbulence value
ε_{ij}	Difference between the solutions
κ	Von Karman constant
μ	Dynamic viscosity
μ_t	Turbulent eddy viscosity
ρ	Fluid density
$\rho\overline{u_i'u_j'}$	Reynolds Stress Tensor
σ_k, σ_ε	Turbulent Schmidt numbers
$\overline{\tau}_{ij}$	Mean viscous stress tensor
Y_M	Dilatation dissipation
φ	Arbitrary solution
$\varphi_{\mathrm{ext}}^{21}$	Extrapolated values
Ψ	Angle of attack

Table 1
Post Panamax 6750-TEU containership data.

Main Particular	Value
L_{OA}	303.98 m
L_{PP}	286.60 m
T	11.98 m
B	40 m
∇	85 634 m^3

Along with computational aerodynamics, wind tunnel tests can be utilized during the design process to ensure that a ship meets the operational and class requirements regarding propulsion, manoeuvring, dynamic positioning, mooring, and stability. Andersen (2013) investigated the effect of the container configuration on the deck of a 9000+ TEU containership on wind loads in a wind tunnel and thus provided experimental results for different container configurations. These findings were used by Prpić-Oršić et al. (2020) to validate the numerical results of the same container configurations for the development of a method based on the Generalized Regression Neural Network (GRNN) which allows a rapid assessment of the wind load coefficients for other container configurations. The authors suggested that uncertainty and reliability analyses should be conducted with additional container configurations using numerical simulations to enlarge the available database for the training of the neural network. Martić et al. (2021) developed an Artificial Neural Network (ANN) model to estimate the added resistance in waves in different sea states. The numerical model yields satisfactory accuracy in a short time without the need to perform complex hydrodynamic calculations. Janssen et al. (2017) conducted CFD simulations of the airflow around a 9000+ TEU containership and investigated the impact of the geometry simplifications on the wind loads. The authors validated the results with the published experimental data in (Andersen, 2013) and showed that the geometry simplification can result in different wind loads even though the projected windage areas were similar. The obtained absolute average difference between the numerical and the wind tunnel results was about 5.9% for the detailed containership geometry. Based on the results obtained in (Janssen et al., 2017), Ricci et al. (2020) assessed the influence of the built environment around a nautical port on the wind loads of the ship. The case study consisted of a large cruise ship moored at the quay of the Rotterdam Cruise Terminal in which the used wind speeds and

directions were validated with on-site measurements. The authors used the wind velocity profile at the inlet boundary in numerical simulations which were based on wind tunnel measurements. Wnek and Guedes Soares (2015) used CFD simulations to assess the wind loads on a Liquefied Natural Gas (LNG) carrier and floating platform models. The authors used a cylindrical computational domain with the inlet and outlet boundaries on the lateral surface of the cylinder to reduce the computational time and avoid the influence of the side walls on the results. A similar method was previously proposed by Kaup (2006) where the author used an octagonal computational domain to determine ship aerodynamic forces. The author validated the numerical results with those obtained from wind tunnel measurements and showed satisfactory agreement even with the simplified ship geometry. Torre et al. (2021) investigated the reduction of the aerodynamic coefficient using the example of a cruise ship moored in the Port of Monfalcone due to the sheltering surroundings with Experimental Fluid Dynamics (EFD). The experiments were conducted in a wind tunnel on a 1:600 model of a large cruise ship and the results showed a reduction of the aerodynamic forces by up to 60% for the wind directions perpendicular to the ship. In this way, the authors demonstrated that complex surrounding buildings may increase port safety. Nguyen et al. (2017) utilized numerical simulations to assess the air resistance of a large containership with a fully loaded deck with containers. The authors showed a significant reduction of air resistance in oblique winds by up to 50% by using the full side covers to close the gap flow. Deng et al. (2022) investigated the wind resistance of a large containership using CFD and EFD and showed that significant reductions in wind resistance can be obtained using different types of forecastle fairings, as well as different container configurations. The influence of the position and the shape of the accommodation on the air resistance of a ship was studied by means of CFD by van He et al. (2016). The authors showed that significant reductions in air resistance can be obtained with streamlined accommodation located on the fore deck. Seok and Park (2020) conducted numerical simulations based on Reynolds Averaged Navier-Stokes (RANS) equations of the flow around the hull of an 8000 TEU Kriso containership with a superstructure and containers and without a superstructure to compare the total resistance, trim, and sinkage. The authors showed good agreement with the results obtained using EFD in the validation study. The obtained quantitative differences of the total resistance were approximately less than 3%. However, large differences were observed in the trim and sinkage values obtained at different Froude numbers.

This study focuses on determining the wind load coefficients and air resistance of a containership at open sea using CFD. The scientific contribution of this study is the assessment of the influence of trim and different container configurations on wind load coefficients as well as ship speed on air resistance. The verification study is performed along with a validation study by comparing available wind tunnel results. The rest of the paper is organized as follows: the theoretical background of the numerical simulations is briefly discussed, and the numerical setup is explained in detail in Section 2. In Section 3, the results, including the verification and validation studies, are presented and discussed. Finally, conclusions from the study are given in Section 4.

2. Methods

Full-scale numerical simulations based on RANS equations were conducted with the aim to determine the wind and air resistance of a post Panamax 6750-TEU containership. RANS equations represent an unclosed set of equations, and hence a turbulence model must be applied to close these equations. In this paper, the Realizable $k-\varepsilon$ (RKE) Two-Layer turbulence model is used as a compromise between accuracy and computational time. This turbulence model is applied in similar studies related to the determination of wind resistance (Wnek and Guedes Soares, 2015), (Janssen et al., 2017). The Finite Volume Method (FVM) is used for the discretization of the governing equations to obtain an algebraic system of equations which can be numerically solved. Within the governing equations, the convection and gradient terms are solved utilizing the second order scheme, while only the temporal terms are solved using the first order scheme (Grlj et al., 2022). In unsteady simulations, overset mesh is used to rotate the ship to obtain different wind angles of attack. The commercial software package STAR-CCM+ was used to numerically solve the required differential equations and to post-process the results.

2.1. Geometry

The 3D model of the post Panamax 6750-TEU containership is used as a case study. Table 1 shows the main particulars of the full-scale ship while Fig. 1 presents the body plan (Kim and Kim, 2016) and the 3D model of the containership fully loaded with containers.

It should be noted that containers are not randomly distributed on the deck, but are loaded for easy access in ports, depending on the weight of the individual container and taking into account trim and stability (Andersen, 2013). Therefore, in service, a containership can experience various trim angles depending on loading conditions caused by realistic container configurations. In this study, the influence of the trim angle on wind and air resistance is investigated. Therefore, two additional loading conditions which include a trim angle of 0.5° by stern and bow are considered, as done in (Islam and Soares, 2019). Table 2 presents the main particulars of the investigated containership at different loading conditions, where the positive trim angle corresponds to trim by bow, and the negative trim angle corresponds to trim by stern.

2.2. Mathematical model

In the commercial software package STAR-CCM+, a mathematical model based on the RANS equations is used. These equations arise from the mass and momentum conservation laws. For an incompressible, unsteady case, the equations read:

$$\frac{\partial \overline{u}_i}{\partial x_i} = 0 \tag{1}$$

$$\rho \frac{\partial \overline{u}_i}{\partial t} + \rho \frac{\partial}{\partial x_j}\left(\overline{u}_i \overline{u}_j + \overline{u_i' u_j'}\right) = -\frac{\partial \overline{p}}{\partial x_i} + \frac{\overline{\tau}_{ij}}{\partial x_j} \tag{2}$$

where ρ is the fluid density, $\overline{u}_i$ is the averaged Cartesian components of the velocity vector, $\rho\overline{u_i' u_j'}$ is the Reynolds Stress Tensor (RST), $\overline{p}$ is the mean pressure, and $\overline{\tau}_{ij}$ is the mean viscous stress tensor defined by:

$$\overline{\tau}_{ij} = \mu\left(\frac{\partial \overline{u}_i}{\partial x_j} + \frac{\partial \overline{u}_j}{\partial x_i}\right) \tag{3}$$

where μ is the dynamic viscosity of the fluid. Turbulence models are used to close the system of equations (1) and (2).

2.2.1. Realizable $k-\varepsilon$ Two-Layer turbulence model

RANS turbulence models are based on the modelling of RST. The stress tensor is modelled as a function of the mean flow quantities. The model used in this study belongs to the group of eddy viscosity models, which use the concept of turbulent eddy viscosity μ_t to model the stress tensor. RST is modelled based on the Boussinesq approximation as follows:

$$-\rho\overline{u_i' u_j'} = \mu_t\left(\frac{\partial \overline{u}_i}{\partial x_j} + \frac{\partial \overline{u}_j}{\partial x_i}\right) - \frac{2}{3}\rho k \delta_{ij} \tag{4}$$

where k is the turbulent kinetic energy.

The RKE turbulence model is a two-equation model that solves transport equations for the turbulent kinetic energy k and the turbulent dissipation rate ε. The eddy viscosity in this model is described with the following equation:

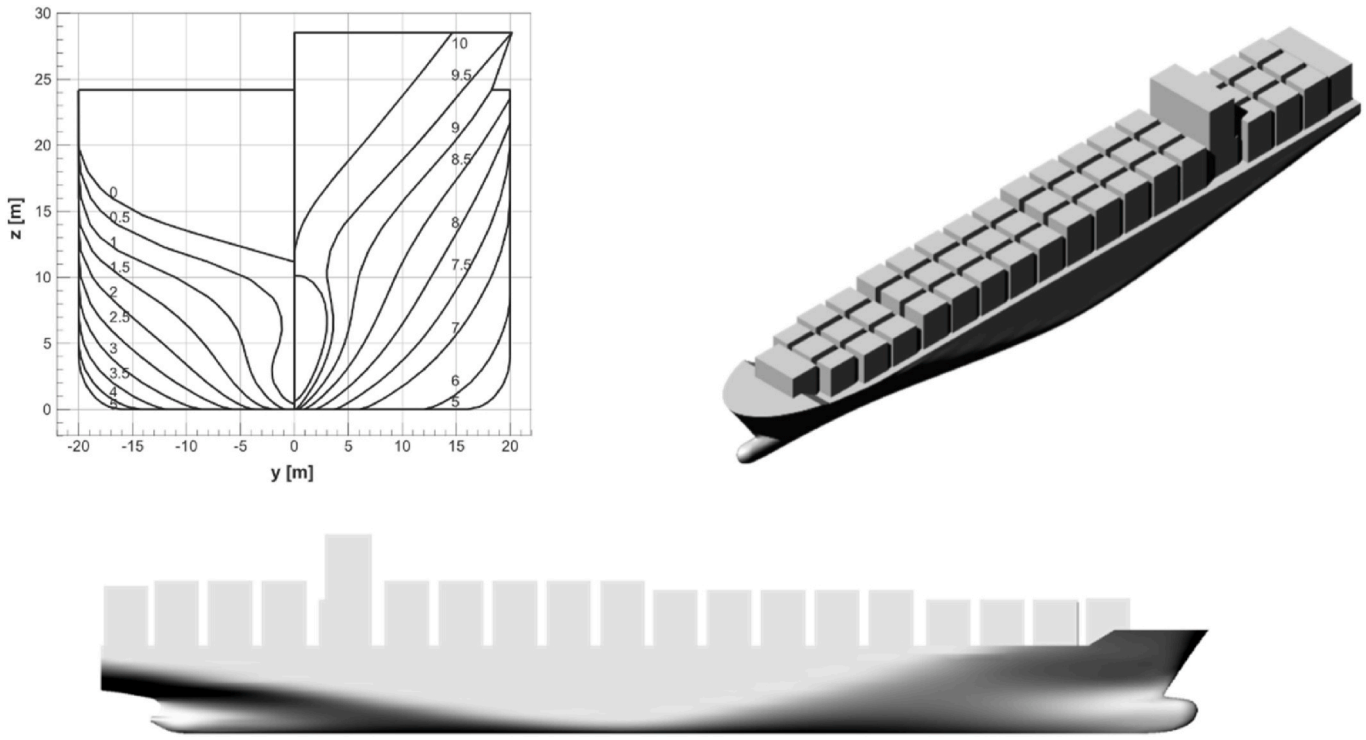


Fig. 1. Geometry of the fully loaded post Panamax 6750-TEU containership.

Table 2
Different loading conditions of the containership.

Trim angle	−0.5°	0°	0.5°
L_{WL}	291.693 m	292.479 m	285.43 m
T_{mid}	11.85 m	11.98 m	12.07 m
T_{aft}	13.10 m	11.98 m	11.01 m
T_{fwd}	10.60 m	11.98 m	13.26 m

$$\mu_t = \rho C_\mu \frac{k^2}{\varepsilon} \tag{5}$$

where C_μ is the model coefficient. The transport equations for k and ε read as follows:

$$\frac{\partial}{\partial t}(\rho k) + \frac{\partial}{\partial x_i}(\rho k \overline{u}_i) = \frac{\partial^2 k}{\partial x_i^2}\left(\mu + \frac{\mu_t}{\sigma_k}\right) + f_c G_k + G_b - Y_M - \rho(\varepsilon - \varepsilon_0) + S_k \tag{6}$$

$$\frac{\partial}{\partial t}(\rho \varepsilon) + \frac{\partial}{\partial x_i}(\rho \varepsilon \overline{u}_i) = \frac{\partial^2 \varepsilon}{\partial x_i^2}\left(\mu + \frac{\mu_t}{\sigma_\varepsilon}\right) + \frac{1}{T_e} C_{\varepsilon 1}(f_c S k + C_{\varepsilon 3} G_b) - C_{\varepsilon 2} f_2 \rho \left(\frac{\varepsilon}{T_e} - \frac{\varepsilon_0}{T_0}\right) + S_\varepsilon \tag{7}$$

where σ_k and σ_ε are turbulent Schmidt numbers, f_c is the curvature correction factor, G_k is the turbulent production term, G_b is the buoyancy production term, ε_0 is the ambient turbulence value that counteracts turbulence decay, Y_M is the dilatation dissipation, $C_{\varepsilon 1}$, $C_{\varepsilon 2}$, and $C_{\varepsilon 3}$ are the model depending coefficients, S is the modulus of the mean strain tensor, and finally S_k and S_ε are the user-defined source terms.

2.3. Wind loads

The results obtained from the numerical simulations are reported according to the ITTC recommendations (ITTC, 2021). Within the ITTC guidelines, a coordinate system is defined for the determination of wind load coefficients. Fig. 2 shows the coordinate system and sign convention used for the determination of the forces, moment, and angle of attack (Ψ).

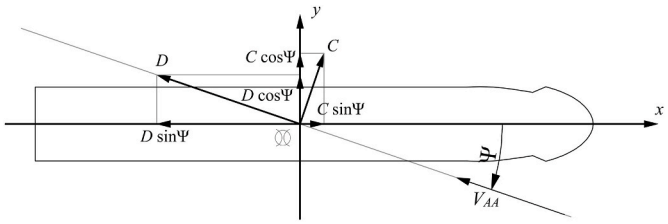


Fig. 2. The coordinate system for the determination of wind load coefficients.

From Fig. 2, the axes are defined as follows.

- the x-axis is positive forward,
- the y-axis is positive portside,
- the z-axis is positive upward.

The origin of the coordinate system is located at the ship centreline halfway between the fore and aft perpendiculars.

The tangential (D) and the normal component (C) of an aerodynamic force are the forces acting on the ship and are obtained from the numerical simulations. The components of the forces are projected onto the ship coordinate system $Oxyz$, Fig. 2. The longitudinal and transverse forces are thus defined as:

$$R_{AAX}(\Psi) = D\cos\Psi - C\sin\Psi \tag{8}$$

$$R_{AAY}(\Psi) = D\sin\Psi + C\cos\Psi \tag{9}$$

The non-dimensional wind load coefficients read as follows:

$$C_{DAX}(\Psi) = \frac{R_{AAX}(\Psi)}{q_A A_{VX}} \tag{10}$$

$$C_{DAY}(\Psi) = \frac{R_{AAY}(\Psi)}{q_A A_{VY}} \tag{11}$$

$$C_N(\Psi) = \frac{M_z(\Psi)}{q_A A_{VY} L_{OA}} \tag{12}$$

where A_{VX} is the transverse projected (frontal windage) area, A_{VY} is the lateral projected (side windage) area, and q_A is the dynamic pressure defined as:

$$q_A = \frac{1}{2}\rho_A V_{AA}^2 \tag{13}$$

where V_{AA} is the representative wind speed which is calculated using the height average wind velocities V_{A1} and V_{A2} for the calculation of $C_{DAX}(\Psi)$ and $C_{DAY}(\Psi)$, respectively. The height averaged wind velocities V_{A1} and V_{A2} used for non-dimensionalizing the forces and moment are obtained by integrating the wind velocity profile and dividing the result by the representative heights H_{BR} and H_L (Kume et al., 2019). H_{BR} is defined as the height from the sea surface to the top of the navigation bridge, while H_L is the average height calculated with the side projected area A_{VY} with the length overall L_{OA}. The procedure and nomenclature are explained in detail in the ITTC recommendations (ITTC, 2021).

2.4. Numerical setup

The computational domain of the airflow around the full-scale containership is discretized using an unstructured hexahedral mesh (Siemens, 2022). It consists of a cylinder-shaped tank as a background region and an overset mesh is defined in the vicinity of the containership. Rotation is defined for the overset mesh around the z axis with 10° intervals. The results obtained with the overset mesh were compared to the results obtained with a fixed grid for a specific angle of attack, and close agreement was achieved. Therefore, the authors decided to use the overset mesh since only one grid is needed to obtain the wind load coefficients for the entire range of angles of attack.

The domain boundaries are placed far enough away to avoid their influence on the airflow around the containership. The inlet and outlet boundaries are set at $3.5L_{PP}$, while the top boundary is set at $1.6L_{PP}$ from the ship. Boundary conditions are chosen as the velocity profile at the inlet boundary, and constant pressure is assigned at the outlet boundary. Symmetry is applied at the top boundary, while the bottom boundary is set as the no-slip wall or symmetry depending on the type of numerical simulation. Symmetry is applied for the determination of air resistance, while the no-slip wall is applied for the determination of wind resistance. The reason for the no-slip wall boundary condition at the bottom is the fact that due to the wind the natural boundary layer is formed. The airflow due to the ship movement does not form a boundary layer and thus the velocity profile is constant, i.e., not a function of height. The ship surface is defined as the no-slip wall boundary condition. Special attention is given to the discretization around the ship windage area. Prism layers are carefully created to keep the non-dimensional wall distance $y^+ > 30$. The distance between the wall and the centre of the first cell near the wall is defined using the following equation (Deng et al., 2013):

$$y^+ = 0.172\left(\frac{y}{L_{PP}}\right)Re^{0.9} \tag{14}$$

Fig. 3 shows the computational domain with the overset mesh enclosing the containership along with the described boundary conditions.

The wind profile is set at the inlet boundary as a function of the domain height. The vertical mean wind speed and streamwise turbulence intensity were measured by Andersen (2013) who provided the wind velocity profile with the following equation:

$$U(z) = U_{\text{ref}}\left(\frac{z}{z_{\text{ref}}}\right)^{\alpha} \tag{15}$$

where $U_{\text{ref}} = 45$ m/s is the reference velocity, $z_{\text{ref}} = 10$ m is the reference height, and $\alpha = 0.11$ is the velocity profile exponent. At the inlet boundary, the turbulent dissipation rate and the turbulent kinetic energy profiles are set based on the following equations:

$$\varepsilon(z) = \frac{(u^*)^3}{\kappa(z + z_0)} \tag{16}$$

$$k(z) = \frac{(u^*)^2}{\sqrt{C_\mu}} \tag{17}$$

where $\kappa = 0.41$ is the von Karman constant, $z_0 = 0.0002$ m is the aerodynamic roughness length, which is estimated according to the updated Davenport roughness classification for the sea surface (Wieringa, 1992), $C_\mu = 0.09$ is a constant, and u^* is the frictional velocity calculated with the following equation:

$$u^* = \frac{\kappa U(z)}{\ln\left(\frac{z_{\text{ref}}+z_0}{z_0}\right)} \tag{18}$$

The roughness of the bottom boundary is defined with the modified logarithmic law wall functions which use the equivalent sand-grain roughness height established by Blocken et al. (2007). The equivalent sand-grain roughness height k_s is defined as:

$$k_s = \frac{9.793 z_0}{C_s} \tag{19}$$

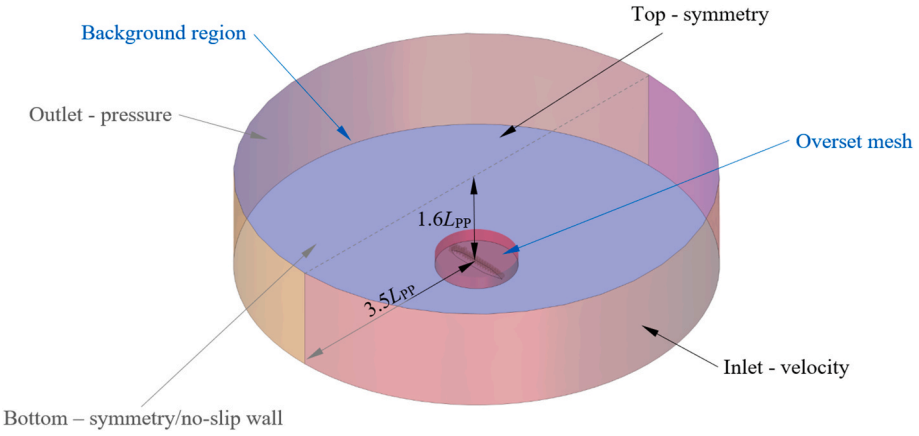


Fig. 3. Detailed view of the computational domain with boundary conditions.

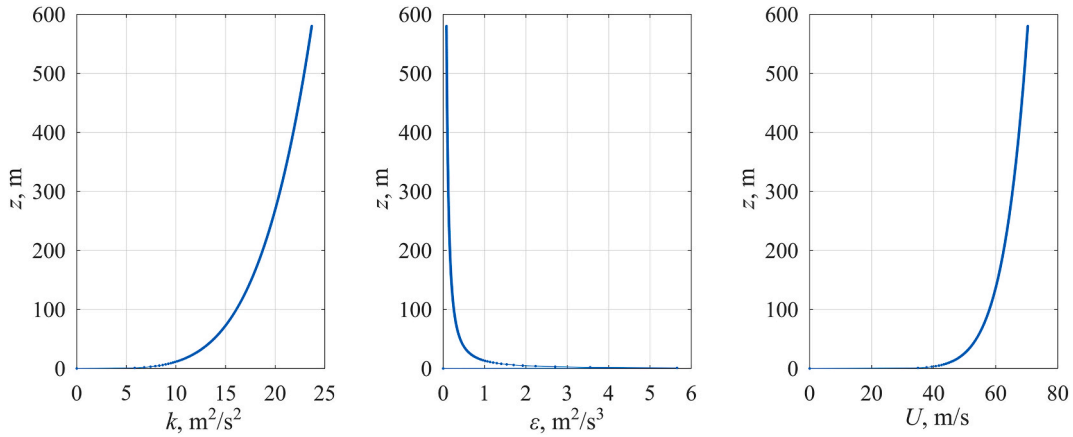


Fig. 4. Turbulent kinetic energy (left), turbulent dissipation rate (middle) and wind velocity (right) profiles used in the numerical simulations at the inlet boundary.

where $C_s = 1$ is the roughness constant.

Fig. 4 shows the turbulent kinetic energy, turbulent dissipation rate, and velocity profiles set at the inlet boundary within the numerical simulations for the determination of wind resistance.

Figs. 5–7 show details of the fine grid used within the numerical simulations for the determination of wind resistance. The region around the ship is refined because in this study the overset mesh is used to obtain different angles of attack. Fig. 7 shows the boundary layers around the containers and on the bottom surface of the domain. The bottom surface is refined to be able to capture the wind profile imposed at the inlet boundary which propagates to the rest of the computational domain. It should be noted that mesh within the numerical simulations for the determination of air resistance does not include prism layers at the bottom boundary and overset mesh. The boundary layer is discretized around the ship windage area to maintain the non-dimensional wall distance greater than 30 so that wall functions can be used.

Fig. 8 shows the obtained non-dimensional wall distance y^+ at an angle of attack of 180°. The obtained y^+ at the first cell is greater than 30 over the entire ship windage area, and thus the boundary layer can be solved utilizing wall functions.

Fig. 9 shows the dynamic pressure distributions for the fully loaded containership at angles of attack of 0° and 180°. The distributions are shown only for the stern and bow regions. It can be noticed that the dynamic pressure is lower on the leeward side of the ship, which for a 0° angle of attack it is the stern region and for 180° it is the bow region.

Fig. 10 shows the wind load coefficients as a function of time for the fully loaded containership. It can be noticed that all the wind load coefficients converged after approximately 40 s of simulation at all angles of attack.

2.5. The verification study

The Grid Convergence Index (GCI) method (Celik et al., 2008) is used for the verification study described in this subsection. Firstly, it is necessary to calculate the apparent order of the method p using the following equations:

$$p = \frac{1}{\ln r_{21}} \cdot \left| \ln \left| \frac{\varepsilon_{32}}{\varepsilon_{21}} \right| + q(p) \right| \tag{20}$$

$$q(p) = \ln\left(\frac{r_{21}^{p} - s}{r_{32}^{p} - s} \right) \tag{21}$$

$$s = 1 \cdot \mathrm{sgn}\left(\frac{\varepsilon_{32}}{\varepsilon_{21}} \right) \tag{22}$$

where r is the grid refinement ratio, ε_{ij} is defined as $\varepsilon_{ij} = \varphi_i - \varphi_j$, with φ being the solution. The order of the method can be obtained by iteratively solving equations (20)–(22).

Extrapolated values are defined by the following equation:

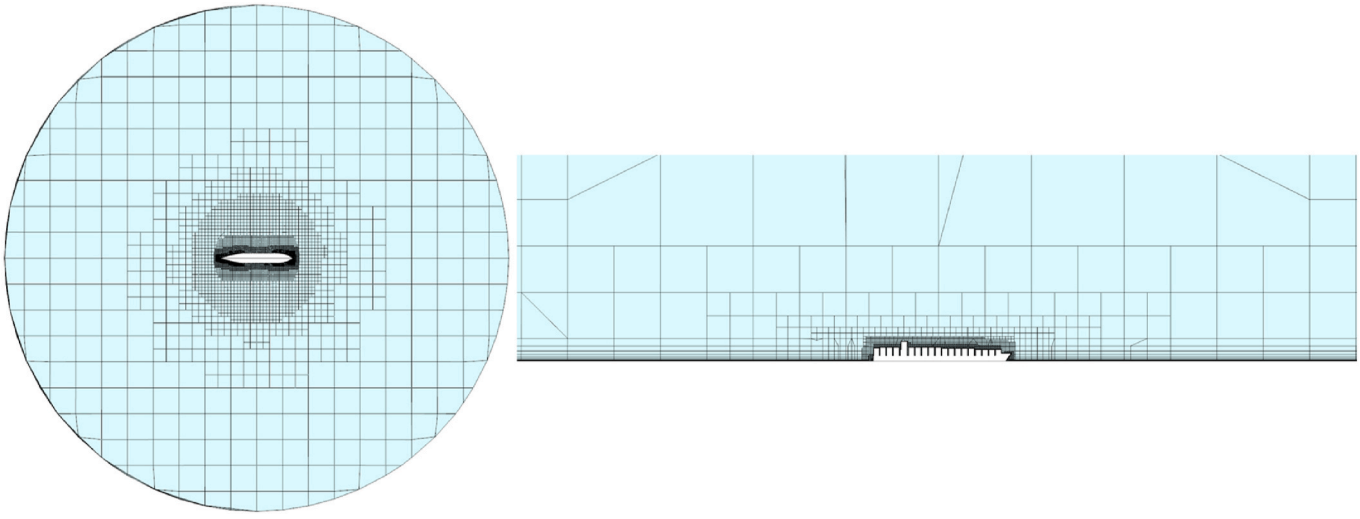


Fig. 5. Fine grid used within the numerical simulations for the determination of wind resistance. Profile view cross section (left) and top view cross section (right).

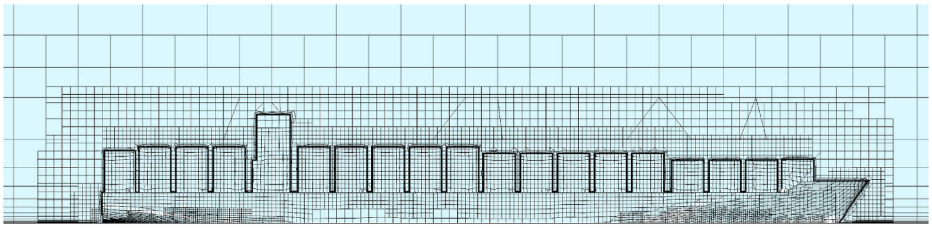


Fig. 6. Detailed view of the grid refinements in the region around the ship.

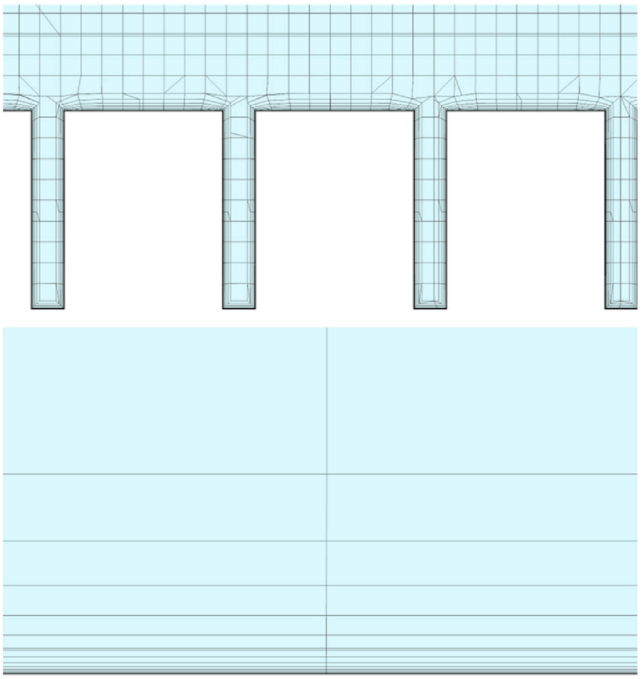


Fig. 7. Grid refinements around the containers (top) and the boundary layer at the bottom of the domain (bottom).

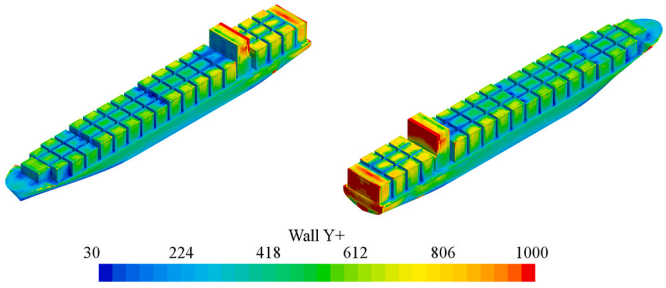


Fig. 8. Non-dimensional wall distance y^+ at the first cell near the wall for the fully loaded containership at a wind angle of attack of 180°.

$$\varphi_{\text{ext}}^{21} = \frac{r_{21}^{p}\varphi_1 - \varphi_2}{r_{21}^{p} - 1} \tag{23}$$

The approximate relative error is calculated as follows:

$$e_{\text{a}}^{21} = \left|\frac{\varphi_1 - \varphi_2}{\varphi_1}\right| \tag{24}$$

The extrapolated relative error is defined as:

$$e_{\text{ext}}^{21} = \left|\frac{\varphi_{\text{ext}}^{21} - \varphi_1}{\varphi_{\text{ext}}^{21}}\right| \tag{25}$$

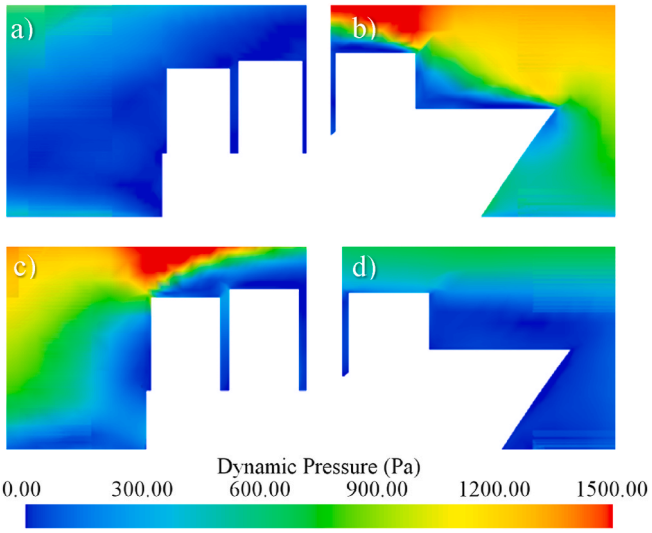


Fig. 9. Dynamic pressure distributions at an angle of attack of 0° - stern region (a), bow region (b), and at an angle of attack of 180° - stern region (c) and bow region (d).

Finally, the fine-grid convergence index can be calculated with the equation:

$$GCI_{\text{fine}}^{21} = \frac{1.25e_{\text{a}}^{21}}{r_{21}^{p} - 1} \tag{26}$$

For an evaluation of the extrapolated values, the convergence of the values must be determined with the possible convergence conditions being.

1. Monotonic convergence: $0 < R < 1$,
2. Oscillatory convergence: $R < 0$,
3. Divergence: $R > 1$.

The same method can be used to calculate the uncertainty due to time step. Fine grid is applied for the determination of temporal uncertainty with three time steps.

3. Results and discussion

3.1. The verification study

Three verification studies were carried out to assess simulation numerical uncertainty using the GCI method. The iteration uncertainty is omitted in the calculation of the simulation numerical uncertainty since it is often one order of accuracy lower than the uncertainty due to grid resolution and the time step size. The uncertainty for the grid size is obtained using three grids with the same setup but different cell numbers. The uncertainty for the time step is determined using three numerical simulations with different time steps. The uncertainty is defined using the following equation:

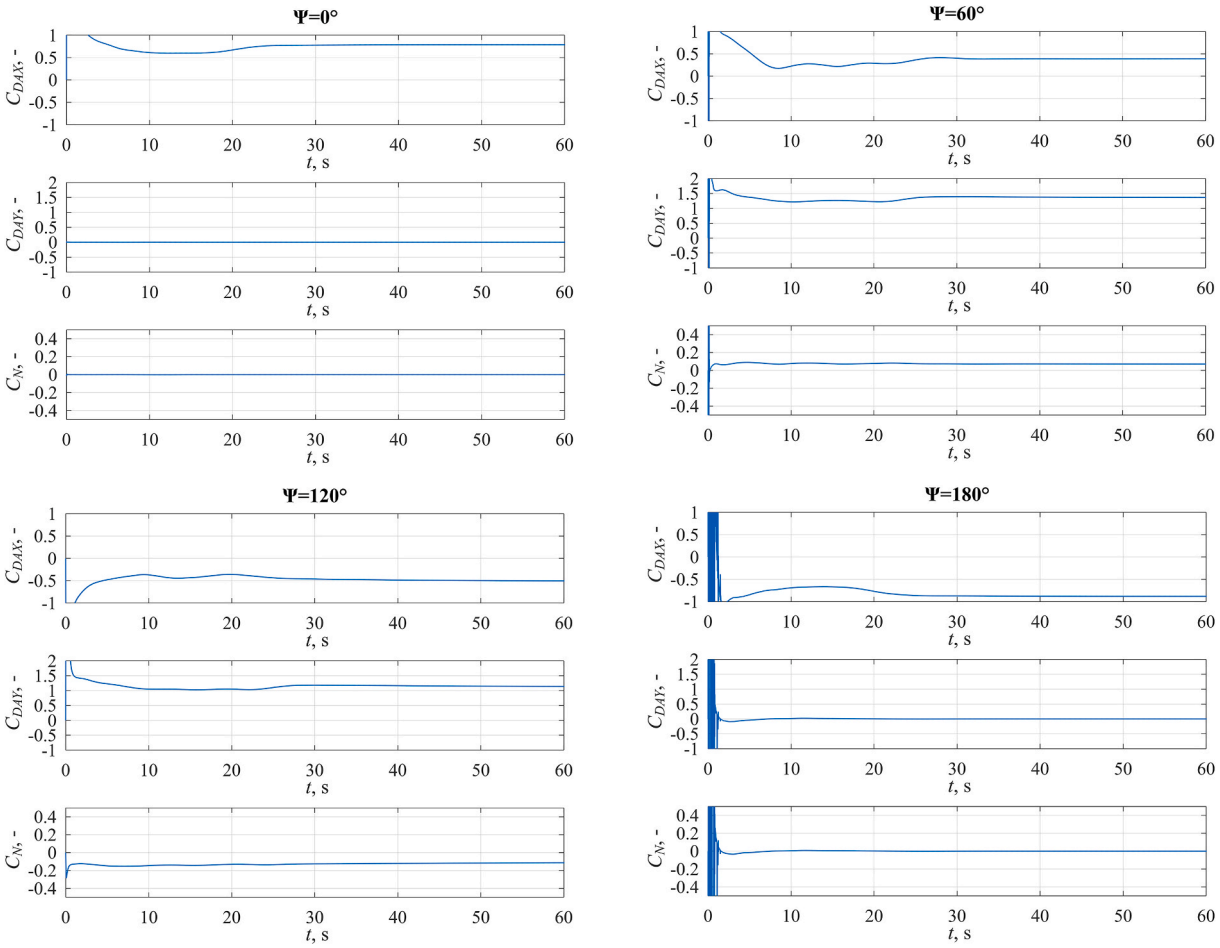


Fig. 10. Convergence of the wind load coefficients for the fully loaded containership at angles of attack of 0°, 60°, 120° and 180°.

$$U_{SN}{}^2 = U_G^2 + U_T^2 \tag{27}$$

where U_{SN} is the simulation numerical uncertainty, U_G is the grid size uncertainty, and U_T is the time step uncertainty.

The grid spacing h is calculated with the STAR-CCM + software package using the following equation:

$$h = \sqrt[3]{\frac{1}{N}\sum_{i=1}^{N}(\Delta V_i)} \tag{28}$$

where N is the total number of cells and V_i is the volume of the i-th cell.

The first verification study is performed for the case of a 9000+ TEU containership since experimental (Andersen, 2013) and numerical (Prpić-Oršić et al., 2020) results are available in the literature. Table 3 shows the number of cells and grid spacing used within the verification study.

Table 4 shows the refinement ratio for coarse-medium r_{32} and medium-fine r_{21} grid sizes and time steps, as well as the calculated GCIs for the longitudinal C_{DAX} and transverse C_{DAY} wind load coefficients. The presented wind load coefficients are calculated differently from the ITTC recommendations to be able to compare them with the available experimental and numerical results. The equations for the wind load coefficients used in the validation study read as follows:

$$C_{DAX} = \frac{R_{AAX}}{\frac{1}{2}\rho_A U_{ref}^2 A_{VX}} \tag{29}$$

$$C_{DAY} = \frac{R_{AAY}}{\frac{1}{2}\rho_A U_{ref}^2 A_{VY}} \tag{30}$$

Table 3
Details of the grids used for the first verification study.

Index	N	h, m
1	260 713	0.0444
2	163 618	0.0510
3	99 867	0.0615

The GCIs in Table 4 are calculated using the wind load coefficients C_{DAX} and C_{DAY} for the range of the angles of attack Ψ from 0° to 180°. The GCIs for both studies are below 5%, with the GCIs for the time step being noticeably lower than the ones for the grid size. Thus, it can be concluded that the fine grid size is adequate for the validation study. More details can be found in Tables 5–6 where the two verification study procedures for the grid size and time step are shown for different angles of attack. For most angles of attack, oscillatory convergence with few exceptions is obtained.

The second verification study is performed for the case of the fully loaded post Panamax 6750-TEU containership on an even keel. The time steps selected for the verification study are 0.02 s, 0.03 s, and 0.045 s, which means that the refinement ratio is 1.5 and thus the iterative procedure for calculating the order of the method is avoided. Table 7 shows details of the considered grids where the indices 1, 2 and 3 are for the fine, medium, and coarse mesh, respectively. The results of the second verification study are shown in Table 8, where the refinement ratios and GCIs are listed for both the verification study for the grid size and time step. It can be noticed that GCI for the fine grid size is below 4% for both the longitudinal and transverse wind load coefficients, so the

Table 4
Verification study for a 9000+ TEU containership.

	Grid size		Time step	
	C_{DAX}	C_{DAY}	C_{DAX}	C_{DAY}
r_{32}	1.206		1.500	
r_{21}	1.149		1.500	
p	6.216	6.849	5.350	4.214
GCI^{21}_{fine}, %	4.632	3.387	0.048	0.031

fine grid is adequate and will be used in the remaining numerical simulations. From Tables 9 and 10, it can be seen that, again, oscillatory convergence is obtained for most of the angles of attack. In the rest of the tables the extrapolated values and approximate and extrapolated relative errors are listed, as well as the GCI values at the bottom of the tables.

The third verification study is performed using the numerical results obtained within the numerical simulations for the determination of the air resistance. In these numerical simulations, a fixed mesh is used with the velocity profile at the inlet boundary being a constant since only the air resistance coefficient is determined. Table 11 shows the number of cells and grid spacing and Table 12 shows the results of the verification study. The third verification study shows satisfactory results, with the R value showing monotonic convergence, and GCI for the air resistance coefficient being under 3%.

3.2. Validation study

Experimental results for a 9000+ TEU containership are available in the literature (Andersen, 2013) and multiple authors have conducted CFD simulations of a similar setup. Prpić-Oršić et al. (2020) conducted numerical simulations of flow around a ship inside a wind tunnel to match the setup that Andersen (2013) used for her experiments. In the first set of numerical simulations, the influence of the wind tunnel walls is neglected and thus larger discrepancies between the transverse wind load coefficients are reported. The authors then included the influence of the walls in the simulations and showed a significant improvement in the numerical results when compared to the experimental ones. In this paper, the computational domain is cylindrical, with the inlet and outlet boundaries enclosing the region of the flow around the ship, and hence the influence of the walls is neglected. For the validation study, eight container configurations are used as shown in Fig. 11.

Fig. 12 presents a comparison of the obtained wind load coefficients with the experimental (Andersen, 2013) and uncorrected numerical (Prpić-Oršić et al., 2020) results. Significant discrepancies between the numerical and experimental results can be seen which is expected since the influence of the wind tunnel walls is neglected in the numerical simulations. The transverse wind load coefficient C_{DAY} is the most affected by the influence of the walls, which was recognized by Prpić-Oršić et al. (2020). Table 13 shows the median relative deviations calculated using the numerical and experimental results. Firstly, the

Table 5
Verification study of grid size for a 9000+ TEU containership at different angles of attack.

	C_{DAX}			C_{DAY}		
Ψ, °	20	90	160	20	90	160
r_{32}	1.125					
r_{21}	1.402					
ε_{32}	0.155	0.120	−0.038	0.012	−0.027	−0.019
ε_{21}	−0.040	−0.016	−0.092	0.007	−0.030	0.038
R	−0.259	−0.131	2.448	0.532	1.117	−1.967
p	7.664	11.261	11.021	7.664	11.261	11.021
$\varphi^{21}_{\text{ext}}$	−1.050	−0.606	1.416	0.366	1.288	0.293
e^{21}_{a}	0.038	0.026	0.066	0.018	0.023	0.125
e^{21}_{ext}	0.020	0.007	0.018	0.009	0.006	0.036
GCI^{21}_{fine}, %	2.473	0.856	2.291	6.755	4.493	10.498

Table 6
Verification study of time step for a 9000+ TEU containership at different angles of attack.

	C_{DAX}			C_{DAY}		
Ψ, °	20	90	160	20	90	160
r_{32}	1.500					
r_{21}	1.500					
ε_{32}	0.000	0.001	0.000	0.000	0.000	0.000
ε_{21}	0.000	0.011	0.000	0.000	−0.008	−0.001
R	0.064	9.182	−1.369	−1.848	−16.497	−4.811
p	6.790	5.469	0.774	6.790	5.469	0.774
$\varphi^{21}_{\text{ext}}$	−1.071	−0.612	1.390	0.369	1.281	0.305
e^{21}_{a}	0.000	0.018	0.000	0.000	0.006	0.002
e^{21}_{ext}	0.000	0.002	0.000	0.000	0.001	0.005
GCI^{21}_{fine}, %	0.000	0.279	0.048	0.018	0.050	0.055

Table 7
Details of the grids used for the determination of the wind load coefficients.

Index	N	h, m
1	549 846	13.881
2	195 739	19.455
3	144 025	21.886

Table 8
Verification study for the determination of wind load coefficients.

	Grid size		Time step	
	C_{DAX}	C_{DAY}	C_{DAX}	C_{DAY}
r_{32}	1.125		1.500	
r_{21}	1.402		1.500	
p	5.498	1.426	1.829	3.541
GCI^{21}_{fine}, %	2.759	3.871	1.258	0.713

Table 9
Verification study of grid size at different angles of attack.

	C_{DAX}			C_{DAY}		
Ψ, °	20	90	170	20	90	170
r_{32}	1.125					
r_{21}	1.402					
ε_{32}	0.101	0.000	−0.044	0.002	−0.003	−0.003
ε_{21}	0.008	0.025	−0.062	−0.016	0.088	0.018
R	0.080	−67.895	1.420	−10.540	−29.831	−5.673
p	22.140	8.040	3.283	22.140	8.040	3.283
$\varphi^{21}_{\text{ext}}$	0.872	0.290	−1.009	0.490	1.401	0.101
e^{21}_{a}	0.009	0.087	0.059	0.033	0.063	0.164
e^{21}_{ext}	0.000	0.006	0.030	0.000	0.004	0.088
GCI^{21}_{fine}, %	0.001	0.772	3.664	1.059	0.950	8.883

Table 10
Verification study of time step at different angles of attack.

	C_{DAX}			C_{DAY}		
Ψ, °	20	90	170	20	90	170
r_{32}	1.500					
r_{21}	1.500					
ε_{32}	0.000	−0.041	0.003	−0.002	−0.087	−0.001
ε_{21}	0.003	0.019	0.001	−0.001	0.058	0.008
R	−11.837	−0.458	0.418	0.589	−0.664	−7.920
p	6.095	1.927	2.152	6.095	1.927	2.152
$\varphi^{21}_{\text{ext}}$	0.872	0.276	−1.041	0.490	1.358	0.105
e^{21}_{a}	0.003	0.064	0.001	0.003	0.041	0.072
e^{21}_{ext}	0.000	0.057	0.001	0.000	0.036	0.055
GCI^{21}_{fine}, %	0.035	6.782	0.096	0.520	10.157	1.305

Table 11
Details of the grids used for the determination of air resistance.

Index	N	h, m
1	175 441	20.208
2	106 013	23.887
3	83.995	25.809

Table 12
Results of the verification study for the determination of air resistance using the fixed grid.

Parameter	Value
r_{32}	1.081
r_{21}	1.182
ε_{32}	0.057
ε_{21}	−0.028
R	−0.491
p	6.782
$\varphi_{\text{ext}}^{21}$	0.592
e_{a}^{21}	0.049
e_{ext}^{21}	0.022
GCI_{fine}, %	2.866

numerical results obtained within this study are compared to the experimental results, and thereafter with the numerical results obtained by Prpić-Oršić et al. (2020). Lastly, the numerical results obtained by Prpić-Oršić et al. (2020) are compared to the experimental results. High relative deviations are obtained for all cases, which confirms that the influence of the wind tunnel walls is high. The obtained numerical results from this study show slightly better results than those obtained by Prpić-Oršić et al. (2020). The largest median relative deviations from the experimental results are obtained for the moment coefficient C_N and is equal to 59.9% for container configuration 7. Even when compared to the uncorrected numerical results, the relative deviation is still high for that specific container configuration.

3.3. Wind resistance

In this subsection, the effects of trim on wind resistance are investigated in detail. The wind resistance is defined using the non-dimensional wind load coefficients described in Section 2. Numerical simulations of the flow around a post Panamax 6750-TEU containership are carried out for the design loading condition as well as two loading conditions keeping the displacement constant: trim of 0.5° by stern and by bow. Since the ship is symmetrical with respect to the longitudinal centreline, the range of angles of attack is selected from 0° to 180°. Different container configurations are used within the numerical simulations defined similarly to Andersen's experimental setups, Fig. 13. The first configuration, which is used for the verification studies, is the fully loaded containership. This setup is defined according to the IMO Safety of Life at Sea regulation (IMO, 2001), which requires the ship operator to have a line of sight from the bridge equal to 500 m or two ship lengths, whichever is smaller. Configurations 2 and 3 are the empty containership and the containership loaded with only one row of containers above the deck. The following configurations 4 and 5 are defined by removing whole stacks of containers in every other bay. In configuration 6, the containership is equally loaded with stacks being 6 containers high which is one less than the maximum number of containers per stack. The last three configurations 7–9 are defined by streamlining the container configuration and adding containers in the aft or fore deck.

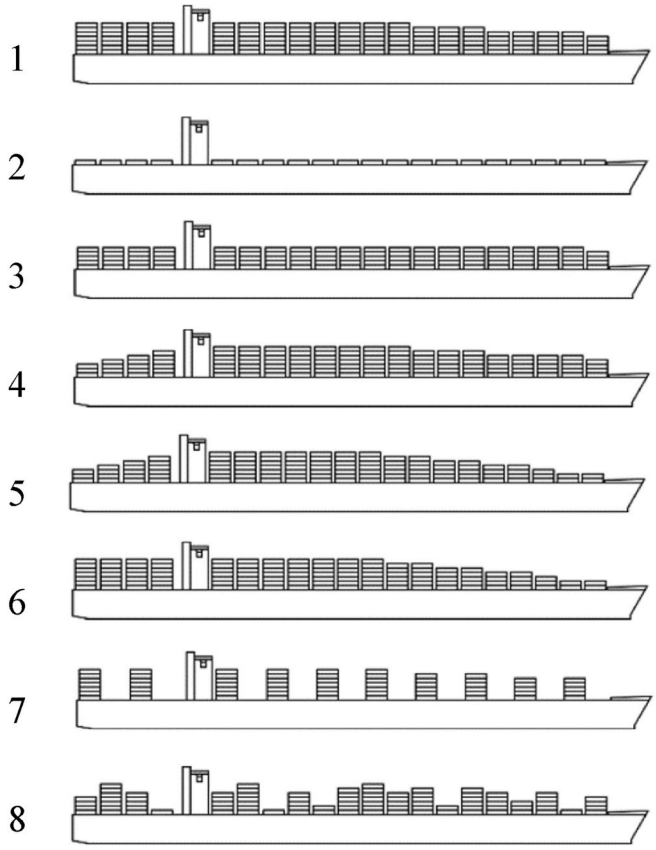


Fig. 11. Container configurations for the validation study.

Figs. 14–16 show the longitudinal C_{DAX}, transverse C_{DAY} wind load coefficients, and the yawing moment coefficient C_N. It can be seen that the investigated trim does not significantly affect the coefficients in most cases. The moment coefficient C_N seems to be the most affected by the trim. A positive trim angle yields higher values of the moment coefficient, while the trim angle with the same absolute value yields lower values over the whole range of angles of attack. The highest absolute values of the longitudinal wind load coefficients are obtained for container configurations 4 and 5, which can be attributed to the fact that every other bay is empty and thus more recirculations occur in these gaps. The transverse wind load coefficient C_{DAY} does not seem to be affected by the trim of the containership.

The relative deviations for the wind load coefficients for all container configurations with respect to even keel conditions are given in Table 14. It can be noticed that the trim angle has the greatest influence on the yawing moment coefficient with the median of the results obtained for all configurations equal to 7.434% for a trim of 0.5° by stern and 9.768% for a trim of 0.5° by bow.

3.4. Air resistance

The air resistance is determined within the numerical simulations in which a constant velocity profile is applied at the inlet boundary. In this study, steady-state numerical simulations are conducted for nine container configurations. The grid in this case is fixed and the air resistance coefficient is calculated. Both the transverse force R_{AAY} and the moment M_z are assumed to be equal to zero, so they are not reported in this subsection. The influence of different loading conditions defined

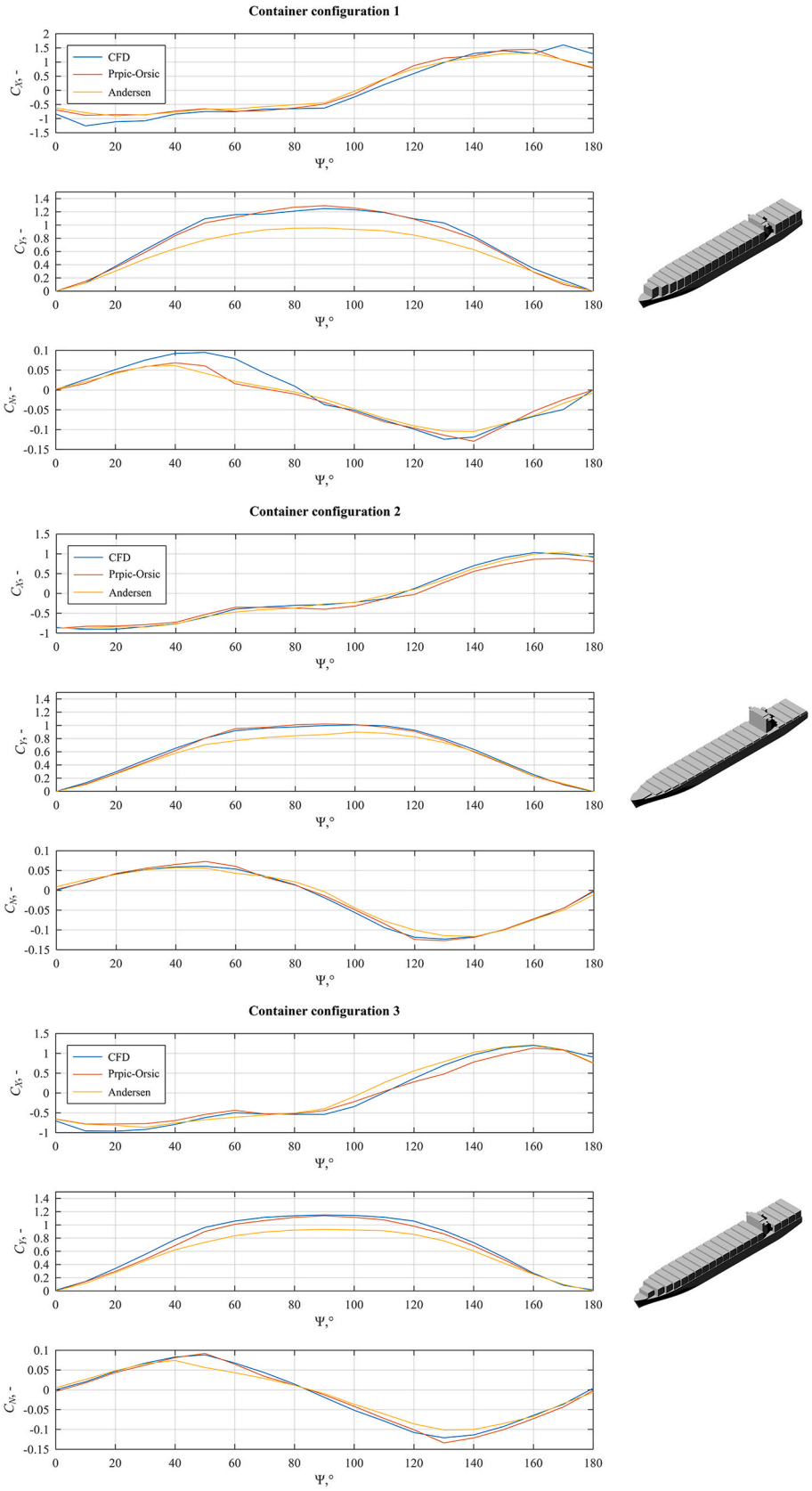


Fig. 12. The obtained wind load coefficients and 3D models of the containership for the analysed container configurations.

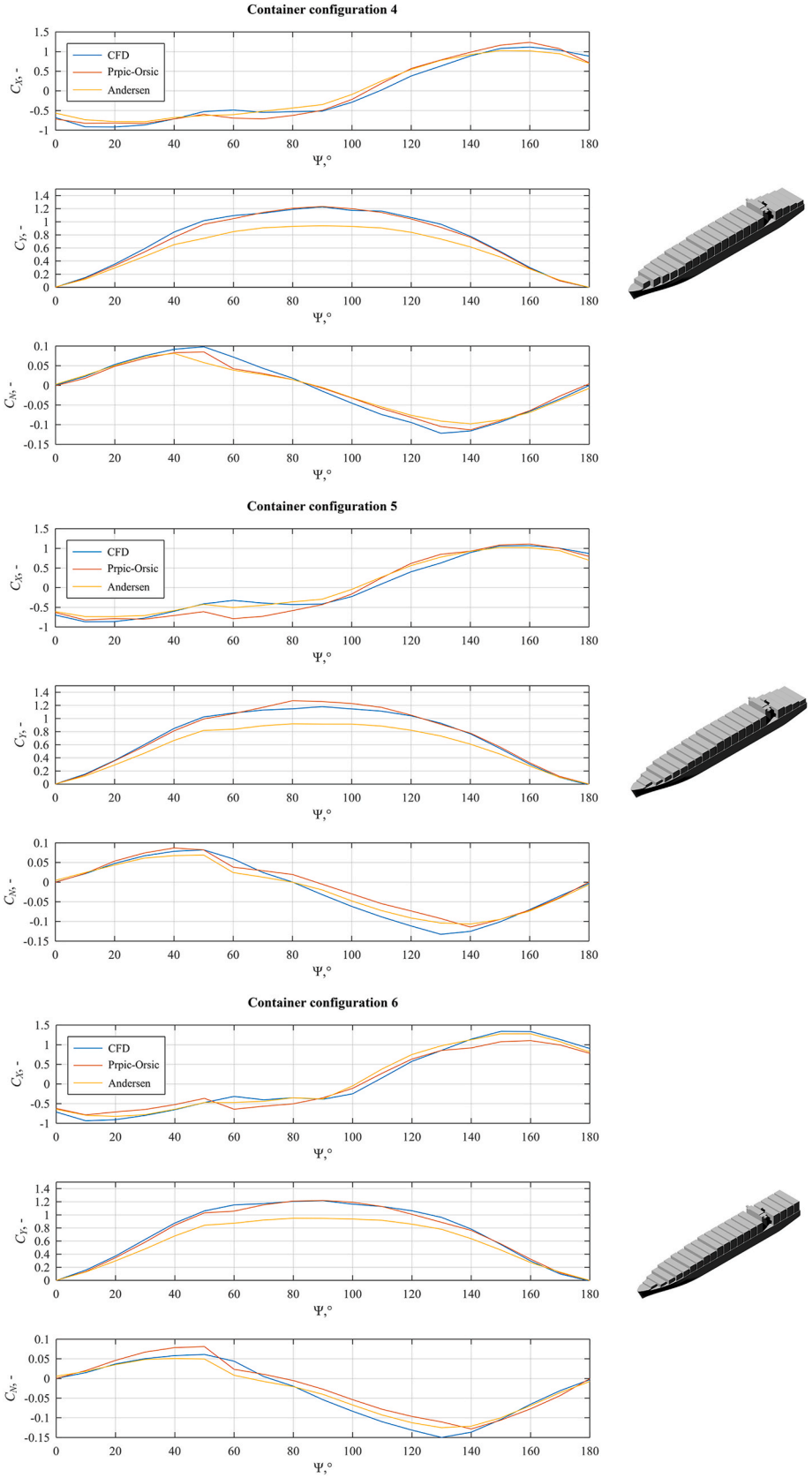


Fig. 12. (*continued*).

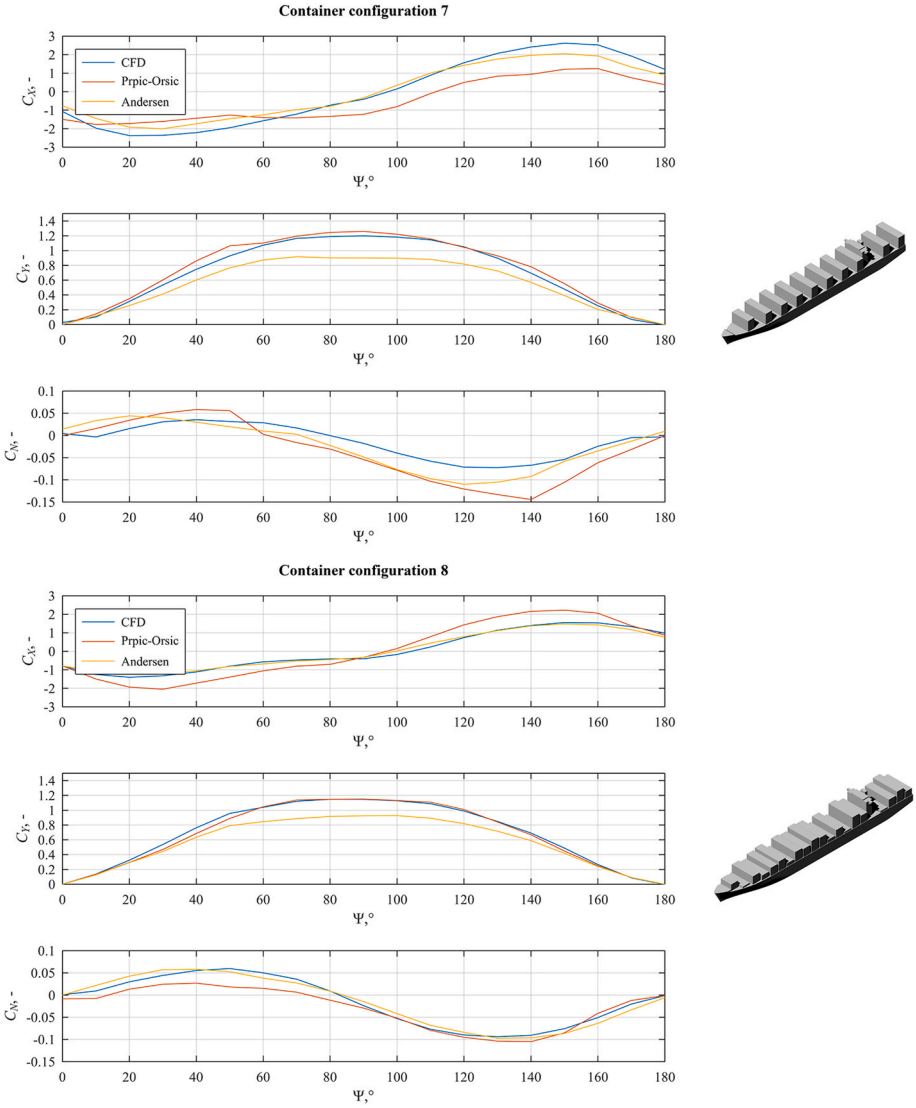


Fig. 12. (*continued*).

Table 13
Relative deviations of results from the validation study.

Relative deviations	$\frac{\varphi_{CFD}-\varphi_{EFD}}{\varphi_{EFD}}\cdot 100\%$			$\frac{\varphi_{CFD}-\varphi_{Prpić-Oršić\ et\ al.}}{\varphi_{Prpić-Oršić\ et\ al.}}\cdot 100\%$			$\frac{\varphi_{Prpić-Oršić\ et\ al.}-\varphi_{EFD}}{\varphi_{EFD}}\cdot 100\%$		
Coefficient/Container configuration	C_X	C_Y	C_N	C_X	C_Y	C_N	C_X	C_Y	C_N
1	23.23	30.90	28.71	20.36	4.69	28.27	9.84	28.88	19.18
2	7.01	12.96	10.17	12.20	4.31	6.07	12.65	11.14	10.64
3	7.75	23.48	25.32	19.06	6.77	9.69	10.84	16.17	18.79
4	18.70	26.91	25.51	11.93	4.07	24.09	13.34	24.21	9.28
5	17.48	25.97	22.01	10.50	4.49	15.34	11.92	26.00	22.88
6	8.53	24.91	17.35	24.40	5.35	28.91	15.70	21.32	30.89
7	25.55	27.02	59.90	66.68	11.10	54.83	46.47	36.71	56.02
8	7.78	20.85	22.52	35.40	3.46	67.45	57.53	17.32	60.26
Average:	14.50	24.12	26.44	25.07	5.53	29.33	22.29	22.72	28.49

by the container configurations and the trim as well as sailing speeds on the air resistance is investigated. Table 15 shows the air resistance coefficient for the design loading condition and trim angle of 0.5° by stern and bow. It can be seen from Table 15 that the influence of the trim on the air resistance coefficient is negligible. The highest absolute value of the relative deviation is equal to 6.759% for container configuration 7 for a trim of 0.5° by stern and the lowest relative deviation is obtained for the fully loaded containership for a trim of 0.5° by bow and is equal

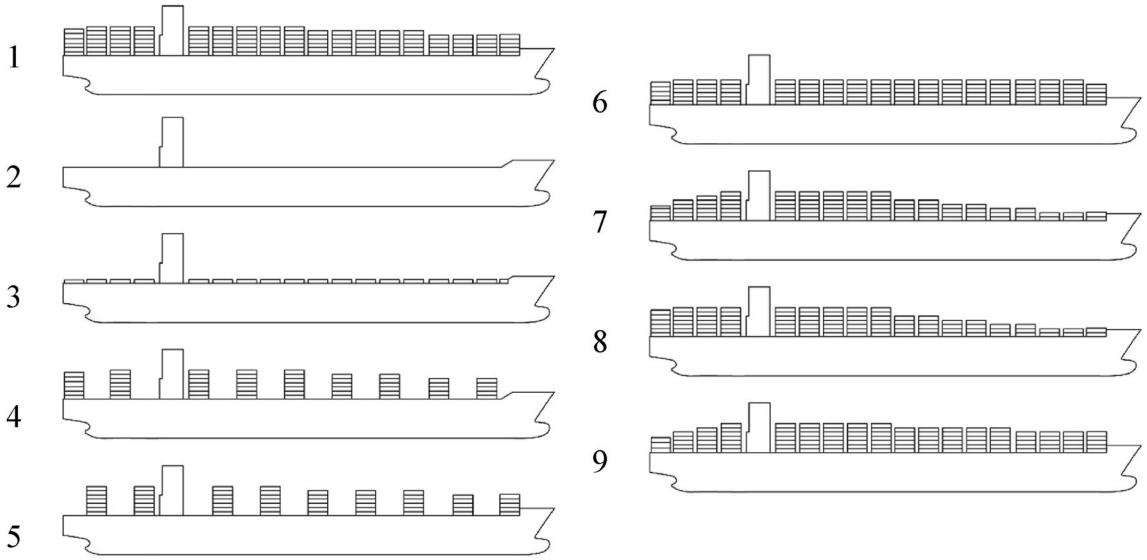


Fig. 13. Container configurations for a post Panamax 6750 TEU containership.

to 0.173%. The results also show that trim by stern causes an increase, while trim by bow causes a decrease of the air resistance coefficient. Greater differences are obtained for trim by bow for all container configurations except for the empty containership. Fig. 17 shows the velocity distribution for container configuration 7 since the relative deviations are highest for this container configuration. The reason for the increase in the air resistance coefficient for trim by stern is the larger flow separation region behind the ship compared to an even keel. The opposite is true for trim by bow, where a lower flow separation region behind the ship can be noticed compared to an even keel. This effect is greater for trim by bow, and thus the absolute values of the relative deviations are greater.

The influence of speed is investigated within the steady-state numerical simulations by varying the sailing speed. The steps are determined according to the number of iterations needed for the air resistance coefficient to converge. The obtained air resistance is presented in Fig. 18 as a function of the speed for the analysed container configurations. From Fig. 18 it can be seen that the highest air resistance is obtained for container configuration 2, which can be related to higher vorticity behind the superstructure as opposed to container configuration 1, Fig. 20. In (Grlj et al., 2022), the total resistance of the post Panamax 6750-TEU containership without a superstructure was determined to be 2387.2 kN at 25 knots. The portion of air resistance within total resistance varies from 3.5% (container configuration 9) to 5.8% (container configuration 2). In Fig. 19, the influence of trim on the air resistance for container configuration 1 is shown and it can be seen that it is insignificant for all analysed ship speeds.

4. Conclusions

In this study, numerical simulations were conducted systematically to assess the influence of different loading conditions on the wind and air resistance of a full-scale post Panamax 6750-TEU containership. The loading conditions are defined with the trim angle and the container configurations. To obtain different loading conditions, the displacement volume is maintained constant, while the trim angle is varied with the following values: 0.5°, 0° and 0.5°. The container configurations consist of different arrangements of containers on the deck of the ship and nine configurations are specified within the study. The wind profile is defined using the power law with reference values corresponding to those from the available wind tunnel test results. The wind loads are reported using two methods for calculating the coefficients. The first method is used for the validation study since the available experimental data and numerical results were reported using the same coefficients. The second method is described in the ITTC recommendations which are based on the study done by Kume et al. (2019). The air resistance of the ship is determined within the numerical simulations with a fixed grid. The influence of the ship speed is investigated using different constant speeds as the inlet velocity profile.

The following conclusions are drawn based on the findings of this study.

- Detailed verification studies have been carried out for three numerical setups used within this study and the obtained numerical uncertainty is relatively low. The obtained numerical results are validated against the available experimental data, and close agreement is shown.
- The influence of trim on wind resistance is negligible when compared to the influence of different container configurations on the deck of the containership.
- The numerical results suggest that the yawing moment coefficient is most influenced by the trim while relatively small differences are noted for the longitudinal and transverse wind load coefficients. The highest longitudinal wind load coefficients are obtained for container configurations 4 and 5, which can be attributed to the fact that every other bay is empty and thus more recirculations occur in these gaps. This is confirmed by the wind tunnel tests carried out by Andersen (2013), where the author concluded that the longitudinal force increases if there is a significant difference between the height of individual bays.
- The results show a certain influence of the trim angle on the air resistance coefficient where trim by bow causes lower values of air resistance and trim by stern causes higher values. This can be attributed to the flow separation behind the ship.
- It has been shown that container configurations affect air resistance, and the portion of air resistance within total resistance varies from 3.5% up to 5.8% for container configurations 9 and 2, respectively.

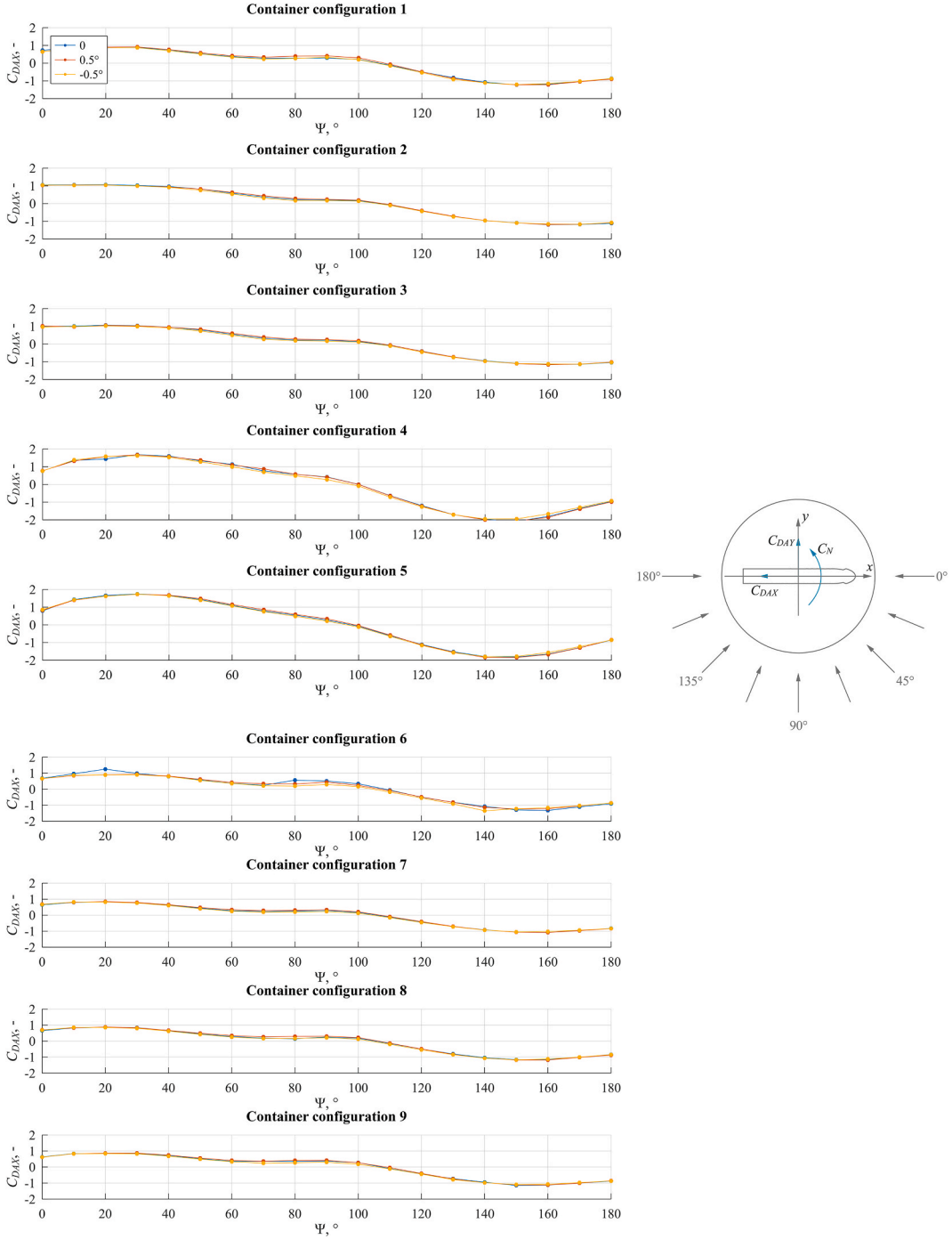


Fig. 14. Longitudinal wind load coefficient C_{DAX} as a function of angle of attack Ψ.

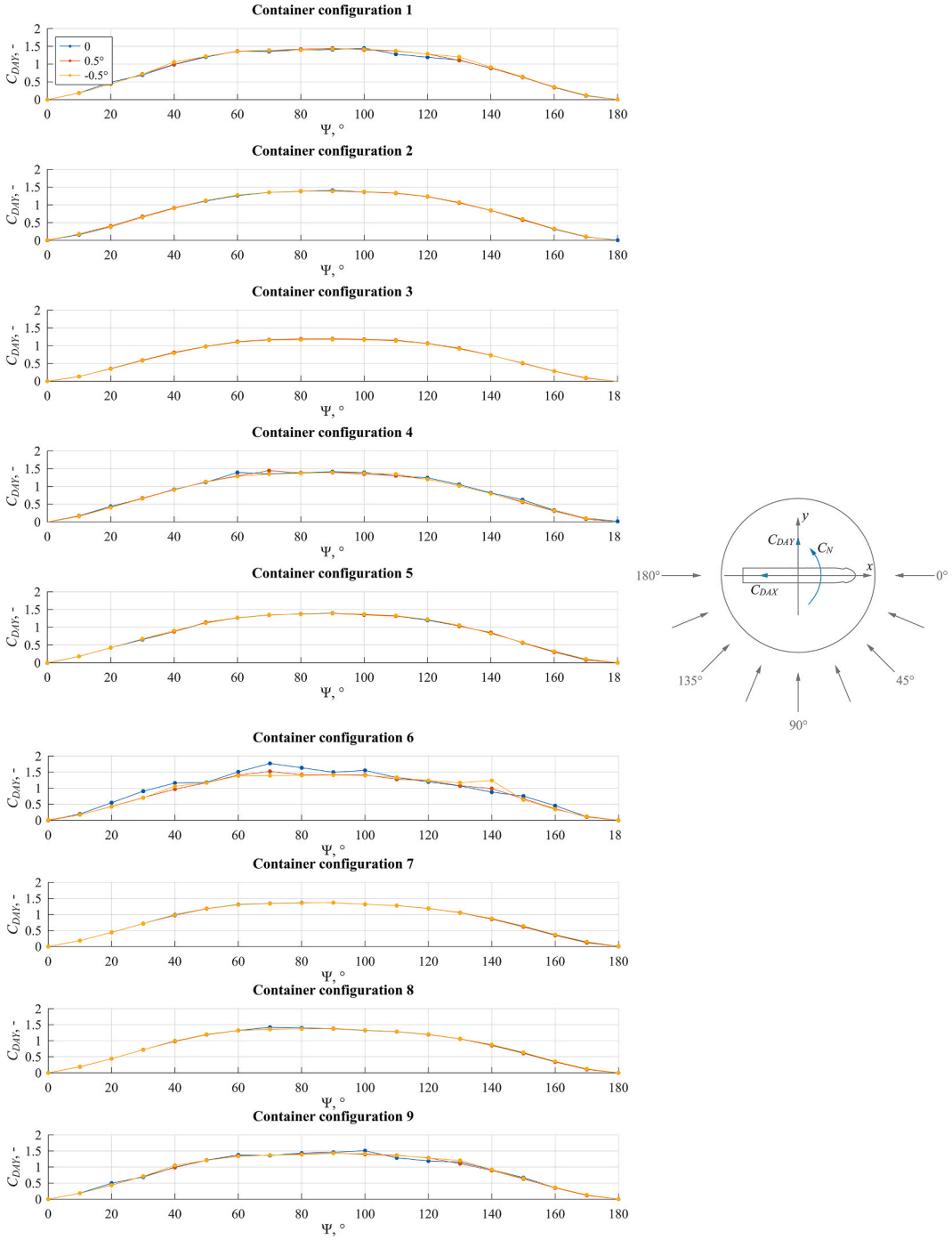


Fig. 15. Transverse wind load coefficient C_{DAY} as a function of angle of attack Ψ.

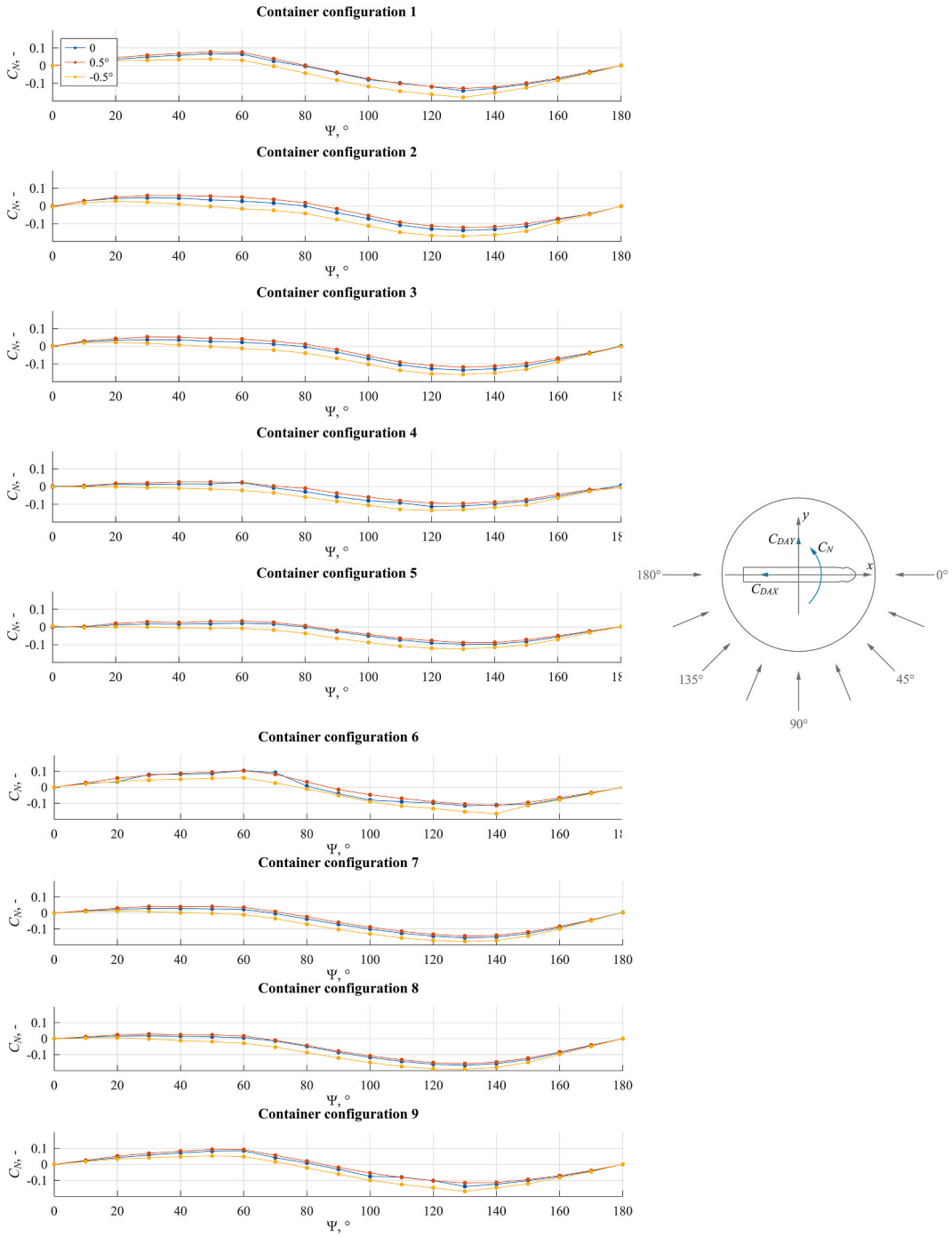


Fig. 16. Yawing moment coefficient C_N as a function of angle of attack Ψ.

Table 14
Relative deviations calculated for the wind load coefficients.

Trim angle	0.5°			−0.5°		
Coefficient/Container configuration	C_{DAX}	C_{DAY}	C_N	C_{DAX}	C_{DAY}	C_N
1	3.629	0.690	−0.498	−1.280	1.962	9.768
2	−0.483	0.131	−7.434	−2.502	0.398	8.408
3	1.159	0.000	−11.572	−3.304	−1.056	8.179
4	1.020	−1.696	−12.768	−3.763	−1.470	18.899
5	1.046	−0.566	−9.566	−2.186	−0.450	18.631
6	−4.451	−11.041	−8.407	−5.472	−8.332	3.744
7	1.215	−0.312	−7.303	−2.622	0.161	11.907
8	2.426	−1.222	−6.403	−1.243	0.184	13.761
9	−0.025	−1.864	0.833	−3.271	0.172	9.319
Medians:	1.159	0.690	7.434	2.622	0.450	9.768

Table 15
Air resistance coefficient for different container configurations and loading conditions.

Container configuration	Trim angle			Relative deviation, %	
	0°	−0.5°	0.5°	$\frac{\varphi_{-0.5°}-\varphi_{0°}}{\varphi_{0°}}\cdot 100\%$	$\frac{\varphi_{0.5°}-\varphi_{0°}}{\varphi_{0°}}\cdot 100\%$
1	0.578	0.579	0.548	0.173	−5.354
2	0.968	0.946	0.959	−2.273	−0.930
3	0.916	0.925	0.894	0.983	−2.402
4	0.725	0.728	0.706	0.414	−2.621
5	0.643	0.645	0.640	0.311	−0.467
6	0.591	0.594	0.573	0.508	−3.141
7	0.651	0.679	0.607	4.301	−6.759
8	0.660	0.686	0.620	3.939	−6.061
9	0.568	0.573	0.550	0.880	−3.169

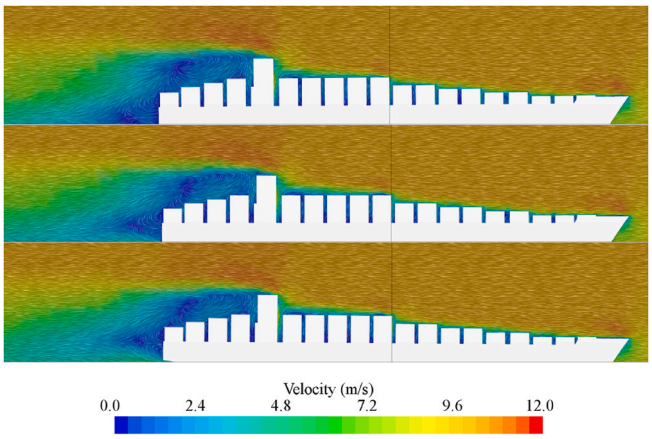


Fig. 17. Velocity distributions at a profile view cross section for container configuration 7 at different trim angles – trim by stern (top), even keel (middle) and trim by bow (bottom).

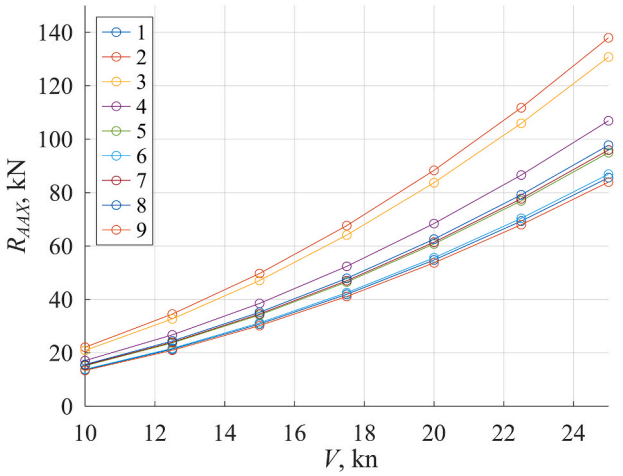


Fig. 18. Air resistance as a function of speed for different container configurations.

Due to the lack of available results of wind tunnel tests in the literature regarding wind loads on containerships, this study demonstrates that CFD can be a viable tool for the assessment of wind and air resistance. Future research should focus on investigating the wind and air resistance coefficients for different containership hull forms and sizes, as well as container configurations. Further, since in this study full-scale numerical simulations were conducted, it would be interesting to determine whether there are scale effects in the determination of wind and air resistances.

CRediT authorship contribution statement

Carlo Giorgio Grlj: Conceptualization, Methodology, Software, Formal analysis, Investigation, Resources, Writing – original draft, Writing – review & editing, Visualization. **Nastia Degiuli:** Conceptualization, Methodology, Formal analysis, Investigation, Resources, Writing – original draft, Writing – review & editing, Visualization, Supervision. **Željko Tuković:** Conceptualization, Methodology, Formal analysis, Investigation, Writing – review & editing, Supervision. **Andrea Farkas:** Conceptualization, Methodology, Software, Investigation, Resources, Writing – original draft, Writing – review & editing. **Ivana Martić:** Conceptualization, Methodology, Formal analysis, Investigation, Resources, Writing – original draft, Writing – review & editing.

Declaration of competing interest

The authors declare that they have no known competing financial

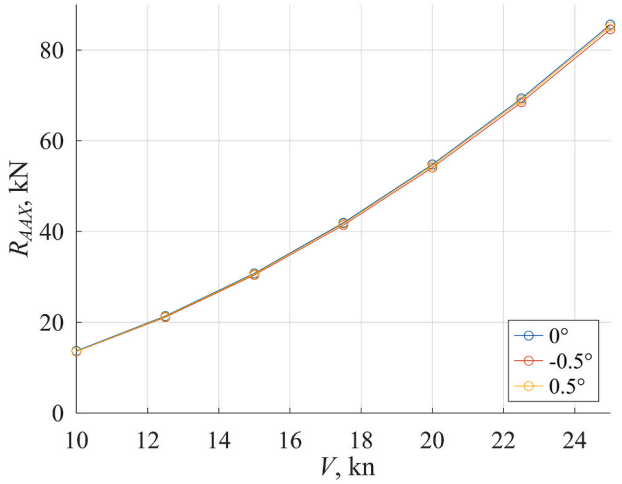


Fig. 19. The influence of trim on air resistance for container configuration 1.

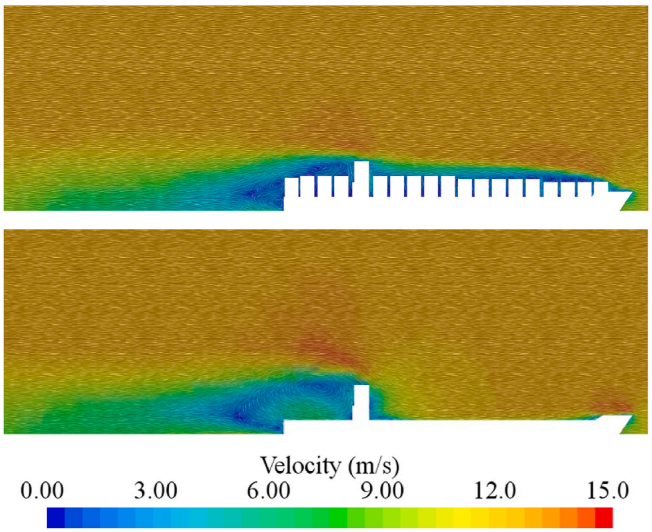


Fig. 20. Velocity distribution for container configurations 1 (upper) and 2 (lower).

interests or personal relationships that could have appeared to influence the work reported in this paper.

Data availability

Data will be made available on request.

Acknowledgments

This study has been fully supported by the Croatian Science Foundation under project IP-2020-02-8568.

References

Andersen, I.M.V., 2013. Wind loads on post-panamax container ship. Ocean Eng. 58, 115–134.
Blocken, B., Carmeliet, J., Stathopoulos, T., 2007. CFD evaluation of wind speed conditions in passages between parallel buildings—effect of wall-function roughness modifications for the atmospheric boundary layer flow. J. Wind Eng. Ind. Aerod. 95 (9–11), 941–962.
Celik, I.B., Ghia, U., Roache, P.J., Freitas, C.J., 2008. Procedure for estimation and reporting of uncertainty due to discretization in CFD applications. Journal of fluids Engineering-Transactions of the ASME 130 (7).
Deng, R., Huang, D.B., Zhou, G.L., Sun, H.W., 2013. Investigation on some factors effecting ship resistance calculation with CFD code FLUENT. J. Ship Mech. 17 (6), 616–624.
Deng, R., Song, Z., Ren, H., Li, H., Wu, T., 2022. Investigation on the effect of container configurations and forecastle fairings on wind resistance and aerodynamic performance of large container ships. Engineering Applications of Computational Fluid Mechanics 16 (1), 1279–1304.
Farkas, A., Degiuli, N., Martić, I., 2018. Assessment of hydrodynamic characteristics of a full-scale ship at different draughts. Ocean Eng. 156, 135–152.
Farkas, A., Degiuli, N., Martić, I., Dejhalla, R., 2019. Numerical and experimental assessment of nominal wake for a bulk carrier. J. Mar. Sci. Technol. 24 (4), 1092–1104.
Grlj, C.G., Degiuli, N., Farkas, A., Martić, I., 2022. The influence of numerical parameters on the total resistance of a container ship. In: Proceedings of the 19th International Congress of the International Maritime Association of the Mediterranean, Istanbul, Turkey, pp. 33–40.
International Maritime Organization, 2001. SOLAS. Consolidated Edition, 2001.
ITTC, 2021. ITTC-recommended procedures and guidelines, 7.5-03-02-05. Guideline on the CFD-based determination of wind resistance coefficients. ITTC Quality System Manual.
Islam, H., Soares, C.G., 2019. Effect of trim on container ship resistance at different ship speeds and drafts. Ocean Eng. 183, 106–115.
Janssen, W.D., Blocken, B., van Wijhe, H.J., 2017. CFD simulations of wind loads on a container ship: validation and impact of geometrical simplifications. J. Wind Eng. Ind. Aerod. 166, 106–116.
Kaup, J., 2006. Metodyka numerycznego wyznaczania współczynników oporu nadwodnej części statku. Zeszyty Naukowe Akademii Morskiej w Szczecinie 11 (83), 131–140.
Kim, Y., Kim, J.H., 2016. Benchmark study on motions and loads of a 6750-TEU containership. Ocean Eng. 119, 262–273.
Kume, K., Ohba, H., Orihara, H., Mizokami, S., 2019. Wind velocity profile and representative wind velocity for wind resistance measurement of ship models. J. Jpn. Soc. Nav. Archit. Ocean Eng. 30, 1–13.
Majidian, H., Azarsina, F., 2019. Numerical simulation of container ship in oblique winds to develop a wind resistance model based on statistical data. Journal of International Maritime Safety, Environmental Affairs, and Shipping 2 (2), 67–88.
Martić, I., Degiuli, N., Majetić, D., Farkas, A., 2021. Artificial neural Network model for the evaluation of added resistance of container ships in head waves. J. Mar. Sci. Eng. 9 (8), 1–23.
Nguyen, T.V., Shimizu, N., Kinugawa, A., Tai, Y., Ikeda, Y., 2017. Numerical studies on air resistance reduction methods for a large container ship with fully loaded deck-containers in oblique winds. In: Proceedings of the VII International Conference on Computational Methods in Marine Engineering, *MARINE 2017*, Nantes, France, pp. 1040–1051.
Prpić-Oršić, J., Valčić, M., Čarija, Z., 2020. A hybrid wind load estimation method for container ship based on computational fluid dynamics and neural networks. J. Mar. Sci. Eng. 8 (7), 539.
Ricci, A., Janssen, W.D., van Wijhe, H.J., Blocken, B., 2020. CFD simulation of wind forces on ships in ports: case study for the Rotterdam Cruise Terminal. J. Wind Eng. Ind. Aerod. 205, 104315.
Seok, J., Park, J.C., 2020. Comparative study of air resistance with and without a superstructure on a container ship using numerical simulation. J. Mar. Sci. Eng. 8 (4), 267.
Siemens, 2022. STAR-CCM + User Guide.
Torre, S., Burlando, M., Ruscelli, D., Repetto, M.P., Camauli, G., 2021. Wind tunnel experimental investigation of the aerodynamic coefficients reduction due to sheltering surroundings on a cruise ship moored in port. J. Wind Eng. Ind. Aerod. 218, 104731.
van He, N., Mizutani, K., Ikeda, Y., 2016. Reducing air resistance acting on a ship by using interaction effects between the hull and accommodation. Ocean Eng. 111, 414–423.
Vinayak, P.P., Krishna Prabu, C.S., Vishwanath, N., Prakash, S.O., 2021. Numerical simulation of ship navigation in rough seas based on ECMWF data. Brodogradnja 72 (1), 19–58.
Wang, W., Wu, T., Zhao, D., Guo, C., Luo, W., Pang, Y., 2019. Experimental–numerical analysis of added resistance to container ships under presence of wind–wave loads. PLoS One 14 (8), e0221453.
Wieringa, J., 1992. Updating the Davenport roughness classification. J. Wind Eng. Ind. Aerod. 41 (1–3), 357–368.
Wnek, A.D., Guedes Soares, C., 2015. CFD assessment of the wind loads on an LNG carrier and floating platform models. Ocean Eng. 97, 30–36.
Zhang, Y., Wang, P., Liu, Y., Hu, J., 2021. Nonlinear rolling stability and chaos research of trimaran vessel with variable layouts in regular and irregular waves under wind load. Brodogradnja 72 (3), 97–123.

Article X

Article published by Faculty of Mechanical Engineering and Naval Architecture of the University of Zagreb in Brodogradnja: an international journal of naval architecture and ocean engineering for research and development on 10 May 2026, available online: https://brodogradnja.fsb.hr/vol-77-no-4-77405/

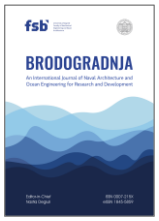
Brodogradnja Volume 77 Number 4 (2026) 77405

University of Zagreb
Faculty of Mechanical
Engineering and Naval
Architecture

journal homepage: www.brodogradnja.fsb.hr

Brodogradnja

An International Journal of Naval Architecture and
Ocean Engineering for Research and Development



Optimization of marine propeller characteristics for maximum open water efficiency using an ANN-GA tool trained on experimental data

Carlo Giorgio Grlj[1,*], *Nastia Degiuli*[1], *Ivana Martić*[1], *Marta Pedišić Buča*[2]

[1]*University of Zagreb, Faculty of Mechanical Engineering and Naval Architecture, Ivana Lučića 5, Zagreb 10000, Croatia*
[2]*Jadranbrod d.d., Avenija Većeslava Holjevca 20, Zagreb, 10000, Croatia*

ARTICLE INFO

Keywords:
Preliminary propeller design
Open water characteristics
Artificial Neural Network
Surrogate model
Bayesian regularization
Optimization
Genetic algorithm

ABSTRACT

This study proposes a numerical approach for identifying the propeller characteristics that achieve maximum open water efficiency for a specific ship, considering its propulsion characteristics and defined operating conditions. The proposed method combines an artificial neural network (ANN) with an optimization procedure based on the genetic algorithm. The ANN is trained using experimentally obtained open water characteristics of 143 propellers, enabling accurate prediction of thrust and torque coefficients as well as the open water efficiency as functions of propeller geometric parameters. The optimal ANN achieved an R^2 of 0.95 and *RMSE* of 0.20 on the validation set. Once trained, the ANN is integrated into the optimization procedure to explore the design space and identify the optimal propeller, while satisfying the imposed constraints. The approach is validated on several benchmark ships. The obtained results show good agreement with those from literature, despite the relatively small training dataset used in the present work. The obtained open water efficiencies are higher than those of the original propellers for all ships considered. It is demonstrated that the required propulsion characteristics used as input parameters can be obtained from different sources, including numerical simulations, experimental data, and empirical prediction methods such as the approach proposed by Holtrop and Mennen. For practical implementation, a standalone application was developed in MATLAB, integrating the trained ANN and genetic algorithm (GA) optimization procedure into a user-friendly environment.

1. Introduction

In ship design, the hydrodynamic performance of the propeller has a critical role in the determination of the ship overall efficiency, fuel consumption and, consequently, the environmental impact. Conventionally, propeller design can be carried out using systematic series data or regression formulae [1]. From the propeller main particulars: the pitch ratio P/D, expanded area ratio A_E/A_0, blade number Z, the corresponding open water characteristics are derived from systematic propeller series such as Wageningen B [2], Gawn [1], or Kaplan series. The final selection of the propeller is typically based on maximising open water efficiency η_O

* Corresponding author.
E-mail address: carlo.g.grlj@fsb.unizg.hr

https://doi.org/10.21278/brod77405
Received 23 March 2026; Received in revised form 24 April 2026; Accepted 09 May 2026
Available online 10 May 2026
ISSN 0007-215X; eISSN 1845-5859

while satisfying the imposed constraints. This method relies on the open water curves derived from the towing tank tests for the different propeller series. Also, the optimal propellers from different series cannot be directly compared, as each design is optimized within the constraints of its respective series [3].

Recent advances in data-driven modelling have enabled more flexible and efficient alternatives. Artificial Neural Networks (ANN), owing to their capability to approximate highly nonlinear relationships, have been increasingly applied in ship design. In particular, ANNs have been used as surrogate models to predict ship resistance and propulsion characteristics, thereby significantly accelerating iterative design. Martić et al. [4] developed an ANN to predict the added resistance coefficient of containerships in regular head waves at various speeds. The data used for training the ANN is derived using boundary integral element method for various hull forms of containerships. This study enables a reliable prediction of added resistance coefficient during the preliminary ship design based on its characteristics and design speed. Ao et al. [5] developed a neural network using the results obtained with a low-fidelity method and with Computational Fluid Dynamics (CFD) simulations to predict the ship total resistance. The authors demonstrated that neural networks can be used to accurately predict the ship hydrodynamic performance. Lee and Lee [6] employed ANN with the intent to replace CFD simulations for the determination of wake distribution and total resistance. The proposed ANN was used in a multi-objective optimization procedure to enhance the wake distribution as well as to reduce the total resistance of a 1000 TEU containership. Degiuli et al. [7] employed different machine learning (ML) methods to develop models for the prediction of wind loads on containerships. The data for training the ML models are derived from CFD simulations for containership loaded with different container configurations at wind angles of attack from 0° to 180° performed by Grlj et al. [8]. More recently, Physics-Informed Neural Networks (PINNs) have been increasingly applied to a range of problems in ship hydrodynamics [9]. Tong and Chen [10] proposed a type of PINN trained on large eddy simulation data for the prediction of propeller wake and showed that a reconstruction of velocity and pressure fields can be obtained with minimal computational demand. Bourchas and Papalambrou [11] developed a PINN for the prediction of ship main engine power with the given loading conditions and sea states. Their results demonstrate that the proposed PINN effectively captures the underlying physical principles, in contrast to conventional ML methods.

The integration of ANN-based surrogate models with optimization algorithms provides a powerful framework for improving ship energy efficiency. Hadavi et al. [12] developed an ANN and coupled it with Genetic Algorithm (GA) to identify optimal designs of ship masts with the aim to minimize the aerodynamic load on the ship. Lefkiou et al. [13] proposed a multitask deep neural network for the prediction of shear and pressure distributions on various Wigley-based hull forms. The trained neural network was incorporated into a GA optimization procedure to obtain an improved hull form that exhibited a 15.77 % reduction in total resistance compared to the baseline geometry. Optimization algorithms can be employed to lower the ship total resistance or improve propulsive efficiency by altering the ship hull or propeller geometry. Cheng et al. [14] generated fully parametric models of a ship, propeller, and rudder for an optimization study with the aim to lower the total resistance. The authors used CFD simulations to obtain the input data needed for the optimization study. An approximately 5 % reduction in delivered power was obtained with respect to the baseline geometry. Liu et al. [15] developed an ANN with numerical results as the training dataset for the prediction of hydrodynamic performance of an Autonomous and Remotely-operated Vehicle (ARV). The trained ANN was used to optimize the ARV geometry with the aim to minimise the dimensionless forces acting on it. Guo et al. [16] performed an optimization of the Korean Research Institute of Ships and Ocean Engineering (KRISO) containership (KCS) hull with the aim to minimise the total resistance by adjusting the bulbous bow. The authors employed Particle Swarm Optimization (PSO) algorithm for the optimization process and CFD simulations for obtaining the hydrodynamic loads acting on the ship. Zhao et al. [17] employed PSO within a numerical framework for selecting the optimal hull, propeller and main engine configuration, showing its potential in the ship design cycle.

In light of recent advancements in data-driven approaches to ship design, several studies have demonstrated the successful application of similar methodologies to preliminary propeller design. Vázquez-Santos et al. [18] employed the Non-dominated Sorting Genetic Algorithm-II (NSGA-II) to optimize the

Wageningen B-series propellers by maximising η_O, while minimising the engine brake power with constraints imposed for thrust and cavitation. The authors investigated the open water characteristics of the obtained propeller by conducting CFD simulations, which were validated against experimental data. Lu et al. [19] performed a multi-objective energy efficiency optimization for ships sailing in realistic conditions. Within the study, the authors optimized the propeller parameters with the objective of increasing propulsion efficiency, while decreasing the specific fuel oil consumption and nitrogen oxides emissions. Vesting and Bensow [20] proposed an optimization method based on PSO algorithm for propeller design. The authors found that the PSO algorithm yields comparable results to NSGA-II but with faster convergence and better solutions regarding constraint violations. Ouyang et al. [21] employed the NSGA-II for multi-objective optimization of rim-driven thrusters which resulted in a 5.78 % improvement of the maximal hydrodynamic efficiency. Zuo et al. [22] developed a Bayesian-optimized back-propagation neural network and employed the NSGA-III algorithm to obtain the optimal propeller design by simultaneously maximizing η_O and K_T while minimizing K_Q. Tadros et al. [3] developed an ANN that uses dimensionless propeller parameters as inputs to predict the corresponding open water characteristics. The trained model was subsequently employed to identify optimal propellers for selected ships across different propeller series. For the training dataset, the authors used the available thrust coefficients K_T and torque coefficients K_Q for propellers from different series. The developed ANN was trained on 4424 propeller designs. Similarly, Li et al. [23] developed data-driven surrogate model for the prediction of propeller open water characteristics. The authors identified eight input parameters that are relevant for the determination of propeller open water characteristics through correlation and importance analysis. The main finding of the study is that the support vector regression achieved the highest predictive accuracy on the validation dataset among the considered ML algorithms.

In the present study, a novel procedure for the preliminary design of marine propellers is proposed. An ANN, trained on experimentally obtained propeller open-water characteristics, is coupled with a GA to systematically determine the optimal propeller parameters that maximize η_O while simultaneously satisfying the prescribed design constraints. The proposed framework enables the direct identification of optimal propeller characteristics within the early design stage, thereby providing a structured and computationally efficient decision-support tool for designers. The developed procedure is demonstrated through selected case studies involving various hull forms of large commercial ships, confirming its robustness and broad applicability. The results further indicate that the ANN is capable of accurately reproducing propeller open water characteristics even when trained on a relatively limited set of experimental data, highlighting the practical feasibility of the proposed procedure as opposed to similar studies where a large database was used for the training of the ML models. To enable practical use of the proposed optimization procedure, a standalone application was developed in MATLAB that integrates the trained ANN with the GA optimization procedure within its graphical user interface. The installation files for the developed tool can be found at https://github.com/carloggrlj/OptiProp . The remainder of the paper is organized as follows: Section 2 describes in detail the procedure for developing the ANN and the optimization approach as well as the ships used as case studies. Section 3 presents the obtained results, and Section 4 summarizes the main findings of the study.

2. Methods

2.1 General overview

The aim of the present study is to obtain an optimal propeller for a ship with the known required thrust T, thrust deduction fraction t, wake fraction w, and propeller loading K_T / J^2. First an ANN is trained to develop a surrogate propeller model that takes the propeller main parameters, i.e., P/D, hub ratio d/D, A_E / A_0, and Z as inputs, and predicts K_T and K_Q over a range of advance coefficients J. Consequently, the η_O is calculated. The trained ANN is subsequently integrated into an optimization procedure based on GA. Within the optimization procedure, the propeller geometric characteristics are varied and η_O is obtained for

specific K_T / J^2. The objective is to obtain the propeller geometric characteristics that yield the maximum η_O while keeping the design variables within the bounds defined by the training dataset and enforcing cavitation and noise criteria through penalty terms. After the GA converges, the optimal propeller corresponding to the specified design speed is identified, its main geometric parameters are extracted, and the results are reported. Figure 1 illustrates schematically the proposed model.

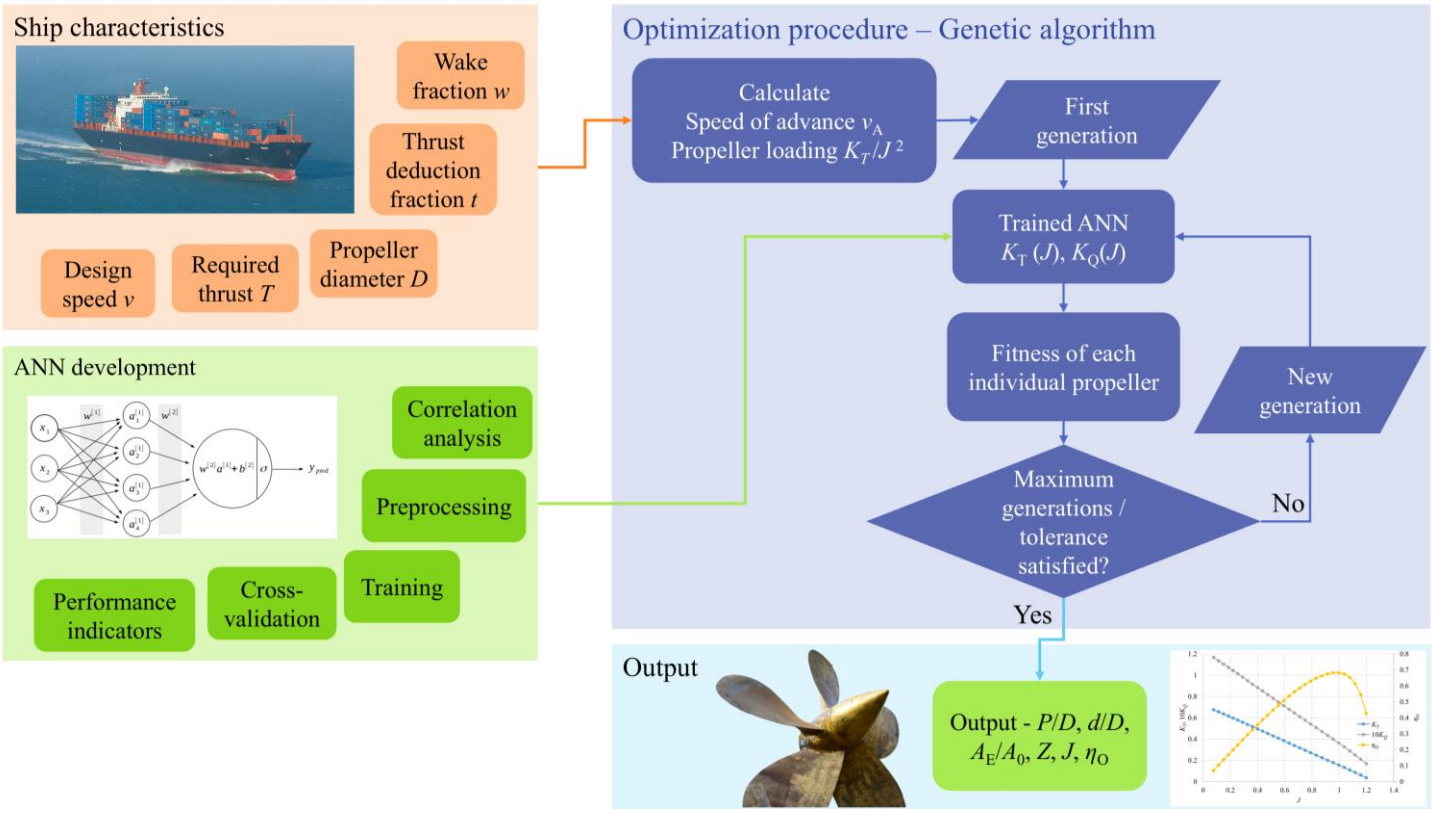


Fig. 1 A schematic illustration of the proposed numerical approach.

2.2 Database

The database used to develop the ANN is based on comprehensive open water tests conducted at the Brodarski Institute (Jadranbrod d.d.) in Zagreb. The open water test consists of the propeller model attached to a horizontal shaft, which is immersed at 1.5 times the propeller diameter D below the free surface. The test is conducted by maintaining the same rate of revolution n while varying the speed at which the propeller model is towed from 0 m/s until the thrust and torque become negative. During the experiment the following physical quantities were measured at each J: the towing speed, i.e. the speed of advance v_A, propeller thrust T, propeller torque Q, and n using the propeller dynamometer and a revolution counter. The K_T and K_Q are calculated for the entire range of J with the following expressions:

$$K_T = \frac{T}{\rho n^2 D^4} \tag{1}$$

$$K_Q = \frac{Q}{\rho n^2 D^5} \tag{2}$$

where ρ is the water density. Based on these physical parameters, J and η_O are calculated with the following expressions:

$$J = \frac{v_A}{nD} \tag{3}$$

$$\eta_O = \frac{K_T}{K_Q}\frac{J}{2\pi} \tag{4}$$

Table 1 Descriptive statistics of propeller characteristics used as inputs

Value	Inputs			
	P/D	d/D	A_E/A_0	Z
Minimum	0.60	0.14	0.30	3.00
Mean	0.98	0.20	0.72	4.05
Median	0.89	0.19	0.65	4.00
Mode	1.00	0.19	1.05	4.00
Maximum	1.80	0.33	1.20	5.00
Standard deviation	0.29	0.05	0.23	0.67

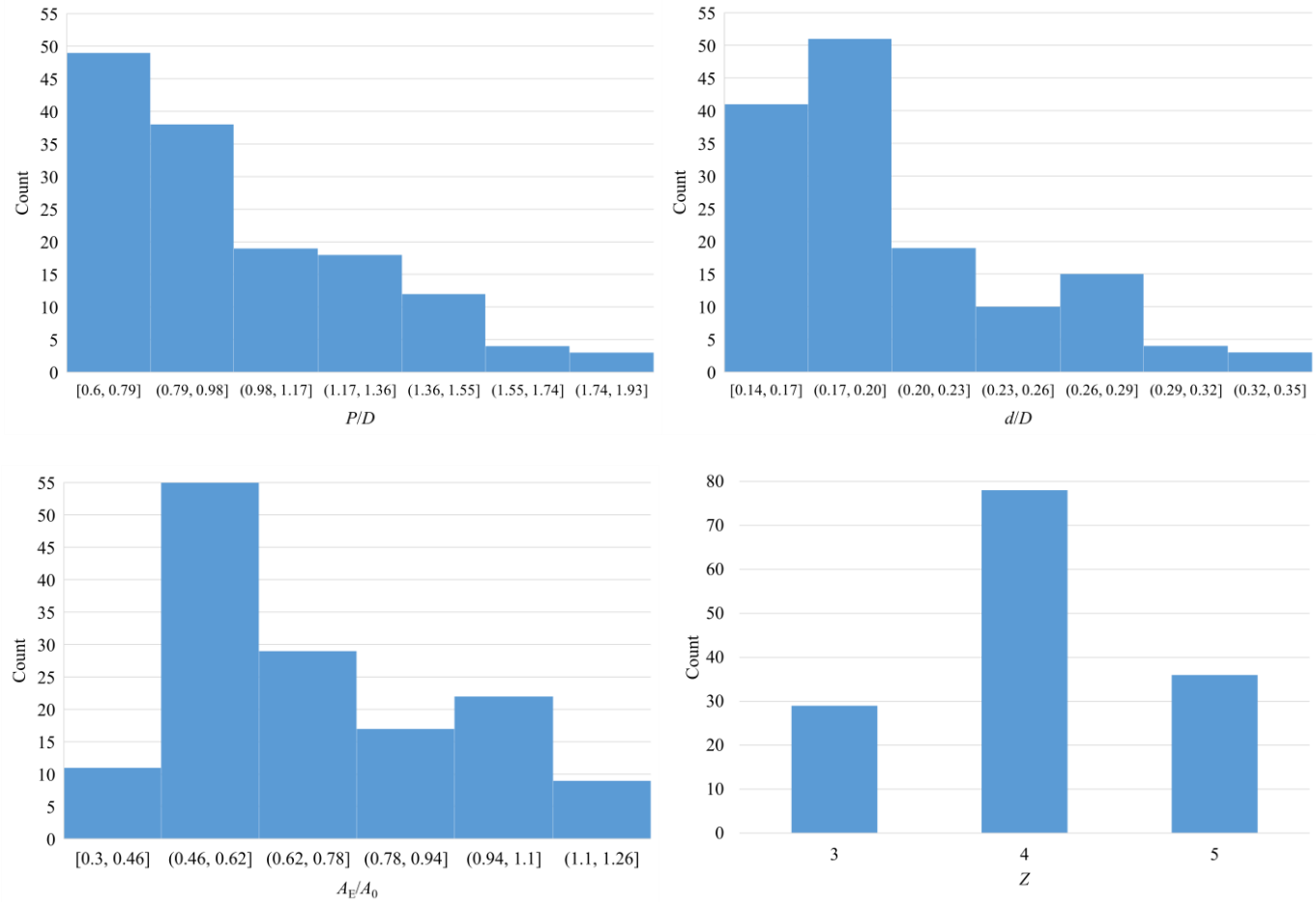


Fig. 2 Histograms of the input variables

The descriptive statistics of propeller characteristics used as inputs can be seen in Table 1. A total of 143 propellers were used to establish the database, with each propeller providing K_T and K_Q values over a range of J. As shown in the histograms in Figure 2, most of the propellers have P/D between 0.6 and 0.98, and d/D between 0.14 and 0.2. As the values P/D and d/D increase, the number of propellers decrease. The number of propellers that have $P/D > 1.55$ or $d/D > 0.29$ is lower than 10. For most of the analysed propellers, the A_E/A_0 ranges between 0.46 and 0.62, with only 10 propellers having $A_E/A_0 < 0.46$. At higher

A_E / A_0 the number of propellers also decreases. Among the 143 propellers, 78 have four blades, 36 have five blades, and 29 have three blades.

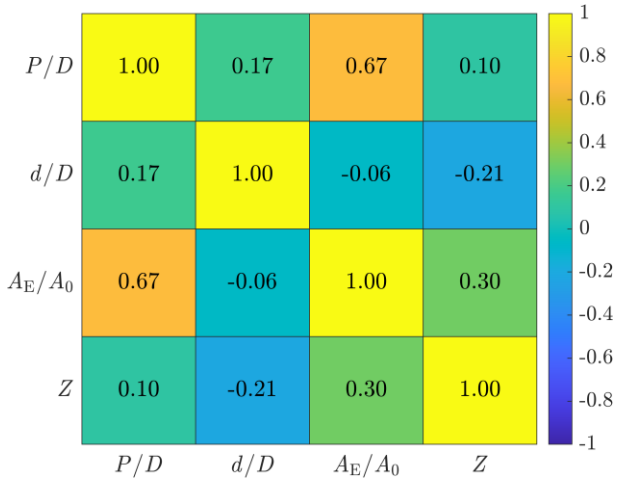


Fig. 3 The correlation matrix of input variables

The results of the correlation analysis presented in Figure 3 shows that most input variables are largely independent, which is beneficial for ANN modelling and reduces the risk of multicollinearity. The strongest correlation observed is between P/D and A_E / A_0, indicating a moderate-to-strong positive relationship where higher pitch ratios tend to coincide with larger expanded area ratios. P/D also has very weak positive correlations with d/D and Z, suggesting minimal association with hub-to-diameter ratio and number of blades. A_E / A_0 and d/D are essentially uncorrelated, while Z shows a weak negative correlation with d/D and a weak positive correlation with A_E / A_0, indicating that the number of blades varies slightly with these geometric parameters but remains largely independent. Overall, the results suggest that the input variables are mostly uncorrelated, which supports robust ANN training and implies that the network can learn the influence of each parameter on the outputs without strong redundancy among inputs.

The scatter diagrams presented in Figure 4 indicate that P/D spans a relatively wide range, however, most propellers are concentrated within the lower-to-moderate interval, with comparatively fewer high pitch designs. As previously noted, d/D is largely confined between 0.14 and 0.20. The distribution of A_E / A_0 shows that medium-area designs predominate within the dataset.

Prior to the training process, the dataset was carefully examined to identify potential outliers, and inconsistencies. Particular attention was given to K_T and K_Q across the range of J. Data points exhibiting non-physical behaviour or clear deviation from expected propeller performance characteristics were excluded from the database. This preprocessing step ensured a consistent, physically meaningful, and reliable dataset, thereby improving the robustness, stability, and predictive capability of the ANN. From the initial 147 propellers, a total of 143 propellers were considered in the study.

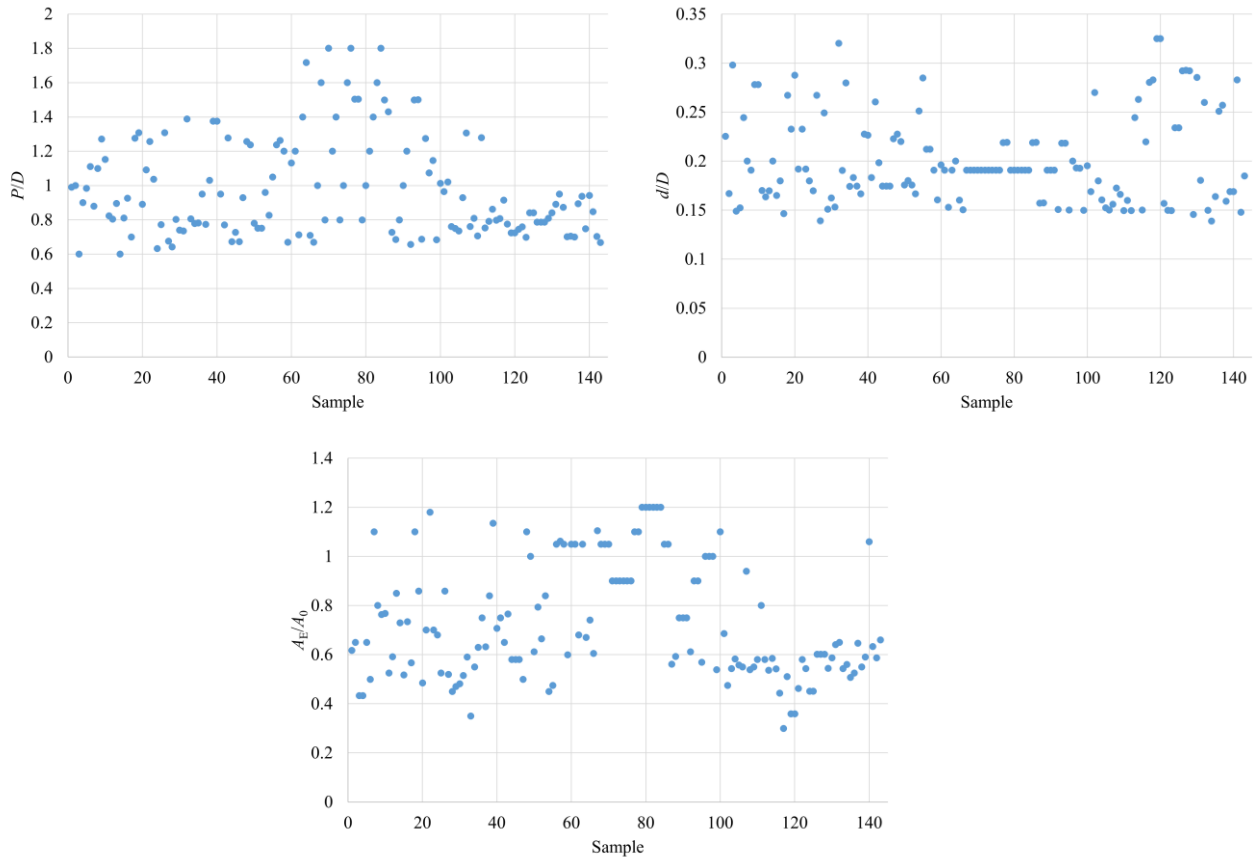


Fig. 4 Scatter diagrams of the input variables

2.3 Artificial neural network

The ANN was developed to predict K_T and K_Q as functions of J based on the four previously defined geometric input parameters. Since the propellers were not experimentally tested at an identical number of J values during the open water tests, the output data were resampled prior to training to ensure that each propeller was represented by an output matrix of uniform dimensions. Resampling was performed using linear interpolation at 30 points for each propeller. The output matrix consists of K_T and K_Q values and the respective J values. Both input and output variables were standardized before the training process to eliminate differences in numerical scale and to ensure that the ANN learned the underlying physical relationships rather than being influenced by magnitude disparities among variables. Initially, four training algorithms were evaluated: Levenberg-Marquardt, scaled conjugate gradient, resilient backpropagation, and Levenberg-Marquardt with Bayesian regularization. The investigated ANN architectures consisted of a single hidden layer with 5, 10, 15, or 20 neurons. Additionally, three activation functions within the neurons in hidden layer were examined:

- Rectified Linear Unit (ReLU):

$$y = \mathrm{ReLU}(x) = \begin{cases} x, x > 0 \\ 0, x \le 0 \end{cases} \tag{5}$$

- Hyperbolic tangent:

$$y = \frac{\mathrm{e}^{x} - \mathrm{e}^{-x}}{\mathrm{e}^{x} + \mathrm{e}^{-x}} \tag{6}$$

- Sigmoid:

$$y = \frac{1}{1+\mathrm{e}^{-x}} \tag{7}$$

In supervised learning, the neural network receives input data along with the corresponding target outputs. The predicted outputs are compared to the target values, and a learning algorithm iteratively adjusts the network weights and biases to reduce the discrepancy between them. This process aims to minimize the defined error function by progressively refining the network parameters. A 5-fold cross-validation procedure was applied to assess model performance more reliably. The complete dataset was partitioned into five equally sized subsets. The training and validation process was repeated five times, each time using one subset as the validation set and the remaining four subsets for training. The final performance indicators were obtained by averaging the results over all five folds. The following metrics have been computed:

- Coefficient of determination:

$$R^2 = 1 - \frac{\sum_{i=1}^{n}(y_i - y_i^{'})^2}{\sum_{i=1}^{n}(y_i - \overline{y}_i)^2} \tag{8}$$

- Root Mean Squared Error:

$$RMSE = \sqrt{\frac{\sum_{i=1}^{n}(y_i - y_i^{'})^2}{n}} \tag{9}$$

where y_i is the actual value, $y_i^{'}$ is the predicted value, $\overline{y}_i$ is the mean of the actual values, and n is the total number of samples.

2.4 Optimization study

The optimization procedure is implemented by employing the GA within the software package MATLAB 2025b [24]. The GA is a population-based evolutionary optimization method inspired by natural selection mechanisms. It consists of a population of candidate solutions, also called individuals, each representing a feasible combination of propeller design variables. For each generation, the fitness of all individuals is evaluated using the trained ANN, which predicts the corresponding open water characteristics. Based on the assigned fitness values, individuals with superior performance are selected to form the next generation. Genetic operators, including crossover and mutation are applied to the selected parent individuals to generate offspring. In this study, the GA is used to identify a surrogate propeller with the maximum η_{O}. The optimization procedure is conducted subject to the cavitation constraint imposed by Keller's criterion [1], which prescribes a minimum allowable A_{E} / A_0 to ensure adequate cavitation performance as well as the noise criterion, which prescribes a maximal propeller tip speed v_{tip}.

The optimization process is defined by minimising an objective function as follows:

$$\min_x f(x) \text{ such that} \begin{Bmatrix} c(x) \le 0 \\ c_{\mathrm{eq}}(x) = 0 \\ A \cdot x \le b \\ A_{\mathrm{eq}} \cdot x = b_{\mathrm{eq}} \\ \mathrm{lb} \le x \le \mathrm{ub} \end{Bmatrix} \tag{10}$$

where x is the input vector, $f(x)$ is the objective function, c and c_{eq} are the inequality and equality constraints, respectively, A and b form the linear inequality constraints, while A_{eq} and b_{eq} form the linear

equality constraints, lb and ub are the lower and upper bounds, respectively. In this study, the equality and inequality constraints are not used, only the lower and upper bounds are defined for each design variable.

The fitness function is defined by combining the objective, the Keller's cavitation [25], and noise constraints as penalties. This way, both the objective and constraints are evaluated in a single equation [26]. Consequently, the problem can be interpreted as an unconstrained optimization with bound constraints, where infeasible solutions are discouraged via penalization rather than strict constraint handling. The fitness function reads as follows:

$$\begin{aligned} \textit{fitness function} = \eta_{\mathrm{O}} + w_{\mathrm{Keller}} \cdot \max\left[0, (A_{\mathrm{E}}/A_0)_{\min} - (A_{\mathrm{E}}/A_0)\right] + \\ + w_{\mathrm{tip,\,speed}} \cdot \max(0, v_{\mathrm{tip}} - v_{\mathrm{tip,\,max}}) \end{aligned} \tag{11}$$

where w_{Keller} and $w_{\mathrm{tip,\,speed}}$ are the cavitation and noise constraint penalty weights, respectively, while the minimum expanded area ratio $(A_{\mathrm{E}}/A_0)_{\min}$ and v_{tip} are defined as:

$$(A_{\mathrm{E}}/A_0)_{\min} = \frac{(1.3+0.3Z)T}{(p_{\mathrm{atm}} + \rho g h_0 - p_v)D^2} + K \tag{12}$$

$$v_{\mathrm{tip}} = Dn\pi \tag{13}$$

where n is the calculated rate of revolution of the considered propeller using v_{A} for the specific ship, p_{atm} is the atmospheric pressure, h_0 is the immersion depth of the propeller shaft and K is the constant equal to 0.2 for the single-screw ships. The Keller's cavitation constraint simply states that the A_{E}/A_0 must be higher than the $(A_{\mathrm{E}}/A_0)_{\min}$ as calculated with Equation (12). To satisfy the noise constraint, the v_{tip} must be below the maximum value as defined by Tadros et al. [3]: maximum tip speed for three- and four-bladed propellers is equal to 53 m/s while for five-bladed propellers is equal to 46 m/s.

Based on a preliminary sensitivity analysis, the population size was set to 100 and the function tolerance equal to 10^{-4}. The maximum number of generations was set as 500, although the simulation stopped much earlier due to the satisfaction of the function tolerance. To avoid the local optima, the GA was performed 10 times in a row. The number of iterations was set to 10, as further repetitions did not yield any significant improvement in the results, indicating convergence. Other GA parameters were set to MATLAB default values: a crossover fraction of 0.8, an elite count of 5 (the number of individuals guaranteed to survive to the next generation), a Gaussian mutation function, and the *selectiontournament* selection method.

2.5 Case studies

The hull forms used in the optimization study are presented in Figures 5 and 6, while the respective main particulars are listed in Table 2. Ships considered in this study are as follows: KCS, Japan Bulk Carrier (JBC), post-Panamax 6750 TEU containership, and Duisburg Test Case (DTC). In the following subsections, each ship is briefly described and the source of input parameters for the present study are given.

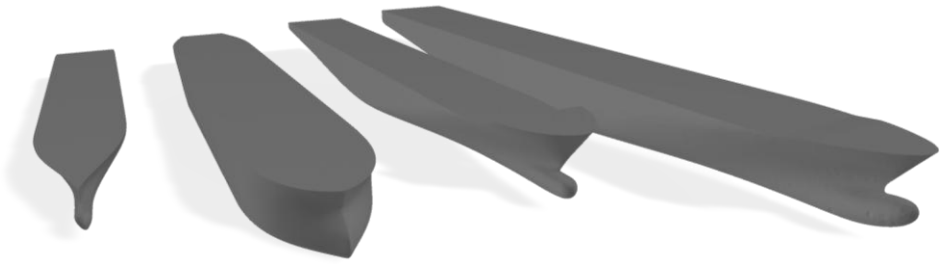


Fig. 5 Ships considered in the optimization study, left to right – KCS, JBC, 6750 TEU containership, DTC

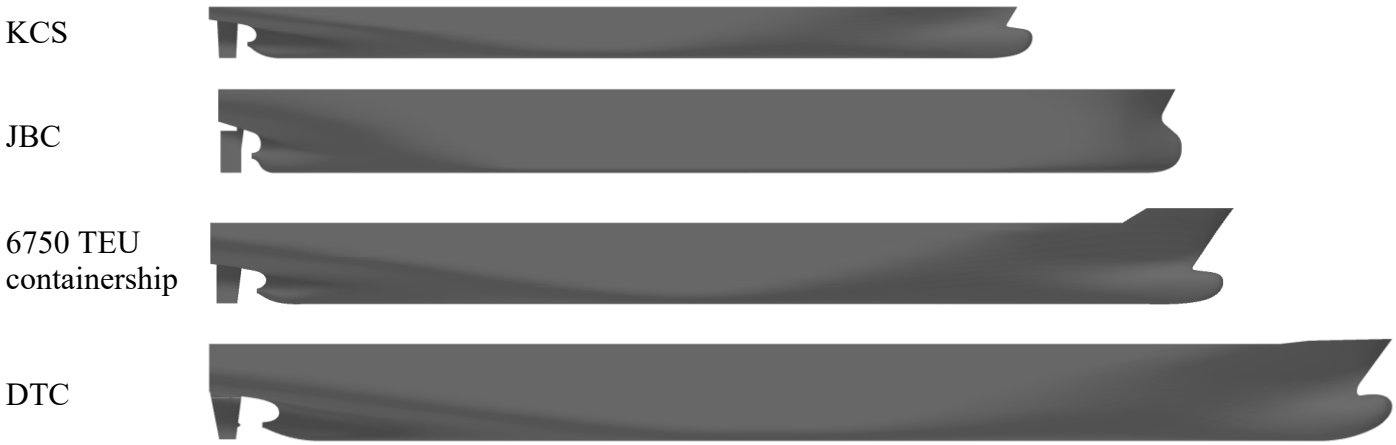


Fig. 6 Side view of the ships considered in the optimization study

Table 2 Main particulars of the ships

Main particular	KCS	JBC	6750 TEU containership	DTC
Length between perpendiculars L_{PP}, m	230	280	286.6	355
Length of waterline L_{WL}, m	233.54	285	292.5	356.1
Length overall L_{OA}, m	243	291	304	372.8
Breadth B, m	32.2	45	40	51
Draught T, m	10.8	16.5	11.98	14.5
Displacement ∇, m^3	52,030	178,420.1	85,562.7	173,467
Propeller shaft immersion h_0, m	6.7	11.32	8.06	9.5
Propeller diameter D, m	7.9	8.12	7.3	8.91
Design speed V, kn	24	14.5	23	25

2.5.1 KRISO containership

The KCS is a 3600 TEU containership developed by KRISO for the International Workshop on CFD in Ship Hydrodynamics in Gothenburg 2000 [27]. Since then, it was used in various experimental and numerical studies. One such study was conducted by Farkas et al. [28], in which the authors performed full-scale numerical simulations of the resistance, open water, and self-propulsion tests for the KCS equipped with the KP505 propeller. The numerical results obtained for the smooth surfaces were used in this study as an input for the optimization study. Also, the required propulsion characteristics were calculated using the Holtrop-Mennen method [29].

2.5.2 Japan Bulk Carrier

The second case study is the JBC which is a benchmark ship developed by the National Maritime Research Institute at the Yokohama National University, and the Ship Building Research Centre of Japan for the CFD workshop in 2015 [30]. It is a bulk carrier with a high block coefficient that consists of a bulbous bow and a transom stern. The JBC was a part of the experimental campaign lead at the Brodarski Institute (Jadranbrod d.d.) in Zagreb [31], and the experimental results were published by Degiuli et al. [32]. The experimental campaign was conducted as a part of the Croatian Science Foundation research project "Sustainable slow steaming for low carbon shipping, IP-2020-02-8568 (STARSHIP)" and consisted of resistance, self-propulsion, open water tests as well as the measurements of the nominal wake. For this study, the required input data for the optimization procedure were obtained from the full-scale numerical results

provided by Grlj et al. [33, 34], the extrapolated towing tank measurements published by Degiuli et al. [27], as well as from calculations performed using the method proposed by Holtrop and Mennen [29].

2.5.3 Post-Panamax 6750 TEU containership

The third case study is the post-Panamax 6750 TEU containership which is a benchmark containership developed for the assessment of the performance of the seakeeping analysis codes as a part of the ITTC-ISSC joint workshop in 2014 [35]. This containership was also investigated in an experimental campaign performed at the Brodarski Institute (Jadranbrod d.d.) [36] by Degiuli et al. [37], where its hydrodynamic characteristics were assessed through resistance, open water, and self-propulsion tests. The experimental campaign was conducted as a part of the Croatian Science Foundation research project "Sustainable slow steaming for low carbon shipping, IP-2020-02-8568 (STARSHIP)". For this study, the required input data for the optimization procedure were obtained from the full-scale numerical results provided by Grlj et al. [38], the extrapolated towing tank measurements published by Degiuli et al. [37], as well as from calculations performed using the method proposed by Holtrop and Mennen [29].

2.5.4 Duisburg Test Case

Finally, the DTC is a 14000 TEU post-Panamax containership developed at the Institute of Ship Technology, Ocean Engineering and Transport Systems [39]. It represents a benchmark case that has been widely used in previous experimental investigations and for the validation of numerical results. It is a single-screw ship with a bulbous bow, large stern overhang and a transom. To assess the hydrodynamic performance of DTC, Farkas et al. [40] conducted numerical simulations of the resistance, open water, and self-propulsion tests. The published numerical results were used in this study, alongside the calculated results with the Holtrop-Mennen method [29] and experimental data provided by Moctar et al. [39].

3. Results and discussion

3.1 Artificial neural network

The ANN trained with Levenberg-Marquardt algorithm using Bayesian regularization demonstrated superior performance compared to the other evaluated learning algorithms, consistent with findings from similar studies [3, 41]. It incorporates a penalty on large network weights directly into the training objective, serving as a built-in regularization mechanism that helps prevent overfitting, which is a common issue with small datasets such as the one used within this study. By balancing network complexity against the training error, it produces models that generalize more effectively to unseen data. Another advantage is that all available data can be used for training without requiring a separate test set, maximizing the information available to the network, an especially valuable feature when working with small datasets. The issue of overfitting with the other learning algorithms was apparent, as the predicted K_T and K_Q curves lacked smoothness. The best-performing topology was found to have 10 neurons in the hidden layer, using the ReLU activation function. The optimal ANN achieved an R^2 of 0.961 on the training set and 0.951 on the validation set. The *RMSE* values for the training and validation datasets are 0.197 and 0.2029, respectively. Although networks with a larger number of neurons in the hidden layer produced a training R^2 exceeding 0.99, their validation set R^2 was substantially lower than that of the optimal model, indicating overfitting.

Figures 7 and 8 present the comparison between predicted and experimentally measured values K_T and K_Q, respectively, for two representative advance ratios, $J = 0.3$ and $J = 0.6$. Overall, the predicted results show strong agreement with the corresponding experimental data. With the exception of a small number of outliers, the majority of data points are closely clustered around the line of perfect agreement, indicating that the model captures the underlying trends with a high degree of accuracy. The dispersion remains limited across both advance ratios, demonstrating consistent predictive capability over different operating regimes.

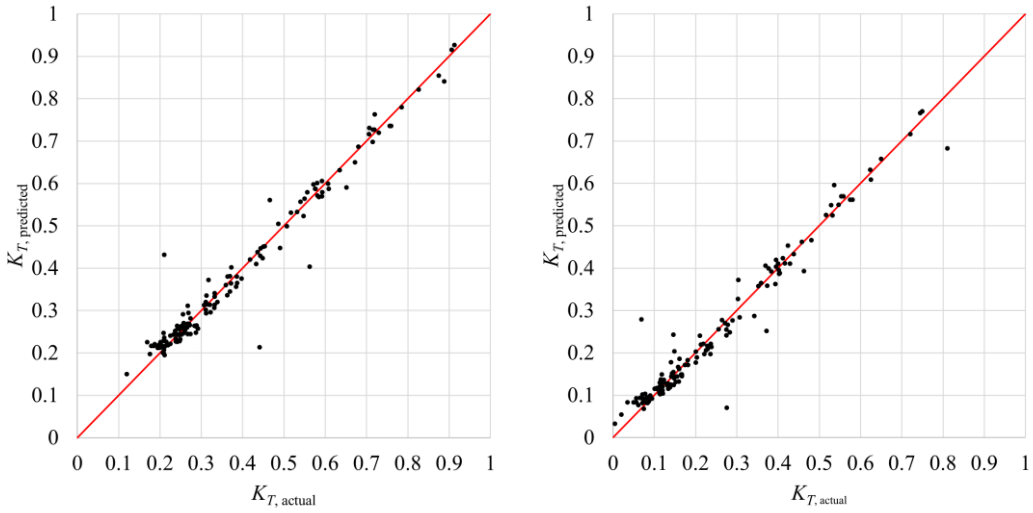


Fig. 7 Predicted vs. actual values for K_T for $J = 0.3$ (left) and $J = 0.6$ (right)

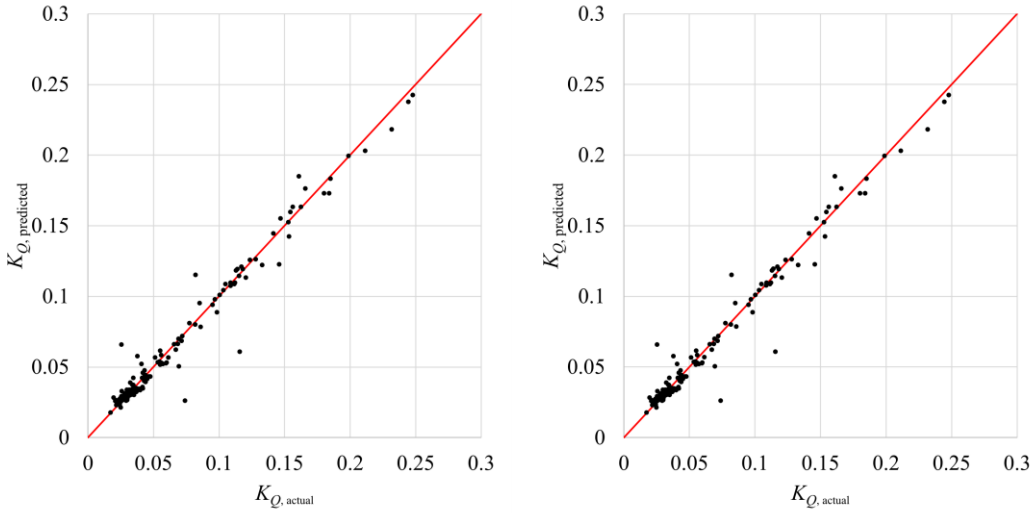


Fig. 8 Predicted vs. actual values for K_Q for $J = 0.3$ (left) and $J = 0.6$ (right)

The open water curves of the original DTC propeller were predicted using the developed ANN. A comparison between the experimentally obtained open water curves and those predicted by the trained ANN is presented in Figure 9. The ANN predicts slightly higher K_Q values compared to the experimental data, while the discrepancies in the K_T curves are negligible, with only minor differences observed at lower J values. As a result, the predicted η_O is slightly lower than the experimental value. This analysis demonstrates that the developed ANN is capable of predicting open water curves with satisfactory accuracy, even for a propeller that was not included in the training or validation sets.

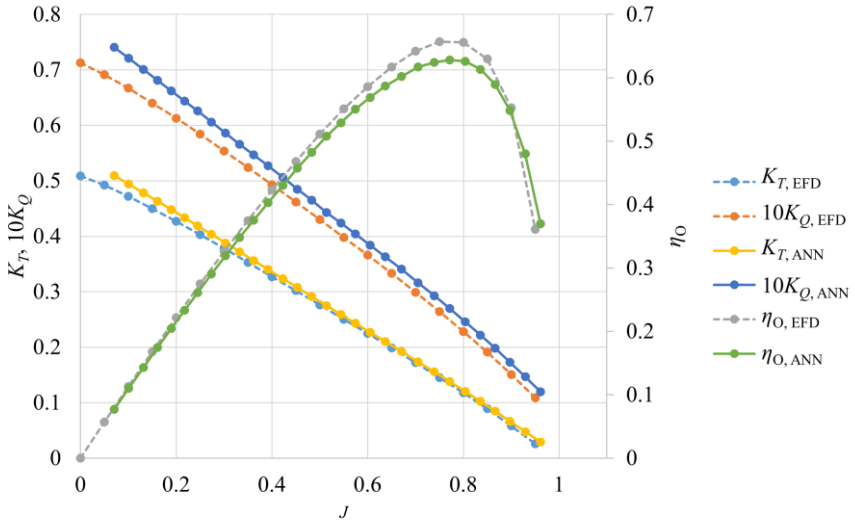


Fig. 9 Comparison between the experimentally obtained open water curves and those predicted by the developed ANN for the DTC

Table 3 Input parameters for the different ships

	KCS			JBC			6570 TEU containership			DTC		
	EFD	CFD	Holtrop	EFD	CFD	Holtrop	EFD	CFD	Holtrop	EFD	CFD	Holtrop
T, kN	1757	1570	1879	1583	1383	1309	1959	1783	2005	3659	3705	4178
t	0.147	0.133	0.165	0.124	0.270	0.208	0.160	0.158	0.176	0.090	0.110	0.195
w	0.197	0.227	0.218	0.490	0.360	0.583	0.271	0.275	0.222	0.187	0.195	0.294
K_T / J^2	0.327	0.310	0.377	1.847	1.229	2.519	0.482	0.527	0.525	0.451	0.476	0.772

3.2 Optimization study

The input data for the optimization study are T, t, w, and K_T / J^2 (Table 3) along with the seawater density $\rho = 1026\ \mathrm{kg/m^3}$, V, D, and h, Table 2. It can be noticed that the different methods yield different results as expected. The biggest differences are obtained for DTC, where Holtrop-Mennen method predicts the highest T. The input data obtained for KCS and the post-Panamax 6750 TEU containership are the most consistent across different methods.

After completing the optimization procedure, the optimal propellers are identified and their corresponding geometric and open water characteristics are summarized in Tables 4-7, together with comparisons against the original propellers for each ship. For most ships, the highest η_O is obtained when CFD-derived input data are used, whereas for the DTC the maximum η_O is achieved using EFD data. When Holtrop-Mennen method is used for the input data, the optimal η_O are lower than those of the original propellers except for the post-Panamax 6750 TEU containership where a slightly higher η_O is obtained. Similar results are obtained when EFD-derived input data is used. The optimal d / D remain close to those of the original propellers, while P / D are generally larger than those of the original propellers, with some deviations observed for the JBC. When the input parameters are determined using the Holtrop-Mennen method, both the achieved η_O and the corresponding geometric characteristics are lower than those obtained using CFD or EFD data, as well as lower than those of the original propellers. The optimal Z is consistently equal to five for all the considered ships, except for the JBC with the Holtrop-Mennen method where the optimization procedure yields a four-bladed propeller. For the post-Panamax 6750 TEU containership, the optimization procedure yields a five-bladed propeller with all the methods applied for obtaining the input data, whereas the original design features four blades. Since propeller performance is strongly influenced by the

wake fraction, the significant differences in the obtained geometric parameters can be attributed to variations in the wake fraction predicted by different methods. The smallest differences in wake fraction are observed for the KCS and the post-Panamax 6750 TEU containership. Consequently, the optimized geometric parameters are consistent for these cases. In contrast, the JBC and DTC results exhibit significant differences in wake fraction, which leads to corresponding variations in the optimal propeller.

Table 4 Original and optimal propeller obtained for KCS with different input data

	Original	EFD	CFD	Holtrop
P/D	0.997	1.1855	1.1855	1.1855
d/D	0.180	0.1932	0.1932	0.1932
A_E/A_0	0.800	0.7552	0.7384	0.8884
Z	5	5	5	5
J	0.679	0.8344	0.8432	0.8217
K_T	0.195	0.2278	0.2209	0.2544
K_Q	0.032	0.0458	0.0446	0.0516
η_O	0.650	0.6599	0.664	0.6452

Table 5 Original and optimal propeller obtained for JBC with different input data

	Original	EFD	CFD	Holtrop
P/D	0.736	1.1057	1.1855	0.6904
d/D	0.190	0.1936	0.1930	0.1618
A_E/A_0	0.640	0.6884	0.7384	0.4954
Z	5	5	5	4
J	0.351	0.4510	0.5539	0.2921
K_T	0.199	0.3756	0.3769	0.2149
K_Q	0.026	0.0599	0.0665	0.0244
η_O	0.452	0.4502	0.4998	0.4101

Table 6 Original and optimal propeller obtained for post-Panamax 6750 TEU containership with different input data

	Original	EFD	CFD	Holtrop
P/D	0.890	1.1855	1.1855	1.1602
d/D	0.169	0.1932	0.1932	0.1905
A_E/A_0	0.750	0.8884	0.8884	0.9884
Z	4	5	5	5
J	0.622	0.7307	0.7495	0.7488
K_T	0.186	0.3065	0.2957	0.2944
K_Q	0.029	0.0595	0.0579	0.0581
η_O	0.603	0.5986	0.6093	0.6035

Table 7 Original and optimal propeller obtained for DTC with different input data

	Original	EFD	CFD	Holtrop
P/D	0.959	1.1602	1.1602	1.2145
d/D	0.176	0.1905	0.1905	0.1886
A_E/A_0	0.800	0.9884	0.9884	1.1884
Z	5	5	5	5
J	0.615	0.7814	0.77	0.6782
K_T	0.316	0.2756	0.2822	0.3548
K_Q	0.054	0.0552	0.0562	0.0724
η_O	0.592	0.6207	0.6148	0.5291

Overall, the optimized propellers demonstrate higher A_E/A_0 compared to the original ones, which is in agreement with the findings from Tadros et al. [3]. In particular, the results obtained for the KCS show close agreement with those reported by Tadros et al. [3]. The optimized KCS propeller exhibits higher η_O, P/D, and A_E/A_0 compared to the original propeller. These results indicate that an optimal propeller design can be successfully obtained using an ANN trained on a relatively small dataset.

Finally, the obtained open water curves for each ship using the input data from CFD are presented in Figure 9. It can be observed that the obtained values of K_T, K_Q, and η_O for each ship are smooth and free of outliers, indicating that the ANN does not exhibit overfitting and demonstrates strong generalization capability. The open water curves for KCS and JBC are similar since the obtained optimal propellers have similar geometric parameters. A similar trend is observed for the post-Panamax 6750 TEU containership and the DTC, whose optimized propellers also yield closely matching open water curves.

To facilitate the practical implementation of the proposed optimization procedure, a standalone application called OptiProp was developed using MATLAB App Designer within the software package MATLAB. The application integrates the trained ANN with the optimization procedure based on GA into a user-friendly graphical interface. It enables the user to define the ship propulsion characteristics and its operating conditions. After the calculations are performed, the results are shown within the same graphical interface. The tool provides the propeller geometric parameters, open water characteristics, including K_T, K_Q, and η_O in a table and plots the curves in a diagram. Figure 10 shows the graphical interface of the developed application, where the input and output can be seen.

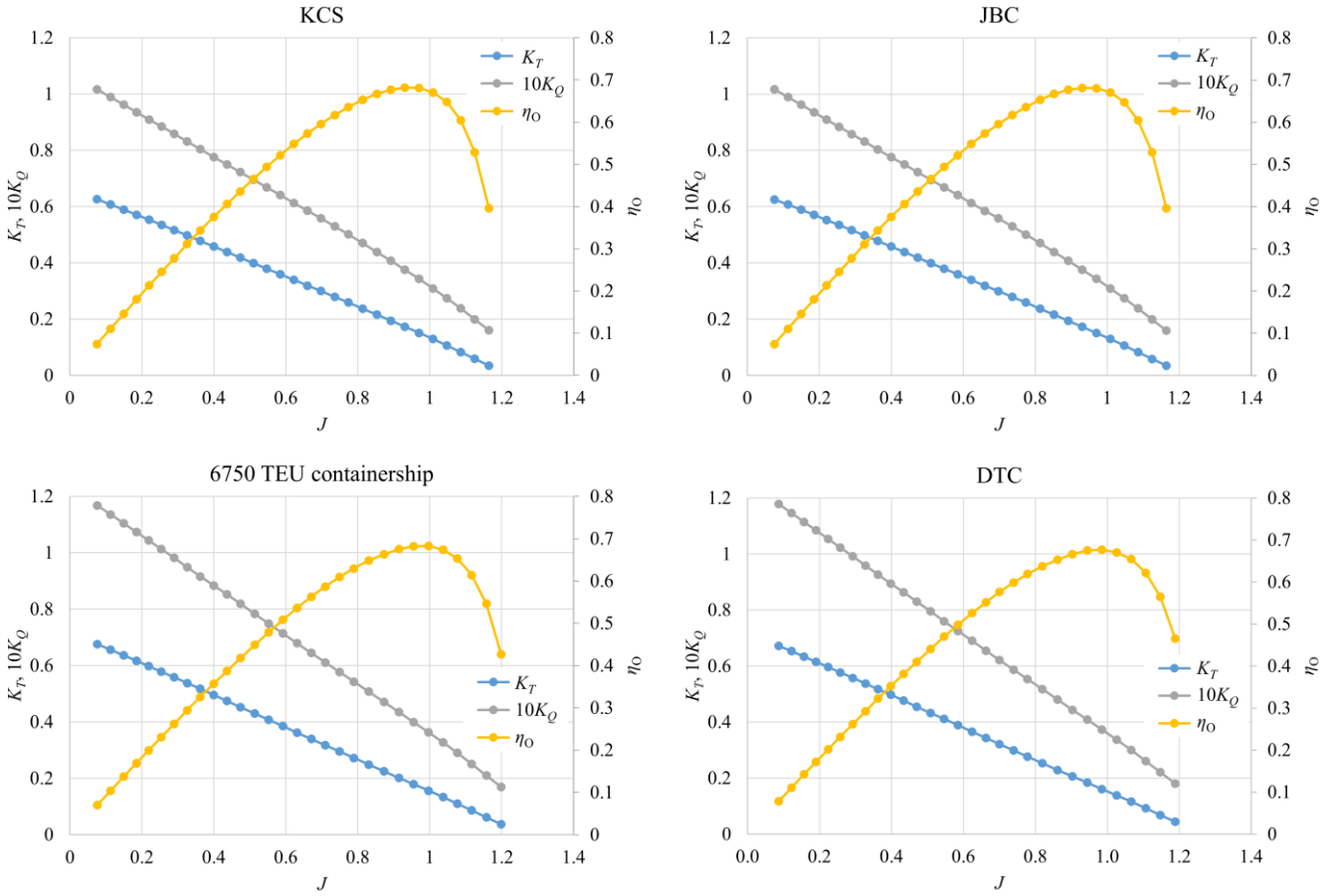


Fig. 9 Open water curves obtained for each case study using the input data from CFD

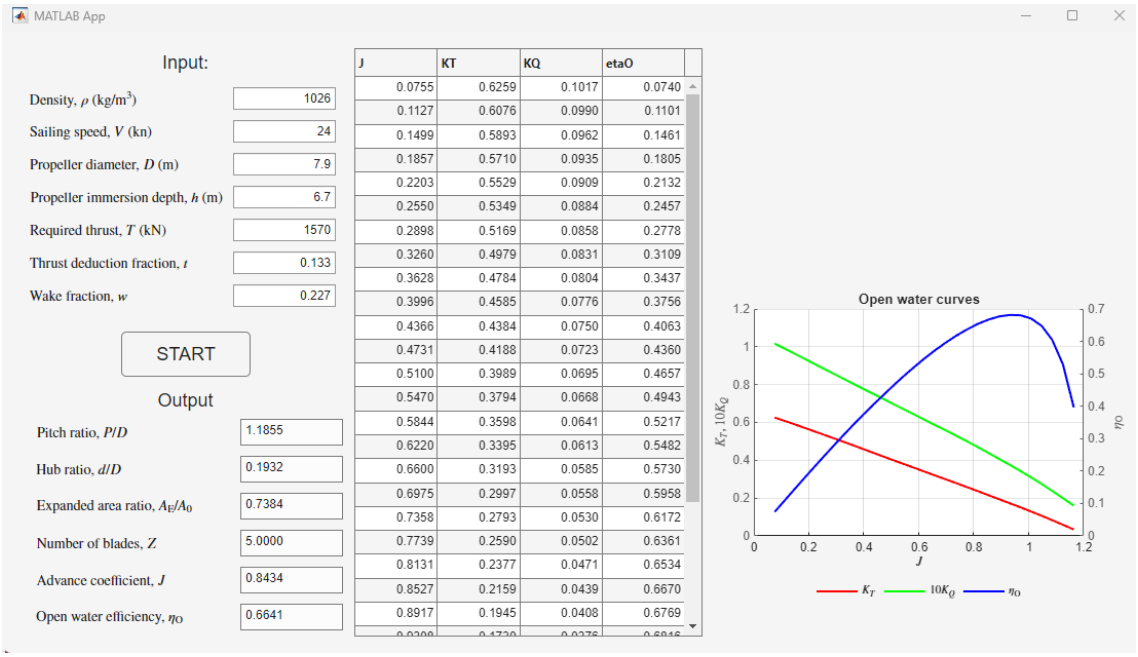


Fig. 10 The OptiProp graphical interface

4. Conclusions

In this study, a numerical approach is proposed for the determination of a propeller characteristics with maximum open water efficiency for a given ship, taking into account its propulsion characteristics and

prescribed operating conditions. The methodology combines a data-driven surrogate model based on an artificial neural network with an optimization procedure employing the genetic algorithm. The artificial neural network is trained on experimentally obtained open water characteristics of 143 various propeller designs, with the dataset provided by the Brodarski Institute (Jadranbrod d.d.). By learning the relationship between key geometric parameters and the resulting thrust and torque coefficients, the artificial neural network serves as a fast and reliable surrogate model suitable for optimization procedure.

The trained artificial neural network is subsequently integrated into an optimization procedure based on genetic algorithm, enabling efficient exploration of the design space while satisfying the imposed design and operational constraints. The results demonstrate that the proposed approach can successfully identify propellers with higher open water efficiency compared to the original ones. In particular, the results obtained for the KRISO containership show close agreement with those reported by Tadros et al. [3], despite the significantly smaller training dataset used in the present study. This confirms that satisfactory and practically relevant results can be achieved even when the artificial neural network is trained on a relatively limited number of experimental data.

An additional advantage of the proposed approach lies in its flexibility with respect to input data source. The propulsion characteristics required for the optimization procedure can be obtained from various sources, including high-fidelity numerical simulations and towing tank tests, or low-fidelity empirical prediction methods. In this study, input data were derived from both numerical and experimental investigations, as well as from calculations based on the empirical method proposed by Holtrop and Mennen. The results indicate that the optimization framework remains applicable and robust across different levels of input-data fidelity, highlighting its potential as a practical tool for preliminary propeller design.

Finally, a standalone application named *OptiProp*, was developed in MATLAB to integrate the trained artificial neural network and optimization procedure based on the genetic algorithm into a graphical interface. The installation files for the developed tool can be found at https://github.com/carloggrlj/OptiProp The tool allows the user to define the ship propulsion characteristics and operating conditions, executes the optimization process, and presents the optimized propeller geometric parameters together with the predicted open water characteristics in both tabular and graphical form, thereby facilitating the practical implementation of the proposed method.

The scientific contributions of this study can be summarized as follows:

- An artificial neural network is developed as a surrogate model based on experimental data, rather than on systematic series data.
- A comparative analysis of optimal propellers obtained with different input data is presented.
- A standalone optimization tool, OptiProp, is developed based on the proposed methodology.

This study demonstrates that optimal propeller designs can be obtained for the design operating condition using the proposed method. The same approach can be extended to other loading conditions or operating speeds, provided that appropriate input data are available. Additionally, the training database for the artificial neural network can be expanded to include a wider range of propellers. Finally, the performance of the optimized propellers should be validated through detailed numerical simulations or experimental investigations, such as self-propulsion tests.

ACKNOWLEDGEMENTS

This work was supported by the Croatian Science Foundation under the project number IP-2025-02-4779.

FUNDING

This work was funded by the Croatian Science Foundation under the project number IP-2025-02-4779.

REFERENCES

[1] Carlton, J., 2018. Marine Propellers and Propulsion. *Butterworth-Heinemann*.

[2] Oosterveld, M.W.C., van Oossanen, P., 1975. Further computer-analyzed data of the Wageningen B-screw series. *International Shipbuilding Progress*, 22, 251-262. https://doi.org/10.3233/ISP-1975-2225102

[3] Tadros, M., Shi, W., Xu, Y., Song, Y., 2024. A unified cross-series marine propeller design method based on machine learning. *Ocean Engineering*, 314, 119691. https://doi.org/10.1016/j.oceaneng.2024.119691

[4] Martić, I., Degiuli, N., Grlj, C.G., 2023. Prediction of Added Resistance of Container Ships in Regular Head Waves Using an Artificial Neural Network. *Journal of Marine Science and Engineering*, 11(7), 1293. https://doi.org/10.3390/jmse11071293

[5] Ao, Y., Li, S., Li, Y., Gong, J., 2024. The construction of a neural network proxy model for ship hull design based on multi-fidelity datasets and the parameter freezing strategy. *Journal of Marine Engineering & Technology*, 23, 270-280. https://doi.org/10.1080/20464177.2024.2330174

[6] Lee, M.-K., Lee, I., 2023. Optimal Design of Flow Control Fins for a Small Container Ship Based on Machine Learning. *Journal of Marine Science and Engineering*, 11(6), 1149. https://doi.org/10.3390/jmse11061149

[7] Degiuli, N., Grlj, C.G., Martić, I., Baressi Šegota, S., Anđelić, N., Majnarić, D., 2025a. Machine Learning Models for the Prediction of Wind Loads on Containerships. *Journal of Marine Science and Engineering*, 13(3), 417. https://doi.org/10.3390/jmse13030417

[8] Grlj, C.G., Degiuli, N., Tuković, Ž., Farkas, A., Martić, I., 2023b. The effect of loading conditions and ship speed on the wind and air resistance of a containership. *Ocean Engineering*, 273, 113991. https://doi.org/10.1016/j.oceaneng.2023.113991

[9] Yang, Z., Xu, Y., Jing, J., Fu, X., Wang, B., Ren, H., Zhang, M., Sun, T., 2023. Investigation of physics-informed neural networks to reconstruct a flow field with high resolution. *Journal of Marine Science and Engineering*, 11(11), 2045. https://doi.org/10.3390/jmse11112045

[10] Tong, Z., Chen, R., 2026. Physics-informed spatiotemporal neural network for unsteady propeller wake prediction via least squares finite-difference framework. *Physics of Fluids*, 38(2), 025132. https://doi.org/10.1063/5.0311065

[11] Bourchas, O., Papalambrou, G., 2025. Physics informed neural networks for vessel main engine power prediction. *Ocean Engineering*, 332, 121344. https://doi.org/10.1016/j.oceaneng.2025.121344

[12] Hadavi, M., Akbarivakilabadi, K., Nikabadi, S., Ghasri, M., 2025. Data-Driven Structural and Aerodynamic Optimization of Ship Masts Using ANN-GA Framework Integrated with FEA and CFD Analysis. *Engineering Reports*, 7, e70362. https://doi.org/10.1002/eng2.70362

[13] Lefkiou, C., Koukouvinis, P., Chatzis, S., Xyfolis, S., 2026. Predicting ship hull flow-field distributions using a soft-constrained ANN model. *International Journal of Naval Architecture and Ocean Engineering*, 18, 100712. https://doi.org/10.1016/j.ijnaoe.2025.100712

[14] Cheng, X., Huang, X., Xu, D., Zhao, Z., Liu, H., Kong, M., Ji, R., 2024. Ship Optimization Based on Fully-Parametric Models for Hull, Propeller and Rudder. *Journal of Marine Science and Engineering*, 12(9), 1635. https://doi.org/10.3390/jmse12091635

[15] Liu, J., Yue, Q., Wu, S., Yue, X., 2024. Hydrodynamic shape optimization of an autonomous and remotely-operated vehicle via a multi-surrogate model. *Brodogradnja*, 75(3), 75301. https://doi.org/10.21278/brod75301

[16] Guo, S., Zhang, B., Tian, Z., Liu, J., Tang, H., 2024. Automatic Optimal Design Method for Minimum Total Resistance Hull Based on Enhanced FFD Method. *Brodogradnja*, 75(4), 75407. https://doi.org/10.21278/brod75407

[17] Zhao, Y., Yu, M.H., Yuan, W., Su, Z., Shen, C.W., 2026. Research on a novel hull, main engine and propeller matching design framework. *Results in Engineering*, 29, 109296. https://doi.org/10.1016/j.rineng.2026.109296

[18] Vázquez-Santos, A., Camacho-Zamora, N., Hernández-Hernández, J., Herrera-May, A.L., Santos-Cortes, L. del C., Tejeda-del-Cueto, M.E., 2024. Numerical Analysis and Validation of an Optimized B-Series Marine Propeller Based on NSGA-II Constrained by Cavitation. *Journal of Marine Science and Engineering*, 12(2), 205. https://doi.org/10.3390/jmse12020205

[19] Lu, D., Wang, A., Gan, H., Su, Y., Ao, X., 2025. A multi-objective collaborative optimization method of ship energy efficiency based on NSGA-II and TOPSIS. *Brodogradnja*, 76(3), 76301. https://doi.org/10.21278/brod76301

[20] Vesting, F., Bensow, R.E., 2018. Particle swarm optimization: an alternative in marine propeller optimization? *Engineering Optimization*, 50, 70-88. https://doi.org/10.1080/0305215X.2017.1302438

[21] Ouyang, W., Zhang, Z., Nie, Y., Liu, B., Vanierschot, M., 2025. Parametric modeling and collaborative optimization of a rim-driven thruster considering propeller-duct interactions. *Ocean Engineering*, 337, 121746. https://doi.org/10.1016/j.oceaneng.2025.121746

[22] Zuo, H., Zhao, Y. and Jia, J., 2025. Bayesian-optimized BP neural network for marine propeller design optimization with improved NSGA-III. *Ocean Engineering*, 340, 122375. https://doi.org/10.1016/j.oceaneng.2025.122375

[23] Li, L., Chen, Y., Xie, S., Xiao, Y., Fang, T., Wang, C., 2025. Comprehensive feature-based machine learning for fast prediction of marine propeller's open-water performance. *Applied Ocean Research*, 154, 104310. https://doi.org/10.1016/j.apor.2024.104310

[24] Mathworks, 2025. MATLAB Help Center.

[25] Auf'm Keller, W. H., 1973. Extended diagrams for determining the resistance and required power for single-screw ships. *International Shipbuilding Progress*, 20, 133-142. https://doi.org/10.3233/ISP-1973-2022501

[26] Tadros, M., Ventura, M., Guedes Soares, C., 2023. Optimization procedures for a twin controllable pitch propeller of a ROPAX ship at minimum fuel consumption. *Journal of Marine Engineering & Technology*, 22, 167-175. https://doi.org/10.1080/20464177.2022.2106623

[27] Larsson, L., Stern, F., Bertram, V., 2003. Benchmarking of Computational Fluid Dynamics for Ship Flows: The Gothenburg 2000 Workshop. *Journal of Ship Research*, 47, 63-81. https://doi.org/10.5957/jsr.2003.47.1.63

[28] Farkas, A., Soonseok, S., Degiuli, N., Martić, I., Demirel, Y. K., 2020. Impact of biofilm on the ship propulsion characteristics and the speed reduction. *Ocean Engineering*, 199, 107033. https://doi.org/10.1016/j.oceaneng.2020.107033

[29] Holtrop, J., Mennen, G. G. J., 1978. A statistical power prediction method. *International Shipbuilding Progress*, 25, 253-256. https://doi.org/10.3233/ISP-1978-2529001

[30] NMRI, 2015. Tokyo 2015 A Workshop on CFD in Ship Hydrodynamics. https://t2015.nmri.go.jp/index.html (Accessed 26 February 2026)

[31] Brodarski Institute, 2022a. Report 6652-M. Resistance, self-propulsion and 3D wake measurement test results, *Brodarski Institute*. Zagreb.

[32] Degiuli, N., Martić, I., Farkas, A., Pedišić Buča, M., Dejhalla, R., Grlj, C.G., 2023. Experimental assessment of the hydrodynamic characteristics of a bulk carrier in off-design conditions. *Ocean Engineering*, 280, 114936. https://doi.org/10.1016/j.oceaneng.2023.114936

[33] Grlj, C.G., Degiuli, N., Martić, I., 2025a. Assessment of the effect of speed and scale on the total resistance and its components for a bulk carrier. *Results in Engineering*, 26, 105095. https://doi.org/10.1016/j.rineng.2025.105095

[34] Grlj, C.G., Degiuli, N., Martić, I., 2025b. Scale effects on the resistance and propulsion characteristics of the Japan Bulk Carrier. *Ocean Engineering*, 339, 122059. https://doi.org/10.1016/j.oceaneng.2025.122059

[35] Kim, Y., Kim, J.-H., 2016. Benchmark study on motions and loads of a 6750-TEU containership. *Ocean Engineering*, 119, 262-273. https://doi.org/10.1016/j.oceaneng.2016.04.015

[36] Brodarski Institute, 2022b. Report 6655-M. Resistance, self-propulsion and 3D wake measurement test results, *Brodarski Institute*. Zagreb.

[37] Degiuli, N., Martić, I., Pedišić Buča, M., Grlj, C.G., 2025b. Benchmark study on resistance and propulsion characteristics of a 6750-TEU container ship. *Ocean Engineering*, 319, 120300. https://doi.org/10.1016/j.oceaneng.2025.120300

[38] Grlj, C.G., Degiuli, N., Martić, I., 2023a. The Impact of Numerical Parameters on the Resistance Characteristics of a Container Ship at the Model and Full Scale. *Journal of Marine Science and Engineering*, 11(9), 1672. https://doi.org/10.3390/jmse11091672

[39] Moctar, O.E., Shigunov, V., Zorn, T., 2012. Duisburg Test Case: Post-Panamax Container Ship for Benchmarking. *Ship Technology Research*, 59, 50-64. https://doi.org/10.1179/str.2012.59.3.004

[40] Farkas, A., Degiuli, N., Martić, I., Mikulić, A., 2023. Benefits of slow steaming in realistic sailing conditions along different sailing routes. *Ocean Engineering*, 275, 114143. https://doi.org/10.1016/j.oceaneng.2023.114143

[41] Martić, I., Degiuli, N., Majetić, D., Farkas, A., 2021. Artificial Neural Network Model for the Evaluation of Added Resistance of Container Ships in Head Waves. *Journal of Marine Science and Engineering*, 9(8), 826. https://doi.org/10.3390/jmse9080826